UNIVERSIDADE FEDERAL DO CEARÁ

CENTRO DE CIÊNCIAS

DEPARTAMENTO DE BIOQUÍMICA E BIOLOGIA MOLECULAR

PROGRAMA DE PÓS-GRADUAÇÃO EM BIOQUÍMICA

JACKSON LIMA AMARAL

BIOLOGIA MOLECULAR *IN SILICO*: DA BIOINFORMÁTICA À DINÂMICA MOLECULAR E BIOQUÍMICA QUÂNTICA COM APLICAÇÕES NA SAÚDE HUMANA

FORTALEZA

2022

JACKSON LIMA AMARAL

BIOLOGIA MOLECULAR *IN SILICO*: DA BIOINFORMÁTICA À DINÂMICA MOLECULAR E BIOQUÍMICA QUÂNTICA COM APLICAÇÕES NA SAÚDE HUMANA

Tese apresentada ao Programa de Pós-Graduação em Bioquímica, do Departamento de Bioquímica e Biologia Molecular, da Universidade Federal do Ceará, como parte dos requisitos obrigatórios para a obtenção do título de Doutor em Bioquímica.

Orientadora: Profa. Dra. Daniele de Oliveira Bezerra de Sousa.

FORTALEZA

2022

Dados Internacionais de Catalogação na Publicação
Universidade Federal do Ceará
Sistema de Bibliotecas
Gerada automaticamente pelo módulo Catalog, mediante os dados fornecidos pelo(a) autor(a)

A514b Amaral, Jackson Lima.
Biologia molecular in silico: da bioinformática à dinâmica molecular e bioquímica quântica com aplicações na saúde humana. / Jackson Lima Amaral. – 2023.
328 f. : il. color.

Tese (doutorado) – Universidade Federal do Ceará, Centro de Ciências, Programa de Pós-Graduação em Bioquímica , Fortaleza, 2023.
Orientação: Prof. Dr. Daniele de Oliveira Bezerra de Sousa.

1. Covid. 2. Candida. 3. Câncer. 4. Albumina. 5. Bioquímica quântica. I. Título.

CDD 572

JACKSON LIMA AMARAL

BIOLOGIA MOLECULAR *IN SILICO*: DA BIOINFORMÁTICA À DINÂMICA MOLECULAR E BIOQUÍMICA QUÂNTICA COM APLICAÇÕES NA SAÚDE HUMANA

Tese apresentada ao Programa de Pós-Graduação em Bioquímica, do Departamento de Bioquímica e Biologia Molecular, da Universidade Federal do Ceará, como parte dos requisitos obrigatórios para a obtenção do título de Doutor em Bioquímica.

Orientadora: Profa. Dra. Daniele de Oliveira Bezerra de Sousa.

Aprovada em: 08/11/2022.

BANCA EXAMINADORA

_____
Profa. Dra. Daniele de O. B. de Sousa (Orientadora)
Universidade Federal do Ceará (UFC)

_____
Prof. Dr. Valder Nogueira Freire
Universidade Federal do Ceará (UFC)

_____
Prof. Dr. Hernandes Faustino de Carvalho
Universidade Estadual de Campinas (UNICAMP)

_____
Profa. Dra. Kellen Brunaldi
Universidade Estadual de Maringá (UEM)

_____
Prof. Dr. Paulo de Tarso Cavalcante Freire
Universidade Federal do Ceará (UFC)

À Deus.

Espíritos de luz e familiares.

AGRADECIMENTOS

Aos órgãos financiadores CNPq, FUNCAP e CAPES, pelo apoio financeiro para o desenvolvimento deste trabalho e outros durante o período do doutorado.

À Profa. Dra. Daniele de Oliveira Bezerra de Sousa pela confiança durante o doutorado. Agradeço a liberdade de pesquisar temas que sempre me interessei, demonstrando que orientar é conduzir caminhos e não os impor. Gratidão por sua excelente orientação, preocupação e paciência.

Ao professor Dr. Valder Nogueira Freire pela orientação, por ser um grande cientista inspirador. Agradeço por tudo que fez por mim e por todos os ensinamentos práticos para a vida. Sem dúvidas, tudo me transformei na vida acadêmica foi graças a você.

Ao professor participante da banca examinadora Hernandes Faustino de Carvalho por sempre estar disposto a ajudar e por todas as colaborações.

À professora participante da banca examinadora Kellen Brunaldi pelas colaborações realizadas e por toda preocupação durante o período da pandemia.

Ao professor participante da banca examinadora Paulo de Tarso Cavalcante Freire por ter se disponibilizado a participar da banca e por todas as colaborações, principalmente na Espectroscopia Raman.

Aos parceiros do Laboratório de Biofísica Aplicada, por estarmos unidos nos momentos de alegria e sofrimento.

À toda minha família pela motivação e apoio ao longo de toda jornada acadêmica. Todos foram essenciais para meu desenvolvimento intelectual.

A todos meus amigos, por todos os risos compartilhados e pelos bons momentos externos à UFC.

O presente trabalho foi realizado com apoio da Coordenação de Aperfeiçoamento de Pessoal de Nível Superior – Brasil (CAPES) – Código de Financiamento 001.

RESUMO

Na biologia e em outras ciências experimentais, a pesquisa *in silico* (do pseudo latin '*in silicon*', que em Latin seria '*in silício*') é aquela realizada tendo o computador como ferramenta auxiliar principal, o que contrasta com a pesquisa realizada utilizando-se organismos vivos *in vitro* e *in vivo*. Nesta tese, fazemos uma descrição dos fundamentos da Biologia Molecular *in silico*, dando uma visão sucinta do que é a Bioinformática, Dinâmica Molecular e Bioquímica Quântica no contexto das pesquisas que realizamos em alguns sistemas biológicos. Utilizamos sequências de resíduos/estruturas de proteínas de sistemas biológicos (dados do UNIPROT e do PDB), e sua interação com ligantes (pequenas moléculas e outras proteínas) visando um entendimento (com base molecular) dos processos biológicos em foco, e de aplicações voltadas à criação, melhoria, reposicionamento e desenvolvimento de fármacos (pequenas moléculas e polipeptídeos). No escopo da biologia molecular *in silico* e/ou *in vivo*, descrevemos nesta tese pesquisas básicas e aplicações desenvolvidas com a *Candida* spp (*in vitro*), Covid, Imunologia do Câncer, e Ligação do Pesticida Atrazina à Albumina Sérica Humana (HSA). Elas foram fundamentadas nas sequências dos resíduos e estruturas de proteínas (UNIPROT e PDB), modelagem de proteínas por homologia, *docking* em proteínas (ClusPro, Frodock e Vina), dinâmica molecular em proteínas e membranas (CHARMM e GROMACS), e bioquímica quântica (função dielétrica não-homogênea e metodologia dividir para conquistar – MFCC) da interação de pequenas moléculas e polipeptideos com as proteínas-alvo de cada sistema biológico. Das atividades e colaborações realizadas durante o desenvolvimento da tese resultaram cinco publicações sobre a *Candida* spp., seis publicações sobre o COVID, e duas publicações sobre a interação do adoçante stevia e do pesticida atrazina com a HSA/BSA, o que fornece informações sobre como estas importantes moléculas são transportadas pelo sangue.

Palavras-chave: Covid; Candida; Câncer; Albumina; Bioquímica quântica.

ABSTRACT

In biology and other experimental sciences, in silico research (from the pseudo-Latin *'in silicon'*, which in Latin would be *'in silício'*) is carried out with the computer as the main auxiliary tool, which contrasts with research carried out using whether living organisms *in vitro* and *in vivo*. In this thesis, we describe the fundamentals of Molecular Biology *in silico*, giving a succinct description of what Bioinformatics, Molecular Dynamics, and Quantum Biochemistry are in the context of the research we carry out in some biological systems. We use sequences of residues/structures of proteins from biological systems (data from UNIPROT and PDB), and their interaction with ligands (small molecules and other proteins) aiming for a (molecular-based) understanding of the biological processes in focus, and applications aimed at the creation, improvement, repositioning, and development of drugs (small molecules and polypeptides). In the scope of *in silico* and/or *in vivo* molecular biology, we describe in this thesis basic research and applications developed with *Candida* spp (*in vitro*), Covid, Cancer Immunology, and Atrazine Pesticide Binding to Human Serum Albumin (HSA). They were based on the sequences of residues and structures of proteins (UNIPROT and PDB), modeling of proteins by homology, docking in proteins (ClusPro, Frodock, and Vina), molecular dynamics in proteins and membranes (CHARMM and GROMACS), and quantum biochemistry (non-homogeneous dielectric function and divide-and-conquer methodology (MFCC) of the interaction of small molecules and polypeptides with the target proteins of each biological system. The activities and colaborations carried out during the development of the thesis resulted in five publications on *Candida* spp., six publications on COVID, and two publications on the interaction of the sweetener stevia and the pesticide atrazine with HSA/BSA, which provides information on how these important molecules are carried by the blood.

Keywords: Covid; Candida; Cancer; Albumin; Quantum biochemistry.

LISTA DE FIGURAS

LISTA DE TABELAS

SUMÁRIO

1 INTRODUÇÃO

Com o avanço da computação e descobertas realizadas no campo da biologia estrutural, possibilitou-se estudos de biologia *in silico*, ou seja, pesquisas em biologia realizadas por simulações computacionais (BEHL *et al.,* 2021; SHULI *et al.,* 2022).

Diversas metodologias estão, constantemente, sendo desenvolvidas e melhoradas para facilitar e desenvolver a biologia computacional. Entre as metodologias mais utilizadas, pode-se citar a modelagem de proteínas por homologia, o *docking* molecular, as simulações de dinâmica molecular e, mais recentemente, a bioquímica quântica (ALBUQUERQUE *et al.,* 2020; MORRIS; CORTE, 2021; STANZIONE; GIANGRECO; COLE, 2021).

Nosso grupo de pesquisa é um dos pioneiros com o estudo de bioquímica quântica no Brasil, sendo o primeiro trabalho publicado em 2012, demonstrando os cálculos quânticos da inibição da HMG-CoA redutase pelas estatinas (DA COSTA *et al.,* 2012). Nesses 10 anos de pesquisa (a partir da primeira publicação), mais de 35 artigos envolvendo diferentes sistemas proteicos foram publicados e mais de 10 drogas já foram sugeridas pelo grupo liderado pelo professor Valder Nogueira Freire.

Nosso laboratório desenvolveu e disponibilizou para o mundo um novo método capaz de calcular a função dielétrica não homogênea para aplicar em bioquímica quântica de sistemas proteicos, o que melhorou os cálculos realizados, tornando-os mais acurados. Em 2021, o professor líder do grupo publica o livro "*Quantum Chemistry Simulation of Biological Molecules*" na editora Cambridge University Press descrevendo as pesquisas e avanços alcançados por nosso grupo.

A partir de toda a expertise do grupo, esta tese foi desenvolvida abordando diferentes temas e sistemas proteicos e, ao longo do meu doutorado, foram publicados 14 artigos. Para compor o corpo da tese, foram escolhidos os 4 primeiros artigos dos 14 listados abaixo. Os demais encontram-se nos apêndices.

Artigo 1: Quantum biochemistry, molecular docking, and dynamics simulation revealed synthetic peptides induced conformational changes affecting the topology of the catalytic site of SARS-CoV-2 main protease. DOI: https://doi.org/10.1080/07391102.2021.1920464

Figura 1. Capa do livro "*Quantum Chemistry Simulation of Biological Molecules*" publicado pelo professor Valder Nogueira Freire na Cambridge University Press.

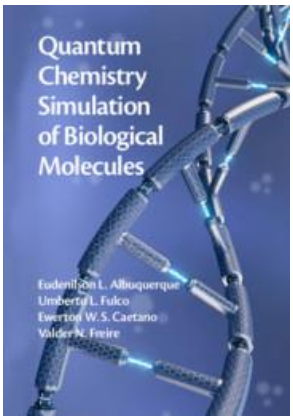

Fonte: ALBUQUERQUE *et al.,* 2020

Nesse artigo demonstramos a capacidade de peptídeos sintéticos interagirem com a Mpro de SARS-CoV-2 e ocasionarem mudanças conformacionais, reduzindo o volume do sítio proteolítico da enzima, figura2. O artigo completo que foi publicado na revista *Journal of Biomolecular Structure & Dynamics* encontra-se no 3.2 desta tese.

Artigo 2: ACE2-derived peptides interact with the RBD domain of SARS-CoV-2 spike glycoprotein, disrupting the interaction with the human ACE2 receptor. DOI: http://dx.doi.org/10.1080/07391102.2020.1871415

A interação entre o domínio RBD da proteína S de SARS-CoV-2 com a proteína ECA2 de humanos é crucial para a invasão do vírus às células. Descreveu-se através de bioquímica quântica as interações existentes entre as duas proteínas (RBD da proteína S com ECA2) e identificou-se os principais resíduos de aminoácidos nessa interação. A partir disso, desenhou-se peptídeos derivados da ECA2 que seriam capazes de inibir a interação da proteína S de SARS-CoV-2 com a proteína humana, ou mesmo ocorrer uma interação de forma anormal, inibindo, dessa forma, a entrada do vírus e evitando a doença, figura 3. O artigo completo que foi publicado na revista *Journal of Biomolecular Structure & Dynamics* encontra-se no tópico 3.3.

Figura 2. Peptídeos sintéticos interagem com Mpro e reduzem o volume do sítio ativo da enzima.

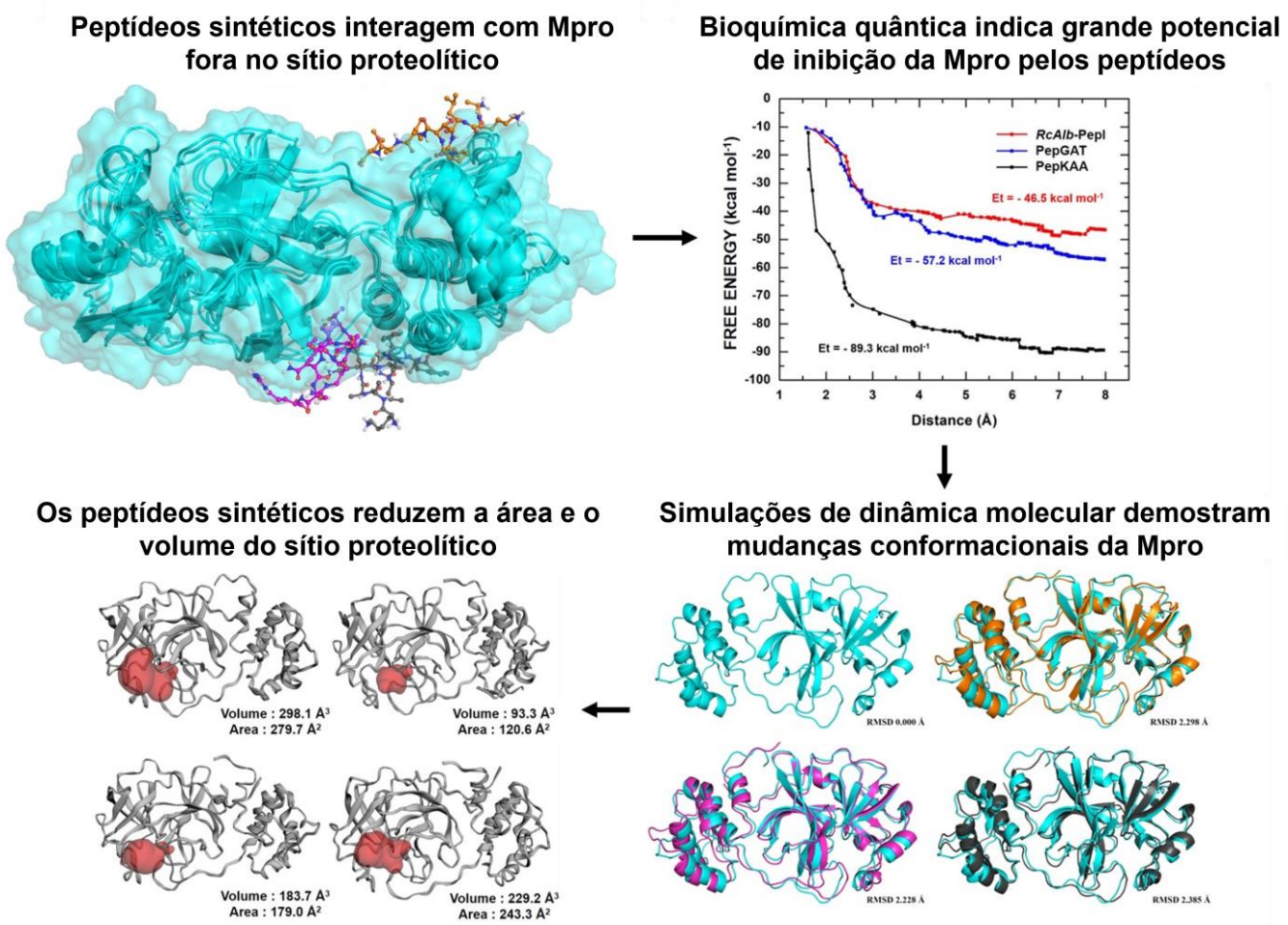

Fonte:Elaborado pelo autor a partir das figuras de AMARAL; OLIVEIRA; *et al.,* 2021.

Artigo 3: Quantum biochemistry in cancer immunotherapy: New insights about CTLA-4/ipilimumab and design of ipilimumab-derived peptides with high potential in cancer treatment. DOI: https://doi.org/10.1016/j.molimm.2020.09.013.

O artigo completo que foi publicado na revista *Molecular Immunology*, encontra-se no tópico 4.1. O câncer consegue escapar do sistema imune através da produção de ligantes que mascaram proteínas *checkpoints*. Com a aplicação de anticorpos monoclonais, é possível impedir a ligação desses ligantes às proteínas e, então, o sistema imune consegue identificar e destruir células cancerígenas. Apesar das vantagens, os anticorpos ainda apresentam algumas desvantagens que podem ser superadas através do desenho de peptídeos cíclicos miméticos inspirados nos anticorpos. Nesse trabalho, realizou-se o cálculo de bioquímica quântica entre o anticorpo Ipilimumab e a proteína CTLA-4. A partir dos dados obtidos dos cálculos,

foi possível desenhar peptídeos das regiões que apresentam maior afinidade do anticorpo com CTLA-4. Os peptídeos desenhados possuem diversas vantagens

Figura 3. Peptídeos sintéticos derivados da proteína humana ECA2 interagem com a proteína S de SARS-CoV-2 e induzem interações anormais com a ECA2, sugerindo uma inibição da invasão do vírus a células humanas.

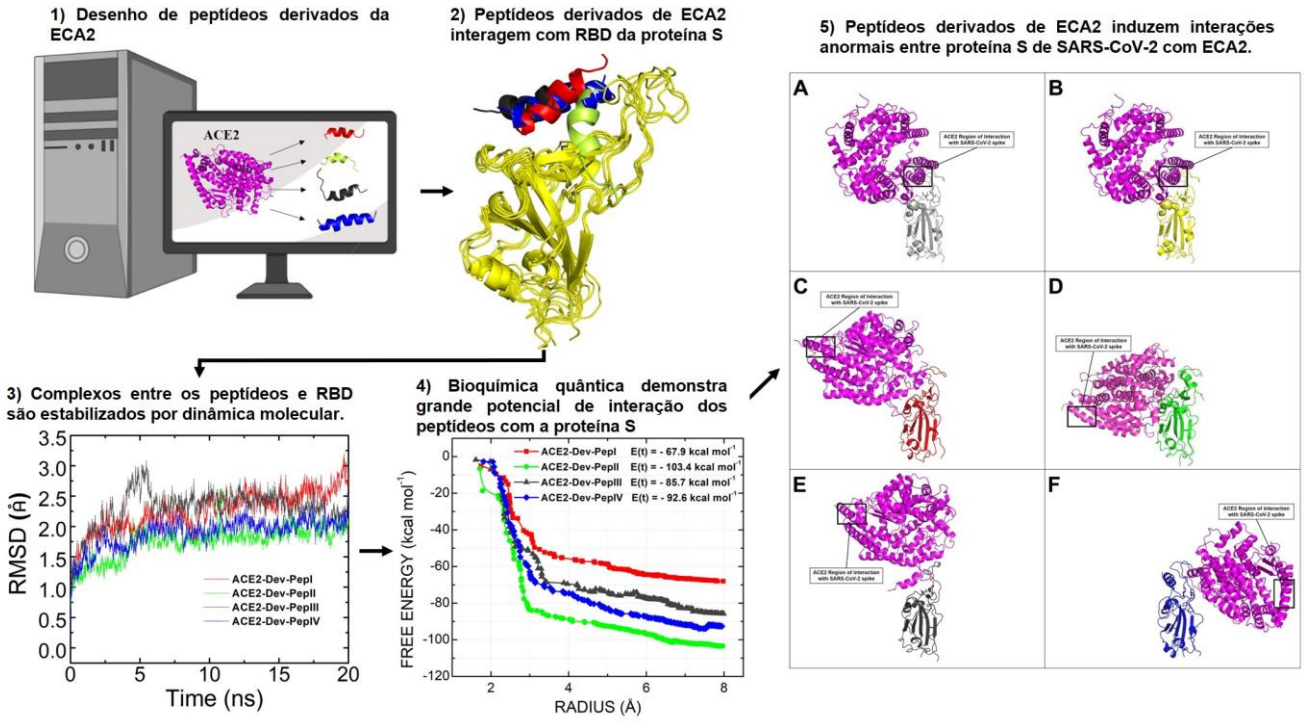

Fonte: Elaborado pelo autor a partir das figuras de SOUZA *et al.,* 2022

como maior resistência a proteólise do que a utilização do anticorpo inteiro. Um esquema dos principais resultados obtidos no trabalho é apresentado na figura 4.

Artigo 4: Characterization of the binding interaction between atrazine and human serum albumin: Fluorescence spectroscopy, molecular dynamics and quantum biochemistry. DOI: http://dx.doi.org/10.1016/j.cbi.2022.110130

A atrazina é um dos pesticidas mais utilizados no mundo e possui vários efeitos tóxicos para humanos como: redução da fertilidade, aumento do risco de câncer de próstata e toxicidade neuroendócrina. Nesse trabalho foi avaliado como esse herbicida interage com a principal proteína presente no sangue: albumina sérica humana (HSA). O estudo da interação entre o pesticida e a albumina fornece dados relevantes para estudos farmacocinéticos de farmacodinâmica e de toxicidade da

atrazina. Utilizando espectroscopia de fluorescência, docking, dinâmica molecular e bioquímica, obteve-se que a atrazina interage principalmente nos sítios FA3/4 e FA8, realizando, em ambos, ligações de hidrogênio, interações de van der Waals e interações hidrofóbicas, como demonstrado no resumo gráfico do artigo (figura 5). O artigo completo, que foi publicado na revista *Chemico-Biological Interactions,* encontra-se no tópico 5.1.

Figura 4. Desenvolvimento de peptídeos miméticos ao anticorpo Ipilimumab para tratamento de câncer.

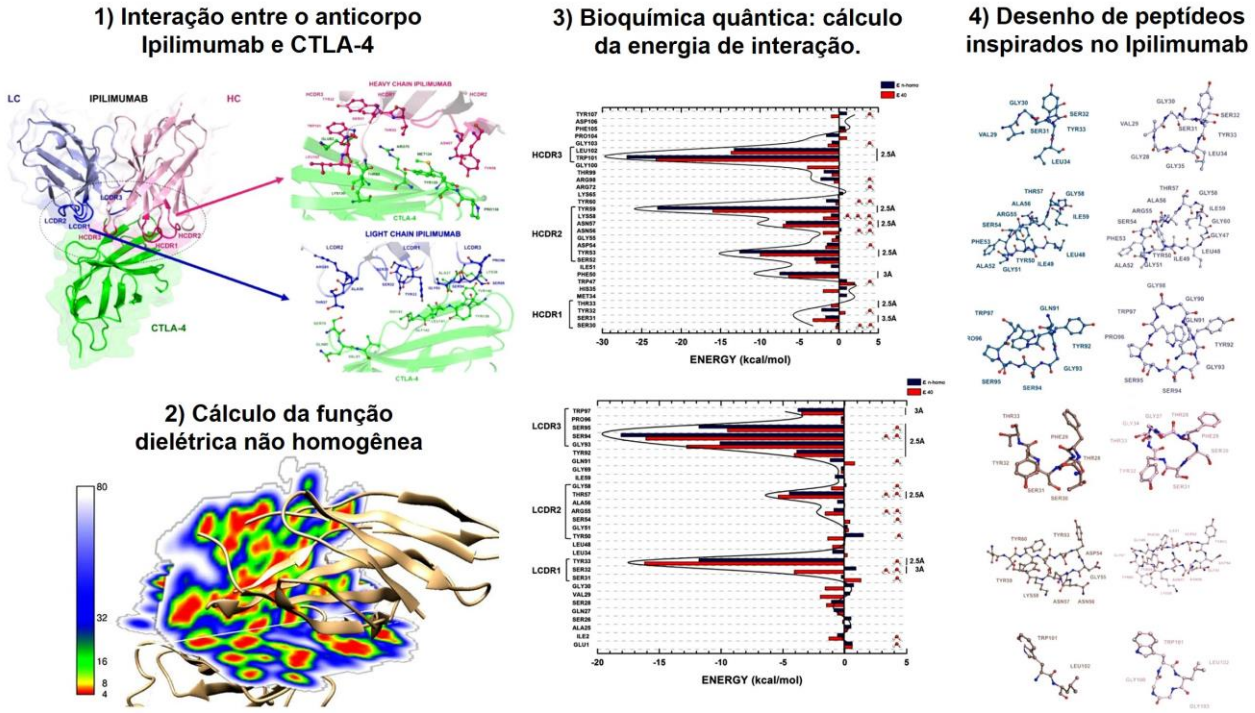

Fonte: Elaborado pelo autor com as figuras de AMARAL *et al.,* 2020.

Figura 5. Atrazina interage com a albumina sérica humana nos sítios FA3/4 e FA8.

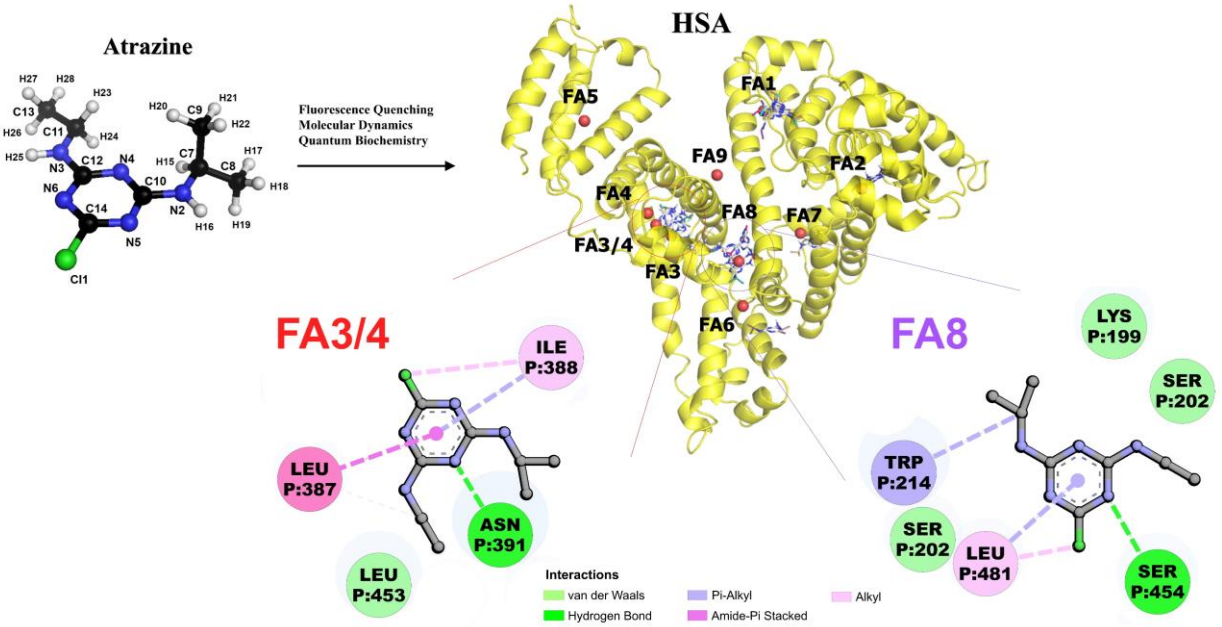

Fonte: FRANÇA *et al.,* 2022

Artigo 5: Computational approach, scanning electron and fluorescence microscopies revealed insights into the action mechanisms of anticandidal peptide *Mo*-CBP$_3$-PepIII. DOI: https://doi.org/10.1016/j.lfs.2021.119775.

Esse artigo completo, que foi publicado na revista *Life Sciences,* encontra-se no apêndice A da tese. Resumidamente, avaliou-se os mecanismos de ação do peptídeo *Mo*-CBP$_3$-PepIII contra *Candida* spp. Utilizou-se docking molecular para avaliar a interação do peptídeo com as proteínas SAP1, SAP5, CYP51 e exo-β-1,3-glucanase de *Candida albicans*. Bem como, analisou-se interação desse peptídeo com uma membrana mimética de *Candida* spp. através de simulações de dinâmica molecular. Constatou-se, assim, que o peptídeo possui maior afinidade com exo-β-1,3-glucanase que o inibidor comercial castanospermina e que o peptídeo é capaz de penetrar na membrana da levedura e induz a formação de poros, demonstrado na figura 6.

Figura 6. Principais mecanismos de ação do peptídeo *Mo*-CBP$_3$-PepIII contra *Candida* spp.

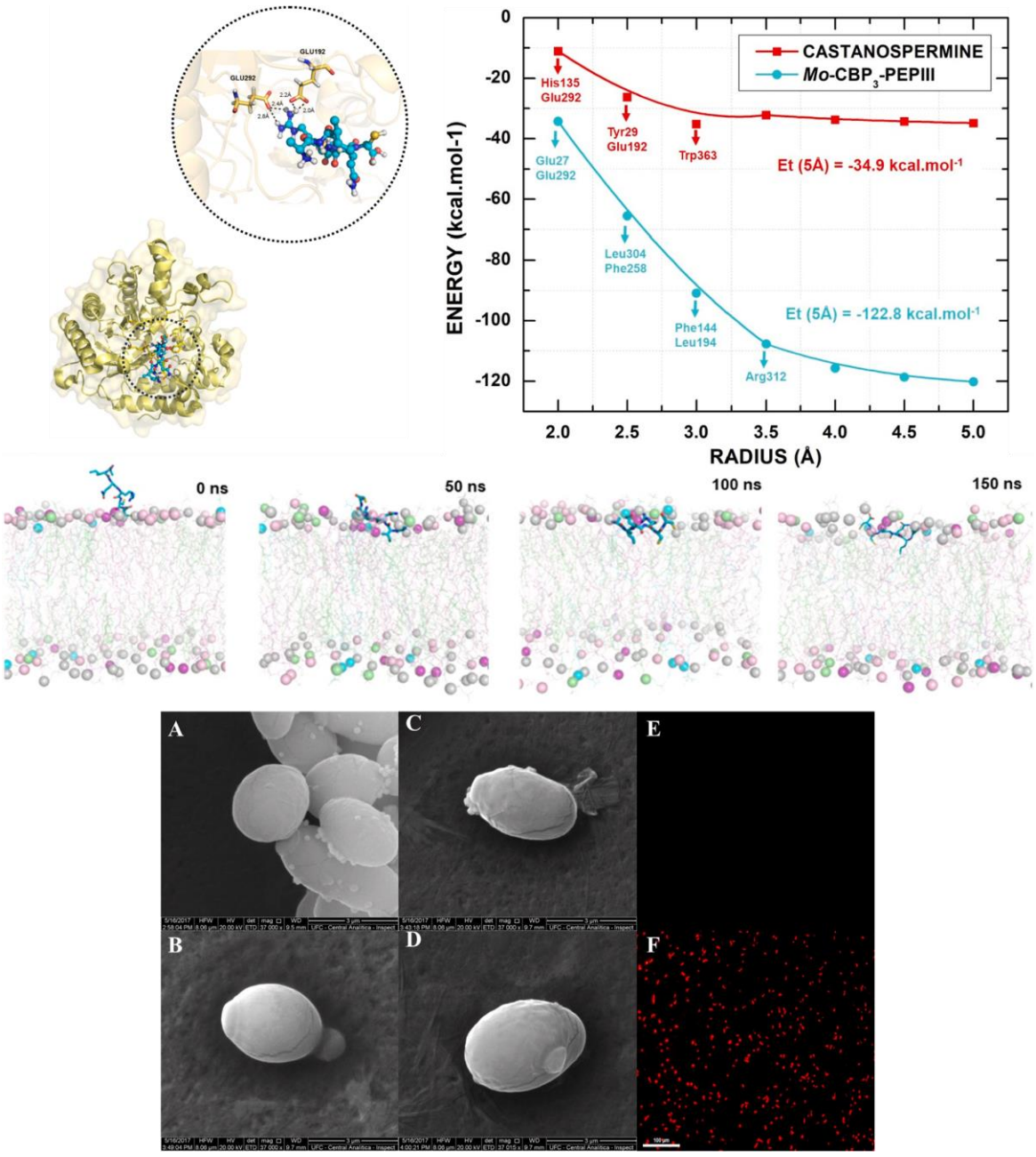

Fonte: AMARAL; SOUZA; *et al.*, 2021.

Artigo 6: Peptide fraction from latex of *Calotropis procera* exhibits

antifungal and insecticidal activities. DOI: http://dx.doi.org/10.1007/s11829-021-09828-2

O látex é um fluido endógeno exsudado por algumas plantas após lesão. É rico em diferentes moléculas e tem demonstrado muitas atividades biológicas contra diferentes fungos e insetos. Neste trabalho, isolou-se uma fração peptídica do látex de *Calotropis procera* (PepCp) e avaliou-se sua atividade contra dois fungos e um inseto. PepCp (1,25 mg mL^{-1}) inibiu o crescimento micelial de *C. gloeosporioides* em 80% e reduziu o peso larval do inseto *Callosobruchus maculatus* em 90% a 0,1%, e a 0,2%, sendo nenhuma larva encontrada, demonstrando o potencial dessa fração peptídica contra fungos e insetos, figura 7. Artigo completo, que foi publicado na revista *Arthropod-Plant Interactions,* encontra-se no apêndice B.

Figura 7. Fração peptídica do látex de *C. procera* possui atividade antifúngica e inseticida.

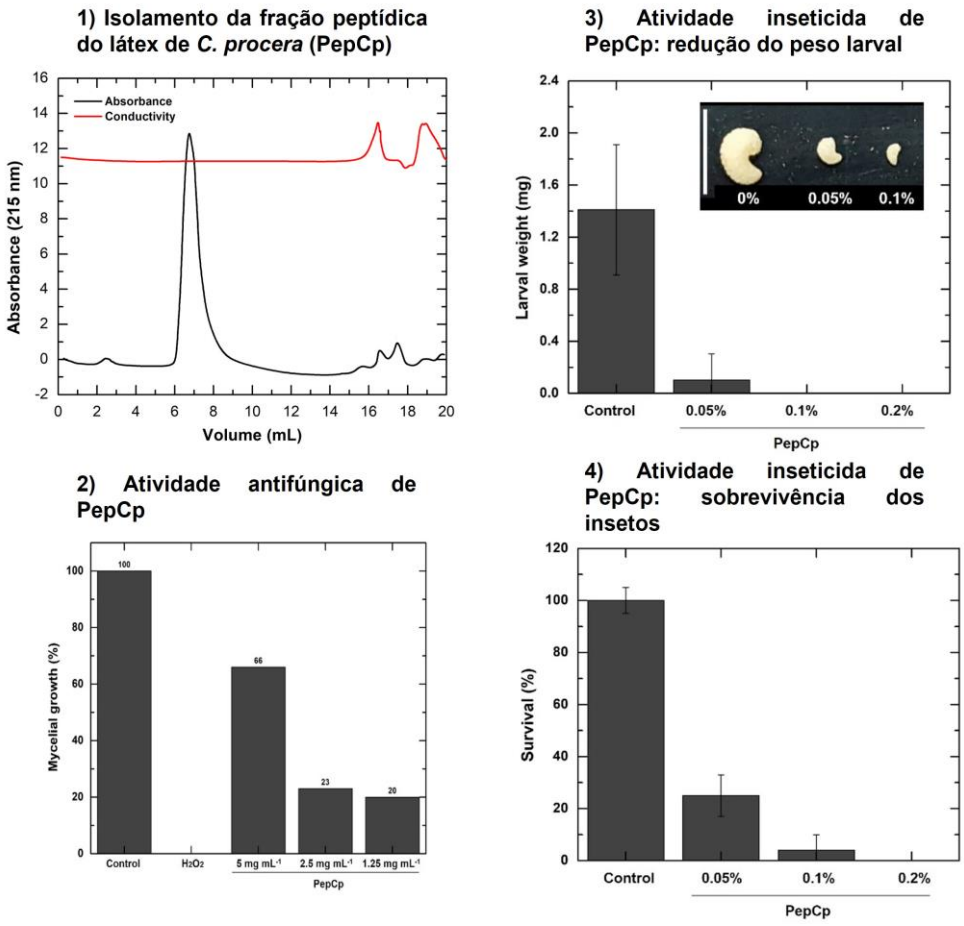

Fonte: AMARAL; FREITAS; *et al.,* 2021.

Artigo 7: Synthetic antimicrobial peptides: Characteristics, design, and potential as alternative molecules to overcome microbial resistance. DOI:

http://dx.doi.org/10.1016/j.lfs.2021.119647

O aumento da resistência antimicrobiana, percebido recentemente, tem recebido atenção da Organização Mundial da Saúde e alertado o mundo sobre a necessidade de desenvolver novas drogas, bem como racionalizar o uso de antimicrobianos. Peptídeos antimicrobianos sintéticos (SAMPs) são considerados eficientes para combater micro-organismos multirresistentes. Nesse artigo, revisou-se as pesquisas sobre o desenvolvimento e testes de SAMPs, incluindo os AMPs naturais, mecanismos de ação e aplicações como novas drogas ou, até mesmo, como moléculas que possuem efeito sinérgico com drogas comerciais, resumido na figura 8. O artigo completo que foi publicado na revista *Life Sciences,* encontra-se no apêndice C.

Figura 8. Peptídeos sintéticos são drogas potenciais para o combate de micro-organismos multirresistentes. Esses peptídeos possuem como principais mecanismos de ação a formação de poros na membrana que induzem a morte celular.

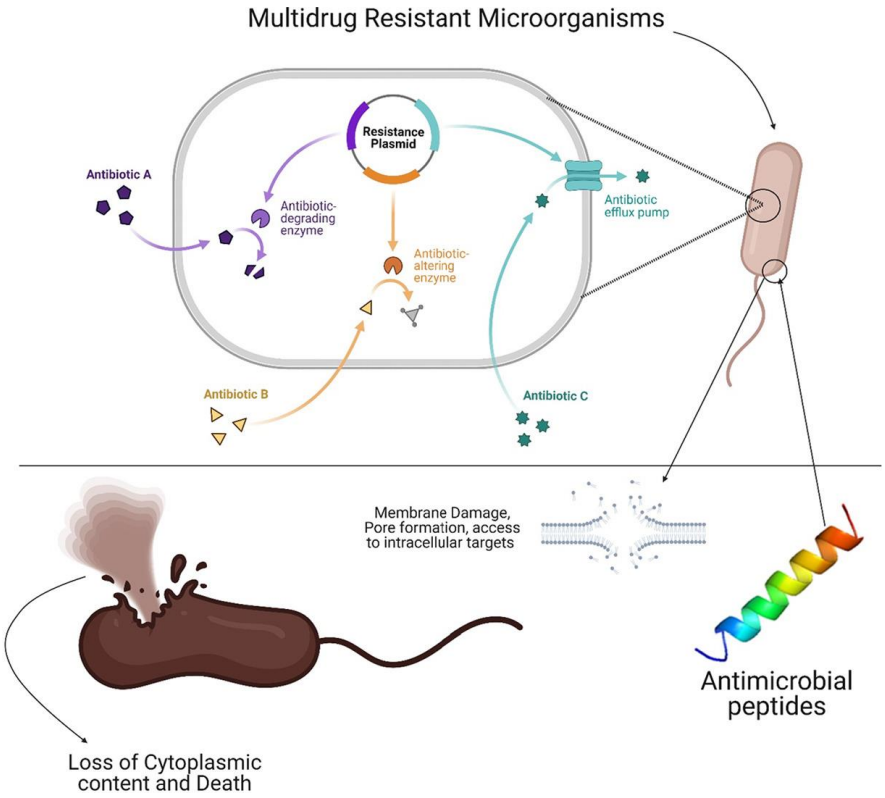

Fonte: LIMA *et al.*, 2021

Artigo 8: Combined antibiofilm activity of synthetic peptides and antifungal drugs against *Candida* spp.. DOI: http://dx.doi.org/10.2217/fmb-2022-0053

Leveduras do gênero *Candida* ssp. causam infecções sistêmicas e mortes, sendo esses micro-organismos capazes de formar uma estrutura de resistência denominada biofilme, tornando o tratamento mais complicado. Nesse artigo, avaliou-se o efeito sinérgico entre peptídeos sintéticos e drogas antifúngicas convencionais. Foi possível observar que as drogas e os peptídeos, utilizados de forma isolada, não são capazes de destruir biofilmes estabelecidos, entretanto, quando aplicada a combinação droga-peptídeo, observou-se uma redução no biofilme, como demonstrado na figura 9. Constatou-se, ainda, que os peptídeos são capazes de reduzir o efeito hemolítico das drogas, reduzindo suas citotoxicidades. O artigo completo, que foi publicado na revista *Future Microbiology,* encontra-se no apêndice D.

Figura 9. Combinação entre peptídeos sintéticos e drogas (itraconazol e nistatina) reduzem a massa de biofilmes estabelecidos de *C. krusei*.

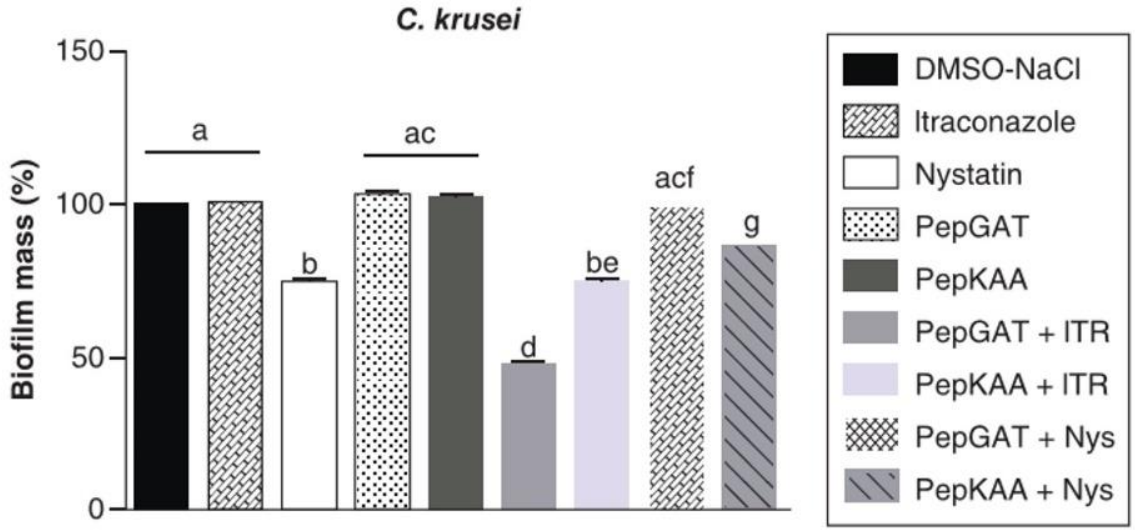

Fonte: BEZERRA; SILVA; *et al.*, 2022.

Artigo 9: Synergistic Antifungal Activity of Synthetic Peptides and Antifungal Drugs against *Candida albicans* and *C. parapsilosis* Biofilms. DOI: http://dx.doi.org/10.3390/antibiotics11050553

Nesse estudo, pesquisamos a atividade antibiofilme dos peptídeos *Mo*-CBP$_3$-PepI e *Mo*-CBP$_3$-PepIII isolados, bem como seus efeitos sinérgicos com as drogas itraconazol e nistatina contra biofilmes de *C. albicans* e *C. parapsilosis,* figura

10. Observou-se que os peptídeos foram capazes de melhorar a atividade antibiofilme das drogas de 2 a 4 vezes. Os resultados de docking molecular sugerem que os peptídeos interagem fracamente com as drogas, indicando que o efeito sinérgico ocorra no alvo, diretamente. Dessa forma, os peptídeos podem ser utilizados como drogas adjuvantes para serem aplicados contra biofilmes de *Candida* spp. O artigo completo, que foi publicado na revista *Antibiotics,* encontra-se no apêndice E.

Figura 10. *Mo*-CBP$_3$-PepI e *Mo*-CBP$_3$-PepIII possuem efeito sinérgico com itraconazol e nistatina para atividade antibiofilme contra *Candida albicans* e *C. Parapsilosis*

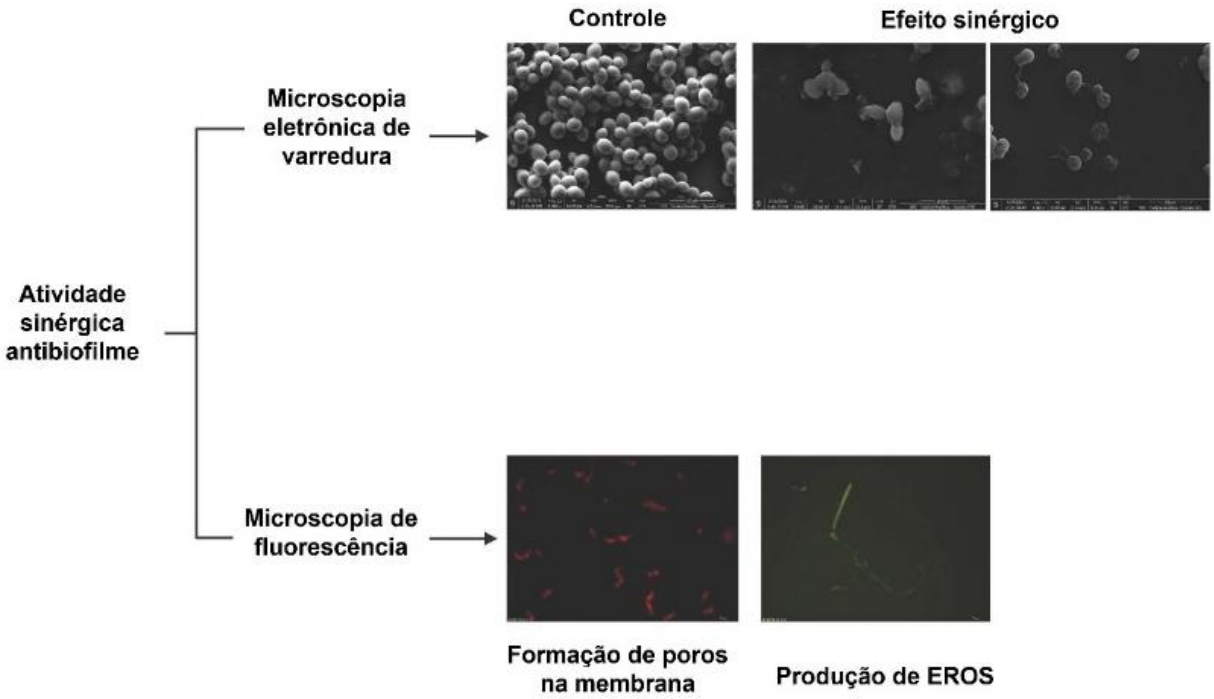

Fonte: BEZERRA; FREITAS; *et al.*, 2022.

Artigo 10: A molecular docking study revealed that synthetic peptides induced conformational changes in the structure of SARS-CoV-2 spike glycoprotein, disrupting the interaction with human ACE2 receptor. DOI: http://dx.doi.org/10.1016/j.ijbiomac.2020.07.174

Nesse artigo avaliou-se a capacidade de peptídeos sintéticos interagirem com a proteína S de SARS-CoV-2 e induzirem uma interação incorreta com a proteína humana ECA2. Os estudos foram realizados utilizando docking molecular

dos peptídeos com a proteína S e, após dela, com a ECA2.

Observou-se que os peptídeos sintéticos se ligam à proteína spike do vírus, induzem mudanças conformacionais na estrutura dessa proteína e, na presença dos peptídeos, a proteína S interage com a ECA2 de maneira incorreta, possivelmente impedindo a entrada do vírus a células humanas, figura 11. O artigo completo, que foi publicado na revista *International Journal of Biological Macromolecules,* encontra-se no apêndice F.

Figura 11. Peptídeo sintético *Mo*-CBP$_3$-PepII interagem com a proteína S de SARS-CoV-2 e induzem uma interação incorreta entre a proteína S e a ECA2 de humanos. A- Local de interação do peptídeo. B e C – Interações entre peptídeo e proteína S. Conformação correta seria o domínio SB interagindo com PD.

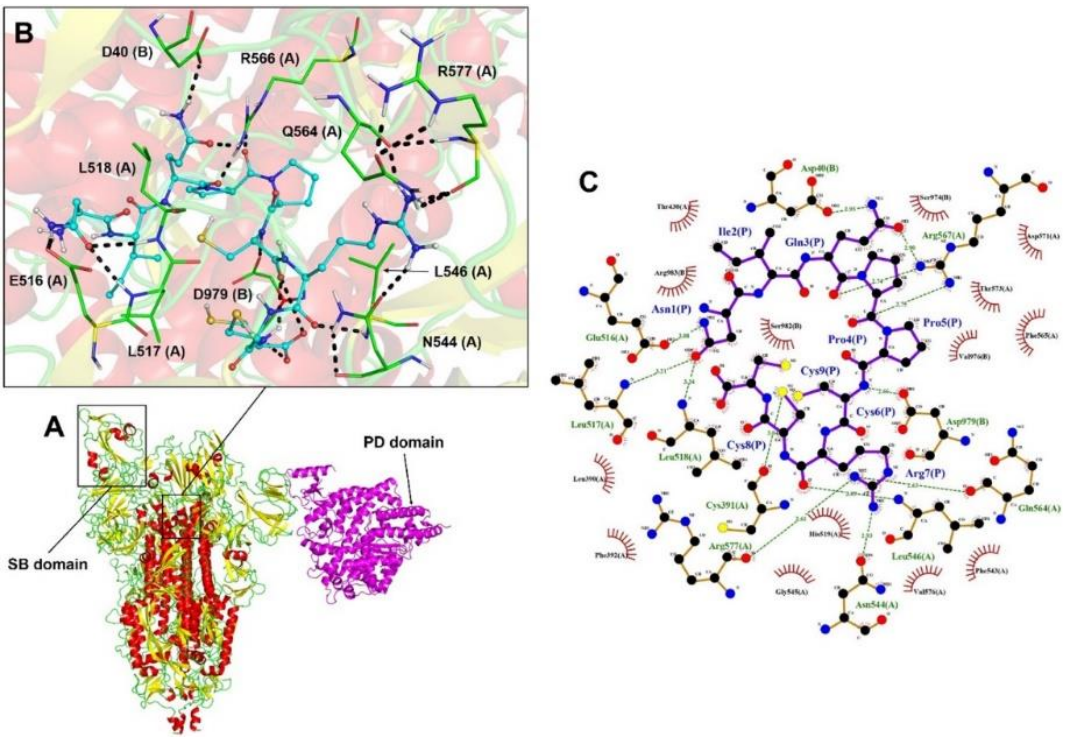

Fonte: SOUZA *et al.*, 2020.

Artigo 11: The human pandemic coronaviruses on the show: The spike glycoprotein as the main actor in the coronaviruses play. DOI: http://dx.doi.org/10.1016/j.ijbiomac.2021.02.203

Neste artigo de revisão, demonstramos o papel central da proteína spike na infecção de células humanas pelos coronavírus. Nas últimas 2 décadas foram observados 3 surtos causados por: MERS-CoV, SARS-CoV e SARS-CoV-2. Possuindo eles alto grau de similaridade genômica e proteômica, porém, as

diferenças moleculares presentes são responsáveis pelos diferentes comportamentos observados. Como a proteína spike é uma proteína chave no processo de infecção e transmissão dos coronavírus, realizamos um estudo analisando as diferenças de sequências e estruturas dos três coronavírus, sendo possível notar as mutações que tornaram o SARS-CoV-2 mais agressivo, como demonstrado na figura 12. O artigo completo publicado na revista *International Journal of Biological Macromolecules,* encontra-se no apêndice G.

Figura 12. Diferenças estruturais observadas nas proteínas spike dos coronavírus MERS-CoV, SARS-CoV e SARS-CoV-2.

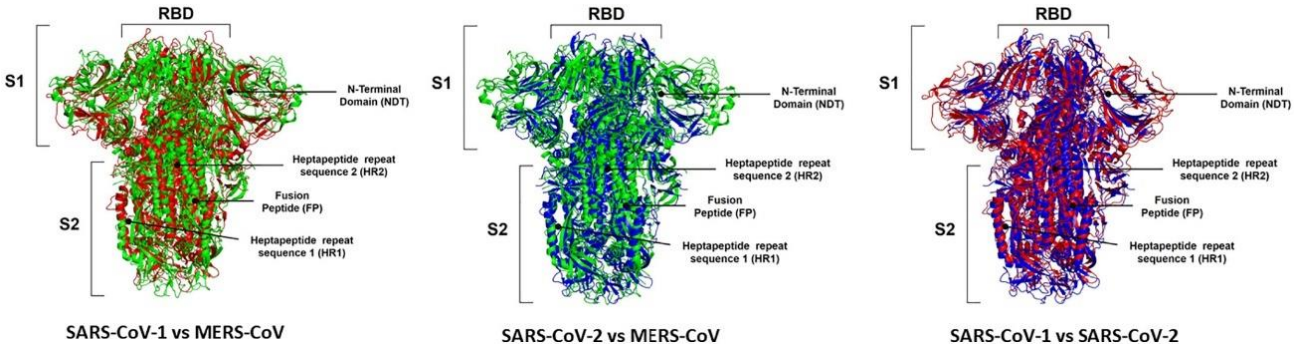

Fonte: SOUZA *et al.,* 2021.

Artigo 12: Neutralizing Effect of Synthetic Peptides toward SARS-CoV-2. DOI: http://dx.doi.org/10.1021/acsomega.2c02203

Testou-se quatro peptídeos sintéticos quanto à capacidade de proteger as células Vero E6 da infecção por SARS-CoV-2 e sua toxicidade para células humanas e embriões de peixe-zebra. Dockings molecular indicaram que todos os peptídeos que interagem e induzem alterações conformacionais na proteína spike, figura 13. PepKAA foi o mais eficaz e inibiu a infecção de SARS-CoV-2 em 50% na concentração de 0,15 $mg.mL^{-1}$, sendo um forte candidato para desenvolvimento de uma nova droga. O artigo completo que foi publicado na revista ACS Omega encontra-se no apêndice H.

Figura 13. Peptídeos sintéticos inibem a infectividade de SARS-CoV-2 através da ligação com a proteína spike do vírus.

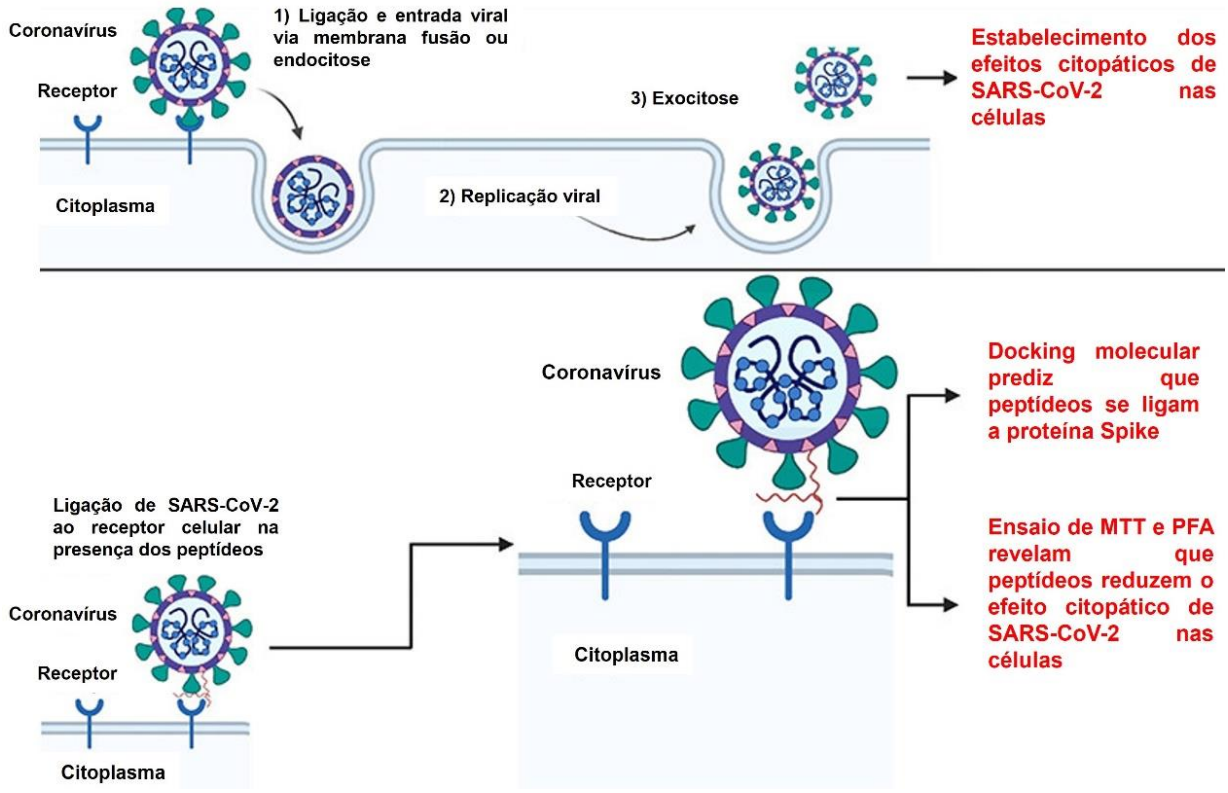

Fonte: SOUZA; VANTILBURG; *et al.,* 2022.

Artigo 13: The spike glycoprotein of SARS-CoV-2: A review of how mutations of spike glycoproteins have driven the emergence of variants with high transmissibility and immune escape. DOI: https://doi.org/10.1016/j.ijbiomac.2022.03.058

A glicoproteína spike desempenha um papel central na infecção, patogenicidade, transmissão e evolução do vírus SARS-CoV-2. Nesse trabalho, revisamos e discutimos as mutações nessa proteína que levaram ao surgimento das variantes do coronavírus, que aumentaram a transmissibilidade e poderiam ocasionar um escape imunológico, figura 14. O trabalho completo que foi publicado na revista *International Journal of Biological Macromolecules,* encontra-se no apêndice I.

Figura 14. Interação entre a proteína spike das diferentes variantes de SARS-CoV-2 com o receptor humano ECA2.

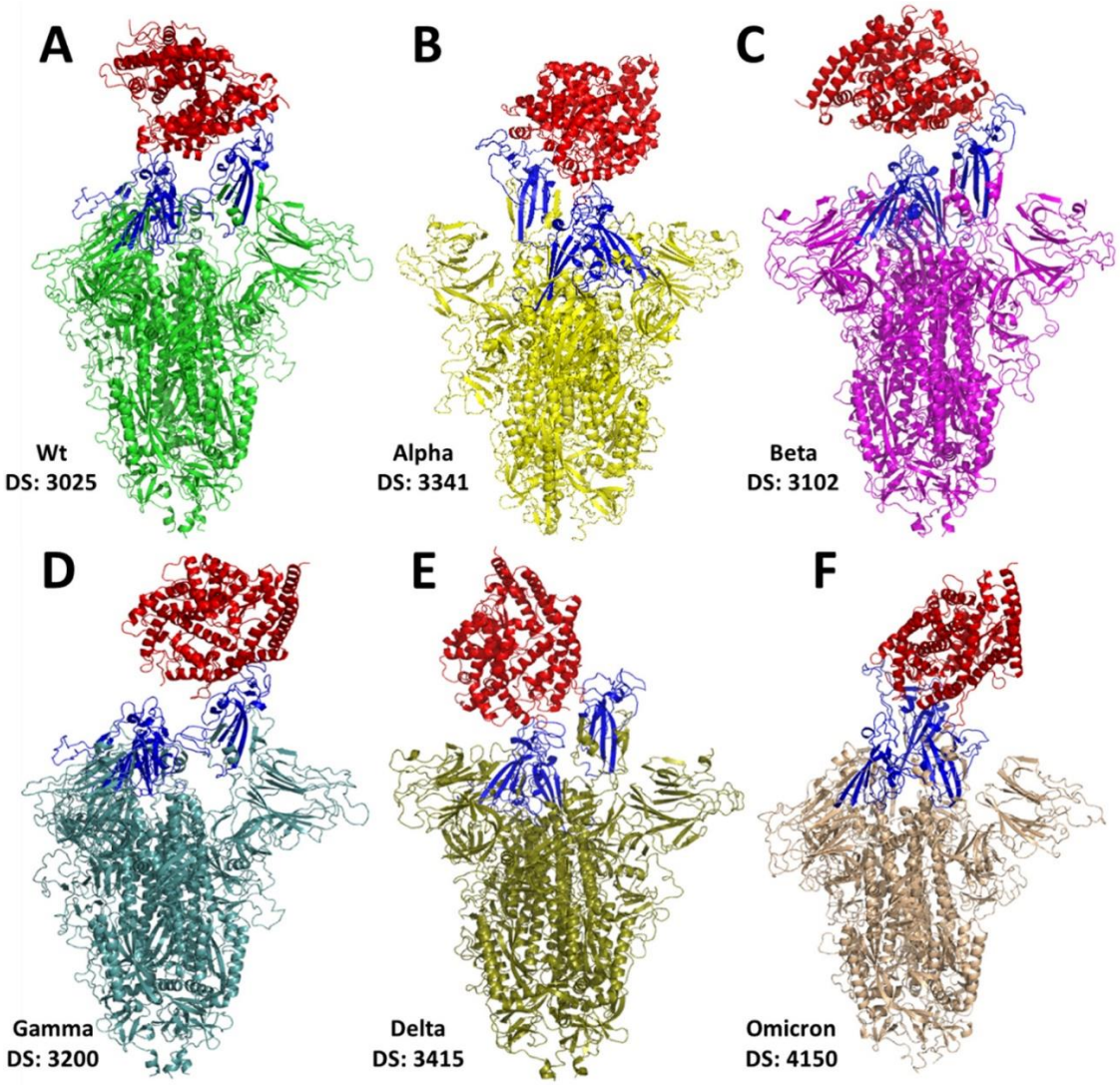

Fonte: SOUZA; MESQUITA; *et al.,* 2022.

Artigo 14: Molecular Insight On The Binding Of Stevia Glycosides To Bovine Serum Albumin. DOI: http://dx.doi.org/10.1016/j.cbi.2021.109526

Neste artigo, estudou-se a interação do esteviol e seus glicosídeos (SG) com albumina sérica bovina (BSA) através de espectroscopia de fluorescência e docking molecular. Observou-se a interação dos derivados de estévia com a BSA através do *quenching* da fluorescência, sendo constatada a formação de ligações de hidrogênio e interações de van der Waals entre os ligantes e a proteína. Docking molecular apontou os sítios de ligação FA1 e FA9 de BSA como os prováveis locais de ligação de esteviol e SG, respectivamente, demonstrado no resumo gráfico do artigo e representado na figura 15. O artigo completo e publicado na revista

Chemico-Biological Interactions encontra-se no apêndice J.

Figura 15. Estivol e seus glicosídeos interagem com a albumina sérica bovina nos sítios FA1 e FA9.

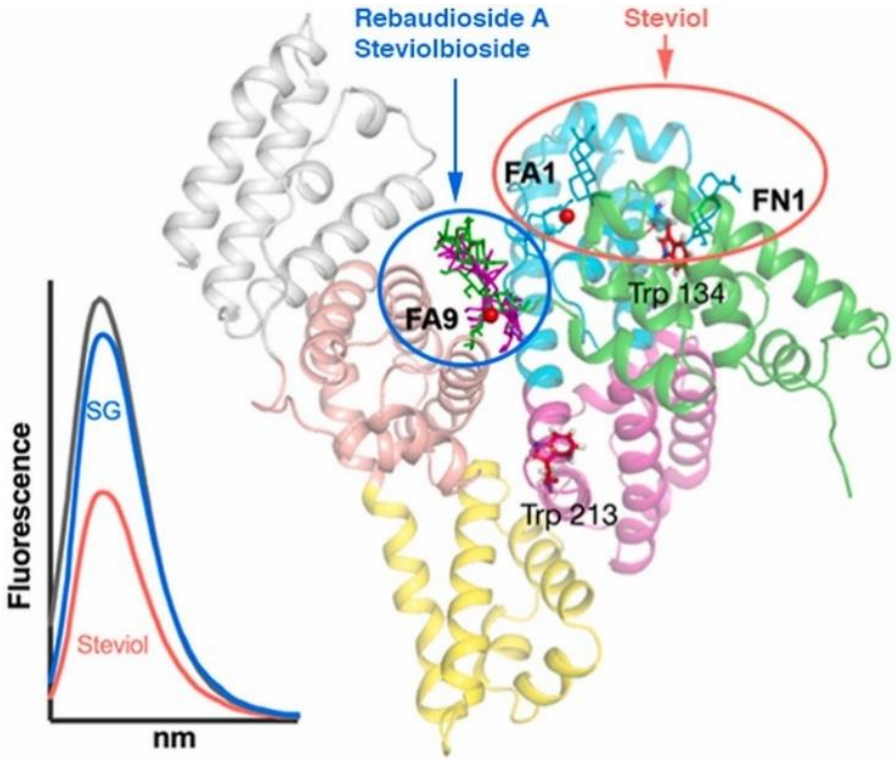

Fonte: SERGIO *et al.,* 2021.

2 FUNDAMENTAÇÃO TEÓRICA

2.1 Sequências e estruturas de proteínas: PDB e UNIPROT

A primeira proteína a ter sua estrutura tridimensional resolvida foi a mioglobina em 1958 e logo depois a hemoglobina (BOLTON; PERUTZ, 1970). Para resolver as estruturas foi utilizada a técnica de cristalografia de raio-X, metodologia demostrada na figura 16. Após essas primeiras resoluções, observou-se um crescimento no número de estruturas elucidadas e, então, foi criado o banco de estruturas de proteínas Protein Data Bank (PDB) (BERMAN, H. M., 2000).

O banco de estruturas de proteínas PDB possui mais de 195 mil estruturas elucidadas e depositadas. Essas estruturas são elucidadas por diferentes técnicas, principalmente por cristalografia de raio-X, Ressonância Magnética Nuclear (RMN) e, recentemente, através da Criomicroscopia Eletrônica de Transmissão (Crio-EM) (BERMAN, Helen M., 2021; BURLEY; BERMAN, 2021; YOUNG; BERRISFORD; CHEN, 2021).

Figura 16. Metodologia utilizada para resolução de estrutura tridimensional de proteínas utilizando cristalografia de raio-X.

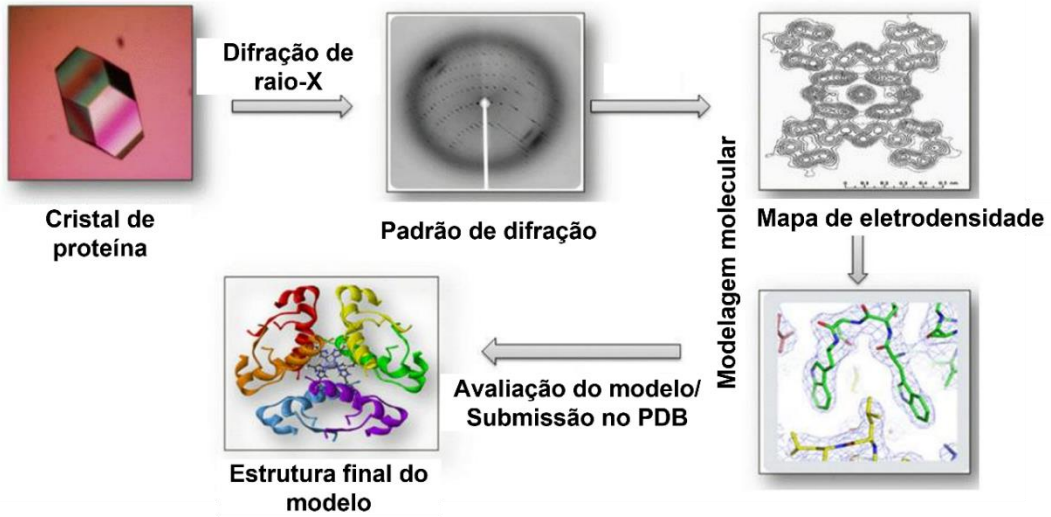

Fonte: GAWAS; MANDREKAR; MAJIK, 2019. Adaptada.

As estruturas tridimensionais das proteínas depositadas no PDB podem ser obtidas através do sítio eletrônico do banco (https://www.rcsb.org/). Cada estrutura depositada recebe um código para ser identificada no banco, esse código é

composto por 4 dígitos, com números e letras. No PDB também é possível obter diversas informações acerca da estrutura, bem como informações biológicas da proteína. O banco descreve o nome da proteína, sua espécie de origem, seu sistema de expressão e se ocorreu alguma mutação na sua sequência. Após isso, dados experimentais são informados, como a metodologia que foi utilizada para a resolução da estrutura e a resolução da estrutura em Å. Esses dados são importantes para o trabalho com biologia *in silico*, visto que quanto menor a resolução da estrutura, melhor é a estrutura e as informações dos átomos presentes nela. A maioria das estruturas depositadas no PDB possuem resoluções maiores que 1 Å, dessa forma, não possuem os átomos de hidrogênio. Utilizando-se inteligência artificial está sendo possível melhorar a qualidade e a resolução das estruturas tridimensionais (MIYAGUCHI *et al.,* 2021) Antes de qualquer trabalho com as estruturas obtidas no PDB, é necessário realizar o cálculo de protonação para adicionar os hidrogênios que não são encontrados nelas, bem como uma minimização de energia da estrutura para ajustar a localização dos átomos de hidrogênios na conformação de menor energia. Utiliza-se o software Protein Prepare para realizar o cálculo da protonação da proteína e o Discovery Studio para otimizar a estrutura (MARTÍNEZ-ROSELL; GIORGINO; DE FABRITIIS, 2017; PAWAR; ROHANE, 2021). Esse passo no estudo *in silico* é extremamente importante, visto que em diferentes valores de pH, as proteínas possuem diferentes protonações e podem obter resultados completamente diferentes dos reais, se a preparação dos arquivos não for realizada de forma correta (CHEN *et al.,* 2021).

No PDB também é possível encontrar outras informações acerca da estrutura, como a presença de pequenas moléculas que foram cocristalizadas e utilizadas na metodologia para resolução da estrutura, principalmente de tampões e ligantes empregados para estabilizar a proteína e conseguir obter cristais. Vale salientar que para estudos *in silico* é necessário retirar essas pequenas moléculas e estabilizar a estrutura da proteína e obter uma com menor valor de energia em condições fisiológicas. Para obter a estrutura da proteína com o menor valor de energia, sem as pequenas moléculas e em condições fisiológicas, pode-se utilizar uma simulação de dinâmica molecular da proteína em caixa de água e sais (LIN *et al.,* 2021).

O banco de dados Uniprot (https://www.uniprot.org/) contém sequências e informações funcionais das proteínas. Neste banco é possível identificar a

localização subcelular da proteína, suas interações, classificação da estrutura secundária, sequências, isoformas e proteínas similares. Também é possível obter a estrutura tridimensional das proteínas, realizar alinhamento da sequência (exemplo na figura 17) e visualizar as publicações que envolvem a proteína.

Figura 17. Exemplo do alinhamento de sequências de proteínas com estrutura tridimensional determinadas.

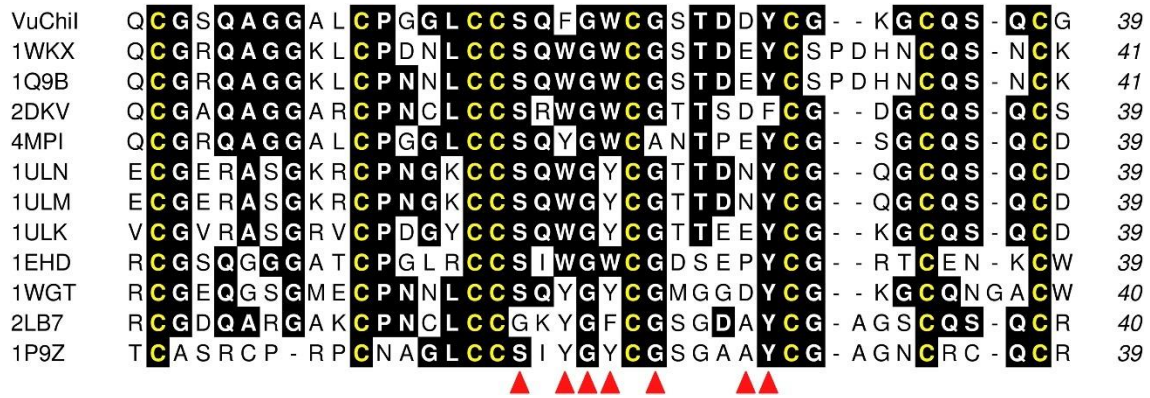

Fonte: (LANDIM *et al.,* 2017)

2.2 Modelagem de proteínas por homologia (PEPFold, SWISS-MODEL e AlphaFold)

Aproximadamente 100 mil proteínas possuem estruturas tridimensionais determinadas por métodos experimentais representando apenas uma pequena parte de bilhões de sequências de proteínas conhecidas. Dessa forma, a modelagem de proteínas por homologia é um método que acelera o processo de obtenção das estruturas tridimensionais, sendo um método rápido, com alta acurácia e com baixo custo. Utilizar estruturas e sequências de proteínas que já foram cristalizadas e elucidadas como molde para obtenção de estruturas de proteínas que não foram cristalizadas, economiza tempo e dinheiro que seriam utilizados nos procedimentos experimentais. Através da obtenção de estruturas por modelagem por homologia é possível obter modelos para diversos estudos, como análises pontuais de mutações, interação entre os complexos proteicos, análises dos sítios ativos (CHOWDHURY *et al.,* 2022; DU *et al.,* 2021; JUMPER *et al.,* 2021a).

O servidor PEPFOLD é utilizado para obtenção de modelos

tridimensionais de peptídeos de 5 a 50 resíduos de aminoácidos. Esse servidor utiliza uma abordagem de cálculo de energia dos peptídeos levando em consideração todos os átomos. Para obter a estrutura, são realizadas 100 simulações que, posteriormente, são ranqueadas em *clusters* de conformações com pequenas variações. A taxa de acurácia dos modelos gerados no PEPFOLD é de 95%, quando comparados os modelos com os dados obtidos experimentalmente (BINETTE; MOUSSEAU; TUFFERY, 2022; SHEN *et al.,* 2014). Ao longo desta tese, várias estruturas de peptídeos foram obtidas utilizando este servidor.

O SWISS-MODEL (https://swissmodel.expasy.org/) é um servidor online no qual é possível realizar a modelagem de proteínas por homologia. Para realizar a modelagem nesse servidor algumas entradas são possíveis: 1) utilizando apenas a sequência da proteína e o servidor encontra uma proteína que possua semelhança e modela a proteína baseado na estrutura tridimensional mais próxima do PDB; e 2) utilizando como entrada a sequência e uma estrutura tridimensional desejável. Nesse segundo modo, é interessante para estudar o efeito das mutações em uma estrutura de uma proteína que já está sendo estudada na conformação nativa. O SWISS-MODEL constrói o modelo da estrutura tridimensional da proteína em quatro passos principais. O primeiro passo é a identificação de modelos estruturais que já possuem estruturas tridimensionais resolvidas por métodos experimentais. O segundo passo é o alinhamento das sequências e estruturas para encontrar as diferenças entre elas. No terceiro passo, o modelo da proteína é construído realizando trocas dos aminoácidos que são diferentes e reduzindo a energia da estrutura para obter conformações de menor energia, logo, a mais estável. Esse modelo construído no terceiro passo é então testado quanto à sua qualidade no quarto passo. Nele, os átomos dos resíduos de aminoácidos são analisados se estão em conformações favoráveis, caso a estrutura satisfaça as condições, o modelo estará pronto. Vale salientar que, mesmo o software realizando essa avaliação do modelo, é necessário validar a estrutura utilizando outros programas, como o MolProbity (BIENERT *et al.,* 2017; STUDER *et al.,* 2021, 2020; WATERHOUSE *et al.,* 2018).

O programa AlphaFold (https://alphafold.ebi.ac.uk/) foi considerado o melhor software para realizar predições de estruturas tridimensionais de proteínas no 14° *Community Wide Experiment on the Critical Assessment of Techniques for Protein Structure Prediction* (CASP14). Utilizando inteligência artificial para realizar

as predições de estruturas proteicas e com uma metodologia de alta acurácia, como demonstrado na figura 18, o AlphaFold obteve uma média de variação de RMSD de 1.5 Å entre as estruturas modeladas e as estruturas nativas das proteínas, enquanto o software que ganhou o segundo lugar do desafio obteve uma média de variação de RMSD de 3.5 Å. Além da sua alta acurácia, o AlphaFold possui metodologia capaz de obter estruturas que não possuem proteínas similares com estruturas elucidadas, ou seja é capaz de realizar predição *de novo*, o que ainda é considerado um desafio até mesmo para resolução de estruturas de proteínas por métodos experimentais, como a cristalografia de raios-X. Em 2022, o AlphaFold possui mais de 200 milhões de proteínas com estruturas modeladas. Para demonstrar a revolução alcançada por esse software, pode-se comparar a quantidade de proteínas com estruturas depositadas no PDB (195 mil estruturas) e no AlphaFold com 200 milhões de estruturas (JUMPER *et al.,* 2021b; TUNYASUVUNAKOOL *et al.,* 2021).

Figura 18. Modelagem de proteínas utilizando o software AlphaFold. O software utiliza inteligência artificial e possui alta acurácia.

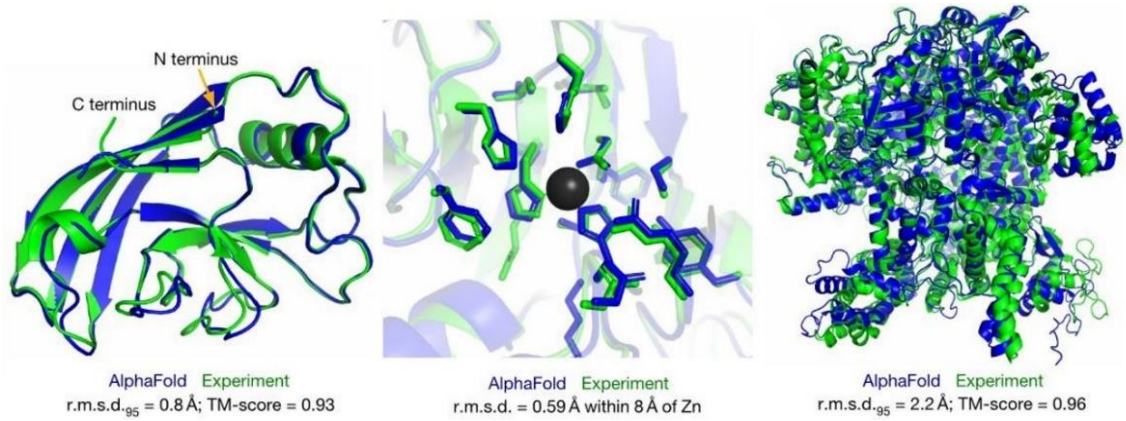

Fonte: JUMPER *et al.,* 2021b

2.3 Docking molecular em proteínas (AutoDock Vina, FRODOCK e ClusPRO)

Docking molecular na tradução para o português significa encaixe molecular. Como o nome faz referência, o docking molecular representa um encaixe entre moléculas, seja entre duas proteínas, de uma proteína com um peptídeo e mesmo entre uma proteína e pequenos ligantes. No docking molecular se busca encaixes entre as duas moléculas, todavia esse encaixe deve ser o mais próximo do

que acontece na natureza, logo, diversas metodologias são utilizadas para obter o melhor, como a busca por estruturas com menor energia livre, conformações favoráveis entres as moléculas, encaixe em sítios ativos, como é possível de observar na figura 19 (GOUTHAMI *et al.,* 2022).

Figura 19. Procedimento padrão para realização de docking molecular.

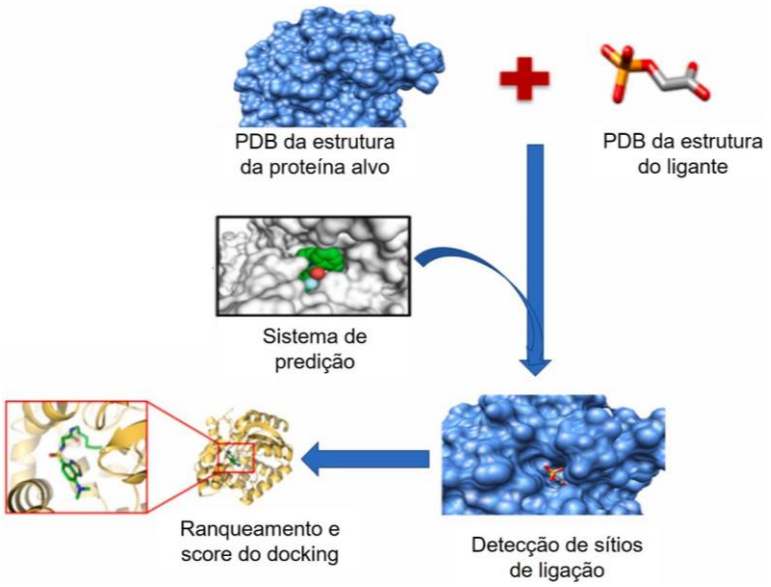

Fonte: GOUTHAMI *et al.,* 2022.

Para o docking molecular possuir uma alta acurácia é necessário atentar-se para a preparação dos arquivos, que é uma etapa crucial e, frequentemente, não realizada por pesquisadores que não possuem expertise no assunto. Na etapa de preparação de arquivos, realiza-se um estudo das protonações das moléculas e adiciona-se os átomos de hidrogênio que não estão presentes em estruturas tridimensionais cristalográficas.

Diversos softwares estão disponíveis para realizar docking molecular. Dessa forma, é necessário sempre testar o programa que será utilizado com o sistema de interesse antes de realizar as simulações. O teste inicial pode ser realizado através de um processo chamado redocking, no qual utiliza-se complexos com estruturas tridimensionais disponíveis, com elas se separam as cadeias de proteínas ou mesmo a proteína do ligante que será testado. Após, essas moléculas separadas, são utilizadas como entrada para o docking molecular (HOFNY *et al.,* 2021). Caso o software de docking possua uma alta acurácia para o sistema em

questão, o resultado deve ser muito próximo à estrutura do complexo obtida experimentalmente (FEDERICO *et al.,* 2021). Com o método de docking testado através do redocking, pode-se simular a interação com outras moléculas.

A escolha do software para realização do docking molecular também deve levar em consideração as metodologias que possuem maior acurácia descrita na literatura. Semestralmente, ocorre o desafio CAPRI (*Critical Assessment of PRediction of Interactions*), no qual vários grupos de pesquisas se unem e testam seus softwares de docking molecular para diferentes sistemas proteicos e os resultados são divulgados na forma de artigo na revista *Proteins: Structure, Function, and Bioinformatics* (LENSINK *et al.,* 2020). É importante que os pesquisadores que trabalham ou desejem trabalhar com docking molecular estejam sempre atentos aos resultados do desafio CAPRI, visto que são divulgados os melhores métodos de docking. Além do desafio de CAPRI, outros estudos na literatura fazem pesquisas de comparação (Benchmark) entre os métodos de docking molecular disponíveis (FAN *et al.,* 2021; GARCÍA-ORTEGÓN *et al.,* 2022; NGO *et al.,* 2021).

O AutoDocking Vina é um software utilizado para docking entre pequenas moléculas e proteínas. Possuem as vantagens de ser rápido e com alta acurácia. No teste de acurácia, o programa conseguiu atingir 78% de acerto no modo de interação das moléculas com proteínas com uma variação de RMSD menor que 2 Å. Por ser rápido, não exige muito tempo para realizar as simulações e é possível fazê-las utilizando pouco recurso computacional. Além disso, é uma metodologia bastante utilizada, sendo citada por mais mil artigos científicos (EBERHARDT *et al.,* 2021; TROTT; OLSON, 2009). Uma desvantagem do programa é que seu código é fechado, ou seja, a metodologia utilizada para realizar as simulações não é divulgada.

O FRODOCK (*Fast Rotational DOCKing*) é um programa online de docking molecular utilizado para obter interações entre proteínas. Ao realizar o processo utilizando o FRODOCK é possível escolher uma opção de interação entre as proteínas: enzima-substrato, anticorpo-antígeno, outras ou desconhecidas. Nos trabalhos desenvolvidos nesta tese, o FRODOCK foi utilizado para analisar as interações entre peptídeos e proteínas, visto que no estudo comparativo de Agrawal e colaboradores (2019), o FRODOCK foi considerado o melhor software para docking entre peptídeo e proteína.

ClusPRO foi o software que ganhou o desafio CAPRI entre os anos 2016

e 2019 e foi considerado o melhor programa para realização de docking molecular entre proteínas (LENSINK *et al.,* 2020). Esse programa utiliza três passos principais para a realização da predição: 1) Docking rígido entre as proteínas, ou seja, as proteínas não mudam as posições dos seus átomos e são gerados mais de um bilhão de modelos, considerando as rotações possíveis das proteínas, bem como as interações eletrostáticas; 2) Todos os modelos são agrupados de acordo com as menores variações (RMSD) entre eles e os mais parecidos são agrupados em um único cluster; 3) Por fim, os modelos agrupados passam por uma minimização de energia para obter a estrutura mais estável e os resultados são disponibilizados, como é possível observar na figura 20. Os desenvolvedores do ClusPRO afirmam que apesar da metodologia possuir alta acurácia, seu ranqueamento final ainda se encontram muitas falhas, sendo uma desvantagem do programa (DESTA *et al.,* 2020; KOZAKOV *et al.,* 2017a).

2.4 Simulação de dinâmica molecular

2.4.1 Simulações com proteínas

Simulações de dinâmica molecular são realizadas para obtenção da trajetória dos átomos nas moléculas. Para isso, são utilizados campos de forças que possuem a parametrização dos potenciais de interações das moléculas de interesse, seja proteínas, carboidratos ou lipídios. Através das simulações é possível compreender a termodinâmica, a cinética e a mecânica das moléculas envolvidas (ORTEGA *et al.,* 2022; WANG, Jinan *et al.,* 2021).

Todos os cálculos realizados na dinâmica molecular ainda possuem a desvantagem de considerarem a matéria estritamente como partícula e utilizarem apenas as equações de movimento de Newton nas simulações. O ideal seria utilizar física quântica para prever esse movimento, pois consideraria a dualidade partícula-onda da matéria. Entretanto, uma simulação utilizando física quântica requereria um custo computacional muito grande, sendo praticamente impossível com os recursos atuais (ALBUQUERQUE *et al.,* 2020). Apesar disso, utilizando-se simulações de dinâmica molecular é possível obter resultados próximos aos observados experimentalmente (WANG, Jinan *et al.,* 2021).

Figura 20. Comparação entre resultado do docking molecular realizado no ClusPro (proteínas em azul) e dados experimentais (proteínas em magenta) com e sem restrições aplicadas.

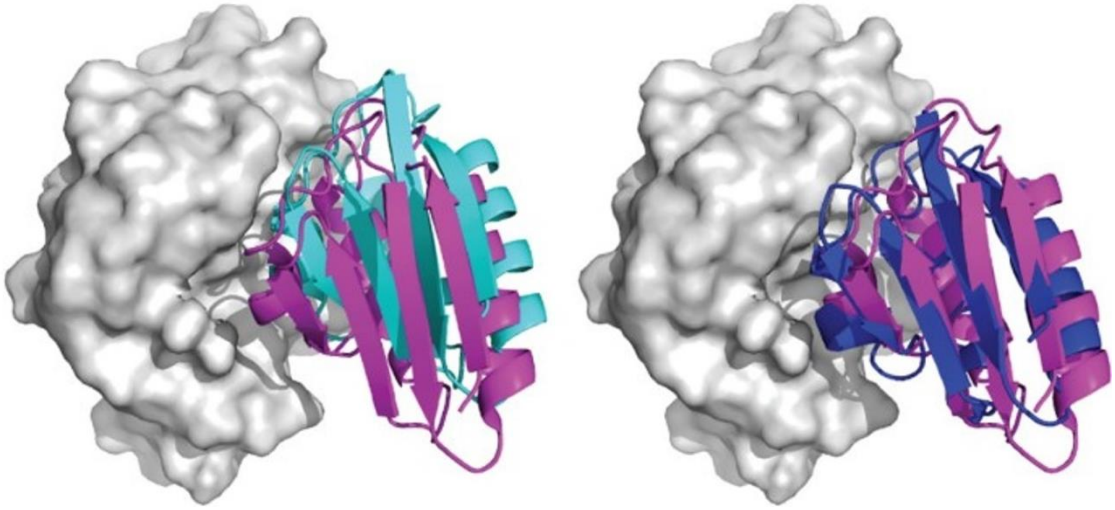

Fonte: KOZAKOV *et al.,* 2017b.

Diversos pacotes de programas são possíveis para realização de simulações de dinâmica molecular, como GROMACS, UMBER, NAMD. Nesta tese foi utilizado, principalmente, o pacote GROMACS por ser grátis e possuir um custo computacional menor, logo, sendo mais rápido (PÁLL *et al.,* 2020)..

O primeiro passo realizado na simulação de dinâmica molecular é a escolha do campo de força que irá trabalhar. O GROMACS disponibiliza 16 campos de forças para realizar as simulações: CHARMM36, AMBER03, AMBER94, AMBER96, AMBER99, AMBER99SB, AMBER99SB-ILDN, AMBERGS, CHARMM27, GROMOS96 43ª1, GROMOS96 43ª2, GROMOS96 45ª3, GROMOS96 53ª5, GROMOS96 53ª6, GROMOS96 54ª7 e OPLS-AA/L. A escolha do campo de força que será utilizado na simulação deve ser feita levando em consideração a parametrização das moléculas de interesse, ou seja, é necessária uma pesquisa na literatura para identificar o campo de força que melhor parametriza as moléculas de interesse (JING *et al.,* 2019)..

Após a escolha do campo de força, é realizada a solvatação do sistema. Nesse passo, o sistema de estudo é adicionado dentro de uma caixa de água. Podendo utilizar o modelo de água explicita, no qual as moléculas de água estarão presentes durante a simulação, ou modelo de água implícita, em que as moléculas de água não estão presentes na simulação e é utilizada uma função dielétrica que

considera os espaços vazios como água. Ao utilizar o modelo de água implícita, economiza-se tempo computacional. Todavia, as interações realizadas entre as macromoléculas e as moléculas de água são desconsideradas. A caixa de água pode ser construída em diferentes geometrias, como cúbica e paralelepipédica, esférica. Estudos demonstram que a geometria da caixa não interfere nos resultados da simulação, entretanto interfere no tempo para a realização da simulação.

Com a caixa de água construída, o próximo passo é realizar a ionização. Nessa etapa, íons são adicionados à caixa. A adição de íons vai depender do objetivo de cada estudo, porém normalmente é utilizada a ionização do padrão fisiológico: 0,15 M do íon positivo sódio (Na^+) e 0,15 M do íon negativo cloreto (Cl^-). Em alguns estudos, adicionam-se íons apenas para neutralizar a caixa de água, para que possua carga líquida final igual a 0. Um modelo de caixa de água solvatada e com íons é demonstrado na figura 21. Com os íons adicionados, executa-se a minimização de energia ou também denominado otimização de geometria. Nesse passo, a estrutura tridimensional de todas as moléculas presentes na caixa é otimizada e encontrada um mínimo de energia local. Posteriormente à minimização, é necessário realizar o equilíbrio de temperatura e pressão da caixa. Na fase de equilíbrio, a temperatura e a pressão são aumentadas de forma lenta até obter a temperatura e impressão desejável.

Após todas as preparações, realiza-se a simulação de dinâmica molecular. Essa etapa é a fase mais demorada e depende do tempo de dinâmica molecular que será utilizado (LEMKUL, 2019). Atualmente, no último trimestre de 2022, é razoável realizar pelo menos três simulações, triplicata, de pelo menos 100 ns, cada uma, para complexo entre proteínas. Com o avanço da tecnologia e das técnicas, os revisores exigem maior tempo de simulação, bem como repetições. Um tutorial completo de simulação de dinâmica molecular encontra-se disponível em: http://www.mdtutorials.com/gmx/.

Alguns sistemas não estabilizam com apenas 100 ns, logo, é necessário realizar simulações de dinâmica molecular mais longas. É possível detectar se o sistema estabilizou na simulação através da observação da variação de RMSD (*Root Mean Square Deviation*). A variação de RMSD é a distância entre as posições atômicas das proteínas sobrepostas, geralmente calculado em Å (AIER; VARADWAJ; RAJ, 2016). Considera-se que o sistema está estabilizado após pelo menos 20 ns de simulação com uma variação de RMSD menor que 1 Å, como demonstrado na figura

22.

Figura 21. Passos para simulação de dinâmica molecular.

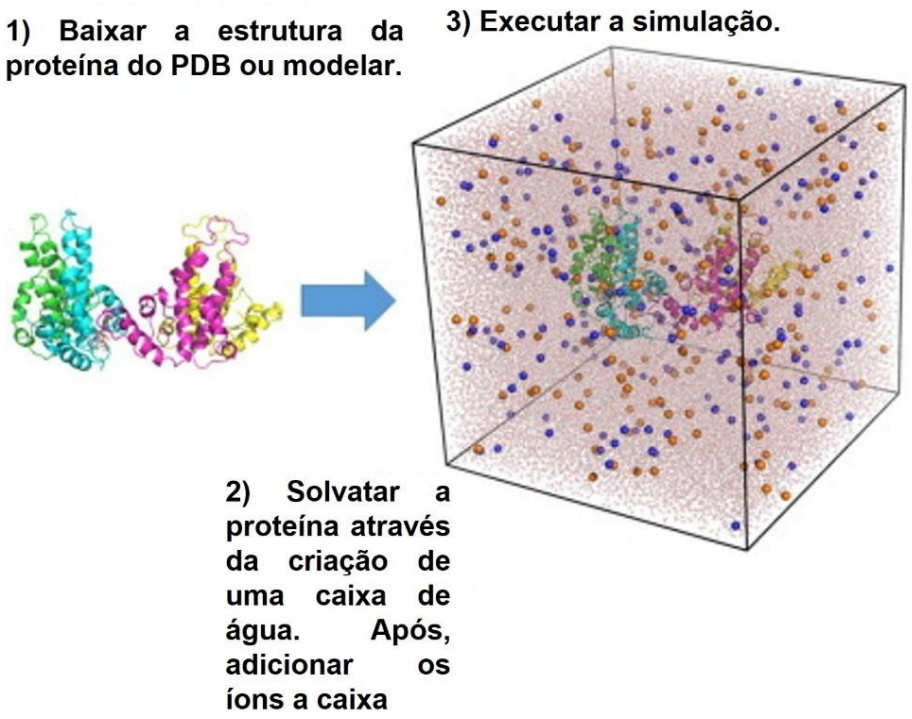

Fonte: MORGNANESI *et al.,* 2015.

2.4.2 Simulações com membranas

O processo de simular a dinâmica molecular com membranas é similar ao processo com proteínas, porém, com alguns passos adicionais. Para início é necessário obter a membrana alvo para simular. Muitos artigos utilizam membranas simples compostas apenas pelo fosfolipídio fosfatidilcolina (POPC) (VELASCO-BOLOM; CORZO; GARDUÑO-JUÁREZ, 2018; VENABLE; KRÄMER; PASTOR, 2019). Entretanto, observa-se que a utilização de membranas biomiméticas que simulam as membranas de interesse têm aumentado. Apesar de requerer um custo computacional maior, simular dinâmicas moleculares com membranas mais realísticas aproxima-se mais da realidade, logo os resultados possuem maior acurácia, como demostrado na figura 23 (FREIRE *et al.,* 2021; RZYCKI; KRASZEWSKI; DRABIK, 2021; TIMMONS *et al.,* 2019).

Figura 22. Exemplos de simulações de dinâmica molecular com proteínas. A estabilização das estruturas é observada quando a variação de RMSD é menor que 1 Å.

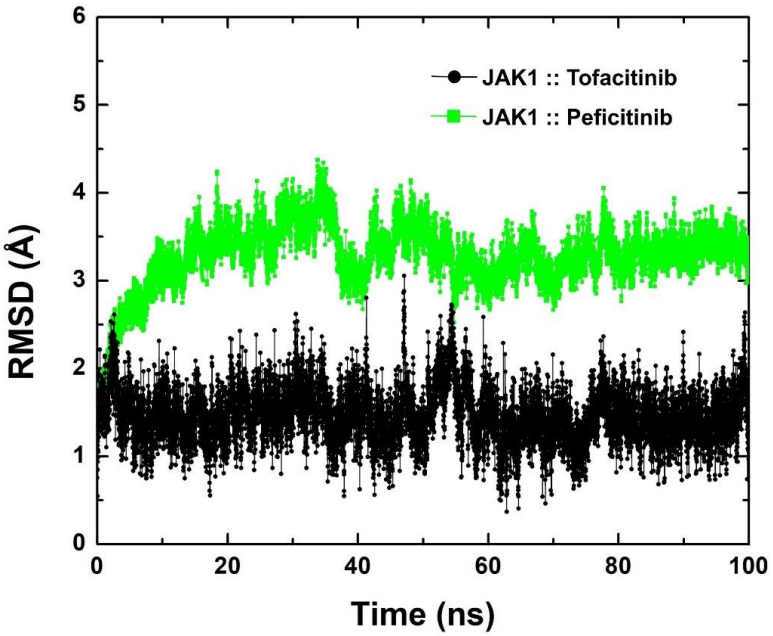

Fonte: Elaborado pelo autor.

Antes de iniciar a construção da membrana, é necessário pesquisar na literatura a composição da membrana de interesse. Após obter as informações dos fosfolipídios e esteróis que compõem a membrana, pode-se utilizar o software CHARMM-GUI (https://www.charmm-gui.org/) para construí-la. O CHARMM-GUI é um software online e gratuito, sendo necessário apenas realizar um cadastro. Nesse programa, é possível construir diversos tipos e tamanhos de membranas com diferentes fosfolipídios e esteróis. Também é possível construir complexos entre proteínas ou peptídeos com membranas. O pesquisador consegue escolher a quantidade de componentes na membrana, bem como a quantidade de cada, logo, é possível construir membranas com diferentes composições e mais realísticas (JO *et al.,* 2009; LEE, Jumin *et al.,* 2019).

Após a construção da membrana, o CHARMM-GUI realiza a solvatação e a ionização do sistema e disponibiliza todos os arquivos de parametrização da membrana. Isso é muito importante, visto que esses arquivos serão utilizados como entrada na simulação de dinâmica molecular, ou seja, o software já constrói as membranas com o objetivo da realização da simulação e esses arquivos podem ser utilizados como entrada em diversos programas de dinâmica molecular, como

GROMACS, AMBER, NAMD, OpenMM e CHARMM.

Figura 23. Simulação de dinâmica molecular do peptídeo CaD23 que interage com membrana mimética de bactéria, mas não interage com membrana de mamífero.

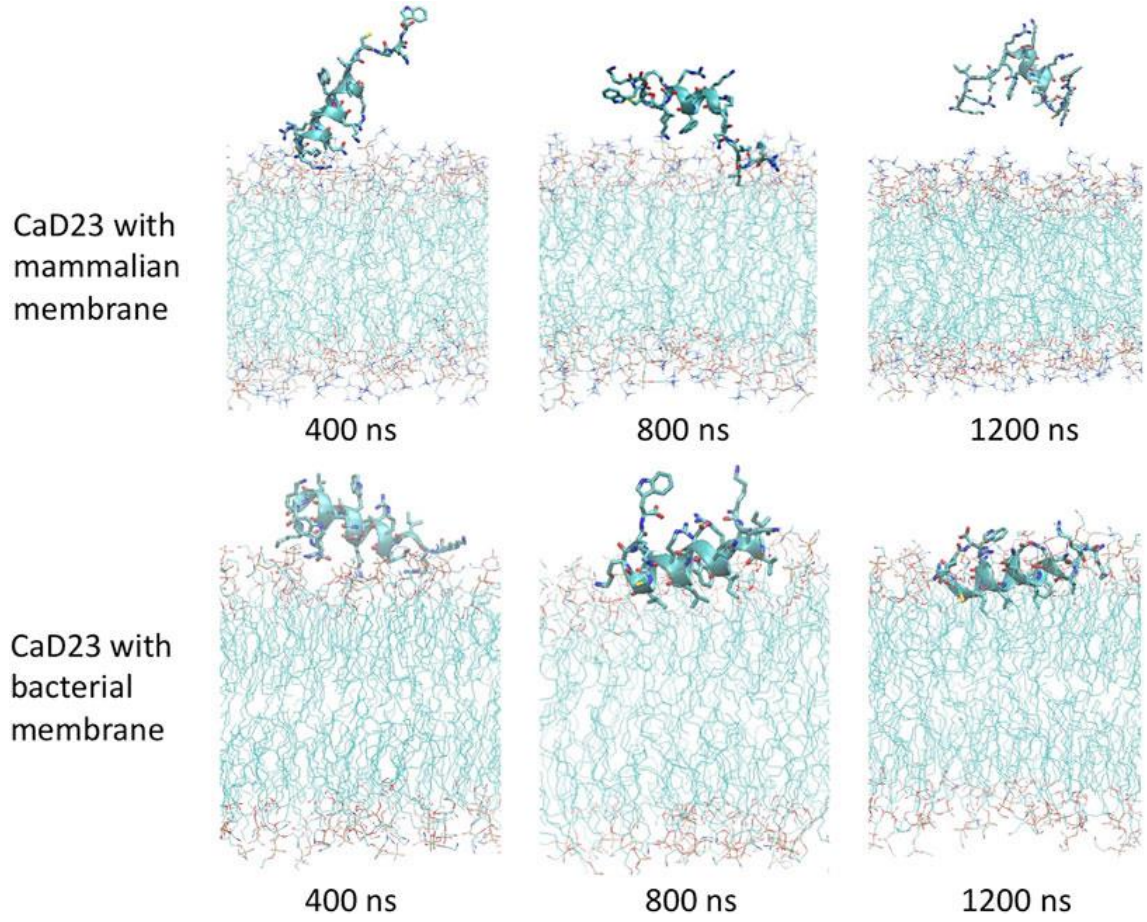

Fonte: TING *et al.,* 2021.

O tempo de simulação utilizado nas simulações de dinâmica molecular com membranas é variável na literatura. Observa-se um padrão dos artigos com simulações de membranas de 1000 ns ou 1 µs. Como já foi comentado anteriormente, quanto maior o tempo da simulação maior será o custo computacional. Alguns grupos de pesquisas já conseguem realizar dinâmicas moleculares por um tempo de 5000 ns (HONG *et al.,* 2021; KIM; YOO; LEE, 2022; PANDEY *et al.,* 2020; UPPAL *et al.,* 2023). Logicamente, quanto maior o tempo da dinâmica mais próximo de um mínimo de energia global é alcançado.

Diversas aplicações são possíveis utilizando-se dinâmica molecular de membranas, como um dos trabalhos desta tese, em que se avalia a entrada de um peptídeo sintético numa membrana biomimética de levedura. Outras aplicações são

possíveis, como entrada de fármacos em compartimentos celulares, estudos envolvendo lipossomas, interação de moléculas com proteínas integrais de membrana.

2.5 Bioquímica quântica: MFCC e função dielétrica não homogênea

2.5.1 Fracionamento molecular com capas conjugadas (MFCC)

O estudo da interação entre proteínas e proteínas com ligantes através de dinâmica molecular fornece bons resultados de trajetória, entretanto, há algumas limitações, visto que as simulações de dinâmica utilizam apenas mecânica clássica, as equações de Newton para calcular as trajetórias e os campos de forças são aproximações dos dados experimentais (ALBUQUERQUE *et al.,* 2020). Sabe-se que o ideal seria utilizar a mecânica quântica para observar o comportamento das moléculas, porém seria necessário um custo computacional muito grande, que ainda é impossível. Para conseguir resolver esses problemas, utiliza-se uma metodologia híbrida, na qual aplicamos a bioquímica quântica no cálculo das energias de interação.

Para calcular as energias de interação de duas proteínas completas através de bioquímica quântica seria inviável, visto o custo computacional muito grande. Dessa forma, desenvolveu-se o método de fracionamento molecular com capas conjugadas (MFCC), também citado como dividir para conquistar. Nesse método, os resíduos de aminoácidos que estão presentes na superfície de contato entre as duas proteínas são cortados em trio, o resíduo de interesse e os que estão ligados a ele por ligação peptídica. De cada resíduo da área de contato é lançado um raio de 8 Å e todos os resíduos da outra proteína que estiverem dentro desse raio são utilizados para o cálculo de energia de interação. Junto com os resíduos que estão presentes dentro do raio, também são utilizadas suas capas que são os resíduos vizinhos que estão ligados por ligações peptídicas, como observado na figura 24. Esse procedimento é realizado para obter um conjunto com menos de 100 átomos sendo possível a execução dos cálculos quânticos.

Com as trincas de resíduos de aminoácidos de cada proteína, separa-se em quatro novos arquivos com o objetivo de obter apenas a energia de interação

entre os dois resíduos de interesse. No primeiro arquivo, é calculada a energia total do sistema com os resíduos de interesse e suas capas. No segundo arquivo, calcula-se a energia do sistema, porém sem o resíduo de interesse da proteína j. No terceiro, calcula-se a energia de todos os resíduos sem o resíduo de interesse da proteína i. Por fim, no quarto, a energia calculada é apenas das capas dos resíduos, como demonstrado na figura 25.

Figura 24. Demonstração hipotética dos resíduos utilizados para o cálculo da energia de interação. O resíduo da proteína i, que está presente na superfície de contato com a proteína j, é utilizado para lançar um raio 8 Å e todos os resíduos que estão dentro desse raio na proteína j são utilizados para o cálculo quântico. Tanto os resíduos de interesse da proteína i como os da proteína j são acompanhados dos resíduos ligados covalentemente a eles no cálculo (R_{i-1}, R_{i+1}, R_{j-1} e R_{j+1}).

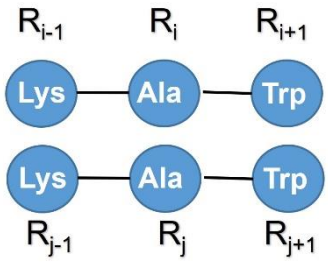

Fonte: Elaborado pelo autor.

Finalmente, a energia de interação entre os resíduos das duas proteínas é calculada de acordo com a equação:

$$E_I\ (R_i - R_j) = E\ (C_{i-1}R_iC_{i+1} + C_{j-1}R_jC_{j+1}) - E\ (C_{i-1}R_iC_{i+1} + C_{j-1}\ C_{j+1}) - E\ (C_{i-1}\ C_{i+1} + C_{j-1}R_jC_{j+1}) + E\ (C_{i-1}\ C_{i+1} + C_{j-1}\ C_{j+1})$$

Figura 25. O cálculo de energia de interação entre dois resíduos de duas proteínas é realizado utilizando-se quatro arquivos. No primeiro, todos os resíduos; no segundo sem o resíduo da proteína i; no terceiro sem o resíduo da proteína j e, por fim, apenas as capas conjugadas.

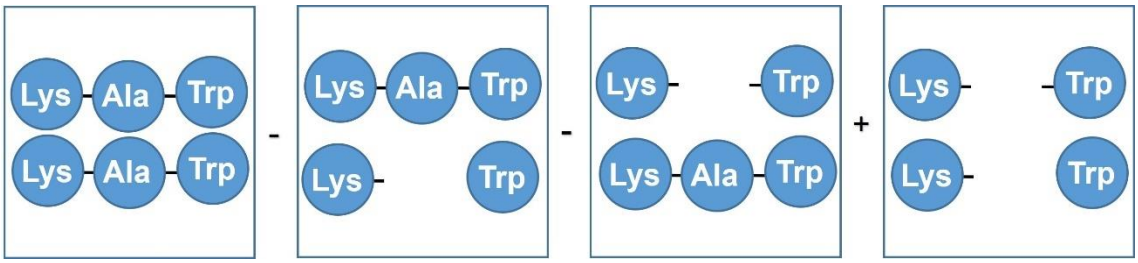

Fonte: Elaborado pelo autor.

Esses cálculos são realizados com todos os resíduos que participam da interface das duas proteínas. Na realização do cálculo quântico é utilizada a teoria do funcional da densidade (DFT).

2.5.2 Função dielétrica não homogênea

Caso o sistema apresente moléculas de água explícitas, são consideradas para o cálculo as moléculas que estão até 3 Å de distância dos resíduos de interesse. Alguns estudos desconsideram as moléculas de água explícitas e utilizam um modelo de água implícita no cálculo, através de uma função dielétrica homogênea, o que reduz o custo computacional do cálculo, porém esse modelo apresenta a desvantagem de subestimar ou superestimar as interações eletrostáticas com as moléculas de água (MORAIS *et al.,* 2020).

A função dielétrica da água é em torno de 80, enquanto o vácuo seria 0. Observando isso, no complexo de proteínas as regiões mais externas possuem função dielétrica próxima a 80 e regiões mais internas e apolares seriam mais próximas de zero. Constata-se que utilizando valores de funções dielétricas baixos, como foi utilizado em alguns estudos o valor 4, ocorre uma superestimação da energia de interação entre as moléculas. Isso é possível de visualizar principalmente quando se analisa o gráfico de convergência de energia de interação desses estudos, pois não apresentam uma convergência e tendem ao -∞. Outros estudos utilizam a função dielétrica igual a 40, entretanto, sabe-se que em regiões mais internas das proteínas esse valor seria muito alto, o que ocasionaria uma subestimação da energia de interação (DANTAS et al., 2015).

Visando resolver esse problema, nosso grupo de pesquisa desenvolveu um método capaz de calcular a função dielétrica não homogênea, dessa forma, calculamos uma média da função dielétrica em cada região da proteína, como mostrado na figura 26. Com isso, é possível obter resultados com maior acurácia do que utilizando uma função dielétrica homogênea.

Figura 26. Representação da função dielétrica não homogênea do complexo uPA-uPAR. Primeiro sistema proteico com função dielétrica calculada.

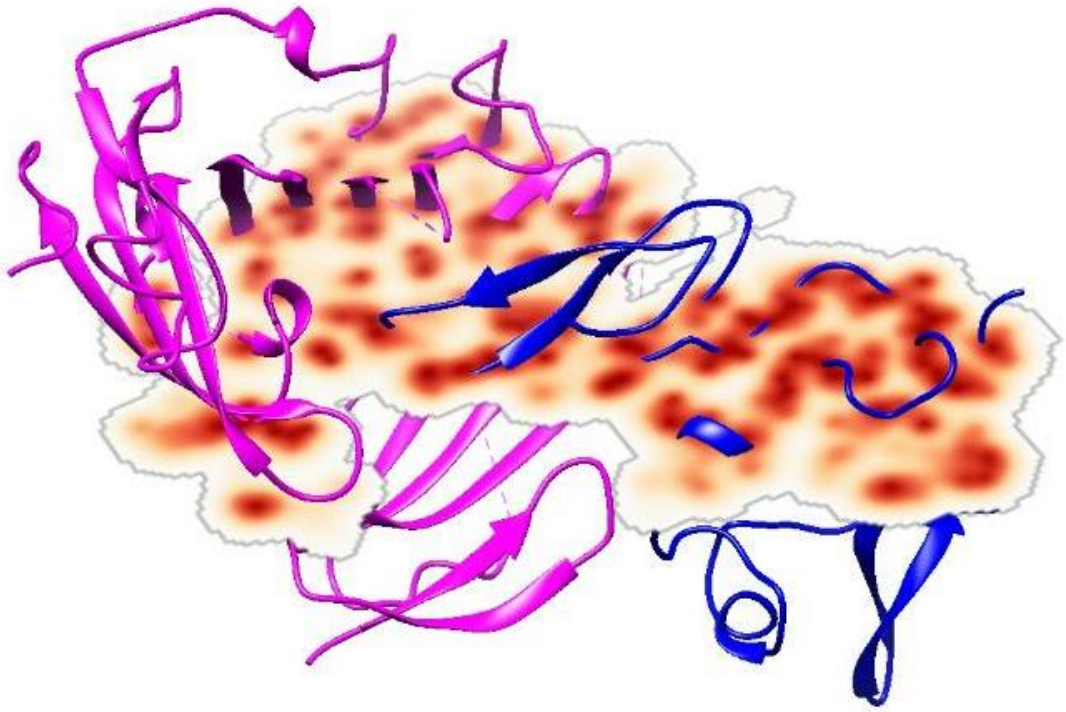

Fonte: MORAIS *et al.,* 2020.

3 NO AUGE DA PANDEMIA COVID

3.1 A pandemia Covid e nossas contribuições

SARS-CoV-2 pertence à família Coronaviridae, sendo um vírus envelopado apresentando um RNA de fita simples positiva com tamanho estimado de 30 kB, figura 27 (HU *et al.,* 2021). O SARS-CoV-2 é o agente etiológico causador da pandemia de covid-19 que já registrou mais de 630 milhões de casos e 6,5 milhões de mortes. Segundo a Organização Mundial de Saúde (OMS), esses números são subestimados devido à subnotificação. A OMS estima que o total de mortes causadas, diretamente ou indiretamente, por covid-19 seja próximo a 15 milhões, no mundo.

Figura 27. Estrutura do vírus SARS-CoV-2.

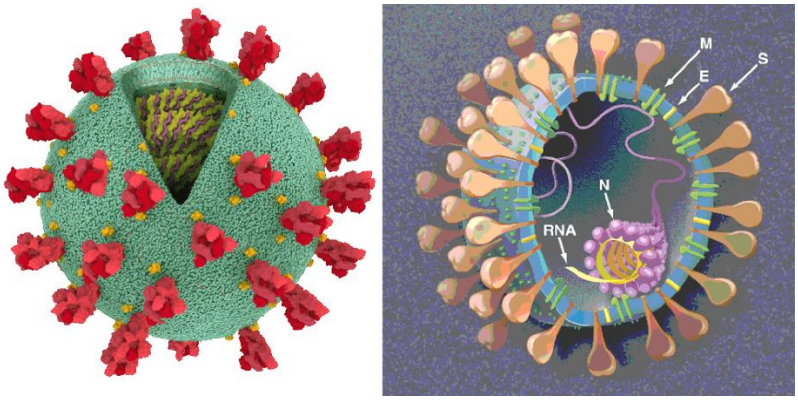

Legenda: M: membrana lipídica; S: espícula de contato do vírus com receptores celulares; E: envoltório glicoproteico; RNA+: material genético viral; N: capsídeo proteico.
Fonte: UZUNIAN, 2020

SARS-CoV-2 possui uma similaridade de, aproximadamente, 78% com SARS-CoV-1, entretanto, as diferenças entre eles são responsáveis pela grande diferença observada no número de casos, bem como na alta transmissibilidade do SARS-CoV-2, o qual rapidamente ocasionou uma pandemia global, enquanto os surtos de SARS-CoV-1 e MERS-CoV aconteciam de forma endêmica em regiões específicas (SOUZA *et al.,* 2021). A transmissão do coronavírus entre humanos ocorre principalmente por gotículas de secreções do nariz e da boca. A doença, em alguns casos, apresenta apenas sintomas brandos semelhantes aos da gripe, como febre e tosse, porém casos mais graves da doença ocasionam a morte do paciente

(RASMUSSEN; POPESCU, 2021).

A invasão do vírus a células humanas ocorre através da interação do domínio de ligação ao receptor (RBD) da glicoproteína spike (proteína S) do vírus com a enzima conversora de angiotensina 2 (ECA2, em inglês ACE2) de humanos, como demostrado na figura 28. Após entrar na célula humana, o vírus controla a maquinária celular para sintetizar o seu genoma e suas proteínas (MALDONADO; BERTELLI; KAMENETZKY, 2021).

Figura 28. Interação entre proteína spike do SARS-CoV-2 com proteína ECA2 de humano.

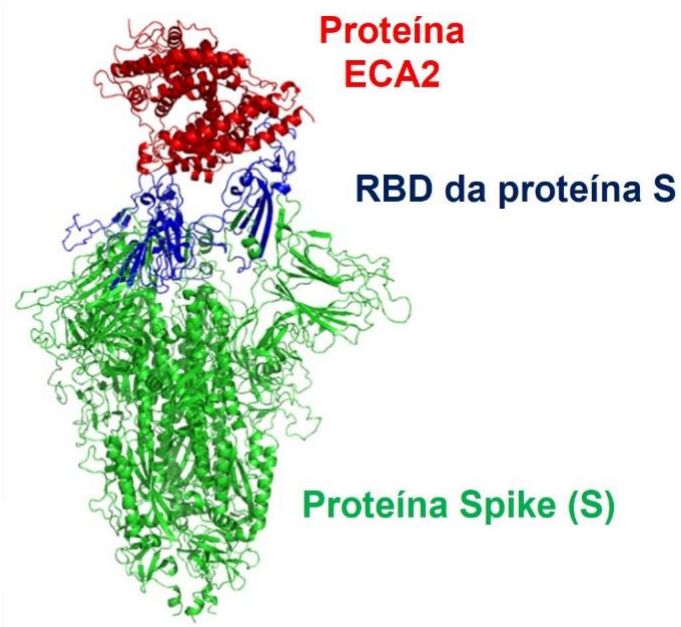

Fonte: SOUZA et al., 2022, adaptada.

Alterações na proteína S do SARS-CoV-2, principalmente na região RBD, aumentaram a afinidade entre a proteína do vírus com a proteína humana ECA2, o que explica a diferença de transmissibilidade quando comparado com SARS-CoV e MERS-CoV. A afinidade entre a proteína S de SARS-CoV-2 é em torno de 20 vezes mais forte com ECA2 de humanos que a afinidade entre SARS-CoV com ECA2, resultando em uma transmissão mais rápida de SARS-CoV-2 entre humanos (SOUZA *et al.,* 2021).

Observando essa interação importante para o estabelecimento da covid-19 pelo SARS-CoV-2, diversos estudos avaliaram o potencial de drogas para impedir

que a interação ocorra, bloqueando a entrada do vírus nas células. Nosso grupo de pesquisa também utilizou essa interação como alvo chave para o desenvolvimento de medicamentos capazes de inibir o SARS-CoV-2. No primeiro estudo, analisamos a capacidade de 8 peptídeos antimicrobianos sintéticos de impedir a interação entre a proteína S e a ECA2 através de docking molecular. Observamos que os peptídeos *Mo*-CBP$_3$-PepII and PepKAA são capazes de interagir com a proteína S na região do RBD, o que alteraria a conformação da região, resultando em um encaixe incorreto entre a proteína S e a ECA2. Nesse mesmo estudo, avaliamos a capacidade desses peptídeos interagirem com a ECA2 e foi constatado que a interação com a ECA2 ocorre de forma fraca e não causa alterações conformacionais nessa proteína. Artigo presente no apêndice F.

Após esse estudo, realizamos o cálculo quântico da interação entre as proteínas S e ECA2, obtendo as principais regiões de interações, bem como os resíduos de aminoácidos principais para interação. A partir desse resultado, propomos peptídeos derivados da ECA2, os quais são capazes de interagir com a proteína S, visto que são baseados em regiões da ECA2 que já interagiam com a proteína S, assim bloqueando a interação da proteína S com a ECA2 ou mesmo ocasionando uma alteração na forma de interação, o que impediria a entrada do vírus as células. Artigo presente no tópico 3.3.

Além da proteína S de SARS-CoV-2, outras proteínas também são importantes para o vírus, como a principal protease do vírus (M^{pro}) que é uma enzima chave envolvida na transcrição e replicação de SARS-CoV-2, sendo uma enzima essencial. Logo, a inibição de M^{pro} é uma forma de combater o vírus. Observando isso, realizamos estudos *in silico* para testar se nossos peptídeos seriam capazes de inibir a atividade dessa enzima. Dos 8 peptídeos testados, *Rc*Alb-PepI, PepGAT e PepKAA apresentaram menores energias de interação, desse modo, interações mais fortes. Constatamos, ainda, que esses peptídeos não interagem no sítio da ativo da protease, mas em outras regiões, indicando uma possível inibição alostérica. Através da simulação de dinâmica molecular, visualizamos que a interação desses peptídeos com a protease reduziu o volume do sítio ativo da protease, o que resultaria na inibição da enzima. O artigo completo está adicionado na tese no próximo tópico.

3.2 Quantum biochemistry, molecular docking, and dynamics simulation revealed synthetic peptides induced conformational changes affecting the topology of the catalytic site of SARS-CoV-2 main protease

Artigo publicado na revista: Journal of Biomolecular Structure & Dynamics.
DOI: https://doi.org/10.1080/07391102.2021.1920464

Running Head: The Catalytic Site of SARS-CoV-2 Main Protease is affected by Synthetic peptides

Jackson L. Amaral[a,*], Jose T. A. Oliveira[a], Francisco E.S. Lopes[a,c], Cleverson D. T. Freitas[a], Valder N. Freire[b], Leonardo V. Abreu[a], Pedro F. N. Souza[a,*]

[a]*Department of Biochemistry and Molecular Biology, Federal University of Ceará, Fortaleza, Ceará, Brazil - CEP 60.440-554.*
[b]*Department of Physics, Federal University of Ceará, Fortaleza, Ceará, Brazil - CEP 60.440-554.*
[c]*Center for Permanent Education in Health Care-CEATS / School of Public Health of Ceará-ESP-CE*

Corresponding Author
*****Corresponding author: Biochemistry and Molecular Biology Department, Federal University of Ceará, CE, Brazil, Laboratory of Plant Defense Proteins, Av. Mister Hull, P.O. Box: 60451 Fortaleza, CE, Brazil. Tel: +55 85 33669823; Fax: +55 85 33669789.
Email: pedrofilhobio@gmail.com, jacksoncesarc@gmail.com

ORCID: 0000-0003-2524-4434 (P. F. N. Souza), 0000-0002-8745-1247 (Jackson L. Amaral)

Abstract

The recent outbreak caused by SARS-CoV-2 continues to threat and take many lives all over the world. The lack of an efficient pharmacological treatments are serious

problems to be faced by scientists and medical staffs worldwide. In this work, an *in silico* approach based on the combination of molecular docking, dynamics simulations, and quantum biochemistry revealed that the synthetic peptides *RcAlb*-PepI, PepGAT, and PepKAA, strongly interact with the main protease (Mpro) a pivotal protein for SARS-CoV-2 replication. Although not binding to the proteolytic site of SARS-CoV-2 Mpro, *RcAlb*-PepI, PepGAT, and PepKAA interact with other protein domain and allosterically altered the protease topology. Indeed, such peptide-SARS-CoV-2 Mpro complexes provoked dramatic alterations in the 3D structure of Mpro leading to area and volume shrinkage of the proteolytic site, which could affect the protease activity and thus the virus replication. Based on these findings, it is suggested that *RcAlb*-PepI, PepGAT, and PepKAA could interfere with SARS-CoV-2 Mpro role *in vivo*. Also, unlike other antiviral drugs, these peptides have no toxicity to human cells. This pioneering *in* silico investigation opens up opportunity for further *in vivo* research on these peptides, towards discovering new drugs and entirely new perspectives to treat COVID-19.

Keywords: SARS-CoV-2 main protease; COVID-19; Synthetic Peptides.

3.2.1 Introduction

The current coronavirus outbreak caused by SARS-CoV-2 (Severe Acute Respiratory Syndrome Coronavirus 2) is the third epidemic event related to Coronaviruses in the last twenty years. The other two outbreaks that were caused by SARS-CoV-1 (Severe Acute Respiratory Syndrome Coronavirus 1) and MERS-CoV (Middle East Respiratory Syndrome Coronavirus) absolutely were not as severe and aggressive as SARS-CoV-2 [1,2]. To date, SARS-CoV-2 has infected 20,972,577 people in 215 countries with 750,377deaths [3–5] and transmission still continues to accelerate in different geographic region of the world. Often, the main problem caused by SARS-CoV-2 in infected patients is the immune response triggered against the virus infection. This immune reaction is characterized by overproduction of the proinflammatory cytokines TNF (tumor necrosis factors) and interleukins IL 6 and 1, known as the “cytokine storm”, which is a hyperinflammatory state that led to multiple-organ damage and dysfunction, specially of lungs, heart, liver, and kidneys [6–8].

First identified in Wuhan, China, genomic data analysis revealed that the human coronavirus SARS-CoV-2 has 70% genetic similarity with SARS-CoV-1 [9–11]. One of the common features amongst these coronaviruses is that they entry in human cells by physical interaction of the viral spike glycoprotein (S protein) with the human ACE2 (Angiotensin-Converting Enzyme 2) receptor, which is located at the cell membrane. Subsequently, conformational alteration of the S protein permits both the viral envelope to combine with the outer membrane and the transport of the virus' genetic material inside the human cell. However, amino acid sequence data analysis showed the SARS-CoV-2 S protein possesses mutations in the receptor-binding domain (RBD), in relation to that of SARS-CoV-1 S protein. Such genetic alteration leads to 20-fold increased affinity of SARS-CoV-2 S protein to ACE2, compared to SARS-CoV-1 S protein, and enhanced infectivity and velocity of SARS-CoV-2 spreading in humans [10,12,13]. Once inside the target cells, SARS-CoV-2 uses its main protease (Mpro), a pivotal protein for SARS-CoV-2 replication process, across the mechanism of viral replication [14]. Therefore, besides the viral spike glycoprotein (S protein), SARS-CoV-2 Mpro has taken as other potential pharmacological target for drug action against SARS-CoV-2 infection [15–18].

Although SARS-CoV-2 belongs to the genus Coronavirus, as SARS-CoV-1 and MERS-CoV, its infection leads to a completely novel and unknown disease, COVID-19 (Coronavirus Disease 2019), which is ending human life and taking over the economy globally [19]. Indubitable, there is an urgent need to discover and develop effective drugs to combat the virus and discontinue the disastrous consequences it has brought to mankind. To speed up novel drug discovery and development for COVID-19 treatment, the integrated use of bioinformatics approaches, such as molecular docking, dynamics simulations, and quantum analysis [17,20,21] allows to select potential antiviral molecules to be subsequently tested *in vitro* and *in vivo* against SARS-CoV-2 and other viruses.

Recently, our research group, by using bioinformatics approaches, found out that the synthetic peptides *Mo*-CBP3-PepII and PepKAA targeted SARS-CoV-2 spike protein and induced conformational alterations that disrupt its correct binding to the ACE2 receptor [22]. In this current study, which was conducted to further exploit the peptide-based therapeutic approach to treat COVID-19, the integrated use of these above mentioned bioinformatics methods was employed to assess whether any out of the following eight synthetic small peptides, *Mo*-CBP_3-PepI, *Mo*-CBP_3-

PepII, *Mo*-CBP$_3$-PepIII [23], *RcAlb*-PepI, *RcAlb*-PepII, *RcAlb*-PepIII [24], PepGAT, and PepKAA [25], which were designed based on plant proteins purified by our research group, could physically interact with SARS-CoV-2 Mpro and inhibit both its binding to ACE2 cell membrane receptor and its crucial activity. Briefly, amongst the tested peptides, RcAlb-PepI, PepGAT, and, particularly, PepKAA interact with SARS-CoV-2 Mpro at a region far away from the active site, but induce conformational alterations of the protease that promote shrinkage of its catalytic domain. These results suggest that *RcAlb*-PepI, PepGAT, and PepKAA could allosterically inhibit the SARS-CoV-2 Mpro activity and theoretically prevent viral replication and, consequently, *spread* of SARS-CoV-2 infection. Certainly, this hypothesis must be tested *in vitro* before being tested *in vivo*.

3.2.2 Methodology

3.2.2.1 Three-dimensional (3D) structures

The 3D structures of *Mo*-CBP$_3$-PepI, *Mo*-CBP$_3$-PepII, and *Mo*-CBP$_3$-PepIII were identical to those used by Oliveira et al. [23]. The 3D structures of *Rc*Alb-PepI, *Rc*Alb-PepII, and *Rc*Alb-PepIII were equal to those employed by Dias et al.[24]. The PepGAT and PepKAA 3D structures were identical to those used by Souza et al. [25]. The 3D structure files of SARS-CoV-2 main protease (Mpro) (PDB: 6M03) were downloaded from Protein Data Bank (PDB, https://www.rcsb.org/).

3.2.2.2 Molecular Docking (MD) Assays

Blind molecular docking analyses were carried out in FRODOCK 3.12 [26] and ClusPro 2.0 (https://cluspro.org), using the synthetic peptides as ligands against SARS-CoV-2 Mpro. Docking scores were used to select the peptides with the highest potential for interaction with SARS-CoV-2 Mpro. A score of 1 was assigned to the peptide with the highest docking value (referred to as the top scored pose). The scores of the subsequent peptides were decreased successively by a factor of 0.125 as the docking values decreased in relation to that of the peptide that received score 1. The peptide score obtained in the FRODOCK was added to that generated by

ClusPro. Based on the sum of scores, the three peptides with the highest potential were used to conduct the subsequent studies.

3.2.2.3 Molecular Dynamics Simulation

To stabilize the complexes formed between SARS-CoV-2 Mpro and the studied peptides before molecular dynamics simulation using Gromacs version 2018.4 [27], they were minimized and equilibrated. OPLS-AA/L all-atom force field [28,29] was used to build molecular topology. Then, a cubic water box of edge length 2 nm was created. Box solvation was done with the SPC/E water model, the systems were neutralized, and Na^+ and Cl^- added at 0.15 M concentration. Energy minimization of the complex structure was carried out until a negative potential energy and a maximum force below 10^3 kJ mol^{-1} nm^{-1} were attained. Next, temperature and pressure equilibration were performed during 100 ps simulation. Molecular dynamics simulations, in duplicate, were performed during 100 ns and the final structures generated were used for further analysis.

3.2.2.4 Interface analysis of the complexes formed between SARS-CoV-2 Mpro and the studied peptides

This analysis was carried out using the Protein Interactions Calculator (PIC) webserver (http://pic.mbu.iisc.ernet.in/). The 2D figures showing hydrogen bonds and hydrophobic interactions were built using the Ligplot software [30]. The Pymol software was used to generate 3D structures and to calculate RMSD (root mean square deviation) [31]. CASTp 3.0 [32] was used to assess changes in the area and volume of the proteolytic site of the SARS-CoV-2 main protease (SARS-CoV-2 Mpro) when alone and complexed with the studied peptides.

3.2.2.5 Quantum Biochemistry Calculation

This was performed according to a protocol established previously by Zhang and Zhang [33]. Molecular fractionation with conjugate caps (MFCC) was

carry out to calculate *in silico* the full quantum mechanical interaction energies between two pairs of specific amino acid residues (Ri and Rj) involving the studied peptides and SARS-CoV-2 Mpro, as follows, based on the work of Amaral et al. [34]:

$$E(R_i - R_j) = E(C_{i-1}\,R_i\,C_{i+1} + C_{j-1}\,R_j\,C_{j+1}) - E(C_{i-1}\,R_i\,C_{i+1} + C_{j-1}\,C_{j+1}) - E(C_{i-1}\,C_{i+1} + C_{j-1}\,R_j\,C_{j+1}) + E(C_{i-1}\,C_{i+1} + C_{j-1}\,C_{j+1})$$

Where $E(C_{i-1}\,R_i\,C_{i+1} + C_{j-1}\,R_j\,C_{j+1})$, the first term of the equation, is the total energy of the system formed by the residues Ri and Rj correctly capped; $E(C_{i-1}\,R_i\,C_{i+1} + C_{j-1}\,C_{j+1})$, the second term, is the total energy of the system formed by the capped residue Ri and the caps of the residue Rj; the third term, $E(C_{i-1}\,C_{i+1} + C_{j-1}\,R_j\,C_{j+1})$, represents the total energy of the system formed by the capped residue Rj and the caps of the residue Ri; and the last term, $E(C_{i-1}\,C_{i+1} + C_{j-1}\,C_{j+1})$, accounts for the total energy of the system formed by the caps of both residues Ri and Rj. The caps $C_{i-1}(C_{i+1})$ and $C_{j-1}(C_{j+1})$ are made from the residues covalently bound to the amine (carboxyl) groups of Ri and Rj. In the MFCC method used, all interaction between amino acid residues of the studied peptides and SARS-CoV-2 Mpro separated from each other within a 8 Å range were calculated, considering a dielectric function approaches of 40 (ε=40) for all interactions. The structural files (PDB format) obtained after molecular dynamics simulation and MFCC were used as inputs for density functional theory (DFT) calculations with DMOL^3 [35].

3.2.3. Results

3.2.3.1 Molecular Docking parameters of the interaction between the synthetic peptides and SARS-CoV-2 Mpro

Before molecular dynamics and quantum biochemistry analyses, molecular docking simulations were run on the FRODOCK 3.12 and ClusPro 2.0 webservers to find out which peptides best interact with SARS-CoV-2 Mpro. Both servers calculated that the eight studied peptides bind strongly to SARS-CoV-2 Mpro with score values that varied from 1700.10 to 2182.11 (Table 1). ClusPro 2.0 was used to calculate the free energies (ΔG) of interactions, which were low and varied from –579.1 to –736.5 kcal.mol^{-1} (Table 1). The sum of the punctuations provided by FRODOCK and ClusPro 2.0 was used to select *RcAlb*-pepII, PepGAT, and PepKAA as the best peptides, in relation to their capacity of binding to SARS-CoV-2 Mpro, with punctuation values of 1.500, 1.375, and 1.375, respectively (Table 1). Molecular docking analysis also revealed that these peptides do not bind to the proteolytic site of SARS-CoV-2 Mpro (His^{41} and Cys^{145}) (Fig. 29). Nevertheless, *RcAlb*-pepII, PepGAT, and PepKAA were further analyzed using molecular dynamics and quantum biochemistry.

3.2.3.2 Molecular Dynamics (MD) Simulation

MD simulations were done with SARS-CoV-2 Mpro alone and complexed with the peptides *RcAlb*-pepII, PepGAT, and PepKAA. RMSD of SARS-CoV-2 Mpro alone and complexed with the peptides increased gradually up to 1.5 Å within 50 ns and then remained stable until 100 ns, with RMSD fluctuation below 1 Å (Fig. 30). The stable conformation obtained from each MD simulation was used to perform further analyzes.

Table 1**.** Molecular docking parameters of the interactions between the studied synthetic peptides and SARS-CoV-2 Mpro

Peptide	FRODOCK[a]	Punctuation[b]	ClusPro[c]	Punctuation[d]	Sum[e]
Mo-CBP3-PepI	1816.15	0.375	-603.5	0.250	0.625
Mo-CBP3-PepII	1809.39	0.250	-736.5	1.000	1.250
Mo-CBP3-PepIII	1700.10	0.125	-654.0	0.625	0.750
RcAlb-PepI	2021.32	0.750	-579.1	0.125	0.875
RcAlb-PepII	2002.75	0.625	-694.5	0.875	1.500
RcAlb-PepIII	1871.59	0.500	-654.7	0.750	1.250
PepGAT	2061.69	0.875	-642.2	0.500	1.375
PepKAA	2182.11	1.000	-632.7	0.375	1.375

[a] Calculated using the FRODOCK v.3.12 server.
[b,d] Punctuation is associated with both the FRODOCK score and the ClusPro lowest binding free energy (kcal mol^{-1}), respectively. A score of 1 was assigned to the peptide with the highest docking value (referred to as the top scored pose). The scores of the subsequent peptides were decreased successively by a factor of 0.125 as the docking values decreased in relation to that of the peptide that received score 1.
[c] The lowest binding free energy (ΔG) calculated using ClusPro 2.0.
[e] Represents the sum of the scores (punctuation) in b and d.

Figure 29. Complexes formed by docking of the peptides *RcAlb*-PepII (A), PepGAT (B), and PepKAA (C) on SARS-CoV-2 Mpro.

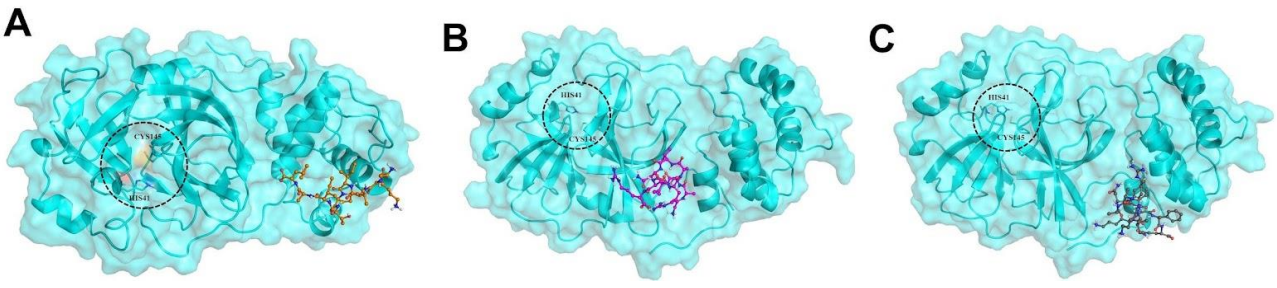

Fonte: AMARAL *et al.,* 2022.

Figure 30. RMSD plot of the conformation stability of SARS-CoV-2 Mpro alone and of the complexes formed by docking of *RcAlb*-PepII, PepGAT, and PepKAA on SARS-CoV-2 Mpro as a function of time (ns).

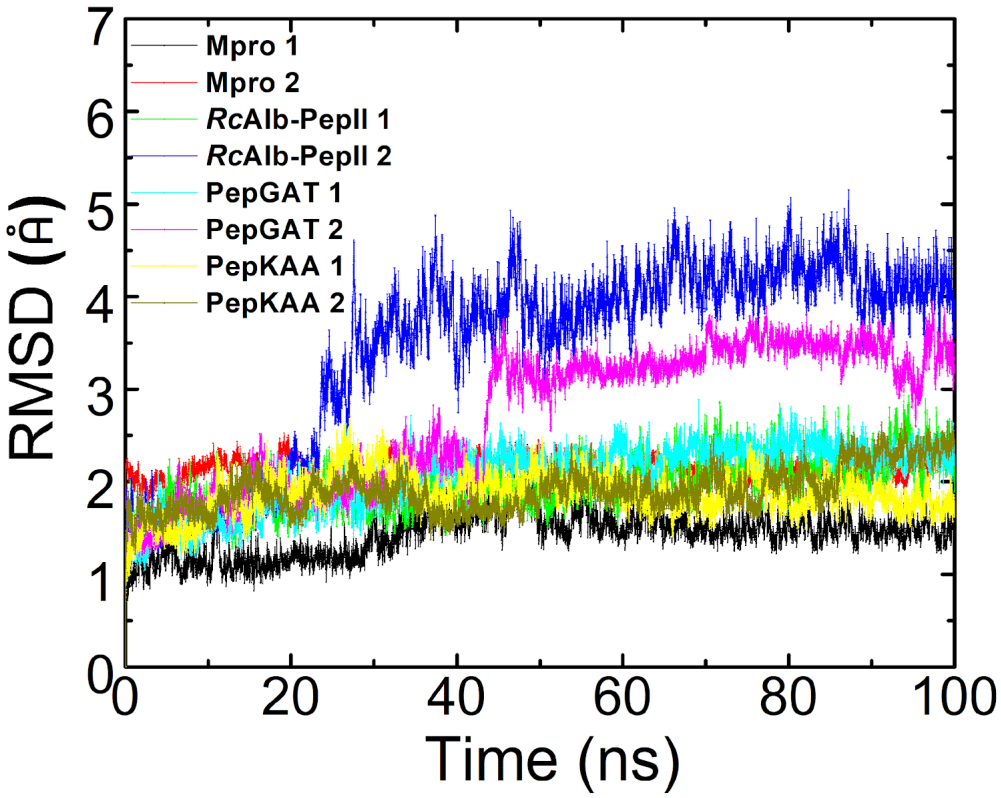

Fonte: AMARAL *et al.,* 2022.

3.2.3.3 Interaction between SARS-CoV-2 Mpro with RcAlb-PepII

The key amino acid residues responsible for the multi-point binding interactions between SARS-CoV-2 Mpro and *RcAlb*-PepII were Lys^{137}, Asn^{274}, Met^{276}, Tyr^{237}, and Asn^{277} with Leu^{9}, Lys^{2}, Lys^{2}, Pro^{5}, and Lys^{2} (Table 2; Fig. 31A, B, and D) with interaction energy of -12.13, -8.30, -4.82, -4.60, and -3.75 kcal.mol^{-1}, respectively (Table 2). Repulsive interactions occur between the amino acid residues Asp^{197}, Lys^{137}, and Glu^{290} of SARS-CoV-2 Mpro with Leu^{9}, Ala^{8}, and Leu^{9} of *RcAlb*-PepII, with interaction energy of +1.64, +1.66, and +1.92 kcal mol^{-1} and distance of 1.64, 1.66, and 1.92 Å, respectively (Table 2). Supplementary Table 1 shows the quantum parameters of the multi-point binding interactions between the amino acid residues of SARS-CoV-2 Mpro and those of *RcAlb*-PepII at distances up to 8 Å. The complex formed between SARS-CoV-2 Mpro and *RcAlb*-PepII is molded through hydrophobic interactions established by the amino acid residues Tyr^{237},

Tyr^{239}, Tyr^{239}, Leu^{271}, Leu^{272}, Leu^{272}, Met^{276}, Leu^{286}, Leu^{286}, Leu^{286}, Leu^{287}, and Leu^{287} of SARS-CoV-2 Mpro with Pro^{5}, Ile^{4}, Leu^{9}, Ile^{4}, Ile^{4}, Pro^{5}, Ile^{4}, Ile^{4}, Ile^{7}, Leu^{9}, Ile^{4}, and Leu^{9} of *Rc*Alb-PepII (Fig. 31A, B and D). Hydrogen bonds are established between the amino acid residues Met^{276} and Asn^{274} of SARS-CoV-2 Mpro with Lys^{2} of *Rc*Alb-PepII (Fig. 31A, B and D). The individual interaction energy of the residues Ala^{1}, Lys^{2}, Leu^{3}, Ile^{4}, Pro^{5}, Thr^{6}, Ile^{7}, Ala^{8}, Leu^{9} was -5.28, -20.44, -3.55, -10.60, -5.86, -0.74, -11.58, -5.98, and -10.83 kcal.mol^{-1}, respectively (Fig. 31C).

Table 2. Quantum parameters of the multi-point binding interactions between the amino acid residues of SARS-CoV-2 Mpro and those of *RcAlb*-PepII

Amino acid residues		**Distance**	**Free energy of interaction**	**Residue charge**		**Residue atom**	
SARS-CoV-2 Mpro	*RcAlb*-PepII	(Å)	(kcal mol^{-1})	SARS-CoV-2 Mpro	*RcAlb*-PepII	SARS-CoV-2 Mpro	*RcAlb*-PepII
LYS137	LEU9	1.80	-12.13	1	-1	HZ3	O2
ASN274	LYS2	2.79	-8.30	0	1	O	HZ1
MET276	LYS2	2.17	-4.82	0	1	H	O
TYR237	PRO5	2.57	-4.60	0	0	CE1	HG1
ASN277	LYS2	2.39	-3.75	0	1	OD1	HD2
LEU287	ILE4	2.33	-2.99	0	0	HD1	HD1
LEU287	LEU9	2.33	-2.86	0	-1	HB2	HD11
LEU286	LEU9	2.42	-2.82	0	-1	HD1	HB2
LEU272	ILE4	2.44	-2.77	0	0	HA	HB
GLY275	LYS2	2.44	-2.75	0	1	HA1	O
LEU286	ILE7	2.82	-2.75	0	0	HD2	HG21
LEU272	PRO5	2.50	-2.63	0	0	HA	HD2
ARG131	LEU9	5.02	-2.08	1	-1	HH1	O1
THR199	LEU9	2.63	-1.94	0	-1	HG23	HD12
LEU271	ILE4	2.68	-1.88	0	0	HB2	HG11
ASP197	LEU9	6.44	1.64	-1	-1	OD1	O2
LYS137	ALA8	5.44	1.66	1	0	HZ3	C
GLU290	LEU9	5.70	1.92	-1	-1	OE2	O1

Figure 31. The 3D and 2D structure representations of the complex formed by docking of *RcAlb*-PepII (Ala[1]-Lys-Leu-Ile-Pro-Thr-Ile-Ala-Leu[9]) on SARS-CoV-2 Mpro

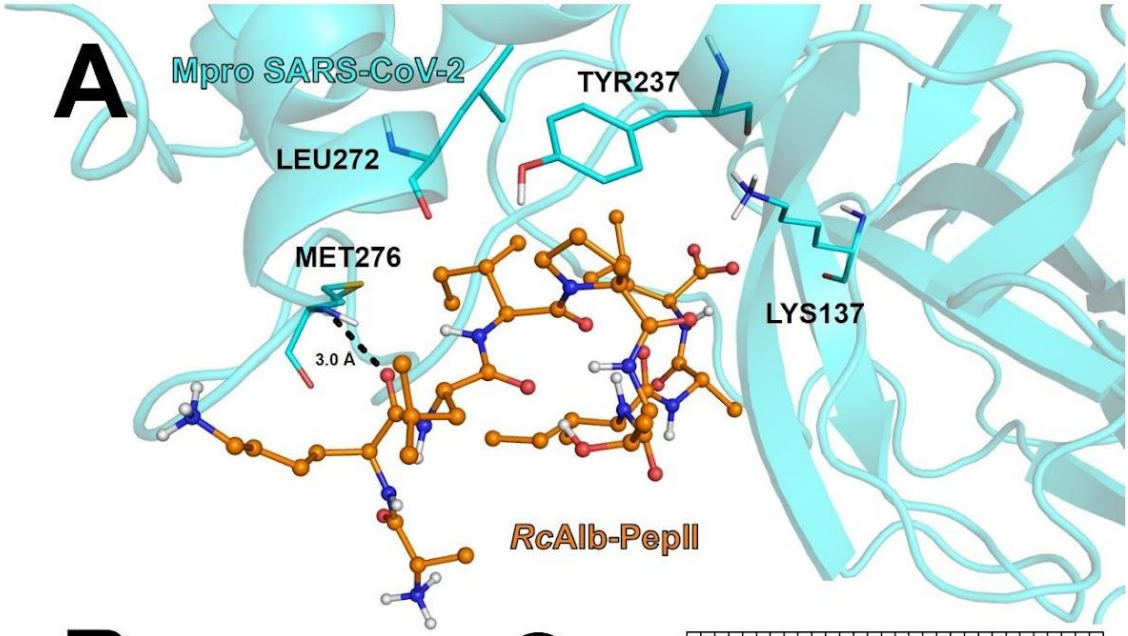

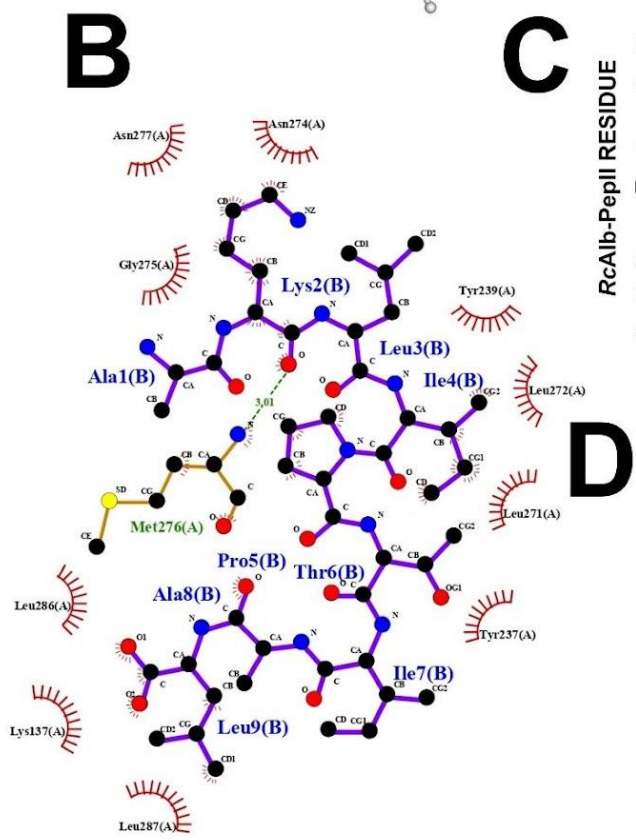

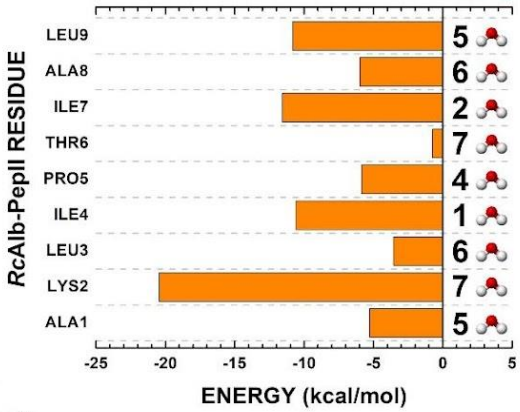

D

Interaction	Mpro Residue	*Rc* Alb-PepII Residue
Hydrophobic	TYR237	PRO5
	TYR239	ILE4
	TYR239	LEU9
	LEU271	ILE4
	LEU272	ILE4
	LEU272	PRO5
	MET276	ILE4
	LEU286	ILE4
	LEU286	ILE7
	LEU286	LEU9
	LEU287	ILE4
	LEU287	LEU9
Hydrogen bond	MET276	LYS2
	ASN274	LYS2

The 3D and 2D structure representations of the complex formed by docking of *RcAlb*-PepII (Ala[1]-Lys-Leu-Ile-Pro-Thr-Ile-Ala-Leu[9]) on SARS-CoV-2 Mpro are depicted in A and B, respectively. The interaction energies of the amino acid residues of *RcAlb*-PepII with those of SARS-CoV-2 Mpro, and the amino acid residues that participate in the hydrophobic interactions and hydrogen bonds between *RcAlb*-PepII and SARS-CoV-2 Mpro are shown in C and D, respectively. Fonte: AMARAL *et al.,* 2022.

3.2.3.4 Interaction between SARS-CoV-2 Mpro with PepGAT

Distances (Å), total free energy of interaction (kcal mol^{-1}), amino acid residue charge and amino acid residue atom closest (up to 8 Å) to the interactions between SARS-CoV-2 Mpro and PepGAT are shown in the supplementary Table 2. Interaction between SARS-CoV-2 Mpro and PepGAT was establish predominantly by Gln^{306}, Gln^{306}, Asp^{153}, Asp^{248}, Phe^{294}, Gln^{110}, Ile^{249}, Phe^{294}, and Asp^{245} with Gly^{1}, Arg^{5}, Gly^{1}, Arg^{10}, Arg^{5}, Thr^{3}, Arg^{10}, Ala^{2}, and Arg^{10}, with interaction energy of -19.62, -12.35, -11.12, -10.39, -6.28, -4.73, -4.51, -3.96, and -3.89 kcal.mol^{-1}, and distances of 1.57, 2.32, 2.50, 2.80, 2.31, 2.23, 2.10, 4.12, and 2.54 Å, respectively, to form stable complex (Table 3; Fig. 32A and B). Repulsive interactions occur mainly between the amino acid residues Arg^{298}, Lys^{102}, and Phe^{305} of the protease with Gly1 of the peptide, with interaction energy of +1.47, +2.26, and +2.79 kcal.mol^{-1} and distances of 6.14, 5.39, and 3.49 Å, respectively (Table 3).

Supplementary Table 2 shows the quantum parameters of the multi-point binding interactions between the amino acid residues of SARS-CoV-2 Mpro and those of PepGAT at distances up to 8 Å. SARS-CoV-2 Mpro establishes hydrophobic, ionic, cation-pi and hydrogen bond interactions with PepGAT. Hydrogen bonds are established between the amino acid residues Gln^{110}, Asp^{153}, and Asp^{248} of SARS-CoV-2 Mpro with Thr^{3}, Gly^{1}, and Arg^{10} of PepGAT (Fig. 32 A, B, and D). The ionic interactions occur between the amino acid residues Asp^{245} and Asp^{248} of Mpro with Arg^{10} of PepGAT (Fig. 32 A, B and D). A cation-pi interaction is formed by Phe^{294} of SARS-CoV-2 Mpro with Arg^{10} of PepGAT. Hydrophobic interactions are established by the amino acid residues Val^{104}, Ile^{249}, Phe^{294}, and Phe^{294} of SARS-CoV-2 Mpro with Ile^{4}, Ala^{6}, Ala^{2}, and Ala^{6} of PepGAT (Fig. 32 B and D). The individual interaction energy of the residues Gly^{1}, Ala^{2}, Thr^{3}, $Ileu^{4}$, Arg^{5}, Ala^{6}, Val^{7}, Asn^{8}, Ser^{9}, and Arg^{10} of PepGAT was -19.73, -6.59, -12.20, -12.10, -16.45, -3.56, -6.26, -0.80, -0.74, and -22.80 kcal.mol^{-1}, respectively (Fig. 32 C).

Table 3. Quantum parameters of the multi-point binding interactions between the amino acid residues of SARS-CoV-2 Mpro and those of PepGAT.

Amino acid residues		**Distance**	**Free energy of interaction**	**Residue charge**		**Residue atom**	
SARS-CoV-2 Mpro	PepGAT	(Å)	(kcal mol^{-1})	SARS-CoV-2 Mpro	PepGAT	SARS-CoV-2 Mpro	PepGAT
GLN306	GLY1	1.57	-19.62	-1	1	O1	H3
GLN306	ARG5	2.32	-12.35	-1	1	O1	HH21
ASP153	GLY1	2.50	-11.12	-1	1	OD2	H2
ASP248	ARG10	2.80	-10.39	-1	0	OD1	HH12
PHE294	ARG5	2.31	-6.28	0	1	HD1	HD1
GLN110	THR3	2.23	-4.73	0	0	HE22	O
ILE249	ARG10	2.10	-4.51	0	0	HG21	HH22
PHE294	ALA2	4.12	-3.96	0	0	HB1	O
ASP245	ARG10	2.54	-3.89	-1	0	OD1	HH22
PHE294	ARG10	3.02	-2.94	0	0	HE1	HG2
GLN107	VAL7	2.76	-2.32	0	0	HG2	HG11
ILE106	THR3	2.86	-2.15	0	0	HG21	HB
ASP295	ALA2	2.41	-2.05	-1	0	HB1	HB2
ASP295	GLY1	1.92	-1.87	-1	1	HB1	C
PHE294	ALA6	2.92	-1.87	0	0	HE2	HA
ILE249	ALA6	3.83	-1.82	0	0	HG21	HA
GLN107	ALA6	6.92	-1.79	0	0	OE1	HB1
ARG298	GLY1	6.14	1.47	1	1	HD2	HA1
LYS102	GLY1	5.39	2.26	1	1	HZ3	H2
PHE305	GLY1	3.49	2.79	0	1	HD2	HA1

Fonte: AMARAL *et al.,* 2022.

Figure 32. The 3D and 2D structure representations of the complex formed by docking of PepGAT (Gly[1]-Ala-Thr-Ileu-Arg-Ala-Val-Asn-Ser-Arg[10]) on SARS-CoV-2 Mpro.

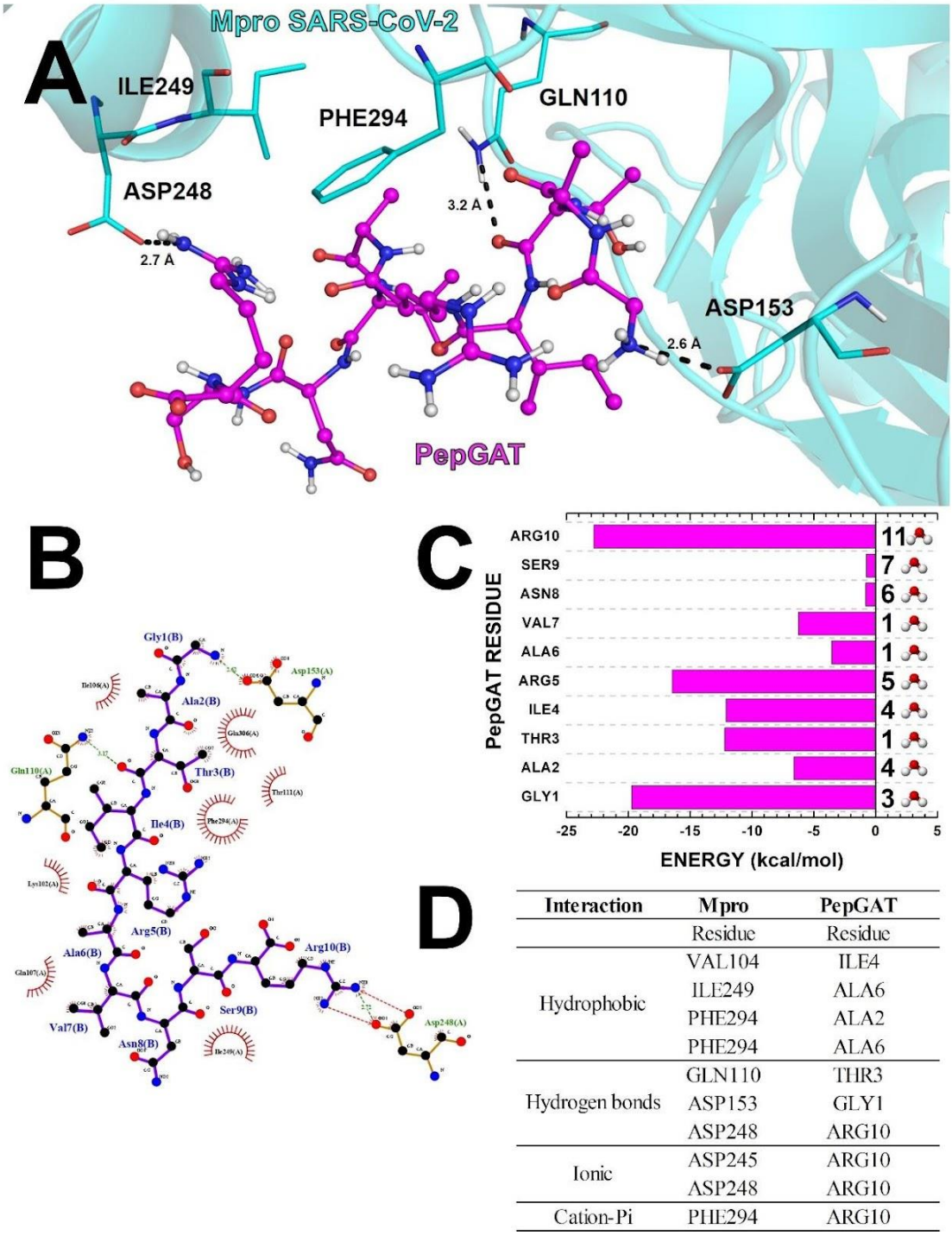

Interaction	Mpro	PepGAT
	Residue	Residue
Hydrophobic	VAL104	ILE4
	ILE249	ALA6
	PHE294	ALA2
	PHE294	ALA6
Hydrogen bonds	GLN110	THR3
	ASP153	GLY1
	ASP248	ARG10
Ionic	ASP245	ARG10
	ASP248	ARG10
Cation-Pi	PHE294	ARG10

The 3D and 2D structure representations of the complex formed by docking of PepGAT (Gly[1]-Ala-Thr-Ileu-Arg-Ala-Val-Asn-Ser-Arg[10]) on SARS-CoV-2 Mpro are depicted in A and B, respectively. The interaction energies of the amino acid residues of PepGAT with those of SARS-CoV-2 Mpro, and the amino acid residues that participate in the formation of hydrogen bond, hydrophobic, cation-pi, and ionic interactions between PepGAT and SARS-CoV-2 Mpro are shown in D. Fonte: AMARAL *et al.,*

2022.

3.2.3.5 Interaction between SARS-CoV-2 Mpro with PepKAA

The key amino acid residues responsible for the multi-point binding interactions between SARS-CoV-2 Mpro and PepKAA are Asp^{245}, Asp^{248}, Asp^{248}, Gln^{256}, Phe^{294}, Asp^{153}, Ile^{249}, Pro^{252}, and Val^{297} with Arg^{5}, Arg^{5}, Lys^{1}, Phe^{9}, Tyr^{8}, Lys^{7}, Arg^{5}, Tyr^{8}, and Tyr^{8} with interaction energy of -11.93, -11.32, -10.36, -6.55, -6.08, -4.93, -4.03, -3.60, and -3.29 kcal.mol^{-1} and distances of 1.68, 1.76, 3.71, 2.70, 2.31, 3.79, 2.60, 2.14, and 2.14 Å, respectively (Table 4). The repulsive interactions occur between Val^{247} and Lys^{102} of SARS-CoV-2 Mpro with Arg^{5} and Lys^{7} of PepKAA, with interaction energy of +0.58 and +1.34 kcal.mol^{-1} and distances of 6.08 and 7.05 Å, respectively (Table 4). Supplementary Table 3 shows the quantum parameters of the multi-point binding interactions between the amino acid residues of SARS-CoV-2 Mpro and those of PepKAA at distances up to 8 Å. SARS-CoV-2 Mpro binds to PepKAA through hydrophobic, ionic, aromatic, and hydrogen bond interactions. Hydrogen bonds are formed by Asp^{245} and Asp^{248} of SARS-CoV-2 Mpro with Arg^{5} of PepKAA (Fig. 33A, B and D). Ionic interactions occur between Asp^{153}, Asp^{245}, Asp^{248}, and Asp^{248} of SARS-CoV-2 Mpro with Lys^{7}, Arg^{5}, Lys^{1}, and Arg^{5} of PepKAA, respectively (Fig. 33B and D). Hydrophobic interactions are established by Ile^{213}, Pro^{252}, Pro^{252}, Pro^{252}, Leu^{253}, Leu^{253}, Pro^{293}, Phe^{294}, Val^{296}, and Val^{297} of SARS-CoV-2 Mpro with Phe^{9}, Ile^{6}, Tyr^{8}, Phe^{9}, Tyr^{8}, Phe^{9}, Tyr^{8}, Tyr^{8}, Phe^{9}, and Tyr^{8} of PepKAA. An aromatic interaction is formed by Phe^{294} of SARS-CoV-2 Mpro with Tyr^{8} of PepKAA (Fig. 33A and D). The individual interaction energy of the residues Lys^{1}, Ala^{2}, Ala^{3}, Asn^{4}, Arg^{5}, Ile^{6}, Lys^{7}, Tyr^{8}, Phe^{9}, Gln^{10} of PepKAA was -6.27, -1.06, +0.05, -0.80, -25.54, -2.34, -11.91, -22.90, -13.16, and -8.42 kcal.mol^{-1}, respectively (Fig. 33C).

Table 4. Quantum parameters of the multi-point binding interactions between the amino acid residues of SARS-CoV-2 Mpro and those of PepKAA

Amino acid residues		**Distance**	**Free energy of interaction**	**Residue charge**		**Residue atom**	
SARS-CoV-2 Mpro	PepKAA	(Å)	(kcal mol^{-1})	SARS-CoV-2 Mpro	PepKAA	SARS-CoV-2 Mpro	PepKAA
ASP245	ARG5	1.68	-11.93	-1	1	OD2	HH22
ASP248	ARG5	1.76	-11.32	-1	1	OD2	HH11
ASP248	LYS1	3.71	-10.36	-1	2	OD1	HB1
GLN256	PHE9	2.70	-6.55	0	0	HB1	HB1
PHE294	TYR8	2.31	-6.08	0	0	HD1	HE1
ASP153	LYS7	3.79	-4.93	-1	1	OD1	HZ3
ILE249	ARG5	2.60	-4.03	0	1	HD2	HD2
PRO252	TYR8	2.14	-3.60	0	0	HG1	HB1
VAL297	TYR8	2.14	-3.29	0	0	HG23	HA
ASP245	LYS1	7.09	-2.66	-1	2	OD1	HA
PRO252	ILE6	2.26	-2.60	0	0	HB2	HA
LEU253	PHE9	2.32	-2.50	0	0	HD21	HD2
TYR154	LYS7	3.17	-2.41	0	1	HE2	HE2
LEU253	TYR8	2.41	-2.40	0	0	HD22	HD2
PRO252	PHE9	1.90	-2.31	0	0	HB1	H
CYS300	PHE9	2.70	-1.77	0	0	O	HZ
ASP248	ALA2	4.12	-1.74	-1	0	OD2	H
PRO293	TYR8	2.06	-1.73	0	0	HB1	HE2
VAL247	ARG5	6.08	0.58	0	1	C	HH11
LYS102	LYS7	7.05	1.34	1	1	HZ1	HZ3

Fonte: AMARAL *et al.,* 2022.

Figure 33. The 3D and 2D structure representations of the complex formed by docking of PepKAA (Lys[1]-Ala-Ala-Asn-Arg-Ile-Lys-Tyr-Phe-Gln[10]) on SARS-CoV-2 Mpro

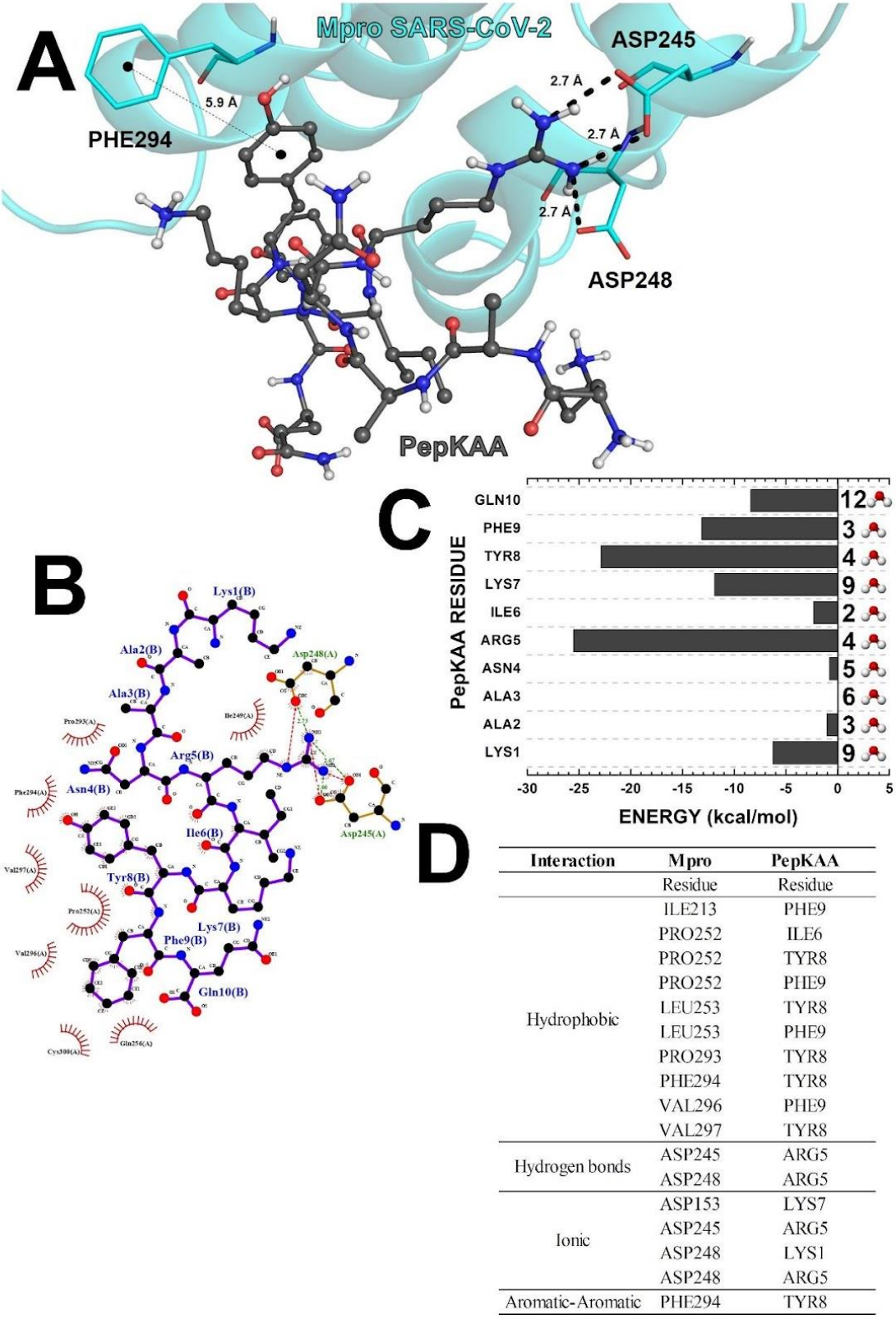

Interaction	Mpro	PepKAA
	Residue	Residue
Hydrophobic	ILE213	PHE9
	PRO252	ILE6
	PRO252	TYR8
	PRO252	PHE9
	LEU253	TYR8
	LEU253	PHE9
	PRO293	TYR8
	PHE294	TYR8
	VAL296	PHE9
	VAL297	TYR8
Hydrogen bonds	ASP245	ARG5
	ASP248	ARG5
Ionic	ASP153	LYS7
	ASP245	ARG5
	ASP248	LYS1
	ASP248	ARG5
Aromatic-Aromatic	PHE294	TYR8

Fonte: AMARAL *et al.,* 2022. The 3D and 2D structure representations of the complex formed by docking of PepKAA (Lys^{1}-Ala-Ala-Asn-Arg-Ile-Lys-Tyr-Phe-Gln^{10}) on SARS-CoV-2 Mpro are depicted in A and B, respectively. The interaction energies of the amino acid residues of PepKAA with those of SARS-CoV-2 Mpro, and the amino acid residues that participate in the formation of hydrogen bond, hydrophobic, ionic, and aromatic interactions between PepKAA and SARS-CoV-2 Mpro are shown in D.

3.2.3.6 Quantum Biochemistry Description

The most important amino acid residues of SARS-CoV-2 Mpro that interact with *RcAlb*-PepII are Leu^{287}, Leu^{286}, Asn^{274}, Gly^{275}, Met^{276}, Lys^{137}, Tyr^{237}, Leu^{272}, and Asn^{277} with interaction energy of -9.36, -9.03, -8.78, -6.47, -6.46, -6.41, -5.97, -5.80, and -5.60 kcal.mol^{-1}, respectively. The Asp^{197}, Asp^{289}, and Glu^{290} residues showed repulsive energies (Fig. 34A). The sum of all free energies of interaction between SARS-CoV-2 Mpro and *RcAlb*-PepII (Et) was –74.85 kcal.mol^{-1} (Fig. 35).

The key amino acid residues involved in the interaction of SARS-CoV-2 Mpro with the PepGAT are Asp^{153}, Gln^{306}, Phe^{294}, Asp^{248}, and Asp^{245} with interaction energy of -12.47, -11.27, -8.36, -6.67, and -4.72 kcal.mol^{-1}, respectively. Residues of Arg^{298}, Phe^{305}, Lys^{102} showed small repulsive energies (Fig. 34B). The sum of all free energies of interaction between SARS-CoV-2 Mpro with PepGAT was –101.2 kcal.mol^{-1} (Fig. 35).

The major amino acid residues of the interaction between SARS-CoV-2 Mpro and PepKAA are Asp^{248}, Pro^{252}, Phe^{294}, Asp^{153}, and Asp^{245}, with interaction energy of -20.14, -11.27, -10.15, -9.57, and -8.17 kcal. mol^{-1}, respectively. Lys^{102} showed a small repulsive energy (Fig. 34C). The sum of all free energies of interaction between SARS-CoV-2 Mpro and PepKAA was –92.35 kcal.mol^{-1} (Fig. 35).

Figure 34. Binding site, interaction energy, and residue domain (BIRD) panel showing the MFCC interaction energies between the main amino acid residues of SARS-CoV-2 Mpro with those of *RcAlb*-PepII (A), PepGAT (B), and PepKAA (C).

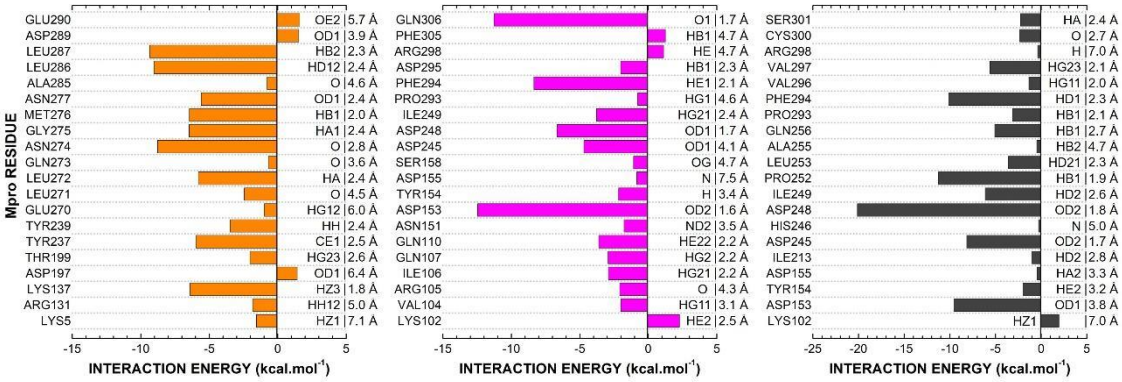

Fonte: AMARAL *et al.,* 2022. The minimal distance (Å) between each residue that participates in the interaction is indicates at the right side of the panel. The amino acid residues at the left side of the panel are from SARS-CoV-2 Mpro.

Figure 35. Total interaction energy between SARS-CoV-2 Mpro and the Peptides as a function of the interaction distance.

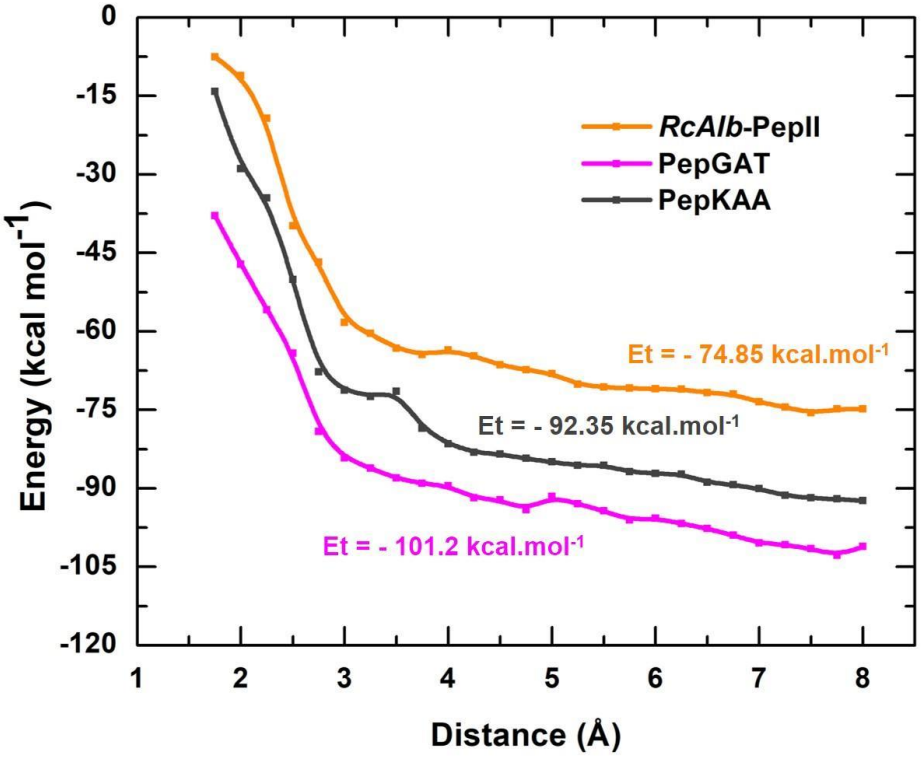

Fonte: AMARAL *et al.,* 2022. Orange, Magenta, and Black squares represent *RcAlb*-PepII, PepGAT, and PepKAA, respectively. Et accounts for the sum of the interaction energies up to 8Å.

3.2.3.7 Assessment of the conformational changes induced by RcAlb-PepII, PepGAT, and PepKAA in the area and volume of the proteolytic site of SARS-CoV-2 Mpro

RMSD analyses revealed that *RcAlb*-PepII, PepGAT, and PepKAA induced alterations in the 3D structure of SARS-CoV-2 Mpro (Fig. 36). The control structure presented RMSD value of 0, which indicates a typical and functional 3D structure (Fig. 36A). However, the structural alignment of SARS-CoV-2 Mpro complexed with *RcAlb*-PepI, PepGAT, or PepKAA revealed several alterations in the SARS-CoV-2 Mpro structure, which was confirmed by the RMSD values of 3.118, 3.164, 3.054 Å, respectively (Fig. 36B-D).

These structural changes in SARS-CoV-2 Mpro induced by interactions with the studied peptides lead to alterations in the area and volume of the SARS-CoV-2 Mpro proteolytic site. SARS-CoV-2 Mpro itself, not complexed with the studied peptides, presented an area and volume of 279.7 $Å^2$ and 298.1 $Å^3$, respectively, (Fig. 37A).

When complexed with *Rc*Alb-PepII, the area and volume of SARS-CoV-2 Mpro proteolytic site reduced to 120.6 $Å^2$ and 93.3 $Å^3$, which represent 68.7% and 56.9% decrease, respectively (Fig. 37B). The structural changes caused by PepGAT also reflected in the area and volume of the SARS-CoV-2 Mpro proteolytic site, which decreased from 298.1 $Å^2$ and 279.7 $Å^3$ to 183.7 $Å^2$ and 179.0 $Å^3$, resulting in a 38.4% and 36.0% decrease, respectively (Fig. 37C). Regarding to PepKAA, its interaction with the protease promoted a 13.0% (279.7 $Å^2$ to 243.3 $Å^2$) and 23.1% (298.1 $Å^3$ to 229.2 $Å^3$) decrease, respectively, in the area and volume of the SARS-CoV-2 Mpro proteolytic site (Fig. 37D).

Figure 36. 3D visualization of the molecular complexes.

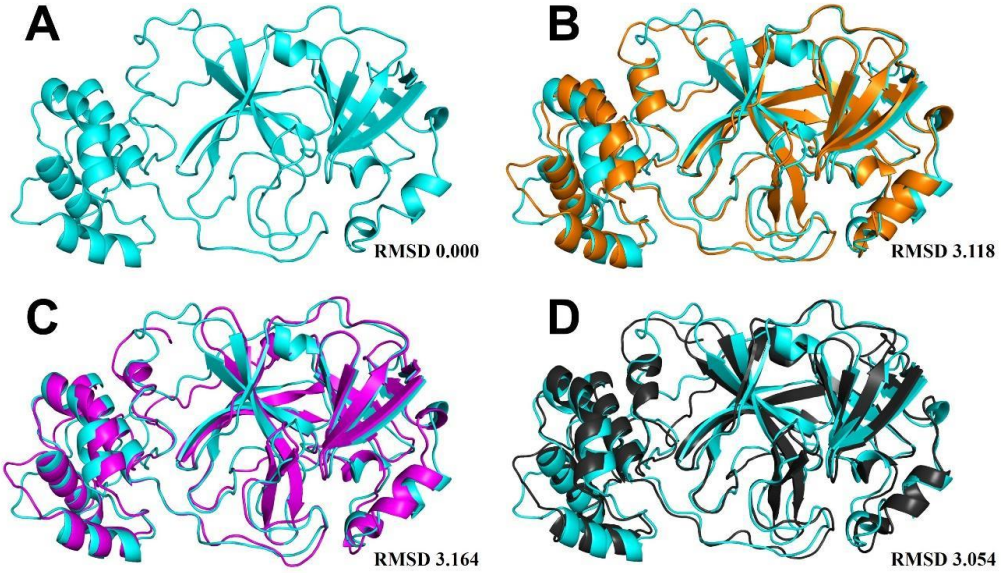

Fonte: AMARAL *et al.,* 2022. 3D visualization of the molecular complexes formed between SARS-CoV-2 Mpro and the peptides with the RMSD values of SARS-CoV-2 Mpro alone (in cyan, A) and when conjugated with *RcAlb*-PepII (B), PepGAT (C), and PepKAA (D). The merged structures suggest conformational alteration induced by the peptides.

Figure 37. Conformational structure of the proteolytic site of SARS-CoV-2 Mpro alone and complexed with the peptides.

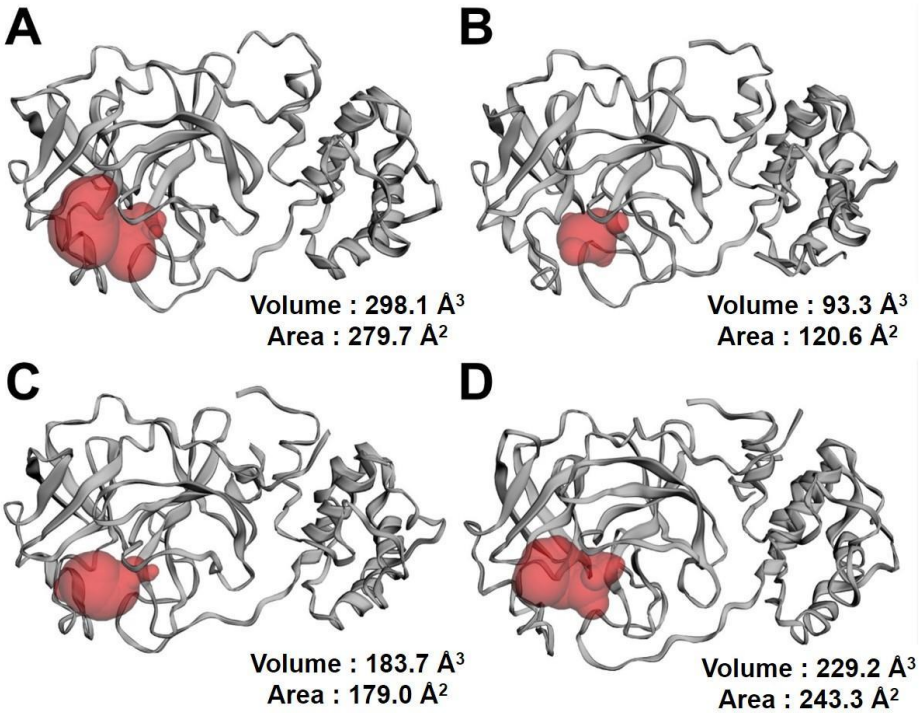

Fonte: AMARAL *et al.,* 2022. The proteolytic site of SARS-CoV-2 Mpro alone (A) presents a volume and area higher than when SARS-CoV-2 Mpro is complexed with *RcAlb*-PepII (B), PepGAT (C), and PepKAA (D).

3.2.4 Discussion

Currently, there are two main ways to find out and develop medicines against SARS-CoV-2. The first one is through drug repositioning in which the antiviral activity of several pharmacological classes of medicines already approved for use in humans is investigated as a possibility for generating new treatments against COVID-19 [36-39]. To date, such attempts have been tried unsuccessfully. The second approach is still a promise, but it is based on systematic investigations conducted to identify novel small molecules designed to target key SARS-CoV-2 factors such as the Spike glycoprotein and RNA polymerase [22]. Such an approach involves the *in silico* molecular docking and molecular dynamics simulation, which are structure-based method employed to predict the binding affinity of a ligand molecule to a target [16–18,40,41].

So, molecular docking and molecular dynamics simulation constitute useful tools to facilitate the drug development process as they allow to predict *in silico* the binding affinity of a designed ligand molecule to a target as SARS-CoV-2 Mpro [40]. Mpro has three-domain (domains I to III) cysteine protease essential for coronavirus replication as it plays a crucial role in the processing of the viral polyproteins into mature proteins [14]. SARS-CoV-2 Mpro and SARS-CoV-1 Mpro primary structures differ by only 12 amino acid residues, which means they have 96% similarity [15]. However, a considerable difference between the catalytic site of SARS-CoV-1 and that of SARS-CoV-2 is observed. In SARS-CoV-1 Mpro, the active site cavity is a well-defined pocket with the area and volume of 256.8 $Å^2$ and 191.24 $Å^3$, respectively, compared to 352.1 $Å^2$ and 323.73 $Å^3$ of that of SARS-CoV-2 Mpro [18]. These differences increase by 15% the proteolytic effectiveness of SARS-CoV-2 Mpro compared to that of SARS-CoV-1 Mpro [15,18,40]. Such higher catalytic efficiency of SARS-CoV-2 Mpro could enhance the virus replication process and formation of new virus particles, which could lead to higher infectivity. Therefore, due to its crucial involvement in maturation of most of the nonstructural proteins that are translated from SARS-CoV-2 RNA, SARS-CoV-2 Mpro is an attractive target to design antiviral drugs [42].

Many studies have tried to either analyze new drugs or already known drugs that could interact with the catalytic site of SARS-CoV-2 Mpro and inhibit its

activity [16–18,40,42]. Moreover, drugs that have been employed to treat HIV by inhibiting the viral protease were also tested [16]. In this current *in silico* study we used molecular docking and dynamics simulations to predict and show that the synthetic peptides *RcAlb*-PepII, PepGAT, and PepKAA, out of eight peptides tested, interact most efficiently with SARS-CoV-2 Mpro (Table 1, Figs. 30-35). These peptides interact with SARS-CoV-2 Mpro at a region far away from the protease catalytic site, which suggests that the peptides may modulate the SARS-CoV-2 Mpro activity allosterically (Figs. 36 and 37). Actually, this is a pioneer study in which quantum biochemistry is employed to analyze the interaction of peptides against SARS-CoV-2 Mpro (Tables 2-4). Quantum biochemistry calculations [21,43] allowed to deduce the individual energies of interactions of each amino acid residue of the studied peptides and those of SARS-CoV-2 Mpro. Therefore, it was possible to predict the hydrogen bonds, ionic, aromatic, and hydrophobic interactions that are important to establish attractive or repulsive interactions between the peptides and SARS-CoV-2 Mpro (Figs. 31-34). Fig 35 shows that, by using quantum biochemistry calculations, the total interaction energy between *RcAlb*-PepII, PepGAT, and PepKAA with SARS-CoV-2 Mpro was –74.85, –101.2, and –92.35 kcal.mol^{-1}, respectively. As this is the first work that analyzes, through quantum biochemistry, interactions of peptides with SARS-CoV-2 Mpro, the results presented herein are compared with those reported by Campos et al. [44], in which the interaction of two peptides against the Zika virus protease was analyzed. The authors demonstrated, by quantum biochemistry, that the interaction energies of the peptides cn-716 and acyl-KR-aldehyde with the protease NS2B–NS3 were –63.35 kcal.mol^{-1} and –71.4 kcal.mol^{-1}, respectively. For instance, *Rc*Alb-PepII, PepGAT, and PepKAA interacts with SARS-CoV-2 Mpro even more strongly than cn-716 and acyl-KR-aldehyde to the protease NS2B–NS3. Nevertheless, interaction of other non-peptide-like antiviral drugs have been tested with the same purpose of inhibiting the proteolytic activity of SARS-CoV-2 Mpro. For example, Ortega et al. [18] tested by molecular docking the interaction of the clinically proven anti-HIV drugs Saquinavir, Lopinavir, and Tripranavir, which act as inhibitors of the HIV protease, with the proteolytic site of SARS-CoV-2 Mpro. Additionally, Jr and Ji [16] reported that Remdesivir, a nucleotide analogue initially developed to treat hepatitis C and later *Ebola* and *Marburg virus*, also binds to the proteolytic site of SARS-CoV-2 Mpro. These two later studies are

referred as drug reposition or drug repurposing, which is an approach to speed up the drug discovery process through identification of a novel clinical use for an existing drug approved for a different indication [39]. Moreover, Ngo et al. [17] docked some natural compounds and found that cannabisin A and isoacteoside interacted with the proteolytic site of SARS-CoV-2 Mpro. Currently, the most reliable inhibitor of SARS-CoV-2 Mpro, as seen by molecular docking and proven *in vitro*, is 13b, an α-ketoamide that is a protease inhibitor of coronavirus that strongly binds to the proteolytic site of SARS-CoV-2 Mpro [40]. *RcAlb*-PepII, PepGAT, and PepKAA interact with SARS-CoV-2 Mpro at a region far away from the protease active site (Figs. 38, 45, and 46), contrary to these above-mentioned antiviral drugs tested. However, Bzówka et al. [45] showed that the proteolytic site of SARS-CoV-2 Mpro has high flexibility and plasticity, which means it is highly susceptible to genetic mutational change. Such possibility constitutes a serious problem for designing drugs targeting the proteolytic site because a simple genetic mutation could prevent the action of these antiviral drugs. Actually, SARS-CoV-2 is an RNA virus and has high mutational rates [45] and, for example, the antiviral 13b, which strongly binds to the proteolytic site of SARS-CoV-2 Mpro [40], could quickly become ineffective against coronavirus. Prediction that *RcAlb*-PepII, PepGAT, and PepKAA interact with SARS-CoV-2 Mpro at a region far away from the protease active site (Figs. 30, 36 and 37) is an advantage because besides their interactions being unaffected by mutation of the active site of SARS-CoV-2 Mpro, they induce conformational alterations in the 3D structure of this protease (Fig. 36), as shown by the RMSD values of SARS-CoV-2 Mpro complexed with the peptides, compared to SARS-CoV-2 Mpro alone, that could disrupt the proteolytic activity of the viral enzyme, leading to a severe reduction in SARS-CoV-2 replication. Indeed, interaction of *RcAlb*-PepII, PepGAT, and PepKAA reduce the volume and area of SARS-CoV-2 Mpro proteolytic site, respectively, in 56.9% and 68.7% (Fig. 37B), 38.4% and 36.0% (Fig. 37C), and 23.1 and 13.0% (Fig. 37D). In a recent report by our research group, it was shown that PepKAA also induced conformational changes in the SARS-CoV-2 Spike glycoprotein, disrupting its interaction with the ACE2 receptor located at the human cell membrane [22].

As PepKAA shows to interact with two different targets (SARS-CoV-2 Spike glycoprotein [22] and SARS-CoV-2 Mpro of SARS-CoV-2, this particular synthetic peptide is a potential small molecule candidate to be further tested *in vitro*

against SARS-CoV-2, either alone or combined with other peptides like *RcAlb*-PepII, PepGAT. Of utmost importance is that *RcAlb*-PepII, PepGAT, and PepKAA were not toxic to mammalian cells like rabbit erythrocytes and human ABO type red blood cells [23–25], neither to fibroblast (lines L929 and MRC-5) and keratinocytes (Data not shown, manuscript in preparation).

3.2.5 Conclusion

Quantum biochemistry and molecular dynamics simulations allow to predicted that the peptides *RcAlb*-PepII, PepGAT, and PepKAA interact physically with SARS-CoV-2 Mpro and alter its 3D structure and provoke shrinkage of the active site of the protease. These findings suggest that these peptides are likely antiviral small molecules that could potentially inhibit SARS-CoV-2 replication *in vivo*, a hypothesis that requires further investigation in the near future to be proven true. Importantly, besides to be apparently harmless to mammalian cells, *RcAlb*-PepII, PepGAT, and PepKAA do not interact with the active site of SARS-CoV-2 Mpro, unlike most antiviral drugs, and, thus, mutation of this protease domain will not affect the peptide effectiveness. In conclusion, this pioneering *in silico* investigation opens up opportunity for further *in vivo* investigations on these peptides, towards discovering new drugs and entirely new perspectives to treat COVID-19. For instance, peptide-based therapeutics have various advantages in relation to traditional small-molecule drugs, since peptides have higher specificity to selected targets, low toxicity because the possibility for accumulation in the body is improbable, and their synthesis is not a complex, costly, and time-consuming technique [46].

3.2.6 Funding and acknowledgments

This work was supported by grants from the following Brazilian agencies: The National Council for Scientific and Technological Development (CNPq) with a doctoral grant to JLA and research grant (codes 431511/2016-0 and 306202/2017-4) to JTAO; the Council for Advanced Professional Training (CAPES) sponsored PFNS with a Postdoctoral Fellowships; The authors are also grateful to the support received

from the National Center for High Performance Processing - Federal University of Ceara and Center for Permanent Education in Health Care-CEATS/School of Public Health of Ceara (ESP-CE). VNF also acknowledges support from PRONEX FUNCAP/CNPq (PR2-0101-00006.01.00/15).

Reference

[1] Z. Song, Y. Xu, L. Bao, L. Zhang, P. Yu, Y. Qu, H. Zhu, W. Zhao, Y. Han, C. Qin, From SARS to MERS, thrusting coronaviruses into the spotlight, Viruses. 11 (2019). https://doi.org/10.3390/v11010059.

[2] WHO | Middle East respiratory syndrome coronavirus (MERS-CoV), WHO. (2020).

[3] COVIDView: A Weekly Surveillance Summary of U.S. COVID-19 Activity | CDC, (n.d.). https://www.cdc.gov/coronavirus/2019-ncov/covid-data/covidview/index.html (accessed July 24, 2020).

[4] D.S. Hui, E. I Azhar, T.A. Madani, F. Ntoumi, R. Kock, O. Dar, G. Ippolito, T.D. Mchugh, Z.A. Memish, C. Drosten, A. Zumla, E. Petersen, The continuing 2019-nCoV epidemic threat of novel coronaviruses to global health — The latest 2019 novel coronavirus outbreak in Wuhan, China, Int. J. Infect. Dis. 91 (2020) 264–266. https://doi.org/10.1016/j.ijid.2020.01.009.

[5] B.M.J.B. Practice, Coronavirus disease 2019, World Heal. Organ. 2019 (2020) 2633. https://doi.org/10.1001/jama.2020.2633.

[6] H. Li, L. Liu, D. Zhang, J. Xu, H. Dai, N. Tang, X. Su, B. Cao, SARS-CoV-2 and viral sepsis: observations and hypotheses, Lancet. 395 (2020) 1517–1520. https://doi.org/10.1016/S0140-6736(20)30920-X.

[7] D. Ragab, H. Salah Eldin, M. Taeimah, R. Khattab, R. Salem, The COVID-19 Cytokine Storm; What We Know So Far, Front. Immunol. 11 (2020) 1446. https://doi.org/10.3389/fimmu.2020.01446.

[8] Y. Tang, J. Liu, D. Zhang, Z. Xu, J. Ji, C. Wen, Cytokine Storm in COVID-19: The Current Evidence and Treatment Strategies, Front. Immunol. 11 (2020) 1708. https://doi.org/10.3389/fimmu.2020.01708.

[9] A. Wu, Y. Peng, B. Huang, X. Ding, X. Wang, P. Niu, J. Meng, Z. Zhu, Z. Zhang, J. Wang, J. Sheng, L. Quan, Z. Xia, W. Tan, G. Cheng, T. Jiang, Genome Composition and Divergence of the Novel Coronavirus (2019-nCoV) Originating in China, Cell Host Microbe. 27 (2020) 325–328. https://doi.org/10.1016/j.chom.2020.02.001.

[10] K.G. Andersen, A. Rambaut, W.I. Lipkin, E.C. Holmes, R.F. Garry, The proximal origin of SARS-CoV-2, Nat. Med. 26 (2020) 450–452. https://doi.org/10.1038/s41591-020-0820-9.

[11] F. Almazán, I. Sola, S. Zuñiga, S. Marquez-Jurado, L. Morales, M. Becares, L. Enjuanes, Coronavirus reverse genetic systems: Infectious clones and replicons, Virus Res. 189 (2014) 262–270. https://doi.org/10.1016/j.virusres.2014.05.026.

[12] M. Hoffmann, H. Kleine-Weber, S. Schroeder, N. Krüger, T. Herrler, S. Erichsen, T.S. Schiergens, G. Herrler, N.H. Wu, A. Nitsche, M.A. Müller, C. Drosten, S. Pöhlmann, SARS-CoV-2 Cell Entry Depends on ACE2 and TMPRSS2 and Is Blocked by a Clinically Proven Protease Inhibitor, Cell. (2020). https://doi.org/10.1016/j.cell.2020.02.052.

[13] Y. Yuan, D. Cao, Y. Zhang, J. Ma, J. Qi, Q. Wang, G. Lu, Y. Wu, J. Yan, Y. Shi, X. Zhang, G.F. Gao, Cryo-EM structures of MERS-CoV and SARS-CoV spike glycoproteins reveal the dynamic receptor binding domains, Nat. Commun. 8 (2017) 15092. https://doi.org/10.1038/ncomms15092.

[14] J. Ziebuhr, E.J. Snijder, A.E. Gorbalenya, Virus-encoded proteinases and proteolytic processing in the Nidovirales, J. Gen. Virol. 81 (2000) 853–879. https://doi.org/10.1099/0022-1317-81-4-853.

[15] E. Estrada, Topological analysis of SARS CoV-2 main protease, Chaos An Interdiscip. J. Nonlinear Sci. 30 (2020) 61102. https://doi.org/10.1063/5.0013029.

[16] D.C. Hall, H.-F. Ji, A search for medications to treat COVID-19 via in silico molecular docking models of the SARS-CoV-2 spike glycoprotein and 3CL protease., Travel Med. Infect. Dis. (2020) 101646. https://doi.org/10.1016/j.tmaid.2020.101646.

[17] S.T. Ngo, N. Quynh Anh Pham, L. Thi Le, D.-H. Pham, V. V Vu, Computational Determination of Potential Inhibitors of SARS-CoV-2 Main Protease, J. Chem. Inf. Model. (2020). https://doi.org/10.1021/acs.jcim.0c00491.

[18] J.T. Ortega, M.L. Serrano, F.H. Pujol, H.R. Rangel, Unrevealing sequence and structural features of novel coronavirus using in silico approaches: The main protease as molecular target, EXCLI J. 19 (2020) 400–409. https://doi.org/10.17179/excli2020-1189.

[19] A. Saxena, Drug targets for COVID-19 therapeutics: Ongoing global efforts, J. Biosci. 45 (2020). https://doi.org/10.1007/s12038-020-00067-w.

[20] S. Liu, Q. Zheng, Z. Wang, Potential covalent drugs targeting the main protease of the SARS-CoV-2 coronavirus, Bioinformatics. 36 (2020) 3295–3298. https://doi.org/10.1093/bioinformatics/btaa224.

[21] P.A. Morais, F.F. Maia, C. Solis-Calero, E.W.S. Caetano, V.N. Freire, H.F. Carvalho, The urokinase plasminogen activator binding to its receptor: A quantum biochemistry description within an in/homogeneous dielectric function framework with application to uPA-uPAR peptide inhibitors, Phys. Chem. Chem. Phys. 22 (2020) 3570–3583. https://doi.org/10.1039/c9cp06530j.

[22] P.F.N. Souza, F.E.S. Lopes, J.L. Amaral, C.D.T. Freitas, J.T.A. Oliveira, A molecular docking study revealed that synthetic peptides induced conformational changes in the structure of SARS-CoV-2 spike glycoprotein, disrupting the interaction with human ACE2 receptor., Int. J. Biol. Macromol. 164 (2020) 66–76. https://doi.org/10.1016/j.ijbiomac.2020.07.174.

[23] J.T.A. Oliveira, P.F.N. Souza, I.M. Vasconcelos, L.P. Dias, T.F. Martins, M.F. Van Tilburg, M.I.F. Guedes, D.O.B. Sousa, Mo-CBP3-PepI, Mo-CBP3-PepII, and Mo-CBP3-PepIII are synthetic antimicrobial peptides active against human pathogens by stimulating ROS generation and increasing plasma membrane permeability, Biochimie. 157 (2019) 10–21. https://doi.org/10.1016/J.BIOCHI.2018.10.016.

[24] L.P. Dias, P.F.N. Souza, J.T.A. Oliveira, I.M. Vasconcelos, N.M.S. Araújo, M.F. V Tilburg, M.I.F. Guedes, R.F. Carneiro, J.L.S. Lopes, D.O.B. Sousa, RcAlb-PepII, a synthetic small peptide bioinspired in the 2S albumin from the seed cake of Ricinus communis, is a potent antimicrobial agent against Klebsiella pneumoniae and

Candida parapsilosis, Biochim. Biophys. Acta - Biomembr. 1862 (2020) 183092. https://doi.org/10.1016/j.bbamem.2019.183092.

[25] P.F.N. Souza, L.S.M. Marques, J.T.A. Oliveira, P.G. Lima, L.P. Dias, N.A.S. Neto, F.E.S. Lopes, J.S. Sousa, A.F.B. Silva, R.F. Caneiro, J.L.S. Lopes, M. V Ramos, C.D.T. Freitas, Synthetic antimicrobial peptides: From choice of the best sequences to action mechanisms, Biochimie. 175 (2020) 132–145. https://doi.org/10.1016/j.biochi.2020.05.016.

[26] E. Ramírez-Aportela, J. Ramón López-Blanco, P. Chacón, Structural Bioinformatics FRODOCK 2.0: Fast Protein-Protein docking server, (2016) 2008–2010. http://frodock.chaconlab.org.

[27] D. Van Der Spoel, E. Lindahl, B. Hess, G. Groenhof, A.E. Mark, H.J.C. Berendsen, GROMACS: fast, flexible, and free., J. Comput. Chem. 26 (2005) 1701–1718. https://doi.org/10.1002/jcc.20291.

[28] I.H. Moal, P.A. Bates, SwarmDock and the use of normal modes in protein-protein Docking, Int. J. Mol. Sci. 11 (2010) 3623–3648. https://doi.org/10.3390/ijms11103623.

[29] M.J. Robertson, J. Tirado-Rives, W.L. Jorgensen, Improved Peptide and Protein Torsional Energetics with the OPLS-AA Force Field, J. Chem. Theory Comput. 11 (2015) 3499–3509. https://doi.org/10.1021/acs.jctc.5b00356.

[30] R.A. Laskowski, M.B. Swindells, LigPlot+: Multiple ligand-protein interaction diagrams for drug discovery, J. Chem. Inf. Model. 51 (2011) 2778–2786. https://doi.org/10.1021/ci200227u.

[31] R.A. Laskowski, J. Jabłońska, L. Pravda, R.S. Vařeková, J.M. Thornton, PDBsum: Structural summaries of PDB entries, Protein Sci. 27 (2018) 129–134. https://doi.org/10.1002/pro.3289.

[32] W. Tian, C. Chen, X. Lei, J. Zhao, J. Liang, CASTp 3.0: Computed atlas of surface topography of proteins, Nucleic Acids Res. 46 (2018) W363–W367. https://doi.org/10.1093/nar/gky473.

[33] D.W. Zhang, J.Z.H. Zhang, Molecular fractionation with conjugate caps for full quantum mechanical calculation of protein-molecule interaction energy, J. Chem. Phys. 119 (2003) 3599–3605. https://doi.org/10.1063/1.1591727.

[34] J.L. Amaral, S.J.M. Santos, P.F.N. Souza, P.A. de Morais, F.F. Maia, H.F. Carvalho, V.N. Freire, Quantum biochemistry in cancer immunotherapy: New insights about CTLA-4/ipilimumab and design of ipilimumab-derived peptides with high potential in cancer treatment, Mol. Immunol. 127 (2020) 203–211. https://doi.org/10.1016/j.molimm.2020.09.013.

[35] B. Delley, From molecules to solids with the DMol3 approach, J. Chem. Phys. 113 (2000) 7756–7764. https://doi.org/10.1063/1.1316015.

[36] M.S. Diamond, T.C. Pierson, The Challenges of Vaccine Development against a New Virus during a Pandemic, Cell Host Microbe. 27 (2020) 699–703. https://doi.org/10.1016/j.chom.2020.04.021.

[37] M.Z. Tay, C.M. Poh, L. Rénia, P.A. MacAry, L.F.P. Ng, The trinity of COVID-19: immunity, inflammation and intervention, Nat. Rev. Immunol. 20 (2020) 363–374. https://doi.org/10.1038/s41577-020-0311-8.

[38] Y. Zhang, J. Xu, R. Jia, C. Yi, W. Gu, P. Liu, X. Dong, H. Zhou, B. Shang, S. Cheng, X. Sun, J. Ye, X. Li, J. Zhang, Z. Ling, L. Ma, B. Wu, M. Zeng, W. Zhou, B. Sun, Protective humoral immunity in SARS-CoV-2 infected pediatric patients, Cell. Mol. Immunol. (2020) 2–4. https://doi.org/10.1038/s41423-020-0438-3.

[39] M.B. Serafin, A. Bottega, V.S. Foletto, T.F. da Rosa, A. Hörner, R. Hörner, Drug repositioning is an alternative for the treatment of coronavirus COVID-19, Int. J. Antimicrob. Agents. 55 (2020) 105969. https://doi.org/10.1016/j.ijantimicag.2020.105969.

[40] L. Zhang, D. Lin, X. Sun, U. Curth, C. Drosten, L. Sauerhering, S. Becker, K. Rox, R. Hilgenfeld, Crystal structure of SARS-CoV-2 main protease provides a basis for design of improved a-ketoamide inhibitors, Science (80-.). 368 (2020) 409–412. https://doi.org/10.1126/science.abb3405.

[41] W. Dai, B. Zhang, X.M. Jiang, H. Su, J. Li, Y. Zhao, X. Xie, Z. Jin, J. Peng, F. Liu, C. Li, Y. Li, F. Bai, H. Wang, X. Cheng, X. Cen, S. Hu, X. Yang, J. Wang, X. Liu, G.

Xiao, H. Jiang, Z. Rao, L.K. Zhang, Y. Xu, H. Yang, H. Liu, Structure-based design of antiviral drug candidates targeting the SARS-CoV-2 main protease, Science. 368 (2020) 1331–1335. https://doi.org/10.1126/science.abb4489.

[42] P. Sharma, V. Vijayan, P. Pant, M. Sharma, N. Vikram, P. Kaur, T.P. Singh, S. Sharma, Identification of potential drug candidates to combat COVID-19: a structural study using the main protease (mpro) of SARS-CoV-2., J. Biomol. Struct. Dyn. 0 (2020) 1–11. https://doi.org/10.1080/07391102.2020.1798286.

[43] B.L. Sousa, I.L. Barroso-Neto, E.F. Oliveira, E. Fonseca, P. Lima-Neto, L.O. Ladeira, V.N. Freire, Explaining RANKL inhibition by OPG through quantum biochemistry computations and insights into peptide-design for the treatment of osteoporosis, RSC Adv. 6 (2016) 84926–84942. https://doi.org/10.1039/c6ra16712h.

[44] D.M.O. Campos, K.S. Bezerra, S.C. Esmaile, U.L. Fulco, E.L. Albuquerque, J.I.N. Oliveira, Intermolecular interactions of cn-716 and acyl-KR-aldehyde dipeptide inhibitors against Zika virus, Phys. Chem. Chem. Phys. 22 (2020) 15683–15695. https://doi.org/10.1039/d0cp02254c.

[45] M. Bzówka, K. Mitusińska, A. Raczyńska, A. Samol, J.A. Tuszyński, A. Góra, Structural and Evolutionary Analysis Indicate That the SARS-CoV-2 Mpro Is a Challenging Target for Small-Molecule Inhibitor Design, Int. J. Mol. Sci. 21 (2020) 3099. https://doi.org/10.3390/ijms21093099.

[46] S. VanPatten, M. He, A. Altiti, K. F Cheng, M.H. Ghanem, Y. Al-Abed, Evidence supporting the use of peptides and peptidomimetics as potential SARS-CoV-2 (COVID-19) therapeutics, Future Med. Chem. 2 (2020). https://doi.org/10.4155/fmc-2020-0180.

3.3 ACE2-derived peptides interact with the RBD domain of SARS-CoV-2 spike glycoprotein, disrupting the interaction with the human ACE2 receptor

Artigo publicado na revista: Journal of Biomolecular Structure & Dynamics.
DOI: http://dx.doi.org/10.1080/07391102.2020.1871415

Running Head: ACE2-derived peptide block RBD-ACE2 interaction

Pedro F. N. Souza[a,]*, Jackson L. Amaral[ab], Leandro P. Bezerra[a], Francisco E.S. Lopes[c], Valder N. Freire[b], Jose T. A. Oliveira[a], Cleverson D. T. Freitas[a]

[a]*Department of Biochemistry and Molecular Biology, Federal University of Ceará, Fortaleza, Ceará, Brazil - CEP 60.440-554.*

[b]*Department of Physics, Federal University of Ceará, Fortaleza, Ceará, Brazil - CEP 60.440-554.*

[c]*Center for Permanent Education in Health Care-CEATS / School of Public Health of Ceará-ESP-CE*

Corresponding Author

*****Corresponding author: Biochemistry and Molecular Biology Department, Federal University of Ceará, CE, Brazil, Laboratory of Plant Defense Proteins, Av. Mister Hull, P.O. Box: 60451 Fortaleza, CE, Brazil. Tel: +55 85 33669823; Fax: +55 85 33669789.

Email: pedrofilhobio@gmail.com

ORCID: 0000-0003-2524-4434 (P. F. N. Souza)

Abstract

Vaccines could be the solution to the current SARS-CoV-2 outbreak. However, some studies have shown that the immunological memory only lasts three months. Thus, it is imperative to develop pharmacological treatments to cope with COVID-19. Here, the *in silico* approach by molecular docking, dynamic simulations, and quantum biochemistry revealed that ACE2-derived peptides strongly interact with the SARS-CoV-2 RBD domain of spike glycoprotein (S-RBD). ACE2-Dev-PepI, ACE2-Dev-PepII, ACE2-Dev-PepIII, and ACE2-Dev-PepIV complexed with S-RBD provoked alterations in the 3D structure of S-RBD, leading to disruption of the correct interaction with the ACE2 receptor, a pivotal step for SARS-CoV-2 infection. This wrong interaction between S-RBD and ACE2 could inhibit the entry of SARS-CoV-2 in cells, and thus virus replication and the establishment of COVID-19 disease. Therefore, we suggest that ACE2-derived peptides can interfere with recognition of ACE2 in human cells by SARS-CoV-2 *in vivo*. Bioinformatic prediction showed that these peptides have no toxicity or allergenic potential. By using ACE2-derived peptides against SARS-CoV-2, this study points to opportunities for further *in vivo* research on these peptides, seeking to discover new drugs and entirely new perspectives to treat COVID-19.

Keywords: SARS-CoV-2 RBD; COVID-19; ACE2 receptor; ACE2-Derived peptides

3.3.1 Introduction

Coronaviruses (CoVs) are enveloped and pleomorphic viruses belonging to the Coronaviridae family. They share a typical morphology with the non-segmented positive single-stranded RNA genome, estimated to have length of 30 Kb [1,2]. The human-to-human spread of the coronaviruses is mainly by nose and mouth secretion droplets. These viruses cause disease that ranges from mild cold symptoms to atypically severe pneumonia, with many complications, resulting in death [1].

The current pandemic caused by the SARS-CoV-2 (severe acute respiratory syndrome coronavirus 2) has claimed many lives and threatened

thousands worldwide. COVID-19 (Coronavirus Disease 2019) is less lethal and by far more transmissible than the diseases caused by the viruses involved in other recent outbreaks, such as in 2002 by SARS-CoV (Severe Acute Respiratory Syndrome Coronavirus) and MERS-CoV (Middle East Respiratory Syndrome Coronavirus). A way to measure that is the case fatality rate (CRF) of each outbreak. The CRF of SARS-CoV, MERS-CoV and SARS-CoV-2 is, respectively, of 9.7, 34 and 1%, which indicates that SARS-CoV-2 is not one of the worst coronaviruses. However, its higher transmissibility has resulted in 10 million of infected people with 500 000 deaths, by far a larger number compared to other outbreaks [3–5].

SARS-CoV-2 is close to SARS-CoV-1, sharing similarities accounting nearly 80% in the genome sequence. Additionally, both coronaviruses employ the same RBD (receptor-binding domain) in the spike glycoprotein (S protein) to interact with human ACE2 (Angiotensin I Converting Enzyme 2) of the host cell to start the infection. The virus takes control of the cellular machinery to synthesize its own genome and proteins. Despite similarities, the SARS-CoV-2 S protein has accumulated mutations, leading to modifications in the RBD region that enhance its affinity for human ACE2 20-fold compared to SARS-CoV S protein, resulting in faster transmission from human to human [4,6,7].

Despite the similarities, it is important to highlight the differences between SARS-CoV-1 and SARS-CoV-2 receptor recognition as they are involved in virus transmissibility, infectivity and pathology. It is known that the SARS-CoV-2 RBD has a higher ACE2-binding affinity than SARS-CoV-1, a characteristic which could lead to a more efficient cell entry and transmissibility [6, 8]. In contrast, ACE2 affinity towards the entire SARS-CoV-2 S protein is lower than that of SARS-CoV entire S protein suggesting that SARS-CoV-2 RBD, besides being strongest, is probably less exposed than SARS-CoV RBD [4-8]. In addition, SARS-CoV-2 S protein also held substitution D614G during the coronavirus disease 2019 (COVID-19) pandemic [9]. An elegant experiment using the cryoelectron microscopy (cryo-EM) revealed that the change from D614 to G614 eliminates the requirements of side-chain hydrogen bond, increasing mainchain flexibility and altering interactions and modulates glycosylation enhancing the cell entry, infectivity, transmissibility, stability of virions, and high viral loads in the airways [9, 10]. Besides these differences, a new feature is the high nanomechanical stability of the SARS-CoV-2 S-ACE2 interaction compared

to SARS-CoV-1 [11]. Moreira et al. [11] revealed that high mechanical stability in the SARS-CoV-2 S-ACE2 has several biological implications such as cell-recognition, viral attachment, fusion and entry. Thus, mechanical stability might play a role in the increasing spread of COVID-19 [11].

Still regarding the importance of S-ACE2 interaction for SARS-CoV-2 cell entry, there recently have been reported that mutations far from RBD could affect the S-ACE2 interaction [12]. For example, Qiao and de la cruz [12] reported mutations non-RBD sited but altering the polybasic cleavage could result in 34% the S-RBD strength of interaction. This result suggests the role of polybasic cleavage in enhancement of S-ACE2 interaction [12].

Given the importance of the S-ACE2 interaction to COVID-19 establishment, many studies have focused on finding drugs (either already available or new ones) that can interfere with this interaction, making S protein a promising target in *silico* assays. Other groups have been investigating existing drugs used to treat other viral infections, in a process called repositioning or repurposing, but without success [13]. Nevertheless, computational screening is an exciting approach to develop new drugs faster and more precisely. Therefore, many research groups are employing molecular docking (MD) and molecular dynamic simulation (MDS) to find new molecules targeting the SARS-CoV-2 S protein [13,14].

Recently, our research group performed MD and MDS studies using eight synthetic antimicrobial peptides (*Mo*-CBP3-PepI, *Mo*-CBP3-PepII, *Mo*-CBP3-PepIII, *RcAlb*-PepI, *RcAlb*-PepII, *RcAlb*-PepIII, PEPGAT and PEPKAA) to target the SARS-CoV-2 S glycoprotein [14]. Of those, *Mo*-CBP3-PepII and PEPKAA strongly interacted with the SARS-COV-2 S protein, changing its native conformation and topology, leading to wrong interaction with ACE2 [14].

The most crucial feature of the SARS-CoV-2 S protein is the high affinity of the RBD domain to the human ACE2 receptor, leading to higher levels of infection compared to SARS-CoV and MERS-CoV. Based on that, in this study we employed the sequence to design antiviral peptides targeting the SARS-CoV-2 S protein RBD domain (S-RBD). Altogether, molecular docking, dynamic simulations, and quantum biochemical analyses revealed that all peptides strongly bind to the RBD domain of SARS-CoV-2 S protein. Through this binding, the peptides can stop the correct cross talk between the cell and SARS-CoV-2, which is a critical step in the viral infection.

Therefore, the inhibition or induction of incorrect interaction of the RBD domain and the human ACE2 receptor could be a potentially valuable strategy to combat COVID-19 caused by SARS-CoV-2.

3.3.2 Methodology

3.3.2.1 Design of peptides

The design of peptides followed the pipeline produced by Souza et al. [15]. The protein sequence chosen was angiotensin-converting enzyme 2 from *Homo sapiens* (ACE2), freely available in the NCBI database (https://www.ncbi.nlm.nih.gov/) under accession number Q9BYF1. The server used for the design was the AVPpred server (http://crdd.osdd.net/servers/avppred/) according to [16]. First, the sequence of ACE2 was fractioned using AVPpred to produce peptides with chain lengths of 10, 15, and 20 amino acid residues. Then, all the peptides were run in AVPpred to find potential antiviral peptides. The AVPpred algorithm employs three criteria to select peptides: (1) alignment model; (2) composition model; and (3) physicochemical model. Based on those, the server classifies the sequences as AVP to potential antiviral peptides and non-AVP to non-potential antiviral peptides.

After the design, the best sequences selected by AVPpred were also run in the iAMPpred tool (http://cabgrid.res.in:8080/amppred/) [17] to calculate the probability of the sequences selected by AVPpred to be antiviral. The best sequences based on antiviral potential prediction were selected and characterized by physicochemical and biological properties using the iAMPpred tool.

The PEPFold server (https://bioserv.rpbs.univ-paris-diderot.fr/services/PEP-FOLD3/), a widely used computational tool to predict three-dimensional (3D) structures of linear peptides between 5 and 50 amino acids [18], was employed to build the 3D structure of ACE-2-derived peptides. The Pymol program was employed to evaluate the peptides' 3D structures and their interaction with the ACE2 human protein.

3.3.2.2 Molecular docking (MD) assays

FRODOCK 3.12 (http://frodock.chaconlab.org/) [19], one of the best servers for peptide-protein interaction, was used to perform all blind molecular docking assays. The peptides with the highest potential were chosen based on the docking score and repetition of poses in the output.

3.3.2.3 Molecular dynamic simulation

The complexes generated by the molecular docking tests were minimized and balanced to stabilize them before the molecular dynamic assays. The force field of all OPLS-AA/L atoms [20,21] was used to perform the topology, after which a 2 nm cubic box was created. Then the SPC/E model of water was used for solvation of the box, the systems were neutralized, and the Na+ e Cl- ions were added at a concentration of 0.15 M. To perform the minimization until it reached negative potential energy and the lower maximum force of 1000 kJ mol^{-1} nm^{-1}. The pressure and temperature balance was performed to 100 ps. Subsequently, molecular dynamic simulations were performed for 100 ns, and the resulting structures were used for the further analyses.

3.3.2.4 Interface analysis of the complexes formed between S-RBD and the studied peptides

The Protein Interactions Calculator (PIC) server was used to analyze the interface interactions of the complexes. The PIC server (http://pic.mbu.iisc.ernet.in/) also determines the accessible surface area and distance of a residue from the protein's surface based on analysis of a set of 3D structure coordinates. The PyMOL software, a molecular graphics tool widely used for three-dimensional visualization of molecules, was used to generate 3D figures and perform RMSD calculations. The Ligplot software [22] was used to generate 2D figures with the respective representations of hydrophobic interactions and hydrogen bonds.

3.3.2.5 Quantum biochemistry calculation

This was performed according to a protocol established previously [23]. Molecular fractionation with conjugate caps (MFCC) was carried out to calculate the full quantum mechanical interaction energies between two pairs of specific amino acid residues (Ri and Rj) involving the studied peptides and SARS-CoV-2 Mpro, as follows, based on the work of Amaral et al. [24]:

$$E(R_i - R_j) = E(C_{i-1}\,R_i\,C_{i+1} + C_{j-1}\,R_j\,C_{j+1}) - E(C_{i-1}\,R_i\,C_{i+1} + C_{j-1}\,C_{j+1}) - E(C_{i-1}\,C_{i+1} + C_{j-1}\,R_j\,C_{j+1}) + E(C_{i-1}\,C_{i+1} + C_{j-1}\,C_{j+1})$$

Where $E(C_{i-1}\,R_i\,C_{i+1} + C_{j-1}\,R_j\,C_{j+1})$, the first term of the equation, is the total energy of the system formed by the residues Ri and Rj correctly capped; $E(C_{i-1}\,R_i\,C_{i+1} + C_{j-1}\,C_{j+1})$, the second term, is the total energy of the system formed by the capped residue Ri and the caps of the residue Rj; the third term, $E(C_{i-1}\,C_{i+1} + C_{j-1}\,R_j\,C_{j+1})$, represents the total energy of the system formed by the capped residue Rj and the caps of the residue Ri; and the last term, $E(C_{i-1}\,C_{i+1} + C_{j-1}\,C_{j+1})$, accounts for the system's total energy, formed by the caps of both residues Ri and Rj. The caps $C_{i-1}(C_{i+1})$ and $C_{j-1}(C_{j+1})$ are made from the residues covalently bound to the amine (carboxyl) groups of Ri and Rj. In the MFCC method used, all interaction between amino acid residues of the studied peptides and SARS-CoV-2 Mpro separated from each other within an 8 Å range were calculated, considering a dielectric function approach of 40 (ε=40) for all interactions. The structural files (PDB format) obtained after molecular dynamic simulation and MFCC were used as inputs for density functional theory (DFT) calculations with DMOL^3 [25].

3.3.3 Results

3.3.3.1 ACE2-derived peptide design

The AVPpred was set up to use the ACE2 sequence to produce peptides with 10, 15, and 20 amino acid residues. There were 100, 80, and 79 peptides generated, with 10, 15, and 20 amino acid residues, respectively, for a total

of 259 peptides (Tables S1-S3). Of those, AVPpred selected four peptides with antiviral potential, which were named ACE2-Dev-PepI, ACE2-Dev-PepII, ACE2-Dev-PepIII, and ACE2-Dev-PepIV. (Table 5).

As summarized in Table 1, all peptides were cationic, with positive charges ranging from +1 to +3, hydrophobic ratio from 45 to 60%, and calculated molecular mass ranging from 1802.16 to 2587.14. Regarding biological properties, the iAMPpred tool revealed antiviral potentials of 80, 75, 63, and 35, respectively, for ACE2-Dev-PepI, ACE2-Dev-PepII, ACE2-Dev-PepIII and ACE2-Dev-PepIV (Table 2), corroborating the analysis of AVPpred. The *in silico* analyses revealed that all peptides had no hemolytic, allergenic or toxic potential (Table 2). This is interesting because designing peptides from the ACE2 human receptor can reduce any collateral effect.

In silico analyses also revealed that, all peptides possibly interacted with DNA and RNA (Table 6). The interaction with RNA is particularly interesting because SARS-CoV-2 and other coronaviruses have RNA as genetic material. Looking forward to clinical application, we tested the resistance of these peptides in the intestinal-like environment. ACE2-Dev-PepIII presented a half-life of 0.021 s, indicating low stability, which means that enzymes promptly digest it. ACE2-Dev-PepIV showed normal stability, as indicated by the half-life of 0.614 s. ACE2-Dev-PepI and ACE2-Dev-PepII presented high stability, with half-life values of 3.461 and 1.669 s, respectively (Table 6). These values indicate the possibility of oral administration of the last two peptides.

The PEPFold server predicted that all ACE2-dev peptides contain long helices as secondary structures (Supplementary Fig. S1). The Ramachandran plot (Table 1) revealed 98%, 99%, 95%, and 99% of favorable regions for helix formation, respectively, for ACE2-Dev-PepI, ACE2-Dev-PepII, ACE2-Dev-PepIII, and ACE2-Dev-PepIV (Table 5).

Table 5. Physicochemical properties of the ACE2-derived peptides

Properties/Peptides	ACE2-Dev-Pep-I	ACE2-Dev-Pep-II	ACE2-Dev-Pep-III	ACE2-Dev-Pep-IV
Sequence	CLPAHLLGDMWGRFW	MRQYFLKVKNQMILF	PFTYMLEKWRWMVFKGEIPK	CLPAHLLGDMWGRFWTNLYS
[a] pI	6.7	10.3	9.5	6.3
[b] Calculated molecular mass (Da)	1802.16	1959.45	2587.14	2380.78
[b] Hydrophobic ratio (%)	60	53	45	50
[b] Net charge	**+**1	+3	+2	+1
[c] Ramachandran plot (%)	98	99	95	99
[d] Tm	0.470	0.335	0.223	0.537
[d] sOPEP	-32.2	-29.49	-48.60	-46.57

Fonte: SOUZA *et al.,* 2022.
[a] Calculated by using the ProtParam tool (https://web.expasy.org/protparam/protpar-ref.html).
[b] Data generated by the Antimicrobial Peptide Database (APD, http://aps.unmc.edu/AP/).
[c] Calculated by using the program Rampage (http://mordred.bioc.cam.ac.uk/~rapper/rampage.php).
[d] Calculated by using the PepFOLD 3.0 server (http://mobyle.rpbs.univ-paris-diderot.fr/cgi-bin/portal.py#forms::PEP-FOLD).

Table 6. ACE2-derived peptides properties obtained by bioinformatic analyses.

Properties/Peptides	ACE2-Dev-Pep-I	ACE2-Dev-Pep-II	ACE2-Dev-Pep-III	ACE2-Dev-Pep-IV
[a]Allergic potential	No	No	No	No
[b]Hemolytic potential (%)	0	0	1	0
[c]Toxic potential	Non-toxic	Non-toxic	Non-toxic	Non-toxic
[d]Antiviral prediction	Yes	Yes	Yes	Yes
[e]Antiviral potential (%)	80	75	63	35
[f]DNA-binding	Yes	Yes	Yes	Yes
[g]RNA-binding	Yes	Yes	Yes	Yes
[h]Half-life	3.461	1.669	0.021	0.614
[i]Stability	High	High	Low	Normal

Fonte: SOUZA *et al.,* 2022.

[a]The allergic potential was calculated using the Antigenic Prediction tool (http://imed.med.ucm.es/Tools/antigenic.pl). [b] The hemolytic potential was calculated by the HemoPI tool (http://crdd.osdd.net/raghava/hemopi/submitfreq.php?ran=44366).[c] The toxin potential was calculated using ToxinPred (http://crdd.osdd.net/raghava/toxinpred/design.php). [d] The antiviral potential was calculated using the AVpred (http://crdd.osdd.net/servers/avppred/). [e] The antiviral potential was calculated using the iAMPpred tool (http://cabgrid.res.in:8080/amppred/). [f] The DNA-binding potential was assessed by using DNAbinder (http://crdd.osdd.net/cgibin/dnabinder/valid1.pl). [g] The RNA-binding potential was assessed by using RNApred (http://crdd.osdd.net/raghava/rnapred/submit.html). [h] The half-life in seconds was calculated using the Half-Life Prediction tool (http://crdd.osdd.net/raghava/hlp/help.html), which predicts the proteolytic activity in the intestinal-like environment.[i] Stability was calculated using the Half-Life Prediction tool (http://crdd.osdd.net/raghava/hlp/help.html). Half-life < 0.1 s means low stability; half-life from 0.1 to 1.0 s means normal stability; half-life > 1.0 s means high stability.

3.3.3.2 Molecular docking and dynamic simulations revealed interaction and stabilization between the ACE2-derived peptides and S-RBD

Given the large size of the entire SARS-CoV-2 S protein, many research groups have chosen to perform molecular docking and dynamic simulations using only the RBD structure [23–26]. Here, we followed the same approach. Molecular docking analyses showed that all ACE2-derived peptides interacted with S-RBD in the same region, with different scores, as revealed by the FRODDOCK server (Fig. 38). The peptides ACE2-Dev-PepI, ACE2-Dev-PepII, ACE2-Dev-PepIII, and ACE2-Dev-PepIV presented scores of 3003.43, 2909.40, 2829.25, and 3251.67 kj.mol^{-1}, respectively.

Molecular dynamic simulation showed the stabilization of the complexes formed by ACE2-Dev-PepI, ACE2-Dev-PepII, ACE2-Dev-PepIII, and ACE2-Dev-PepIV with S-RBD after assay of 30 ns, remaining stable up to 100 ns, with RMSD variations below 1Å after 30 ns (Fig. 39). The stable conformation obtained from each MD simulation was used to perform all further analyses.

3.3.3.3 Interaction between S-RBD and ACE2-Dev-PepI

The most relevant interactions among the amino acid residues from S-RBD and ACE2-Dev-PepI were by: Tyr^{489}, Tyr^{473}, Tyr^{489}, Phe^{456}, Ala^{475}, Tyr^{489}, Leu^{455}, Lys^{458}, Tyr^{489}, and Ala^{475} of RBD with Phe^{14}, Trp^{15}, Trp^{11}, Trp^{15}, Phe^{14}, Trp^{15}, Trp^{11}, Trp^{15}, Met^{10}, and Trp^{15} of ACE2-Dev-PepI. The interaction energies of interaction were, respectively, -7.40, -7.22, -6.65, -5.54, -5.41, -4.57, -3.11, -2.90, -2.86, and -2.72 kcal.mol^{-1}, with distances of 1.69, 1.76, 2.63, 2.54, 2.17, 2.40, 2.26, 4.70, 2.04, and 2.65 Å, respectively. All existing interactions up to a distance of 8Å are reported in Supplementary Table 4.

The complex ACE2-Dev-PepI::S-RBD is supported by many interactions, such as hydrophobic, and aromatic-aromatic interactions, along with hydrogen bonds (Fig. 40A, B, and D). The hydrophobic interactions were with residues Tyr^{489}, Leu^{455}, Tyr^{489}, Ala^{475}, Tyr^{489}, Phe^{456}, Tyr^{473}, and Tyr^{489} of S-RBD with Met^{10}, Trp^{11}, Trp^{11}, Phe^{14}, Phe^{14}, Trp^{15}, Trp^{15}, and Trp^{15} of ACE2-Dev-PepI (Fig. 40B and D). The hydrogen bonds occurred between residues Phe^{489} and Tyr^{489} of S-RBD and residues Met^{10} and Phe^{14}of ACE2-Dev-PepI (Fig. 40A, B and D). The aromatic-

aromatic interactions were formed between residues Tyr^{489} and Phe^{456} of S-RBD and residues Trp^{11} and Trp^{15} of ACE2-Dev-PepI (Fig. 40A and D).

Met10, Trp11, Phe14, and Trp15 were the most relevant amino acid residues of ACE2-Dev-PepI in the interaction with S-RBD, with respective interaction energies of -6.78, -15.40, -17.24, and -23.81kcal.mol^{-1} (Fig. 40C).

3.3.3.4 Interaction of S-RBD with ACE2-Dev-PepII

Regarding the complex ACE2-Dev-PepII::S-RBD, interactions occurred between residues Arg^{403}, Glu^{484}, Leu^{492}, Tyr^{473}, Gln^{493}, Phe^{456}, Leu^{455}, Tyr^{505}, Tyr^{489}, Leu^{455}, and Phe^{490} of S- RBD and residues Phe^{15}, Lys^{9}, Lys^{9}, Phe^{5}, Lys^{9}, Phe^{5}, Val^{8}, Phe^{15}, Leu^{6}, Lys^{9}, and Lys^{9} of ACE2-Dev-PepII. The interaction energies of those interactions were, respectively, -13.81, -11.00, -5.14, -4.98, -4.61, -4.34, -4.23, -3.91, -3.61, -3.21, and -2.93 kcal.mol^{-1} with distances of 1.63, 1.57, 2.18, 2.39, 2.85, 2.57, 2.39, 2.33, 2.31, 2.35, and 2.15 Å. The ACE2-Dev-PepII::S-RBD complex presented a repulsive interaction between Arg^{403} of S-RBD and Leu^{14} of ACE2-Dev-PepII, with interaction energy of +1.47 kcal.mol^{-1} and distance of 5.09 Å. Supplementary Table 5 summarizes all interactions between ACE2-Dev-PepII and SARS-CoV-2 RBD up to a distance of 8Å.

Figure 38**.** Molecular docking revealed that peptides derived from ACE2 human protein can interact with SARS-CoV-2 RBD.

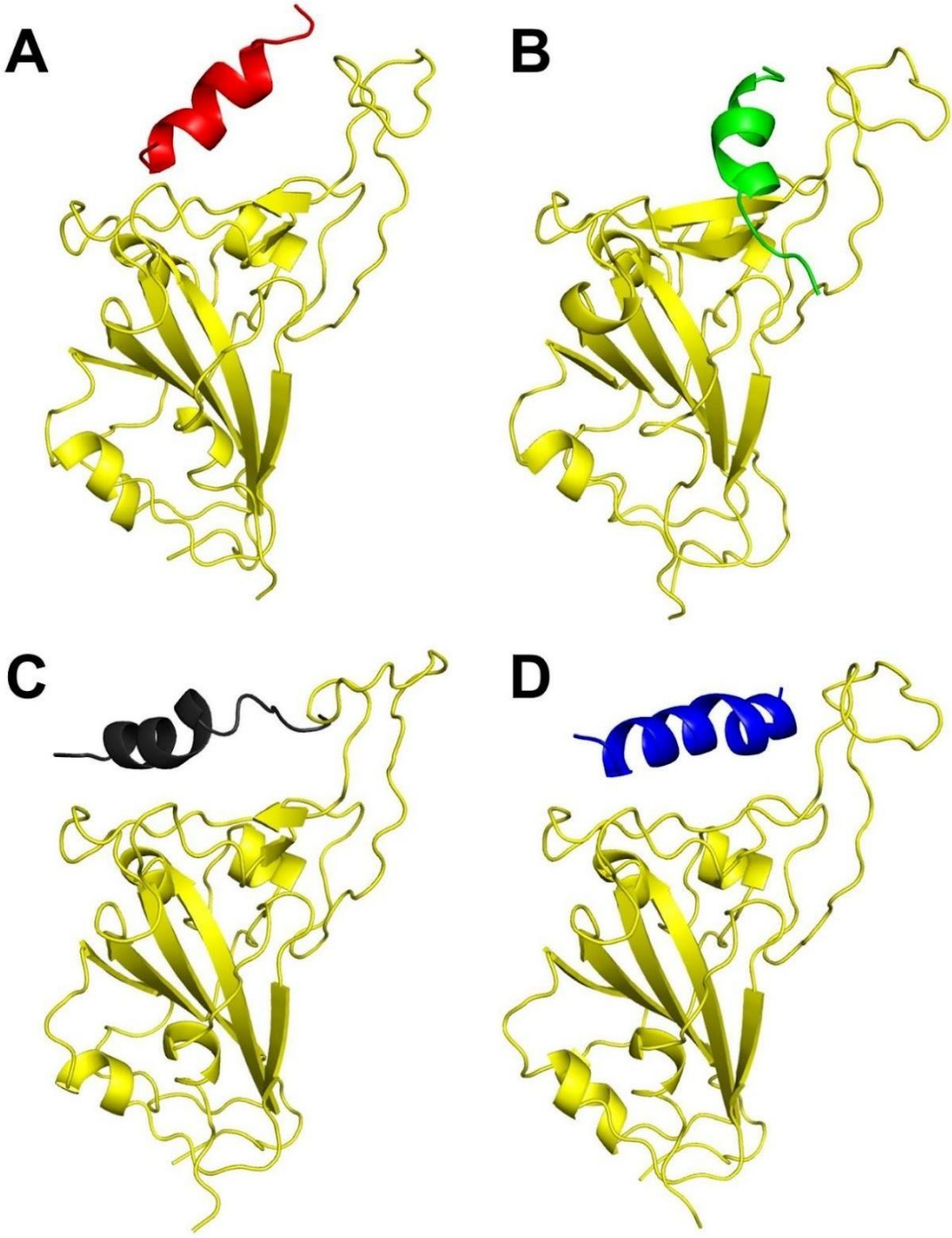

The target SARS-CoV-2 RBD is represented in cartoon yellow and ACE2-Dev-PepI in red (A), ACE2-Dev-PepII in green (B), ACE2-Dev-PepIII in black (C), and ACE2-Dev-PepIV in blue (D).

Figure 39. Molecular dynamic simulations obtaining stable structures.

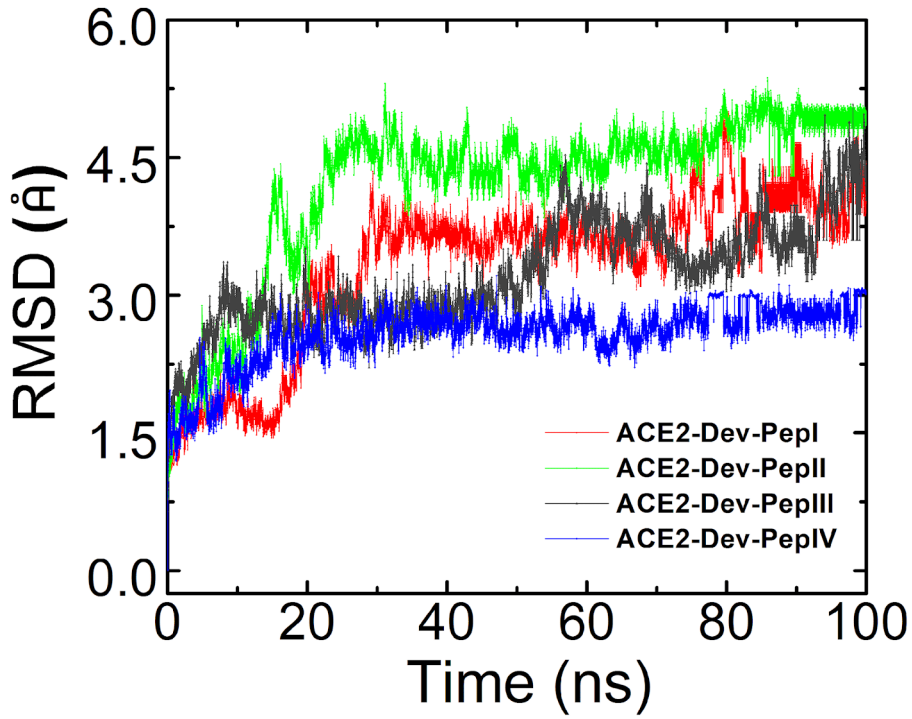

Fonte: SOUZA *et al.,* 2022. The complexes formed between the four peptides derived from ACE2 and SARS-CoV-2 were examined by molecular dynamics, and stable structures were obtained after 100 ns. Each RMSD variation demonstrated stability during the simulation after 30 ns.

The interaction between ACE2-Dev-PepII and S-RBD occurred through hydrophobic, ionic, aromatic-aromatic, cation-pi, and hydrogen bonds (Fig 41A, B, and C). Tyr^{489}, Phe^{456}, Phe^{456}, Tyr^{473}, Ala^{475}, Ala^{475}, Tyr^{489}, Leu^{455}, Phe^{456}, Pro^{491}, Tyr^{453}, Leu^{455}, and Tyr^{505} of S-RBD had hydrophobic interactions with residues Met^{1}, Tyr^{4}, Phe^{5}, Phe^{5}, Phe^{5}, Leu^{6}, Leu^{6}, Val^{8}, Val^{8}, Val^{8}, Met^{12}, Met^{12}, Phe^{15} of ACE2-Dev-PepII peptide (Fig. 41B and C). Hydrogen bonds occurred between residues Phe^{490}, Leu^{492}, Glu^{484}, and $Tyr^{453}$of S-RBD and residues Lys^{9}, Lys^{9}, Lys^{9}, and Met^{12} of ACE2-Dev-PepII (Fig. 41A, B and C).

Ionic interaction occurred between the Glu^{484} residue of S-RBD and Lys^{9} residue of ACE2-Dev-PepII. Four cation-pi interactions happened between residues Lys^{458}, Arg^{403}, Tyr^{489}, and Phe^{490} of S-RBD and residues Phe^{5}, Phe^{15}, Lys^{9}, and $Lys^{9}$of ACE2-Dev-PepII (Fig. 41C). Finally, the Phe^{456}, Phe^{456}, Tyr^{473}, and Tyr^{505}residues of S-RBD had aromatic-aromatic interactions with the residues Tyr^{4}, Phe^{5}, Phe^{5}, and Phe^{15} of ACE2-Dev-PepII (Fig. 41C).

Figure 40. Energies and interaction between SARS-CoV-2 RBD and ACE2-Dev-PepI.

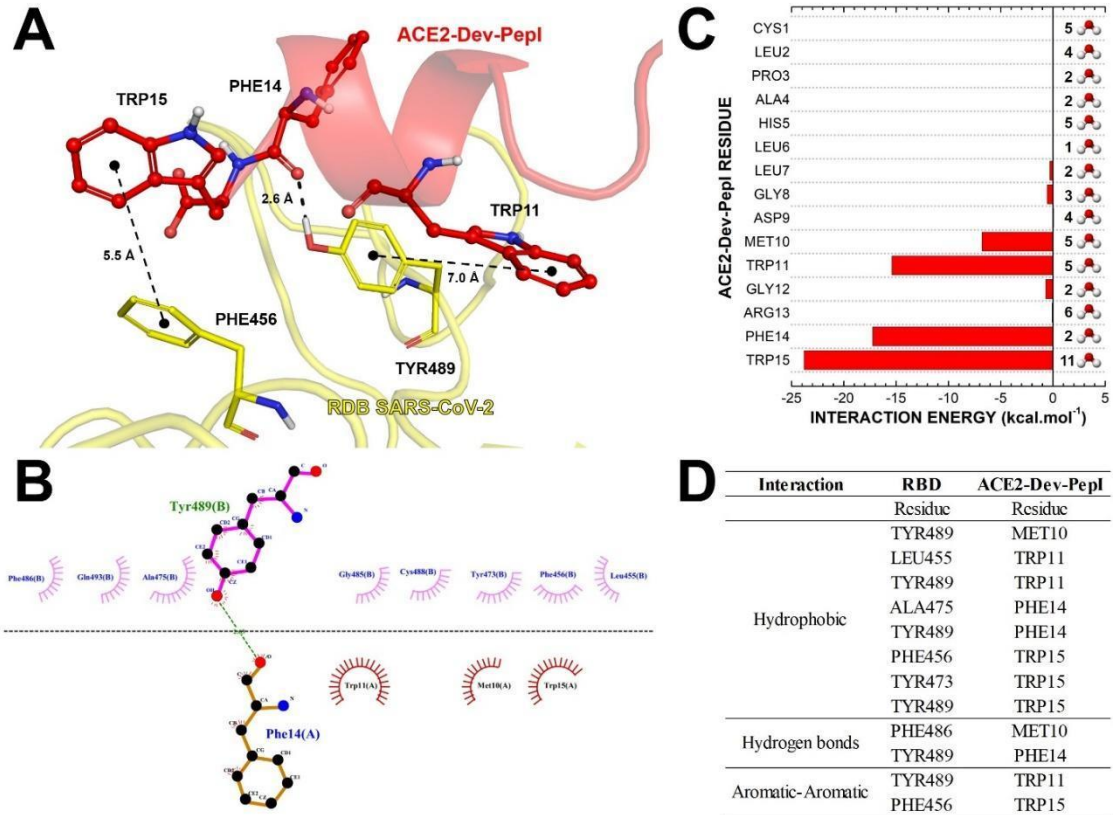

Interaction	RBD Residue	ACE2-Dev-PepI Residue
Hydrophobic	TYR489	MET10
	LEU455	TRP11
	TYR489	TRP11
	ALA475	PHE14
	TYR489	PHE14
	PHE456	TRP15
	TYR473	TRP15
	TYR489	TRP15
Hydrogen bonds	PHE486	MET10
	TYR489	PHE14
Aromatic-Aromatic	TYR489	TRP11
	PHE456	TRP15

Fonte: SOUZA *et al.,* 2022. Energies and interaction between SARS-CoV-2 RBD (yellow) and ACE2-Dev-PepI (red). A and B represent the 3D interactions and 2D interactions, respectively. C represents the individual energy contribution of each amino acid residue of ACE2-Dev-PepI, and D denotes all interactions between SARS-CoV-2 RBD and ACE2-Dev-PepI.

The most relevant amino acid residues of ACE2-Dev-PepII that interacted with S-RBD were Phe5, Leu6, Val8, Lys9, Met12, and Phe15 with the interaction energies of -16.11, -12.78, -9.23, -31.58, -5.95, and -20.79 kcal.mol^{-1}, respectively (Fig. 41D).

3.3.3.5 Interaction between S-RBD and ACE2-Dev-PepIII

In the complex formed between ACE2-Dev-PepIII::S-RBD, the main interactions were by residues Lys^{417}, Arg^{408}, Tyr^{453}, Glu^{406}, Tyr^{489}, Leu^{455}, Gln^{493}, Gln^{493}, Gln^{493}, and Phe^{456} of S-RBD with residues Glu^{7}, Phe^{2}, Arg^{10}, Arg^{10}, Phe^{14}, Phe^{14}, Trp^{9}, Val^{13}, Arg^{10}, and Phe^{14} of ACE2-Dev-PepIII. The interaction energies were, respectively, -11.04, -8.78, -5.04, -4.88, -3.90, -3.81, -3.34, -3.24, -3.22, and -3.04 kcal.mol^{-1} and distances of 1.59, 2.53, 1.89, 4.01, 2.48, 2.23, 2.01, 2.66, 2.51, 2.62 Å, respectively. Repulsive interactions occurred between residues Glu^{406} and

Arg^{403} of SARS-CoV-2 RBD and residues Glu^{7} and Arg^{10} of ACE2-Dev-PepIII, with interaction energies of +1.42 and +1.98 kcal.mol^{-1}, respectively. All interactions between ACE2-Dev-PepIII and SARS-CoV-2 RBD up to a distance of 8Å are reported in Supplementary Table 6.

ACE2-Dev-PepIII interacted with S-RBD through hydrophobic, ionic, aromatic-aromatic, cation-pi interactions and hydrogen bonds. The residues Tyr^{505}, Tyr^{505}, Leu^{455}, Leu^{455}, Phe^{456}, and Tyr^{489} of S-RBD were involved in hydrophobic interactions with Met^{5}, Trp^{9}, Val^{13}, Phe^{14}, Phe^{14}, and Phe^{14} of ACE2-Dev-PepIII (Fig. 42B and D). Tyr505, Phe456, and Tyr489 of S-RBD and Trp9, Phe14, and Phe14 of ACE2-Dev-PepIII (Fig. 42A and D), drove aromatic-aromatic interactions. Hydrogen bonds occurred between Gln^{493}, Gln^{493}, Tyr^{453}, and Lys^{417} residues of S-RBD and the Trp^{9}, Trp^{9}, Arg^{10}, and Glu^{7} residues of ACE2-Dev-PepIII (Fig. 42A, B and D).

Phe^{2}, Leu^{6}, Glu^{7}, Trp^{9}, Arg^{10}, Val^{13}, Phe^{14}, and Lys^{15} were the main amino acid residues of ACE2-Dev-PepIII that interacted with S-RBD, with interaction energy values of -13.98, -6.13, -11.52, -9.74, -14.52, -7.07, -13.85, and -4.38 kcal.mol^{-1}.

3.3.3.6 Interaction between S-RBD and ACE2-Dev-PepIV

The main interactions between amino acid residues were driven by Tyr^{449}, Gln^{493}, Tyr^{489}, Phe^{490}, Leu^{455}, Gln^{498}, Gln^{498}, Phe^{456}, Phe^{456}, Phe^{456}, and Leu^{455} of S-RBD and residues Leu^{18}, Trp^{11}, Leu^{7}, Trp^{11}, Leu^{6}, Leu^{18}, Asn^{17}, Leu^{7}, Pro^{3}, Leu^{6}, and Leu^{7} of ACE2-Dev-PepIV. The interaction energies were -5.27, -5.07, -4.99, -4.14, -4.05, -3.91, -3.85, -3.82, -3.40, -3.04, and -3.03 kcal.mol^{-1}, with distances of 2.22, 2.92, 2.18, 2.25, 2.25, 3.43, 1.71, 2.22, 2.51, 2.12, and 2.22 Å, respectively. The repulsive interaction was between the residue Gly^{485} of S-RBD and Leu^{7} of ACE2-Dev-PepIV, with the interaction energy of +0.54 kcal.mol^{-1}. All interactions between ACE2-Dev-PepIV and SARS-CoV-2 RBD up to a distance of 8Å are reported in Supplementary Table 7.

Figure 41. Energies and interaction between SARS-CoV-2 RBD (yellow) and ACE2-Dev-PepII (green).

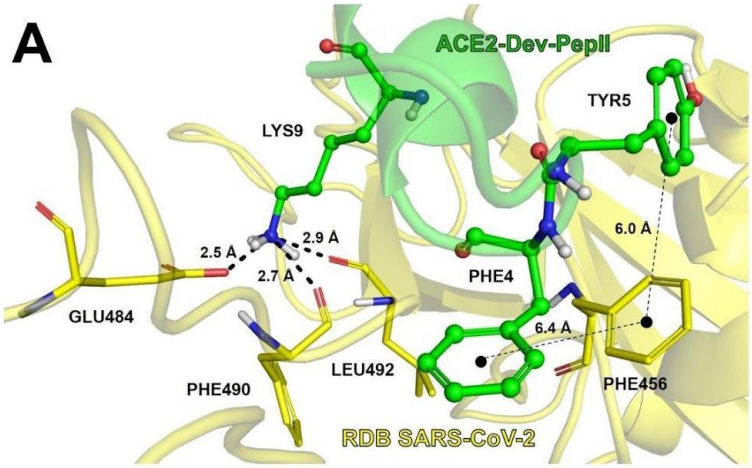

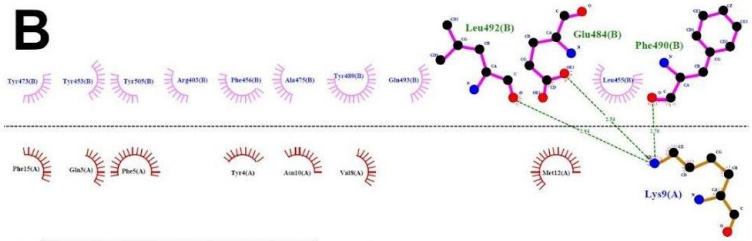

C

Interaction	RBD Residue	ACE2-Dev-PepII Residue
Hydrophobic	TYR489	MET1
	PHE456	TYR4
	PHE456	PHE5
	TYR473	PHE5
	ALA475	PHE5
	ALA475	LEU6
	TYR489	LEU6
	LEU455	VAL8
	PHE456	VAL8
	PRO491	VAL8
	TYR453	MET12
	LEU455	MET12
	TYR505	PHE15
Hydrogen bonds	PHE490	LYS9
	LEU492	LYS9
	GLU484	LYS9
	TYR453	MET12
Ionic	GLU484	LYS9
Aromatic-Aromatic	PHE456	TYR4
	PHE456	PHE5
	TYR473	PHE5
	TYR505	PHE15
Cation-Pi	LYS458	PHE5
	ARG403	PHE15
	TYR489	LYS9
	PHE490	LYS9

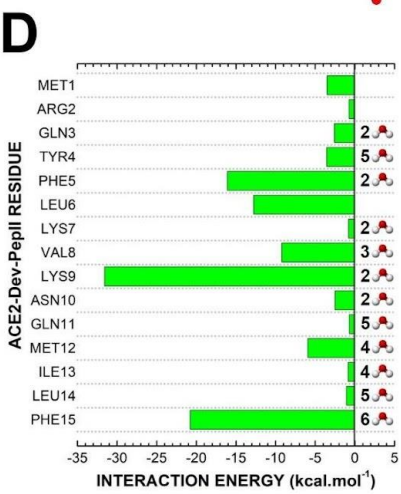

Fonte: SOUZA *et al.,* 2022. Energies and interaction between SARS-CoV-2 RBD (yellow) and ACE2-Dev-PepII (green). A and B represent the 3D interactions and 2D interactions, respectively. C denotes all interactions between SARS-CoV-2 RBD and ACE2-Dev-PepII and D represents the individual energy contribution of each amino acid residue of ACE2-Dev-PepII.

Figure 42. Energies and interaction between SARS-CoV-2 RBD (yellow) and ACE2-Dev-PepIII (black).

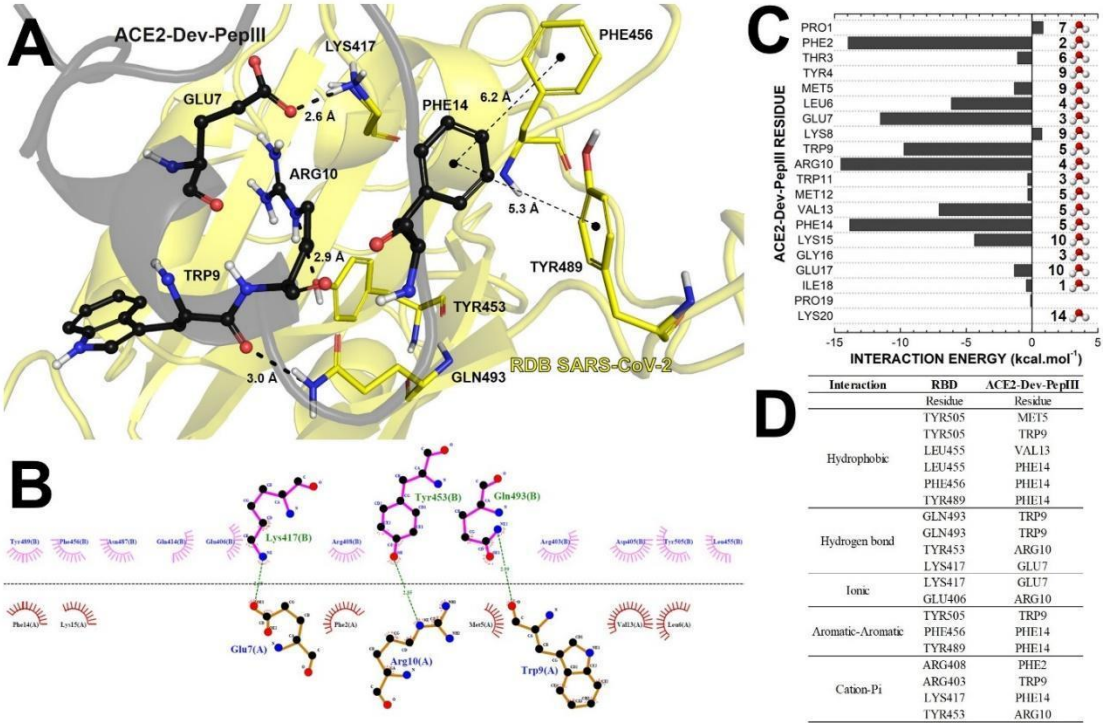

Interaction	RBD Residue	ACE2-Dev-PepIII Residue
Hydrophobic	TYR505	MET5
	TYR505	TRP9
	LEU455	VAL13
	LEU455	PHE14
	PHE456	PHE14
	TYR489	PHE14
Hydrogen bond	GLN493	TRP9
	GLN493	TRP9
	TYR453	ARG10
	LYS417	GLU7
Ionic	LYS417	GLU7
	GLU406	ARG10
Aromatic-Aromatic	TYR505	TRP9
	PHE456	PHE14
	TYR489	PHE14
Cation-Pi	ARG408	PHE2
	ARG403	TRP9
	LYS417	PHE14
	TYR453	ARG10

Fonte: SOUZA *et al.,* 2022. A and B represent the 3D interactions and 2D interactions, respectively. C represents the individual energy contribution of each amino acid residue of ACE2-Dev-PepIII, and D denotes all interactions between SARS-CoV-2 RBD and ACE2-Dev-PepIII.

Hydrophobic, and aromatic-aromatic interactions along with hydrogen bonds are the interactions that stabilize the ACE2-Dev-PepIV::S-RBD complex. Hydrophobic interactions occurred between ACE2-Dev-PepIV and residues Phe^{456}, Phe^{456}, Ala^{475}, Tyr^{489}, Tyr^{489}, Tyr^{421}, Leu^{455}, Phe^{456}, Leu^{455}, Phe^{456}, Tyr^{473}, Tyr^{489}, Pro^{491}, Leu^{455}, Leu^{455}, Phe^{490}, Tyr^{453}, Leu^{455}, and Tyr^{449} of S-RBD (Fig. 43B and D). Eight hydrogen bonds occurred between residues Phe^{490}, Gln^{493}, Gln^{493}, Gln^{493}, Gln^{498}, Gln^{498}, Gln^{498}, and Gln^{498} of S-RBD and residues Trp^{11}, Trp^{15}, Phe^{14}, Phe^{14}, Asn^{17}, Asn^{17}, Tyr^{19}, and Tyr^{19} of ACE2-Dev-PepIV, respectively (Fig. 43A, B and D). Aromatic-aromatic interaction occurred between $Phe^{490}$of S-RBD and Trp^{11} residue of ACE2-Dev-PepIV, respectively (Fig. 43A and D).

Pro^{3}, Leu^{6}, Leu^{7}, Trp^{11}, Phe^{14}, Asn^{17}, and Leu^{18} were the main amino acid residues of ACE2-Dev-PepIV that interacted with S-RBD, with interaction energies of -8.55, -10.54, -19.27, -16.08, -10.03, -8.26, -14.77 kcal.mol^{-1} (Fig. 43C).

3.3.3.7 Quantum biochemistry description

ACE2-Dev-PepI mainly interacted with residues Tyr^{489}, Ala^{475}, Tyr^{473}, Phe^{456}, Leu^{455}, Asn^{487}, and Lys^{458} of S-RBD, with interaction free energies of -21.54, -8.78, -7.23, -6.27, -3.91, -3.17, and -2.90 kcal.mol^{-1}, respectively (Fig. 44A). The ACE2-Dev-PepII peptide interacted primarily with residues Arg^{403}, Glu^{484}, Gln^{493}, Leu^{455}, Phe^{456}, Tyr^{489}, Tyr^{473}, Leu^{492}, Pro^{491}, Asn^{487}, Tyr^{505}, Ala^{475}, and $Phe^{490\ 94}$ of S-RBD ,with interaction energies of -12.67, -11.03, -10.64, -10.23, -9.92, -9.42, -7.04, -5.29, -4.87, -4.42, -4.07, -3.78, and -3.43 kcal.mol^{-1}, respectively (Fig. 44B). The ACE2-Dev-PepIII peptide mainly interacted with the amino acid residues Lys^{417}, Gln^{493}, Arg^{408}, Leu^{455}, Tyr^{453}, Glu^{406}, Tyr^{489}, Gln^{409}, Phe^{456}, Tyr^{505}, and Asp^{405} of the S-RBD, with interaction energies of -12.13, -10.56, -9.40, -8.79, -6.08, -5.02, -4.85, -3.92, -3.55, -3.31, and -3.31 kcal.mol^{-1}, respectively (Fig. 44C). ACE2-Dev-PepIV mainly interacted with residues Leu^{455}, Phe^{456}, Gln^{498}, Gln^{493}, Tyr^{489}, Tyr^{449}, Phe^{490}, Ser^{494}, Pro^{491}, Tyr^{453}, Ala^{475}, and Gly^{496} of S-RBD, with interaction energies of -14.65, -13.38, -11.44, -10.72, -10.58, -6.60, -6.22, -4.19, -4.07, -3.22, -3.14, and -3.12 kcal.mol^{-1}, respectively (Fig. 44D).

The ACE2-Dev-PepII and ACE2-Dev-PepIV peptides had the lowest interaction energy, of -112.8 and -113.9 kcal. mol^{-1}, respectively, with S-RBD, so they have highest potentials to inhibit the interaction between S-RBD and ACE2 receptor. ACE2-Dev-PepI and ACE2-Dev-PepIII presented total interaction energies, E(t), equal to -64.9 and -84.6 kcal.mol^{-1}, respectively (Fig. 45). Energy convergence was observed in all complexes formed between ACE2-derived peptides and S-RBD after a distance greater than 6Å, with minimal variations seen after that distance (Fig. 45).

3.3.3.8 ACE2-derived peptides induced wrong interaction between S-RBD and the ACE2 receptor

All ACE2-derived peptides induced incorrect binding of S-RBD with the ACE2 receptor. The redocking confirmed the reliability of the docking tool, since the conformation generated by the redocking (Fig. 46B) was similar to the crystal structure used as control (Fig. 46A). When S-RBD was bound to ACE2-Dev-PepI, ACE2-Dev-PepII, ACE2-Dev-PepIII, or ACE2-Dev-PepIV peptides could not recognize the ACE2 receptor in the correct conformation (Fig. 46C, D, E, and F). The

ACE2 region that generally interacts with S-RBD was no longer able to interact in the correct conformation with S-RBD.

Figure 43**.** Energies and interaction between SARS-CoV-2 RBD (yellow) and ACE2-Dev-PepIV (blue).

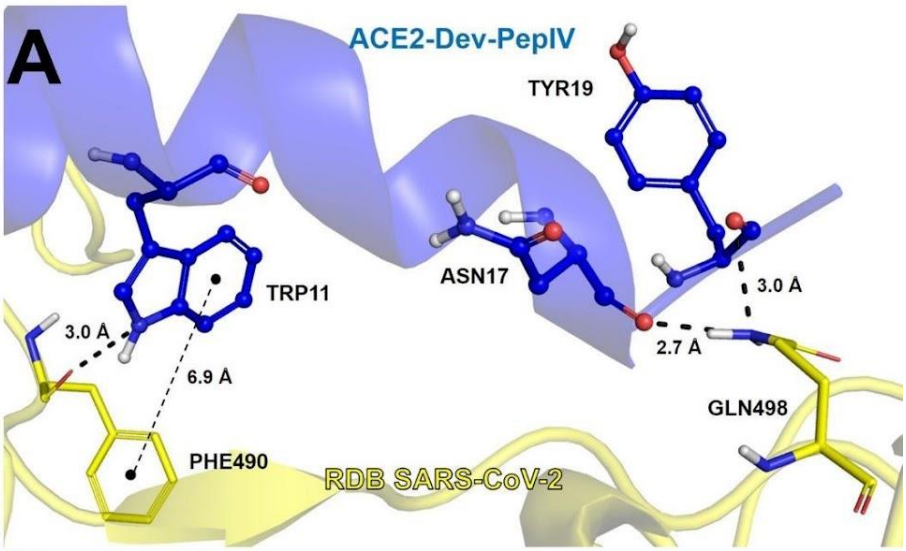

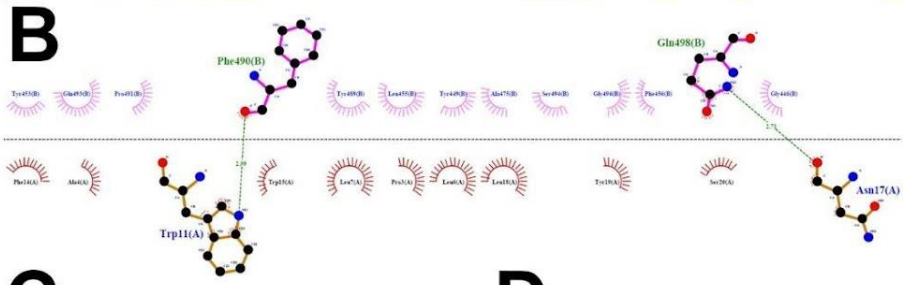

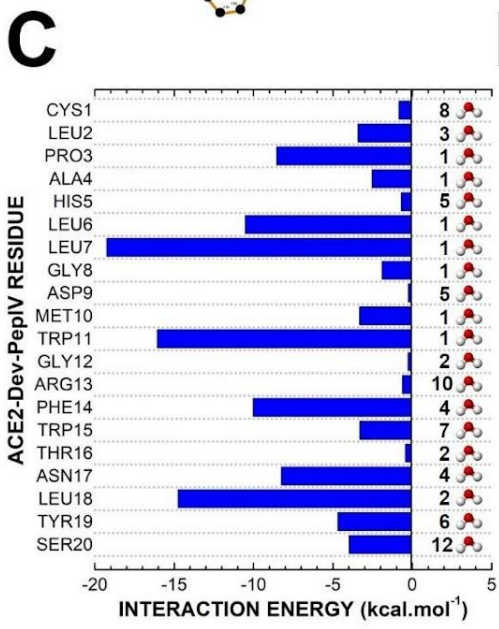

D

Interaction	RBD Residue	ACE2-Dev-PepIV Residue
Hydrophobic	PHE456	LEU2
	PHE456	PRO3
	ALA475	PRO3
	TYR489	PRO3
	TYR489	ALA4
	TYR421	LEU6
	LEU455	LEU6
	PHE456	LEU6
	LEU455	LEU7
	PHE456	LEU7
	TYR473	LEU7
	TYR489	LEU7
	PRO491	LEU7
	LEU455	MET10
	LEU455	TRP11
	PHE490	TRP11
	TYR453	PHE14
	LEU455	PHE14
	TYR449	LEU18
Hydrogen bonds	PHE490	TRP11
	GLN493	TRP15
	GLN493	PHE14
	GLN493	PHE14
	GLN498	ASN17
	GLN498	ASN17
	GLN498	TYR19
	GLN498	TYR19
Aromatic-Aromatic	PHE490	TRP11

Fonte: SOUZA *et al.,* 2022. A and B represent the 3D interactions and 2D interactions, respectively. C represents the individual energy contribution of each amino acid residue of ACE2-Dev-PepIV, and D denotes all interactions between SARS-CoV-2 RBD and ACE2-Dev-PepIV.

Figure 44. Binding site, interaction energy, and residue domain (BIRD) panel showing the MFCC interaction energies between the central amino acid residues of SARS-CoV-2 RBD and ACE2-Derived peptides.

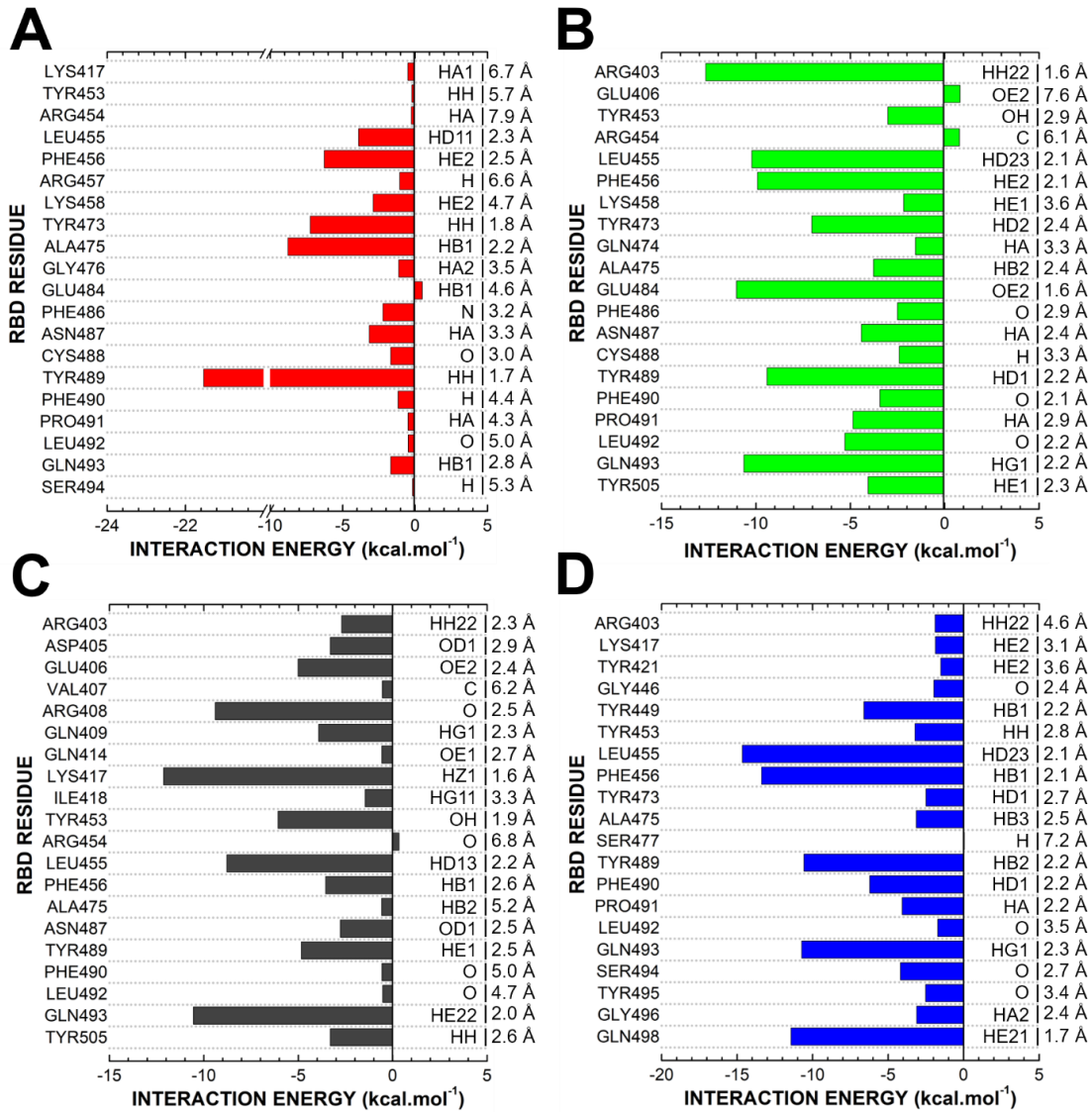

Fonte: SOUZA *et al.*, 2022. ACE2-Dev-PepI (A), ACE2-Dev-PepII (B), ACE2-Dev-PepIII (C), and ACE2-Dev-PepIV (D) The minimal distance (Å) between each residue that participates in the interaction is indicated at the right side of the panel. The amino acid residues at the left side of the panel are from SARS-CoV-2 RBD.

Figure 45. Total interaction energy between SARS-CoV-2 RBD and the ACE2 derived peptides as a function of the interaction distance.

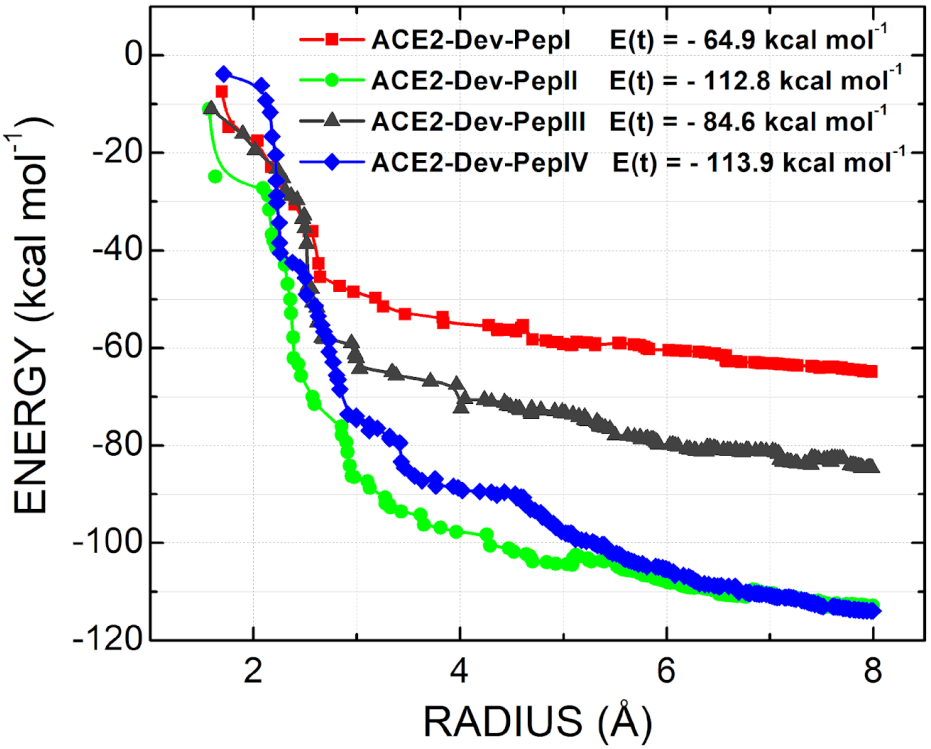

Fonte: SOUZA *et al.,* 2022. Red, Green, Black, and Blue squares represent ACE2-Dev-PepI, ACE2-Dev-PepII, ACE2-Dev-PepIII, and ACE2-Dev-PepIV, respectively. E(t) is the sum of the interaction energies up to 8Å.

Figure 46. The ACE2-derived peptides induced an abnormal interaction between SARS-CoV-2 RBD and the human ACE2 protein.

Fonte: SOUZA *et al.,* 2022. Redocking (B) confirmed the accuracy of the molecular docking method used, with no difference for the crystallized structure (A). When SARS-CoV-2 RBD interacted with ACE2-Dev-PepI (C), ACE2-Dev-PepII (D), ACE2-Dev-PepIII (E), and ACE2-Dev-PepIV (F), the peptides could not interact correctly with human ACE2.

3.3.4 Discussion

The development of vaccines is the most crucial measure to block SARS-CoV-2 spread and infection. Even though many research groups worldwide are rushing to develop an efficient vaccine against SARS-CoV-2, an undesirable problem has arisen. Some studies have shown the immunological memory mediated by IgGs anti-SARS-CoV-2 is brief, only around three months. Besides that, there are reports of patients infected twice by SARS-CoV-2 [30–31]. This problem related to immunity offered by the vaccine to SARS-CoV-2 represents a considerable challenge to the world population. Therefore, research for new molecules is imperative to abolish or even attenuate its symptoms.

One approach to develop therapies quickly is repositioning of already available antiviral drugs to treat SARS-CoV-2 [8], which has not been successful so far. The most employed way to discover possible alternative compounds against SARS-CoV-2 is computational screening [30,31]. By employing computational screening, it is possible to choose as target a vital protein to SARS-CoV-2 infection, such as RNA polymerase, a main protease, and S protein [14,35]. For instance, Elfiky [32] used molecular docking to test many conventional antiviral drugs such as galidesivir, remdesivir, and tenofovir against the RNA polymerase of SARS-CoV-2. In turn, Wu et al. [26] performed molecular docking simulation of drugs such as antihypertensives, antifungals and anticoagulants against SARS-CoV-2 targets.

The spike glycoprotein of coronaviruses is an essential protein to infection. It has two portions, S1 outside the virus envelope, which is connected to S2, a transmembrane portion attached to the virus envelope. S1 possesses the RBD domain, which interacts with ACE2. After this interaction, the S2 portion is responsible for membrane fusion and virus entry [7,36]. The S-RBD domain possesses high mutational rates, characterizing it as the most variable region of the coronavirus genome [26,37].

In SARS-CoV-like viruses, there are six amino acid residues critical to the interaction between the RBD domain and the ACE2 receptor. The mutations accumulated by SARS-CoV-2 lead to five amino acid residues that are different from in to SARS-CoV. In SARS-CoV, the residues are Tyr^{455}, Leu^{486}, Asn^{494}, Asp^{495}, Tre^{501}, and Tyr^{506}. In contrast, in SARS-CoV-2, the residues are Leu^{455}, Phe^{486}, Glu^{494}, Ser^{495}, Asn^{501}, and Tyr^{506} [4,6]. These differences in the SARS-CoV-2 RBD

domain allow it to bind to ACE2 with an affinity 20 times higher than SARS-CoV [4]. The ACE2 receptor is expressed in different human tissues, such as kidneys, gut, brain, liver, heart, and lungs. By using it to enter the cells, SARS-CoV-2 can infect nearly all these tissues, causing SARS-CoV-2 viral sepsis, meaning the virus can infect several tissues at the same time [38].

Given the importance of interaction between S-RBD and ACE2, several research groups have been seeking molecules that can block this interaction, either by interaction with S-RBD or with the ACE2 receptor, [26,28,39]. Choudhary et al. [28] employed molecular dynamic simulations to find ligand molecules that interact with the ACE2 receptor and thus block interaction with SARS-CoV-2 RBD. This can be a two-way road, because by blocking the ACE2 receptor, SARS-CoV-2 cannot recognize it and does not establish infection. However, choosing to block the ACE2 receptor at the same time makes it unavailable to the cells, and hence produces several collateral effects. In a virtual screening, Wu et al. [26] found a flavonoid from citrus fruit, called hesperidin, which interacted with RBD, blocking its interaction with ACE2. However, hesperidin has two highly undesired side effects: it induces bleeding disorders and low blood pressure. Oliveira et al. [39] tested azithromycin, hydroxychloroquine and chloroquine by molecular dynamics against SARS-CoV-2 RBD. These drugs do bind to RBD, but with low energy.

Here, we employed an *in silico* approach but with a different idea, focused on SARS-CoV-2 spike protein, specifically in the RBD domain. Instead of looking for molecules to interact with the ACE2 receptor, we used the sequence of the human ACE2 receptor to design synthetic peptides derived from it to target S-RBD. Out of 259 peptides (Tables S1-S3), ACE2-dev-pepI, ACE2-dev-pepII, ACE2-dev-pepIII, ACE2-dev-pepIV deserved attention.

Molecular docking and dynamic simulations revealed that all ACE2-derived peptides interacted efficiently with S-RBD (Table 1, Figs. 38-45). This is a pioneer study employing quantum biochemistry to analyze peptides' interaction against SARS-CoV-2 RBD (Tables 4-7). Quantum biochemistry calculations [40] revealed the individual contribution of each amino acid residue of the ACE2-derived peptides and those of S-RBD. Therefore, these analyses showed that hydrogen bonds and ionic, aromatic, cation-pi and hydrophobic interactions are essential to attractive or repulsive interactions between the ACE2-derived peptides and S-RBD (Figs. 40-44). As shown in Fig 45, the quantum biochemical calculations taking in

consideration each amino acid energy level, showed that the total interaction energy values between SARS-CoV-2 RBD and ACE2-dev-pepI, ACE2-dev-pepII, ACE2-dev-pepIII, ACE2-dev-pepIV were –64.9, –112.8, –84.6, and 1139 kcal.mol^{-1}, respectively (Fig. 45). Further based on the quantum calculations, ACE2-dev-pepIV was the peptides with the highest affinity to bind with S-RBD, followed by ACE2-dev-pepII, ACE2-dev-pepIII and ACE2-dev-pepI.

Since this is the first study to apply quantum biochemistry calculations to analyze the interactions of peptides with S-RBD, our results can only be compared with those reported by Campos et al. [41], who also investigated the interaction of two peptides against the Zika virus protease. By quantum biochemistry, the authors showed that the interaction energies of the peptides cn-716 and acyl-KR-aldehyde with the protease NS2B–NS3 were –63.35 kcal.mol^{-1} and –71.4 kcal.mol^{-1}, respectively. Our peptides interacted with S-RBD even more strongly than did cn-716 and acyl-KR-aldehyde to the protease NS2B–NS3.

Moreover, the effectiveness of other non-peptide-like antiviral drugs against S-RBD has been assayed. For example, Oliveira et al. [39] tested by molecular docking the interaction of the drugs azithromycin, hydroxychloroquine and chloroquine, which are used to treat bacterial infection and malaria, respectively study is about drug repositioning or repurposing, employed to speed up the drug discovery process by identifying a novel clinical use for an existing drug approved for a different indication [8]. Our results revealed that ACE-derived peptides strongly bind to S-RBD. However, two questions remain; what are the consequences of that interaction? Can these peptides block or induce a wrong interaction between S-RBD and ACE2? The results presented here guide us to answer yes. As presented in Fig. 9, the crystal structure (Fig. 46A) and the redocking of those structures (Fig. 46B), all ACE2-derived peptides when complexed with S-RBD did not block interaction between S-RBD and the ACE2 receptor, instead inducing an incorrect interaction between them (Fig. 46C-F). These results strongly suggest that ACE2-derived peptides are efficient to prevent SARS-CoV-2 entry in cells, greatly reducing SARS-CoV-2 replication and avoiding COVID-19 establishment.

As expected, the ACE2-derived peptides presented high affinity to bind with S-RBD, and the results suggest these peptides are efficient to block SARS-CoV-2 infection. Additionally, for being designed from a human protein, these peptides will likely cause no serious collateral effects, unlike other drugs. The *in silico* analyses

revealed these peptides have no toxic, allergenic, or hemolytic potential against humans. Additionally, stability tests suggested high stability of ACE2-Dev-pepI, ACE2-Dev-pepII, and ACE2-Dev-pepIV in the intestinal environment indicating possible oral administration.

3.3.5 Conclusion

Quantum biochemistry and molecular dynamic simulations revealed that the ACE2-derived peptides interact physically with S-RBD, blocking its interaction with the ACE2 receptor and thus virus entry in the cell. These findings suggest that ACE2-derived peptides are small antiviral molecules that can potentially prevent cell invasion by SARS-CoV-2 and thus its replication *in vivo*. However, further investigation is required to prove this hypothesis. In conclusion, this pioneering *in silico* investigation opens an opportunity for further *in vivo* investigations of these peptides, aiming to discover new drugs and entirely new perspectives to treat COVID-19. For instance, peptide-based therapeutics have various advantages compared to traditional small-molecule drugs, such as higher specificity to selected targets; low toxicity because accumulation in the body is improbable; and less complex, costly, and time-consuming synthesis [8].

3.3.6 Funding and acknowledgments

Grants from the following Brazilian agencies supported this work: The National Council for Scientific and Technological Development (CNPq), with a doctoral grant to JLA and a research grant (codes 431511/2016-0 and 306202/2017-4) to JTAO; the Office to Coordinate Improvement of University Personnel (CAPES) sponsored PFNS with a postdoctoral fellowship. The authors are also grateful for the support received from the National Center for High-Performance Processing - Federal University of Ceará and Center for Ongoing Education in Health Care-CEATS/School of Public Health of Ceará (ESP-CE).

References

[1] C.J. Burrell, C.R. Howard, F.A. Murphy, Fenner and White's Medical Virology (Fifth Edition): Chapter 13 - Coronaviruses, (2017) 437–446. https://doi.org/10.1016/B978-0-12-375156-0.00031-X.

[2] J.S.M. Peiris, Coronaviruses, in: Med. Microbiol., Elsevier, 2012: pp. 587–593. https://doi.org/10.1016/B978-0-7020-4089-4.00072-X.

[3] Q. Li, X. Guan, P. Wu, X. Wang, L. Zhou, Y. Tong, R. Ren, K.S.M. Leung, E.H.Y. Lau, J.Y. Wong, X. Xing, N. Xiang, Y. Wu, C. Li, Q. Chen, D. Li, T. Liu, J. Zhao, M. Liu, W. Tu, C. Chen, L. Jin, R. Yang, Q. Wang, S. Zhou, R. Wang, H. Liu, Y. Luo, Y. Liu, G. Shao, H. Li, Z. Tao, Y. Yang, Z. Deng, B. Liu, Z. Ma, Y. Zhang, G. Shi, T.T.Y. Lam, J.T. Wu, G.F. Gao, B.J. Cowling, B. Yang, G.M. Leung, Z. Feng, Early Transmission Dynamics in Wuhan, China, of Novel Coronavirus-Infected Pneumonia, N. Engl. J. Med. 382 (2020) 1199–1207. https://doi.org/10.1056/NEJMoa2001316.

[4] K.G. Andersen, A. Rambaut, W.I. Lipkin, E.C. Holmes, R.F. Garry, The proximal origin of SARS-CoV-2, Nat. Med. 26 (2020) 450–452. https://doi.org/10.1038/s41591-020-0820-9.

[5] Z. Song, Y. Xu, L. Bao, L. Zhang, P. Yu, Y. Qu, H. Zhu, W. Zhao, Y. Han, C. Qin, From SARS to MERS, thrusting coronaviruses into the spotlight, Viruses. 11 (2019). https://doi.org/10.3390/v11010059.

[6] A.C. Walls, Y.-J. Park, M.A. Tortorici, A. Wall, A.T. McGuire, D. Veesler, Structure, Function, and Antigenicity of the SARS-CoV-2 Spike Glycoprotein, Cell. 181 (2020) 281-292.e6. https://doi.org/10.1016/j.cell.2020.02.058.

[7] Y. Yuan, D. Cao, Y. Zhang, J. Ma, J. Qi, Q. Wang, G. Lu, Y. Wu, J. Yan, Y. Shi, X. Zhang, G.F. Gao, Cryo-EM structures of MERS-CoV and SARS-CoV spike glycoproteins reveal the dynamic receptor binding domains, Nat. Commun. 8 (2017) 15092. https://doi.org/10.1038/ncomms15092.

[8] R. Yan, Y. Zhang, Y. Li, L. Xia. L, Y. Guo, Q. Zhou, Structural basis for the recognition of SARS-CoV-2 by full-length human ACE2, Science. 367 (2020) 367:1444–1448. DOI: 10.1126/science.abb2762.

[9] B. Korber, W. M. Fischer, S. Gnanakaran, H. Yoon, J. Theiler, W. Abfalterer, N. Hengartner, E. E.Giorgi, T. Bhattacharya, B. Foley, K. M. Hastie, M. D. Parker, D. G.Partridge, C. M. Evans, T. M. Freeman, T. I. Silva, Tracking Changes in

SARS-CoV-2 Spike: Evidence that D614G Increases Infectivity of the COVID-19 Virus, Cell. 182, (2020) 812–827

[10] D. Wrapp, N. Wang, K. S. Corbett, J. A. Goldsmith, C. L. Hsieh, O. Abiona, B. S. Graham, J. S. McLellan, Cryo-EM structure of the 2019-nCoV spike in the prefusion conformation, Science. 367 (2020) 1260-1263. DOI: 10.1126/science.abb2507.

[11] R. A. Moreira, M. Chwastyk, J. L. Baker, H. V. Guzman, A. B. Poma, Quantitative determination of mechanical stability in the novel coronavirus spike protein, Nanoscale. 12 (2020) 16409-16413. https://doi.org/10.1039/D0NR03969A.

[12] B. Qiao, M. Olvera de la Cruz, Enhanced Binding of SARS-CoV-2 Spike Protein to Receptor by Distal Polybasic Cleavage Sites, ACS nano. 14 (2020) 10616-10623. https://doi.org/10.1021/acsnano.0c04798

[13] P. Calligari, S. Bobone, G. Ricci, A. Bocedi, Molecular Investigation of SARS–CoV-2 Proteins and Their Interactions with Antiviral Drugs, Viruses. 12 (2020) 445-460. doi: 10.3390/v12040445

[14] P.F.N. Souza, F.E.S. Lopes, J.L. Amaral, C.D.T. Freitas, J.T.A. Oliveira, International Journal of Biological Macromolecules A molecular docking study revealed that synthetic peptides induced conformational changes in the structure of SARS-CoV-2 spike glycoprotein , disrupting the interaction with human ACE2 receptor, Int. J. Biol. Macromol. 164 (2020) 66–76. https://doi.org/10.1016/j.ijbiomac.2020.07.174.

[15] P.F.N. Souza, L.S.M. Marques, J.T.A. Oliveira, P.G. Lima, L.P. Dias, N.A.S. Neto, F.E.S. Lopes, J.S. Sousa, A.F.B. Silva, R.F. Caneiro, J.L.S. Lopes, M. V. Ramos, C.D.T. Freitas, Synthetic antimicrobial peptides: From choice of the best sequences to action mechanisms, Biochimie. 175 (2020) 132–145. https://doi.org/10.1016/j.biochi.2020.05.016.

[16] N. Thakur, A. Qureshi, M. Kumar, AVPpred: collection and prediction of highly effective antiviral peptides, Nucleic Acids Res. 40 (2012) W199–W204. https://doi.org/10.1093/nar/gks450.

[17] P.K. Meher, T.K. Sahu, A.R. Rao, Prediction of donor splice sites using random forest with a new sequence encoding approach, BioData Min. 9 (2016) 4. https://doi.org/10.1186/s13040-016-0086-4.

[18] Y. Shen, J. Maupetit, P. Derreumaux, P. Tufféry, Improved PEP-FOLD Approach for Peptide and Miniprotein Structure Prediction, J. Chem. Theory Comput. 10 (2014) 4745–4758. https://doi.org/10.1021/ct500592m.

[19] E. Ramírez-Aportela, J.R. López-Blanco, P. Chacón, FRODOCK 2.0: Fast protein-protein docking server, Bioinformatics. 32 (2016) 2386–2388. https://doi.org/10.1093/bioinformatics/btw141.

[20] I.H. Moal, P.A. Bates, SwarmDock and the Use of Normal Modes in Protein-Protein Docking, Int. J. Mol. Sci. 11 (2010) 3623–3648. https://doi.org/10.3390/ijms11103623.

[21] M.J. Robertson, J. Tirado-Rives, W.L. Jorgensen, Improved Peptide and Protein Torsional Energetics with the OPLS-AA Force Field, J. Chem. Theory Comput. 11 (2015) 3499–3509. https://doi.org/10.1021/acs.jctc.5b00356.

[22] R.A. Laskowski, M.B. Swindells, LigPlot+: Multiple ligand-protein interaction diagrams for drug discovery, J. Chem. Inf. Model. 51 (2011) 2778–2786. https://doi.org/10.1021/ci200227u.

[23] D.W. Zhang, J.Z.H. Zhang, Molecular fractionation with conjugate caps for full quantum mechanical calculation of protein-molecule interaction energy, J. Chem. Phys. 119 (2003) 3599–3605. https://doi.org/10.1063/1.1591727.

[24] J.L. Amaral, S.J.M. Santos, P.F.N. Souza, P.A. de Morais, F.F. Maia, H.F. Carvalho, V.N. Freire, Quantum biochemistry in cancer immunotherapy: New insights about CTLA-4/ipilimumab and design of ipilimumab-derived peptides with high potential in cancer treatment, Mol. Immunol. 127 (2020) 203–211. https://doi.org/10.1016/j.molimm.2020.09.013.

[25] B. Delley, From molecules to solids with the DMol3 approach, J. Chem. Phys. 113 (2000) 7756–7764. https://doi.org/10.1063/1.1316015.

[26] C. Wu, Y. Liu, Y. Yang, P. Zhang, W. Zhong, Y. Wang, Q. Wang, Y. Xu, M. Li, X. Li, M. Zheng, L. Chen, H. Li, Analysis of therapeutic targets for SARS-CoV-2 and discovery of potential drugs by computational methods, Acta Pharm. Sin. B. 10 (2020) 766–788. https://doi.org/10.1016/j.apsb.2020.02.008.

[27] R. Henderson, R.J. Edwards, K. Mansouri, K. Janowska, V. Stalls, S.M.C. Gobeil, M. Kopp, D. Li, R. Parks, A.L. Hsu, M.J. Borgnia, B.F. Haynes, P. Acharya, Controlling the SARS-CoV-2 spike glycoprotein conformation, Nat. Struct. Mol. Biol. (2020). https://doi.org/10.1038/s41594-020-0479-4.

[28] S. Choudhary, Y.S. Malik, S. Tomar, Identification of SARS-CoV-2 Cell Entry Inhibitors by Drug Repurposing Using in silico Structure-Based Virtual Screening Approach, Front. Immunol. 11 (2020). https://doi.org/10.3389/fimmu.2020.01664.

[29] H. Othman, Z. Bouslama, J.-T. Brandenburg, J. da Rocha, Y. Hamdi, K. Ghedira, N. Srairi-Abid, S. Hazelhurst, Interaction of the spike protein RBD from SARS-CoV-2 with ACE2: Similarity with SARS-CoV, hot-spot analysis and effect of the receptor polymorphism, Biochem. Biophys. Res. Commun. 527 (2020) 702–708. https://doi.org/10.1016/j.bbrc.2020.05.028.

[30] M.S. Diamond, T.C. Pierson, The Challenges of Vaccine Development against a New Virus during a Pandemic, Cell Host Microbe. 27 (2020) 699–703. https://doi.org/10.1016/j.chom.2020.04.021.

[31] M.Z. Tay, C.M. Poh, L. Rénia, P.A. MacAry, L.F.P. Ng, The trinity of COVID-19: immunity, inflammation and intervention, Nat. Rev. Immunol. 20 (2020) 363–374. https://doi.org/10.1038/s41577-020-0311-8.

[32] Y. Zhang, J. Xu, R. Jia, C. Yi, W. Gu, P. Liu, X. Dong, H. Zhou, B. Shang, S. Cheng, X. Sun, J. Ye, X. Li, J. Zhang, Z. Ling, L. Ma, B. Wu, M. Zeng, W. Zhou, B. Sun, Protective humoral immunity in SARS-CoV-2 infected pediatric patients, Cell. Mol. Immunol. 17 (2020) 768–770. https://doi.org/10.1038/s41423-020-0438-3.

[33] D.C. Hall, H.-F. Ji, A search for medications to treat COVID-19 via in silico molecular docking models of the SARS-CoV-2 spike glycoprotein and 3CL protease, Travel Med. Infect. Dis. 35 (2020) 101646. https://doi.org/10.1016/j.tmaid.2020.101646.

[34] S.T. Ngo, N. Quynh Anh Pham, L. Thi Le, D.-H. Pham, V. V. Vu, Computational Determination of Potential Inhibitors of SARS-CoV-2 Main Protease, J. Chem. Inf. Model. (2020). https://doi.org/10.1021/acs.jcim.0c00491.

[35] A.A. Elfiky, Ribavirin, Remdesivir, Sofosbuvir, Galidesivir, and Tenofovir against SARS-CoV-2 RNA dependent RNA polymerase (RdRp): A molecular docking study, Life Sci. 253 (2020) 117592. https://doi.org/10.1016/j.lfs.2020.117592.

[36] M. Hoffmann, H. Kleine-Weber, S. Schroeder, N. Krüger, T. Herrler, S. Erichsen, T.S. Schiergens, G. Herrler, N.H. Wu, A. Nitsche, M.A. Müller, C. Drosten, S. Pöhlmann, SARS-CoV-2 Cell Entry Depends on ACE2 and TMPRSS2 and Is Blocked by a Clinically Proven Protease Inhibitor, Cell. (2020). https://doi.org/10.1016/j.cell.2020.02.052.

[37] P. Zhou, X. Lou Yang, X.G. Wang, B. Hu, L. Zhang, W. Zhang, H.R. Si, Y. Zhu, B. Li, C.L. Huang, H.D. Chen, J. Chen, Y. Luo, H. Guo, R. Di Jiang, M.Q. Liu, Y. Chen, X.R. Shen, X. Wang, X.S. Zheng, K. Zhao, Q.J. Chen, F. Deng, L.L. Liu, B. Yan, F.X. Zhan, Y.Y. Wang, G.F. Xiao, Z.L. Shi, A pneumonia outbreak associated with a new

coronavirus of probable bat origin, Nature. 579 (2020) 270–273. https://doi.org/10.1038/s41586-020-2012-7.

[38] H. Li, L. Liu, D. Zhang, J. Xu, H. Dai, N. Tang, X. Su, B. Cao, SARS-CoV-2 and viral sepsis: observations and hypotheses, Lancet. 395 (2020) 1517–1520. https://doi.org/10.1016/S0140-6736(20)30920-X.

[39] O.V. de Oliveira, G.B. Rocha, A.S. Paluch, L.T. Costa, Repurposing approved drugs as inhibitors of SARS-CoV-2 S-protein from molecular modeling and virtual screening, J. Biomol. Struct. Dyn. (2020) 1–10. https://doi.org/10.1080/07391102.2020.1772885.

[40] P.A. Morais, F.F. Maia, C. Solis-Calero, E.W.S. Caetano, V.N. Freire, H.F. Carvalho, The urokinase plasminogen activator binding to its receptor: A quantum biochemistry description within an in/homogeneous dielectric function framework with application to uPA-uPAR peptide inhibitors, Phys. Chem. Chem. Phys. 22 (2020) 3570–3583. https://doi.org/10.1039/c9cp06530j.

[41] D.M.O. Campos, K.S. Bezerra, S.C. Esmaile, U.L. Fulco, E.L. Albuquerque, J.I.N. Oliveira, Intermolecular interactions of cn-716 and acyl-KR-aldehyde dipeptide inhibitors against Zika virus, Phys. Chem. Chem. Phys. 22 (2020) 15683–15695. https://doi.org/10.1039/d0cp02254c.

4. IMUNOTERAPIA DO CÂNCER

Câncer é um grupo de doenças que envolve o crescimento desordenado de células anormais com o potencial de invadir e se espalhar para outras partes do corpo (SOUZA *et al.,* 2021). O sistema imune é composto por células, tecidos e órgãos que trabalham em conjunto com a finalidade de proteger o corpo de ameaças, tais como germes, vírus e doenças e, entre elas, pode-se citar o câncer (MA *et al.,* 2021).

As células cancerígenas são comuns no corpo humano, todavia o sistema imune é capaz de identificar e destruí-las, entretanto, essas células podem sofrer mutações e se adaptarem, não podendo ser identificadas pelo nosso sistema imune, permitindo sua proliferação e espalhamento, por este motivo conseguem se desenvolver e ocasionar problemas a saúde humana (DHARA *et al.,* 2022).

As células tumorosas são identificadas pelo sistema imune através da identificação do aumento da expressão das proteínas CTLA-4 e PD-1, principalmente. Para não serem identificadas, elas expressam ligantes que camuflam a presença dessas proteínas e escapam das atividades antitumorais. Desta forma, suprimem a proliferação de células imune, logo, sobrevivendo e se proliferando, como demostrado na figura 47 (WOJTUKIEWICZ et al., 2021).

A Imunoterapia é a área que potencializa o próprio sistema imune do corpo para lutar contra o câncer, impedindo que os ligantes camuflem as proteínas checkpoints, deste modo, o sistema imune consegue reconhecer e destruir as células cancerígenas. Comparada a tratamentos convencionais para o câncer, como cirurgia, quimioterapia e radiação, a imunoterapia possui uma grande especificidade, visto que, permite que as células cancerígenas sejam alvos exclusivos, deixando as outras células livres da ação, além de possuir menos limitações ao uso em diferentes estágios do câncer (AMARAL *et al.,* 2020).

A maioria dos estudos com inibidores de imuno-*checkpoints* são anticorpos monoclonais anti-CTLA-4, anti-PD-1 e anti-PD-L1, os quais regulam as vias regulatórias de células T para o aumento das respostas antitumorais (WILLSMORE *et al.,* 2021).

Figura 47. Vias de regulação da ativação das células T pela CTLA-4 e CD28.

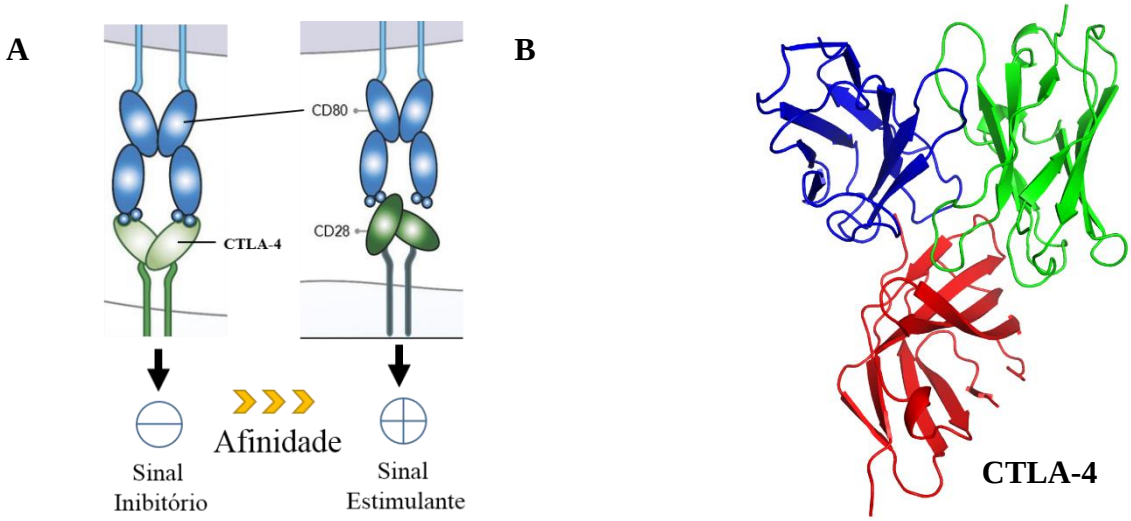

Legenda: **A**. CD80 é a proteína B7-1 a qual pode interagir tanto com a CTLA-4, emitindo um sinal inibitório da ativação das células T, como com o CD28, interação que emite um sinal estimulante da ativação das células T. B7-1 possui uma maior afinidade com a CTLA-4 do que com CD28, assim apresenta uma maior sensibilidade na inibição da ativação das células T do que uma estimulação. **B**. Estrutura cristalográfica do anticorpo comercial Ipilimumab com a proteína imuno-*checkpoint* CTLA-4, a qual permite estudos aprofundados de bioquímica quântica. Em azul e denominado como CL indica a cadeia leve do anticorpo e em verde e denominado como CP a cadeia pesada do mesmo. Em vermelho tem-se a proteína CTLA-4.
Fonte: **A**. ROWSHANRAVAN; HALLIDAY; SANSOM, 2018. Adaptado. **B**. Elaborada pelo autor.

Apesar de todas as vantagens vistas com o tratamento com anticorpos monoclonais, há desvantagens que podem ser melhoradas, como: o custo do tratamento que é altíssimo, baixa estabilidade dos anticorpos, a via de administração que é, obrigatoriamente, intravenosa e não pode ser oral e, em alguns casos de respostas autoimune, chega a atacar células saudáveis, bem como alguns sintomas relacionados ao trato digestório, como perda do apetite e fadiga. Diante das desvantagens dos anticorpos, os peptídeos miméticos e pequenas moléculas surgem como uma nova alternativa. Tendo como alvo a inibição da ligação entre as proteínas imune-*checkpoints* e seus ligantes (WANG, Lei *et al.,* 2022).

Para o desenvolvimento de peptídeos bioinspirados nos anticorpos comercializados, faz-se necessário o conhecimento dos principais resíduos das proteínas envolvidas na interação do complexo e da contribuição energética individual de cada resíduo. Deste modo, pode-se sugerir modificações pontuais na sequência e na estrutura para melhorar a inibição da formação dos complexos entre proteínas imuno-*checkpoints* e seus ligantes, tornando o tratamento mais efetivo e específico (MATSOUKAS *et al.,* 2021).

Observando isso, nosso grupo de pesquisa realizou cálculos quânticos da interação entre a proteína checkpoint CTLA-4 e o anticorpo monoclonal Ipilimumab. Com os cálculos, foi possível identificar as principais regiões de interação entre as proteínas e sugerir peptídeos cíclicos com grande potencial para o tratamento do câncer. O artigo completo encontra-se no próximo tópico.

4.1 Quantum biochemistry in cancer immunotherapy: New insights about CTLA-4/ipilimumab and design of ipilimumab-derived peptides with high potential in cancer treatment

Artigo publica na revista: Molecular Immunology
DOI: https://doi.org/10.1016/j.molimm.2020.09.013

Jackson L. Amaral[af], Samuel J. M. Santos[b], Pedro F. N. Souza[a], Pablo A. de Morais[c], F. F. Maia Jr.[d], Hernandes F. Carvalho[e], Valder N.Freire[f]

[a]Department of Biochemistry and Molecular Biology, Federal University of Ceará, Fortaleza, Ceará, CEP 60.440-554, Brazil
[b]Federal Institute of Education, Science and Technology of Rio Grande Do Sul, Feliz, Rio Grande Do Sul, CEP 95770-000, Brazil
[c]Federal Institute of Education, Science and Technology of Ceará, Horizonte, Ceará, CEP 62.884-105, Brazil
[d]Department of Nature Sciences, Mathematics and Statistics, Federal Rural University of Semi-arid, Mossoró, Rio Grande Do Norte, CEP 59.625-900, Brazil
[e]Department of Structural and Functional Biology, Institute of Biology, State University of Campinas, Campinas, SP, CEP 13.083-862, Brazil
[f] Department of Physics, Federal University of Ceará, Fortaleza, Ceará, CEP 60.440-970, Brazil

Abstract
Cancer is a group of diseases involving disordered growth of abnormal cells with the potential to invade and spread to other parts of the body. Today, immunotherapy is the most efficient treatment, with fewer side effects. Notably, the employment of monoclonal antibodies to inhibit checkpoint proteins, such as CTLA-4, has caused

much excitement among cancer immunotherapy researchers. Thus, in-depth analysis through quantum biochemistry and molecular dynamics simulations was performed to understand the complex formed by ipilimumab and its target CTLA-4. Our computational results provide a better understanding of the binding mechanisms and new insights about the CTLA-4: ipilimumab interaction, identifying essential amino acid residues to support the complex. Additionally, we report new interactions such as aromatic-aromatic, aromatic-sulfur, and cation-pi interactions to stabilize the CTLA-4:ipilimumab complex. Finally, quantum biochemistry analyses reveal the most important amino acid residues involved in the CTLA-4:ipilimumab interface, which were used to design synthetic peptides to inhibit CTLA-4. The computational results presented here provide a better understanding of the CTLA-4:ipilimumab binding mechanisms, and can support the development of alternative antibody-based drugs with high relevance in cancer immunotherapy.

Keywords: Cancer, Immunotherapy, Checkpoint proteins.

4.1.1 Introduction

Cancer is a group of diseases involving disordered growth of abnormal cells with the potential to invade and spread to other parts of the body. More than 100 types of cancer affect humans. In 2018, 9.6 million people died of cancer in the world, equivalent to 1/6 of the total deaths that year (World Health Organization, 2018). The immune system can identify and destroy cancer cells. However, they easily mutate and adapt to trick the immune system, allowing them to proliferate and spread, leading in some cases to systemic spread to healthy tissues (Lee et al., 2016).

Immunotherapy strengthens the immune system to fight cancer by increasing the ability to recognize tumor cells for destruction. Compared to conventional cancer treatments, such as surgery, chemotherapy and radiation, immunotherapy has high specificity. It only targets cancer cells, without causing any damage to healthy cells. Additionally, it only has a few limitations on treatment and can be used in different stages of cancer progression (Galluzzi et al., 2018).

T-cell receptors (TCRs) can recognize tumor antigens in antigen-presenting cells (APCs) to eradicate tumor cells and induce anti-tumor immunity. After TCRs recognize antigens, a second signal, a co-stimulatory signal, is necessary

for the activation of T-cells. In contrast, cytotoxic T-lymphocyte-associated protein 4 (CTLA-4) and programmed cell death protein 1 (PD-1) transmit inhibitory signals when linked to their ligands, B7-1/B7-2 and PD -L1/PD-L2, respectively, in APCs or tumor cells. These proteins are called immune-checkpoint proteins (IMCP). Tumor cells can exploit the inhibitory mechanism carried out by CTLA-4 and PD-1 proteins to escape the immune system (Almagro et al., 2017; Konstantinidou et al., 2018).

Immune checkpoint protein inhibitors have been developed to control the escape of cancer cells from immune control. Most studies of immunological checkpoint inhibitors have investigated anti-CTLA-4, anti-PD-1 or anti-PD-L1 monoclonal antibodies, which regulate T-cell regulatory pathways to increase anti-tumor responses (Acúrcio et al., 2018).

The main co-stimulatory signals are the links between the B7-1 and B7-2 proteins present in APCs with the CD28 present in T-cells, activating T-cells to destroy specific targets. Unlike CD28, CTLA-4 produces an inhibitory signal when bound to B7-1 or B7-2, competing with CD28. It was reported that the affinity between CTLA-4/B7-1 and B7-2 is approximately 20 times higher than that between CD28/B7-1 and B7-2. This high affinity prevents autoimmune diseases by attenuating T-cells (Schwartz et al., 2001; Stamper et al., 2001). Cancer cells inhibit T-cell activation by impairing the interaction of CTLA-4 and B7-1/B7-2 with CTLA-4. Based on that, it has been suggested that the co-stimulatory signal of CD28 with B7-1/B7- 2 to activate T-cells makes it possible to detect and destroy cancer cells. This approach was successful by employing the first anti-CTLA-4 monoclonal antibody, ipilimumab. Recently, ipilimumab was approved by the Food and Drug Administration (FDA) in the United States for the treatment of advanced-stage melanomas (He et al., 2017).

Several studies with antibodies have been performed to block the inhibition of the immune system caused by cancer cells. This approach has brought results and benefits never before seen in oncology. The resistance of cancer cells to chemotherapeuticals is prevented by employing antibodies, and some patients have been free of cancer progression for many years (Lee et al., 2016). Despite the advantages of using monoclonal antibodies, there are some disadvantages, such as the high cost of treatment, the low stability of antibodies, the possible autoimmune responses associated with the administration route, and the attack on healthy cells (Kroschinsky et al., 2017).

Based on that, mimetic peptides and small molecules are new alternatives,

by inhibiting the interaction between immune-checkpoint proteins and their ligands (Guzik et al., 2019). For the development of bioinspired peptides from commercial antibodies, it is necessary to know the central residues of the proteins involved in the interaction and the individual energy contribution of each residue to suggest specific changes in the sequence, making treatment more effective and specific (Tavares et al., 2018).

Quantum biochemistry is a powerful tool to discover new molecules for immunotherapy. It is possible to know the individual energetic contributions of amino acid residues in the interaction of the immuno-checkpoint protein complex with their ligands, with antibodies or with small commercial and experimental molecules. While most studies of the development of mimetic peptides consider only the distances of antibodies to targets, quantum biochemistry provides a more specific way through the calculation of energies, thus making it possible to develop new drugs with greater efficiency and specificity.

4.1.2 Material and Methods

4.1.2.1 Structural data

All structural analyses were performed using X-ray crystal structure data on ipilimumab in complex with CTLA-4 (PDB ID: 5XJ3) (He et al., 2017), with 3.2 Å resolution. The protonation was adjusted according to data obtained from PROPKA 3.1 (Olsson et al., 2011), using the PDB2PQR server (http://server.poissonboltzmann.org/pdb2pqr) (Dolinsky et al., 2004). Protonation was adjusted using the Discovery Studio software.

4.1.2.2 Molecular dynamics

Molecular dynamics (MD) simulations were performed using NAMD v. 2.12 (Phillips et al., 2005). The system was submitted to cubic box solvation with the TIP3 water model. After that, chloride and sodium ions were added to obtain a final salt concentration of 0.15 M. Next, the system was minimized in 1000 steps, the temperature was adjusted from 100 K to 300 K, and the simulation was finally performed during 20 ns with a time step of 2 fs. After the simulation, the RMSD along

the simulation was calculated using the VMD software (Humphrey et al., 1996) and the final and stable structure was used in further analyses.

4.1.2.3 Molecular fractionation with conjugate caps (MFCC)

To obtain quantum detail of the interactions between the ipilimumab antibody and CTLA-4, the molecular fractionation with conjugate caps scheme was used to perform quantum calculations (Chen et al., 2005; He and Zhang, 2005; Zhang and Zhang, 2003). To perform the calculation, interactions up to a radius of 8Å were considered and the interaction energy between two residues (Ri and Rj) was calculated as follows:

$$E_I(R_i–R_j) = E(C_{i-1}R_iC_{i+1} + C_{j-1}R_jC_{j+1}) - E(C_{i-1}R_iC_{i+1} + C_{j-1}C_{j+1}) – E(C_{i-1}C_{i+1} + C_{j-1}R_jC_{j+1}) + E(C_{i-1}C_{i+1} + C_{j-1}C_{j+1}) \quad (1)$$

Where the Ck terms refer to the amino acid residues neighboring the residues of interest in the calculation. By this means, it is possible obtain a more reliable result, since the local environment of the amino acid residue is reproduced (Wu et al., 2007). The bonds that are missing due to the cut made by the MFCC are completed with H atoms. On the right-hand side of the equation, the first term, $E(C_{i-1}R_iC_{i+1} + C_{j-1}R_jC_{j+1})$, is the total energy of the system formed by two interacting residues with their caps. The second term, $E(C_{i-1}R_iC_{i+1} + C_{j-1}C_{j+1})$, gives the total energy of the system formed by the capped residue R_i without the residue R_j. The third term, $E(C_{i-1}C_{i+1} + C_{j-1}R_jC_{j+1})$, is the total energy of the system formed by R_j without the residue R_i. Finally, $E(C_{i-1}C_{i+1} + C_{j-1}C_{j+1})$ is the total energy of the system formed by the caps only.

Calculations were performed using either a constant dielectric function equal to 40 or a non-homogeneous dielectric function, calculated following the method of Morais et al. (2020). Finally, the interaction energies were calculated through the density functional theory (DFT) using the PDB files generated in the MFCC as input. The calculations were performed using the DMOL3 code (Delley, 2000).

After quantum biochemistry, the main hotspots were used to design mimetic peptides. The cyclic peptides were constructed using the Discovery Studio

software.

4.1.2.4 Protein-protein interactions

Protein interactions were calculated using the Protein Interactions Calculator (PIC) webserver (Tina et al., 2007) (http://pic.mbu.iisc.ernet.in/) to obtain all interactions between ipilimumab and CTLA-4.

4.1.2.5 In silico analyses of cleavage sites and resistance to intestinal-like environment

To evaluate the presence of cleavage sites in the heavy and light chains of ipilimumab and the peptide sequences, the molecules were submitted to cleavage by trypsin, chymotrypsin, pepsin (pH 1.3), and pepsin (pH>2) using the peptide cutter server (Gasteiger et al., 2003) (http://web.expasy.org/peptide_cutter/). Additionally, to evaluate the resistance to the intestinal-like environment, all the sequences were analyzed in the server half-life in an intestine-like environment (http://crdd.osdd.net/raghava/hlp/help.html)(Gasteiger et al., 2007).

4.1.3 Results and Discussion

4.1.3.1 General characterization of ipilimumab/CTLA-4

The ipilimumab antibody is divided into the heavy chain (HC) and light chain (LC), each of which has three complementarity-determining regions (CDRs), the light chain called LCDRs and the heavy chain HCDRs (Ramagopal et al., 2017; Singh et al., 2019). CDRs are the main points of interaction with CTLA-4 and define the specificity of the antibody for the protein (Ramagopal et al., 2017). The central amino acid residues in HCDR1 were Ser^{31} and Thr^{33}, in HCDR2 were Asn^{57} and Tyr^{59} and, in HCDR3 were Trp^{101} and Leu^{102} (Fig. 48). HCDRs interacted mainly with the residues Glu^{83}, Lys^{130}, Thr^{82}, Arg^{70}, Met^{134}, Tyr^{135}, and Pro^{136} of CTLA-4, while the LCDRs of ipilimumab interacted with Ser^{79}, Gln^{80}, Val^{81}, Iso^{143}, Gly^{142}, Leu^{141}, Tyr^{139} and Tyr^{140} of CTLA-4 (Fig. 48). All these results are in agreement with those reported by Ramagopal (2017) regarding the interactions supporting the CTLA-4:ipilimumab

complex.

4.1.3.2 Molecular dynamics simulations

To the best of our knowledge, this is the first report of molecular dynamics analyses aiming to characterize the stability of the CTLA-4:ipilimumab complex. Molecular dynamics simulations are employed to explore conformational space and energy of interactions showing the most stable conformation assumed by the complex (Hospital *et al*., 2015). After 20 ns of molecular dynamics simulation, it was possible to verify the stabilization of the CTLA-4:ipilimumab complex with a RMSD variation smaller than 1Å (Fig. Suppl. 56), indicating that a very stable complex was formed (Hospital *et al*., 2015). After 13 ns, the RMSD variation was minimal, so the last frame of the molecular dynamics, after stabilization and minimization by molecular dynamics simulation, was used for the subsequent analyses.

4.1.3.3 Dielectric function

The protein's dielectric function varied widely depending on the region of the protein. In more external regions outside the 3D structure, the dielectric function was close to the dielectric function of water (ε = 80). In contrast, in more internal regions of the protein, which are more hydrophobic, the dielectric function was close to 4. The region of interest in the interaction is shown in a 2D plane in Figure 49. Morais et al. (2020) obtained similar results by analyzing the variation of the dielectric function in the uPA-uPAR complex.

Figure 48. Structure of the CTLA-4/ipilimumab complex (PDB ID:5XJ3). (A) The general structure of the complex.

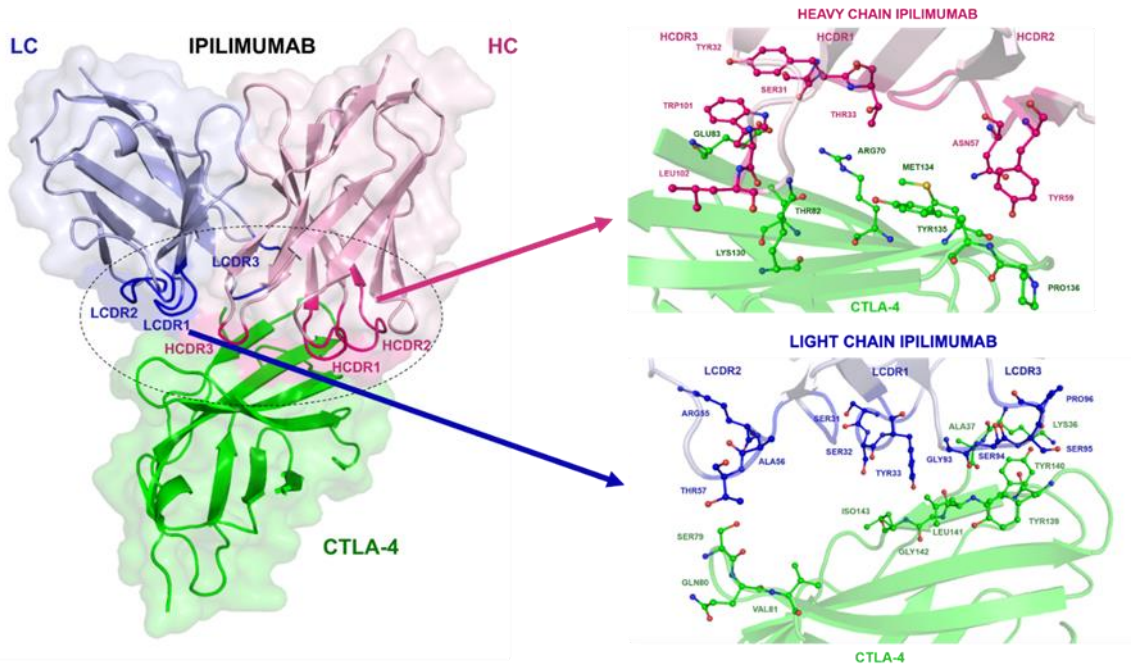

Legenda:CTLA-4 colored in green, light chain (LC) in blue, heavy chain (HC) in pink, LCDRs in dark blue, and HCDRs in dark pink. (B) The central residues of the interaction between HCDRs/CTLA-4 and LCDRs/CTLA-4.
Fonte: AMARAL *et al.,* 2020.

4.1.3.4 Quantum biochemistry description

For comparison, we used the calculated non-homogeneous dielectric function and the homogeneous dielectric function equal to 40. This was the same approach used by Morais et al. (2020) to analyze the interactions of uPA–uPAR by quantum biochemistry. The HCDRs and LCDRs showed higher interaction energies with the CTLA-4 protein. In HCDR1, the residues Tyr^{32} and Ser^{31} showed the best interaction energies, of -2.2 and -1.7 kcal.mol^{-1} when using a non-homogeneous dielectric function, and +0.8 and -3.3 kcal.mol^{-1} when using a constant dielectric function. This is a new and interesting result revealed by quantum analyses. Ramagopal et al. (2017) did not mention the contributions of these amino acid residues in their study about the CTLA-4:ipilimumab complex, which seems important for the understanding of this complex.

HCDR1 revealed total energy levels of -5.9 and -2.2 kcal.mol^{-1} when

using constant and non-homogeneous dielectric functions, respectively. In HCDR2, the residues Tyr^{59}, Lys^{58}, Asn^{57}, Asp^{54}, Tyr^{53}, and Ser^{52} had energies of -23, -6.7, -1.5, -12.6, -3.1 and -1 kcal.mol^{-1} using a non-homogeneous dielectric function, and energies of -16, -7.1, -1.7, -10 and -2.9 kcal.mol^{-1} using ε = 40. These are the same residues reported by Ramagopal et al. (2017). However, quantum analysis identified an additional residue, Lys^{58}, which is important for that interaction.

Figure 49. Dielectric function variation in the CTLA-4/ipilimumab interaction.

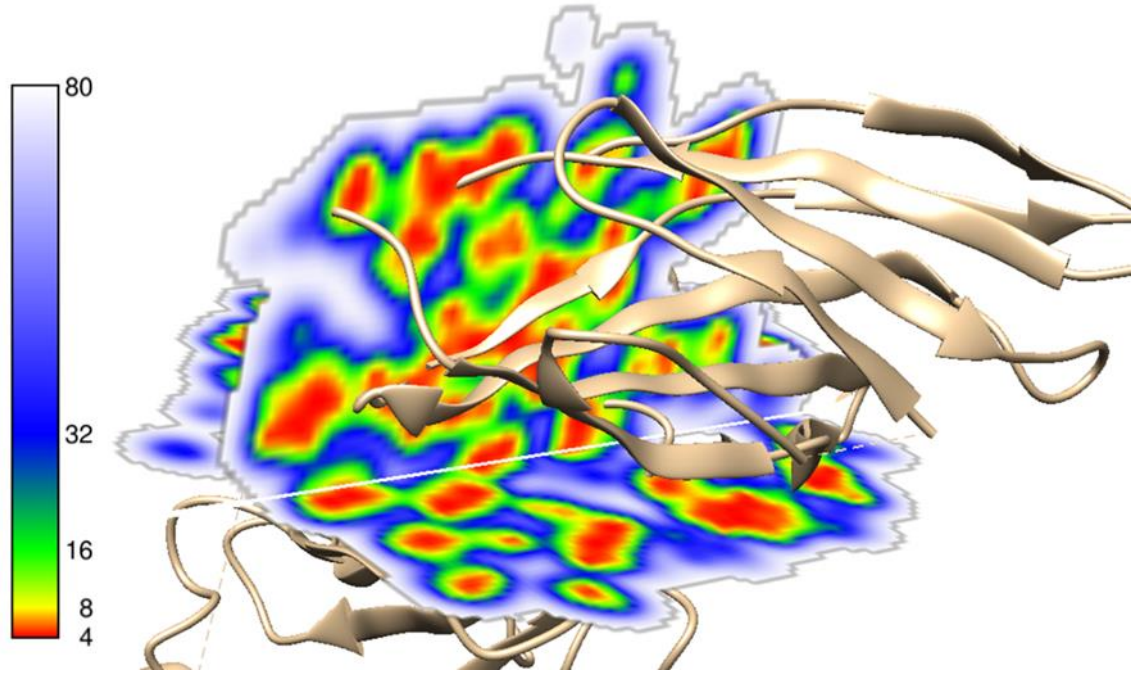

Legenda: Dielectric function variation in the CTLA-4/ipilimumab interaction. White represents dielectric constant ε = 80 and red ε = 4.
Fonte: AMARAL *et al.,* 2020.

The total energy levels of HCDR2 were -48 and -42 kcal.mol^{-1} using non-homogeneous and homogeneous ε = 40, respectively. In the HCDR3, only residues Gly^{100}, Trp^{101}, Leu^{102} and Gly^{103} obtained high attraction energies, with values of +0.1, -26.9, -13.3 and -0.9 kcal.mol^{-1} with a non-homogeneous dielectric function, and -4, -23.2, -13.7 and -1.4 kcal.mol^{-1} using a homogeneous dielectric function. For HCDR3, quantum analyses revealed two additional amino acid residues, Gly^{100} and Gly^{103}, as important to HCDR3 interaction with CTLA-4, as compared to the results reported by Ramagopal et al. (2017). The total energy sums of HCDR3 were -41.0 and -42.3

kcal.mol^{-1} with non-homogeneous and homogeneous dielectric functions, respectively.

In the CDRs of the ipilimumab light chain, we found that LCDR3 was the main chain involved in the interaction, as reported before by Ramagopal et al. (2017). The main residues of LCDR3 were Trp^{97}, Ser^{95}, Ser^{94}, Gly^{93} and Tyr^{92}, with interaction energies of -3.8, -11.8, -18.1, -10.1 and -3.9 kcal.mol^{-1} using a non-homogeneous dielectric function. When applying the uniform dielectric function ε = 40, the values obtained were -3.5, -9.5, -16.1, -12.8 and -4.1 kcal.mol^{-1}, respectively.

Compared to the results of Ramagopal et al. (2017), quantum analyses revealed Tyr^{92} as an important interaction residue. Thus, the total energies of the LCDR3 were equal to -48 and -46.3 kcal.mol^{-1} using a non-homogeneous dielectric function and ε = 40, respectively. The LCDR2 obtained total interaction energies of -4.3 and -8.8 kcal.mol^{-1} using a non-homogeneous dielectric function and ε = 40, respectively. The main residues of LCDR2 were Thr^{57}, Arg^{55} and Tyr^{50}, with energies of -4.5, -0.9 and +1.5 kcal.mol^{-1} and -5.4, -1.6 and -1.4 kcal.mol^{-1} using a non-homogeneous and homogeneous dielectric function ε = 40, respectively. Ramagopal et al. (2017) reported that only Tyr^{50} was important for LCDR2 interaction with CTLA-4. However, we found other amino acid residues involved in the interaction.

LCDR1 obtained total interaction energies of -11.2 and -19 kcal.mol-1 using a non-homogeneous dielectric function and ε = 40, respectively. The main residues of LCDR1 were Ser^{31}, Ser^{32}, and Tyr^{33}, with energies equal to -0.3, +0.9 and -11.8 kcal.mol^{-1} using a non-homogeneous dielectric function and +1.3, -4.1 and -16.2 kcal.mol^{-1} when using the constant dielectric function ε = 40 (Fig. 50B). This analysis highlighted the importance of Tyr^{33} for the interaction between LCDR1 with CTLA-4.

The ipilimumab antibody has 19 sites of hydrophobic interactions with CTLA-4; 7 and 12 interactions between the antibody light chain and the heavy chain, respectively. The ipilimumab light and heavy chains presented 5 and 8 hydrogen bonds with CTLA-4, respectively, totaling 13 hydrogen bonds between the antibody and the protein. Only one ionic interaction formed between Asp54 in the antibody heavy chain and Arg70 of CTLA-4. An aromatic-aromatic interaction was observed between the Trp97 of the antibody light chain and the Tyr139 residue of CTLA-4, with a distance of 5.58 Å between the centroids. The Phe50 and Tyr53 residues of the antibody heavy chain presented aromatic-sulfur and cation-pi interactions with CTLA-4 residues Met134 and Arg70, respectively (Table 7).

Figure 50. Energy profile for each ipilimumab chain on the recognition surface.

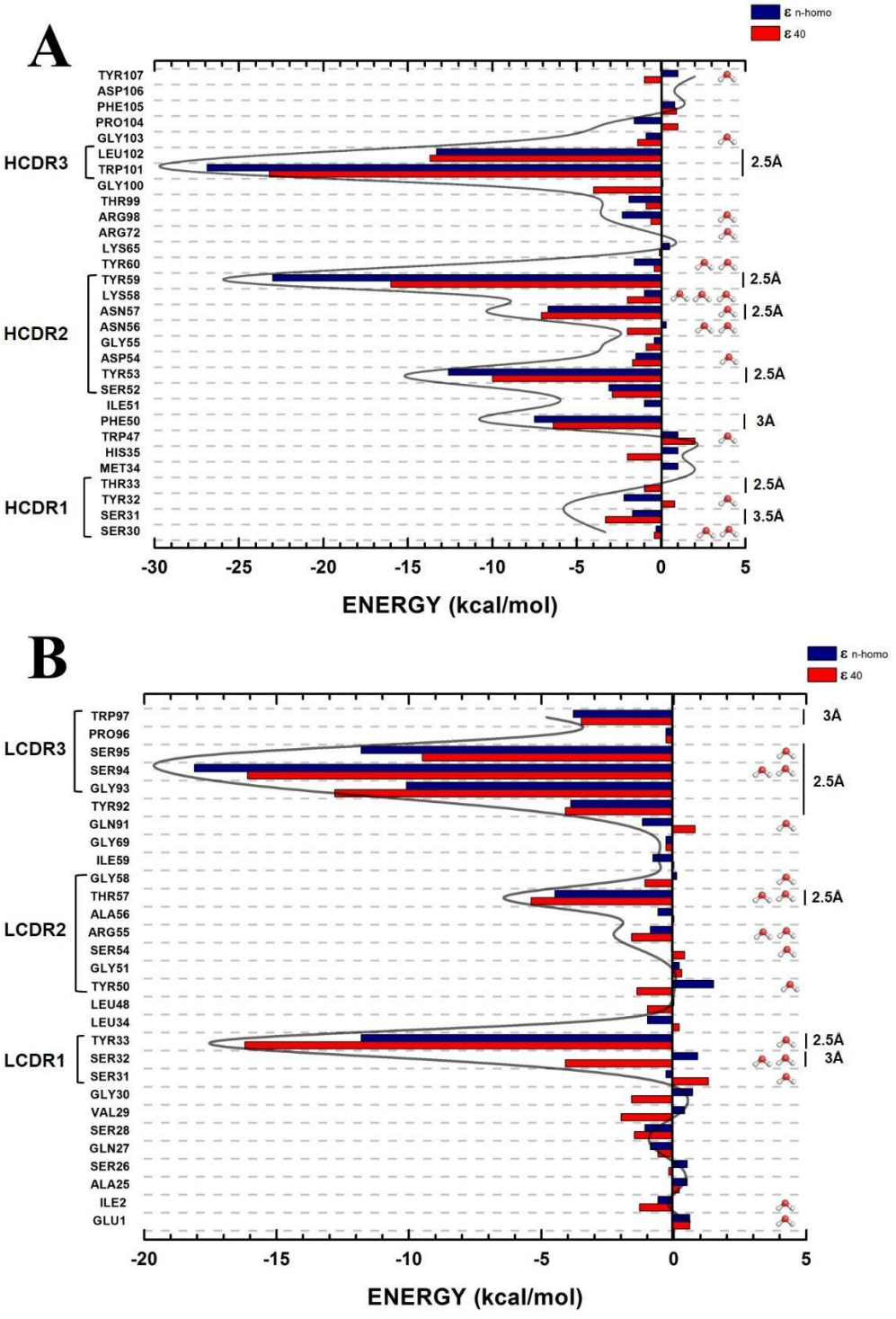

Legenda: (A) This figure represents the interaction energies of the amino acid residues in the heavy chain. (B) The interaction energies of the amino acid residues in the light chain, using either the dielectric function ε = 40 (red) or the non-homogenous dielectric function (blue).
Fonte: AMARAL *et al.,* 2020.

Table 7. The interactions between Ipilimumab antibody and CTLA-4.

Interaction	Pos	Residue	Chain	Pos	Residue	Chain	Distance (Å)
HYDROPHOBIC	33	TYR	LIGHT	141	LEU	CTLA-4	
	33	TYR	LIGHT	143	ILE	CTLA-4	
	33	TYR	LIGHT	37	ALA	CTLA-4	
	92	TYR	LIGHT	141	LEU	CTLA-4	
	92	TYR	LIGHT	143	ILE	CTLA-4	
	97	TRP	LIGHT	139	TYR	CTLA-4	
	97	TRP	LIGHT	141	LEU	CTLA-4	
	50	PHE	HEAVY	139	TYR	CTLA-4	
	50	PHE	HEAVY	134	MET	CTLA-4	
	53	TYR	HEAVY	134	MET	CTLA-4	
	59	TYR	HEAVY	135	TYR	CTLA-4	
	59	TYR	HEAVY	137	PRO	CTLA-4	
	59	TYR	HEAVY	139	TYR	CTLA-4	
	101	TRP	HEAVY	81	VAL	CTLA-4	
	101	TRP	HEAVY	74	LEU	CTLA-4	
	102	LEU	HEAVY	74	LEU	CTLA-4	
	102	LEU	HEAVY	81	VAL	CTLA-4	
	102	LEU	HEAVY	128	ILE	CTLA-4	
	102	LEU	HEAVY	143	ILE	CTLA-4	
HYDROGEN BONDS	33	TYR	LIGHT	143	ILE	CTLA-4	3.09
	33	TYR	LIGHT	143	ILE	CTLA-4	3.43
	57	THR	LIGHT	79	SER	CTLA-4	3.29
	93	GLY	LIGHT	141	LEU	CTLA-4	2.63
	95	SER	LIGHT	139	TYR	CTLA-4	2.88
	53	TYR	HEAVY	132	GLU	CTLA-4	2.79
	53	TYR	HEAVY	132	GLU	CTLA-4	3.09
	57	ASN	HEAVY	68	GLU	CTLA-4	2.6
	57	ASN	HEAVY	68	GLU	CTLA-4	2.6
	57	ASN	HEAVY	68	GLU	CTLA-4	2.6
	57	ASN	HEAVY	68	GLU	CTLA-4	2.6
	59	TYR	HEAVY	134	MET	CTLA-4	2.65
	101	TRP	HEAVY	130	LYS	CTLA-4	2.7
Ionic	54	ASP	HEAVY	70	ARG	CTLA-4	
Aromatic-Aromatic	97	TRP	LIGHT	139	TYR	CTLA-4	5.58
Aromatic-Sulphur	50	PHE	HEAVY	134	MET	C	5

Cation-Pi	53	TYR	HEAVY	70	ARG	C	4.52

Figure 51. Variation of the interaction energy as a function of the CTLA-4 radius.

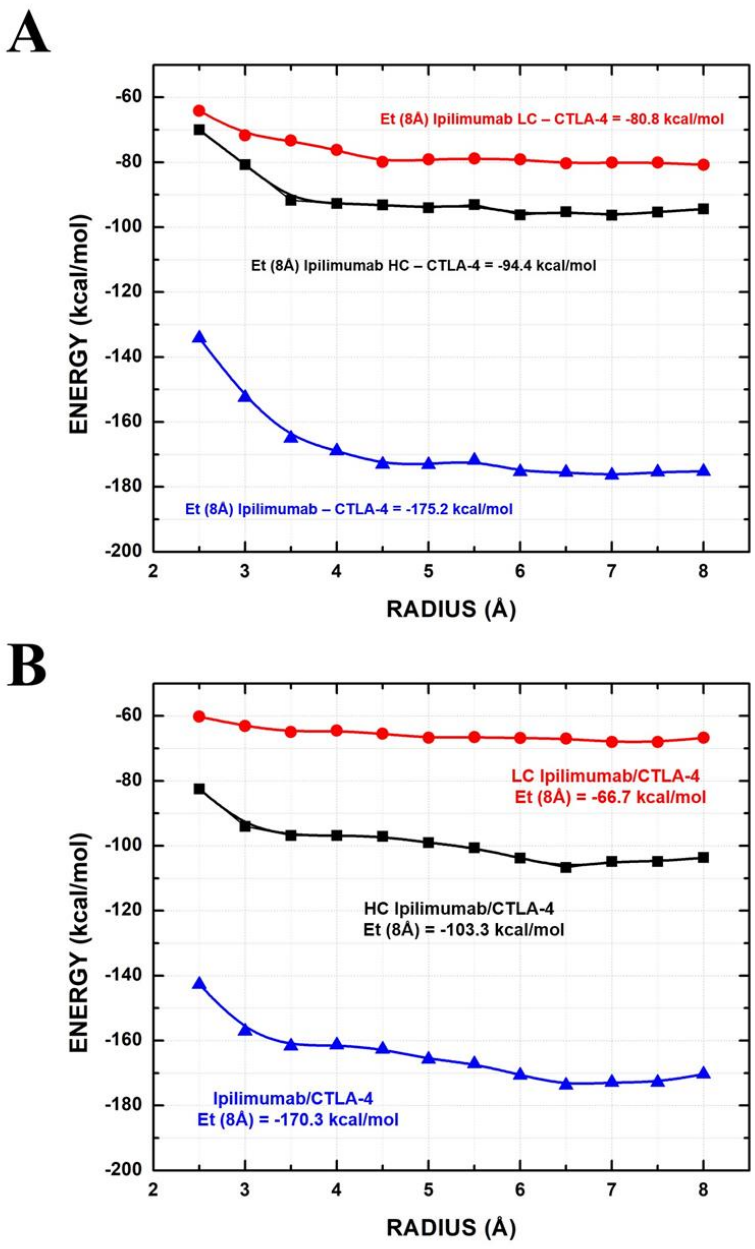

Legenda:Variation of the interaction energy as a function of the CTLA-4 radius for light chain (red), heavy chain (black), and the sum of the HC and LC energies (blue). (A) Interaction energies using the dielectric function ε = 40 and (B) using the non-homogenous dielectric function.
Fonte: AMARAL *et al.,* 2020.

The total interaction energy presented by ipilimumab/CTLA-4 complex was

1.3-fold higher than the energy presented by pembrolizumab/PD-1 (Tavares et al., 2018), considering the same dielectric function. Similar to the results presented by Tavares et al. (2018), the most important contribution to antibody interaction was made by the heavy chain. This suggests that the heavy chain could be a target to bioinformatics aiming to improve this interaction and produce a more efficient inhibitor of those cancer-related proteins, and hence strengthen the immune system even more to overcome cancer.

Tyr^{139} was the main residue of CTLA-4 in the interaction with ipilimumab, with interaction energy of -27 $kcal.mol^{-1}$. This residue interacts with both the heavy and light chains of the antibody. This is an important finding that has not been reported previously, and can be used to design more efficient molecules for the treatment of cancer. Tyr^{140}, Leu^{141} and Ile^{143} presented energies of -17, -10.3 and -10.5 $kcal.mol^{-1}$, respectively, and had interaction mainly with the antibody light chain. The main residues of CTLA-4 that interacted with the heavy chain were Arg^{70}, Leu^{74}, Thr^{82}, Glu^{83}, Lys^{130}, Met^{134} and Tyr^{135} , with respective interaction energies equal to -7, -5.3, -5.9, -9, -14.2, -15.5 and -5.9 $kcal.mol^{-1}$ (Fig. 52).

Using a non-homogeneous dielectric function, it was possible to observe more realistic results. By employing a constant dielectric function, it is possible to overestimate or underestimate some interactions, especially those with charges involved. These results corroborate the results obtained by Morais (2020) in the uPA-uPAR interaction.

4.1.3.5 Mimetic peptides

Based on the results of quantum biochemistry, we designed 12 mimetic peptides. The peptide derived from the LCDR1 was named Pep-Ipi-L1 (Fig. 53A), consisting of the residues Val^{29} to Leu^{34} of the ipilimumab light chain. The cyclic peptide from the same region was obtained by adding a peptide bond between two glycine residues at the ends and was named Pep-Cyclo-Ipi-L1 (Fig. 53B). The third peptide designed from LCDR2 consisted of the residues Leu^{48} to Ile^{59} and was named Pep-Ipi-L2 (Fig. 53C). The corresponding cyclic peptide was designed and named Pep-Cyclo-Ipi-L2 (Fig. 53D). From LCDR3, Pep-Ipi-L3 was designed and consisted of the residues Gln^{91} to Trp^{97} (Fig. 53E), while the corresponding cyclical

form was called Pep-Cyclo-Ipi-L3 (Fig. 53F).

Figure 52. Hotspot of the CTLA-4 chain on the recognition surface.

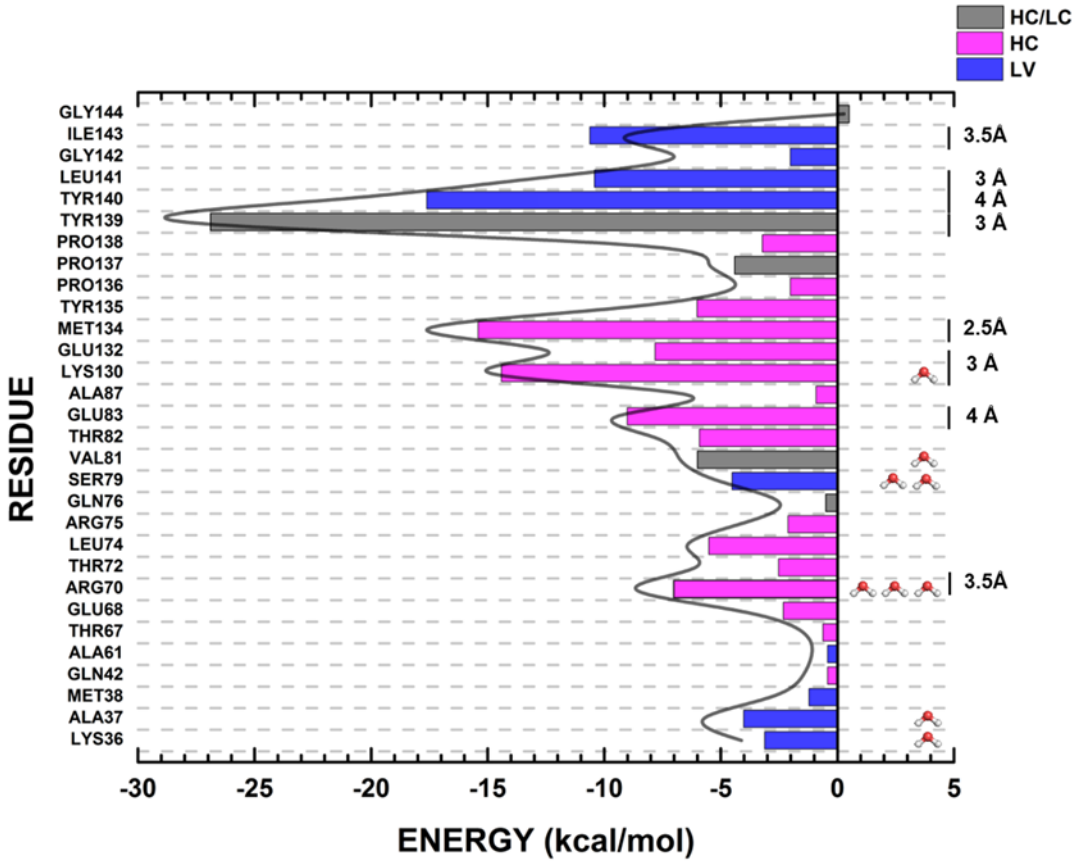

Legenda:The colors represent the main chains involved in the interaction. The light chain (LC) is represented in blue, the heavy chain (HC) in pink, and interaction involving both the light and heavy chains (HC/LC) in gray.
Fonte: AMARAL *et al.,* 2020.

Using the same approach, Pep-Ipi-H1 was designed from HCDR1, which consisted of the Thr^{28} to Thr^{33} residues (Fig. 53G), while its cyclic form was Pep-Cyclo-Ipi-H1 (Fig. 53H). From HCDR2, Pep-Ipi-H2 corresponded to the residues Tyr^{53} to Tyr^{60} (Fig. 53I) and the cyclic form was called Pep-Cyclo-Ipi-H2 (Fig. 53J). Finally, the peptides Pep-Ipi-H3 and Pep-Cyclo-Ipi-H3 consisted of the residues Trp^{101}-Leu^{102} (Fig. 53K and 53L).

Synthetic peptides have recently gained more attention due to increasing microbial resistance to antibiotics (Souza et al., 2020). They have also been investigated in other application, such as antiviral (Souza et al., 2020) and anticancer therapies (Arias et al., 2020). Thus, the approach of designing peptides from the best

ipilimumab amino acid residues that interacted with CTLA-4 followed these guidelines. By doing this, three advantages were obtained: (1) the peptides composed from the best amino acid residues could have a better affinity to bind with CTLA-4 than ipilimumab itself; (2) for being designed from ipilimumab, the peptides could have no or slight toxic effects; and (3) by using peptides it is possible to solve the problem of low proteolytic resistance of ipilimumab and thus assess the possibility of oral administration, avoiding the collateral effects of intravenous application (Kroschinsky et al., 2017).

4.1.3.6 Comparison of the proteolytic resistance of ipilimumab and ipilimumab-derived peptides

The low resistance of antibodies to proteolysis is a problem that has to be considered during clinical trials. Ipilimumab has become an essential molecule in cancer treatment. However, its administration route results in some undesired side effects. A solution to that problem is the design of peptides from the ipilimumab sequence that present the same activity and are resistant to proteolysis.

Using the online server Peptide Cutter (Gasteiger et al., 2003), it was possible to evaluate the presence and number of cleavage sites in ipilimumab's heavy and light chains. Both chains are highly susceptible to digestion by trypsin, chymotrypsin, and pepsin at pH 1.3 and pH>2. All designed peptides presented high stability to digestion by trypsin, chymotrypsin and pepsin at pH 1.3 and pH>2. Some peptides did not show any site for cleavage by trypsin, chymotrypsin or pepsin at pH 1.3.All peptides had pepsin cleavage sites at pH>2. The peptide with the greatest number was Pep-Cyclo-Ipi-L2, with 6 sites susceptible to pepsin at pH>2. However, this value is 9 and 10 times lower than the presented by the light and heavy chain, respectively (Table 8).

Figure 53. Mimetics peptides derived of antibody Ipilimumab.

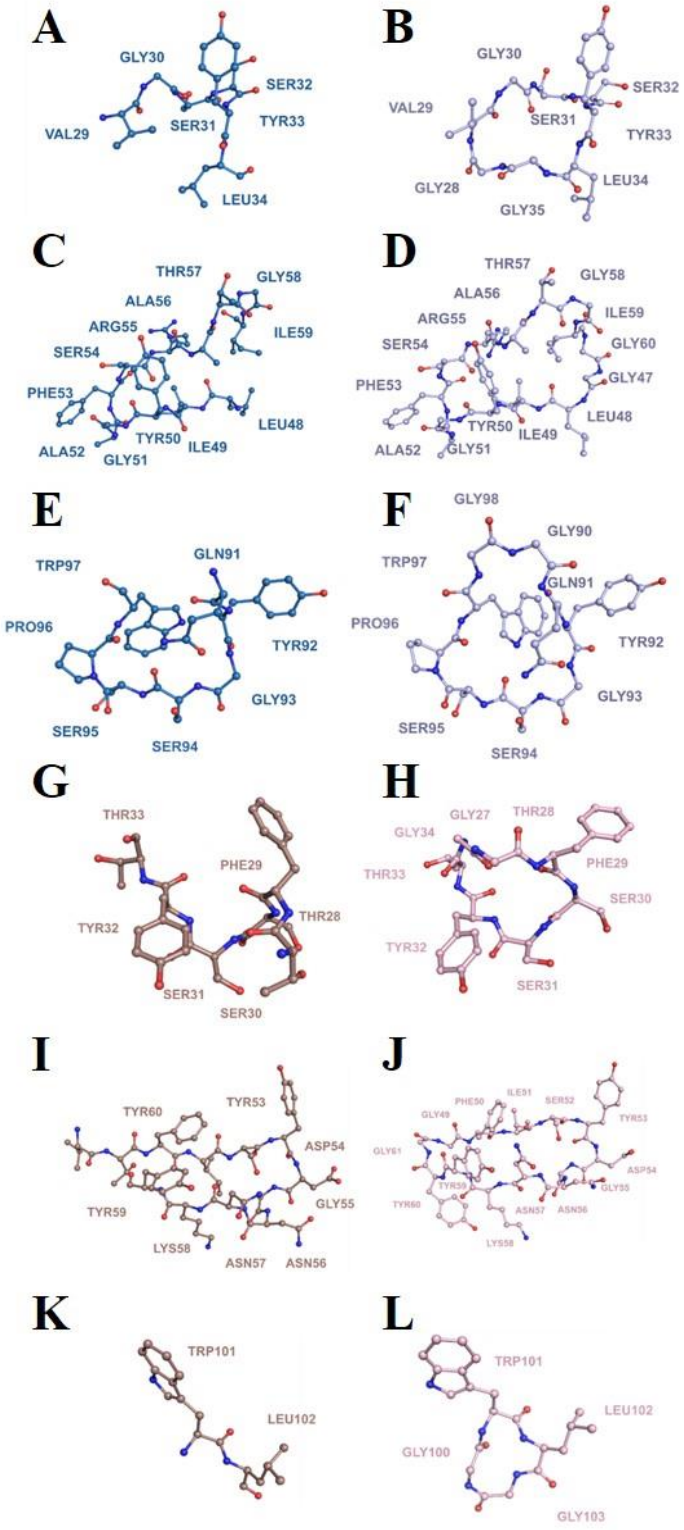

Legenda: Original HCDRs and LCDRs (dark blue and salmon, respectively) and mimetic peptides (light blue and pink, respectively).
Fonte: AMARAL *et al.,* 2020.

Other analyses were performed to evaluate the stability of ipilimumab and derived peptides to the intestinal-like environment. The light and heavy chains presented calculated half-lives of 0.212 and 0.221 sec, respectively. These findings suggests that both chains were promptly digested in the presence of intestinal enzymes, confirming their low stability. All peptides presented a half-life longer than 1 sec. The highest value was that of Pep-Cyclo-Ipi-H1, achieving 1.615 sec (Table 8). Therefore, the peptides presented higher stability in the presence of intestinal enzymes. Souza et al. (2020) designed two synthetic antimicrobial peptides presented high stability, which was later confirmed by *in vitro* digestion and mass spectrometry analyses, corroborating the data of the *in silico* analyses. Altogether, these results demonstrate the feasibility of obtaining peptides as potential inhibitors of CTLA-4, with excellent potential for application in cancer immunotherapy, possibly by oral administration.

Table 8. Cleavages site obtained from bioinformatics analysis of Ipilimumab and Ipilimumab-derived peptides

Samples	Trypsin[a]	Chymotrypsin[a]	Pepsin (pH 1.3) [a]	Pepsin (pH>2) [a]	Half-life [b]	Stability [c]
	Number of cleavage sites[a]					
Ipilimumab light chain	19	20	38	55	0.212	low
Ipilimumab heavy chain	19	21	38	60	0.221	low
Pep-Cyclo-Ipi-L1	0	0	2	3	1.083	high
Pep-Cyclo-Ipi-L2	1	2	4	6	1.178	high
Pep-Cyclo-Ipi-L3	0	0	0	3	1.341	high
Pep-Cyclo-Ipi-H1	0	0	2	4	1.343	high
Pep-Cyclo-Ipi-H2	1	0	0	4	1.491	high
Pep-Cyclo-Ipi-H3	0	0	2	2	1.615	high

Legenda: [a]The cleavage sites was analyzed using the Peptide Cutter (http://web.expasy.org/peptide_cutter/).
[b]The half-life in seconds was calculated using the Half Life Prediction tool (http://crdd.osdd.net/raghava/hlp/help.html), which predicts the proteolytic activity in the intestinal-like environment.
[c]Stability was calculated using the Half Life Prediction tool (http://crdd.osdd.net/raghava/hlp/help.html). Half-life < 0.3 s means low stability; half-life from 0.1 to 1.0 s means normal stability; half-life > 1.0 s means high stability.
Fonte: AMARAL *et al.,* 2020.

4.1.4. Conclusion

Here we report the results of quantum analysis of the CTLA-4:ipilimumab complex at both molecular and energetic levels by depicting proteins as amino acid fragments and calculating the residue-residue interaction energies to assess the global interaction energy. The use of quantum biochemistry for the calculations provided a detailed characterization and new insights into molecular features, shedding light on new and relevant amino acid interactions. Altogether, the results presented here favor the development of new compounds targeting the CTLA-4: ipilimumab complex. Finally, using quantum biochemistry, we designed synthetic peptides from the CTLA-4:ipilimumab interface complex, whose calculated binding energy suggests they can mimic antibodies to block CTLA-4. The obtained peptides are good alternatives to ipilimumab, by showing higher protease resistance and stability in the intestinal environment. Furthermore, these new molecules could reduce the costs of treatment and increase the benefits not only in clinical oncology trials but also in pharmaceutical medicine, improving cancer therapy.

REFERENCE

1 World Health Organization, *WHO guidelines for the pharmacological and radiotherapeutic management of cancer pain in adults and adolescents*, 2018.

2 J. Y. Lee, H. T. Lee, W. Shin, J. Chae, J. Choi, S. H. Kim, H. Lim, T. Won Heo, K. Y. Park, Y. J. Lee, S. E. Ryu, J. Y. Son, J. U. Lee and Y. S. Heo, Structural basis of checkpoint blockade by monoclonal antibodies in cancer immunotherapy, *Nat. Commun.*, 2016, **7**, 1–10.

3 L. Galluzzi, T. A. Chan, G. Kroemer, J. D. Wolchok and A. López-Soto, The hallmarks of successful anticancer immunotherapy., *Sci. Transl. Med.*, , DOI:10.1126/scitranslmed.aat7807.

4 M. Konstantinidou, T. Zarganes-Tzitzikas, K. Magiera-Mularz, T. A. Holak and A. Dömling, Immune Checkpoint PD-1/PD-L1: Is There Life Beyond Antibodies?, *Angew. Chem. Int. Ed. Engl.*, 2018, **57**, 4840–4848.

5 J. C. Almagro, T. R. Daniels-Wells, S. M. Perez-Tapia and M. L. Penichet, Progress and Challenges in the Design and Clinical Development of Antibodies for Cancer Therapy., *Front. Immunol.*, 2017, **8**, 1751.

6 R. C. Acúrcio, A. Scomparin, J. Conniot, J. A. R. Salvador, R. Satchi-Fainaro, H. F. Florindo and R. C. Guedes, Structure-Function Analysis of Immune Checkpoint Receptors to Guide Emerging Anticancer Immunotherapy., *J. Med. Chem.*, 2018, **61**, 10957–10975.

7 C. C. Stamper, Y. Zhang, J. F. Tobin, D. V Erbe, S. Ikemizu, S. J. Davis, M. L. Stahl, J. Seehra, W. S. Somers and L. Mosyak, Crystal structure of the B7-1/CTLA-4 complex that inhibits human immune responses, *Nature*, 2001, **410**, 608–611.

8 J. C. Schwartz, X. Zhang, A. A. Fedorov, S. G. Nathenson and S. C. Almo, Structural basis for co-stimulation by the human CTLA-4/B7-2 complex., *Nature*, 2001, **410**, 604–608.

9 M. He, Y. Chai, J. Qi, C. W. H. Zhang, Z. Tong, Y. Shi, J. Yan, S. Tan and G. F. Gao, Remarkably similar CTLA-4 binding properties of therapeutic ipilimumab and tremelimumab antibodies., *Oncotarget*, 2017, **8**, 67129–67139.

10 F. Kroschinsky, F. Stölzel, S. von Bonin, G. Beutel, M. Kochanek, M. Kiehl and P. Schellongowski, New drugs, new toxicities: severe side effects of modern targeted and immunotherapy of cancer and their management., *Crit. Care*, 2017, **21**, 89.

11 K. Guzik, M. Tomala, D. Muszak, M. Konieczny, A. Hec, U. Błaszkiewicz, M. Pustuła, R. Butera, A. Dömling and T. A. Holak, Development of the Inhibitors that Target the PD-1/PD-L1 Interaction-A Brief Look at Progress on Small Molecules, Peptides and Macrocycles., *Molecules*, , DOI:10.3390/molecules24112071.

12 A. B. M. L. A. Tavares, J. X. Lima Neto, U. L. Fulco and E. L. Albuquerque, Inhibition of the checkpoint protein PD-1 by the therapeutic antibody pembrolizumab outlined by quantum chemistry, *Sci. Rep.*, 2018, **8**, 1840.

13 D. W. Zhang and J. Z. H. Zhang, Molecular fractionation with conjugate caps for full quantum mechanical calculation of protein-molecule interaction energy, *J. Chem. Phys.*, 2003, **119**, 3599–3605.

14 X. He and J. Z. H. Zhang, A new method for direct calculation of total energy of protein, *J. Chem. Phys.*, , DOI:10.1063/1.1849132.

15 X. Chen, Y. Zhang and J. Z. H. Zhang, An efficient approach for ab initio energy calculation of biopolymers., *J. Chem. Phys.*, 2005, **122**, 184105.

16 E. L. Wu, Y. Mei, K. L. Han and J. Z. H. Zhang, Quantum and molecular dynamics study for binding of macrocyclic inhibitors to human α-thrombin, *Biophys. J.*,

2007, **92**, 4244–4253.
17 P. A. Morais, F. F. Maia, C. Solis-Calero, E. W. S. Caetano, V. N. Freire and H. F. Carvalho, The urokinase plasminogen activator binding to its receptor: A quantum biochemistry description within an in/homogeneous dielectric function framework with application to uPA-uPAR peptide inhibitors, *Phys. Chem. Chem. Phys.*, 2020, **22**, 3570–3583.
18 B. Delley, From molecules to solids with the DMol3 approach, *J. Chem. Phys.*, 2000, **113**, 7756–7764.
19 A. S. Singh, B. Chmielowski, J. R. Hecht, L. S. Rosen, W. A. Chow, X. Wang, S. Brackert, C. Adame, J. Bovill, E. Schink, M. Douek, J. Chantharasamee, K. Wong, F. C. Eilber and J. A. Glaspy, A randomized phase II study of nivolumab monotherapy versus nivolumab combined with ipilimumab in advanced gastrointestinal stromal tumor (GIST)., *J. Clin. Oncol.*, 2019, **37**, 11017.
20 U. A. Ramagopal, W. Liu, S. C. Garrett-Thomson, J. B. Bonanno, Q. Yan, M. Srinivasan, S. C. Wong, A. Bell, S. Mankikar, V. S. Rangan, S. Deshpande, A. J. Korman and S. C. Almo, Structural basis for cancer immunotherapy by the first-in-class checkpoint inhibitor ipilimumab, *Proc. Natl. Acad. Sci. U. S. A.*, 2017, **114**, E4223–E4232.
21 A. Hospital, J. R. Goñi, M. Orozco and J. L. Gelpí, Molecular dynamics simulations: advances and applications., *Adv. Appl. Bioinform. Chem.*, 2015, **8**, 37–47.
22 P. F. N. Souza, F. E. S. Lopes, J. L. Amaral, C. D. T. Freitas and J. T. A. Oliveira, A molecular docking study revealed that synthetic peptides induced conformational changes in the structure of SARS-CoV-2 spike glycoprotein, disrupting the interaction with human ACE2 receptor., *Int. J. Biol. Macromol.*, 2020, **164**, 66–76.
23 M. Arias, E. F. Haney, A. L. Hilchie, J. A. Corcoran, M. E. Hyndman, R. E. W. Hancock and H. J. Vogel, Selective anticancer activity of synthetic peptides derived from the host defence peptide tritrpticin, *Biochim. Biophys. Acta - Biomembr.*, 2020, 183228.

5 LIGAÇÃO DO PESTICIDA ATRAZINA À ALBUMINA HUMANA

Pesticidas são utilizados na agricultura com objetivo de reduzir as perdas causadas por pestes. Com sua utilização, observa-se um aumento da produtividade de alimentos. Entretanto, esses pesticidas são tóxicos na natureza e possuem diversos riscos para o meio ambiente e para saúde dos seres humanos, como: diabetes, distúrbios reprodutivos, disfunção neurológica, câncer e distúrbios respiratórios (ZHOU; ZHAO, 2021).

A atrazina [6-cloro-N-etil-N´(1-metiletil)-1,3,5-triazina-2,4-diamina] é um dos pesticidas mais utilizados no mundo. Assim como os outros herbicidas, possui efeitos deletérios na natureza, como a contaminação de água, bioacumulação, magnificação trófica e diversos efeitos prejudiciais à saúde humana. Esse pesticida foi proibido na União Europeia em 2003, porém diversos países continuam realizando sua aplicação nas plantações, como os Estados Unidos e o Brasil, mesmo já sendo relatado sua toxicidade neuroendócrina e disfunções sexuais (ROSTAMI *et al.,* 2021).

A albumina sérica humana (HSA) é a proteína em maior quantidade no sangue, sendo envolvida no transporte, metabolismo e eliminação de diversas moléculas. Desse modo, é crucial entender como os pesticidas e outras moléculas se ligam a HSA, pois através do estudo da interação entre as moléculas com a HSA é possível compreender os parâmetros farmacocinéticos, farmacodinâmicos, bem como a toxicidade das mesmas (MOLAEI *et al.,* 2022).

Nosso grupo de pesquisa realizou estudos da interação entre a albumina sérica humana (HSA) com o pesticida atrazina, utilizando espectroscopia de fluorescência, simulações de docking e dinâmica molecular, bem como cálculos quânticos da interação desse pesticida em diferentes sítios ativos da HSA. Foi possível constatar que o principal sítio ativo de ligação da atrazina a HSA foi o FA8 e demonstrar os principais tipos de interações que ocorrem no complexo. O artigo completo com todas as informações encontra-se no tópico seguinte.

Além de estudar os pesticidas interagindo com a HSA, nosso grupo também estudou a interação do adoçante stevia e dois derivados à albumina sérica bovina. O artigo desse trabalho encontra-se no apêndice J.

5.1 Characterization of the binding interaction between atrazine and human serum albumin: Fluorescence spectroscopy, molecular dynamics and quantum biochemistry

Artigo publicado na revista: Chemico-Biological Interactions.
DOI: http://dx.doi.org/10.1016/j.cbi.2022.110130

Victor L. B. França[a], Jackson L. Amaral[a], Yandara A. Martins[b], Ewerton W. S. Caetano[c], Kellen Brunaldi[d], Valder N. Freire[a*]

[a]Departament of Physics, Federal University of Ceará, Fortaleza 60440-900, Brazil.
[b]Departament of Physiology and Biophysics, Institute of Biomedical Sciences, University of São Paulo, São Paulo 05508-000, Brazil.
[c]Federal Institute of Education, Science and Technology of Ceará, Fortaleza 60040-531, Brazil.
[d]Departament of Physiological Sciences, State University of Maringá, Maringá 87020-900, Brazil.

*Corresponding author:
Kellen Brunaldi - Av. Colombo 5790, Sala 117, Bloco H79, Departamento de Ciências Fisiológicas, Universidade Estadual de Maringá, Maringá, PR 870020-900, Brazil;
Phone: (+55) 44-30114703; Email: kbrunaldi@uem.br

Highlights

- Direct interaction of ATR with TRP214 (FA8) quenches HSA fluorescence.
- Molecular dynamics predicts FA3/4 and FA8 as primary binding sites of ATR.
- Quantum biochemistry indicates FA8 as the main binding site of ATR.
- Pi-alkyl and van der Waals interactions contribute to the ATR/FA8 complexation.

Abstract

Atrazine (ATR), one of the most used herbicides worldwide, causes persistent contamination of water and soil due to its high resistance to degradation. ATR is associated with low fertility and increased risk of prostate cancer in humans, as well as birth defects, low birth weight and premature delivery. Describing ATR binding to human serum albumin (HSA) is clinically relevant to future studies about pharmacokinetics, pharmacodynamics and toxicity of ATR, as albumin is the most abundant carrier protein in plasma and binds important small biological molecules. In this work we characterize, for the first time, the binding of ATR to HSA by using fluorescence spectroscopy and performing simulations using molecular docking, classical molecular dynamics and quantum biochemistry based on density functional theory (DFT). We determine the most likely binding sites of ATR to HSA, highlighting the fatty acid binding site FA8 (located between subdomains IA-IB-IIA and IIB-IIIA-IIIB) as the most important one, and evaluate each nearby amino acid residue contribution to the binding interactions explaining the fluorescence quenching due to ATR complexation with HSA. The stabilization of the ATR/FA8 complex was also aided by the interaction between the atrazine ring and SER454 (hydrogen bond) and LEU481(alkyl interaction).

Keywords: triazine; herbicide; docking; quenching; molecular dynamics; density functional theory

5.1.1 Introduction

Pesticides avoid crop losses and warrant food availability to mankind. Different pesticides such as herbicides, insecticides, fungicides, rodenticides, and nematicides are essential in order to maintain the increase in the food production. Population growth estimates indicate that the food industry needs to increase pesticide production by 50% to meet the nutritional demand of world population by 2050. Herbicides corresponded to 47.5% of the pesticide world production in 2019, the largest proportion among different pesticide groups [1]. It is crucial to focus studies on binding mechanisms as a basis for informed discussions of sustainability and pesticide use in the agricultural system [2] .

Atrazine (ATR) is one of the most common worldwide herbicides, with an

annual usage ranging from 70,000 to 90,000 tons (notwithstanding its banning from the European Union since 2003). The USA consumed 36,000 tons of ATR in 2019, while in Brazil it was the second most used herbicide [3-5]. Chemically, ATR (2-ethylamino-4-isopropylamino-6-chloro-s-triazine; Figure 54 is a water-soluble chlorotriazine widely applied in corn crops to control broadleaf and grassy weeds [6]. ATR inhibits efficiently photosynthesis by targeting the D1 protein of photosystem II [7]. Unfortunately, the indiscriminate and widespread use of ATR has led to soil and water contamination [8, 9]. More importantly, ATR persists in the environment due to its high resistance to degradation (long half-life, low vapor pressure, and low pKa) and molecular mobility [10, 11].

The general population is exposed to ATR from drinking water and food, which pose widespread danger to public health [5, 12]. Consumption of contaminated food with hazardous pesticides has been estimated to 20,000 deaths a year in developing countries [1]. ATR is a potent endocrine disruptor with detrimental effects on gonadal development and fertility of fish, amphibians, and rodents. Additionally, ATR causes neurotoxicity and depresses immune function. In humans, it is associated with decreased sperm count, low semen quality, low fertility, and an increased risk of prostate cancer. Epidemiological studies have also reported birth defects, low birth weight, and small gestational age in populations exposed to ATR [13, 14].

Figure 54. Molecular structure of atrazine (ATR) and human serum albumin (HSA).

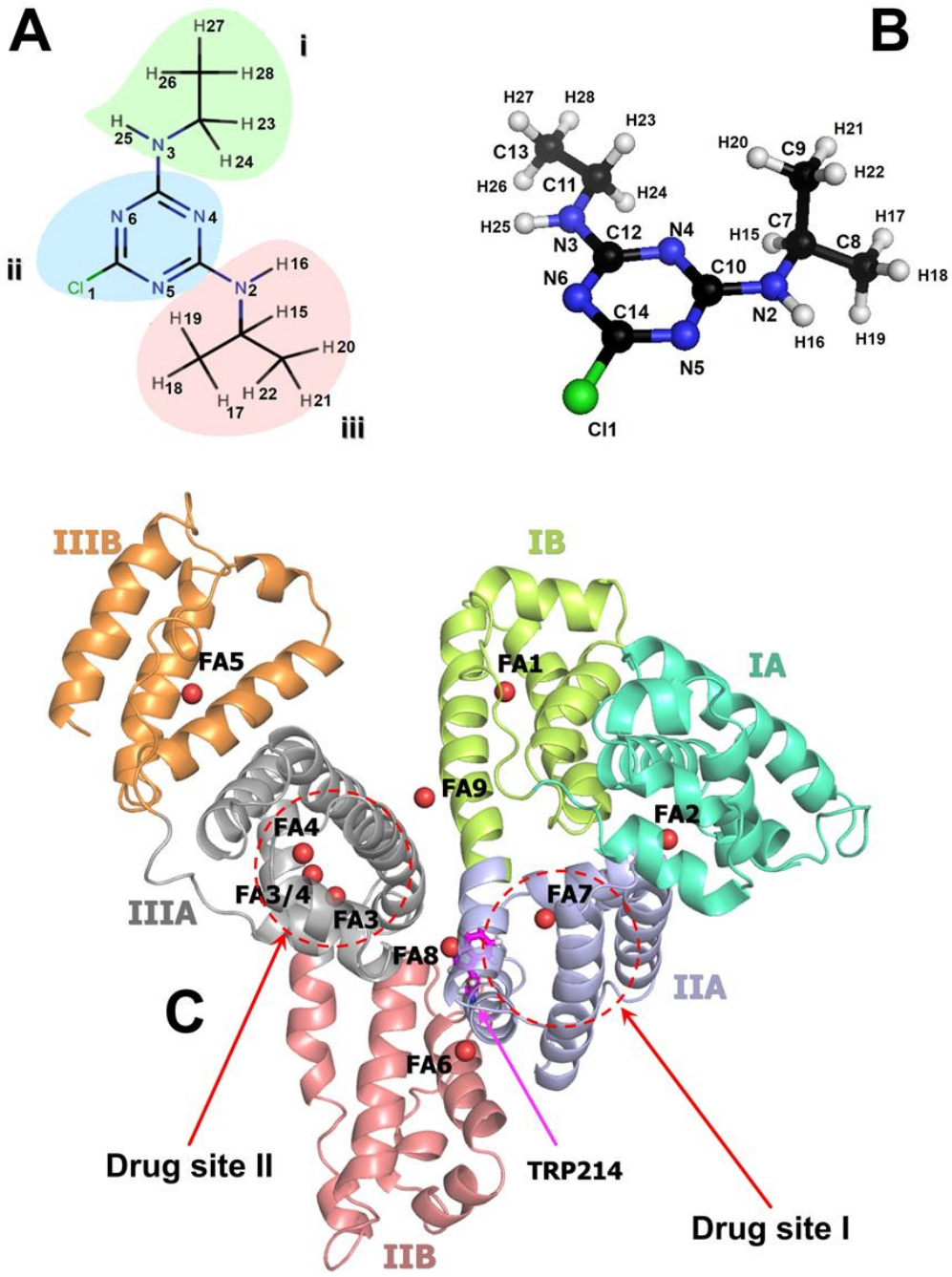

Legenda: **A.** Wide-frame representation of the ATR molecule separated into three regions: i (2-ethylamine group), ii (6-chloro-s-triazine ring), and iii (4-isopropylamine group). **B.** Ball and stick representation of the ATR molecule with atom labels (Cl 1; N 2-6; C 7-14 and, H 15-28). **C**. The overall structure of HAS determined by x-ray crystallography (ID 4Z69 [15] with its subdomains and the fatty binding sites (FA1-FA9).
Fonte: FRANÇA *et al.,* 2022.

Many aspects of distribution, metabolism, and elimination of small molecules are strongly correlated to their interactions with serum albumin. Therefore,

characterizing of the binding interaction of ATR with human serum albumin (HSA) is of great significance to understand pharmacokinetics, pharmacodynamics and toxicity of ATR in the human body. HSA is the most abundant carrier protein in plasma (60% of the total serum proteins) for a diverse range of exogenous and endogenous ligands through reversible noncovalent binding [16]. HSA consists of 585 amino acids arranged in three homologous helical domains (I-III), each one comprising two subdomains (A and B). Nine structurally distinct sites for long and medium-chain fatty acids (FA) are distributed through the HSA domains, with major drug-binding sites located at the hydrophobic pockets of sub-domains II-A (Drug site I/FA7) and III-A (Drug site II/FA3) (Figure 54) [17-21].

ATR spontaneously binds to HSA by forming covalent adducts with cysteine 34 [22] and by electrostatic interactions with site II/FA3/4 [7, 23]. However, the binding sites of ATR in the HSA structure have not been rigorously assigned. Several studies have used spectroscopy methods and molecular models to describe interactions between serum albumins and small molecules such as drugs and pesticides. For example, the binding of the fungicide iprodione to HSA has been investigated through docking, calorimetry, UV-visible, fluorescence and CD spectroscopy revealing structural changes of HSA upon iprodione binding [24]. A similar approach was employed to study the interaction of conazole pesticides with HSA [25], as well as 9-hydroxyphenanthrene, a polycyclic aromatic hydrocarbon with carcinogenic properties [26].

With the advances in the structure organization of albumin by x-ray crystallography [19, 21, 27-29] and NMR spectroscopy [17, 18, 30] newer methods in computational biology allow the investigation of protein-drug complexes, beyond molecular docking [31, 32], such as classical molecular dynamics [33-35], molecular mechanics [36, 37] and semiempirical quantum methods [38, 39]. Quantum biochemistry calculations through the application of density functional theory (DFT) [40-46] combined with molecular fractionation strategies [47-54] is more accurate to estimate interaction energies, and our research group has been successfully applied it for the description of protein-drug, protein-peptide and protein-protein interactions at the amino acid residue level [55-70].

In this work we present the results of molecular docking, molecular dynamics, and quantum biochemistry along with fluorescence spectroscopy to obtain basic data helpful for further elucidation of the binding mechanism of ATR to HSA,

clarifying the potential toxicity of ATR to human health, and aiding in the biomonitoring of ATR safety levels in the human body.

5.1.2 Material and methods

5.1.2.1 Reagents

ATR (2-ethylamino-4-isopropylamino-6-chloro-s-triazine), HSA, and Tris buffer were obtained from Sigma-Aldrich.

5.1.2.2 Fluorescence quenching

Fluorescence emission spectra were obtained with an RF-6000 Shimadzu spectrofluorometer (Kyoto, Japan) equipped with a 1 cm quartz cell and a thermostatic bath. HSA was excited (λ_{exc}) at 280 nm and the emission was recorded between 300 and 500 nm. The excitation and emission slit widths were set to 5 nm each. HSA at the concentration of 10 µM was prepared in Tris-HCL buffer pH 7.4. ATR was added to the HSA solution to obtain 5 solutions at the final concentrations of 5 mM, 10 mM, 20 mM, 40 mM, and 80 mM. All measurements were performed in triplicate at 25 ºC.

5.1.2.3 Acquiring and preparing the structures of HSA and ATR

The 3D structure of HSA was obtained from a protein data bank (PDB file ID 4Z69 – Resolution 2.19 Å) [71]. Water, ligands, and one protein chain were removed from the crystal structure of HSA using Discovery Studio 3.1 (Dassault Systemes BIOVIA). The protonation state of HSA was calculated at pH 7.4 with the PDB2PQR software [72]. Protonation changes of HSA residues, hydrogen adjustments, and total energy minimization were also performed using Discovery Studio 3.1. The 3D structure of ATR was obtained from the PubChem Database (https://pubchem.ncbi.nlm.nih.gov/), CID 2256, and submitted to charge analysis at pH 7.4 using MarvinSketch 18.24 (Marvin Beans Suite, ChemAxon), being afterwards submitted to Discovery Studio 3.1 for geometry optimization.

5.1.2.4 Molecular docking

HSA and ATR were prepared using AutoDockTools 1.5.6. (The Scripps Research Institute) and executed with Autodock Vina 1.1.2 (The Scripps Research Institute) [73], which uses quasi-Newton and Broyden-Fletcher-Goldfarb-Shanno (BFGS) methods [74]. AutoDockTools was used to retain the polar hydrogens of HSA, to determine the torsion tree of ATR, and to add partial charges to ATR and HSA through Kollman united charges [75]. Receptor (HSA) and ligand (ATR) were both treated as flexible molecules. The grid box was defined as 72 Å x 108 Å x 94 Å with HSA in the center. Exhaustiveness was set at 500 with the remaining settings kept as default. The twenty top-ranked poses were analyzed and classified according to the binding site, docking score, and recurrence. Three binding sites were selected for the following simulations.

5.1.2.5 Molecular dynamics (MD)

ATR poses in the FA1, FA3/4, and FA8 binding sites of HSA, previously predicted by the molecular docking, were prepared using the Visual Molecular Dynamics (VMD) software version 1.9.1. ATR and HSA molecules were merged and inserted into a water box (TIP3 model), and the concentration of NaCl was adjusted to 0.15 M. ATR parameters were generated by SwissParam (https://www.swissparam.ch/) using the CHARMM force field 22 [76]. ATR/HSA complexes were initially refined by energy minimization using 1000 steps and a temperature gradient from 100 to 299 K. A simulation of 50 ns was performed (299 K and 1 bar) using NAMD 2.9 (University of Illinois at Urbana-Champaign) [77]. The root-mean-square deviation of the atomic positions (RMSD) of HSA and ATR was also calculated during the simulation. Following the MD procedure, energy minimization using 10000 steps was achieved. Finally, the interactions among ligand, protein, and water molecules were obtained from the last coordinates of each complex (ATR-HSA:FA1, ATR-HSA:FA3/4, ATR-HSA:FA8) using VMD 1.9.1.

5.1.2.6 ATR/HSA binding interactions

2D diagrams of the interaction of ATR with the binding sites FA1, FA3/4, FA8 (coordinates previously generated by MD) were obtained using the Discovery Studio 2020 Receptor-Ligand Interactions Package (Dassault Systemes BIOVIA). The analysis of the ATR/HSA binding interaction was restricted to a distance of 4 Å from the ATR molecule considering a high ligand quality and preserving hydrogen interactions. Finally, the main interactions between ATR and HSA were represented in a 3D format using the Pymol software (Schrödinger, Inc).

5.1.2.7 Molecular fractionation with conjugate caps (MFCC) and quantum biochemistry

The interaction energy between the ATR molecule and HSA residues was calculated using Density Functional Theory (DFT) [42] through the Molecular Fractionation with Conjugate Caps (MFCC) strategy. The MFCC approach makes possible the investigation of many residues in a protein at a reduced computational time while maintaining accuracy [47, 78, 79]. To limit the number of residues to be analyzed without missing important interactions, non-covalent interactions within 10 Å from the ATR molecule were considered, as well as water molecules within 2.5 Å from each HSA residue and ATR.

The interaction energy between the i-th HSA residue of interest (R_i) and ATR was calculated as follows. First, we defined four auxiliary systems: (S1) R_i plus its respective conjugate caps C_{i-1} and C_{i+1} (the caps are attached to the amine and carboxyl parts of R_i and reflect the electronic environment of its neighborhood); (S2) R_i plus its conjugate caps only; (S3) the conjugate caps of R_i and ATR; (S4) the conjugate caps of R_i only. For each system, the total energy E_{Si} were evaluated using the DFT formalism. All dangling bonds were passivated with hydrogen atoms and the caps were formed from the immediate neighbor residues of R_i in the protein chain, $C_{i+1} = R_{i+1}$. The interaction energy between ATR and each amino acid residue was given by:

$$E(ATR - R_i) = E_{S1} - E_{S2} - E_{S3} + E_{S4} \qquad \text{(Eq. 1)}$$

All DFT calculations were performed using the DMOL3 code [80, 81]. A Double Numerical plus Polarization (DNP) basis set was selected to expand the Kohn-Sham orbitals of all electrons. The exchange-correlation functional of Perdew-

Burke-Ernzerhof (PBE) within the generalized gradient approximation (GGA) [82] and, the Tkatchenko-Scheffler dispersion correction (GGA + TS) [83] scheme were chosen to evaluate electronic energies. The orbital cutoff radius was set to 4 Å and the self-consistent field (SCF) convergence threshold was adjusted to 10^{-6} Ha. Water solvation was implemented through the COSMO implicit solvation model [84] with dielectric constant of 40 and include explicit water molecules within a radius of 2.5 Å relative to the ATR-R_i centroid.

5.1.3 Results and discussion

5.1.3.1 Fluorescence quenching experiments

The interaction of ATR with HSA is clinically relevant. HSA binds to a wide variety of drugs, increasing their half-life at the expense of decreasing their free active concentration [85]. In the case of ATR, binding to HSA may have an important role in enhancing ATR low solubility in water [6] and, consequently, changing its distribution throughout body compartments and toxicity.

As depicted in Figure 55, ATR caused a concentration-dependent quenching of HSA fluorescence, a clear sign of ATR binding to HSA. Although HSA presents 40 aromatic residues (31 phenylalanine, 18 tyrosine, and only one tryptophan residue) [15], its intrinsic fluorescence is mainly attributed to the TRP214 residue found at the surface of subdomain II (site FA8) [86, 87]. Lack of shift in the maximum emission peak of HSA (approximately at 330 nm) in our measurements suggests no change in the microenvironment hydrophobicity around TRP214 upon ATR binding [88].

Our fluorescence quenching results are in accordance with those previously reported for ATR [7] and prometryn (diamino-1,3,5 triazine with SCH3 group at position 6) [23]. In these studies, HSA quenching occurred by a static mechanism (quencher interacts with the fluorophore in the ground state). Thermodynamic parameters derived from the quenching data pointed towards a spontaneous complexation of the triazine herbicides and HSA ($\Delta G < 0$) ruled mostly by electrostatic, hydrophobic interactions and hydrogen bonding.

Figure 55. Steady-state fluorescence spectra of HSA in the presence of increasing concentrations of ATR.

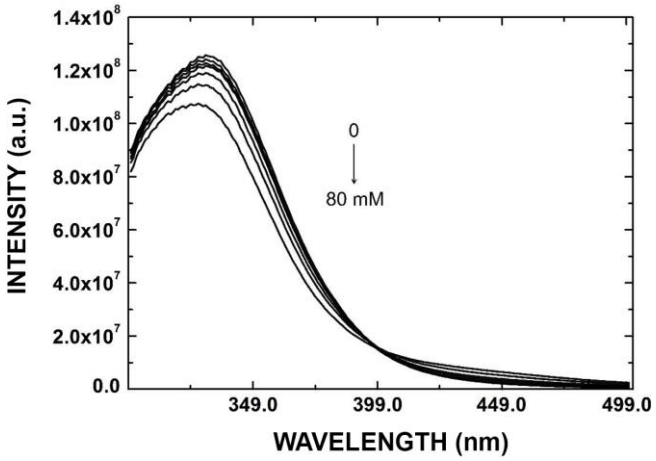

Legenda:Each spectrum corresponds to one aqueous solution of 10 µM HSA and ATR (0, 5, 10, 20, 40 and 80 mM) in Tris-HCL buffer (pH 7.4). Excitation: 280 nm. Emission and excitation slits were 5 nm each.
Fonte: FRANÇA *et al.,* 2022.

Thermodynamics of the association between triazine herbicides and HSA seems to occur via an enthalpy–entropy compensation mechanism [23]. Negative entropies were explained by degrees of freedom of the herbicide being lost when it was included in the HSA cavity. However, the association mechanism was enthalpically driven by the replacement of weak herbicide–bulk solvent interactions with van der Waal and polar interactions. The importance of the hydrophobic effect on the triazine herbicide binding mechanism was discussed as well. The strength of complexation to HSA increased with hydrophobicity/bulkiness of the herbicide. For instance, ATR (region iii = 4-isopropylamine) bound more strongly to HSA than simazine (region iii = 2-ethylamine) whereas binding was significantly decreased by the presence of a chloro group (ATR and simazine) compared to a –S–CH3 (or –O–CH3) group (prometryne, ametryne, terbutryne, desmetryne and secbumeton).

5.1.3.2 Docking and molecular dynamics simulations

Prediction of the interaction of HSA with small ligands has been widely investigated through docking and molecular dynamics simulations [7, 24, 59, 88-90]. HSA can bind up to nine molecules of long-chain fatty acids (FA), represented by the binding sites FA1-FA9 with different affinities for FA (Figure 54). FA4 and FA5 are

high-affinity sites that provide the most enclosed binding environments in the HSA structure; FA2 is a medium affinity site entirely contained within the N-terminal half of the protein, between subdomains IA and IIA; FA8 and FA9 are usually considered as supplementary binding sites, displaying ligand occupancy only in the presence of short-chain FAs (FA8) or in the presence of saturating FA concentration (FA9). In addition to FA and other endogenous ligands, a wide range of drugs bind to HSA. Drug and FA bindings sites overlap: FA7 with drug site I; FA3/4 with drug site II [17-21].

Most of the predicted conformation poses after the docking simulations were associated with sites FA3/4 (or drug site II; 6 poses), FA1 (5 poses), and FA8 (5 poses) (Figure 55). The presence of TRP214 at FA8 (pose 9) and TYR138, TYR161 at FA1 (pose 1) agree with our observations of HSA fluorescence quenching by ATR (Figure 55).

Site marker displacement experiments have suggested drug sites II (sites FA3 and FA4) and I (site FA7) as the main binding sites of ATR [7] and prometryn [23], respectively. Moreover, molecular docking simulations confirmed the binding of prometryn to the large hydrophobic cavity of drug site I [23]. However, those investigation [7] did not analyze the contribution of other bindings sites of HSA to herbicide/HSA complexation, such as site FA8.

Figure 56. ATR/HSA docking

Pose	D. Score*	Site
1	-6.2	FA1
2	-6.2	FA1
3	-6.1	FA2
4	-6	FA1
5	-6	FA3/4
6	-6	FA2
7	-6	FA3/4
8	-5.9	FA3
9	-5.9	FA8
10	-5.8	FA8
11	-5.8	FA8
12	-5.8	FA1
13	-5.8	FA3
14	-5.7	FA8
15	-5.7	FA1
16	-5.7	FA3
17	-5.7	FA3/4
18	-5.7	FA6
19	-5.6	FA7
20	-5.6	FA8

* In Kcal/mol

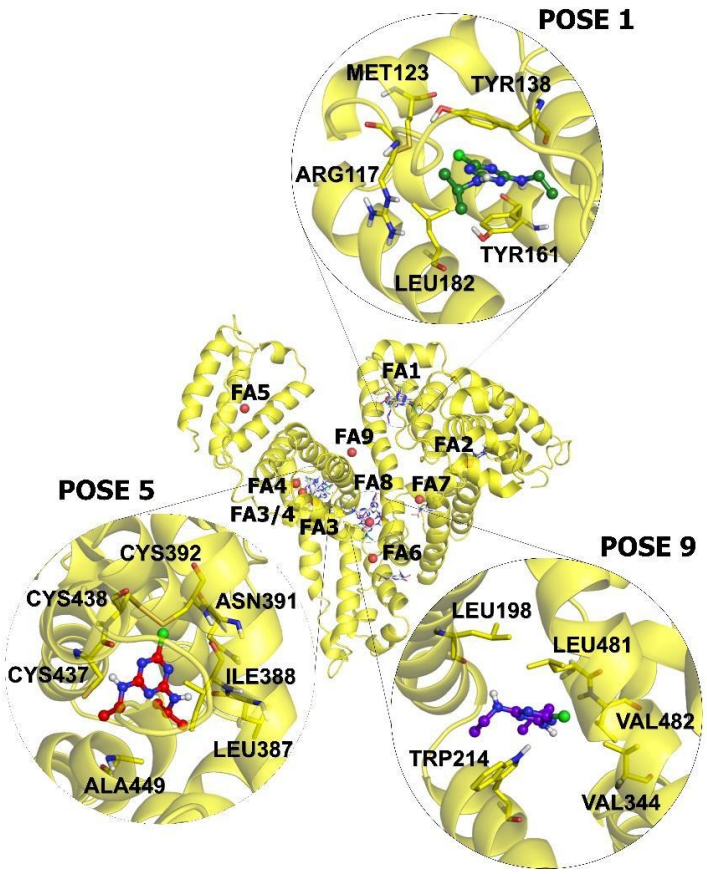

Legenda:The chart lists the binding energy (docking score) of the 20 predicted conformational poses generated by the ATR/HSA docking procedure (binding sites FA1-FA8). Poses with the highest docking scores (in red) are represented in the 3D approximation cartoon.
Fonte: FRANÇA *et al.,* 2022.

To further characterize the ATR/HSA binding interaction, MD simulations were performed. The time dependence of the root mean square deviation (RMSD) of the HSA atomic coordinates without ligand and the HSA-ATR complexes with highest docking scores (pose 1 - FA1, pose 5 - FA3/4, and FA8 - pose 9) is shown in Figure 57. The binding sites FA2, FA6, and FA7 were discarded due to their smaller docking frequency.

The RMSD variations of ATR complexed with sites FA3/4 and FA8 were smaller than 1 Å, indicating structural stabilization [91-94]. MD simulation runs of 20 ns showed variations of 0.84 and 0.82 Å for HSA and ATR/HSA:FA3/4 and 1.49 and 0.61 Å for HSA and ATR/HSA:FA8, respectively. Conversely, the larger RMSD variation of the ATR-HSA:FA1 complex of 0.96 Å, compared to the other complexes, indicated weaker stabilization.

MD simulation data (RMSD) pointed sites FA3/4 and FA8 as the most probable binding sites of ATR on HSA, with the maximum structural stabilization (lower RMSD) observed for FA3/4. Considering that FA3/4 is part of drug site II, the MD results are in agreement with literature that has identified drug site II as the experimental binding site of ATR [7] and prometryn [23].

5.1.3.3 Quantum biochemistry simulations

Figures 58-61 describe in detail the non-covalent interactions and the residue-ATR binding energies at sites FA1, FA3/4, and FA8 considering all residues within 10 Å from the ATR molecule. For the sake of our analysis, the ATR molecule was divided into three regions: i (2-ethylamine group), ii (6-chloro-s-triazine ring), and iii (4-isopropylamine group) (Figure 54). Furthermore, in tables S1-S3 of the Supplementary Data, the interaction energies, electric charges, and atoms involved in each binding interaction are listed.

Figure 57. Root-mean-square deviation as a function of time.

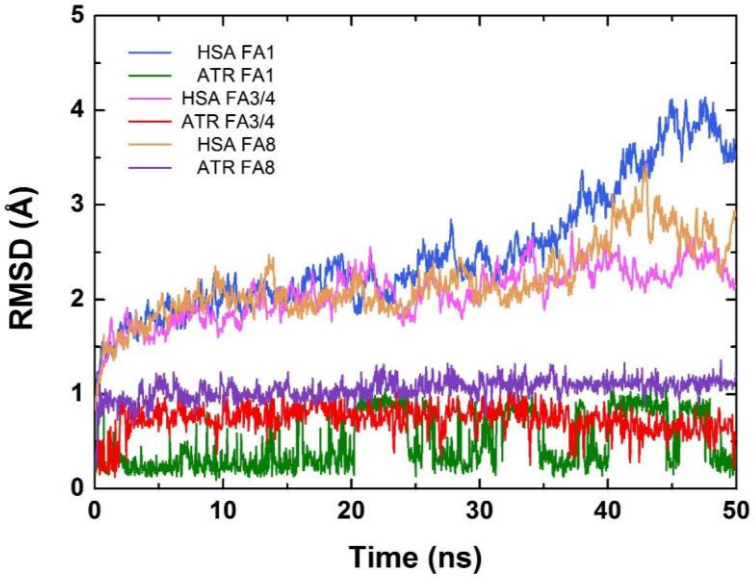

Legenda: Root-mean-square deviation (RMSD) as a function of time in the MD simulation for the sites FA1, FA3/4, and FA8 of HSA and HSA bound to ATR.
Fonte: FRANÇA *et al.,* 2022.

The quantum mechanical calculations highlighted hydrogen, pi-alkyl, amide-pi stacked, alkyl, and van der Waals interactions between HSA and all three

regions of ATR. The highest binding affinity (smallest interaction energy), in decrescent order, was observed with TRP214 (pi-alkyl interaction with region iii) at FA8, ASN391 (hydrogen-bond with region ii) at FA3/4, and TYR138, TYR161 (pi-alkyl interaction with regions i and iii, respectively) at FA1. Among the three binding sites, the complexation of ATR with FA8 exhibited the strongest interaction, in agreement with fluorescence quenching data (figure 55).

5.1.3.4 ATR binding to FA1 site

The FA1 site is a narrow and deep D-shaped cavity located in subdomain IB that can extend and accommodate ligands of different sizes, such as bilirrubin and heme. In comparison to the other major FA binding pockets on HSA, FA1 is relatively open and solvent accessible [17-21].

As shown in Figure 58A, ten HSA residues at the FA1 site (LEU115, PRO118, PHE134, LEU135, LEU139, ILE142, ALA158, PHE165, ASP183, and ARG186) exhibited van der Waals interactions with ATR, while TYR138 (3.65 Å), TYR161 (4.24 Å and 5.28 Å), and LEU182 (4.83 Å) establish pi-alkyl interactions. Alkyl-type interactions were observed between ATR and ARG117 (4.14 Å), MET123 (4.68 Å), and LEU182 (4.74 Å).

The main HSA residues involved in the formation of the ATR/FA1 complex were ARG117 (2.32 Å), TYR138 (2.41 Å), TYR161 (2.15 Å), and LEU182 (2.2 Å) (figure 57A-B). As shown in Figure 58C, the most energetically favorable interactions occurred between region i of ATR (2-ethylamine group) and TYR138 (-6.49 kcal.mol^{-1}, including 5 water molecules), and between region iii (4-isopropylamine group) and TYR161 (-6.34 kcal.mol^{-1}, including 6 water molecules). The binding interactions of region iii with LEU182 (5 water molecules) and ARG117 (7 water molecules) presented energies of -4.60 kcal.mol^{-1} and -3.90 kcal.mol^{-1}, respectively. Small repulsion interactions of about 1 kcal.mol^{-1} were observed for ARG145 and ARG160, at 6 and 8 Å of distance from ATR, respectively. All the remaining residues attracted ATR with energies ranging between -3 and -1 kcal.mol^{-1} approximately.

The quantum biochemistry simulations did not predict interactions between the triazine ring (region ii) and FA1 site. However, the thiol group of CYS-4 (at FA1) has been recently reported to form covalent adducts with the triazine ring, without prior metabolic transformation of ATR [22]. CYS34 is of physiological importance since it is

the only free CYS residue present in HSA, which makes HSA a powerful plasma antioxidant and detoxicant due to its covalent binding to endogenous ligands, metal ions, free radicals, and xenobiotics [95].

Figure 58. Quantum biochemistry results for the ATR/FA1 complexation.

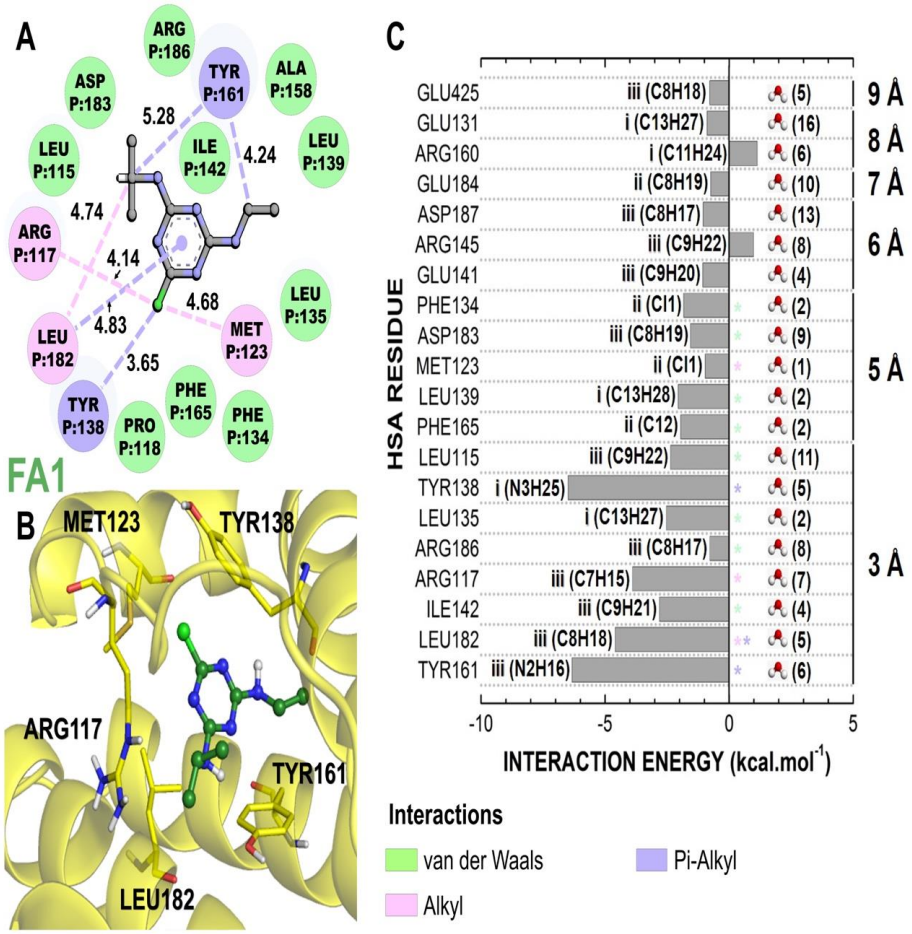

Legenda: **A.** Non-covalent interactions within 10 Å from the ATR molecule. Distances (in Å) for each interaction are shown. **B.** 3D diagram illustrating the most energetically relevant ATR interactions at FA1. **C.** BIRD panel (Binding site, Interaction energy, and Residues Domain) showing the interaction energy of each residue with the ATR molecule (regions i, ii, and iii). The distance of each residue to the ATR centroid is given at the right side of the panel. The number of explicit water molecules and the type of interaction (asterisk symbols) participating in the ATR/FA1 complexation are also indicated.
Fonte: FRANÇA *et al.,* 2022.

The interaction of ATR with TYR138 and TYR161 might have a direct effect on the adjustment of FA1 to ligands, leading eventually to steric exclusion and the compromise of HSA antioxidant properties. In the absence of a ligand, the FA1 cavity is partially occluded by TYR138 and TYR161, which stack on top of one another. However, upon ligand binding (heme, FA) the sidechains of TYR138 and TYR161 rotate, causing the opening of the binding pocket and clamping the ligand in place

[17-21].

5.1.3.5 ATR binding to FA3/4 site

Sites FA3 and FA4 are located in a large cavity in subdomain IIIA and together constitute the drug site II, which is the preferential binding site of aromatic carboxylates with an extended conformation (i.e. ibuprofen, diflunisal). Drug site II is generally selective for drugs with an electronegative group peripherally located due to the presence of a basic polar patch close to one side of the binding pocket entrance, centered on TYR411, ARG410, LYS414, and SER489 [17-21].

As presented in Figure 59A, the binding of ATR to sites FA3 and FA4 involved eight van der Waals (LEU394, PHE403, LEU407, LEU430, GLY431, GLY434, ARG445, and LEU453) and five alkyl type interactions (ILE388 - 4.44 Å, CYS392 - 4.97 Å, CYS437 - 4.42 Å, CYS438 - 4.48 Å, and ALA449 - 4.14 Å). Further inquiry indicated the formation of a single hydrogen bond (ASN391 - 2.01 Å), one amide-pi stacked (LEU387- 5.13 Å) and two pi-alkyl interactions (ILE388 - 5.16 Å and ALA449 - 4.40 Å). Among them, the most relevant binding was to ASN391 (2.01 Å, -8.30 kcal.mol^{-1}, 7 water molecules), ILE388 (2.52 Å, -4.15 kcal.mol^{-1}, 3 water molecules), LEU387 (2.44 Å, - 3.45 kcal.mol^{-1}, 3 water molecules) and LEU453 (2.20 Å, -3,43 kcal.mol^{-1}, 6 water molecules) (Figures 59B-C). The residues GLU382 and GLU442, between 9 and 10 Å of distance from ATR were slightly repulsive, with positive interaction energies of about 0.15 kcal.mol^{-1}, while all remaining residues at the binding pocket were attractive. A clear trend to decrease the binding energy as the distance from ATR increases was observed for distances larger than 3 Å, as occurred for FA1 site.

None of the ATR interactions at FA3/4 involved the basic polar patch of the drug site II [17-21]. This can be explained by the neutral (uncharged) character of the ATR molecule at physiological pH (7.4, Tables S.1-3). Moreover, contrary to the observed for FA1, all regions of the ATR molecule interacted with FA3/4: region i (H24) with LEU387, region ii (N6 and N4) with ILE388 and ASN391, and region iii (H20) with LEU453. These results indicate that the ATR molecule is entirely entrapped by the FA3/4 cavity (drug site II), with the triazine ring (region ii) playing an important role in stabilizing the ATR/FA3/4 complex mainly by the hydrogen bond between N4 and ASN391 (table S2 and figure 59B-C).

Figure 59. Quantum biochemistry results for the ATR/FA3/4 complexation.

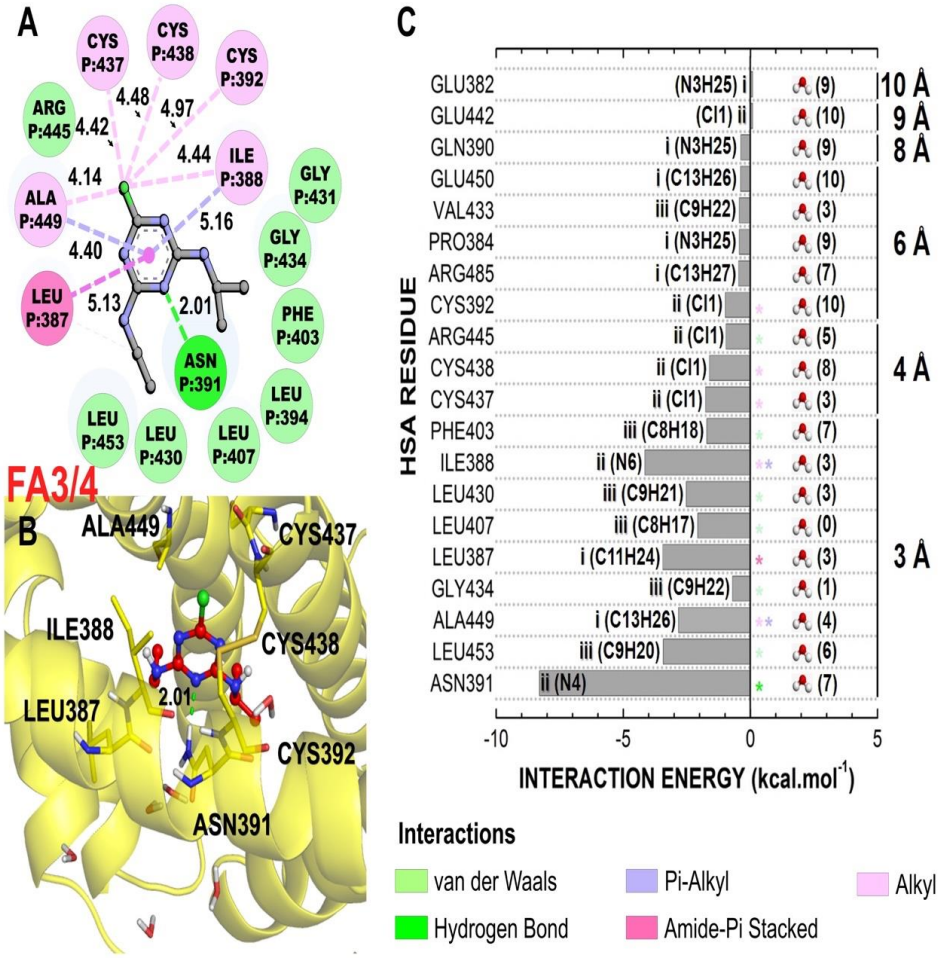

Legenda: **A.** Non-covalent interactions within 10 Å from the ATR molecule. Distances (in Å) for each interaction are shown. **B.** 3D diagram illustrating the most energetically relevant ATR interactions at FA1. **C.** BIRD panel (Binding site, Interaction energy, and Residues Domain) showing the interaction energy of each residue with the ATR molecule (regions i, ii, and iii). The distance of each residue to the ATR centroid is given at the right side of the panel. The number of explicit water molecules and the type of interaction (asterisk symbols) participating in the ATR/FA1 complexation are also indicated.
Fonte: FRANÇA *et al.,* 2022.

5.1.3.6 ATR binding to FA8 site

Site FA8 is located at the base of the gap between subdomains IA–IB–IIA on one side and subdomains IIB–IIIA–IIIB on the other side. Due to volume restrictions, site FA8 only accommodates short-chain FA. The hydrophobic cavity of FA8 is formed by the methylene tail of the short-chain FA bound to FA6 and, by polar residues (LYS195, LYS199, ARG218, ASP451, and SER454) that stabilize the polar head of the ligand [17-21].

As depicted in Figure 60, there were nine residues at the FA8 binding site forming van der Waals interactions with ATR (LYS195, LYS199, SER202, ALA210, PHE211, LEU347, GLU450, ASP451, VAL455). Pi-alkyl (TRP214 - 4.13 Å, LEU481 - 4.23 Å) and alkyl (VAL344 - 4.15 Å, LEU481 - 4.38 Å, VAL482 - 4.90 Å) interactions were identified as well, plus one hydrogen bond (SER454 - 2.17 Å).

The residues presenting the most energetically favorable interactions with ATR were TRP214 (2.42 Å, -8.98 kcal.mol^{-1}, 2 water molecules considered), SER202 (1.91 Å, -7.01 kcal.mol^{-1} and 3 water molecules); LEU481 (2.93 Å, -5.74 kcal.mol^{-1}, 6 water molecules), SER454 (2.17 Å, -5.33 kcal.mol^{-1}, 3 water molecules), and LYS199 (2.28 Å, -4.31 kcal.mol^{-1}, 2 water molecules). These residues interacted strongly with regions ii (SER202, LEU481, SER454) and iii (TRP214, LYS199) of ATR. One can also mention PHE211 (-3.20 kcal.mol^{-1}, through a van der Waals interaction within 3 Å of ATR and 3 water molecules included) and LEU198 (-2.95 kcal.mol^{-1}, alkyl interaction within 4 Å of ATR and an alkyl interaction, near 5 water molecules). There were no residues with repulsive interaction to ATR up to 10 Å, except for GLU479, with interaction energy of 0.08 kcal.mol^{-1}. The interaction energy decreased consistently for residues beyond 4 Å from the ATR centroid.

Figure 61 shows the electrostatic potential isosurface constructed from the DFT calculations, colored according to the electric charge density of ATR and TRP214. Similar figures are presented in the Supplementary Data for other residues at the FA1, FA3/4, and FA8 binding pockets (figures S1-S3, respectively). Atoms with large (O, N) and small (C, H) electron density are depicted, with the largest values being observed in the region ii of ATR (near the nitrogen atoms) and in the carboxyl and amino groups of TRP214. The ATR/TRP214 conformation promotes a pi-alkyl type interaction between them within a range of approximately 2.4 Å. This interaction is responsible for the fluorescence quenching observed in our measurements (figure 54).

Figure 60. Quantum biochemistry results for the ATR/FA8 complexation

.

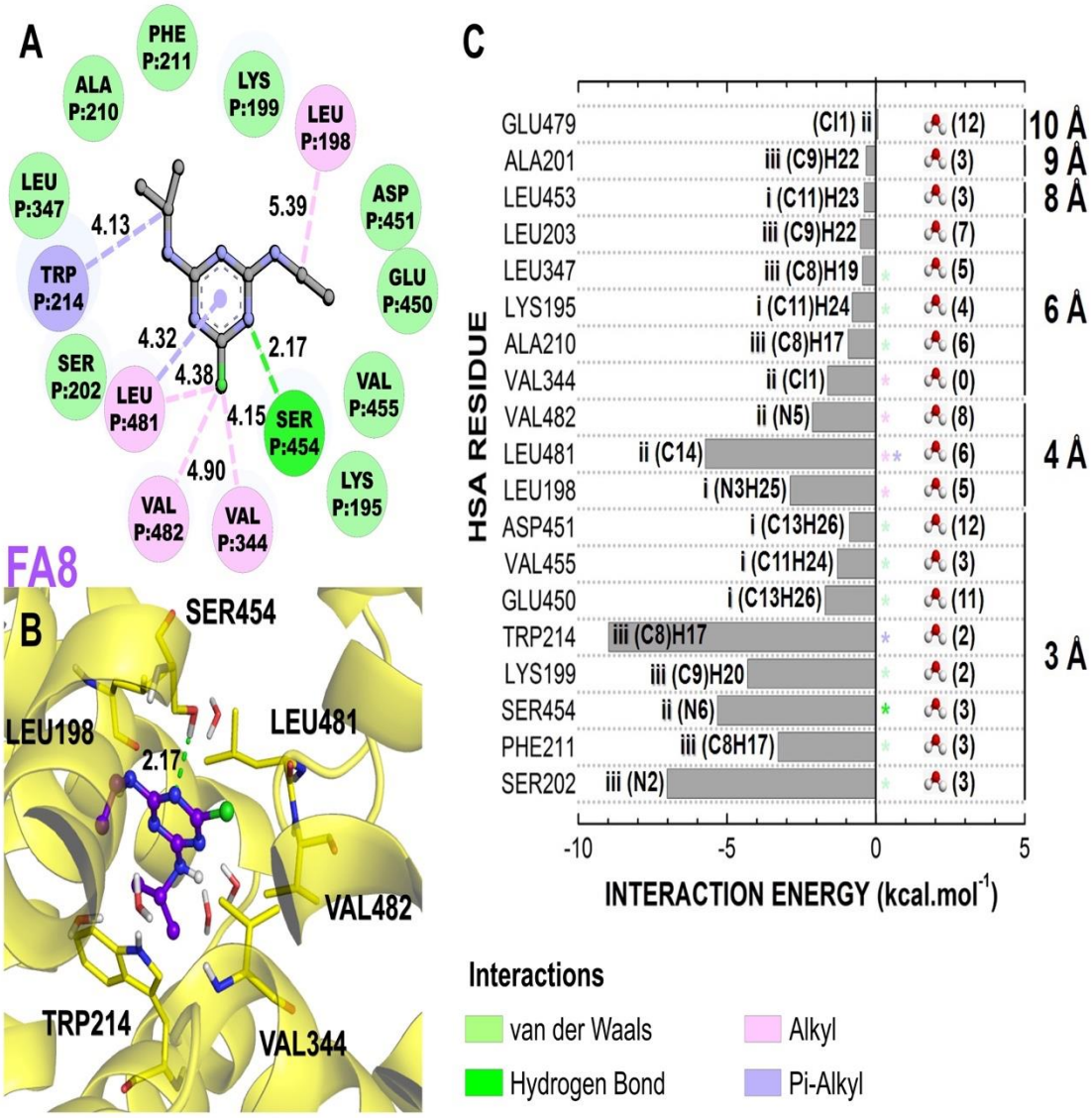

Legenda: **A.** Non-covalent interactions within 10 Å from the ATR molecule. Distances (in Å) for each interaction are shown. **B.** 3D diagram illustrating the most energetically relevant ATR interactions at FA1. **C.** BIRD panel (Binding site, Interaction energy, and Residues Domain) showing the interaction energy of each residue with the ATR molecule (regions i, ii, and iii). The distance of each residue to the ATR centroid is given at the right side of the panel. The number of explicit water molecules and the type of interaction (asterisk symbols) participating in the ATR/FA1 complexation are also indicated.
Fonte: FRANÇA *et al.,* 2022.

Figure 61. Electron density of ATR and TRP214 (site FA8).

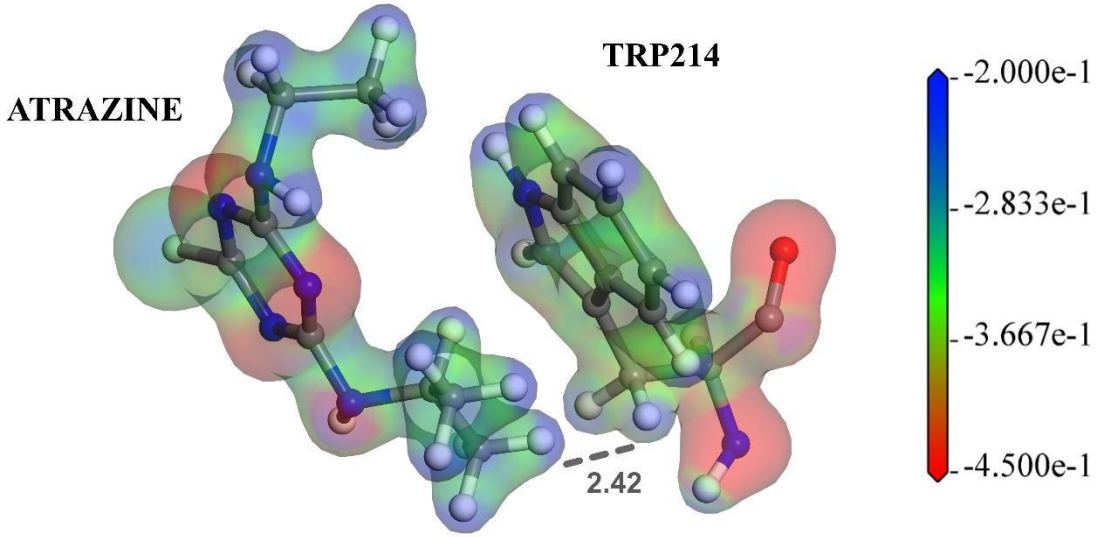

Legenda: A pi-alkyl type interaction is shown between region iii of the ATR molecule and TRP214.
Fonte: FRANÇA *et al.,* 2022.

One can point out that the quantum biochemistry simulations were performed without fatty acids in the environment. However, the absence of fatty acids does not invalidate our results. Drug site II (FA3/4) overlaps with one high affinity (FA4) and one low affinity (FA3) FA binding site. Thus, in physiological condition, it would be expected drug site II to be more susceptible to displacement by FA [17]. This observation reinforces the case in favor of the low-affinity binding site FA8 as the main promoter of ATR complexation to HSA. On the other hand, the FA8 site is probably not capable of holding multiple ATR molecules due to volume restrictions. This is not observed, for instance, in the big hydrophobic cavity of drug site I (FA7), which is usually the place of interactive association of drugs [17-21].

5.1.3.7 Binding pocket sizes and total binding energies of ATR/HSA complexation

One can define the binding pocket size of a molecule bound to a protein by constructing a sphere centered at the molecule centroid and adding up the interaction energies with the molecule only for residues inside the sphere. As the sphere radius increases, the total interaction energy must stabilize, defining an

effective binding pocket size.

Figure 62. Total interaction energy E_T between ATR and the residues of the three binding sites of HAS.

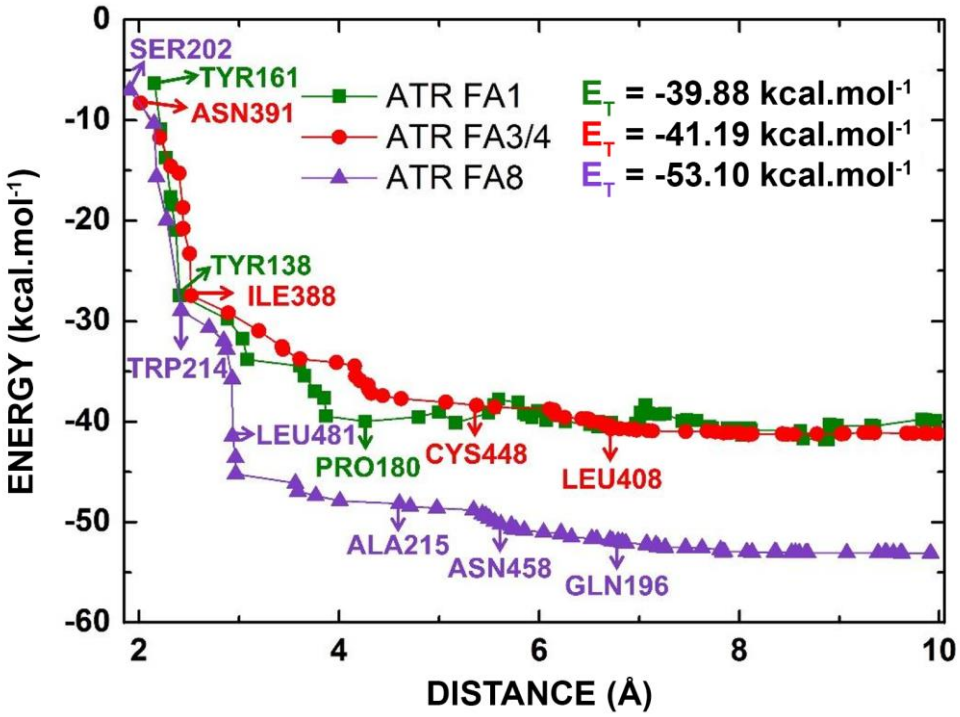

Legenda: Total interaction energy E_T between ATR and the residues of the three binding sites of HSA (FA1, FA3/4, and FA8) as a function of the binding site radius (all residues within the given distance from ATR are considered to obtain the interaction energy) from the quantum biochemistry calculations. Some relevant amino acid residues are identified.
Fonte: FRANÇA *et al.,* 2022.

We have performed this procedure for ATR and each albumin binding site using quantum biochemistry. As shown in Figure 62, the total interaction energy stabilized for a 8 Å radius from the ATR centroid for both the ATR-HSA:FA3/4 and ATR-HSA:FA1 complexes, reaching approximately nearly the same value. For the ATR-HSA:FA8 complex, one can observe a very sharp decrease in interaction energy at 3 Å in comparison to ATR-HSA:FA1 and ATR-HSA:FA3/4, which is attributed to the interaction with LEU481. A subsequent energy reduction occurred near 5.5 Å followed by energy stabilization at 8 Å associated to a significant smaller energy than that observed for the other binding sites. At 10 Å, the complex ATR-HSA:FA8 exhibited a binding energy of 53.10 kcal.mol^{-1}, more than 10 kcal.mol^{-1} larger than those reported for ATR-HSA:FA1 (39.88 kcal.mol^{-1}) and ATR-HSA:FA3 (41.19 kcal.mol^{-1}).

5.1.4 Conclusions

The indiscriminate and often widespread use of ATR is a potential harm to public health [13, 14]. The detailed insights into HSA/ATR binding interactions reported here provide an invaluable structural framework for the interpretation of the pharmacodynamics and toxicity of ATR.

In summary, we have investigated the interaction between the herbicide ATR and HSA through experimental and computational techniques. On the experimental side, we have confirmed the binding interaction of ATR and HSA by observing a concentration-dependent quenching of HSA intrinsic fluorescence as ATR interacts directly with TRP214 presented in FA8 site.

ATR docking simulations performed for the FA binding sites of HSA provided 20 poses, which were subsequently submitted to molecular dynamics simulations. The results revealed sites FA1, FA3/4 and FA8 as the most relevant for the binding interaction between ATR and HSA. RMSD analysis indicated stability of ATR especially for the FA8 binding site (followed by FA3/4), in contrast with previous studies that suggested sites FA3/FA4 and FA7 as the main binding sites of triazine herbicides [7, 23].

A detailed analysis using quantum biochemistry was then performed to evaluate the specific residue contributions to ATR binding to FA1, FA3/4, and FA8 sites. In the case of FA1, residues TYR138 and TYR161 were highlighted, with interaction energies of -6.49 kcal.mol^{-1} and -6.34 kcal.mol^{-1} involving the ethylamine and isopropylamine groups of ATR, respectively. At FA3/4 site, there was a very strong interaction via hydrogen bonding with ASN391 (-8.30 kcal.mol^{-1}). For the FA8 binding site, there were three residues with significant affinity for ATR: TRP214 (-8.98 kcal.mol^{-1}), SER202 (-7.01 kcal.mol^{-1}), and LEU481 (-5.74 kcal.mol^{-1}). All these interactions are affected by the presence of water molecules and decrease consistently when the residues are beyond 4 Å.

Adding-up the interaction energies of all residues in the three distinct binding pockets of HSA, one finds that FA1 and FA3/4 presented approximately the same energetic affinity for ATR, about -40 kcal.mol^{-1}, while the FA8 site was the preferential binding site with interaction energy of about -53 kcal.mol^{-1}, contrasting with a previous study that suggested FA3/FA4 and FA7 sites as the more likely sites of interest for complexation with ATR [7, 23]. These results correlate well with the

fluorescence quenching observed in the performed experiments.

5.1.5 Acknowledgments

V. N. F. is a senior researcher from the Brazilian National Research Council (CNPq) and would like to acknowledge the financial support received during the development of this work. E. W. S. C. received financial support from CNPq through projects 425348/2018-0 and 304935/2019-0. This study was also financed in part by the Coordenação de Aperfeiçoamento de Pessoal de Nível Superior - Brasil (CAPES) - Finance Code 001 (PROEX 23038.000509/2020-82).

References

[1] S. Sabzevari, J. Hofman, A worldwide review of currently used pesticides' monitoring in agricultural soils, Science of The Total Environment, (2021) 152344.
[2] M. Lykogianni, E. Bempelou, F. Karamaouna, K.A. Aliferis, Do pesticides promote or hinder sustainability in agriculture? The challenge of sustainable use of pesticides in modern agriculture, Science of The Total Environment, 795 (2021) 148625.
[3] H. Sadeghnia, S. Shahba, A. Ebrahimzadeh-Bideskan, S. Mohammadi, A.M. Malvandi, A. Mohammadipour, Atrazine neural and reproductive toxicity, Toxin Reviews, (2021) 1-14.
[4] N. Bakaraki Turan, B.T. Zaman, D.S. Chormey, G. Onkal Engin, S. Bakırdere, Atrazine: From Detection to Remediation–A Minireview, Analytical Letters, 55 (2022) 411-426.
[5] E.M. Brovini, B.C.T. de Deus, J.A. Vilas-Boas, G.R. Quadra, L. Carvalho, R.F. Mendonça, R. de Oliveira Pereira, S.J. Cardoso, Three-bestseller pesticides in Brazil: Freshwater concentrations and potential environmental risks, Science of The Total Environment, 771 (2021) 144754.
[6] N.P. Cheremisinoff, P. Rosenfeld, P. Rosenfeld, Handbook of pollution prevention and Cleaner production, Elsevier2009.
[7] M. Zhu, L. Wang, Y. Wang, J. Zhou, J. Ding, W. Li, Y. Xin, S. Fan, Z. Wang, Y. Wang, Biointeractions of herbicide atrazine with human serum albumin: UV-Vis, fluorescence and circular dichroism approaches, International journal of environmental research and public health, 15 (2018) 116.
[8] S. Frıas, M. Sánchez, M. Rodrıguez, Determination of triazine compounds in ground water samples by micellar electrokinetic capillary chromatography, Analytica Chimica Acta, 503 (2004) 271-278.
[9] T. Satapanajaru, P. Anurakpongsatorn, P. Pengthamkeerati, H. Boparai, Remediation of atrazine-contaminated soil and water by nano zerovalent iron, Water, air, and soil pollution, 192 (2008) 349-359.
[10] E. Blume, M. Bischoff, T.B. Moorman, R.F. Turco, Degradation and binding of atrazine in surface and subsurface soils, Journal of Agricultural and Food Chemistry, 52 (2004) 7382-7388.
[11] I.F. Chowdhury, M. Rohan, B.J. Stodart, C. Chen, H. Wu, G.S. Doran, Persistence of atrazine and trifluralin in a clay loam soil undergoing different temperature and moisture conditions, Environmental Pollution, 276 (2021) 116687.
[12] A. Concilla, H. Liu, Presence of agricultural herbicide atrazine in water, foods, and human urine samples, Int J Environ Monit Anal, 5 (2017) 9-13.
[13] T.B. Hayes, Atrazine has been used safely for 50 years?, Wildlife Ecotoxicology, Springer2011, pp. 301-324.
[14] V. Galbiati, E. Buoso, R. d'Emmanuele di Villa Bianca, R.D. Paola, F. Morroni, G. Nocentini, M. Racchi, B. Viviani, E. Corsini, Immune and Nervous Systems Interaction in Endocrine Disruptors Toxicity: The Case of Atrazine, Frontiers in Toxicology, 3 (2021) 649024.
[15] Y. Zhang, P. Lee, S. Liang, Z. Zhou, X. Wu, F. Yang, H. Liang, Structural basis of non-steroidal anti-inflammatory drug diclofenac binding to human serum albumin, Chemical biology & drug design, 86 (2015) 1178-1184.
[16] T. Peters Jr, All about albumin: biochemistry, genetics, and medical applications, Academic press1995.
[17] J.R. Simard, P.A. Zunszain, J.A. Hamilton, S. Curry, Location of high and low affinity fatty acid binding sites on human serum albumin revealed by NMR drug-competition analysis, Journal of molecular biology, 361 (2006) 336-351.
[18] E.S. Krenzel, Z. Chen, J.A. Hamilton, Correspondence of fatty acid and drug binding sites on human serum albumin: a two-dimensional nuclear magnetic resonance study, Biochemistry, 52 (2013) 1559-1567.
[19] A.A. Bhattacharya, T. Grüne, S. Curry, Crystallographic analysis reveals common modes of binding of medium and long-chain fatty acids to human serum albumin, Journal of molecular biology, 303 (2000) 721-732.

[20] J. Ghuman, P.A. Zunszain, I. Petitpas, A.A. Bhattacharya, M. Otagiri, S. Curry, Structural basis of the drug-binding specificity of human serum albumin, Journal of molecular biology, 353 (2005) 38-52.
[21] S. Curry, H. Mandelkow, P. Brick, N. Franks, Crystal structure of human serum albumin complexed with fatty acid reveals an asymmetric distribution of binding sites, Nature structural biology, 5 (1998) 827-835.
[22] S. Chu, R.J. Letcher, Identification and characterization of serum albumin covalent adduct formed with atrazine by liquid chromatography mass spectrometry, Journal of Chromatography B, 1163 (2021) 122503.
[23] L. Ismaili, C. André, L. Nicod, T.T. Truong, J. Millet, M. Thomassin, E. Cavalli, J.P. Chaumont, A. Xicluna, Y.C. Guillaume, Triazine–human serum albumin association: thermodynamic approach and sodium effect, Journal of Chromatography B, 780 (2002) 467-474.
[24] A. Ahmed, A. Shamsi, M.S. Khan, F.M. Husain, B. Bano, Probing the interaction of human serum albumin with iprodione, a fungicide: spectroscopic and molecular docking insight, Journal of Biomolecular Structure and Dynamics, 37 (2019) 857-862.
[25] K. Golianová, S. Havadej, V. Verebová, J. Uličný, B. Holečková, J. Staničová, Interaction of conazole pesticides epoxiconazole and prothioconazole with human and bovine serum albumin studied using spectroscopic methods and molecular modeling, International journal of molecular sciences, 22 (2021) 1925.
[26] J. Zhang, X. Gao, J. Huang, H. Wang, Probing the interaction between human serum albumin and 9-hydroxyphenanthrene: a spectroscopic and molecular docking study, ACS omega, 5 (2020) 16833-16840.
[27] P.A. Zunszain, J. Ghuman, T. Komatsu, E. Tsuchida, S. Curry, Crystal structural analysis of human serum albumin complexed with hemin and fatty acid, BMC Structural biology, 3 (2003) 1-9.
[28] I. Petitpas, T. Grüne, A.A. Bhattacharya, S. Curry, Crystal structures of human serum albumin complexed with monounsaturated and polyunsaturated fatty acids, Journal of molecular biology, 314 (2001) 955-960.
[29] P.A. Zunszain, J. Ghuman, A.F. McDonagh, S. Curry, Crystallographic analysis of human serum albumin complexed with 4Z, 15E-bilirubin-IXα, Journal of molecular biology, 381 (2008) 394-406.
[30] J.A. Hamilton, NMR reveals molecular interactions and dynamics of fatty acid binding to albumin, Biochimica et Biophysica Acta (BBA)-General Subjects, 1830 (2013) 5418-5426.
[31] D.B. Kitchen, H. Decornez, J.R. Furr, J. Bajorath, Docking and scoring in virtual screening for drug discovery: methods and applications, Nature reviews Drug discovery, 3 (2004) 935-949.
[32] S.Z. Grinter, X. Zou, Challenges, applications, and recent advances of protein-ligand docking in structure-based drug design, Molecules, 19 (2014) 10150-10176.
[33] A. Ganesan, M.L. Coote, K. Barakat, Molecular dynamics-driven drug discovery: leaping forward with confidence, Drug discovery today, 22 (2017) 249-269.
[34] H. Zhao, A. Caflisch, Molecular dynamics in drug design, European journal of medicinal chemistry, 91 (2015) 4-14.
[35] G.R. Smith, M.J. Sternberg, Prediction of protein–protein interactions by docking methods, Current opinion in structural biology, 12 (2002) 28-35.
[36] A.K. Rappé, C.J. Casewit, K. Colwell, W.A. Goddard III, W.M. Skiff, UFF, a full periodic table force field for molecular mechanics and molecular dynamics simulations, Journal of the American chemical society, 114 (1992) 10024-10035.
[37] D.A. Pearlman, D.A. Case, J.W. Caldwell, W.S. Ross, T.E. Cheatham III, S. DeBolt, D. Ferguson, G. Seibel, P. Kollman, AMBER, a package of computer programs for applying molecular mechanics, normal mode analysis, molecular dynamics and free energy calculations to simulate the structural and energetic properties of molecules, Computer Physics Communications, 91 (1995) 1-41.
[38] W. Thiel, Semiempirical quantum–chemical methods, Wiley Interdisciplinary Reviews: Computational Molecular Science, 4 (2014) 145-157.

[39] A.S. Christensen, T. Kubar, Q. Cui, M. Elstner, Semiempirical quantum mechanical methods for noncovalent interactions for chemical and biochemical applications, Chemical Reviews, 116 (2016) 5301-5337.
[40] A.D. Becke, Density-functional thermochemistry. I. The effect of the exchange-only gradient correction, The Journal of chemical physics, 96 (1992) 2155-2160.
[41] N. Mardirossian, M. Head-Gordon, Thirty years of density functional theory in computational chemistry: an overview and extensive assessment of 200 density functionals, Molecular Physics, 115 (2017) 2315-2372.
[42] R.O. Jones, Density functional theory: Its origins, rise to prominence, and future, Reviews of modern physics, 87 (2015) 897.
[43] J. Antony, S. Grimme, Fully ab initio protein-ligand interaction energies with dispersion corrected density functional theory, Journal of computational chemistry, 33 (2012) 1730-1739.
[44] S. Ehrlich, J. Moellmann, S. Grimme, Dispersion-corrected density functional theory for aromatic interactions in complex systems, Accounts of chemical research, 46 (2013) 916-926.
[45] J. Antony, S. Grimme, Density functional theory including dispersion corrections for intermolecular interactions in a large benchmark set of biologically relevant molecules, Physical Chemistry Chemical Physics, 8 (2006) 5287-5293.
[46] S.J. Fox, J. Dziedzic, T. Fox, C.S. Tautermann, C.K. Skylaris, Density functional theory calculations on entire proteins for free energies of binding: application to a model polar binding site, Proteins: Structure, Function, and Bioinformatics, 82 (2014) 3335-3346.
[47] D.W. Zhang, J. Zhang, Molecular fractionation with conjugate caps for full quantum mechanical calculation of protein–molecule interaction energy, The Journal of chemical physics, 119 (2003) 3599-3605.
[48] N. Jiang, J. Ma, Y. Jiang, Electrostatic field-adapted molecular fractionation with conjugated caps for energy calculations of charged biomolecules, The Journal of chemical physics, 124 (2006) 114112.
[49] X. Wang, J. Liu, J.Z. Zhang, X. He, Electrostatically embedded generalized molecular fractionation with conjugate caps method for full quantum mechanical calculation of protein energy, The Journal of Physical Chemistry A, 117 (2013) 7149-7161.
[50] M.A. Collins, R.P. Bettens, Energy-based molecular fragmentation methods, Chemical reviews, 115 (2015) 5607-5642.
[51] M.S. Gordon, D.G. Fedorov, S.R. Pruitt, L.V. Slipchenko, Fragmentation methods: A route to accurate calculations on large systems, Chemical reviews, 112 (2012) 632-672.
[52] P.r. Söderhjelm, F. Aquilante, U. Ryde, Calculation of protein− ligand interaction energies by a fragmentation approach combining high-level quantum chemistry with classical many-body effects, The Journal of Physical Chemistry B, 113 (2009) 11085-11094.
[53] A. Saha, K. Raghavachari, Analysis of different fragmentation strategies on a variety of large peptides: Implementation of a low level of theory in fragment-based methods can be a crucial factor, Journal of Chemical Theory and Computation, 11 (2015) 2012-2023.
[54] J. Liu, J.M. Herbert, Pair–pair approximation to the generalized many-body expansion: an alternative to the four-body expansion for ab initio prediction of protein energetics via molecular fragmentation, Journal of Chemical Theory and Computation, 12 (2016) 572-584.
[55] P.A. Morais, F.F. Maia, C. Solis-Calero, E.W.S. Caetano, V.N. Freire, H.F. Carvalho, The urokinase plasminogen activator binding to its receptor: a quantum biochemistry description within an in/homogeneous dielectric function framework with application to uPA–uPAR peptide inhibitors, Physical Chemistry Chemical Physics, 22 (2020) 3570-3583.
[56] C. Rodrigues, J. Oliveira, U. Fulco, E. Albuquerque, R. Moura, E. Caetano, V. Freire, Quantum biochemistry study of the T3-785 tropocollagen triple-helical structure, Chemical Physics Letters, 559 (2013) 88-93.
[57] J.X.L. Neto, K.S. Bezerra, D.N. Manso, K.B. Mota, J.I. Oliveira, E.L. Albuquerque, E.W. Caetano, V.N. Freire, U.L. Fulco, Energetic description of cilengitide bound to integrin, New Journal of Chemistry, 41 (2017) 11405-11412.

[58] K. Mota, J.L. Neto, A.L. Costa, J. Oliveira, K. Bezerra, E. Albuquerque, E. Caetano, V. Freire, U. Fulco, A quantum biochemistry model of the interaction between the estrogen receptor and the two antagonists used in breast cancer treatment, Computational and Theoretical Chemistry, 1089 (2016) 21-27.
[59] D.S. Dantas, J.I. Oliveira, J.X.L. Neto, R.F. da Costa, E.M. Bezerra, V.N. Freire, E.W. Caetano, U.L. Fulco, E.L. Albuquerque, Quantum molecular modelling of ibuprofen bound to human serum albumin, RSC Advances, 5 (2015) 49439-49450.
[60] G. Zanatta, G. Della Flora Nunes, E.M. Bezerra, R.F. da Costa, A. Martins, E.W. Caetano, V.N. Freire, C. Gottfried, Two binding geometries for risperidone in dopamine D3 receptors: Insights on the fast-off mechanism through docking, quantum biochemistry, and molecular dynamics simulations, ACS Chemical Neuroscience, 7 (2016) 1331-1347.
[61] G. Zanatta, I.L. Barroso-Neto, V. Bambini-Junior, M. Dutra, E. Bezerra, R. da Costa, E. Caetano, B. Cavada, V. Freire, C. Gottfried, Quantum biochemistry description of the human dopamine D3 receptor in complex with the selective antagonist eticlopride, J Proteomics Bioinform, 5 (2012) 155-162.
[62] G. Zanatta, G. Nunes, E.M. Bezerra, R.F. da Costa, A. Martins, E.W. Caetano, V.N. Freire, C. Gottfried, Antipsychotic Haloperidol Binding to the Human Dopamine D3 Receptor: Going beyond Docking Through QM/MM Re-finement for the Design of Improved Schizophrenia Medicines.
[63] I.L. Barroso-Neto, J.o.P.C. Marques, R.F. da Costa, E.W. Caetano, B.S. Cavada, C. Gottfried, V.N. Freire, Inactivation of ovine cyclooxygenase-1 by bromoaspirin and aspirin: a quantum chemistry description, The Journal of Physical Chemistry B, 116 (2012) 3270-3279.
[64] A. Martins, P. De-Lima-Neto, E. Caetano, V. Freire, An improved quantum biochemistry description of the glutamate–GluA2 receptor binding within an inhomogeneous dielectric function framework, New Journal of Chemistry, 41 (2017) 6167-6179.
[65] A.C.V. Martins, P. de Lima-Neto, I.L. Barroso-Neto, B.S. Cavada, V.N. Freire, E.W. Caetano, An ab initio explanation of the activation and antagonism strength of an AMPA-sensitive glutamate receptor, Rsc Advances, 3 (2013) 14988-14992.
[66] K.S. Bezerra, J.L. Neto, J. Oliveira, E. Albuquerque, E. Caetano, V. Freire, U. Fulco, Computational investigation of the α 2 β 1 integrin–collagen triple helix complex interaction, New Journal of Chemistry, 42 (2018) 17115-17125.
[67] P.F. Souza, J.L. Amaral, L.P. Bezerra, F.E. Lopes, V.N. Freire, J.T. Oliveira, C.D. Freitas, ACE2-derived peptides interact with the RBD domain of SARS-CoV-2 spike glycoprotein, disrupting the interaction with the human ACE2 receptor, Journal of Biomolecular Structure and Dynamics, (2021) 1-14.
[68] R.F. da Costa, V.N. Freire, E.M. Bezerra, B.S. Cavada, E.W. Caetano, J.L. de Lima Filho, E.L. Albuquerque, Explaining statin inhibition effectiveness of HMG-CoA reductase by quantum biochemistry computations, Physical Chemistry Chemical Physics, 14 (2012) 1389-1398.
[69] G. Ourique, J.d.F. Vianna, J.L. Neto, J. Oliveira, P.W. Mauriz, M.S.d. Vasconcelos, E. Caetano, V. Freire, E.L.d. Albuquerque, U.L. Fulco, A quantum chemistry investigation of a potential inhibitory drug against the dengue virus, RSC advances, 6 (2016) 56562-56570.
[70] J.X.L. Neto, U.L. Fulco, E.L. Albuquerque, G. Corso, E.M. Bezerra, E.W. Caetano, R.F. da Costa, V.N. Freire, A quantum biochemistry investigation of willardiine partial agonism in AMPA receptors, Physical Chemistry Chemical Physics, 17 (2015) 13092-13103.
[71] Y. Zhang, P. Lee, S. Liang, Z. Zhou, X. Wu, F. Yang, H. Liang, Structural basis of non-steroidal anti-inflammatory drug diclofenac binding to human serum albumin, Chem Biol Drug Des, 86 (2015) 1178-1184.
[72] T.J. Dolinsky, J.E. Nielsen, J.A. McCammon, N.A. Baker, PDB2PQR: an automated pipeline for the setup of Poisson–Boltzmann electrostatics calculations, Nucleic acids research, 32 (2004) W665-W667.
[73] O. Trott, A. Olson, Software news and update AutoDock Vina: improving the speed and accuracy of docking with a new scoring function, Efficient Optimization, and Multithreading, (2009).

[74] J. Nocedal, S. Wright, Numerical Optimization, Second, ITM Web of Conferences itmconf/201.
[75] B.L. Sousa, I.L. Barroso-Neto, E.F. Oliveira, E. Fonseca, P. Lima-Neto, L.O. Ladeira, V.N. Freire, Explaining RANKL inhibition by OPG through quantum biochemistry computations and insights into peptide-design for the treatment of osteoporosis, RSC advances, 6 (2016) 84926-84942.
[76] W. Humphrey, A. Dalke, K. Schulten, VMD: visual molecular dynamics, Journal of molecular graphics, 14 (1996) 33-38.
[77] J. Phillips, R. Braun, W. Wang, J. Gumbart, E. Tajkhorshid, E. Villa, and Schulten, K. 2005, Scalable molecular dynamics with NAMD. Journal of Computational Chemistry, 26 (2005) 1781-1802.
[78] X. Chen, Y. Zhang, J.Z. Zhang, An efficient approach for ab initio energy calculation of biopolymers, The Journal of chemical physics, 122 (2005) 184105.
[79] X. He, J.Z. Zhang, A new method for direct calculation of total energy of protein, The Journal of chemical physics, 122 (2005) 031103.
[80] B. Delley, From molecules to solids with the DMol 3 approach, The Journal of chemical physics, 113 (2000) 7756-7764.
[81] B. Delley, An all-electron numerical method for solving the local density functional for polyatomic molecules, The Journal of chemical physics, 92 (1990) 508-517.
[82] J.P. Perdew, K. Burke, M. Ernzerhof, Generalized gradient approximation made simple, Physical review letters, 77 (1996) 3865.
[83] A. Tkatchenko, M. Scheffler, Accurate molecular van der Waals interactions from ground-state electron density and free-atom reference data, Physical review letters, 102 (2009) 073005.
[84] A. Klamt, G. Schüürmann, COSMO: a new approach to dielectric screening in solvents with explicit expressions for the screening energy and its gradient, Journal of the Chemical Society, Perkin Transactions 2, (1993) 799-805.
[85] G. Fanali, A. Di Masi, V. Trezza, M. Marino, M. Fasano, P. Ascenzi, Human serum albumin: from bench to bedside, Molecular aspects of medicine, 33 (2012) 209-290.
[86] Y. Moriyama, D. Ohta, K. Hachiya, Y. Mitsui, K. Takeda, Fluorescence behavior of tryptophan residues of bovine and human serum albumins in ionic surfactant solutions: a comparative study of the two and one tryptophan (s) of bovine and human albumins, Journal of protein chemistry, 15 (1996) 265-272.
[87] N. Tayeh, T. Rungassamy, J.R. Albani, Fluorescence spectral resolution of tryptophan residues in bovine and human serum albumins, Journal of pharmaceutical and biomedical analysis, 50 (2009) 107-116.
[88] L.M. Sergio, Y.A. Martins, J.L. Amaral, V.L.B. França, C.F. de Freitas, A.M. Neto, N. Hioka, M.I. Ravanelli, C. Mareze-Costa, S. Claudio da Costa, V.N. Freire, K. Brunaldi, Molecular insight on the binding of stevia glycosides to bovine serum albumin, Chem Biol Interact, 344 (2021) 109526.
[89] Y. Wang, G. Zhang, L. Wang, Interaction of prometryn to human serum albumin: insights from spectroscopic and molecular docking studies, Pesticide biochemistry and physiology, 108 (2014) 66-73.
[90] M.F. Siddiqui, M.S. Khan, F.M. Husain, B. Bano, Deciphering the binding of carbendazim (fungicide) with human serum albumin: A multi-spectroscopic and molecular modelling studies, Journal of Biomolecular Structure and Dynamics, 37 (2019) 2230-2241.
[91] L.G. Astrakas, C. Gousias, M. Tzaphlidou, Structural destabilization of chignolin under the influence of oscillating electric fields, Journal of Applied Physics, 111 (2012) 074702.
[92] K. Sargsyan, C. Grauffel, C. Lim, How molecular size impacts RMSD applications in molecular dynamics simulations, Journal of chemical theory and computation, 13 (2017) 1518-1524.
[93] J. Zondagh, V. Balakrishnan, I. Achilonu, H.W. Dirr, Y. Sayed, Molecular dynamics and ligand docking of a hinge region variant of South African HIV-1 subtype C protease, Journal of Molecular Graphics and Modelling, 82 (2018) 1-11.

[94] A.I. Uba, K. Yelekçi, Crystallographic structure versus homology model: a case study of molecular dynamics simulation of human and zebrafish histone deacetylase 10, Journal of Biomolecular Structure and Dynamics, 38 (2020) 4397-4406.
[95] J.M. Chalker, G.J. Bernardes, Y.A. Lin, B.G. Davis, Chemical modification of proteins at cysteine: opportunities in chemistry and biology, Chemistry–An Asian Journal, 4 (2009) 630-640.

6 FOCO NA *CANDIDA* SPP.

Espécies de *Candida spp*. são fungos oportunistas, sendo o fungo responsável pelo maior número de mortes de pacientes imunossuprimidos no mundo, o que representa um sério problema de saúde pública (FIRACATIVE, 2020). Candidemia é a infecção hospitalar mais frequente e responsável por mais de 15% de todas as infecções sanguíneas, se considerar apenas infecções causadas por fungos, sendo as diferentes espécies de *Candida spp*. responsáveis por 40 a 70% dessas infecções (FIORITI *et al.,* 2022). As infecções fúngicas invasivas ameaçam a vida com uma taxa de mortalidade por ano mais alta que a da malária, do câncer de mama e de próstata (VAN DIJCK *et al.,* 2018).

Candida albicans é a espécie mais encontrada quando se isolam os agentes causadores das infecções, porém, outras espécies, como *C. parapsilosis, C. tropicalis, C. krusei, C. glabrata* e *C. famata* têm aumentado, significativamente, os índices de infecções, principalmente em pacientes imunodeprimidos, tais como aqueles portadores do vírus HIV (SINGH; TÓTH; GÁCSER, 2020)

Espécies de *Candida spp*. apresentam uma grande flexibilidade em seus modos de vida, sendo capazes de crescer em ambientes extremamente diferentes, no que se refere à disponibilidade de nutrientes, variação de temperatura, pH, osmolaridade e à quantidade de oxigênio disponível (BARTNICKA *et al.,* 2019). Superfícies contaminadas com *Candida spp*., como mesas, cadeiras e sondas possuem colonização persistentes por 28 dias, tornando-se um problema no processo de desinfecção hospitalar (FU *et al.,* 2020). Esse fato associado ao grande desenvolvimento de resistência das leveduras pelos antifúngicos já descobertos, bem como a capacidade de formar biofilmes com outras espécies, torna o genêro *Candida spp*. um sério risco para a saúde humana, sendo necessário o desenvolvimento contínuo de novas drogas com diferentes mecanismos de ação para se garantir um eficiente tratamento aos pacientes (AMARAL; SOUZA; *et al.,* 2021).

6.1 Estudos *in silico* e experimentais com peptídeos contra *Candida* spp.

Peptídeos antimicrobianos naturais são moléculas compostas por uma sequência de 10 a 50 resíduos de aminoácidos, que são carregados positivamente (+2 a +9), e possuem tanto resíduos hidrofóbicos como resíduos hidrofílicos, o que permite sua solubilidade em meio aquoso, como também em meios com membranas hidrofóbicas. São classificados em diferentes grupos dependendo da sua composição, tamanho, sequência, estrutura, hidrofobicidade e anfipaticidade, características cruciais para sua atividade antimicrobiana (LIMA *et al.,* 2021).

Diferentemente das drogas convencionais que possuem uma proteína alvo ou um constituinte específico da membrana, os PAMs possuem ação principalmente na permeabilização da membrana de micro-organismos através de interações iônicas e hidrofóbicas com os fosfolipídios presentes em sua estrutura. O que dificulta a sua resistência, visto que, o patógeno trocar sua composição da membrana, resultaria em um custo energético alto. Assim, os PAMs induzem nenhuma ou pouca resistência dependendo do micro-organismo (HOLLMANN *et al.,* 2018). Mesmo com a membrana sendo o alvo mais provável dos PAMs, é observado que esses peptídeos também possuem alvos intracelulares e extracelulares, como na interferência da produção da parede celular, na síntese de RNA/DNA e proteínas, na atividade enzimática e no enovelamento de proteínas (KALSY *et al.,* 2020; LEE, Hyunhee *et al.,* 2019).

Apesar dos PAMs apresentarem diversas vantagens e alguns estarem em fase de teste clínico, a maioria deles apresentam características não desejáveis para aplicação clínica, demostrando várias limitações farmacocinéticas, como a susceptibilidade, a degradação por enzimas, citotoxicidade contra células de mamíferos e baixa biodisponibilidade (GALDIERO *et al.,* 2019; SHWAIKI; LYNCH; ARENDT, 2021). Assim, o desenvolvimento dos PAMs sintéticos através da bioinformática tem sido considerada a alternativa mais promissora para o desenvolvimento de novos fármacos, visto que melhoram os parâmetros farmacocinéticos e farmacodinâmicos dos PAMs naturais (MOOKHERJEE *et al.,* 2020). Além disso, apenas pequenas regiões dos PAMs naturais são responsáveis pela ação antimicrobiana desempenhada, dessa forma, desenhando PAMs sintéticos é possível reduzir o tamanho do peptídeo, o que resulta na redução do preço de produção, diminuição dos efeitos colaterais, bem como na redução do seu potencial

de imunogenicidade (FERNÁNDEZ DE ULLIVARRI *et al.,* 2020). Outra vantagem observada nos PAMs sintéticos, é o melhoramento da sua suscetibilidade contra proteólise e a redução da toxicidade, tornando-se mais estável para aplicação terapêutica (LAI *et al.,* 2022).

Os PAMs sintéticos são bioinspirados em PAMs naturais, bem como em fragmentos de proteínas com grandes atividades antimicrobiana. Diversos softwares estão disponíveis online e com acesso gratuito para fazer predições de PAMs sintéticos, considerando as características bioquímicas dos peptídeos, como na análise de suas sequências com atividade comprovada, na hidrofobicidade, nas cargas, anfipacidade e conformações (LIMA *et al.,* 2021), sendo possível o desenvolvimento de PAMs sintéticos com atividade antimicrobiana, eficazes e seguros para aplicação clínica contra micro-organismos multirresistentes.

Com o avanço da bioinformática, é possível realizar estudos envolvendo proteínas e membrana alvo dos peptídeos. As espécies de *Candida* spp. possuem várias proteínas que podem ser alvos para o desenvolvimento de drogas, como a proteína CYP51 que é o alvo do grupo de drogas azóis (fluconazol, isavuconazol, itraconazol, posaconazol e voriconazol) e a β-1,3-glucanase e β-1,3-glucano sintetase que são alvos do grupo de drogas chamados equinocandinas (caspofungina, micafungina e anidulafungina). Outros alvos proteicos são considerados como chave para o desenvolvimento de novas drogas, como as proteases aspárticas secretadas por *Candida*. Além de proteínas, os peptídeos antimicrobianos (PAMs) possuem como alvo principal a membrana plasmática do micro-organismo. O estudo das interações dos PAMs com proteínas e com membranas a nível molecular é possível através da utilização de simulações de bioinformática.

No nosso artigo, que foi tema da minha dissertação de mestrado e durante o doutorado realizei os experimentos finais e publiquei, demonstrei que o peptídeo *Mo*-CBP$_3$-PepIII interage com proteínas alvo de *Candida* spp. através de docking, dinâmica molecular e bioquímica quântica, bem como simulei a interação desse PAM com uma membrana mimética de levedura através de dinâmica molecular. Esse estudo completo encontra-se no apêndice A da tese. Durante minha graduação, realizei um trabalho de isolamento de peptídeos do látex de *Calotropis procera* e testei as atividades desse isolado. Observei que o isolado peptídico possui atividade inseticida e fungicida, incluindo contra *Candida* spp., como demonstrado

no artigo completo no apêndice B que também foi finalizado e publicado durante o período do meu doutorado. Além do estudo diretamente entre os peptídeos e os alvos, também realizei parcerias para analisar a interação de peptídeos com drogas já conhecidas e demostrar o sinergismo que ocorre entre elas. Essas colaborações renderam os trabalhos que encontram-se nos apêndices C, D e E.

7 TRABALHOS EM FINALIZAÇÃO

Além dos trabalhos publicados, que estão nesta tese, vários estudos estão sendo desenvolvidos utilizando as mesmas metodologias por nosso grupo de pesquisa. Estamos desenvolvendo peptídeos miméticos do anticorpo Infliximabe, que é o anticorpo mais comercializado no Brasil atualmente. Outros peptídeos miméticos estão sendo desenvolvidos a partir do anticorpo Trastuzumabe, que possui como alvo a proteína HER2, que desempenha um papel importante no câncer de mama. Como os resultados não estão finalizados desses anticorpos, iremos demonstrar aqui os principais resultados de outros dois artigos que estão submetidos e serão publicados em breve. Dessa forma, além dos artigos já publicados, espera-se que quatro artigos ainda sejam publicados a partir desse trabalho de doutorado.

7.1 Interação de SARS-CoV-2 com animais

O primeiro trabalho é um estudo entre a interação da proteína S do SARS-CoV-2 com a proteína ECA2 de 53 espécies de animais. O objetivo deste trabalho é observar quais espécies poderiam ser infectadas com SARS-CoV-2, podendo ser um reservatório natural do vírus. As proteínas ECA2 dos animais foram modeladas por homologia, após realizarmos o docking molecular com a proteína S de SARS-CoV-2. Das 53 espécies testadas, apenas 11 tiveram um encaixe semelhante ao encaixe da proteína S com a ECA2 humana, como pode ser observado na figura 63.

Com esse resultado de docking molecular foi possível predizer que as outras espécies testadas não são infectadas por SARS-CoV-2. Dessa forma, realizamos dinâmica molecular e bioquímica quântica do complexo proteína S e ECA2 das 11 espécies de animais. A bioquímica quântica demonstrou que a proteína

S de SARS-CoV-2 possui energia de interação pela proteína ECA2 das espécies na seguinte ordem, do que possui maior afinidade para o menor: *Sapajus apella* (macaco-prego), *Rhinolophus sinicus* (morcego ferradura ruivo chinês), *Gorilla gorilla gorilla* (gorila-do-ocidente), *Chinchilla lanigera* (chinchila de cauda longa), *Aotus nancymaae* (uma espécie de macaco-da-noite), *Pan paniscus* (bonobo ou chimpanzé-pigmeu), *Saccopteryx bilineata* (morcego da família Emballonuridae), *Neovison vison* (visão americano), *Homo sapiens*, *Numida meleagris* (galinha-d'angola), *Macaca nemestrina* (Macaco-de-cauda-de-porco-do-sul) e *Emballonura alecto* (morcego da família Emballonuridae), como mostrado na figura 64.

Figura 63. Proteína S de SARS-CoV-2 interage com onze animais de maneira semelhante à interação com a proteína ECA2 de humanos.

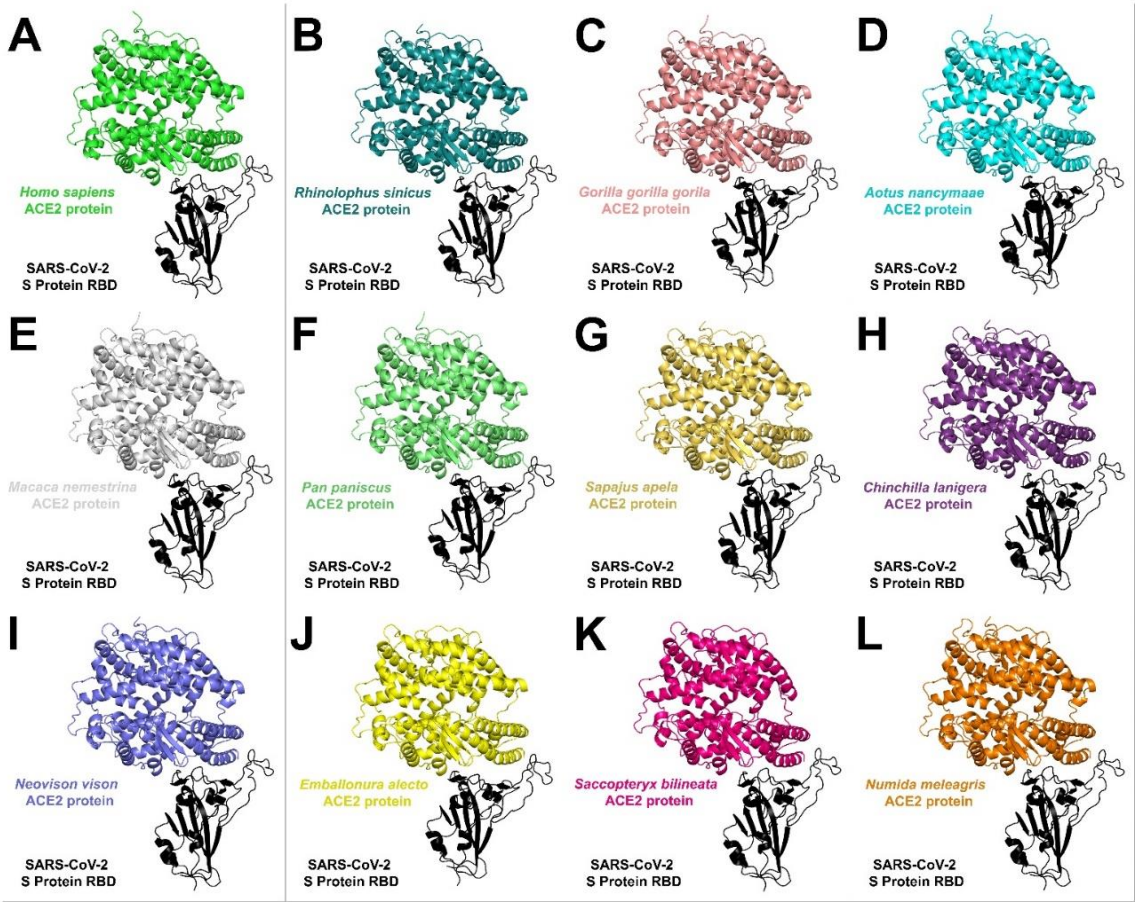

Fonte: Elaborado pelo autor.

Figura 64. Convergência e somatório da energia de interação entre a proteína S de SARS-CoV-2 e a proteína ECA2 das 11 espécies testadas e a do ser humano.

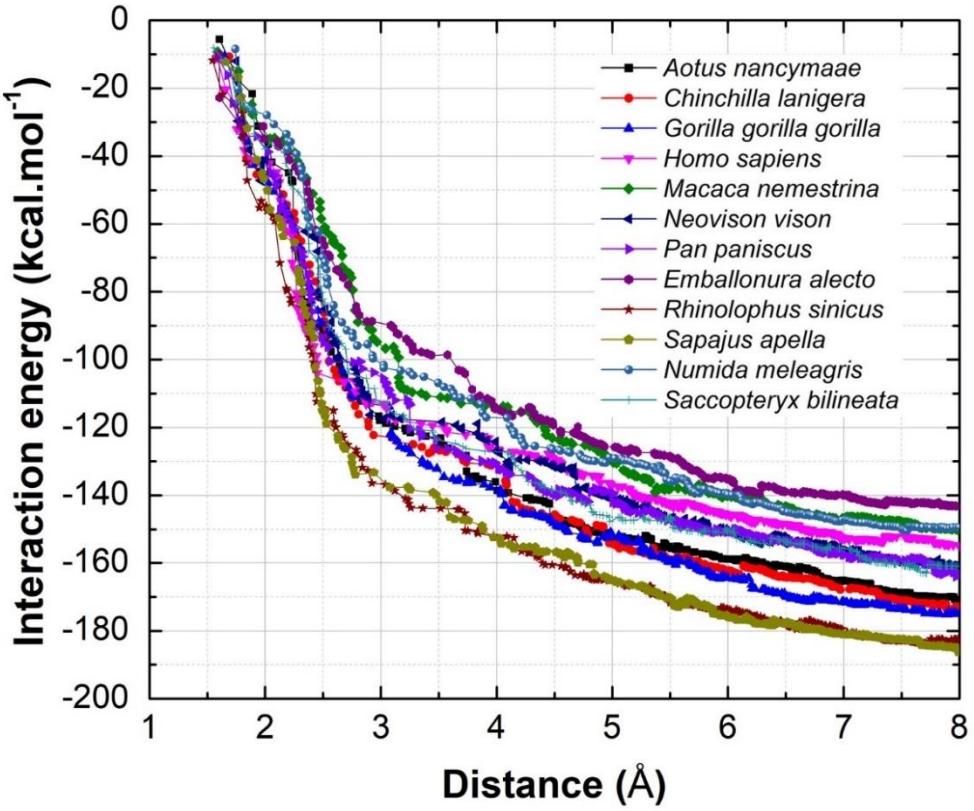

Fonte: Elaborado pelo autor.

Das 11 espécies que o SARS-CoV-2 pode interagir, de acordo com as simulações, 5 são espécies de macacos, o que era um resultado esperado devido a grande similaridade das proteínas ECA2. Outras 3 espécies indicadas são de morcegos, o que já é constatado na literatura, visto que os morcegos são reservatórios de coronavírus, desde o vírus MERS-CoV. O *Neovison vison* (vison americano) e a *Chinchilla lanigera* (chinchila de cauda longa) já são relatados com a capacidade de ser infectado e a Austrália sacrificou milhões desses animais para impedir a circulação de SARS-CoV-2. Assim, apenas *Numida meleagris* (galinha-d'angola) apresenta-se como uma novidade ainda não relatada na literatura, apesar de ser relatado o potencial de infectividade das aves por vírus. Através desse estudo podemos observar a acurácia que as simulações possuem e alertar o mundo para o potencial da galinha-d'angola ser um reservatório de SARS-CoV-2.

7.2 Interação das drogas Tofacitinib e Peficitinib com a enzima JAK1

O segundo trabalho que encontra-se submetido, entitula-se “*Tofacitinib and Peficitinib inhibitors of Janus kinase for autoimmune diseases treatments: A Quantum Biochemistry Description*”. Esse manuscrito descreve a pesquisa das diferenças e semelhanças na interação entre as Tofacitinib e Peficitinib, drogas utilizadas para o tratamento de artrite reumatóide, que possuem como alvo a proteína janus quinase 1 (JAK1). O sítio ativo de interação das drogas é o mesmo e muitos átomos são sobrepostos, como demostrado na Figura 65.

Figura 65. Visão geral da interação do Tofacitinib e Peficitinib com JAK1.

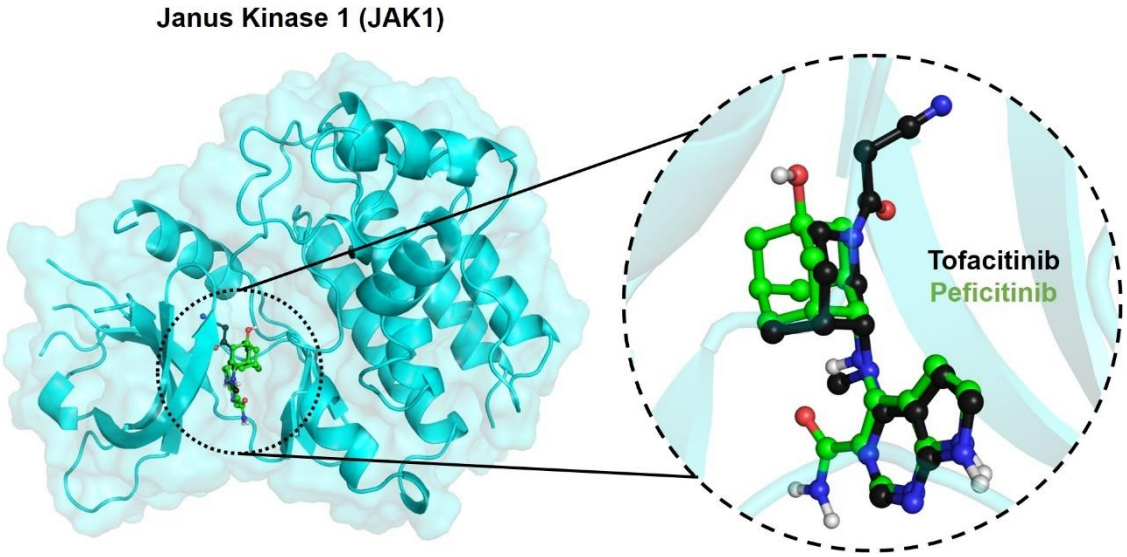

Fonte: Elaborado pelo autor.

Como comentado na introdução, uma das técnicas desenvolvidas pelo nosso grupo de pesquisa foi o cálculo da função dielétrica, a qual permite realizar o cálculo quântico com maior acurácia, visto que realizamos os cálculos com função dielétrica mais próximo da realidade evitando sub ou superestimações. Calculamos então a função dielétrica para esse sistema, como demonstrado na figura 66. Apesar da figura demostrar uma representação 2D, o cálculo é realizado em cada ponto do espaço. Esses valores de função dielétrica são utilizados como entrada para o cálculo quântico das energias de interação.

Após isso, o cálculo quântico foi realizado para observar quais resíduos de aminoácidos interagem de forma mais significante (maior afinidade) com as drogas e quais as diferenças entre elas. O resultado pode ser observado na figura

67.

Figura 66. Representação de mapa 2D da função dielétrica não homogênea nos sistemas de proteínas. A barra de cores mostra a função dielétrica variando de 4 a 80.

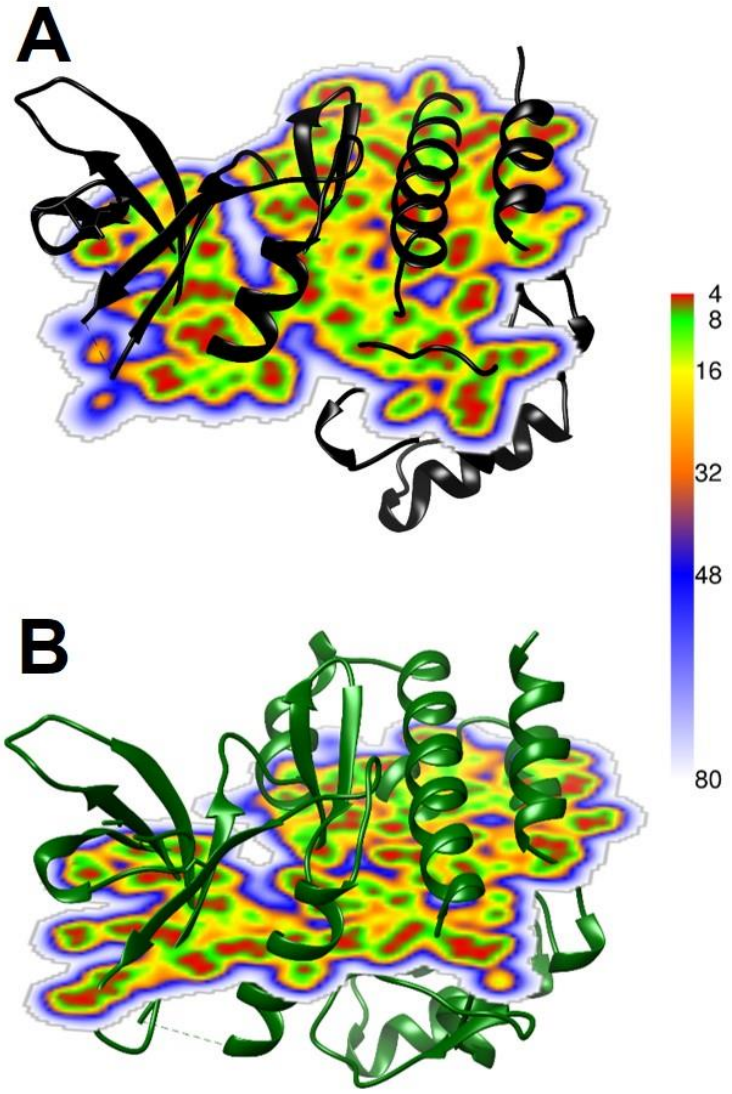

Fonte: Elaborado pelo autor.

Os principais resíduos da JAK1 que interagem com Tofacitinib e Peficitib são PHE958 e LEU959. Diferenças na energia de interação quando se utiliza função dielétrica homogênea e não homogênea também são possíveis de observar. Utilizando a função dielétrica homogênea é observado que a energia de interação de alguns resíduos é superestimada, enquanto, em outros, ocorre uma subestimação, demonstrando que, para obter resultados com maior acurácia é necessário utilizar a função dielétrica não homogênea.

Figura 67. Principais resíduos de aminoácidos da JAK1 que interagem com Tofacitinib e Peficitinib utilizando função dielétrica constate (40) e não homogênea.

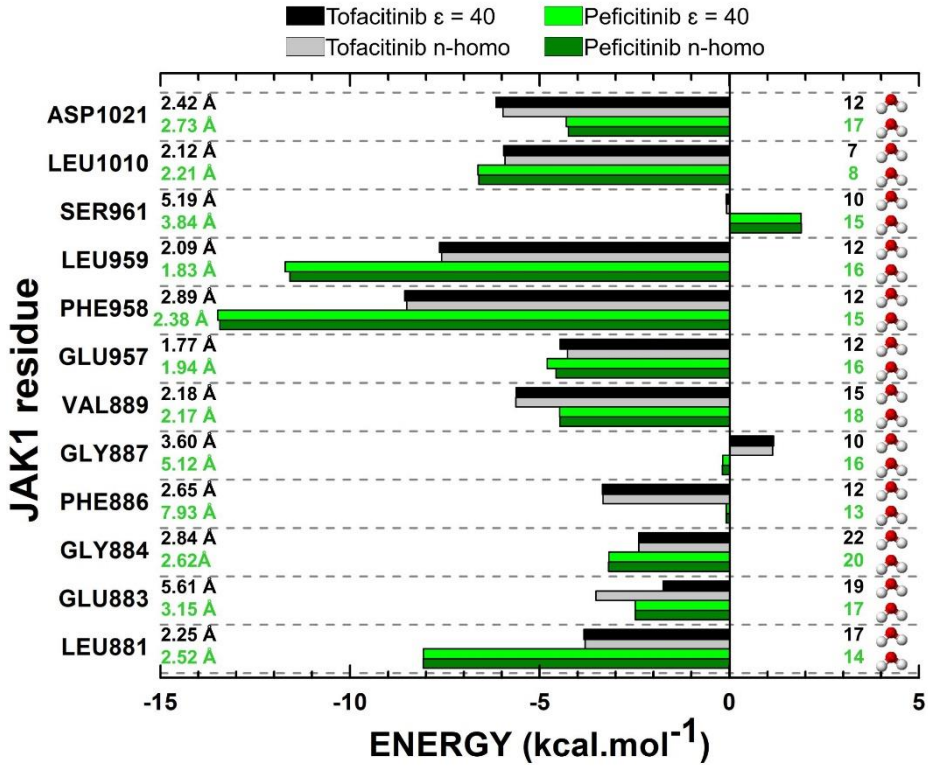

Fonte: Elaborado pelo autor.

Para entender as diferenças de energia de interação observada, realizou-se um estudo molecular das interações presentes entre a JAK1 e as drogas. Nota-se que as principais interações que estabilizam os complexos são Van der Waals, ligações de hidrogênio, Alquil, Pi-Alquil e Pi-Enxofre, figura 68, Constatou-se que a principal interação presente entre as drogas e a JAK1 é van der Waals com aproximadamente 39% da energia de interação total; Ligação de hidrogênio representa 16% da energia de interação entre JAK1 e Tofacitinib, enquanto as ligações de hidrogênio representam 21% da energia de interação com Peficitinib. Já as interações alquil e pi-alquil representam apenas 6% da energia de interação e outras interações apresentam porcentagem menores.

Um dos ganhos na energia de interação pelo Peficitinib com a JAK1 ocorre nas ligações de hidrogênio realizadas com o grupo hidroxiadamanta, que é uma das principais diferenças entre os dois fármacos. Com esse grupo, o Peficitinib realiza uma ligação de hidrogênio a mais do que o Tofacitinib, podendo ser uma região da droga a ser melhorada para obter valor de concentração inibitória menores,

logo, drogas mais eficientes.

Figura 68. Interações entre as drogas Tofacitinib e Peficitinib com a proteína JAK1. A e B- figura 2D das interações. C e D- figuras 3D das interações.

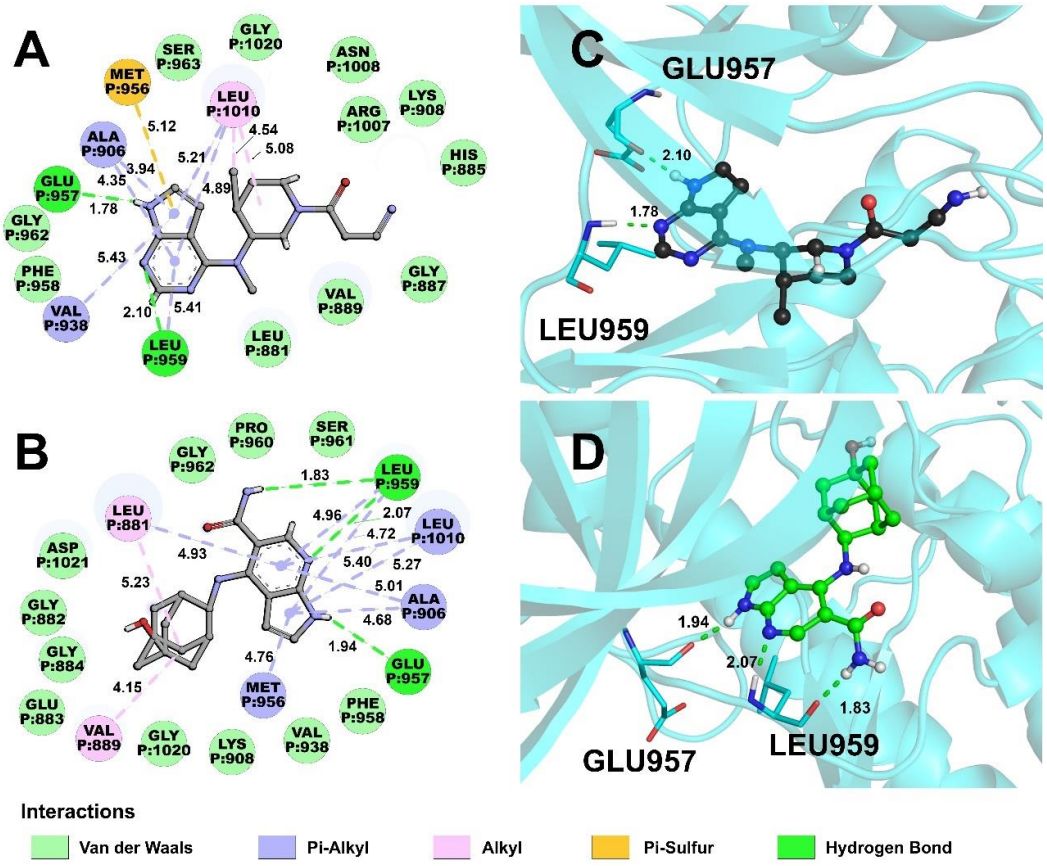

Fonte: Elaborado pelo autor.

8. CONCLUSÃO E PERSPECTIVA

Comprovamos que o peptídeo *Mo*-CBP$_3$-PepIII apresenta atividade *in vitro* contra *Candida* spp., assim como perpectiva futura dessa linha de pesquisa é a realização do teste *in vivo* desse peptídeo, visto que muito peptídeos apresentam atividade *in vitro*, mas fracassam nos testes *in vivo*. Testes *in vivo* para *Candida albicans* utilizando invertebrados (nematóides) como modelo estão sendo estabelecidos. Objetivamos continuar investigando a atividade do peptídeo *in vivo* utilizando invertebrados como modelo antes da realização de pesquisas com vertebrados.

Peptídeos sintéticos impedem a entrada do SARS-CoV-2 nas células através da interação com a principal protease do vírus e com a glicoproteína spike. Demonstramos *in silico* e *in vitro* que o peptídeo PepKAA possui grande potencial para ser aplicado contra SARS-CoV-2 e não possui efeito tóxico contra o modelo peixe zebra. Entretanto, nos testes realizados *in vitro* utilizamos as células Vero E6 (células de macacos verde africano) como alvo do SARS-CoV-2, apesar da grande semelhança entre as células Vero e as células humanas, é necessário testar se o peptídeo impede a invasão de SARS-CoV-2 nas células de humanos, bem como testar sua atividade *in vivo*. Estamos contactando alguns pesquisadores para realizar esses testes em colaboração.

A utilização de peptídeos miméticos a anticorpos possue diversas vantagens. Utilizando bioquímica quântica, desenhamos e propomos 6 peptídeos com grande potencial de serem aplicados contra câncer. Nesse linha de pesquisa, ainda estamos na fase inicial de validação dos peptídeos, finalizamos os testes *in silico*. Como perspectiva futura, buscaremos parcerias para realizar os teste *in vitro* dos peptídeos contra o câncer.

A grande utilização de pesticidas no mundo tem causado consequências relacionadas com a saúde animal e humana, bem como consequências ao meio ambiente. Confirmamos que a atrazina interage com a albumina sérica humana (HSA) e demonstramos a nível molecular como ocorre a interação. O sítio FA8 da HSA é o principal sítio de interação da atrazina, mas o herbicida também interage nos sítios FA1 e FA3/4. Uma das principais perspectiva dessa linha de pesquisa é divulgar os resultados para que desperte o interesse de outros pesquisadores estudarem os efeitos da atrazina a nível fisiológico.

Concluimos que modelagem, docking e simulação de dinâmica molecular unidos à bioquímica quântica são metodologias *in silico* com grande potencial para serem aplicadas em diversos problemas e obter resoluções com alta acurácia, rapidez e baixo custo. Os artigos desta tese demostraram a aplicabilidade dessas metodologias como uma fase anterior aos experimentos *in vitro* ou *in vivo* através do desenvolvimento racional de drogas e análise de interações entre proteínas e proteínas com ligantes. Conclui-se também que as simulações *in silico* podem ser aplicadas após a validação de dados experimentais, pois são poderosas ferramentas para o melhoramento de drogas estabelecidas, por exemplo, através do entendimento dos mecanismos de ação e as interações dessas drogas.

Planejamos utilizar os resultados obtidos ao longo do período do doutorado para publicar mais 4 artigos científicos, que estão em fase de finalização.

REFERÊNCIAS

AIER, I.; VARADWAJ, P. K.; RAJ, U. Structural insights into conformational stability of both wild-type and mutant EZH2 receptor. **Scientific Reports**, Londres, vol. 6, n.1, p. 1-10, 2016.

ALBUQUERQUE, E.; FULCO, U. L.; CAETANO, E.; FREIRE, V. **Quantum Chemistry Simulation of Biological Molecules**. 1. ed. Londres: Cambridge University Press, 2020.

AMARAL, J. L.; FREITAS, C. D. T.; RODRIGUES, J. P. V.; HUSSAIN, G.; RAMOS, M. V.; SOUZA, P. F. N. Peptide fraction from latex of Calotropis procera exhibits antifungal and insecticidal activities. **Arthropod-Plant Interactions**, Berlim, vol. 15, n. 3, p. 431–438, 2021.

AMARAL, J. L.; OLIVEIRA, J. T. A.; LOPES, F. E. S.; FREITAS, C. D. T.; FREIRE, V. N.; ABREU, L. V.; SOUZA, P. F. N. Quantum biochemistry, molecular docking, and dynamics simulation revealed synthetic peptides induced conformational changes affecting the topology of the catalytic site of SARS-CoV-2 main protease. **Journal of Biomolecular Structure and Dynamics**, Oxon, vol. 40, n. 19, p. 8925-8937, 2021.

AMARAL, J. L.; SANTOS, S. J.M.; SOUZA, P. F.N.; DE MORAIS, P. A.; MAIA, F.F.; CARVALHO, H. F.; FREIRE, V. N. Quantum biochemistry in cancer immunotherapy: New insights about CTLA-4/ipilimumab and design of ipilimumab-derived peptides with high potential in cancer treatment. **Molecular Immunology**, Oxford, vol. 127, p. 203–211, 2020.

AMARAL, J. L.; SOUZA, P. F.N.; OLIVEIRA, J. T.A.; FREIRE, V. N.; SOUSA, D. O.B. Computational approach, scanning electron and fluorescence microscopies revealed insights into the action mechanisms of anticandidal peptide Mo-CBP3-PepIII. **Life Sciences**, Oxford, vol. 281, p. 1-11, 2021.

BARTNICKA, D.; KARKOWSKA-KULETA, J.; ZAWROTNIAK, M.; SATAŁA, D.; MICHALIK, K.; ZIELINSKA, G.; BOCHENSKA, O.; KOZIK, A.; CIASTON, I.; KOZIEL, J.; DUTTON, L. C.; NOBBS, A. H.; POTEMPA, B.; BASTER, Z.; RAJFUR, Z.; POTEMPA, J.; RAPALA-KOZIK, M. Adhesive protein-mediated cross-talk between Candida albicans and Porphyromonas gingivalis in dual species biofilm protects the anaerobic bacterium in unfavorable oxic environment. **Scientific Reports**, Londres, vol. 9, n. 1, p. 4376, 2019.

BEHL, T.; KAUR, I.; SEHGAL, A.; SINGH, S.; BHATIA, S.; AL-HARRASI, A.; ZENGIN, G.; BABES, E. E.; BRISC, C.; STOICESCU, M.; TOMA, M. M.; SAVA, C.; BUNGAU, S. G. Bioinformatics Accelerates the Major Tetrad: A Real Boost for the Pharmaceutical Industry. **International Journal of Molecular Sciences**, Basel, vol. 22, n. 12, p. 6184, 2021.

BERMAN, H. M. The Protein Data Bank. **Nucleic Acids Research**, Oxford, vol. 28, n. 1, p. 235–242, 2000.

BERMAN, H. M. Synergies between the Protein Data Bank and the community. **Nature Structural & Molecular Biology**, Nova Iorque, vol. 28, n. 5, p. 400–401, 2021.

BEZERRA, L. P.; FREITAS, C. D. T.; SILVA, A. F. B.; AMARAL, J. L.; NETO, Nilton A. S.; SILVA, R. G. G.; PARRA, A. L. C.; GOLDMAN, G. H.; OLIVEIRA, J. T. A.; MESQUITA, F. P.; SOUZA, P. F. N. Synergistic Antifungal Activity of Synthetic Peptides and Antifungal Drugs against Candida albicans and C. parapsilosis Biofilms. **Antibiotics**, Basel, vol. 11, n. 5, p. 553, 2022.

BEZERRA, L. P; SILVA, A. FB; SANTOS-OLIVEIRA, R.; ALENCAR, L. M.R.; AMARAL, J. L; NETO, N. A.S.; SILVA, R. G.G.; BELÉM, M. O.; DE ANDRADE, C. R; OLIVEIRA, J. T. A.; FREITAS, C. D. T.; SOUZA, P. F.N. Combined antibiofilm activity of synthetic peptides and antifungal drugs against *Candida* spp. **Future Microbiology**, Londres, vol. 17, n. 14, p. 1133–1146, 2022.

BIENERT, S.; WATERHOUSE, A.; DE BEER, T. A. P.; TAURIELLO, G.; STUDER, G.; BORDOLI, L.; SCHWEDE, T. The SWISS-MODEL Repository—new features and functionality. **Nucleic Acids Research**, Oxford, vol. 45, n. 1, p. D313–D319, 2017.

BINETTE, Vincent; MOUSSEAU, Normand; TUFFERY, Pierre. A Generalized Attraction–Repulsion Potential and Revisited Fragment Library Improves PEP-FOLD Peptide Structure Prediction. **Journal of Chemical Theory and Computation**, Nova Iorque, vol. 18, n. 4, p. 2720–2736, 2022.

BOLTON, W.; PERUTZ, M. F. Three Dimensional Fourier Synthesis of Horse Deoxyhaemoglobin at 2.8 Å Resolution. **Nature**, Londres, vol. 228, n. 5271, p. 551–552, 1970.

BURLEY, S. K.; BERMAN, H. M. Open-access data: A cornerstone for artificial intelligence approaches to protein structure prediction. **Structure**, Cambridge, vol. 29, n. 6, p. 515–520, 2021.

CHEN, J.; ZHANG, S.; WANG, W.; SUN, H.; ZHANG, Q.; LIU, X. Binding of Inhibitors to BACE1 Affected by pH-Dependent Protonation: An Exploration from Multiple Replica Gaussian Accelerated Molecular Dynamics and MM-GBSA Calculations. **ACS Chemical Neuroscience**, Nova Iorque, vol. 12, n. 14, p. 2591–2607, 2021.

CHOWDHURY, R.; BOUATTA, N.; BISWAS, S.; FLORISTEAN, C.; KHARKAR, A.; ROY, K.; ROCHEREAU, C.; AHDRITZ, G.; ZHANG, J.; CHURCH, G. M.; SORGER, P. K.; ALQURAISHI, M. Single-sequence protein structure prediction using a language model and deep learning. **Nature Biotechnology**, Nova Iorque, vol. 40, p. 1617–1623, 2022.

DA COSTA, R. F.; FREIRE, V. N.; BEZERRA, E. M.; CAVADA, B. S.; CAETANO, E. W. S.; DE LIMA FILHO, J. L.; ALBUQUERQUE, E. L. Explaining statin inhibition effectiveness of HMG-CoA reductase by quantum biochemistry computations. **Physical Chemistry Chemical Physics,** Londres, vol. 14, n. 4, p. 1389–1398, 2012.

DANTAS, D. S.; OLIVEIRA, J. I. N.; LIMA NETO, J. X.; DA COSTA, R. F.; BEZERRA,

E. M.; FREIRE, V. N.; CAETANO, E. W. S.; FULCO, U. L.; ALBUQUERQUE, E. L. Quantum molecular modelling of ibuprofen bound to human serum albumin. **RSC Advances**, Londres, vol. 5, n. 61, p. 49439–49450, 2015.

DESTA, I. T.; PORTER, K. A.; XIA, B.; KOZAKOV, D.; VAJDA, S.. Performance and Its Limits in Rigid Body Protein-Protein Docking. **Structure**, Cambridge, vol. 28, n. 9, p. 1071-1081, 2020.

DHARA, V.; SHETTY, S. S.; DE ARRUDA, J. A. A.; SILVA, T. A.; RUSSO, R. C.; SHETTY, N. J.; PIDAPARTHI, M.; WOLLENBERG, B.; RAO, V. U.S.; GOPINATH, T. P.S. Decoding the influence of the immune system and immunotherapy targets on carcinomas: A hidden prism in oral cancer therapy. **Disease-a-Month**, Chicago, vol. 69, n. 1, p. 101353, 2022.

DU, Z.; SU, H.; WANG, W.; YE, L.; WEI, H.; PENG, Z.; ANISHCHENKO, I.; BAKER, D.; YANG, J. The trRosetta server for fast and accurate protein structure prediction. **Nature Protocols**, Nova Iorque, vol. 16, n. 12, p. 5634–5651, 2021.

EBERHARDT, J.; SANTOS-MARTINS, D.; TILLACK, A. F.; FORLI, S.. AutoDock Vina 1.2.0: New Docking Methods, Expanded Force Field, and Python Bindings. **Journal of Chemical Information and Modeling**, Washington, vol. 61, n. 8, p. 3891–3898, 2021.

FAN, W.; MENCIUS, J.; DU, W.; FAN, H.; ZHU, H.; WEI, D.; ZHOU, M.; QUAN, S. Online bioinformatics teaching practice: Comparison of popular docking programs using SARS-CoV-2 spike RBD–ACE2 complex as a benchmark. **Biochemistry and Molecular Biology Education**, Albania, vol. 49, n. 6, p. 833–840, 2021.

FEDERICO, L. B.; SILVA, G. M.; DA SILVA HAGE-MELIM, L. I.; GOMES, S. Q.; BARCELOS, M. P.; GALINDO FRANCISCHINI, I. A.; TOMICH DE PAULA DA SILVA, C. H. Identification of known drugs as potential SARS-CoV-2 Mpro inhibitors using ligand- and structure-based virtual screening. **Future Medicinal Chemistry**, Londres, vol. 13, n. 16, p. 1353–1366, 2021.

FERNÁNDEZ DE ULLIVARRI, M.; ARBULU, S.; GARCIA-GUTIERREZ, E.; COTTER, P. D. Antifungal Peptides as Therapeutic Agents. **Frontiers in Cellular and Infection Microbiology**, Lausanne, vol. 10, n. 105, p. 1-22, 2020.

FIORITI, S.; BRESCINI, L.; PALLOTTA, F.; CANOVARI, B.; MORRONI, G.; BARCHIESI, F. Antifungal Combinations against Candida Species: From Bench to Bedside. **Journal of Fungi**, Basel, vol. 8, n. 10, p. 1077, 2022.

FIRACATIVE, C. Invasive fungal disease in humans: are we aware of the real impact? **Memórias do Instituto Oswaldo Cruz**, Rio de Janeiro, vol. 115, n. 200430, p. 1-9, 2020.

FRANÇA, V. L.B.; AMARAL, J. L.; MARTINS, Y. A.; CAETANO, E. W.S.; BRUNALDI, K.; FREIRE, V. N. Characterization of the binding interaction between atrazine and human serum albumin: Fluorescence spectroscopy, molecular dynamics and quantum biochemistry. **Chemico-Biological Interactions**, Limerick, vol. 366, p.

110130, 2022.

FREIRE, R. V.M.; PILLCO-VALENCIA, Y.; DA HORA, G. C.A.; RAMSTEDT, M.; SANDBLAD, L.; SOARES, T. A.; SALENTINIG, S. Antimicrobial peptide induced colloidal transformations in bacteria-mimetic vesicles: Combining in silico tools and experimental methods. **Journal of Colloid and Interface Science**, Nova Iorque, vol. 596, p. 352–363, 2021.

FU, L.; LE, T.; LIU, Z.; WANG, L.; GUO, H.; YANG, J.; CHEN, Q.; HU, J.. Different efficacies of common disinfection methods against candida auris and other candida species. **Journal of Infection and Public Health**, Riyadh, vol. 13, n. 5, p. 730–736, 2020.

GALDIERO, E.; LOMBARDI, L.; FALANGA, A.; LIBRALATO, G.; GUIDA, M.; CAROTENUTO, R. Biofilms: Novel Strategies Based on Antimicrobial Peptides. **Pharmaceutics**, Basel, vol. 11, nº 7, p. 322, 2019.

GARCÍA-ORTEGÓN, M.; SIMM, G. N. C.; TRIPP, A. J.; HERNÁNDEZ-LOBATO, J. M.; BENDER, A.; BACALLADO, S. DOCKSTRING: Easy Molecular Docking Yields Better Benchmarks for Ligand Design. **Journal of Chemical Information and Modeling**, Washington, vol. 62, n. 15, p. 3486–3502, 2022.

GAWAS, U. B.; MANDREKAR, V. K.; MAJIK, M. S. Structural analysis of proteins using X-ray diffraction technique. *In*: MEENA, S. N.; NAIK, M. M. **Advances in Biological Science Research**. Cambridge: Academic Press, 2019, p. 69–84.

GOUTHAMI, K.; VEERARAGHAVAN, V.; RAHDAR, A.; BILAL, M.; SHAH, A.; RAI, V.; GURUMURTHY, D. M.; FERREIRA, L. F. R.; AMÉRICO-PINHEIRO, J. H. P.; MURARI, S. K.; KALIA, S.; MULLA, S. I. Molecular docking used as an advanced tool to determine novel compounds on emerging infectious diseases: A systematic review. **Progress in Biophysics and Molecular Biology**, Londres, p. 1-24, 2022.

HOFNY, H. A.; MOHAMED, M. F.A.; GOMAA, H. A.M.; ABDEL-AZIZ, S. A.; YOUSSIF, B. G.M.; EL-KOUSSI, N. A.; ABORAIA, A. S. Design, synthesis, and antibacterial evaluation of new quinoline-1,3,4-oxadiazole and quinoline-1,2,4-triazole hybrids as potential inhibitors of DNA gyrase and topoisomerase IV. **Bioorganic Chemistry**, Minneapolis, vol. 112, p. 104920, 2021.

HOLLMANN, A.; MARTINEZ, M.; MATURANA, P.; SEMORILE, L. C.; MAFFIA, P. C. Antimicrobial Peptides: Interaction With Model and Biological Membranes and Synergism With Chemical Antibiotics. **Frontiers in Chemistry**, Lausanne, vol. 6, n. 204, p. 1-13, 2018.

HONG, C.; BYRNE, N. J.; ZAMLYNNY, B.; TUMMALA, S.; XIAO, L.; SHIPMAN, J. M.; PARTRIDGE, A. T.; MINNICK, C.; BRESLIN, M. l J.; RUDD, M. T.; STACHEL, S. J.; RADA, V. L.; KERN, J. C.; ARMACOST, K. A.; HOLLINGSWORTH, S. A.; O'BRIEN, J. A.; HALL, D. L.; MCDONALD, T. P.; STRICKLAND, C.; HOLLENSTEIN, K. Structures of active-state orexin receptor 2 rationalize peptide and small-molecule agonist recognition and receptor activation. **Nature Communications**, Londres, vol. 12, n. 1, p. 815, 2021.

HU, B.; GUO, H.; ZHOU, P.; SHI, Z. L. Characteristics of SARS-CoV-2 and COVID-19. **Nature Reviews Microbiology**, Londres, vol. 19, n. 3, p. 141–154, 2021.

JING, Z.; LIU, C.; CHENG, S. Y.; QI, R.; WALKER, B. D.; PIQUEMAL, J. P.; REN, P. Polarizable Force Fields for Biomolecular Simulations: Recent Advances and Applications. **Annual Review of Biophysics**, Santa Clara, vol. 48, n. 1, p. 371–394, 2019.

JO, S.; LIM, J. B.; KLAUDA, J. B.; IM, W. CHARMM-GUI Membrane Builder for Mixed Bilayers and Its Application to Yeast Membranes. **Biophysical Journal**, Nova Iorque, vol. 97, n. 1, p. 50–58, jul. 2009.

JUMPER, J.; EVANS, R.; PRITZEL, A.; GREEN, T.; FIGURNOV, M.; RONNEBERGER, O.; TUNYASUVUNAKOOL, K.; BATES, R.; ŽÍDEK, A.; POTAPENKO, A.; BRIDGLAND, A.; MEYER, C.; KOHL, S. A. A.; BALLARD, A. J.; COWIE, A.; ROMERA-PAREDES, B.; NIKOLOV, S.; JAIN, R.; ADLER, J.; HASSABIS, D. Highly accurate protein structure prediction with AlphaFold. **Nature**, Londres, vol. 596, nº 7873, p. 583–589, 2021a.

KALSY, M.; TONK, M.; HARDT, M.; DOBRINDT, U.; ZDYBICKA-BARABAS, A.; CYTRYNSKA, M.; VILCINSKAS, A.; MUKHERJEE, K. The insect antimicrobial peptide cecropin A disrupts uropathogenic Escherichia coli biofilms. **npj Biofilms and Microbiomes**, Nova Iorque, vol. 6, n. 1, p. 6, 2020.

KIM, H.; YOO, Y.; LEE, G. Y. Identification of Bacterial Membrane Selectivity of Romo1-Derived Antimicrobial Peptide AMPR-22 via Molecular Dynamics. **International Journal of Molecular Sciences**, Basel, vol. 23, n. 13, p. 7404, 2022.

KOZAKOV, D.; HALL, D. R; XIA, B.; PORTER, K. A; PADHORNY, D.; YUEH, C.; BEGLOV, D.; VAJDA, S. The ClusPro web server for protein–protein docking. **Nature Protocols**, Londres, vol. 12, n. 2, p. 255–278, 2017a.

LAI, Z.; YUAN, X.; CHEN, H.; ZHU, Y.; DONG, N.; SHAN, A. Strategies employed in the design of antimicrobial peptides with enhanced proteolytic stability. **Biotechnology Advances**, Nova Iorque, vol. 59, p. 107962, 2022.

LANDIM, P. G. C.; CORREIA, T. O.; SILVA, F. D.A.; NEPOMUCENO, D. R.; COSTA, H. P.S.; PEREIRA, H. M.; LOBO, M. D.P.; MORENO, F. B.M.B.; BRANDÃO-NETO, J.; MEDEIROS, S. C.; VASCONCELOS, I. M.; OLIVEIRA, J. T.A.; SOUSA, B. L.; BARROSO-NETO, I. L.; FREIRE, V. N.; CARVALHO, C. P.S.; MONTEIRO-MOREIRA, A. C.O.; GRANGEIRO, T. B. Production in Pichia pastoris, antifungal activity and crystal structure of a class I chitinase from cowpea (Vigna unguiculata): Insights into sugar binding mode and hydrolytic action. **Biochimie**, Paris, vol. 135, p. 89–103, 2017.

LEE, H.; LIM, S. I.; SHIN, S. H.; LIM, Y.; KOH, J. W.; YANG, S. Conjugation of Cell-Penetrating Peptides to Antimicrobial Peptides Enhances Antibacterial Activity. **ACS Omega**, Washington, vol. 4, n. 13, p. 15694–15701, 2019.

LEE, J.; PATEL, D. S.; STÅHLE, J.; PARK, S. J.; KERN, N. R.; KIM, S.; LEE, J.; CHENG, Xi; VALVANO, M. A.; HOLST, O.; KNIREL, Y. A.; QI, Y.; JO, S.; KLAUDA, J. B.; WIDMALM, G.; IM, W. CHARMM-GUI *Membrane Builder* for Complex Biological Membrane Simulations with Glycolipids and Lipoglycans. **Journal of Chemical Theory and Computation**, Washington, vol. 15, n. 1, p. 775–786, 2019.

LEMKUL, J. From Proteins to Perturbed Hamiltonians: A Suite of Tutorials for the GROMACS-2018 Molecular Simulation Package. **Living Journal of Computational Molecular Science**, Boulder, vol. 1, n. 1, p. 1-53, 2019.

LENSINK, M. F.; NADZIRIN, N.; VELANKAR, S.; WODAK, S. J. Modeling protein-protein, protein-peptide, and protein-oligosaccharide complexes: CAPRI 7th edition. **Proteins: Structure, Function, and Bioinformatics**, Nova Iorque, vol. 88, n. 8, p. 916–938, 2020.

LIMA, P. G.; OLIVEIRA, J. T.A.; AMARAL, J. L.; FREITAS, C. D.T.; SOUZA, P. F.N. Synthetic antimicrobial peptides: Characteristics, design, and potential as alternative molecules to overcome microbial resistance. **Life Sciences**, Oxford, vol. 278, p. 119647, 2021.

LIN, H. Y.; CHEN, X.; DONG, J.; YANG, J. F.; XIAO, H.; YE, Y.; LI, L. H.; ZHAN, C. G.; YANG, W. C.; YANG, G. F. Rational Redesign of Enzyme via the Combination of Quantum Mechanics/Molecular Mechanics, Molecular Dynamics, and Structural Biology Study. **Journal of the American Chemical Society**, Washington, vol. 143, n. 38, p. 15674–15687, 2021.

MA, L.; DIAO, L.; PENG, Z.; JIA, Y.; XIE, H.; LI, B.; MA, J.; ZHANG, M.; CHENG, L.; DING, D.; ZHANG, X.; CHEN, H.; MO, F.; JIANG, H.; XU, G.; MENG, F.; ZHONG, Z.; LIU, M. Immunotherapy and Prevention of Cancer by Nanovaccines Loaded with Whole-Cell Components of Tumor Tissues or Cells. **Advanced Materials**, Weinheim, vol. 33, n. 43, p. 2104849, 2021.

MALDONADO, L. L.; BERTELLI, A. M.; KAMENETZKY, L. Molecular features similarities between SARS-CoV-2, SARS, MERS and key human genes could favour the viral infections and trigger collateral effects. **Scientific Reports**, Londres, vol. 11, n. 1, p. 4108, 2021.

MARTÍNEZ-ROSELL, G.; GIORGINO, T.; DE FABRITIIS, G.. PlayMolecule ProteinPrepare: A Web Application for Protein Preparation for Molecular Dynamics Simulations. **Journal of Chemical Information and Modeling**, Washington, vol. 57, n. 7, p. 1511–1516, 2017.

MATSOUKAS, J. M.; LIGIELLI, I.; CHASAPIS, C. T.; KELAIDONIS, K.; APOSTOLOPOULOS, V.; MAVROMOUSTAKOS, T. Novel Approaches in the Immunotherapy of Multiple Sclerosis: Cyclization of Myelin Epitope Peptides and Conjugation with Mannan. **Brain Sciences**, Basel, vol. 11, n. 12, p. 1583, 2021.

MIYAGUCHI, I.; SATO, M.; KASHIMA, A.; NAKAGAWA, H.; KOKABU, Y.; MA, B.; MATSUMOTO, S.; TOKUHISA, A.; OHTA, M.; IKEGUCHI, M.. Machine learning to estimate the local quality of protein crystal structures. **Scientific Reports**, Londres,

vol. 11, n. 1, p. 23599, 2021.

MOLAEI, P.; MAHAKI, H.; MANOOCHEHRI, H.; TANZADEHPANAH, H. Binding Sites of Anticancer Drugs on Human Serum Albumin (HSA): A Review. **Protein & Peptide Letters**, Schiphol, vol. 29, n. 8, p. 651–675, 2022.

MOOKHERJEE, N.; ANDERSON, M. A.; HAAGSMAN, H. P.; DAVIDSON, D. J. Antimicrobial host defence peptides: functions and clinical potential. **Nature Reviews Drug Discovery**, Londres, vol. 19, n. 5, p. 311–332, 2020.

MORAIS, P. A.; MAIA, F. F.; SOLIS-CALERO, C.; CAETANO, E. W. S.; FREIRE, V. N.; CARVALHO, H. F. The urokinase plasminogen activator binding to its receptor: a quantum biochemistry description within an in/homogeneous dielectric function framework with application to uPA–uPAR peptide inhibitors. **Physical Chemistry Chemical Physics**, Cambridge, vol. 22, n. 6, p. 3570–3583, 2020.

MORGNANESI, D.; HEINRICHS, E. J.; MELE, A. R.; WILKINSON, S.; ZHOU, S.; KULP, J. L. A computational chemistry perspective on the current status and future direction of hepatitis B antiviral drug discovery. **Antiviral Research**, Amsterdã, vol. 123, p. 204–215, 2015.

MORRIS, C. J.; CORTE, D. Using molecular docking and molecular dynamics to investigate protein-ligand interactions. **Modern Physics Letters B**, Singapura, vol. 35, n. 08, p. 2130002, 2021.

NGO, S. T.; TAM, N. M.; PHAM, M. Q.; NGUYEN, T. H. Benchmark of Popular Free Energy Approaches Revealing the Inhibitors Binding to SARS-CoV-2 Mpro. **Journal of Chemical Information and Modeling**, Washington, vol. 61, n. 5, p. 2302–2312, 2021.

ORTEGA, N.; SÁEZ, L.; PALACIOS, D.; BUSTO, M. D. Kinetic Modeling, Thermodynamic Approach and Molecular Dynamics Simulation of Thermal Inactivation of Lipases from Burkholderia cepacia and Rhizomucor miehei. **International Journal of Molecular Sciences**, Basel, vol. 23, n. 12, p. 6828, 2022.

PÁLL, S.; ZHMUROV, A.; BAUER, P.; ABRAHAM, M.; LUNDBORG, M.; GRAY, A.; HESS, B.; LINDAHL, E. Heterogeneous parallelization and acceleration of molecular dynamics simulations in GROMACS. **The Journal of Chemical Physics**, Nova Iorque, vol. 153, n. 13, p. 134110, 2020.

PANDEY, B.; TYAGI, C.; PRAJAPATI, G. K.; MISHRA, A. K.; HASHEM, A.; ALQARAWI, A. A.; ABD_ALLAH, E. F.; MOHANTA, T. K. Analysis of mutations of defensin protein using accelerated molecular dynamics simulations. **PLOS ONE**, São Francisco, vol. 15, n. 11, p. 241679, 2020.

PAWAR, S. S.; ROHANE, S. H. Review on Discovery Studio: An important Tool for Molecular Docking. **Asian Journal Of Research in Chemistry**, Raipur, vol. 14, n. 1, p. 1–3, 2021.

RASMUSSEN, Angela L.; POPESCU, Saskia v. SARS-CoV-2 transmission without

symptoms. **Science**, Washington, vol. 371, n. 6535, p. 1206–1207, 2021.

ROSTAMI, S.; JAFARI, S.; MOEINI, Z.; JASKULAK, M.; KESHTGAR, L.; BADEENEZHAD, A.; AZHDARPOOR, A.; ROSTAMI, M.; ZORENA, K.; DEHGHANI, M. Current methods and technologies for degradation of atrazine in contaminated soil and water: A review. **Environmental Technology & Innovation**, Amsterdã, vol. 24, p. 102019, 2021.

ROWSHANRAVAN, B.; HALLIDAY, N.; SANSOM, D. M. CTLA-4: a moving target in immunotherapy. **Blood**, Washington, vol. 131, n. 1, p. 58–67, 2018.

RZYCKI, M.; KRASZEWSKI, S.; DRABIK, D. Towards Mimetic Membrane Systems in Molecular Dynamics: Characteristics of E. Coli Membrane System. **Langmuir**, Nova Iorque, vol. 36, n. 14, p. 3826–3835, 2021.

SERGIO, L. M.; MARTINS, Y. A.; AMARAL, J. L.; FRANÇA, V. L.B.; DE FREITAS, C. F.; NETO, A. M.; HIOKA, N.; RAVANELLI, M. I.; MAREZE-COSTA, C.; CLAUDIO DA COSTA, S.; FREIRE, V. N.; BRUNALDI, K. Molecular insight on the binding of stevia glycosides to bovine serum albumin. **Chemico-Biological Interactions**, Limerick, vol. 344, p. 109526, 2021.

SHEN, Y.; MAUPETIT, J.; DERREUMAUX, P.; TUFFÉRY, P. Improved PEP-FOLD Approach for Peptide and Miniprotein Structure Prediction. **Journal of Chemical Theory and Computation**, Washington, vol. 10, n. 10, p. 4745–4758, 2014.

SHULI, Z.; LINLIN, L.; LI, G.; YINGHU, Z.; NAN, S.; HAIBIN, W.; HONGYU, X. Bioinformatics and Computer Simulation Approaches to the Discovery and Analysis of Bioactive Peptides. **Current Pharmaceutical Biotechnology**, Hilversum, vol. 23, n. 13, p. 1541–1555, 2022.

SHWAIKI, L. N.; LYNCH, K. M.; ARENDT, E. K. Future of antimicrobial peptides derived from plants in food application – A focus on synthetic peptides. **Trends in Food Science & Technology**, Oxford, vol. 112, p. 312–324, 2021.

SINGH, D. K.; TÓTH, R.; GÁCSER, A. Mechanisms of Pathogenic Candida Species to Evade the Host Complement Attack. **Frontiers in Cellular and Infection Microbiology**, Lausanne, vol. 10, 2020.

SOUZA, P. F. N.; AMARAL, J. L.; BEZERRA, L. P.; LOPES, F. E. S.; FREIRE, V. N.; OLIVEIRA, J. T. A.; FREITAS, C. D. T. ACE2-derived peptides interact with the RBD domain of SARS-CoV-2 spike glycoprotein, disrupting the interaction with the human ACE2 receptor. **Journal of Biomolecular Structure and Dynamics**, Oxford, vol. 40, n. 12, p. 5493–5506, 2022.

SOUZA, P. F.N.; LOPES, F. E.S.; AMARAL, J. L.; FREITAS, C. D.T.; OLIVEIRA, J.T.A. A molecular docking study revealed that synthetic peptides induced conformational changes in the structure of SARS-CoV-2 spike glycoprotein, disrupting the interaction with human ACE2 receptor. **International Journal of Biological Macromolecules**, Amsterdã, vol. 164, p. 66–76, 2020.

SOUZA, P. F.N.; MESQUITA, F. P.; AMARAL, J. L.; LANDIM, P. G.C.; LIMA, K. R.P.; COSTA, M. B.; FARIAS, I. R.; BELÉM, M. O.; PINTO, Y. O.; MOREIRA, H. H.T.; MAGALHAES, I. C.L.; CASTELO-BRANCO, D. S.C.M.; MONTENEGRO, R. C.; DE ANDRADE, C. R. The spike glycoprotein of SARS-CoV-2: A review of how mutations of spike glycoproteins have driven the emergence of variants with high transmissibility and immune escape. **International Journal of Biological Macromolecules**, Amsterdã, vol. 208, p. 105–125, 2022.

SOUZA, P. F.N.; MESQUITA, F. P.; AMARAL, J. L.; LANDIM, P. G.C.; LIMA, K. R.P.; COSTA, M. B.; FARIAS, I. R.; LIMA, L. B.; MONTENEGRO, R. C. The human pandemic coronaviruses on the show: The spike glycoprotein as the main actor in the coronaviruses play. **International Journal of Biological Macromolecules**, Amsterdã, vol. 179, p. 1–19, 2021.

SOUZA, P. F.N.; VANTILBURG, M. F.; MESQUITA, F. P.; AMARAL, J. L.; LIMA, L. B.; MONTENEGRO, R. C.; LOPES, F. E.S.; MARTINS, R. X.; VIEIRA, L.; FARIAS, D. F.; MONTEIRO-MOREIRA, A. C. O.; FREITAS, C. D.T.; BEZERRA, A. S.; GUEDES, M. I. F.; CASTELO-BRANCO, D. S.C.M.; OLIVEIRA, J. T.A. Neutralizing Effect of Synthetic Peptides toward SARS-CoV-2. **ACS Omega**, Washington, vol. 7, n. 18, p. 16222–16234, 2022.

STANZIONE, F.; GIANGRECO, I.; COLE, J. C. Use of molecular docking computational tools in drug discovery. *In* WITTY, D. R.; COX, B. **Progress in Medicinal Chemistry**, San Diego: Elsevier, 2021. p. 273–343.

STUDER, G.; REMPFER, C.; WATERHOUSE, A. M; GUMIENNY, R.; HAAS, J.; SCHWEDE, Tn. QMEANDisCo—distance constraints applied on model quality estimation. **Bioinformatics**, Oxford, vol. 36, n. 6, p. 1765–1771, 2020.

STUDER, G.; TAURIELLO, G.; BIENERT, S.; BIASINI, M.; JOHNER, N.; SCHWEDE, T. ProMod3—A versatile homology modelling toolbox. **PLOS Computational Biology**, São Francisco, vol. 17, n. 1, p. 1008667, 2021.

TIMMONS, P. B.; O'FLYNN, D.; CONLON, J. M.; HEWAGE, C. M. Structural and positional studies of the antimicrobial peptide brevinin-1BYa in membrane-mimetic environments. **Journal of Peptide Science**, Chichester, vol. 25, n. 11, 2019.

TING, D. S. J.; LI, J.; VERMA, C. S.; GOH, E. T. L.; NUBILE, M.; MASTROPASQUA, L.; SAID, D. G.; BEUERMAN, R. W.; LAKSHMINARAYANAN, R.; MOHAMMED, I.; DUA, H. S. Evaluation of Host Defense Peptide (CaD23)-Antibiotic Interaction and Mechanism of Action: Insights From Experimental and Molecular Dynamics Simulations Studies. **Frontiers in Pharmacology**, Lausanne, vol. 12, 2021.

TROTT, O.; OLSON, A. J. AutoDock Vina: Improving the speed and accuracy of docking with a new scoring function, efficient optimization, and multithreading. **Journal of Computational Chemistry**, Nova Iorque, vol. 31, p. 455-461, 2009.

TUNYASUVUNAKOOL, K.; ADLER, J.; WU, Z.; GREEN, T.; ZIELINSKI, M.; ŽÍDEK, A.; BRIDGLAND, A.; COWIE, A.; MEYER, C.; LAYDON, A.; VELANKAR, S.; KLEYWEGT, G. J.; BATEMAN, A.; EVANS, R.; PRITZEL, A.; FIGURNOV, M.;

RONNEBERGER, O.; BATES, R.; KOHL, S. A. A.; HASSABIS, D.. Highly accurate protein structure prediction for the human proteome. **Nature**, Londres, vol. 596, n. 7873, p. 590–596, 2021.

UPPAL, S.; LIU, T.; GALVAN, E.; GOMEZ, F.; TITTLEY, T.; POLIAKOV, E.; GENTLEMAN, S.; REDMOND, T. M.. An inducible amphipathic α-helix mediates subcellular targeting and membrane binding of RPE65. **Life Science Alliance**, Woodbury, vol. 6, n. 1, p. 202201546, 2023.

UZUNIAN, A. Coronavirus SARS-CoV-2 and Covid-19. **Jornal Brasileiro de Patologia e Medicina Laboratorial**, Rio de Janeiro, vol. 53, n. 3, p. 148-149, 2020.

VAN DIJCK, P.; SJOLLEMA, J.; CAMUE, B. P.A.; LAGROU, K.; BERMAN, J.; D'ENFERT, C.; ANDES, D. R.; ARENDRUP, M. C.; BRAKHAGE, A. A.; CALDERONE, R.; CANTÓN, E.; COENYE, T.; COS, P.; COWEN, L. E.; EDGERTON, M.; ESPINEL-INGROFF, A.; FILLER, S. G.; GHANNOUM, M.; A.R. GOW, N.; THEVISSEN, K. Methodologies for in vitro and in vivo evaluation of efficacy of antifungal and antibiofilm agents and surface coatings against fungal biofilms. **Microbial Cell**, Graz, vol. 5, n. 7, p. 300–326, 2018.

VELASCO-BOLOM, J. L.; CORZO, G.; GARDUÑO-JUÁREZ, R. Molecular dynamics simulation of the membrane binding and disruption mechanisms by antimicrobial scorpion venom-derived peptides. **Journal of Biomolecular Structure and Dynamics**, Oxford, vol. 36, n. 8, p. 2070–2084, 2018.

VENABLE, R. M.; KRÄMER, A.; PASTOR, R. W. Molecular Dynamics Simulations of Membrane Permeability. **Chemical Reviews**, Easton, vol. 119, n. 9, p. 5954–5997, 2019.

WANG, J.; ARANTES, P. R.; BHATTARAI, A.; HSU, R. V.; PAWNIKAR, S.; HUANG, Y. M.; PALERMO, G.; MIAO, Y. Gaussian accelerated molecular dynamics: Principles and applications. **WIREs Computational Molecular Science**, Malden, vol. 11, n. 1521, 2021.

WANG, L.; WANG, N.; ZHANG, W.; CHENG, X.; YAN, Z.; SHAO, G.; WANG, X.; WANG, R.; FU, C.. Therapeutic peptides: current applications and future directions. **Signal Transduction and Targeted Therapy**, Londres, vol. 7, n. 1, p. 48, 2022.

WATERHOUSE, A.; BERTONI, M.; BIENERT, S.; STUDER, G.; TAURIELLO, G.; GUMIENNY, R.; HEER, F. T.; DE BEER, T. A. P.; REMPFER, C.; BORDOLI, L.; LEPORE, R.; SCHWEDE, T. SWISS-MODEL: homology modelling of protein structures and complexes. **Nucleic Acids Research**, Oxford, vol. 46, n. 1, p. 296–303, 2018.

WILLSMORE, Z. N.; COUMBE, B. G. T.; CRESCIOLI, S.; RECI, S.; GUPTA, A.; HARRIS, R. J.; CHENOWETH, A.; CHAUHAN, J.; BAX, H. J.; MCCRAW, A.; CHEUNG, A.; OSBORN, G.; HOFFMANN, R. M.; NAKAMURA, M.; LADDACH, R.; GEH, J. L. C.; MACKENZIE-ROSS, A.; HEALY, C.; TSOKA, S.; KARAGIANNIS, S. N. Combined anti-PD-1 and anti-CTLA-4 checkpoint blockade: Treatment of melanoma and immune mechanisms of action. **European Journal of Immunology**, Weinheim,

vol. 51, n. 3, p. 544–556, 2021.

WOJTUKIEWICZ, M. Z.; REK, M. M.; KARPOWICZ, K.; GÓRSKA, M.; POLITYŃSKA, B.; WOJTUKIEWICZ, A. M.; MONIUSZKO, M.; RADZIWON, P.; TUCKER, S. C.; HONN, K. V. Inhibitors of immune checkpoints—PD-1, PD-L1, CTLA-4—new opportunities for cancer patients and a new challenge for internists and general practitioners. **Cancer and Metastasis Reviews**, Boston, vol. 40, n. 3, p. 949–982, 2021.

YOUNG, J. Y.; BERRISFORD, J.; CHEN, M. wwPDB biocuration: on the front line of structural biology. **Nature Methods**, Londres, vol. 18, n. 5, p. 431–432, 2021.

ZHOU, M.; ZHAO, J.. A Review on the Health Effects of Pesticides Based on Host Gut Microbiome and Metabolomics. **Frontiers in Molecular Biosciences**, Lausanne, vol. 8, n. 632955, p. 1-10, 2021.

APÊNDICE A – COMPUTATIONAL APPROACH, SCANNING ELECTRON AND FLUORESCENCE MICROSCOPIES REVEALED INSIGHTS INTO THE ACTION MECHANISMS OF ANTICANDIDAL PEPTIDE *MO*-CBP$_3$-PEPIII

Life Sciences 281 (2021) 119775

Contents lists available at ScienceDirect

Life Sciences

journal homepage: www.elsevier.com/locate/lifescie

Computational approach, scanning electron and fluorescence microscopies revealed insights into the action mechanisms of anticandidal peptide *Mo*-CBP$_3$-PepIII

Jackson L. Amaral [a,b,*], Pedro F.N. Souza [a], Jose T.A. Oliveira [a], Valder N. Freire [b], Daniele O. B. Sousa [a,*]

[a] Department of Biochemistry and Molecular Biology, Federal University of Ceará, Fortaleza, Ceará CEP 60.440-554, Brazil
[b] Department of Physics, Federal University of Ceará, Fortaleza, Ceará CEP 60.440-554, Brazil

ARTICLE INFO

Keywords:
Mo-CBP$_3$-PepIII
Molecular dynamics
Quantum biochemistry
Membrane insertion

ABSTRACT

Aims: The *Candida* genus is composed of opportunistic pathogens that threaten public health. Given the increase in resistance to current drugs, it is necessary to develop new drugs to treat infections by these pathogens. Antimicrobial peptides are promising alternative molecules with low cost, broad action spectrum and low resistance induction. This study aimed to clarify the action mechanisms of synthetic peptides against *Candida albicans*.

Main methods: The mode of action of the anticandidal peptides *Mo*-CBP$_3$-PepIII were analyzed through molecular dynamics and quantum biochemistry methods against Exo-β-1,3-glucanase (EXG), vital to cell wall metabolism. Furthermore, scanning electron (SEM) and fluorescence (FM) microscopies were employed to corroborate the *in silico* data.

Key findings: Mo-CBP$_3$-PepIII strongly interacted with EXG (−122.2 kcal mol^{-1}) at the active site, higher than the commercial inhibitor pepstatin. Also, molecular dynamics revealed the insertion of *Mo*-CBP$_3$-PepIII into the yeast membrane. SEM analyses revealed that *Mo*-CBP$_3$-PepIII induced cracks and scars of the cell wall and FM analyses confirmed the pore formation on the *Candida* membrane.

Significance: Mo-CBP$_3$-PepIII has strong potential as a new drug with a broad spectrum of action, given its different mode of action compared to conventional drugs.

1. Introduction

The *Candida* genus contains the most important human pathogenic yeasts responsible for invasive candidiasis. Typically, these pathogens cause human mortality mainly in immunosuppressed patients [1,2]. It is estimated that *Candida* ssp. are responsible for 8 to 10% of bloodstream infections in intensive care units (ICUs), and *Candida albicans* cause at least 50% of them [3,4]. Recently, cases of candidiasis caused by other *Candida* species have been reported, such as *C. krusei* and *C. parapsilosis*, with resistance to conventional treatments available [5,6].

Candida spp. have several proteins that are targeted by commercially available drugs. The protein sterol 14-demethylase (CYP51), involved in the synthesis of sterols, is a target of azole drugs such as fluconazole, voriconazole, itraconazole and posaconazole [7]. Exo-1,3-β-glucanases (EXG) and Exo-1,3-β-synthases are responsible for glucan organization in the fungal cell wall. These proteins are targeted by echinocandins, such as caspofungin, micafungin, and anidulafungin [8]. Some secondary metabolites of plants have inhibitory activity against these enzymes, such as the alkaloids castanospermine, a tetrahydroxyindolizidine alkaloid that is a potent inhibitor of exo-1,3-β-glucanases (EXG) [9]. Inhibition of EXG and/or Exo-1,3-β-synthase impairs the turnover of the cell wall, leading to osmotic imbalance, increased membrane permeability, loss of cytoplasmic content, and cell death [10]. The secreted aspartic proteases (SAPs) are indicated as promising targets for the development of new drugs since they participate in fungal extracellular metabolism and are important in the development of biofilms [11]. The resistance to conventional antifungal drugs suggests that the current strategies to treat diseases caused by *Candida* species will soon become

* Corresponding authors at: Biochemistry and Molecular Biology Department, Federal University of Ceará, Laboratory of Plant Defense Proteins, Av. Mister Hull, P. O. Box: 60451, Fortaleza, CE, Brazil.
E-mail addresses: jacksoncesarc@gmail.com (J.L. Amaral), daniele.sousa@ufc.br (D.O.B. Sousa).

https://doi.org/10.1016/j.lfs.2021.119775
Received 26 November 2020; Received in revised form 9 June 2021; Accepted 20 June 2021
Available online 26 June 2021
0024-3205/© 2021 Elsevier Inc. This article is made available under the Elsevier license (http://www.elsevier.com/open-access/userlicense/1.0/).

inefficient [12]. In this context, the development of new active molecules employing different action mechanisms from known drugs is essential to continue obtaining successful treatments.

In this respect, natural antimicrobial peptides (nAMPs) have substantial unexplored potential to develop new drugs [13,14]. However, natural AMPs present some limitations, such as low resistance to proteolysis, high purification cost, low yield, and sometimes toxicity to the host. Therefore, synthetic antimicrobial peptides (sAMP) derived from nAMPs have received more attention as alternatives to produce new drugs. Additionally, the computational approach has been widely employed to develop new drugs because it can provide faster screening of large numbers of molecules with low cost.

Our research group recently developed a sAMP named *Mo*-CBP$_3$-PepIII, with AIQRCC amino acid sequence, mass of 692.85 kDa, net positive charge of +1 and a hydrophobic ratio of 66% [15]. The hydrophobic ratio of *Mo*-CBP$_3$-PepIII is similar to found in known pore-forming peptides, demonstrating its potential to form pores in membranes (Sup. Table 1). Additionally, bioinformatics analysis indicated *Mo*-CBP$_3$-PepIII is a cell-penetrating peptide [15]. *Mo*-CBP$_3$-PepIII presents MIC$_{90\%}$ values at low concentrations of 4.4 and 2.2 μM against *C. albicans* and *C. parapsilosis*, respectively, and MIC$_{50\%}$ values of 17.5 and 2.2 μM against *C. krusei* and *C. tropicalis*, respectively. Moreover, *Mo*-CBP$_3$-PepIII does not exhibit either hemolytic activity against ABO-type human blood cells or toxic activity against Vero cells even at concentration 120 times higher than the antimicrobial concentration. The study also found a 20 kDa pore size in *C. parapsilosis* membranes, indicating membranes are a target of *Mo*-CBP$_3$-PepIII [15].

Therefore, investigation of the molecular dynamics of AMP-membrane interactions and activity against important cell proteins for *C. albicans* survival can provide insights into their mechanism of action. A new approach using realistic membrane simulation is a potent technique to examine membrane complexity and variety of components [13]. The results obtained in this study provide specific insights into the mode of action of *Mo*-CBP$_3$-PepIII and its interaction with a crucial enzyme and biomimetic membranes.

2. Materials and methods

2.1. Structural data

The peptide's 3D structure was the same as predicted by Oliveira et al. [15] using the PEP-FOLD Server (http://bioserv.rpbs.univ-paris-diderot.fr/services/PEP-FOLD/), and this structure was used for molecular dynamics simulation in NAMD during 100 ns under the same conditions as described in 2.3. The final conformation of the simulation was used in the subsequent analyses. All structural analyses were performed with data on the X-ray crystal structures of sterol 14-alpha demethylase (CYP51) (PDB ID: 5V5Z) [16], secreted aspartic proteinase (Sap) 1 (PDB ID: 2QZW), secreted aspartic proteinase (Sap) 5 (PDB ID: 2QZX) [17], and Exo-β-(1,3)-glucanase (EXG) (PDB ID: 1CZ1) [18]. The H^+ state of all receptors was adjusted according to data obtained from the PROPKA 3.1 web server tool (http://propka.ki.ku.dk/) and the protonation tool in the Discovery Studio package.

2.2. Molecular docking

Molecular docking was performed with Autodock Vina, version 1.1.2, which uses the efficient quasi-Newton method and Broyden–Fletcher–Goldfarb–Shanno (BFGS) method for local optimization [19]. The Autodock graphical interface, AutoDockTools, version 1.5.6, was used to retain polar hydrogens and to add partial charges to the proteins and ligands using the Kollman united charges [20]. The receptors and ligand (*Mo*-CBP$_3$-PepIII) were treated as rigid and flexible molecules. The grid box was defined by a cube measuring 60 Å × 60 Å × 60 Å with the receptor in the center. Exhaustiveness was set at 15, and all other parameters were used as default. The ten top-ranked peptide conformations based on the docking score (in kilocalories per mole [kcal mol^{-1}]) were analyzed. The poses were first classified into clusters, in which the poses were grouped using a RMSD-tolerance of 2.0 Å, and the clusters were then analyzed regarding steric criteria. The most suitable result was further ranked based on steric criteria, according to the number of poses of each cluster and the docking score (given as a negative score in kcal mol^{-1}).

2.3. Molecular dynamics

To obtain structures with energy close to minimum global energy and more stable, the two systems of interest (*Mo*-CBP$_3$-PepIII/SAP5 and *Mo*-CBP$_3$-PepIII/EXG) were minimized, equilibrated and submitted to molecular dynamics simulation using GROMACS version 2018.4 [21]. Initially, the topology was recorded using the OPLS-AA/L all-atom force field [22,23], after which a cubic box was created with 2 nm from the box edge. The box solvation was performed with the SPC/E water model. The systems were neutralized and Na^+ and Cl^- ions were added at a concentration of 0.15 M. The minimization was carried out until the potential energy was negative and the maximum force was less than 1000 kJ mol^{-1} nm^{-1}. Next, the equilibration of temperature (canonical NVT) and pressure (NPT ensemble, isothermal-isobaric) was performed for 100 ps using 300 K and 1 bar as reference temperature and pressure, respectively. Finally, the molecular dynamics simulations were performed during 100 ns using a short-range electrostatic and van der Waals cutoff of 1 nm and the particle mesh Ewald method for long-range electrostatics. The final structures were obtained and the stable complexes were used for further analysis. The final structure was visualized using the VMD software.

2.4. Molecular fractionation with conjugate caps (MFCC) and quantum biochemistry

A detailed energetic description of the interaction between the receptors and *Mo*-CBP$_3$-PepIII was performed by quantum mechanics calculations. The MFCC scheme was applied, which is a handy approach that provides an accurate description of biological systems through quantum calculations [24,25]. The method modified by Morais et al. [26] was applied to describe protein-peptide interactions, and the interaction energy between two specific residues (Ri and Rj) was calculated as follows:

$$E_I(R_i - R_j) = E(C_{i-1}R_iC_{i+1} + C_{j-1}R_jC_{j+1}) - E(C_{i-1}R_iC_{i+1} + C_{j-1}C_{j+1}) - E(C_{i-1}C_{i+1} + C_{j-1}R_jC_{j+1}) + E(C_{i-1}C_{i+1} + C_{j-1}C_{j+1})$$

On the right-hand side of the equation, the first term, $E(C_{i-1}R_iC_{i+1} + C_{j-1}R_jC_{j+1})$, is the total energy of the system formed by two interacting residues with their caps; the second term, $E(C_{i-1}R_iC_{i+1} + C_{j-1}C_{j+1})$, gives the total energy of the system formed by the capped residue R_i without the residue R_j; the third term, $E(C_{i-1}C_{i+1} + C_{j-1}R_jC_{j+1})$, is the total energy of the system formed by R_j without the residue R_i; and the fourth term, $E(C_{i-1}C_{i+1} + C_{j-1}C_{j+1})$, is the total energy of the system formed by the caps only.

Based on that, structural files (PDB format) obtained after molecular

dynamics were prepared and used as input for calculations with Density Functional Theory (DFT). The DFT calculations were carried out using the DMol^3 code [27], and a Double Numerical plus Polarization (DNP) basis was chosen to expand the Kohn–Sham orbitals for all electrons. The generalized gradient approximation (GGA) as the theoretical calculation level was employed with the Perdew-Burke-Ernzerhof (PBE) [28] parametrization with the dispersion corrected energy proposed by Tkatchenko and Scheffler [29] (GGA + TS), which accounts to some degree for the relative variation in dispersion parameters of differently bonded atoms. The orbital cutoff was set 4 Å to ensure a good accuracy and less computational time. The total energy variation to achieve self-consistent field (SCF) convergence was set to 10^{-6} Ha. The calculation adopted an implicit system solvation mode and it was applied a dielectric function equal to 40. Additionally, explicit water molecules with a distance of up to 2.5 Å were considered in the calculation.

The energy contribution of all protein-peptide interactions involved in the *Mo*-CBP$_3$-PepIII–receptor complex and the individual contributions of specific amino acid residues are plotted in BIRD panels – an acronym for Binding site, Interaction energy, and Residues Domain. The BIRD panel depicts (i) the interaction energy (in kcal mol^{-1}) of a specific residue, employing horizontal bars, from which one can assess the importance of each residue in the complex formation, whether attractive (negative energy) or repulsive (positive energy); (ii) the binding interface radius to which each interaction/residue belongs, on the right side; and (iii) the molecules of water involved in the interaction [30].

2.5. Energy stabilization

The energy contributions of all the interactions between the *Mo*-CBP$_3$-PepIII and receptors (SAP5 and EXG) were computed following the topic 2.4. For this purpose, *Mo*-CBP$_3$-PepIII residues were used with spheres having initial radius of 2 Å for each residue. These radii were increased by increments of 0.5 Å up to 5 Å. In each radius, the amino acid residues of the receptors with at least one atom within the traced sphere were selected. This enabled obtaining the interaction pairs (the amino acid residues of *Mo*-CBP$_3$-PepIII that interacted with the residues of the receptors) and determining the radius to which each residue belonged. The Discovery Studio version 3.1 software was used to trace the spheres with delimited radii [20].

2.6. Mo-CBP$_3$-PepIII-yeast mimics membrane system

The yeast membrane system was built containing the same components as employed by Balliano and co-workers [30], consisting of 1,2-dioleoyl-sn-glycerol-3-phosphocholine (DOPC), 1-palmitoyl-2-oleoyl-sn-glycerol-3-phosphoethanolamine (POPE), 1-palmitoyl-2-oleoyl-sn-glycerol-3-phosphate (POPA), 1-palmitoyl-2-oleoyl-sn-glycerol-3-phospho-L-serine (POPS), 1,2-dipalmitoyl-sn-glycerol-3-phosphocholine (DPPC), and cholesterol. The initial *Mo*-CBP$_3$-PepIII-membrane systems were constructed based on Lyu and co-workers [31], who used the CHARMM-GUI Membrane Builder module [32–34]. The CHARMM36 force field was used and a 3 nm minimum height was added at the top and the bottom of the system to simulate a fully hydrated bilayer system. A total of 0.15 M of Na^+ and Cl^- salts (both sodium and chloride) was added, determined by simulating the physiological conditions, and the final system had neutral charge. The simulation was performed with NAMD 2.12 to observe the insertion of *Mo*-CBP$_3$-PepIII in the lipid bilayer membrane. Initially, a minimization of 10,000 steps was performed, followed by a simulation of 150 ns with a time step of 2 fs [31,34,35]. To analyze the insertion of the peptide in the membrane, measurements were performed of the center of mass (COM) coordinates of the phospholipid phosphates present on the surface close to the peptide, as well as of the *Mo*-CBP$_3$-PepIII throughout the simulation using the VMD software. With the coordinates of the center of mass, the difference between the Z-direction of the peptide and the phosphates was obtained.

2.7. Scanning electron microscopy (SEM)

To shed light the action of *Mo*-CBP$_3$-PepIII against *C. albicans*, SEM analysis was employed according to the method described by Oliveira et al. [15]. SEM images were obtained with an FEI Inspect™ 50 scanning electron microscope (Oregon USA), with a low energy detector (Everhart-Thornley detector), using an acceleration beam voltage of 20,000 kV, and 20,000 detector magnification. Before the SEM analyses, 100 µL of (2.5 CFU mL^{-1}) *C. albicans* cells were treated with *Mo*-CBP3-PepIII at 2.2 µM for 24 h at 37 °C. The DMSO-NaCl solution alone was used as control. After treatment, cells were recovered by centrifugation (Mikro 200R centrifuge, Hettich, Germany) at 3000*g* for 5 min at 22 ± 2 °C and fixed with 100 µL of a solution composed of 1% (v/v) glutaraldehyde and 4% (v/v) formaldehyde prepared in 0.15 M Na-phosphate buffer at pH 7.2 for 2 h at room temperature (22 ± 2 °C). Then the cells were recovered again by centrifugation as above, washed three times with 0.15 M Na-phosphate buffer, pH 7.2. Nest, cells were treated with 0.2% (m/v) osmium tetroxide for 10 min at room temperature (22 ± 2 °C) and centrifuged again. Subsequently, the samples were dehydrated by incubation with ethanol concentrations (30%, 70%, 100%, 100%, and 100% v/v) for 10 min each, followed by centrifugation as previously described. Finally, the samples were dried by immersion in 50/50 ethanol/hexamethyldisilazane (HMDS) for 10 min and centrifuged with 100% (v/v) HMDS. The cells were mounted on cover slips treated with 0.1% (m/v) gelatin, which were placed on stubs and coated with a 20 nm gold layer with a PET coating machine (Emitech Q150TES, Quorum Technologies, England), and SEM images were obtained.

2.8. Fluorescence microscopy

For fluorescence microscopy analyses, *C. albicans* cells (100 µL at 2.5 CFU mL^{-1}) were incubated either with *Mo*-CBP3-PepIII at 2.2 µM or control solution of DMSO-NaCl for 24 h. Afterwards, cells were recovered by centrifugation (5000*g*, 5 min at 22 ± 2 °C, Mikro 200R centrifuge, Hettich, Germany), and re-incubated with 10^{-3} M of fluorophore propidium iodide according to Lima et al. [36] for 30 min in the dark. Then, the cells were washed three times, mounted on slides in the dark, and analyzed under a fluorescence microscope (Olympus System BX60) with excitation wavelength of 488 nm and emission wavelength of 525 nm.

2.9. Light microscopy

The experiments to detect the ROS overproduction by *C. albicans* cells after treatment with *Mo*-CBP3-PepIII were performed according to Oliveira et al. [11]. Aliquots (100 µL) of *C. albicans* cell suspensions previously treated with the studied *Mo*-CBP3-PepIII at 2.2 µM dissolved in DMSO-NaCl, and DMSO-NaCl alone (blank), were incubated with 100 µL of 3,3′-diaminobenzidine (DAB, 1.0 mg mL^{-1} of ultrapure water) for 1 h at 30 °C. The cells were observed under a light microscope (Olympus System BX 60) to visualize the presence of ROS. All steps were carried out following the method described by Oliveira et al. [15]. Cells were mounted on slides, covered with cover slips and analyzed with the light microscope.

3. Results and discussion

3.1. Molecular docking predicted the interaction of Mo-CBP$_3$-PepIII with C. albicans enzyme

The peptide structure was stabilized after 65 ns of molecular dynamic simulation (Sup. Fig. 1A) with open conformation after molecular dynamics (Sup. Fig. 1B and C). The molecular docking showed that *Mo*-CBP$_3$-PepIII interacted with the sterol 14α-demethylase (CYP51) of *C. albicans* far from the enzyme active site (Sup. Fig. 2 - yellow dashed circle). Additionally, the docking scores were very low, varying between

−5.1 and −6.1 kcal mol^{-1}. This result suggests that *Mo*-CBP$_3$-PepIII employs a different mode against *C. albicans* compared to azoles, which is supported by its interaction with the active site of CYP51, avoiding the formation of ergosterol, an essential component of *C. albicans* membranes. Since the peptide was unable to interact at the active site; further analyses were not carried out with this enzyme.

Mo-CBP$_3$-PepIII interacted at the active site of SAP1 and SAP5, very close to the catalytic residues (Sup. Fig. 3). Regarding SAP1, the *Mo*-CBP$_3$-PepIII presented a docking score of −5.7 kcal mol^{-1} and distances of 3.5 Å and 4.1 Å from catalytic residues Asp32 and Asp218, respectively, as shown in Sup. Fig. 3A (zoomed red dashed circle). The docking score of the interaction between SAP5 and *Mo*-CBP$_3$-PepIII was −7.4 kcal mol^{-1}, suggesting a more favorable interaction compared to SAP1. Besides this, distances between the catalytic residues of SAP5 and the *Mo*-CBP$_3$-PepIII were also shorter: 2.4 Å and 3.2 Å for Asp32 and Asp218, respectively (Sup. Fig. 3B - zoomed blue dashed circle).

Mo-CBP$_3$-PepIII presented a docking score of −7.0 kcal mol^{-1} with Exo-β-(1,3)-glucanase (EXG), interacting with the catalytic residues with distances of 2.0 Å and 2.4 Å from Glu192 and Glu292, respectively (Fig. 1). Similar results were observed by Lum and co-workers [37], but the ten peptides tested in their work presented binding affinity varying from −9.0 kcal mol^{-1} to −10.0 kcal mol^{-1}. This result suggests an interesting inhibitory potential of *Mo*-CBP$_3$-PepIII toward EXG.

It should be noted that the proteins analyzed in this work are a small

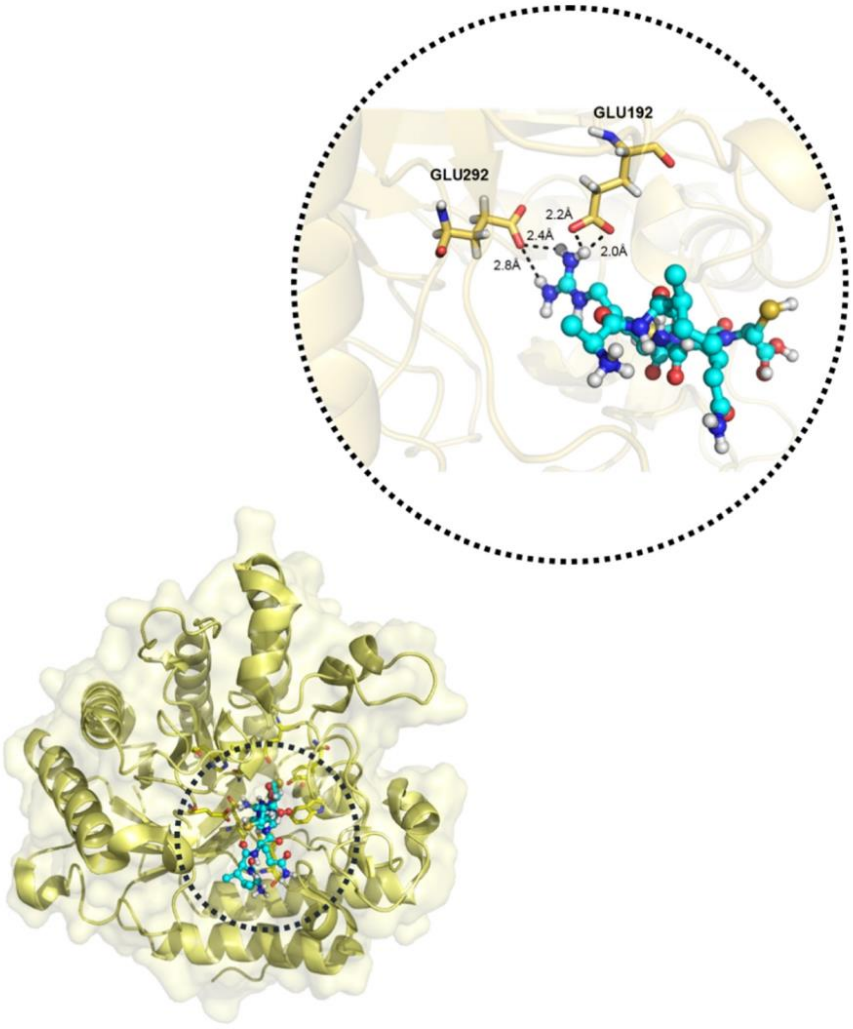

Fig. 1. Predicted interaction between *Mo*-CBP$_3$-PepIII and Exo-β-(1,3)-glucanase (EXG - PDB ID 2QZW). The catalytic residues Glu192 and Glu292 of EXG are represented in yellow and *Mo*-CBP$_3$-PepIII is represented in cyan. The docking score of the interaction was kcal mol^{-1}. The dashed lines represent the distance in Å (small numbers) between the catalytic residues and *Mo*-CBP$_3$-PepIII. (For interpretation of the references to color in this figure legend, the reader is referred to the web version of this article.)

fraction of those present in the proteome of *C. albicans*. The peptide *Mo*-CBP$_3$-PepIII could interact with other putative target proteins of the yeast that have not been analyzed.

3.2. Molecular dynamics

To analyze and obtain a stable structure under conditions similar to the cell environment, the complexes *Mo*-CBP$_3$-PepIII/EXG and *Mo*-CBP3-PepIII/SAP5 were submitted to simulations regarding molecular dynamics. During simulation for 100 ns, the complexes were stabilized from approximately 35 ns (Sup. Fig. 4). After this stabilization, it was possible to observe differences lower than 1 Å in RMSD, indicating that the complexes were stable.

3.3. Interaction between Mo-CBP$_3$-PepIII with EXG and SAP5

Even interacting in the active site of SAP5, quantum biochemical analysis revealed that *Mo*-CBP$_3$-PepIII (−104.9 kcal mol^{-1}) presented lower attraction and higher interaction energy compared to pepstatin (−152.2 kcal mol^{-1}), the commercial inhibitor of SAP5 (Sup. Fig. 5). Based on that, we chose not to continue the analyses with SAP5 enzymes.

Mo-CBP$_3$-PepIII interacted mainly with the residues Phe258, Phe144, Glu27, Glu262, Arg312, Leu304, Ser259, Glu192, and Leu194 of EXG from *C. albicans*. All interaction energies of each amino acid residue are shown in Supplementary Table 2. The strongest interaction occurred with Phe258, with a free energy of −23.4 kcal mol^{-1}. This interaction presented 10 water molecules with a distance of 2.5 Å (Fig. 2). The strong interaction energy of Phe258 is due to the hydrogen bond of its carboxylic group in the main-chain with the nitrogen group of the residue Ile2 of *Mo*-CBP$_3$-PepIII, with a distance of 3.0 Å and energy of −4.7 kcal mol^{-1} (Fig. 3A).

The residue Phe144 presented interaction energy of −14.1 kcal mol^{-1} with *Mo*-CBP$_3$-PepIII. The interaction of Phe144 presented 13 water molecules forming a hydrogen bonds and a radius of 2.5 Å (Fig. 2). The energy of this residue is due to the aromatic-sulphur interaction with the Cys5 of the *Mo*-CBP$_3$-PepIII (Fig. 3B).

The residues Glu27 and Glu262 from EXG presented interaction energies of −13.2 kcal mol^{-1} and −12.8 kcal mol^{-1}, respectively (Fig. 2). The first interacted mainly with the *Mo*-CBP$_3$-PepIII residue Arg4 and presented two hydrogen bonds with distances of 2.6 Å and 2.7 Å (Fig. 3C). Glu262 interacted with the peptide mainly through a hydrogen bond between its carboxylic group present in the side chain and the amino group in the side chain of the Ala1 residue, with a distance of 2.6 Å (Fig. 3D). Arg312 and Leu304 of the EXG enzyme presented interaction energies of −11.3 and −8.2 kcal mol^{-1}, respectively, being present in the 2.5 Å radius (Fig. 2). Arg312 showed repulsive energy to Ala1 residue of *Mo*-CBP$_3$-PepIII and attraction to Arg4, forming a hydrogen bond, as well as to Cys6 (Fig. 3E). Leu304 presented a hydrogen bond with the Arg4 residue of the peptide, which was the

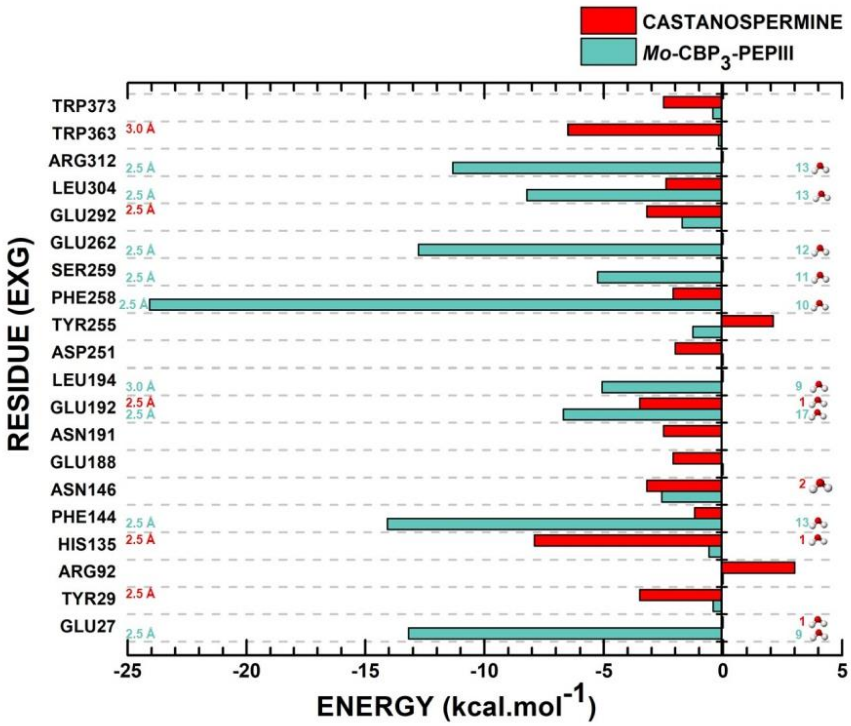

Fig. 2. The binding site, interaction energy, and residue domain (BIRD) panel showing the MFCC energy for the main interactions established of the EXG enzyme with *Mo*-CBP$_3$-PepIII and with the glucanase inhibitor castanospermine. Blue and red bars represent values obtained with *Mo*-CBP$_3$-PEPIII and castanospermine, respectively. Colored numbers at the left side of the panel identify the distance in Å between the residue of EXG and the ligand for each interaction. The number of water molecules involved in each interaction is presented at the right side of the panel. (For interpretation of the references to color in this figure legend, the reader is referred to the web version of this article.)

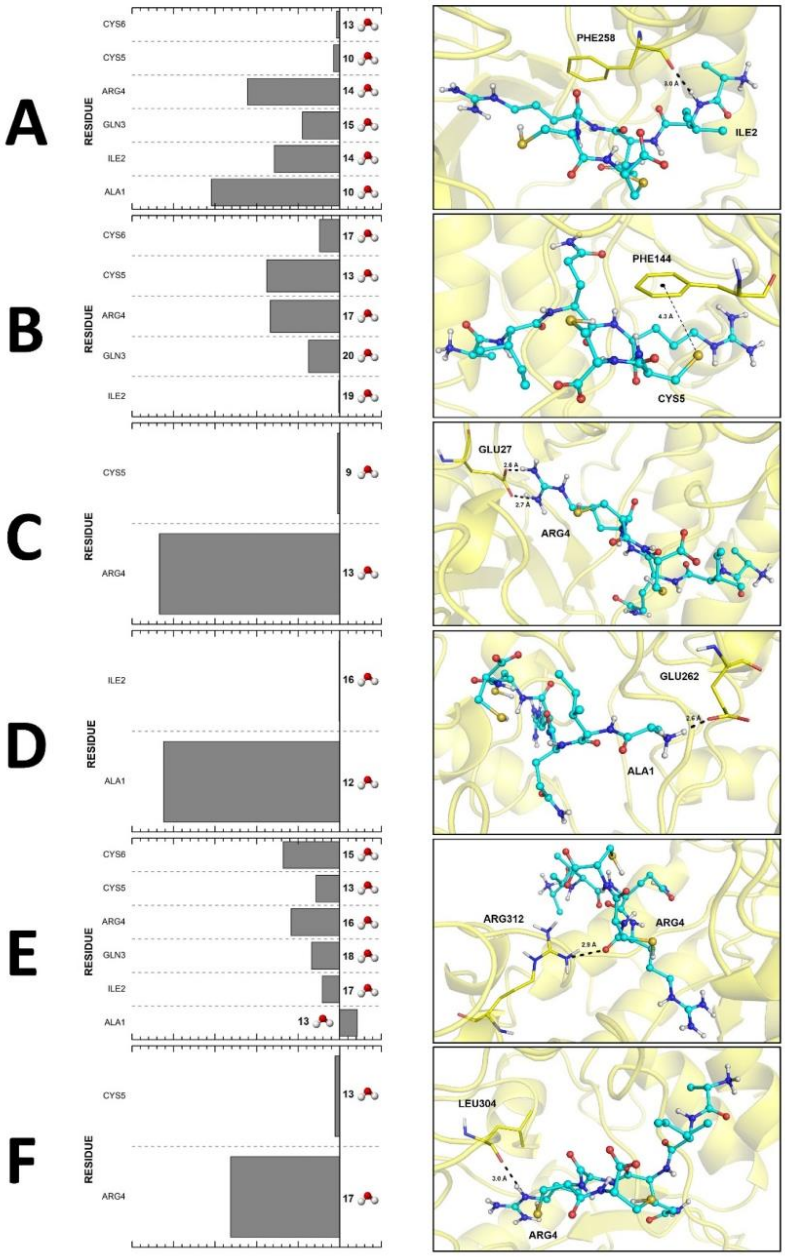

Fig. 3. Amino acid residues involved in *Mo*-CBP$_3$-PepIII anchorage in the EXG enzyme. The binding site, interaction energy and residue domain (BIRD) panels placed at the left side present the MFCC interaction energy for each interaction performed by Phe258 (A), Phe144 (B), Glu27 (C), Glu262 (D), Arg312 (E), and Leu304 (F). The residue coordination is represented on the right side. *Mo*-CBP$_3$-PEPIII is represented in cyan, and residues of EXG are represented in yellow. The main interactions are represented as black dashed lines (distances are indicated in Å). Water representations on the right side of the BIRD panels indicate interactions involving water molecules. (For interpretation of the references to color in this figure legend, the reader is referred to the web version of this article.)

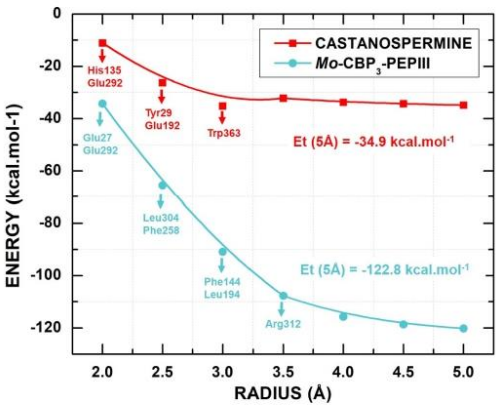

Fig. 4. *Mo*-CBP$_3$-PepIII and castanospermine total interaction energy as a function of the binding pocket radius. Amino acid residues responsible for the regions of the greatest negative variation are highlighted. Blue circles and red squares represent the *Mo*-CBP$_3$-PEPIII and castanospermine values, respectively. Et (5 Å) represents the sum of energies until 5 Å and energy values are represented as kcal mol^{-1}. (For interpretation of the references to color in this figure legend, the reader is referred to the web version of this article.)

main interaction, responsible for almost all of the interaction energy between Leu304 and Mo-CBP3-PepIII (Fig. 3F).

The residues Gln 3 and Arg4 from *Mo*-CBP$_3$-PepIII are located in a region inside the catalytic site of the enzyme and were the only residues that interacted with the residue Glu192 and Glu292. Glu192 presented interaction energy of −6.7 kcal mol^{-1} and the residue Glu292 had interaction energy of −1.7 kcal mol^{-1}.

The main contributions of energy in the interaction between *Mo*-CBP$_3$-PepIII and EXG were in the radii of 2.5 Å and 3.0 Å. Beyond this radius, no significant contributions to the energy were observed (Fig. 4). This result indicates that amino acids with a distance greater than 4 Å have minimal contributions to the interaction energy, given the energy convergence.

For comparison, the energies of the commercial inhibitor castanospermine were calculated. The *Mo*-CBP$_3$-PepIII presented total interaction energy of −122.8 kcal mol^{-1} for EXG, indicating that *Mo*-CBP3-PepIII has the potential to be a potent inhibitor compared to castanospermine, which had interaction energy of −34.9 kcal mol^{-1} until the radius of 5 Å. However, *in vitro* and/or *in vivo* experiments need to be carried out to verify this observed potential. The residues involved in castanospermine and EXG interaction were His135, Glu192, Tyr29, Glu192, and Trp363, different from those observed in the interaction between EXG and *Mo*-CBP$_3$-PepIII (Glu27, Glu292, Leu304, Phe258, Leu194, and Arg312), as depicted in Fig. 4. All interaction energies between castanospermine and EXG are identified in the Supplementary Table 3.

The precise role of EXG in the physiological processes in *Candida* cells is still unclear. However, there is no doubt that EXG enzymes are essential to cell wall metabolism, such as turnover and maintenance of healthy cell walls [38]. By interacting with the active site of EXG, *Mo*-CBP$_3$-PepIII

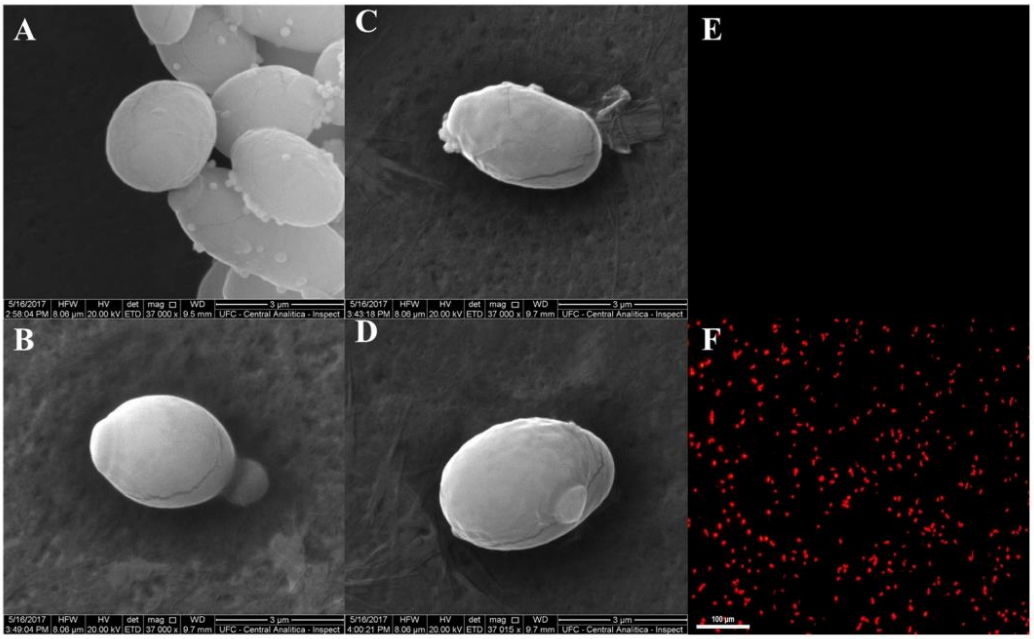

Fig. 5. Damage to *C. albicans* membranes induced by *Mo*-CBP$_3$-PepIII revealed by scanning electron microscopy (SEM) and fluorescence microscopy. (A) The surface of the control *C. albicans* cells is covered by well-defined and organized structures. (B–D) Cells exposed to *Mo*-CBP$_3$-PepIII (2.2 μM) showing considerable alterations in the shape and surface, such as the presence of multiple scars and bud scars, cell wall damage, and internal content loss. (E) Control cells showing an intact membrane with no propidium iodide fluorescence. (F) *Mo*-CBP$_3$-PepIII-treated cells presenting damaged membranes allowing the entry of propidium iodide and showing bright red fluorescence. (For interpretation of the references to color in this figure legend, the reader is referred to the web version of this article.)

could block it, inhibiting enzyme activity. By doing that, *Mo*-CBP$_3$-PepIII could inhibit the essential catalytic process necessary for healthy cell walls, causing damaged cell walls [38]. Indeed, the treatment of *C. albicans* with *Mo*-CBP$_3$-PepIII resulted in damage to the cell wall (Fig. 5). SEM images revealed that *Candida* cells presented cracks all over the cells, indicating this damage to the cell wall (Fig. 5B–D). It was possible to see loss of cytoplasmic content (Fig. 5C). Also, buds, scar buds and roughness were present in the *Mo*-CBP$_3$-PepIII-treated cells (Fig. 5B–C). SEM analyses strongly suggested that *Mo*-CBP$_3$-PepIII has the cell wall as a target. Without a healthy cell wall, it is impossible to maintain the osmotic balance with the environment, leading to loss of internal content and death. In a previous study from our research group [15], we observed lethal damage caused by *Mo*-CBP$_3$-PepIII to the *Candida* cell wall, corroborated by the findings reported here.

3.4. Interaction between Mo-CBP$_3$-PepIII and yeast membrane

To understand how the peptide interacts with the membrane, insert itself and remains in the membrane, we performed molecular dynamics simulations between the *Mo*-CBP$_3$-PepIII and a realistic yeast membrane. At 0 ns, *Mo*-CBP$_3$-PepIII approached the membrane in the initial step of the interaction. This interaction is driven by ionic interactions caused by the attraction between the charges of amino acid residue Gln3, Arg4, and Cys5 of *Mo*-CBP$_3$-PepIII and the phospholipid charges POPE21 in the *C. albicans* mimics membrane (Sup. Fig. 6A) [15]. After 50 ns, *Mo*-CBP$_3$-PepIII was already interacting with the surface of the membrane even without insertion supported by ionic interaction between the phosphates negative charge of POPE36 and POPA55 with the positive charges of amino acid residues Arg4 (Fig. 6 and Sup. Fig. 6B). In this frame, the peptide is closer to the membrane and has hydrophobic interactions with the phospholipids POPA24, POPE21, POPS29, and DOPC34 (Sup. Fig. 6B). Fifty ns later, *Mo*-CBP$_3$-PepIII was inserted in the membrane, as indicated by the 100 ns snapshot (Fig. 6). The insertion of *Mo*-CBP$_3$-PepIII is due to its amphipathicity and hydrophobic moment. In this case, the insertion of *Mo*-CBP$_3$-PepIII is now driven by hydrophobic interaction of hydrophobic and apolar amino acid residues from *Mo*-CBP$_3$-PepIII with the core of the membrane. Hydrophobic interactions are observed with the phospholipid POPA55 and the cholesterols molecules CHL114 and CHL1, as well as hydrogen bonds between the amino acid residues Ala1, Gln3, Arg4, and Cys6 of *Mo*-CBP$_3$-PepIII with the phospholipids POPA24, POPE36, POPE21, and DOPC56, respectively (Sup. Fig. 6C). The peptide remains inserted in the outer leaflet of the membrane until the end of the 150 ns molecular dynamics simulation. As already observed in the 100 ns frame, the peptide continues to interact with the membrane through hydrophobic interactions and hydrogen bonds (Fig. 6D and Sup. Fig. 6D). It is important to note that the interactions shown are of point frames and that at different times these interactions can change due to the dynamics of interactions between the peptide and the membrane.

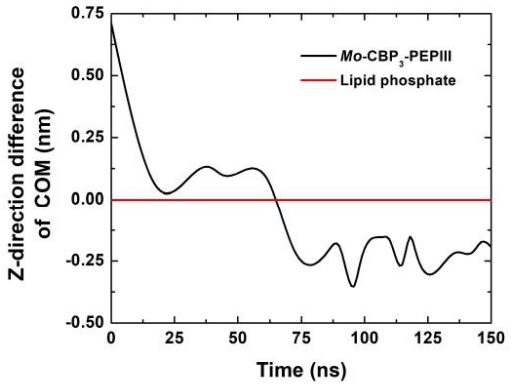

Fig. 7. Peptide insertion in the yeast membrane outer leaflet. Black and red represent the *Z*-direction difference of center of mass (COM) of peptide and phosphates of the outer membrane leaflet, respectively. (For interpretation of the references to color in this figure legend, the reader is referred to the web version of this article.)

This result is similar to the results obtained by Yang and co-workers [39], who also analyzed the insertion of peptides in simple membranes composed of POPG: POPC. They authors demonstrated that some peptides could insert themselves in the membrane after approximately 100 ns. The *Mo*-CBP$_3$-PepIII displayed a mode of interaction with the membrane very similar to that of the BAX core α5 and melittin peptide, by entering the subsurface region of the membrane, as also reported by Flores-Romero and co-workers [40].

The peptide was partially inserted in the outer membrane leaflet with approximately 65 ns of molecular dynamics (Fig. 7). The peptide center of mass exceeded the phosphate center of mass on the surface of the membrane, and the peptide remained inside the membrane during the simulation.

Sahoo and Fujiwara [41] observed similar behavior of BMAP27, also a cationic peptide, but they used simpler membranes, composed only of POPC or DOPG. The authors observed that the first moment of attraction of the peptide to the membrane occurred after 80 ns. After that, they observed slow binding and reorientation until 500 ns. In turn, we observed the same movement during the molecular dynamics simulation, but only until 150 ns. Yang and co-workers [39] observed the interaction of the peptides VT18-KKLV, VT18-CAKKLV, and cVT18-CAKKLV with a membrane during 500 ns. The three peptides analyzed by Yang et al. [37] were able to insert itself the membrane in approximately 90 ns, as seen in our work.

Additionally, our findings corroborate the data on molecular

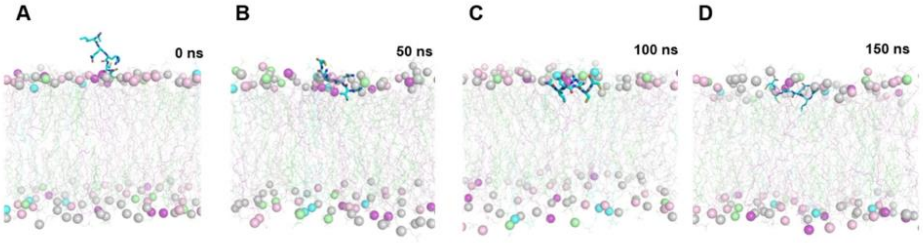

Fig. 6. Snapshots of *Mo*-CBP$_3$-PEPIII inside realistic membranes during molecular dynamics. (A), (B), (C), (D), respectively, represent snapshots of 0, 50, 100, 150 ns. Color code: CHL, green; DOPC, silver; POPE, pink; POPS, cyan; POPA, purple; DPPC, lime. (For interpretation of the references to color in this figure legend, the reader is referred to the web version of this article.)

dynamics of the membrane. The molecular dynamics showed that *Mo*-CBP_3-PepIII interacted with the membrane and inserted itself in the membrane. This result was confirmed by fluorescence microscopy. *C. albicans* cells showed bright red fluorescence, indicating propidium iodide uptake and pores on the membrane (Fig. 5F), compared to the control without fluorescence (Fig. 5E).

By targeting the membranes, unlike conventional antifungal drugs that act on specific biosynthetic pathways (*i.e.*, ergosterol synthesis), *Mo*-CBP_3-PepIII hinders the development of resistance by pathogens because they have to modify the membrane constituents, which is difficult, harmful, and metabolically expensive to cells [42].

3.5. *Mo-CBP_3-PepIII induced ROS overproduction in C. albicans cells*

Given the ROS toxicity, it can rapidly kill the cell by interacting with and destroying membranes, DNA, and proteins [43–45]. Although these damages are known, the triggers and mechanisms involved in ROS production are still unclear [44,45]. As indicated in Fig. 8A–C, control *C. albicans* cells presented no sign of ROS production. In contrast, *Mo*-CBP_3-PepIII-treated (2.2 μ) *C. albicans* cells accumulated high amounts of ROS, as indicated by the dark-brown halos and brown colored cells (Fig. 8D–F – black arrows). It is clear that *Mo*-CBP_3-PepIII induced high accumulation of ROS, causing several damages, leading *C. albicans* death.

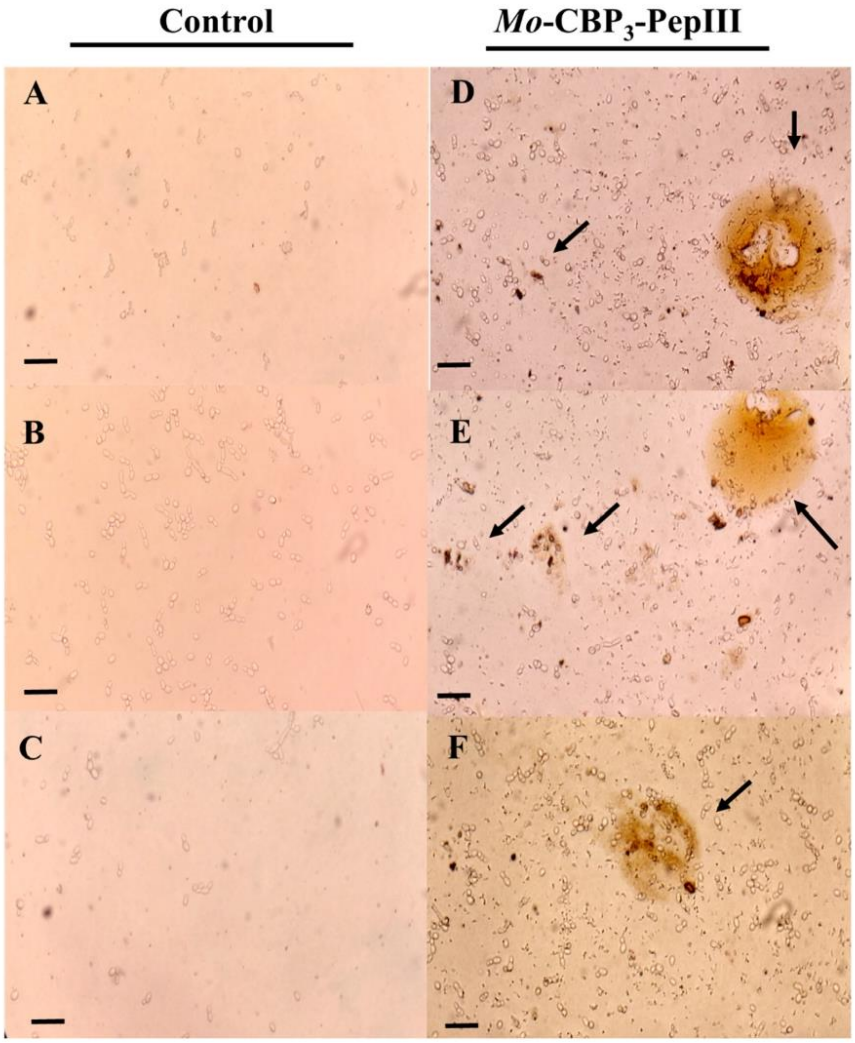

Fig. 8. Reactive oxygen species (ROS) generation by *C. albicans* cells. Light micrograph of cells previously incubated for 24 h, at 37 °C with DMSO-NaCl (A, control) or 2.2 μM *Mo*-CBP_3-PepIII dissolved in DMSO-NaCl (B) followed by incubation with DAB. The presence of ROS was observed in (B) as a reddish-brown staining reaction inside and around cells (black arrows). (For interpretation of the references to color in this figure legend, the reader is referred to the web version of this article.)

4. Conclusion

The *in silico* assays indicated that *Mo*-CBP$_3$-PepIII has a broad spectrum of action against *Candida* cells. *In silico* and microscopic analyses revealed *Mo*-CBP$_3$-PepIII targets both cell wall and membrane of *C. albicans*. Additionally, *Mo*-CBP$_3$-PepIII presented stronger attractive interaction energy with the enzyme Exo-β-(1,3)-glucanase than the commercial inhibitor castanospermine, indicating its possible multiple mechanisms of action and similar action to antifungal agents of the class of echinocandins. The peptide *Mo*-CBP$_3$-PepIII can also interact, enter, and stay in the subsurface region of the fungal membranes.

CRediT authorship contribution statement

The authors made substantial contributions to the following steps: (1) conception and design of the study, acquisition of data and analysis and interpretation of data - JLA, PFNS, JTAO, VNF and DOBS; (2) drafting the article and revising it critically for important intellectual content - JLA, PFNS, and DOBS; and (3) final approval of the version to be submitted - PFNS and DOBS.

Declaration of competing interest

All authors declare no conflicts of interest.

Acknowledgments

This study was supported by CNPq (National Council for Scientific and Technological Development), process numbers 308107/2013-6 and 306202/2017-4. Special thanks go to CAPES (Office to Coordinate Improvement of University Personnel) for providing the postdoctoral research grant to Pedro F. N. Souza. We are also grateful to the central analytical facilities of CENAPAD-UFC.

Ethical approval

None sought.

Appendix A. Supplementary data

Supplementary data to this article can be found online at https://doi.org/10.1016/j.lfs.2021.119775.

References

[1] G. Quindós, Epidemiology of candidaemia and invasive candidiasis. A changing face, Rev. Iberoam. Micol. 31 (2014) 42–48, https://doi.org/10.1016/j.riam.2013.10.001.
[2] J. Schneider, E. Mateo, C. Marcos-Arias, N. Eiró, F. Vizoso, R. Pérez-Fernández, E. Eraso, G. Quindós, Antifungal activity of the human uterine cervical stem cells conditioned medium (hUCESC-CM) against Candida albicans and other medically relevant species of Candida, Front. Microbiol. 9 (2018) 2818. https://www.frontiersin.org/article/10.3389/fmicb.2018.02818.
[3] F.L. Mayer, D. Wilson, B. Hube, Candida albicans pathogenicity mechanisms, Virulence 4 (2013) 119–128, https://doi.org/10.4161/viru.22913.
[4] M. Negri, M. Martins, M. Henriques, T.I.E. Svidzinski, J. Azeredo, R. Oliveira, Examination of potential virulence factors of Candida tropicalis clinical isolates from hospitalized patients, Mycopathologia 169 (2010) 175–182, https://doi.org/10.1007/s11046-009-9246-0.
[5] M. Puig-Asensio, J. Pemán, R. Zaragoza, J. Garnacho-Montero, E. Martín-Mazuelos, M. Cuenca-Estrella, B. Almirante, Impact of therapeutic strategies on the prognosis of Candidemia in the ICU, Crit. Care Med. 42 (2014) 1423–1432, https://doi.org/10.1097/CCM.0000000000000221.
[6] E.L. Berkow, S.R. Lockhart, Fluconazole resistance in Candida species: a current perspective, Infect. Drug Resist. 10 (2017) 237–245, https://doi.org/10.2147/IDR.S118892.
[7] T. Honorato Siqueira, L. Martínez, Molecular simulations of fluconazole-mediated inhibition of sterol biosynthesis, J. Biomol. Struct. Dyn. (2019) 1–11, https://doi.org/10.1080/07391102.2019.1614998.
[8] M. Sumiyoshi, T. Miyazaki, J.N. Makau, S. Mizuta, Y. Tanaka, T. Ishikawa, K. Makimura, T. Hirayama, T. Takazono, T. Saijo, H. Yamaguchi, S. Shimamura, K. Yamamoto, Y. Imamura, N. Sakamoto, Y. Obase, K. Izumikawa, K. Yanagihara, S. Kohno, H. Mukae, Novel and potent antimicrobial effects of caspofungin on drug-resistant Candida and bacteria, Sci. Rep. 10 (2020) 17745, https://doi.org/10.1038/s41598-020-74749-8.
[9] K. Whitby, T.C. Pierson, B. Geiss, K. Lane, M. Engle, Y. Zhou, R.W. Doms, M. S. Diamond, Castanospermine, a potent inhibitor of dengue virus infection in vitro and in vivo, J. Virol. 79 (2005) 8698–8706, https://doi.org/10.1128/JVI.79.14.8698-8706.2005.
[10] A. Ortiz, E. Sansinenea, The chemistry of drugs to treat Candida albicans, Curr. Top. Med. Chem. 19 (2019) 2554–2566, https://doi.org/10.2174/1568026619666191025153124.
[11] D.R. Silva, J. De C.O. Sardi, I.A. Freires, A.C.B. Silva, P.L. Rosalen, In silico approaches for screening molecular targets in Candida albicans: a proteomic insight into drug discovery and development, Eur. J. Pharmacol. 842 (2019) 64–69, https://doi.org/10.1016/j.ejphar.2018.10.016.
[12] L. Czaplewski, R. Bax, M. Clokie, M. Dawson, H. Fairhead, V.A. Fischetti, S. Foster, B.F. Gilmore, R.E.W. Hancock, D. Harper, I.R. Henderson, K. Hilpert, B.V. Jones, A. Kadioglu, D. Knowles, S. Ólafsdóttir, D. Payne, S. Projan, S. Shaunak, J. Silverman, C.M. Thomas, T.J. Trust, P. Warn, J.H. Rex, Alternatives to antibiotics-a pipeline portfolio review, Lancet Infect. Dis. 16 (2016) 239–251, https://doi.org/10.1016/S1473-3099(15)00466-1.
[13] C.D. Fjell, J.A. Hiss, R.E.W. Hancock, G. Schneider, Designing antimicrobial peptides: form follows function, Nat. Rev. Drug Discov. 11 (2012) 37–51, https://doi.org/10.1038/nrd3591.
[14] M.H. Cardoso, E.S. Cândido, K.G.N. Oshiro, S.B. Rezende, O.L. Franco, Peptides containing D-amino acids and retro-inverso peptides: General applications and special focus on antimicrobial peptides, in: Pept. Appl. Biomed. Biotechnol. Bioeng, Elsevier Inc, 2018, pp. 131–155, https://doi.org/10.1016/B978-0-08-100736-5.00005-3.
[15] J.T.A. Oliveira, P.F.N. Souza, I.M. Vasconcelos, L.P. Dias, T.F. Martins, M.F. Van Tilburg, M.I.F. Guedes, D.O.B. Sousa, Mo-CBP3-PepI, Mo-CBP3-PepII, and Mo-CBP3-PepIII are synthetic antimicrobial peptides active against human pathogens by stimulating ROS generation and increasing plasma membrane permeability, Biochimie 157 (2019) 10–21, https://doi.org/10.1016/j.biochi.2018.10.016.
[16] M.V. Keniya, M. Sabherwal, R.K. Wilson, M.A. Woods, A.A. Sagatova, J.D. A. Tyndall, B.C. Monk, Crystal structures of full-length lanosterol 14α-demethylases of prominent fungal pathogens Candida albicans and Candida glabrata provide tools for antifungal discovery, Antimicrob. Agents Chemother. 62 (2018), https://doi.org/10.1128/AAC.01134-18.
[17] C. Borelli, E. Ruge, J.H. Lee, M. Schaller, A. Vogelsang, M. Monod, H.C. Korting, R. Huber, K. Maskos, X-ray structures of Sap1 and Sap5: structural comparison of the secreted aspartic proteinases from Candida albicans, Proteins Struct. Funct. Bioinf. 72 (2008) 1308–1319, https://doi.org/10.1002/prot.22021.
[18] S.M. Cutfield, G.J. Davies, G. Murshudov, B.F. Anderson, P.A. Sullivan, J. F. Cutfield, P.C. Moody, The structure of the exo-ß-(1,3)-glucanase from Candida albicans in native and bound forms: relationship between a pocket and groove in family 5 glycosyl hydrolases 1 1Edited by I. A. Wilson, J. Mol. Biol. 294 (1999) 771–783, https://doi.org/10.1006/jmbi.1999.3287.
[19] O. Trott, A.J. Olson, AutoDock Vina: improving the speed and accuracy of docking with a new scoring function, efficient optimization, and multithreading, J. Comput. Chem. 31 (2010) 455–461, https://doi.org/10.1002/jcc.21334.
[20] B.L. Sousa, I.L. Barroso-Neto, E.F. Oliveira, E. Fonseca, P. Lima-Neto, L.O. Ladeira, V.N. Freire, Explaining RANKL inhibition by OPG through quantum biochemistry computations and insights into peptide-design for the treatment of osteoporosis, RSC Adv. 6 (2016) 84926–84942, https://doi.org/10.1039/c6ra16712h.
[21] D. Van Der Spoel, E. Lindahl, B. Hess, G. Groenhof, A.E. Mark, H.J.C. Berendsen, GROMACS: fast, flexible, and free, J. Comput. Chem. 26 (2005) 1701–1718, https://doi.org/10.1002/jcc.20291.
[22] W.L. Jorgensen, D.S. Maxwell, J. Tirado-Rives, Development and testing of the OPLS, J. Am. Chem. Soc. 118 (1996) 11225–11236, https://doi.org/10.1021/ja9621760.
[23] M.J. Robertson, J. Tirado-Rives, W.L. Jorgensen, Improved peptide and protein torsional energetics with the OPLS-AA force field, J. Chem. Theory Comput. 11 (2015) 3499–3509, https://doi.org/10.1021/acs.jctc.5b00356.
[24] J.L. Amaral, S.J.M. Santos, P.F.N. Souza, P.A. de Morais, F.F. Maia, H.F. Carvalho, V.N. Freire, Quantum biochemistry in cancer immunotherapy: new insights about CTLA-4/ipilimumab and design of ipilimumab-derived peptides with high potential in cancer treatment, Mol. Immunol. 127 (2020) 203–211, https://doi.org/10.1016/j.molimm.2020.09.013.
[25] J.L. Amaral, J.T.A. Oliveira, F.E.S. Lopes, C.D.T. Freitas, V.N. Freire, L.V. Abreu, P. F.N. Souza, Quantum biochemistry, molecular docking, and dynamics simulation revealed synthetic peptides induced conformational changes affecting the topology of the catalytic site of SARS-CoV-2 main protease, J. Biomol. Struct. Dyn. (2021) 1–13, https://doi.org/10.1080/07391102.2021.1920464.
[26] P.A. Morais, F.F. Maia, C. Solis-Calero, E.W.S. Caetano, V.N. Freire, H.F. Carvalho, The urokinase plasminogen activator binding to its receptor: a quantum biochemistry description within an in/homogeneous dielectric function framework

with application to uPA-uPAR peptide inhibitors, Phys. Chem. Chem. Phys. 22 (2020) 3570–3583, https://doi.org/10.1039/c9cp06530j.
[27] B. Delley, From molecules to solids with the DMol3 approach, J. Chem. Phys. 113 (2000) 7756–7764, https://doi.org/10.1063/1.1316015.
[28] J.P. Perdew, K. Burke, M. Ernzerhof, Generalized gradient approximationmade simple, Phys. Rev. Lett. 77 (1996) 3865–3868, https://doi.org/10.1103/PhysRevLett.77.3865.
[29] A. Tkatchenko, M. Scheffler, Accurate molecular van der waals interactions from ground-state electron density and free-atom reference data, Phys. Rev. Lett. 102 (2009), 073005, https://doi.org/10.1103/PhysRevLett.102.073005.
[30] G. Daum, G. Tuller, T. Nemec, C. Hrastnik, G. Balliano, L. Cattel, P. Milla, F. Rocco, A. Conzelmann, C. Vionnet, D.E. Kelly, S. Kelly, E. Schweizer, H.-J. Schüller, U. Hojad, E. Greiner, K. Finger, Systematic analysis of yeast strains with possible defects in lipid metabolism, Yeast 15 (1999) 601–614, https://doi.org/10.1002/(SICI)1097-0061(199905)15:7<601::AID-YEA390>3.0.CO;2-N.
[31] Y. Lyu, N. Xiang, J. Mondal, X. Zhu, G. Narsimhan, Characterization of interactions between curcumin and different types of lipid bilayers by molecular dynamics simulation, J. Phys. Chem. B 122 (2018) 2341–2354, https://doi.org/10.1021/acs.jpcb.7b10566.
[32] E.L. Wu, Y. Mei, K. Han, J.Z.H. Zhang, Quantum and molecular dynamics study for binding of macrocyclic inhibitors to human a-thrombin, Biophys. J. 92 (2007) 4244–4253, https://doi.org/10.1529/biophysj.106.099150.
[33] E.L. Wu, X. Cheng, S. Jo, H. Rui, K.C. Song, E.M. Dávila-Contreras, Y. Qi, J. Lee, V. Monje-Galvan, R.M. Venable, J.B. Klauda, W. Im, CHARMM-GUI membrane builder toward realistic biological membrane simulations, J. Comput. Chem. 35 (2014) 1997–2004, https://doi.org/10.1002/jcc.23702.
[34] S. Jo, T. Kim, W. Im, Automated builder and database of protein/membrane complexes for molecular dynamics simulations, PLoS One. 2 (2007), e880, https://doi.org/10.1371/journal.pone.0000880.
[35] B.R. Brooks, C.L. Brooks, A.D. Mackerell, L. Nilsson, R.J. Petrella, B. Roux, Y. Won, G. Archontis, C. Bartels, S. Boresch, A. Caflisch, L. Caves, Q. Cui, A.R. Dinner, M. Feig, S. Fischer, J. Gao, M. Hodoscek, W. Im, K. Kuczera, T. Lazaridis, J. Ma, V. Ovchinnikov, E. Paci, R.W. Pastor, C.B. Post, J.Z. Pu, M. Schaefer, B. Tidor, R. M. Venable, H.L. Woodcock, X. Wu, W. Yang, D.M. York, M. Karplus, CHARMM: the biomolecular simulation program, J. Comput. Chem. 30 (2009) 1545–1614, https://doi.org/10.1002/jcc.21287.
[36] P.G. Lima, P.F.N. Souza, C.D.T. Freitas, J.T.A. Oliveira, L.P. Dias, J.X.S. Neto, I. M. Vasconcelos, J.L.S. Lopes, D.O.B. Sousa, Anticandidal activity of synthetic peptides: mechanism of action revealed by scanning electron and fluorescence microscopies and synergism effect with nystatin, J. Pept. Sci. 26 (2020), https://doi.org/10.1002/psc.3249.
[37] K.Y. Lum, S.T. Tay, C.F. Le, V.S. Lee, N.H. Sabri, R.D. Velayuthan, H. Hassan, S. D. Sekaran, Activity of novel synthetic peptides against Candida albicans, Sci. Rep. 5 (2015) 9657, https://doi.org/10.1038/srep09657.
[38] R.S. Chambers, M.J. Broughton, R.D. Cannon, A. Carne, G.W. Emerson, P. A. Sullivan, An exo- -(1,3)-glucanase of Candida albicans: purification of the enzyme and molecular cloning of the gene, J. Gen. Microbiol. 139 (1993) 325–334, https://doi.org/10.1099/00221287-139-2-325.
[39] R. Yang, G. Zhang, F. Zhang, Z. Li, C. Huang, Membrane permeabilization design of antimicrobial peptides based on chikungunya virus fusion domain scaffold and its antibacterial activity against gram-positive Streptococcus pneumoniae in respiratory infection, Biochimie 146 (2018) 139–147, https://doi.org/10.1016/j.biochi.2017.12.007.
[40] H. Flores-Romero, M. Garcia-Porras, G. Basañez, Membrane insertion of the BAX core, but not latch domain, drives apoptotic pore formation, Sci. Rep. 7 (2017) 16259, https://doi.org/10.1038/s41598-017-16384-4.
[41] B.R. Sahoo, T. Fujiwara, Membrane mediated antimicrobial and antitumor activity of cathelicidin 6: structural insights from molecular dynamics simulation on multi-microsecond scale, PLoS One. 11 (2016), e0158702, https://doi.org/10.1371/journal.pone.0158702.
[42] C. Ghosh, J. Haldar, Membrane-active small molecules: designs inspired by antimicrobial peptides, ChemMedChem 10 (2015) 1606–1624, https://doi.org/10.1002/cmdc.201500299.
[43] I.K. Maurya, S. Pathak, M. Sharma, H. Sanwal, P. Chaudhary, S. Tupe, M. Deshpande, V.S. Chauhan, R. Prasad, Antifungal activity of novel synthetic peptides by accumulation of reactive oxygen species (ROS) and disruption of cell wall against Candida albicans, Peptides 32 (2011) 1732–1740, https://doi.org/10.1016/j.peptides.2011.06.003.
[44] K. Wang, W. Dang, J. Xie, R. Zhu, M. Sun, F. Jia, Y. Zhao, X. An, S. Qiu, X. Li, Z. Ma, W. Yan, R. Wang, Antimicrobial peptide protonectin disturbs the membrane integrity and induces ROS production in yeast cells, Biochim. Biophys. Acta - Biomembr. 2015 (1848) 2365–2373, https://doi.org/10.1016/j.bbamem.2015.07.008.
[45] J. Lee, D.G. Lee, Antimicrobial peptides (AMPs) with dual mechanisms: membrane disruption and apoptosis, J. Microbiol. Biotechnol. 25 (2015) 759–764, https://doi.org/10.4014/jmb.1411.11058.

APÊNDICE B - PEPTIDE FRACTION FROM LATEX OF CALOTROPIS PROCERA EXHIBITS ANTIFUNGAL AND INSECTICIDAL ACTIVITIES

Arthropod-Plant Interactions (2021) 15:431–438
https://doi.org/10.1007/s11829-021-09828-2

ORIGINAL PAPER

Peptide fraction from latex of *Calotropis procera* exhibits antifungal and insecticidal activities

Jackson L. Amaral[1] · Cleverson D. T. Freitas[1] · João P. V. Rodrigues[2] · Ghulam Hussain[1] · Márcio V. Ramos[1] · Pedro F. N. Souza[1]

Received: 14 October 2020 / Accepted: 26 March 2021 / Published online: 8 April 2021
© The Author(s), under exclusive licence to Springer Nature B.V. 2021

Abstract
Latex is an endogenous fluid exuded by some plants after injury. It is rich in different molecules and has shown many biological activities against different fungi and insects. This work aimed to isolate a peptide fraction from *Calotropis procera* (PepCp) latex and to evaluate its activity against two fungi and an insect. The chromatographic profile showed that PepCp is constituted mainly by 7 kDa peptides. PepCp showed a low effect against the spore germination of both fungi *Colletotrichum gloeosporioides* and *Fusarium solani*. However, PepCp (1.25 mg mL^{-1}) inhibited the mycelial growth of *C. gloeosporioides* by 80%. On the other hand, PepCp, 0.05% (w/w), reduced the larval weight of *Callosobruchus maculatus* by 90%, and at 0.2%, no larva was found. At 0.05%, there was a delay of 2 days in the emergence of adult insects, while at 0.1%, no emergence of adult insects was noticed. Our results corroborate the hypothesis of the defense role played by latex and that PepCp can be an interesting biological source of new fungicidal or insecticidal peptides.

Keywords *Callosobruchus maculatus* · *Colletotrichum gloeosporioides* · *Fusarium solani* · Laticifer · Plant defense · Peptides

Introduction

Plants can be attacked by numerous phytopathogens, insects, and mammals, causing fatal diseases and severe injuries to different organs, such as fruits, seeds, stems, roots, and vascular systems (Pontes et al. 2020). These damages badly affect the crop production, resulting in a considerable loss with consequent increase in the food prices (Motaung et al. 2017).

Handling Editor: Ritu Chaudhary.

✉ Jackson L. Amaral
jacksoncesarc@gmail.com

✉ Cleverson D. T. Freitas
cleversondiniz@ufc.br

[1] Laboratory of Plant Defense Proteins, Department of Biochemistry and Molecular Biology, Federal University of Ceará, Av. Mister Hull, P.O. Box: 60451, Fortaleza, Ceará CEP 60440-554, Brazil

[2] Department of Pharmacy, Federal University of Ceará, Fortaleza, Ceará CEP 60430-160, Brazil

The *Colletotrichum* genus is among the top ten phytopathogens of importance worldwide, because they can cause the anthracnose disease in several plants, such as apple, citrus, papaya, passion fruit, guava, coffee, peach, mango, and avocado, which results in a significant economic impact (Bordoh et al. 2020; Kimaru et al. 2020). Similarly, fungi of the *Fusarium* genus predominantly cause damages in wheat, barley, and corn (Turkington et al. 2016). Additionally, some species of this genus can produce mycotoxins, such as fumonisins and trichothecenes, that are toxic to humans and animals (Wan et al. 2020).

Insects also led to a significant damage to crop production and are responsible for an average loss of 15–20% in food production (Rathee and Dalal 2018). The bean (*Vigna unguiculata* L.) is a very important crop in Brazil, with an estimated cultivation area of 1.5 million hectares. Its seeds can be severely attacked by the insect *Callosobruchus maculatus* (Dutra et al. 2016; Galindo et al. 2020). After oviposition, the *C. maculatus* larvae develop inside the seeds and cause severe damage by reducing their weight, germination rate, and nutritional value (Matos et al. 2020).

The application of pesticides is essential to control infections by the pests in plants. However, their conventional

usage, besides damaging the environment, imposes a selective pressure on the microorganisms and insects, results in evolution of resistance among them (Hawkins et al. 2018). Thus, it is imperative to prospect new fungicides and pesticides based on natural molecules to fight these aggressors in an environment friendly way. In this respect, the plant latex fluids appear as interesting sources of new biologically active molecules (Barbosa et al. 2020).

Latex is an endogenous and milky fluid composed by a solid phase, where the rubber is the main representant, and a liquid phase, which is rich in different proteins and metabolites (Barbosa et al. 2019). The amount of exudate latex depends on the plant species and the area injured (Ramos et al. 2019). *Calotropis procera* is a laticifer plant belonging to the *Apocynaceae* family, known for its medicinal properties. Additionally, its latex is a rich source of biologically active molecules (Ramos et al. 2019). Therefore, this work aimed to purify a peptide fraction of *C. procera* and to evaluate its biological activity against two phytopathogenic fungi and an important crop pest.

Materials and methods

Obtaining of water-soluble peptide fraction from *C. procera* latex (PepCp)

Latex from *Calotropis procera* was collected from healthy plants grown in Fortaleza, Ceará, Brazil, as described by Ramos et al. (2010). After the injury, the exudate latex was harvested in distilled water to finalize a 1:2 dilution (v:v). The mixture was filtered using cotton and then centrifuged at 10,000×*g* for 10 min at 4 °C. The supernatant was filtered again using cotton, and finally passed through a 0.2 µm filter to ensure no residual rubber left. The filtrate was centrifuged (8000×*g* for 20 min at 4 °C) using Vivaspin® tubes with 10 kDa pores. Two fractions were obtained: one having molecules smaller than 10 kDa, where the peptides were found, and the other one having molecules larger than 10 kDa. The fraction containing the peptides was centrifuged again under the same conditions using Vivaspin® tubes with 3 kDa pores to remove salts and small secondary metabolites. In this way, a fraction (the supernatant) containing peptides higher than 3 kDa and less than 10 kDa was obtained and termed herein as PepCp.

Detection of peptides by spectrophotometry and colorimetry

First, the presence of peptides in the PepCp fraction was evaluated by spectrophotometric absorption curve at different wavelengths (200–400 nm). For that, PepCp was dissolved in distilled water (1 mg mL^{-1}) and measurements were taken at 20 nm intervals, using a spectrophotometer (Ultrospec 1000 Amersham Pharmacia). Distilled water was used as blank.

In addition, the ninhydrin method was used to detect peptides in the PepCp fraction as described by Zhou and Tan (2000). The PepCp fraction (10 mg mL^{-1} in distilled water) was applied into thin layer chromatographic plates formed by silica gel (Merck) and incubated with 12 M HCl for 2 min. Finally, the plates were heated using a thermal plate at 110 °C for 10 min and a ninhydrin solution (0.2%) was sprayed. The protein fraction of *C. procera* latex was used as a positive control and distilled water as negative control. The formation of yellow or orange color indicated the presence of peptides/proteins in the sample.

PepCp characterization

The PepCp fraction (10 mg mL^{-1}) was submitted to size exclusion chromatography using the Superdex Peptide 10/300 GL column, coupled to the high-performance liquid chromatography system (AKTA, Purifier GE Healthcare). The flow rate was 0.5 mL min^{-1} and the presence of peptides was detected by spectrophotometry at 215 nm.

Antifungal activity

Obtaining of fungal spores

Colletotrichum gloeosporioides and *Fusarium solani* were cultivated in Petri dishes (100 × 15 mm), containing sterile Potato Dextrose Agar (PDA) medium (200 g of infused potato and 20 g of dextrose, pH 5.6, in 1 L of water). After inoculation, the plates were kept at 27 ± 2 °C, 70% relative humidity, and 12 h photoperiod (light/dark). The methodology described by Ho and Ko (1997) was followed to obtain the spore suspensions. Briefly, 5 mL of sterile distilled water was added to each plate and by using Drigalski spatula the spores were gently rubbed-down to the plates from the surface of the mycelium. Then, the suspensions were collected and filtered in a sterile nylon mesh to remove any remaining hyphae. For mycelial growth inhibition and spore germination tests, the spore suspensions were adjusted to a concentration of 2×10^5 spores mL^{-1}, which were counted using a Neubauer chamber under an optical microscope (Olympus System Microscope BX 60), as described by Souza et al. (2011).

Spore germination inhibition

The effect of PepCp on the germination of *C. gloeosporioides* and *F. solani* spores was evaluated according to the method described by Souza et al. (2011). Briefly, 10 µL aliquots of the spore suspension (2.0×10^5 spores mL^{-1})

were incubated with 10 µL of PepCp (10, 5, 2.5, and 1.25 mg mL^{-1}), which was dissolved in 2 × concentrated Yeast Peptone Dextrose (YPD) medium (20 g of bacteriological peptone, 20 g of glucose, and 10 g of yeast extract, in 1 L of water). YPD medium (1×) and 5 mM hydrogen peroxide were used as negative and positive controls for spore germination inhibition, respectively. The germination plates were kept at 27 °C for 24 h, and the spore germination inhibition was evaluated qualitatively, by absence or decrease of germ tubes or hyphae, using an optical microscope (Olympus System Microscope BX 60).

Mycelial growth inhibition

The effect of PepCp on the mycelial growth of *C. gloeosporioides* and *F. solani* was evaluated, quantitatively, according to Broekaert et al. (1990). The tests were carried out in 96-well flat-bottomed polystyrene microtiter plates adding 10 µL of a spore suspension (2×10^5 spores mL^{-1}) and 90 µL of YPD medium. After 16 h in the dark at 27 °C, 100 µL of PepCp was added (5, 2.5, and 1.25 mg mL^{-1}). The negative and positive controls for growth inhibition were sterile distilled water and 5 mM hydrogen peroxide, respectively. Fungal growth was monitored at 630 nm, at 8 h intervals, until reaching 48 h, using a microplate reader (Biotrak II Plate Reader, Amersham Biosciences).

Insecticidal activity

Seed preparation

Commercial seeds of *V. unguiculata*, susceptible to *C. maculatus*, were crushed using an electric grinder and then macerated with a mortar and pistil to obtain a fine-grained powder. Different quantities of PepCp were carefully mixed with the bean flour to obtain final concentrations of 0.05%, 0.1%, and 0.2% (w/w). The artificial seeds were prepared in a manual encapsulator using gelatin capsules (no. 1). Capsules containing only *V. unguiculata* flour were used as control. The artificial seeds were placed in contact with beans for 24 h before being subjected to oviposition to have the bean's characteristic odor, which allows better acceptance by insects.

Effect of PepCp on the development of *C. maculatus*

The insecticidal activity of PepCp was evaluated on the larvae and adult insects of *C. maculatus,* as described by Ramos et al. (2010). For this assay, four treatments were conducted (PepCp at 0.05%, 0.1%, and 0.2%, and the negative control containing only the bean powder), and performed in quadruplicate. Each experimental group was composed of 5 artificial seeds (total of 20 seeds for a group). Twenty male insects and twenty female, 1-day old, were introduced into each pot for 24 h. After this period, the insects were discarded and the number of eggs was adjusted to 5 per seed. After 21 days at 27 °C, the seeds were opened to assess larval survival and weight. The number of alive larvae was determined and correlated with the total number of hatched eggs to express the percentage of survival.

A second experiment was carried out simultaneously following the same conditions, but the seeds were not opened on the twenty-first day. In this case, complete larval development was allowed until the emergence of adult insects. After the first emergence, the hatching of the eggs was monitored for 11 days, where the number of adult insects and the day of emergence were recorded for each experimental group. The average development time and percentage of adult emergence were calculated, related to the number of eggs hatched.

Statistical analysis

All results are reported as mean ± SD. Assays with fungi were performed with three independent triplicates and those with insects were performed with three independent quadruplicates. All data were analyzed by ANOVA followed by Tukey test to identify the means that differed where the ANOVA test was significant. A p value < 0.05 was considered to be significant.

Results and discussion

Detection and characterization of peptides in PepCp fraction

The spectrophotometric absorption curve of PepCp fraction showed two peaks (Fig. 1a), one close to 220 nm, which is related to peptide bonds, and another one at 280 nm, which is characteristic of peptides and proteins containing amino acids with aromatic side chains, such as tryptophan and tyrosine (Scopes 1994). Similar results have already been reported by the absorbance spectra of a pure pine nut peptide (QWFH) (Zhang et al. 2019) and an iron-binding peptide (QKGTYDDYVEGL) from *Decapterus maruadsi* (Jiang et al. 2019). These results reinforce the presence of peptides in PepCp fraction.

The ninhydrin test was positive for the PepCp fraction (Fig. 1c), which showed an orange/purple coloration, similar to that exhibited by the positive control, which was the fraction protein *C. procera* latex (Fig. 1d). Because the latex fraction of *C. procera* (> 10 kDa) is very rich in proteins, it showed a stronger coloration and closer to purple color was observed in the center of the circumference. Ninhydrin reacts with free amino groups and the reaction product (Ruhemann's Purple) is visualized with an orange/purple

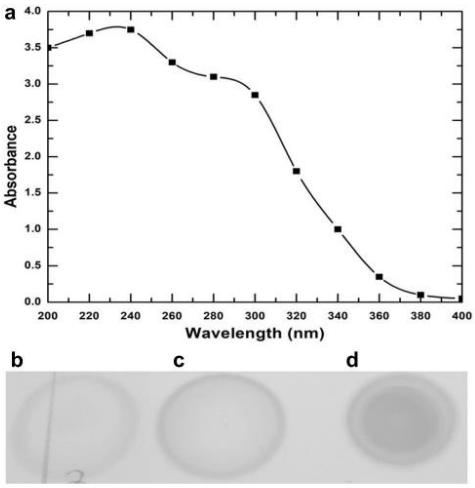

Fig. 1 Absorbance spectrum and detection of peptides using the ninhydrin test in the peptide fraction of *Calotropis procera* latex (PepCp). **a** The readings were taken at 20 nm intervals, from 200 to 400 nm. **b–d** distilled water, PepCp, and CpLP fraction, respectively, after ninhydrin test. For these assays, the samples were dissolved in distilled water at 1 mg mL^{-1}

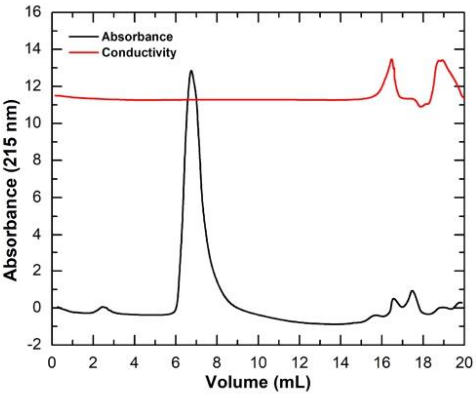

Fig. 2 Chromatographic profile of the PepCp fraction using a column of Superdex Peptide. PepCp, at 1 mg mL^{-1}, was eluted using a 0.5 mL min^{-1} flow rate and peptides were detected at 215 nm

color (Friedman 2004), thereby again confirming the presence of peptides in PepCp.

The size exclusion chromatography using the Superdex Peptide column showed only a peak for PepCp fraction, which was eluted in 7 mL (Fig. 2). According to the column manual, the PepCp fraction has peptides with molecular masses higher than 7 kDa. The chromatographic profile also showed two small peaks between 16 and 18 mL. Compared with a standard chromatography, we reasoned these peaks are composed of very small molecules, based on the exclusion limits of the column, which is 100 Da. Thus, it is suggested that these molecules are left-over salts of the running buffer, presenting molecular mass less than 100 Da and high conductivity (Fig. 2).

Altogether these results confirm the presence of peptides in the latex of *C. procera*, as previously described by Jucá et al. (2013), where the cytotoxic and anti-inflammatory potentials of the dichloromethane and ethyl acetate fractions were observed. In this work, the PepCp fraction was tested against two fungi and an insect.

Antifungal activity

Even using at 10 mg mL^{-1}, PepCp did not affect the spore germination of *F. solani* and *C. gloeosporioides* (Fig. 3). In contrast, all concentrations of PepCp inhibited the mycelial growth of the fungus *C. gloeosporioides* (Fig. 4a). Considering the absorbance of the control as 100% of growth (48 h), PepCp at 5, 2.5, and 1.25 mg mL^{-1} decreased the growth of *C. gloeosporioides* by 34%, 77%, and 80%, respectively (Fig. 4b). On the other hand, PepCp did not affect the mycelial growth of *F. solani* after 48 h and at 5 mg.mL^{-1} (Fig. 4c and d).

The PepCp fraction presented a selective antifungal activity by only inhibiting the mycelial growth of *C. gloeosporioides*. This type of selectivity was already reported about some peptides. Johnson et al. (2015) tested the cationic peptide JH8944 against *Colletotrichum* spp. and *Fusarium* spp., but it showed the activity only against the later. A similar result was observed by Lacerda et al. (2016). Lacerda et al. analyzed the peptide rDrr230a, which was active against genus *Fusarium* and showed only a little activity against *C. gossypii*.

Thus, although fungi have the same general components, the biochemical composition of their cell walls and membranes can be very different, somehow which can explain the selectivity of several antimicrobial peptides (Lopes et al. 2020). In general, the antimicrobial peptides have positive net charge (at least + 1), hydrophobic ratio (40–60%), and α-helix structure (Souza et al. 2011). The positive net charge is critical for the interaction with the negative portion of phospholipids of the cell membrane, while the α-helix structure and hydrophobic portion enable the insertion and pore formation in the membrane (Souza et al. 2011). Further studies are needed to purify, characterize, and evaluate the action mechanism of the peptides in PepCp.

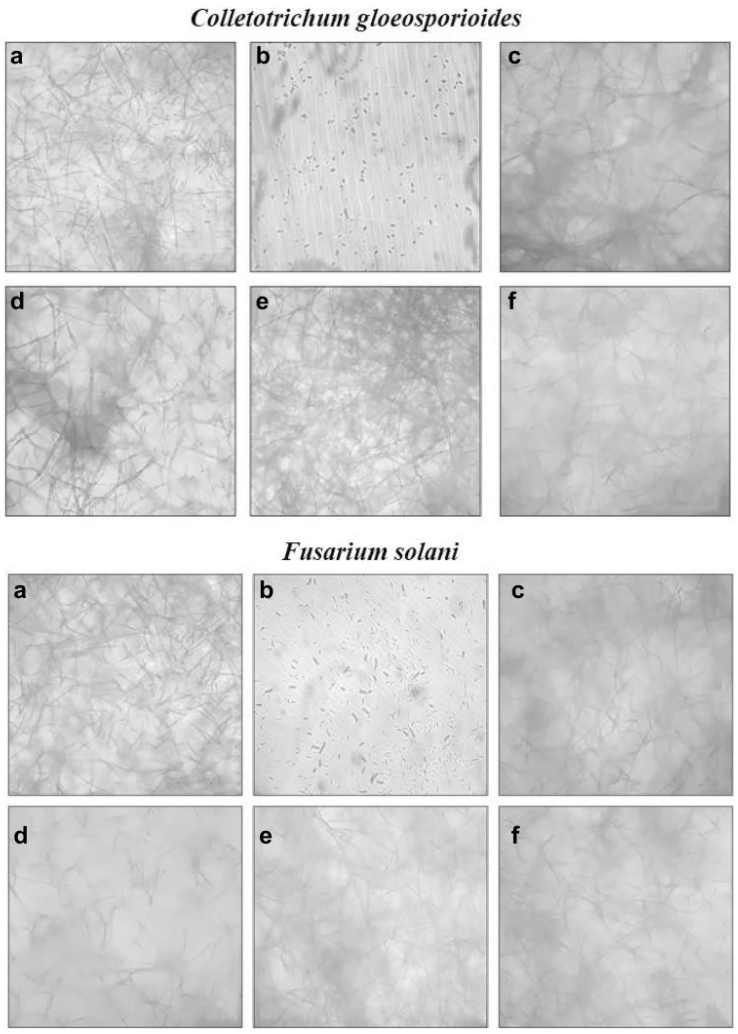

Fig. 3 Assays for inhibiting of the germination of *Colletotrichum gloeosporioides* and *Fusarium solani* spores. **a** Control (YPD medium). **b** Positive control, H_2O_2 (5 mM). **c–e** and **f** PepCp at 10, 5, 2.5, and 1.25 mg mL^{-1}, respectively. After 24 h at 27 °C, the results were visualized using an optical microscope

Insecticidal activity

In all studied parameters, the PepCp fraction showed a significant insecticidal effect against *C. maculatus*. Firstly, larval weight was analyzed after 21 days of development. It was observed that the average weight of larvae grown in the control seeds was 1.41 ± 0.5 mg (Fig. 5a), while the average weight of those grown in seeds containing 0.05% PepCp was 0.10 ± 0.2 mg ($p < 0.05$). At a concentration of 0.1% PepCp, only one larva was able to develop and its weight was negligible (Fig. 5a). At 0.2%, no larva was found. Visually, the sizes of the larvae were also very different among the groups. In the control group, the larvae were approximately 5 mm long after 21 days (Fig. 5a, insert), while the larvae from seeds containing 0.05% PepCp were around 2.0 mm. In the treatment with 0.1% PepCp, the only larva had 1.0 mm and at 0.2% PepCp no larva was found.

After treatment with PepCp, a significant decrease in larval survival rate was also observed (Fig. 5b). At 0.05% and 0.1% PepCp, a reduction of approximately 75% and 96% was observed, respectively ($p < 0.05$). On the 32nd day, adult insects began to emerge from the control artificial

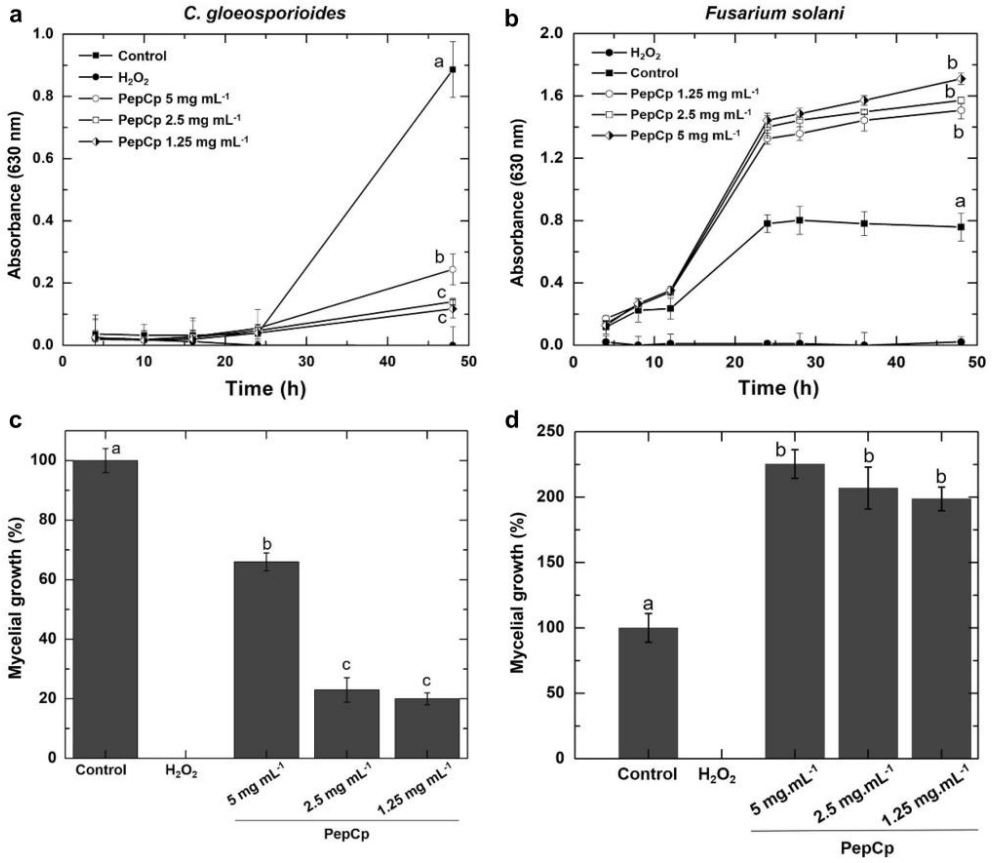

Fig. 4 Growth-inhibiting activity of PepCP fraction against *C. gloeosporioides* and *F. solani*. **a** and **c** PepCp was tested at different concentrations and growth was observed by absorbance at 630 nm. **b** and **d** The data obtained from "a" and "c," after 48 h of assay, were transformed in percentage of inhibition, considering the negative control as 100% of growth. The data were analyzed by one-way ANOVA followed by Tukey test. A p value < 0.05 was considered to be significant

seeds. The average development time for these insects was 36.1 ± 1.1 days, while for those grown in seeds containing 0.05% PepCp was 38.7 ± 1.5 days ($p > 0.05$). The percentage of insects that emerged from the control seeds was the same from seeds containing 0.05% PepCp ($p > 0.05$), while using 0.1% and 0.2% of PepCp, no insect emerged (Fig. 5c and d).

PepCp was very active against *C. maculatus*, when compared to the already used protein fraction from *C. procera* latex (CpLP) by Ramos et al. (2010). CpLP was active only in a concentration higher than 0.25% (w/w) against the insect *C. maculatus*. The peptide fraction studied here (PepCp) showed a lethal dose on larvae at concentrations of 0.1% (w/w). Freitas et al. (2016) showed that chitinases from CpLP reduce the survival of *C. maculatus* by 56%, at a concentration of 0.1% (w/w). In this way, it is possible to visualize the higher potential of PepCp to be applied against *C. maculatus*. Stanisçuaski and Carlini (2012) showed that many peptides have insecticidal activity in the intestines of insects. However, further studies based on the PepCp fraction are necessary to better understand the action mechanism of peptides against *C. maculatus*.

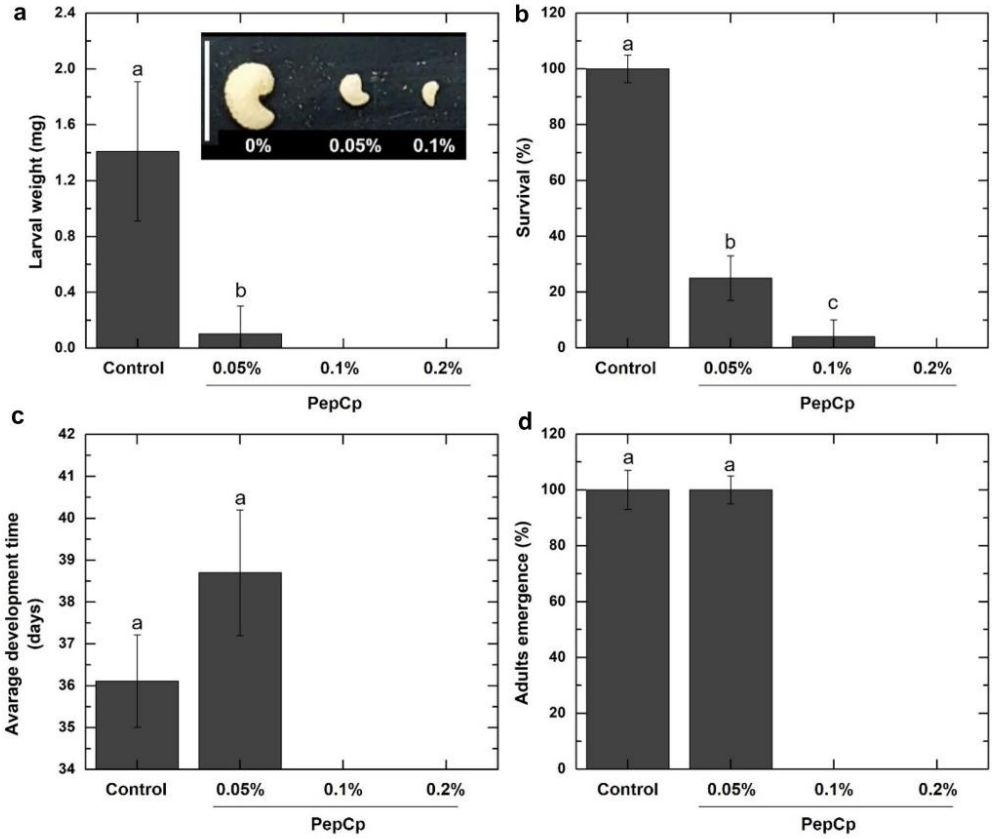

Fig. 5 Insecticidal activity of PepCp on *Callosobruchus maculatus*. **a** Average larval weight after 21 days of oviposition. Inset represents the general overview of larvae after 21 days of assay. The white bar indicates 5 mm. **b** Larvae survival rate after 21 days of assay. **c** Average adult insect development time. **d** Percentage of adult emergence. In case of control seeds, containing no PepCp, survival rate and adult emergence were considered as 100%. The data were analyzed by one-way ANOVA followed by Tukey test. A p value <0.05 was considered to be significant

Conclusion

The peptide fraction (PepCp) from latex of *C. procera* showed selective antifungal activity against *C. gloeosporioides* and *F. solani* and it was highly active against the insect *C. maculatus*. Besides, our results give new insights into the chemical composition of the latex as well as reinforce that the synthesis of different molecules with different activities have guaranteed the evolutionary success of these fluids in plant defense. Finally, this study opened new perspectives to identify and characterize new biomolecules to control agricultural pests.

Author contributions All the authors contributed equally to the overall conception, experimental design, and sampling protocols of this study.

Funding This work was supported by grants from the following Brazilian agencies: Conselho Nacional de Desenvolvimento Científico e Tecnológico (CNPq); Coordenação de Aperfeiçoamento de Pessoal de Nível Superior (CAPES); and Fundação Cearense de Apoio ao Desenvolvimento Científico e Tecnológico (FUNCAP). This study is part of the consortium "Molecular Biotechnology of Plant Latex."

Declarations

Conflict of interest The authors confirm that the contents of this article pose no conflicts of interest.

References

Barbosa MS, da Silva SB, Silva Sales AC et al (2019) Antifungal proteins from plant latex. Curr Protein Pept Sci 21:497–506. https://doi.org/10.2174/1389203720666191119101756

Barbosa MS, da Silva SB, Silva Sales AC et al (2020) Antifungal proteins from plant latex. Curr Protein Pept Sci 21:497–506. https://doi.org/10.2174/1389203720666191119101756

Bordoh PK, Ali A, Dickinson M et al (2020) A review on the management of postharvest anthracnose in dragon fruits caused by Colletotrichum spp. Crop Prot 130:105067. https://doi.org/10.1016/j.cropro.2019.105067

Broekaert WF, Terras FRG, Cammue BPA, Vanderleyden J (1990) An automated quantitative assay for fungal growth inhibition. FEMS Microbiol Lett 69:55–59. https://doi.org/10.1016/0378-1097(90)90412-J

de Dutra KA, de Oliveira JV, Navarro DM et al (2016) Control of *Callosobruchus maculatus* (FABR.) (Coleoptera: Chrysomelidae: Bruchinae) in *Vigna unguiculata* (L.) WALP. with essential oils from four Citrus spp. plants. J Stored Prod Res 68:25–32. https://doi.org/10.1016/j.jspr.2016.04.001

de Pontes JGM, Fernandes dos Santos Vander LSR et al (2020) Virulence factors in the phytopathogen-host interactions: an overview. J Agric Food Chem 68:7555–7570. https://doi.org/10.1021/acs.jafc.0c02389

Freitas CDT, Viana CA, Vasconcelos IM et al (2016) First insights into the diversity and functional properties of chitinases of the latex of *Calotropis procera*. Plant Physiol Biochem 108:361–371. https://doi.org/10.1016/j.plaphy.2016.07.028

Friedman M (2004) Applications of the Ninhydrin reaction for analysis of amino acids, peptides, and proteins to agricultural and biomedical sciences. J Agric Food Chem 52:385–406. https://doi.org/10.1021/jf030490p

Galindo FS, Filho MCMT, Silva EC et al (2020) Technical and economic viability of cowpea co-inoculated with *Azospirillum brasilense* and Bradyrhizobium spp. and nitrogen doses. Rev Bras Eng Agrícola e Ambient 24:304–311

Hawkins NJ, Bass C, Dixon A, Neve P (2018) The evolutionary origins of pesticide resistance. Biol Rev Camb Philos Soc 94:135–155. https://doi.org/10.1111/brv.12440

Ho WC, Ko WH (1997) A simple method for obtaining single-spore isolates of fungi. Bot Bull Acad Sin 38:41–44

Jiang H, Zhang W, Chen F et al (2019) Purification of an iron-binding peptide from scad (*Decapterus maruadsi*) processing by-products and its effects on iron absorption by Caco-2 cells. J Food Biochem 43:1–10. https://doi.org/10.1111/jfbc.12876

Johnson ET, Evans KO, Dowd PF (2015) Antifungal activity of a synthetic cationic peptide against the plant pathogens *Colletotrichum graminicola* and three Fusarium species. Plant Pathol J 31:316–321. https://doi.org/10.5423/PPJ.NT.04.2015.0061

Jucá TL, Ramos MV, Moreno FBMB et al (2013) Insights on the phytochemical profile (cyclopeptides) and biological activities of *Calotropis procera* latex organic fractions. Sci World J. https://doi.org/10.1155/2013/615454

Kimaru KS, Muchemi KP, Mwangi JW (2020) Effects of anthracnose disease on avocado production in Kenya. Cogent Food Agric 6:1799531. https://doi.org/10.1080/23311932.2020.1799531

Lacerda AF, Del Sarto RP, Silva MS et al (2016) The recombinant pea defensin Drr230a is active against impacting soybean and cotton pathogenic fungi from the genera Fusarium, Colletotrichum and Phakopsora. 3 Biotech 6:1–10. https://doi.org/10.1007/s13205-015-0320-7

Lopes TDP, Souza PFN, da Costa HPS, Pereira ML, da Silva Neto JX, de Paula PC, Brilhante RSN, Oliveira JTA, Vasconcelos IM, Sousa DOB (2020) Mo-CBP4, a purified chitin-binding protein from Moringa oleifera seeds, is a potent antidermatophytic protein: In vitro mechanisms of action, in vivo effect against infection, and clinical application as a hydrogel for skin infection. Int J Biol Macromol 149:432–442

Matos LF, da Cruz Lima E, de Andrade Dutra K et al (2020) Chemical composition and insecticidal effect of essential oils from Illicium verum and Eugenia caryophyllus on *Callosobruchus maculatus* in cowpea. Ind Crops Prod 145:112088. https://doi.org/10.1016/j.indcrop.2020.112088

Motaung TE, Saitoh H, Tsilo TJ (2017) Large-scale molecular genetic analysis in plant-pathogenic fungi: a decade of genome-wide functional analysis. Mol Plant Pathol 18:754–764. https://doi.org/10.1111/mpp.12497

Ramos MV, Grangeiro TB, Freire EA et al (2010) The defensive role of latex in plants: detrimental effects on insects. Arthropod Plant Interact 4:57–67. https://doi.org/10.1007/s11829-010-9084-5

Ramos MV, Demarco D, da Costa Souza IC, de Freitas CDT (2019) Laticifers, latex, and their role in plant defense. Trends Plant Sci 24:553–567. https://doi.org/10.1016/j.tplants.2019.03.006

Rathee M, Dalal P (2018) Emerging insect pests in Indian agriculture. Indian J Entomol 80:267. https://doi.org/10.5958/0974-8172.2018.00043.3

Scopes RK (1994) Protein purification: principles and practice/Robert K Scopes. Springer, New York

Souza DP, Freitas CDT, Pereira DA et al (2011) Laticifer proteins play a defensive role against hemibiotrophic and necrotrophic phytopathogens. Planta 234:183–193. https://doi.org/10.1007/s00425-011-1392-1

Stanisçuaski F, Carlini CR (2012) Plant ureases and related peptides: understanding their entomotoxic properties. Toxins 4:55–67. https://doi.org/10.3390/toxins4020055

Turkington TK, Yonow T, Petran A, Kriticos DJ (2016) Fusarium graminearum Pest Geography. Harvest Pest Geogr St Paul, MN InSTePP-HarvestChoice. https://doi.org/10.13140/RG.2.2.12061.31200

Wan J, Chen B, Rao J (2020) Occurrence and preventive strategies to control mycotoxins in cereal-based food. Compr Rev Food Sci Food Saf 19:928–953. https://doi.org/10.1111/1541-4337.12546

Zhang S, Zhang M, Xing J, Lin S (2019) A possible mechanism for enhancing the antioxidant activity by pulsed electric field on pine nut peptide Glutamine-Tryptophan-Phenylalanine-Histidine. J Food Biochem 43:1–12. https://doi.org/10.1111/jfbc.12714

Zhou J, Tan N (2000) Application of a new TLC chemical method for detection of cyclopeptides in plants. Chin Sci Bull 45:1825–1831. https://doi.org/10.1007/BF02886288

Publisher's Note Springer Nature remains neutral with regard to jurisdictional claims in published maps and institutional affiliations.

APÊNDICE C - SYNTHETIC ANTIMICROBIAL PEPTIDES: CHARACTERISTICS, DESIGN, AND POTENTIAL AS ALTERNATIVE MOLECULES TO OVERCOME MICROBIAL RESISTANCE

Life Sciences 278 (2021) 119647

Contents lists available at ScienceDirect

Life Sciences

journal homepage: www.elsevier.com/locate/lifescie

Review article

Synthetic antimicrobial peptides: Characteristics, design, and potential as alternative molecules to overcome microbial resistance

Patrícia G. Lima, Jose T.A. Oliveira, Jackson L. Amaral, Cleverson D.T. Freitas, Pedro F. N. Souza *, **

Department of Biochemistry and Molecular Biology, Federal University of Ceará, CEP 60.440-554 Fortaleza, Ceará, Brazil

ARTICLE INFO

Keywords:
Antimicrobial peptides
Synthetic antimicrobial peptides
Multidrug resistant pathogens
Mechanisms of action
Chemical synthesis

ABSTRACT

Recently, the dramatic emergence of antimicrobial resistance has received attention from World Health Organization. Synthetic antimicrobial peptides (SAMPs) are considered new weapons to fight against infections caused by multi-drug resistant pathogens. Here, the authors provide an overview of the current research on SAMPs. The focus is SAMPs, how to design them, which features must be considered during design, and comparison with natural peptides. This review also includes a discussion about the natural AMPs, mechanisms of action and applications as new drugs or even as adjuvants molecules to enhance commercial drugs activity. The advances in chemical synthesis have reduced the cost to produce synthetic peptides open ways to achieve new antimicrobial agents. Therefore, synthetic peptides are new promising molecules to safeguard human and animal health.

1. Introduction

In the early 1900s, and even before that, the infectious diseases were responsible for high mortality rates worldwide. Thus, the life expectancy was no longer than 40 and 38 years for men and women, respectively. The low life expectancy was due to many bacterial infections such as smallpox, tuberculosis, syphilis and plague [1]. For example, earlier in the 1900s, at least 10% of populations had syphilis with a death rate around 264 per million [2]. Regardless of the high death rate the etiological agent was unknown until 1905. Analyses of patients infected revealed the bacterium *Treponema pallidum* as responsible for the infections. However, the great news became only in 1910; when the first synthetic drug, named Salvarsan, was developed by the group head by Paul Ehrlich to treat syphilis. Later He received the Nobel Prize for that discovery [3]. Even though it is exciting discovery, Salvarsan presented many collateral effects in patients. The arsenic on its composition caused those effects.

A few years later, Salvarsan was overshadowed by the discovery of the first natural antimicrobial molecule from *Penicillium* ssp., named penicillin, in 1928 by Sir Alexander Fleming. In 1942, the first penicillin molecule was purified being available for therapeutic application in 1945, which became known as the beginning of "antibiotic era" [4]. After 1945, from 1950s to 1970s was named as golden era of antibiotics, because this period is marked by the discovery of many other antibiotic molecules such as tetracycline (1950), erythromycin (1953), gentamicin (1967), vancomycin (1972) [4]. The development of antibiotics brought a new breath into the fight against microorganisms. For example, after the development of antibiotics, the increase of life expectancy to change from 47 years in the beginning of the 20th Century to the average life expectancy at birth rose to 78.8 years in the mid of 20th Century [1].

The end of "antibiotic era" was unexpectedly fast. As predicted by evolution, at some point, bacteria would find way to fight back the antibiotics. Thus, the problem was, nobody thought that it could happen so fast. For example, bacterial resistance was found out for penicillin in 1940; however, penicillin became available to population only in 1942 [1]. Beginning in 1940 up today several microorganisms have acquired resistance and multiresistance to drugs such as Methicillin-Resistant *Staphylococcus aureus* (MRSA) and Vancomycin-Resistant *S. aureus* (VRSA), Vancomycin-Resistant *Enterococcus faecium* (VRE), *Streptococcus pneumoniae*, *Mycobacterium tuberculosis* (DRMT). Additionally, Fungi also developed resistance to Fluconazole and griseofulvin such as yeasts and dermatophytes, respectively [1,4–7]. The microbial

* Corresponding author at: Laboratory of Plant Defense Proteins, Biochemistry and Molecular Biology, at Federal University of Ceara, Av. Mister Hull, P.O. Box: 60440-554, Fortaleza Ceara.
** Corresponding author at: Laboratory of Plant Defense Proteins, Av. Mister Hull, P.O. Box: 60451, Fortaleza, CE, Brazil.
E-mail address: pedrofilhobio@gmail.com (P.F.N. Souza).

https://doi.org/10.1016/j.lfs.2021.119647
Received 16 December 2020; Received in revised form 8 May 2021; Accepted 18 May 2021
Available online 24 May 2021
0024-3205/© 2021 Elsevier Inc. This article is made available under the Elsevier license (http://www.elsevier.com/open-access/userlicense/1.0/).

resistance is a natural process; however, the fast development by them was a result of the selective pressure driven by the uncontrolled use of antibiotics over the years [8]. The alarming antimicrobial resistance situation has been recognized by the World Health Organization, which has named antibiotic resistance as one of the three most important public health threats of the 21st century [9].

As such, to overcome microbial resistance, research worldwide have put many efforts to propose new alternative antimicrobial molecules upon the current drugs to develop new treatments. Natural molecules were for many years the best source of new antimicrobial molecules being more than one-third of all new molecular entities approved by FDA [10–17]. Among those molecules, natural antimicrobial peptides (NAMPs) have been received attention as alternative molecules to fight against microbial resistance. However, given several problems in their applications such as toxicity to hosts and low stability, new molecules were still required. In this context, synthetic antimicrobial peptides (SAMPs) have emerged as important molecules to solve the problems presented by NAMPs [18,19].

Thus, in this review will be discussed how to produce and why synthetic peptides are promising molecules to overcome microbial resistance to drugs highlighting structural aspects, mechanisms of action, toxicity, and comparisons between natural and synthetic peptides.

2. Mechanisms of antimicrobial resistance

Prior to talk about AMPs, it is needed to understand how microorganisms developed resistance. Antimicrobial resistance occurs through a variety of mechanisms, depending on genetic and environmental factors. Microorganisms may present inherent or developed resistance to confer resistance to drugs. Other strategy to obtain resistance is by means of either gene mutation or acquiring exogenous genetic material (horizontal gene transfer) (Fig. 1) [20].

The most employed mechanism to obtain resistance is by drug modification, achieved by the action of microbial enzymes able to alter and even destroy these molecules (Fig. 1). For instance, aminoglycoside modifying enzymes (AMEs) catalyze the reactions of acetylation, phosphorylation, or adenylation decreasing the avidity of the modified drug for its target, being present in nearly all medically important bacteria [21]. Some other examples of modifying enzymes are chloramphenicol, streptogramins and lincosamides [22–24]. In the case of the well-known β-lactamases, it acts by destroying the amide bond of the β-lactam ring, present in antibiotics such as penicillin, ampicillin, amoxicillin, imipenem, piperacillin, and ceftazidime [25].

Other common mechanism of antimicrobial resistance is the drug target alteration (Fig. 1). By inserting point mutations in the genes encoding the target site, enzymatic modifications of the binding site, and/or replacement or bypass of the original target, which decrease the affinity for the antibiotic molecule [26]. One example is the mutation of gene encoding for penicillin-binding proteins (PBPs), resulting in PBPs with lower affinity for β-lactam drugs [27,28]. Likewise, this mechanism is the most common form of resistance in pathogenic fungi [29]. For instance, the lanosterol demethylase (encoded by ERG11 in *C. albicans*)

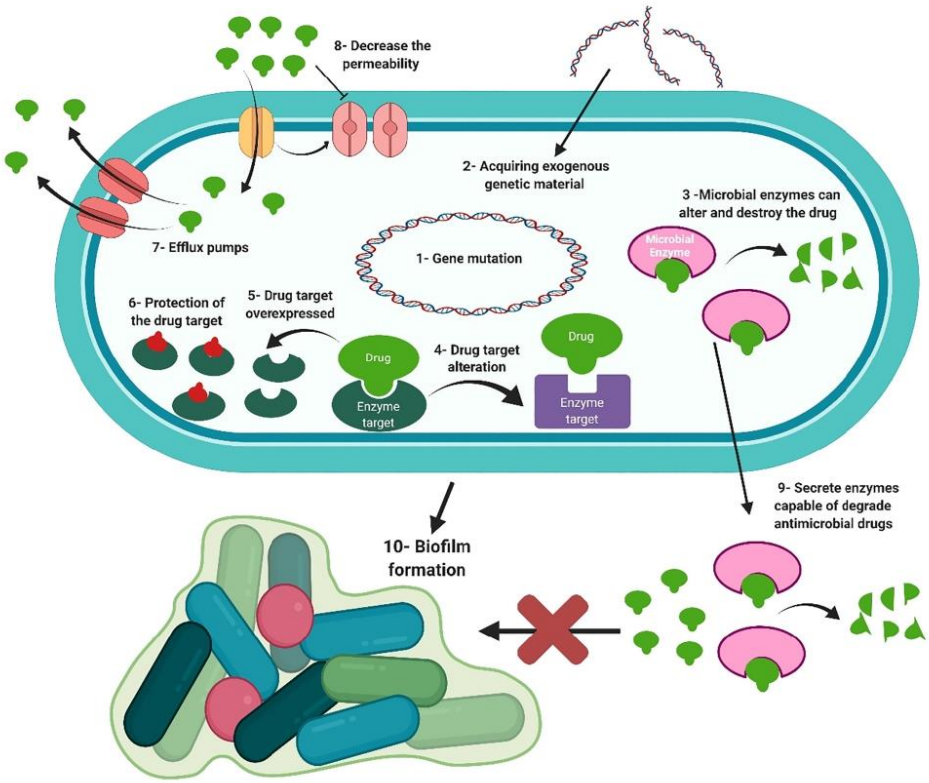

Fig. 1. Mechanisms by which pathogens developed multidrug resistance.

and β-1,3 glucan synthase (encoded by FKS genes in different fungal species) are the targets for binding of the antifungals drugs azoles and echinocandins, respectively, and any alteration, mutation, in these targets make the strain resistant [30].

Moreover, the drug target can also be overexpressed, leading to resistance by setting a higher effective drug concentration to reach (Fig. 1). Some examples are the up-regulation of ERG11, causing azole resistance in *C. albicans* [31]; and the overproduction of dihydrofolate reductase, associated with resistance to trimethoprim in *Escherichia coli* [32]. Lastly, the protection of the drug target site is other possible mechanism of antimicrobial resistance. One example is ribosomal protection proteins (RPPs), which reduces the available target sites by bounding to the ribosome and releasing the tetracycline from it [33]. Also, the Qnr proteins are other example of this mechanism, which act as a DNA analogue and reduce the interaction of the bacterial gyrase and topoisomerase IV with DNA, protecting cells from quinolones by lowering the number of available enzyme targets on chromosome [34].

Furthermore, reduction of the concentration of drug inside the microbial cell is other strategy developed for antimicrobial resistance (Fig. 1). This is achieved by mechanisms such as efflux pumps, which are membrane proteins that expel the drug from inside the cell at a high rate, not allowing them to reach a sufficiently high concentration to elicit an antimicrobial effect (Fig. 1) [35]. Efflux pumps are not specific for a family of antibiotics, they can extrude a wide range of different families of antibiotics including protein synthesis inhibitors, fluoroquinolones, β-lactams, carbapenems, polymyxins and azoles, resulting in multidrug resistant pathogens [36]. Some of the major families of efflux pumps are: the major facilitator superfamily (MFS), the small multidrug resistance family (SMR), the resistance-nodulation-cell-division family (RND), the ATP-binding cassette family (ABC), and the multidrug and toxic compound extrusion family (MATE) [37]. This mechanism is present in *Acinetobacter baumannii* with AdeABC pump, member of the RND superfamily, which confers resistance to several antibiotic classes such as aminoglycosides; also, efflux pumps Tet(A) and Tet(B) of the MFS confers resistance to tetracycline and minocycline [38–40]. In the case of *Candida albicans* the ABC pump Cdr1 is the main cause of azole resistance [41].

In order to achieve lower concentrations of drugs inside the cell of the microorganism, they can also decrease the permeability of the cell membrane (Fig. 1). One of the principal routes of entry of hydrophilic antibiotics through the membrane is by water-filled diffusion channels known as aquaporins [42]. Acquired antibiotic resistance can be obtained by mutations, affecting the expression or the function of porins (porin loss, the modification of the size or conductance of the porins or the reduced expression of porins) [43,44]. For instance, mutations in the membrane porin protein F (ompF) lead to development of resistance in *Escherichia coli* [45,46] and *Serratia marcescens* [47]; in the case of *Klebsiella pneumoniae* the mutation was in ompK [48].

Biofilm is a multicellular microbial structure attached to a surface and formed by assembly of protein, polysaccharide, and DNA in a extracellular polymeric matrix (Fig. 1) [49]. This kind of microbial organization is also one mechanism of antimicrobial resistance. It happens due to mechanical protection of the matrix, preventing antimicrobial diffusion or direct binding to some antibiotics (Fig. 1). Additionally, microorganisms within these structures can also secrete enzymes capable of degrade toxic compounds, such as antimicrobial drugs. Other factor is that microbial cells in deeper layers of the biofilm have low growth rate, and consequently reduced metabolic activity, impacting negatively the efficiency of antimicrobial drugs, which generally target cellular process [50]. Some examples of microorganism that present biofilm as mechanism of resistance to antibiotics are *Pseudomonas aeruginosa*, *Escherichia coli*, *Enterococcus faecalis*, *Streptococcus mutans*, *Aspergillus fumigatus* and *Candida* spp. [51–53].

2.1.1. Why peptides are special?

Antimicrobial peptides (AMPs) occur naturally in all living organisms such as bacteria, fungi, plants, and animals. They compose the first line of defense innate immunity from animals and plants [54]. AMPs share some characteristics as amino acids, size, charge, secondary structure and hydrophobicity. In general, these molecules are small (~2 kDa), cationic (at least +1), hold hydrophobic and/or apolar amino acids residues, alpha helices structures, hydrophobic moment, amphipathicity, sell-association ability (Fig. 2). Usually, when holding an α-helix with amphipathic characteristic and hydrophobic moment [55–58].

This set of structural characteristics is essential for AMPs to perform their activity making them special. Even though many AMPs have their mechanisms of action unclear, what is known still make them special. Virtually, all AMPs target the membranes, directly, either causing damage or destabilizing the membranes, or indirectly by interacting protein attached on the membrane still yet damaging it RNA and proteins [59].

By targeting the membranes, peptides impose a serious problem to the microorganisms. For example, antibiotic from penicillin group target protein involved in cell wall metabolism. Resistant bacteria to those antibiotics have either a new protein or a simple modified protein that is not affected by the antibiotic anymore. This type of modification is very easy to a microorganism like bacteria or fungi. However, in case of AMP that target the membrane, is very hard to a microorganism develop resistance. The membrane was essentially preserved during cellular evolution. Change the membrane composition or structure is even very hard, extremely expensive in energetic terms besides being dangerous to the cell life [60].

3. Synthetic AMPs

New antimicrobial products, including AMPs, can be discovered by isolating them from a natural source. However, this classical path to discover new molecules is not suitable for scale-up process, since it may be time consuming, have low yield of peptide and have high cost of production [61]. Furthermore, natural occurring AMPs may possess some undesirable characteristics, such as instability due to degradation by host proteases, poor selectivity, low hydrosolubility, hemolytic activity, host toxicity, and salt sensitivity [61].

To overcome these drawbacks, SAMPs came up. Designing synthetic peptides from natural AMP's sequences have two aims: (1) to extract the better part, which holds antimicrobial activity; (2) exclude the worse part from that particular sequence, which is toxicity and low resistance to proteolysis [55]. The rational design of these peptides based in the relationship of the structure to the activity of these molecules, since each amino acid is added sequentially to the AMP, being possible to do punctual modifications, analyzing and optimizing these molecules [62,63]. One of the main strategies applied is to use as template the sequence of natural occurring AMPs and then design a new molecule. Other route is the use of AMP libraries, using bioinformatics tools to assist in the screening and combination of new sequences of AMPs [63]. With the assistance of in silico technologies specific amino acids can be changed and possible engineered AMPs can be analyzed for improved antimicrobial activity [64]. Some of these modifications include the addition of hydrophobic and cationic residues for higher antimicrobial activity; others are the use of D-amino acids, cyclization, acetylation and peptidomimetics for improvement of in vivo stability [65,66].

Usually, synthetic peptides are more efficient than natural peptides by exerting the antimicrobial activity at low concentration compared to natural peptides that it came from (Table 1). Table 1 summarizes many times where synthetic peptides are more effective than natural peptides. For example, the natural AamAP1 from *Androctonus amoreuxi* present

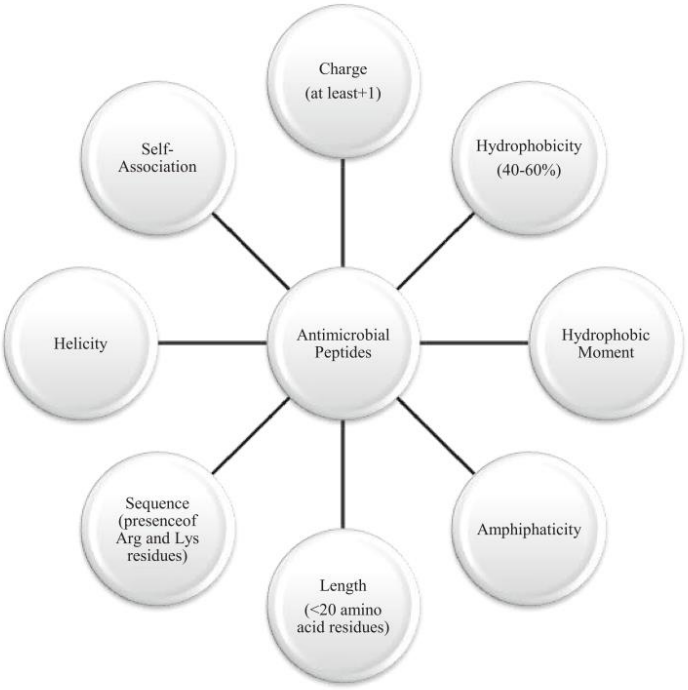

Fig. 2. Characteristics essential for peptides to display antimicrobial activity.

Table 1
Comparison of antimicrobial activity between natural and synthetic peptides.

Microorganisms	NAMP (concentration)	Reference	Microorganisms	SAMP (concentration)	Reference
Staphylococcus aureus, Escherichia coli, Candida albicans	AamAP1 (20 μM −150 μM)	[65]	*Staphylococcus epidermidis, Staphylococcus aureus, Enterococcus faecalis, Eshereschia coli, Salmonella enterica, Pseudomonas aeruginosa, Klebsiella pneumoniae*	AamAP1-Lysine (5–7.5 μM)	[66]
E. coli, K. pneumoniae	Pg-AMP1 (32–72 μM)	[116]	*Escherichia coli, Pseudomonas aeruginosa, Klebsiella pneumoniae, Acinetobacter baumannii, Staphylococcus aureus, Streptococcus pyogenes, Listeria ivanovii, Enterococcus faecalis, Candida albicans, Candida parapsilosis.*	Guavanin 2 (6.25–20 μM)	[117]
Staphylococcus aureus and *Escherichia coli*	PaDBS1 (8–256 μM)	[118]	*Escherichia coli, Staphylococcus aureus, Enterococcus faecalis, Pseudomonas aeruginosa*	PaDBS1R6F10 (4–32 μM)	[119]
Staphylococcus aureus, Pseudomonas aeruginosa, Enterococcus faecalis	Holothuroidin 2 (H2) (12.5 mM)	[120]	*Listeria monocytogenes*	H2d (0.3–1.2 mM)	[121]
Candida parapsilosis, Candida guilliermondii, Candida tropicalis, Candida albicans, Kluyveromyces marxianus; Leishmania amazonensis	*Pv*D1 (25–600 μM)	[122,124]	*Candida albicans* and *Candida buinensis*	$\gamma_{33\text{-}41}$*Pv*D1^{++} (18.35–293.6 μM)	[123]
Fusarium culmorum	Rs-AFP2 (8.5 μM)	[125]	*Fusarium culmorum*	Rs-AFP2(G9R) and Rs-AFP2(V39R) (3.3 and 3.2 μM)	[125]
N. crassa, B. cinerea, F. culmorum, S. cerevisiae, P. pastoris	Ib-AMP1 and Ib-AMP4 (0.5–16 μM)	[126]	*N. crassa, B. cinerea, F. culmorum, S. cerevisiae, P. pastoris*	MCD26, MCD30, MCE01 and MCE02 (0.5–20 μM)	[126]
R. meliloti, X. campestris, C. michiganensis, F. oxysporum, P. cucumerina, B. cinerea	Pp-TH (0.43–20 μM)	[127]	*R. meliloti, X. campestris, C. Michiganensis, F. oxysporum, P. cucumerina, B. cinerea*	Pp-TH(D32R) (0.38–3.3 μM)	[127]

antimicrobial activity against *Staphylococcus aureus*, *Escherichia coli*, and *Candida albicans* with concentration ranging from 20 to 150 μM [67]. However, the synthetic version of AamAP1, AamAP1-Lysine present antimicrobial activity against the same pathogens with a lower concentration range 5–7.5 μM, which is 4–20 times more potent than natural version [68].

In another case, the natural peptide Rs-AFP2 from radish (*Raphanus sativus* L.) has activity against *Fusarium culmorum* at a concentration of

8.5 μM. By mutation insertion, the authors designed two new synthetic derived peptides Rs-AFP2(G9R) and Rs-AFP2(V39R), which have activity against the same pathogen at 3.3 and 3.2 μM, respectively [69]. The synthetic derived peptides Rs-AFP2(G9R) and Rs-AFP2(V39R) were 2.6 times stronger than Rs-AFP2.

Despite the difference in the effectiveness of synthetic and natural peptides, an important point that both, synthetic and natural, shared the same mechanisms of action against pathogens, indicating synthetic and natural antimicrobial peptides have the same characteristics. Therefore, those characteristics could be employed in design synthetic peptide, as discussed below.

4. Antimicrobial peptides characteristics

As stated before, AMPs can be considered as ubiquitous molecules in nature, since all living organisms produce them [70]. Considering it, these peptides share some common characteristics that were cited before but now here in this topic will be discussed in detail. Among all features required for peptides-membrane interaction both, charge and hydrophobicity are essential to the initial attraction. The other ones such helicity, amphiphaticity, self-association are important to peptide-insertion into the membrane (Fig. 2).

4.1. Helicity

Multiple studies demonstrated that peptide helicity is critical for antimicrobial activity (negatively charged membrane) of AMPs (Fig. 3A–C) [55,71–75]. The most convincing contribution about the role of helicity to antimicrobial activity of peptides was provided by Oren and Shai [76] and Chen et al. [75]. In an elegant and wise experiment, Chen and collaborators [75] have made changes in the peptide V13K$_L$ sequences. The substitution of the L-amino acids by D-amino acid residues did not change the charge and hydrophobicity. By monitoring the peptides by reverse-phase coupled to HPLC the authors found that amino acids substitutions had change the ability of peptides to assume correct folded α-helix [75]. Overall, the introduction of D-amino acid residues result in slight change in the hydrophobicity of peptide by sufficient enough to interfere with it interaction with the reverse-phase matrix and thereby changing the retention time of peptide [77]. Chen et al. (2002) reported that the peptides V13K$_L$, with D-amino acids presented a reduction in antimicrobial activity when compared with those composed by L-amino acids.

The critical role of a helicity in antimicrobial activity was proved by many other studies. Lyu et al. (2016) showed that RI18 a fully helical peptide derived from PAMP-36 has antimicrobial activity enhanced in 8-fold compared to PAMP-36. The PAMP-36 peptide possesses a secondary structure with a α-helix with 6 turns followed by a loop structure and a smaller helix with one and half turn. In contrast, RI18 presented only one α-helix with 4 turns [74]. The authors discussed the smaller and stable α-helix of RI18 was the most responsible for the high activity of RI18 compared to PAMP-36.

Lima et al. (2020) have studied the mechanism of action of two peptides (*Mo*-CBP$_3$-PepI and *Mo*-CBP$_3$-PepII) against *Candida albicans*. Even though they share similar mechanism of action, *Mo*-CBP$_3$-PepI is 8 times stronger than *Mo*-CBP$_3$-PepII. Circular dichroism (CD) of peptides in contact to SDS micelles revealed new insights in the mechanisms of those peptides. CD analyses revealed that in aqueous solution both peptides assume disordered structures. However, in contact to SDS, *Mo*-CBP$_3$-PepI changes its secondary structure to a α-helix enhancing the interaction with the SDS micelle. In contrast, *Mo*-CBP$_3$-PepII did not

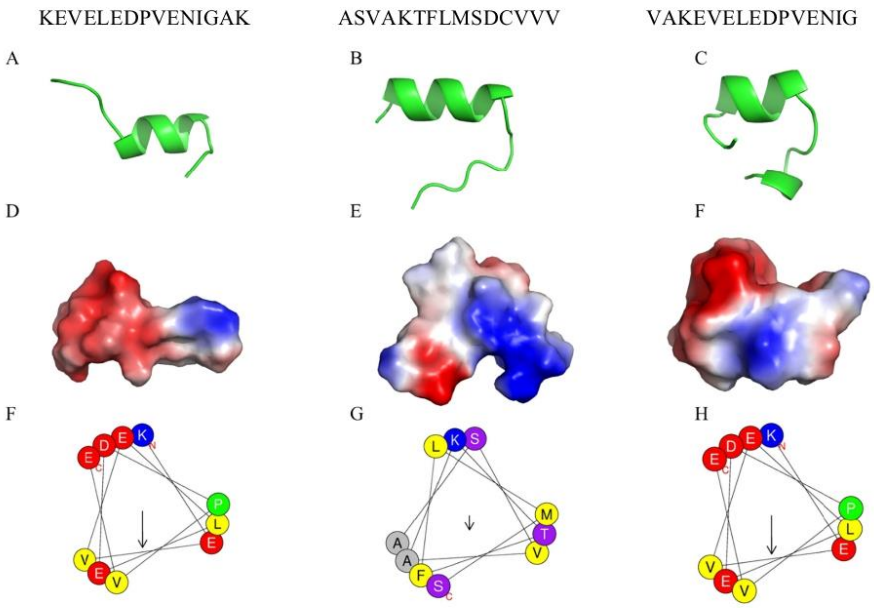

Fig. 3. Structural analyses of secondary of synthetic peptides. (A–C) Secondary structures of SAMPs with α-helix. (D–F) Vacuum electrostatic density maps of secondary structures. (C–E) Blue color represents the portions with a positive charge; Red color represents the apolar/hydrophobic portions; Silver color represents a neutral portion of structures. (F–H) the wheel projection of α-helices revealing the polar and hydrophobic face of it. The blue circle represents positive amino acid residues. The red circle indicates negative amino acid residues. Yellow Circle indicates non-polar amino acid residues. The green circle represents proline residues. The silver circle represents uncharged amino acid residues. The arrow indicates the direction of the hydrophobic face of helices. (For interpretation of the references to color in this figure legend, the reader is referred to the web version of this article.)

change its structure. This experiment simulates the interaction of peptides with the negative membrane of microorganisms and shows the role displayed by α-helices in antimicrobial interaction.

Here, we provide an example of some structures of synthetic peptides summarized in the Fig. 3A–C. As expected, the three peptides designed presented secondary structures in α-helix. All peptides presented α-helices structures mixed with unordered structure in the edges of between helices (Fig. 3A–C).

4.2. Charge

Primarily the electrostatic force drives the interaction of peptides with the microbial membranes. The microbial membrane has a negative charge due to the presence of negative charged lipids outside the membrane [64]. Because of that, the positive charge of peptides is so essential to initial attraction.

Despite the importance of positive charge to antimicrobial activity, there was no correlation about peptides with high positive charge with high activity. It is accepted that, at least a charge of +1, is required for antimicrobial activity [71,73]. For instance, Lima et al. (2020) reported peptides (*Mo*-CBP$_3$-PepI and *Mo*-CBP$_3$-PepII) with a charge of +1 presenting a Minimal Inhibitory Concentration (MIC) of 7 μM to kill 90% (MIC_{90}) of *Candida albicans* [72]. In contrast, Lyu et al. (2016) reported a peptide (PAMP-36) with a charge of +14 that presented a MIC_{90} at a concentration of 128 μM against *C. albicans* [74]. These reports are an example about no correlation of high positive charge with antimicrobial activity. Indeed, this is a very hard task to accomplish. However, the negative correlation is quite easy to follow.

The negative correlation of high positive charged peptides is related with toxicity to erythrocytes. It was reported that peptides with charges higher than +9 presented several damages to erythrocytes. Lyu et al. [74] showed the peptide PMAP-36 (charge of +14) has a hemolytic concentration at 4 μM [74]. In contrast, a PMAP-36 derived peptide, RI12 (charge of +6) has a hemolytic concentration at 128 μM. By showing that is clear to notice the correlation of high positive charge with hemolytic activity.

Experiments have revealed that changes of peptide positive charge affect their biological activity. For example, Jiang et al. [78] have done many experiments altering the positive charge of the antimicrobial peptide V13K to evaluate the influence of charge in the V13K biological activity [78]. By performing many alterations in the V13K sequence such as introduction, substitution of positively charged amino acids by negative it was possible to analyze the role of net charge in antimicrobial activity and hemolytic activity of V13K. Versions of V13K with high positive charges (+9 and +10) presented a dramatic increase in hemolytic activity with no enhancement in antimicrobial activity. These results suggest a critical threshold for the net positive charge of AMPs that governs antimicrobial and hemolytic activities [78]. In contrast, versions of V13K with charges lower than +4 were totally inactive. However, the versions of V13K with charges starting from +4 up to +8 presented high antimicrobial activity with low hemolytic activity (Minimum Hemolytic Concentration 250 $\mu g mL^{-1}$). Further increase in net charge to +9 and +10 improved antimicrobial activity, but also caused a dramatic increase in hemolytic activity.

Fig. 3D–F summarizes the analysis of electronic density of synthetic peptides. The evaluation of electronic density of peptides structures is important to understand the distribution of charges across the structure. Based on the electronic density it is possible to identify the exactly charge in the region of peptides (Fig. 3D–F). The positive charged region in the peptide structure is in blue, the apolar/hydrophobic region is in red, and the neutral regions are presented in silver.

4.3. Hydrophobicity, hydrophobic moment, and amphiphaticity

After electrostatic force, the hydrophobicity is the second force that driven the peptide into the membrane. Different from antibiotic drugs, peptides target the cytoplasmic microbial membranes are the main target of AMPs, and therefore, hydrophobicity is a crucial feature to interact with the membranes and insert itself into the membrane hydrophobic core [79]. In general, increased hydrophobicity of the nonpolar face of an amphipathic α-helical peptide improves antimicrobial activity [80–82].

HP (2–20, AKKVFKRLEKLFSKIQNDK) is an antimicrobial peptide derived from the N-terminus of *Helicobacter pylori* ribosomal protein L1 (RPL1) [83]. Lee et al. (2002) utilized the sequence of native peptide HP (2−20) to design and produce several HP-analogs peptides with amino acid substitutions altering the hydrophobic ratio and evaluate its role on peptide antimicrobial activity. In this study, the substitution of Gln and Asp at positions 17 and 19 of HP by two Trp residues enhanced hydrophobicity and led to a dramatic increase in antimicrobial activity without alteration in hemolytic activity [83]. In contrast, the reduction of hydrophobicity by substituting Leu and Phe at positions 12 and 19 of HP by Ser decreased the antimicrobial activity compared to HP. These results indicated that the hydrophobicity of peptides is critical for its effective antimicrobial activity and may be one of the determinant parameters for peptide interaction with the lipid bilayers of the cell membrane [83].

In another study, Chen et al. (2007) utilized the $V13K_L$ antimicrobial peptide to study the role of hydrophobicity on the peptide action. After the analyses, the authors found an optimal hydrophobicity window that enhance the antimicrobial potential of peptide [84]. The $V13K_L$ has a MIC against *Pseudomonas aeruginosa* and hemolytic activity respectively of 7.8 and 250 $\mu g\ mL^{-1}$ [84]. However, a $V13K_L$-derived peptide (L6A/L21A) with a lower hydrophobicity presented a MIC against *P. aeruginosa* and hemolytic activity respectively of >500 and >1000 $\mu g\ mL^{-1}$ [84]. In contrast, a highly hydrophobic $V13K_L$-derived peptide (A12L/A20L/A23L) presented a low MIC against *P. aeruginosa* (>500 $\mu g\ mL^{-1}$), and a high hemolytic activity (>4.0 $\mu g\ mL^{-1}$). These results revealed, indeed, there is a window to hydrophobic ratio to a great antimicrobial activity, and any modification out of this range could interfere with antimicrobial activity and increase collateral effects of peptide.

Together with hydrophobic ratio, the hydrophobic moment is also a critical feature to drive the antimicrobial activity. The hydrophobic moment is the ability of peptide to shift from a polar face to a hydrophobic face at the time to insert into the membrane [55,85]. Kim et al. (2018) correlated the increase of hydrophobic moment of synthetic peptide Hp1404-T1 with antibacterial activity [85]. The Hp1404-T1, with a hydrophobic moment value of 0.699, was 16-fold less efficient to inhibit bacterial growth than Hp1404-T1e, which showed a hydrophobic moment value of 0.831. This experiment just confirms the role of hydrophobic moment in antimicrobial activity of peptides.

Although they are correlated, there were no directed action between hydrophobic ratio and hydrophobic moment. What is known is that both are critical to peptide insertion into the microbial membrane. As stated before, the electrostatic potential is useful in the primary attraction of peptide to membrane. After that, all the process is driven by hydrophobicity and hydrophobic moment. The hydrophobic moment is essential to peptide shift from the polar to apolar face. Then, hydrophobicity is important to peptides interact with the hydrophobic portion of the lipids in the membrane hydrophobic core.

The amphipathic structure is an important requirement to AMP penetrates the membrane and thus exerts antimicrobial activity. Amphipathicity is defined as the vector sum of the hydrophobicity of individual amino acids [86]. It has been shown that the position of helix during the hydrophobic moment is a crucial factor for antimicrobial activity than hydrophobicity [87,88]. The study of a 17-residue amidated-acetylated peptides when interacting with both neutral and anionic lipids revealed that peptide helicity in water increased the hydrophobic moment. This result demonstrates that helical amphipathicity plays more significant roles in interfacial binding than hydrophobicity does [88].

The wheel projection is an interesting tool to analyze the amphipaticity and hydrophobic moment of the peptide's helices. In the Fig. 3F and H clearly presented a polar face and an apolar face indicating that the peptides have a hydrophobic moment, which is important to shift between from polar and apolar faces. However, the structure presented in Fig. 3G did not has a clear separation between polar and apolar faces.

4.4. Length

AMPs are generally small sized with <20 amino acid residues [89]. This is in consonance with the minimal requirement of 2–4 amino acid residues per turn to produce an alpha helix, 7–8 amino acid residues (two turns) to produce amphipathic faces. In addition, at least, 18 residues are needed to a peptide transverse the lipid bilayers [90]. Given its importance, the impact of size for AMP activity has been largely studied. Benincasa et al. [91] revealed the 15-residue cathelicidin synthetic peptide produced from the C-terminus of melittin, which has 7 times less antimicrobial activity and 300 times less hemolytic activity compared to the original melittin [91]. In another study, the HP-derived synthetic peptide 15 mer peptide HP-A3 (A3-NT) that is smaller than its counterpart presented an increase of antibacterial and antifungal activity at 2- and 4-fold, respectively, without hemolysis, compared to the HP original peptide [92].

Lyu et al. (2016) have demonstrated the importance of length to the antimicrobial activity of peptides by working with the porcine myeloid antimicrobial peptide-36 (PMAP-36). The PMAP-36 is a peptide with 36 residues that presents activity against gram-positive and gram-negative bacteria, as well as is active against candida cells [74]. Attempting to improve its activity, the authors design and synthesized smaller PMAP-36-derived peptides with 21 (RI21), 18 (RI18), 15 (TI15), and 12 (RI12) residues. After testing, the authors did not notice any significant improvement in antimicrobial activity among the peptides. However, it became clear that as small was the peptides less hemolytic it was. These results revealed that the smaller peptides were safer than bigger ones [74].

4.5. Sequence

AMPs have different primary sequences, with approximately 50% hydrophobic residues and to confer at least a charge of +1. In addition, a good peptide sequence confers to it the ability to produce an α-helix. By comparing N-terminal sequences of more than 150 AMPs there was found no conserved pattern [93]. Usually, the positive net charge is provided by arginine or lysine residues. It is not common to find histidine in AMPs given the size of its imidazole group, which could impair peptide insertion into the membrane [94–96]. Comparison between Arg and Lys residues revealed Arg as most critical to antimicrobial activity [95,96].

Arginine residues possess a side chain able to establish both electrostatic and hydrophobic interaction with the membrane. The physicochemical analysis of the arginine side chain revealed a hydrophobic propyl moiety group and a large cationic resonance-stabilized guanidinium group. The guanidinium group has a pKa about 12–13, which means it is protonated and cationic virtually at all conditions [95]. By providing the most essential interaction with the membranes, arginine is critical to antimicrobial activity of peptides.

The hydrophobic content is usually provided by the sequence of amino acid residues classified as apolar and hydrophobic. The hydrophobic residues are not that common given the size of phenol group in the lateral chain. Regarding the apolar residues, the most important are leucine, isoleucine, valine, threonine, and cysteine [71,72]. Related to the cysteine function in the antimicrobial peptide none is known about its contribution to the activity. However, it is indeed, known when present, cysteines must not form disulfide bridges, otherwise peptides could not penetrate the membrane [97]. Schoeder et al., [97] revealed that the treatment of peptide human betadefensin-1 (hDB-1) with DTT to break the disulfide bridges enhanced antimicrobial activity [97]. Additionally, the substitution of cysteine by either alanine or leucine reduced the antimicrobial activity of hDB-1. The mechanisms of how cysteine play it role in antimicrobial activity is not clear, but the result does confirm its importance to peptides action.

4.6. Self-association

Many studies have reported peptide self-association (i. e., the ability to dimerize) as critical requirement for antimicrobial activity [98]. However, in some cases if the self-association ability of a peptide is too strong in aqueous environment it could decrease the antimicrobial potential of peptide. This happens because peptides bind each other in such a way making difficult to dissociate them, turning down the ability to pass through the capsule and cell wall of microorganisms, and to penetrate into the cytoplasmic membrane to kill target cells.

The studies about the self-association of peptide are scarce due to the requirement of powerful techniques to evaluate this process. However, some studies reported requirement to self-association such as the perfect helix and interaction between peptides without lose the ability to interact with membranes. Recently, Lima et al. (2020) proposed a hypothetic model based on their results. By working with two small peptides *Mo*-CPB$_3$-PepI (893.25 Da) and *Mo*-CPB$_3$-PepII (1031.30 Da) produced pores with size of 10 and 6 kDa, respectively, into the membrane of *C. albicans* [72]. The authors reasoned that those peptides were making self-association after fluorescence analyses using the FITC-Dextran with known sizes. However, the results did not allow the authors to make any correlation of pore-size with high efficiency in inhibit *C. albicans* growth, just show that, indeed, self-association happens.

5. Antimicrobial peptides mechanisms of action

Although AMPs share various common characteristics, they can act trough diverse mechanisms that are important to be elucidated for further drug development based on these molecules. One of the AMPs main mode of action, and more vastly studied is the microbial membrane permeabilization [70]. Initially, the concept was that the membrane was the only target of AMPs, but nowadays is known that there are other mechanisms, including intracellular targets [99].

5.1. Membrane disruption

In order to disrupt the membrane or penetrate the microbial cell the AMPs must first interact with the membrane. As stated before, most AMPs share structural characteristics that facilitate those interactions with microbial membranes, being the first of them the electrostatic attraction. This occurs by the attraction of the positively charged peptides to the negatively charged components of microbial membranes, such as negatively charged lipid present on the outer surface of the cytoplasmic membrane [100]. The next step is the AMP insertion into the lipid bilayer, which is aided by the interaction with hydrophobic residues and the amphipathic structure of the peptides [8,101]. The insertion generally happens initially in a parallel orientation to the outer leaflet of the lipid bilayer; as the concentration increases, the AMPs tend to assume a perpendicular orientation to the surface, reaching a critical concentration responsible for inducing a dislocation of lipids and modifications in the membrane structure [8,100]. Some of these changes are membrane thinning, alterations in membrane curvature, electrostatics modifications, pore formation and disturbance of the bilayer permeability barrier [62]. With all these membrane alterations the peptides can be reoriented in the membrane and translocated into the cytoplasm [100].

Some models were proposed to explain the membrane permeabilization action of the AMPs, for instance the barrel-stave, toroidal-pore, and carpet models. In the barrel-stave model the pore is formed by the insertion of the hydrophobic portion of the peptide into the lipid core

of the membrane. Upon reaching a threshold concentration, peptide monomers aggregate, minimizing the exposure of the peptide hydrophilic residues, and forming transmembrane pores within the hydrophobic membrane core [70,102]. Nevertheless, in the toroidal pore model there are no specific peptide-peptide interactions, instead the polar groups of the peptides associate with the polar head groups of the phospholipids [62,103]. Thus, in the barrel-stave pore, the hydrophobic and hydrophilic conformation of the lipids is not altered, whereas in toroidal pores that conformation is disrupted [65].

The mode of action of the carpet model, unlike the other models, does not consist in the specific formation of pores [65]. In this case, the peptides act in a diffuse manner, which can be compared to a detergent action [104]. The positively charged AMPs are electrostatically attracted to the anionic phospholipids head groups on the membrane surface and fold into an amphipathic conformation [8,70]. A high density of peptides accumulates on the membrane surface forming a carpet-like cover, leading to the disintegration of the membrane and formation of micelles [62,65].

5.2. Intracellular targets

Membrane disruption is the most important and the primary mode of action for antimicrobial activity of these peptides, however it is not the only mode of action [8]. Observations showed that some AMPs were able to accomplish their antimicrobial function without causing damage to the cellular membrane, but through the inhibition of cellular functions [62,101]. Thus, intracellular targets represent the main mechanism of cellular death of various AMPs [65]. Once inside the microbial cell the AMPs may inhibit cell wall, DNA, RNA, and protein synthesis as well as inhibit enzymes activity [59,105,106]. The sum of these effects can lead to the collapse of the metabolic pathways and result in cell death [107].

5.3. Immune modulation

In addition to the direct killing modes of action, AMPs can also act by selectively enhancing or regulating host immune mechanism in vivo, promoting resistance to microbial infection [62,108]. The immune responses produced by AMPs include reduction of inflammation by lowering the levels of proinflammatory cytokines produced in response to microbial signature molecules and modulation of the expression of chemokines [108]. These effects are beneficial during microbial infections since they can prevent excessive and harmful proinflammatory responses that can result in organ failure and sepsis [109]. AMPs are also capable of enhancing wound healing by stimulating the production of restructuring metalloproteinases and epithelial cell metabolism as well as the migration of epithelial and keratinocyte cells [110]. Furthermore, AMPs can also promote stimulation of chemotaxis, of angiogenesis, and cellular differentiation of macrophages (leukocytes) and dendritic cells [62]. In order to explain these immune modulation responses of AMPs on mammalian cells some models were suggested, such as directly bind of AMPs to specific cell surface receptors, inducing receptor signaling; AMPs may locally modify the part of membrane that contains the receptor and indirectly alter the activation state and function of the receptor; AMPs can also cause release of a membrane-bound factor, which could then bind to its receptor [109,110].

6. Synergism of AMP with other antimicrobial agents

A synergism occur when the combination of at least of two different compounds result in a higher inhibitory activity than the simply addition of their separated effects [111]. The main reason for the synergic interaction between AMPs and other antimicrobial agents is that the majority of AMPs is able to cause pore formation in the microbial membranes, which facilitates the entry of the antimicrobials in the microbial cell, permitting the inhibition of DNA synthesis, protein synthesis or cell wall synthesis [112]. Accordingly, this combination may be effective to overcome mechanisms of resistance that involves the membrane, such as low microbial penetrability [70]. Other advantage of the combined use is the reduction of the effective dose, consequently reducing the potential toxicity and the economic costs [112]. Thus, it can prevent the development of drug resistance and extend the lifetime of traditional antimicrobial agents [113]. Considering this, AMPs may be employed as adjuvants, facilitating and complementing the action of the conventional antimicrobial agents [112].

The assessment of the type of interaction between antimicrobial agents is usually measured by the fractional inhibitory concentration index (FICI). This index is calculated based on the minimal inhibitory concentration (MIC), by dividing the mean MIC of each compound in combination by the MIC of each compound alone and adding the results, classifying them into antagonistic (FICI $\geq$4.0), indifferent(FICI 0.5–4.0) or synergistic (FICI $\leq$0.5) interaction [114].

Recently, our research group has published a study the synergistic effect between synthetic peptides and antifungal drug against dermatophytes [115]. *Trichophyton mentagrophytes* and *T. rubrum* are the most important drug resistant fungi infecting humans leading to dermatophytosis. Both are resistant to griseofulvin, the most common antifungal drug. In that study, Souza et al. (2020) revealed that alone, griseofulvin only inhibit 40% the growth of *T. mentagrophytes* and 0% of *T. rubrum*. However, when mixed with peptides (5 μg mL^{-1}) the griseofulvin (1000 μg mL^{-1}) thus inhibits 100% of fungal growth. The FICI values of peptides with griseofulvin of 0.22. This FICI value indicates a synergistic effect between peptides and griseofulvin. Lima et al. (2020) showed the synthetic peptide *Mo*-CBP_3-PepI enhanced the activity of nystatin toward *C. albicans* in 200 times with a FICI value of 0.16 [72]. In both studies published by Lima et al. (2020) and Souza et al., 2020 an interesting result was found. Besides enhance the activity of antifungal drugs, the peptides also reduced their toxicity to human erythrocytes. Altogether, these results brought to light the application of peptides as adjuvants to improve the use conventional useless drugs.

7. Conclusion

Given these considerations explained here, it is possible to assure that synthetic peptides are new potential molecules to fight back toward multidrug resistant pathogens. Two factors are the important the most: (1) the synthetic peptides use the ways of natural peptide to affect pathogens; (2) during design is removed from sequence the toxic or allergenic regions to prevent the production of toxic synthetic peptides. So, we reasoned that, together the development of new technologies reaching low price of synthesis and innovative computer-assisted design strategies has considerable potential to boost the discovery of new potential antimicrobial therapeutic peptides and not only for targeting bacteria and fungi but also for targeting disease-causing viruses, helminths, and protozoa.

Ethical approval

Not applicable.

CRediT authorship contribution statement

Conceptualization: Patrícia G. Lima, Jose T. A. Oliveira, Jackson L. Amaral, Cleverson D. T. Freitas, and Pedro F. N. Souza.

Data curation: Patrícia G. Lima and Pedro F.N. Souza.

Formal analysis: Pedro F.N. Souza, Jackson L. Amaral and Patrícia G. Lima.

Funding acquisition: Jose T.A. Oliveira and Cleverson D. T. Freitas.

Resources: Jose T.A. Oliveira and Cleverson D. T. Freitas, Valder N. Freire.

Supervision: Pedro F.N. Souza.

Writing - original draft: Patricia G. Lima and Pedro F.N. Souza.

Writing, review and editing: Pedro F.N. Souza.

Funding and acknowledgments

Grants from the following Brazilian agencies supported this work: The National Council for Scientific and Technological Development (CNPq), with a doctoral and master grant to JLA and PGL a research grant (codes 431511/2016-0 and 306202/2017-4) to JTAO; the Office to Coordinate Improvement of University Personnel (CAPES) sponsored PFNS with a postdoctoral fellowship. The authors are also grateful for the support received from the National Center for High-Performance Processing - Federal University of Ceará.

Declaration of competing interest

All authors declare no conflicts of interest.

References

[1] W.A. Adedeji, The treasure called antibiotics, Ann. Ibadan Postgrad. Med. 14 (2016) 56–57. http://www.ncbi.nlm.nih.gov/pubmed/28337088. (Accessed 23 January 2020).

[2] S. Szreter, The prevalence of syphilis in England and Wales on the eve of the great war: re-visiting the estimates of the royal commission on venereal diseases 1913–1916, Soc. Hist. Med. 27 (2014) 508–529, https://doi.org/10.1093/shm/hkt123.

[3] N.C. Lloyd, H.W. Morgan, B.K. Nicholson, R.S. Ronimus, The composition of Ehrlich's Salvarsan: resolution of a century-old debate, Angew. Chemie - Int. Ed. 44 (2005) 941–944, https://doi.org/10.1002/anie.200461471.

[4] C.L. Ventola, The antibiotic resistance crisis: causes and threats, P T J. 40 (2015) 277–283 (doi:Article).

[5] M. Gross, Antibiotics in crisis, Curr. Biol. 23 (2013), https://doi.org/10.1016/j.cub.2013.11.057.

[6] S. Sengupta, M.K. Chattopadhyay, H.P. Grossart, The multifaceted roles of antibiotics and antibiotic resistance in nature, Front. Microbiol. 4 (2013), https://doi.org/10.3389/fmicb.2013.00047.

[7] B. Spellberg, D.N. Gilbert, The future of antibiotics and resistance: a tribute to a career of leadership by John Bartlett, Clin. Infect. Dis. 59 (2014) S71–S75, https://doi.org/10.1093/cid/ciu392.

[8] K. Sharma, S. Aaghaz, K. Shenmar, R. Jain, Short antimicrobial peptides, Recent Pat. Antiinfect. Drug Discov. 13 (2018) 12–52, https://doi.org/10.2174/1574891x13666180628105928.

[9] ANTIMICROBIAL RESISTANCE Global Report on Surveillance, n.d. https://apps.who.int/iris/bitstream/handle/10665/112642/9789241564748_eng.pdf;jsessionid=582B27405776F1EDD1897A9ECA73029A?sequence=1 (accessed April 8, 2019).

[10] P.F.N. Souza, I.M. Vasconcelos, F.D.A. Silva, F.B. Moreno, A.C.O. Monteiro-Moreira, L.M.R. Alencar, A.S.G. Abreu, J.S. Sousa, J.T.A. Oliveira, A 2S albumin from the seed cake of ricinus communis inhibits trypsin and has strong antibacterial activity against human pathogenic bacteria, J. Nat. Prod. 79 (2016) 2423–2431, https://doi.org/10.1021/acs.jnatprod.5b01096.

[11] H.P. Oliveira, R.G.G. Silva, J.T.A. Oliveira, D.O.B. Sousa, M.L. Pereira, P.F. N. Souza, A.A. Soares, V.M. Gomes, A.C.O. Monteiro-Moreira, F.B.M.B. Moreno, I. M. Vasconcelos, A novel peroxidase purified from Marsdenia megalantha latex inhibits phytopathogenic fungi mediated by cell membrane permeabilization, Int. J. Biol. Macromol. 96 (2017) 743–753, https://doi.org/10.1016/j.ijbiomac.2016.12.083.

[12] T.F. Martins, I.M. Vasconcelos, R.G.G. Silva, F.D.A. Silva, P.F.N. Souza, A.L. N. Varela, L.M. Albuquerque, J.T.A. Oliveira, A Bowman-Birk inhibitor from the seeds of Luetzelburgia auriculata inhibits Staphylococcus aureus growth by promoting severe cell membrane damage, J. Nat. Prod. 81 (2018) 1497–1507, https://doi.org/10.1021/acs.jnatprod.7b00545.

[13] A.J.S. Sousa, P.F.N. Souza, J.M. Gifoni, L.P. Dias, C.D.T. Freitas, J.T.A. Oliveira, D.O.B. Sousa, I.M. Vasconcelos, Scanning electron microscopy reveals deleterious effects of Moringa oleifera seed exuded proteins on root-knot nematode Meloidogyne incognita eggs, Int. J. Biol. Macromol. (2019), https://doi.org/10.1016/j.ijbiomac.2019.10.278.

[14] T.R. Mota, H.V.S. Linhares, J.H. Araújo-Filho, D.M. Veras, H.P.S. Costa, C.M. P. Souza, P.F.N. Souza, T.F. Martins, Protein extract from Cereus jamacaru (DC.) inhibits Colletotrichum gloeosporioides growth by stimulating ROS generation and promoting severe cell membrane damage, Microb. Pathog. 130 (2019) 71–80, https://doi.org/10.1016/j.micpath.2019.02.033.

[15] C.D.T. Freitas, R.O. Silva, M.V. Ramos, C.T.M.N. Porfírio, D.F. Farias, J.S. Sousa, J.P.B. Oliveira, P.F.N. Souza, L.P. Dias, T.B. Grangeiro, Identification, characterization, and antifungal activity of cysteine peptidases from Calotropis procera latex, Phytochemistry 169 (2020), 112163, https://doi.org/10.1016/j.phytochem.2019.112163.

[16] S.E. Rossiter, M.H. Fletcher, W.M. Wuest, Natural products as platforms to overcome antibiotic resistance, Chem. Rev. 117 (2017) 12415–12474, https://doi.org/10.1021/acs.chemrev.7b00283.

[17] E. Patridge, P. Gareiss, M.S. Kinch, D. Hoyer, An analysis of FDA-approved drugs: natural products and their derivatives, Drug Discov. Today 21 (2016) 204–207, https://doi.org/10.1016/j.drudis.2015.01.009.

[18] W. Li, F. Separovic, N.M. O'Brien-Simpson, J.D. Wade, Chemically modified and conjugated antimicrobial peptides against superbugs, Chem. Soc. Rev. 50 (2021) 4932–4973, https://doi.org/10.1039/d0cs01026j.

[19] M. Magana, M. Pushpanathan, A.L. Santos, L. Leanse, M. Fernandez, A. Ioannidis, M.A. Giulianotti, Y. Apidianakis, S. Bradfute, A.L. Ferguson, A. Cherkasov, M. N. Seleem, C. Pinilla, C. de la Fuente-Nunez, T. Lazaridis, T. Dai, R.A. Houghten, R.E.W. Hancock, G.P. Tegos, The value of antimicrobial peptides in the age of resistance, Lancet Infect. Dis. 20 (2020) e216–e230, https://doi.org/10.1016/S1473-3099(20)30327-3.

[20] J.O. Sekyere, J. Asante, Emerging mechanisms of antimicrobial resistance in bacteria and fungi: advances in the era of genomics, Future Microbiol. 13 (2018) 241–262, https://doi.org/10.2217/fmb-2017-0172.

[21] M.S. Ramirez, M.E. Tolmasky, Aminoglycoside modifying enzymes, Drug Resist. Updat. 13 (2010), https://doi.org/10.1016/j.drup.2010.08.003.

[22] L. Huang, H. Yuan, M.-F. Liu, X.-X. Zhao, M.-S. Wang, R.-Y. Jia, S. Chen, K.-F. Sun, Q. Yang, Y. Wu, X.-Y. Chen, A.-C. Cheng, D.-K. Zhu, Type B chloramphenicol acetyltransferases are responsible for chloramphenicol resistance in Riemerella anatipestifer, China, Front. Microbiol. 8 (2017), https://doi.org/10.3389/fmicb.2017.00297.

[23] S. Schwarz, C. Kehrenberg, B. Doublet, A. Cloeckaert, Molecular basis of bacterial resistance to chloramphenicol and florfenicol, FEMS Microbiol. Rev. 28 (2004), https://doi.org/10.1016/j.femsre.2004.04.001.

[24] S. Schwarz, J. Shen, K. Kadlec, Y. Wang, G. Brenner Michael, A.T. Feßler, B. Vester, Lincosamides, streptogramins, phenicols, and pleuromutilins: mode of action and mechanisms of resistance, Cold Spring Harb. Perspect. Med. 6 (2016), https://doi.org/10.1101/cshperspect.a027037.

[25] C.L. Tooke, P. Hinchliffe, E.C. Bragginton, C.K. Colenso, V.H.A. Hirvonen, Y. Takebayashi, J. Spencer, β-Lactamases and β-lactamase inhibitors in the 21st century, J. Mol. Biol. 431 (2019), https://doi.org/10.1016/j.jmb.2019.04.002.

[26] P. Lambert, Bacterial resistance to antibiotics: modified target sites, Adv. Drug Deliv. Rev. 57 (2005), https://doi.org/10.1016/j.addr.2005.04.003.

[27] A. Zapun, C. Contreras-Martel, T. Vernet, Penicillin-binding proteins and β-lactam resistance, FEMS Microbiol. Rev. 32 (2008), https://doi.org/10.1111/j.1574-6976.2007.00095.x.

[28] A. Zapun, C. Morlot, M.-K. Taha, Resistance to β-lactams in Neisseria ssp due to chromosomally encoded penicillin-binding proteins, Antibiotics 5 (2016), https://doi.org/10.3390/antibiotics5040035.

[29] M.C. Fisher, N.J. Hawkins, D. Sanglard, S.J. Gurr, Health and food security - TCLocal, Science 742 (2018) 739–742 (80-.).

[30] A.A. Sagatova, M.V. Keniya, R.K. Wilson, M. Sabherwal, J.D.A. Tyndall, B. C. Monk, Triazole resistance mediated by mutations of a conserved active site tyrosine in fungal lanosterol 14α-demethylase, Sci. Rep. 6 (2016), https://doi.org/10.1038/srep26213.

[31] N. Dunkel, T.T. Liu, K.S. Barker, R. Homayouni, J. Morschhäuser, P.D. Rogers, A gain-of-function mutation in the transcription factor Upc2p causes upregulation of ergosterol biosynthesis genes and increased fluconazole resistance in a clinical Candida albicans isolate, Eukaryot. Cell 7 (2008), https://doi.org/10.1128/EC.00103-08.

[32] G.M. Eliopoulos, P. Huovinen, Resistance to trimethoprim-sulfamethoxazole, Clin. Infect. Dis. 32 (2001), https://doi.org/10.1086/320532.

[33] P.J. Warburton, N. Amodeo, A.P. Roberts, Mosaic tetracycline resistance genes encoding ribosomal protection proteins, J. Antimicrob. Chemother. 71 (2016), https://doi.org/10.1093/jac/dkw304.

[34] K.J. Aldred, R.J. Kerns, N. Osheroff, Mechanism of quinolone action and resistance, Biochemistry 53 (2014), https://doi.org/10.1021/bi5000564.

[35] D. Du, X. Wang-Kan, A. Neuberger, H.W. van Veen, K.M. Pos, L.J.V. Piddock, B. F. Luisi, Multidrug efflux pumps: structure, function and regulation, Nat. Rev. Microbiol. 16 (2018) 523–539, https://doi.org/10.1038/s41579-018-0048-6.

[36] P. Blanco, S. Hernando-Amado, J. Reales-Calderon, F. Corona, F. Lira, M. Alcalde-Rico, A. Bernardini, M. Sanchez, J. Martinez, Bacterial multidrug efflux pumps: much more than antibiotic resistance determinants, Microorganisms 4 (2016), https://doi.org/10.3390/microorganisms4010014.

[37] D. Du, X. Wang-Kan, A. Neuberger, H.W. van Veen, K.M. Pos, L.J.V. Piddock, B. F. Luisi, Multidrug efflux pumps: structure, function and regulation, Nat. Rev. Microbiol. 16 (2018), https://doi.org/10.1038/s41579-018-0048-6.

[38] S. Martí, F. Fernández-Cuenca, A. Pascual, A. Ribera, J. Rodríguez-Baño, G. Bou, J. Miguel Cisneros, J. Pachón, L. Martínez-Martínez, J. Vila, Prevalencia de los genes tetA y tetB como mecanismo de resistencia a tetraciclina y minociclina en aislamientos clínicos de Acinetobacter baumannii, Enferm. Infecc. Microbiol. Clin. 24 (2006), https://doi.org/10.1157/13085012.

[39] I. Marchand, L. Damier-Piolle, P. Courvalin, T. Lambert, Expression of the RND-type efflux pump AdeABC in Acinetobacter baumannii is regulated by the AdeRS two-component system, Antimicrob. Agents Chemother. 48 (2004), https://doi.org/10.1128/AAC.48.9.3298-3304.2004.

[40] S.N. Abdi, R. Ghotaslou, K. Ganbarov, A. Mobed, A. Tanomand, M. Yousefi, M. Asgharzadeh, H.S. Kafil, Acinetobacter baumannii efflux pumps and antibiotic resistance, Infect. Drug Resist. 13 (2020), https://doi.org/10.2147/IDR.S228089.

[41] A.R. Holmes, Y.-H. Lin, K. Niimi, E. Lamping, M. Keniya, M. Niimi, K. Tanabe, B. C. Monk, R.D. Cannon, ABC transporter Cdr1p contributes more than Cdr2p does to fluconazole efflux in fluconazole-resistant Candida albicans clinical isolates, Antimicrob. Agents Chemother. 52 (2008), https://doi.org/10.1128/AAC.00463-08.

[42] J.-M. Pagès, C.E. James, M. Winterhalter, The porin and the permeating antibiotic: a selective diffusion barrier in Gram-negative bacteria, Nat. Rev. Microbiol. 6 (2008), https://doi.org/10.1038/nrmicro1994.
[43] E. Christaki, M. Marcou, A. Tofarides, Antimicrobial resistance in bacteria: mechanisms, evolution, and persistence, J. Mol. Evol. 88 (2020), https://doi.org/10.1007/s00239-019-09914-3.
[44] L. Fernandez, R.E.W. Hancock, Adaptive and mutational resistance: role of porins and efflux pumps in drug resistance, Clin. Microbiol. Rev. 25 (2012), https://doi.org/10.1128/CMR.00043-12.
[45] B.K. Ziervogel, B. Roux, The binding of antibiotics in OmpF porin, Structure 21 (2013), https://doi.org/10.1016/j.str.2012.10.014.
[46] C.C. Chang, C.W. Yan, R. Onal, Y. Zhang, Genetic characterization and investigation of kanamycin susceptibility of ompC and ompF single gene deletion mutants of Escherichia coli K-12, J. Exp. Microbiol. Immunol . 22 (2018) 1–9.
[47] A. Moya-Torres, M.R. Mulvey, A. Kumar, I.J. Oresnik, A.K.C. Brassinga, The lack of OmpF, but not OmpC, contributes to increased antibiotic resistance in Serratia marcescens, Microbiology 160 (2014), https://doi.org/10.1099/mic.0.081166-0.
[48] E. Sugawara, S. Kojima, H. Nikaido, Klebsiella pneumoniae major porins OmpK35 and OmpK36 allow more efficient diffusion of β-lactams than their Escherichia coli homologs OmpF and OmpC, J. Bacteriol. 198 (2016), https://doi.org/10.1128/JB.00590-16.
[49] S. Singh, S.K. Singh, I. Chowdhury, R. Singh, Understanding the mechanism of bacterial biofilms resistance to antimicrobial agents, Open Microbiol. J. 11 (2017), https://doi.org/10.2174/1874285801711010053.
[50] D. Dufour, V. Leung, C.M. Lévesque, Bacterial biofilm: structure, function, and antimicrobial resistance, Endod. Top. 22 (2010), https://doi.org/10.1111/j.1601-1546.2012.00277.x.
[51] C.W. Hall, T.-F. Mah, Molecular mechanisms of biofilm-based antibiotic resistance and tolerance in pathogenic bacteria, FEMS Microbiol. Rev. 41 (2017), https://doi.org/10.1093/femsre/fux010.
[52] E. Mowat, C. Williams, B. Jones, S. Mcchlery, G. Ramage, The characteristics of Aspergillus fumigatus mycetoma development: is this a biofilm? Med. Mycol. 47 (2009) https://doi.org/10.1080/13693780802238834.
[53] S. Silva, C. Rodrigues, D. Araújo, M. Rodrigues, M. Henriques, Candida species biofilms' antifungal resistance, J. Fungi 3 (2017), https://doi.org/10.3390/jof3010008.
[54] M.D.T. Torres, S. Sothiselvam, T.K. Lu, C. de la Fuente-Nunez, Peptide design principles for antimicrobial applications, J. Mol. Biol. (2019), https://doi.org/10.1016/j.jmb.2018.12.015.
[55] P.F.N. Souza, L.S.M. Marques, J.T.A. Oliveira, P.G. Lima, L.P. Dias, N.A.S. Neto, F. E.S. Lopes, J.S. Sousa, A.F.B. Silva, R.F. Caneiro, J.L.S. Lopes, M.V. Ramos, C.D. T. Freitas, Synthetic antimicrobial peptides: from choice of the best sequences to action mechanisms, Biochimie 175 (2020) 132–145, https://doi.org/10.1016/j.biochi.2020.05.016.
[56] M. Zasloff, Antimicrobial peptides of multicellular organisms, Nature 415 (2002) 389–395, https://doi.org/10.1038/415389a.
[57] R. Dhayakaran, S. Neethirajan, X. Weng, Investigation of the antimicrobial activity of soy peptides by developing a high throughput drug screening assay, Biochem. Biophys. Reports 6 (2016), https://doi.org/10.1016/j.bbrep.2016.04.001.
[58] F.E.S. Lopes, H.P.S. da Costa, P.F.N. Souza, J.P.B. Oliveira, M.V. Ramos, J.E. C. Freire, T.L. Jucá, C.D.T. Freitas, Peptide from thaumatin plant protein exhibits selective anticandidal activity by inducing apoptosis via membrane receptor, Phytochemistry 159 (2019) 46–55, https://doi.org/10.1016/j.phytochem.2018.12.006.
[59] B. Bechinger, S.-U. Gorr, Antimicrobial peptides: mechanisms of action and resistance, J. Dent. Res. 96 (2017) 254–260, https://doi.org/10.1177/0022034516679973.
[60] C. Ghosh, J. Haldar, Membrane-active small molecules: designs inspired by antimicrobial peptides, ChemMedChem 10 (2015) 1606–1624, https://doi.org/10.1002/cmdc.201500299.
[61] A. Boto, J. Pérez de la Lastra, C. González, The road from host-defense peptides to a new generation of antimicrobial drugs, Molecules 23 (2018) 311, https://doi.org/10.3390/molecules23020311.
[62] E.F. Haney, S.C. Mansour, R.E.W. Hancock, Antimicrobial peptides: an introduction, in: Methods Mol. Biol, Humana Press Inc., 2017, pp. 3–22, https://doi.org/10.1007/978-1-4939-6737-7_1.
[63] Z.Y. Ong, N. Wiradharma, Y.Y. Yang, Strategies employed in the design and optimization of synthetic antimicrobial peptide amphiphiles with enhanced therapeutic potentials, Adv. Drug Deliv. Rev. 78 (2014) 28–45, https://doi.org/10.1016/j.addr.2014.10.013.
[64] D. Ciumac, H. Gong, X. Hu, J.R. Lu, Membrane targeting cationic antimicrobial peptides, J. Colloid Interface Sci. 537 (2019) 163–185, https://doi.org/10.1016/j.jcis.2018.10.103.
[65] P. Kumar, J. Kizhakkedathu, S. Straus, Antimicrobial peptides: diversity, mechanism of action and strategies to improve the activity and biocompatibility in vivo, Biomolecules 8 (2018) 4, https://doi.org/10.3390/biom8010004.
[66] M.D.T. Torres, S. Sothiselvam, T.K. Lu, C. de la Fuente-Nunez, Peptide design principles for antimicrobial applications, J. Mol. Biol. 431 (2019) 3547–3567, https://doi.org/10.1016/j.jmb.2018.12.015.
[67] A. Almaaytah, M. Zhou, L. Wang, T. Chen, B. Walker, C. Shaw, Antimicrobial/cytolytic peptides from the venom of the North African scorpion, Androctonus amoreuxi: biochemical and functional characterization of natural peptides and a single site-substituted analog, Peptides 35 (2012), https://doi.org/10.1016/j.peptides.2012.03.016.
[68] A. Almaaytah, S. Tarazi, A. Abu-Alhaijaa, Y. Altall, N. Alshar'i, K. Bodoor, Q. Al-Balas, Enhanced antimicrobial activity of Aam AP1-Lysine, a novel synthetic peptide analog derived from the scorpion venom peptide Aam AP1, Pharmaceuticals 7 (2014) 502–516, https://doi.org/10.3390/ph7050502.
[69] G.W. De Samblanx, I.J. Goderis, K. Thevissen, R. Raemaekers, F. Fant, F. Borremans, D.P. Acland, R.W. Osborn, S. Patel, W.F. Broekaert, Mutational analysis of a plant defensin from radish (*Raphanus sativus* L.) reveals two adjacent sites important for antifungal activity, J. Biol. Chem. 272 (1997), https://doi.org/10.1074/jbc.272.2.1171.
[70] J.M. Sierra, E. Fusté, F. Rabanal, T. Vinuesa, M. Viñas, An overview of antimicrobial peptides and the latest advances in their development, Expert. Opin. Biol. Ther. 17 (2017) 663–676, https://doi.org/10.1080/14712598.2017.1315402.
[71] J.T.A. Oliveira, P.F.N. Souza, I.M. Vasconcelos, L.P. Dias, T.F. Martins, M.F. Van Tilburg, M.I.F. Guedes, D.O.B. Sousa, Mo-CBP3-PepI, Mo-CBP3-PepII, and Mo-CBP3-PepIII are synthetic antimicrobial peptides active against human pathogens by stimulating ROS generation and increasing plasma membrane permeability, Biochimie 157 (2019) 10–21, https://doi.org/10.1016/j.biochi.2018.10.016.
[72] P.G. Lima, P.F.N. Souza, C.D.T. Freitas, J.T.A. Oliveira, L.P. Dias, J.X.S. Neto, I. M. Vasconcelos, J.L.S. Lopes, D.O.B. Sousa, Anticandidal activity of synthetic peptides: mechanism of action revealed by scanning electron and fluorescence microscopies and synergism effect with nystatin, J. Pept. Sci. (2020) 1–13, https://doi.org/10.1002/psc.3249.
[73] L.P. Dias, P.F.N. Souza, J.T.A. Oliveira, I.M. Vasconcelos, N.M.S. Araújo, M.F. V. Tilburg, M.I.F. Guedes, R.F. Carneiro, J.L.S. Lopes, D.O.B. Sousa, RcAlb-PepII, a synthetic small peptide bioinspired in the 2S albumin from the seed cake of Ricinus communis, is a potent antimicrobial agent against Klebsiella pneumoniae and Candida parapsilosis, Biochim. Biophys. Acta Biomembr. 1862 (2020), 183092, https://doi.org/10.1016/j.bbamem.2019.183092.
[74] Y. Lyu, Y. Yang, X. Lyu, N. Dong, A. Shan, Antimicrobial activity, improved cell selectivity and mode of action of short PMAP-36-derived peptides against bacteria and Candida, Sci. Rep. 6 (2016), 27258, https://doi.org/10.1038/srep27258.
[75] Y. Chen, C.T. Mant, R.S. Hodges, Determination of stereochemistry stability coefficients of amino acid side-chains in an amphipathic alpha-helix, J. Pept. Res. 59 (2002) 18–33. http://www.ncbi.nlm.nih.gov/pubmed/11906604. (Accessed 10 October 2019).
[76] Z. Oren, Y. Shai, Selective lysis of bacteria but not mammalian cells by diastereomers of melittin: structure–function study †, Biochemistry 36 (1997) https://doi.org/10.1021/bi962507l.
[77] J.M. Kovacs, C.T. Mant, R.S. Hodges, Determination of intrinsic hydrophilicity/hydrophobicity of amino acid side chains in peptides in the absence of nearest-neighbor or conformational effects, Biopolymers 84 (2006), https://doi.org/10.1002/bip.20417.
[78] Z. Jiang, A.I. Vasil, J.D. Hale, R.E.W. Hancock, M.L. Vasil, R.S. Hodges, Effects of net charge and the number of positively charged residues on the biological activity of amphipathic α-helical cationic antimicrobial peptides, Biopolym. - Pept. Sci. Sect. 90 (2008) 369–383, https://doi.org/10.1002/bip.20911.
[79] I. Kabelka, R. Vácha, Optimal hydrophobicity and reorientation of amphiphilic peptides translocating through membrane, Biophys. J. 115 (2018), https://doi.org/10.1016/j.bpj.2018.08.012.
[80] T. Wieprecht, M. Dathe, M. Beyermann, E. Krause, W.L. Maloy, D.L. MacDonald, M. Bienert, Peptide hydrophobicity controls the activity and selectivity of magainin 2 amide in interaction with membranes, Biochemistry 36 (1997), https://doi.org/10.1021/bi9619987.
[81] M. Dathe, T. Wieprecht, H. Nikolenko, L. Handel, W.L. Maloy, D.L. MacDonald, M. Beyermann, M. Bienert, Hydrophobicity, hydrophobic moment and angle subtended by charged residues modulate antibacterial and haemolytic activity of amphipathic helical peptides, FEBS Lett. 403 (1997), https://doi.org/10.1016/S0014-5793(97)00055-0.
[82] D. Avrahami, Y. Shai, Conjugation of a magainin analogue with lipophilic acids controls hydrophobicity, solution assembly, and cell selectivity, Biochemistry 41 (2002), https://doi.org/10.1021/bi011549t.
[83] D.G. Lee, H.N. Kim, Y. Park, H.K. Kim, B.H. Choi, C.-H. Choi, K.-S. Hahm, Design of novel analogue peptides with potent antibiotic activity based on the antimicrobial peptide, HP (2–20), derived from N-terminus of helicobacter pylori ribosomal protein L1, Biochim. Biophys. Acta - Proteins Proteomics 1598 (2002), https://doi.org/10.1016/S0167-4838(02)00373-4.
[84] Y. Chen, M.T. Guarnieri, A.I. Vasil, M.L. Vasil, C.T. Mant, R.S. Hodges, Role of peptide hydrophobicity in the mechanism of action of α-helical antimicrobial peptides, Antimicrob. Agents Chemother. 51 (2007), https://doi.org/10.1128/AAC.00925-06.
[85] M.K. Kim, H.K. Kang, S.J. Ko, M.J. Hong, J.K. Bang, C.H. Seo, Y. Park, Mechanisms driving the antibacterial and antibiofilm properties of Hp1404 and its analogue peptides against multidrug-resistant Pseudomonas aeruginosa, Sci. Rep. 8 (2018), https://doi.org/10.1038/s41598-018-19434-7.
[86] D. Eisenberg, Three-dimensional structure of membrane and surface proteins, Annu. Rev. Biochem. 53 (1984), https://doi.org/10.1146/annurev.bi.53.070184.003115.
[87] N. Pathak, R. Salas-Auvert, G. Ruche, M. Janna, D. McCarthy, R.G. Harrison, Comparison of the effects of hydrophobicity, amphiphilicity, and α-helicity on the activities of antimicrobial peptides, Proteins Struct. Funct. Genet. 22 (1995), https://doi.org/10.1002/prot.340220210.
[88] M. Fernández-Vidal, S. Jayasinghe, A.S. Ladokhin, S.H. White, Folding amphipathic helices into membranes: amphiphilicity trumps hydrophobicity, J. Mol. Biol. 370 (2007), https://doi.org/10.1016/j.jmb.2007.05.016.

[89] R.E. Hancock, Peptide antibiotics, Lancet 349 (1997), https://doi.org/10.1016/S0140-6736(97)80051-7.
[90] Y. Shai, Mode of action of membrane active antimicrobial peptides, Biopolymers 66 (2002), https://doi.org/10.1002/bip.10260.
[91] M. Benincasa, B. Skerlavaj, R. Gennaro, A. Pellegrini, M. Zanetti, In vitro and in vivo antimicrobial activity of two α-helical cathelicidin peptides and of their synthetic analogs, Peptides 24 (2003), https://doi.org/10.1016/j.peptides.2003.07.025.
[92] Y. Park, S.-C. Park, H.-K. Park, S.Y. Shin, Y. Kim, K.-S. Hahm, Structure-activity relationship of HP (2–20) analog peptide: enhanced antimicrobial activity by N-terminal random coil region deletion, Biopolymers 88 (2007), https://doi.org/10.1002/bip.20679.
[93] A. Tossi, L. Sandri, A. Giangaspero, Amphipathic, α-helical antimicrobial peptides, Biopolymers 55 (2000), https://doi.org/10.1002/1097-0282(2000)55:1<4::AID-BIP30>3.0.CO;2-M.
[94] J. Portelinha, Examining the Role of Histidine in the Antimicrobial Peptide Gaduscidin-1, 2018, pp. 1–59.
[95] K. Hristova, W.C. Wimley, A look at arginine in membranes, J. Membr. Biol. 239 (2011) 49–56, https://doi.org/10.1007/s00232-010-9323-9.
[96] M. Arias, K. Piga, M. Hyndman, H. Vogel, Improving the activity of Trp-rich antimicrobial peptides by Arg/Lys substitutions and changing the length of cationic residues, Biomolecules 8 (2018), https://doi.org/10.3390/biom8020019.
[97] B.O. Schroeder, Z. Wu, S. Nuding, S. Groscurth, M. Marcinowski, J. Beisner, J. Buchner, M. Schaller, E.F. Stange, J. Wehkamp, Reduction of disulphide bonds unmasks potent antimicrobial activity of human β 2-defensin 1, Nature 469 (2011) 419–423, https://doi.org/10.1038/nature09674.
[98] Y. Chen, C.T. Mant, S.W. Farmer, R.E.W. Hancock, M.L. Vasil, R.S. Hodges, Rational design of α-helical antimicrobial peptides with enhanced activities and specificity/therapeutic index, J. Biol. Chem. 280 (2005), https://doi.org/10.1074/jbc.M413406200.
[99] H. Ulm, M. Wilmes, Y. Shai, H.G. Sahl, Antimicrobial host defensins specific antibiotic activities and innate defense modulation, Front. Immunol. 3 (2012) 1–4, https://doi.org/10.3389/fimmu.2012.00249.
[100] C.D. Fjell, J.A. Hiss, R.E.W. Hancock, G. Schneider, Designing antimicrobial peptides: form follows function, Nat. Rev. Drug Discov. 11 (2012) 37–51, https://doi.org/10.1038/nrd3591.
[101] K.A. Brogden, Antimicrobial peptides: pore formers or metabolic inhibitors in bacteria? Nat. Rev. Microbiol. 3 (2005) 238–250, https://doi.org/10.1038/nrmicro1098.
[102] M.R. Yeaman, N.Y. Yount, Mechanisms of antimicrobial peptide action and resistance, Cardiovasc. Res. 55 (2003) 27–55, https://doi.org/10.1124/pr.55.1.2.27.
[103] W.C. Wimley, Describing the mechanism of antimicrobial peptide action with the interfacial activity model, ACS Chem. Biol. 5 (2010) 905–917, https://doi.org/10.1021/cb1001558.
[104] M.R. Yeaman, Mechanisms of antimicrobial peptide action and resistance, Pharmacol. Rev. 55 (2003) 27–55, https://doi.org/10.1124/pr.55.1.2.
[105] F. Guilhelmelli, N. Vilela, P. Albuquerque, L. da S. Derengowski, I. Silva-Pereira, C.M. Kyaw, Antibiotic development challenges: the various mechanisms of action of antimicrobial peptides and of bacterial resistance, Front. Microbiol. 4 (2013) 353, https://doi.org/10.3389/fmicb.2013.00353.
[106] A. Krizsan, D. Volke, S. Weinert, N. Sträter, D. Knappe, R. Hoffmann, Insect-derived proline-rich antimicrobial peptides kill bacteria by inhibiting bacterial protein translation at the 70 S ribosome, Angew. Chemie - Int. Ed. 53 (2014) 12236–12239, https://doi.org/10.1002/anie.201407145.
[107] S. Sharma, N. Sahoo, A. Bhunia, Antimicrobial Peptides and their Pore/Ion Channel Properties in Neutralization of Pathogenic Microbes, (n.d.).
[108] J. Wang, X. Dou, J. Song, Y. Lyu, X. Zhu, L. Xu, W. Li, A. Shan, Antimicrobial peptides: promising alternatives in the post feeding antibiotic era, Med. Res. Rev. 39 (2019) 831–859, https://doi.org/10.1002/med.21542.
[109] M. Mahlapuu, J. Håkansson, L. Ringstad, C. Björn, Antimicrobial peptides: an emerging category of therapeutic agents, Front. Cell. Infect. Microbiol. 6 (2016) 194, https://doi.org/10.3389/fcimb.2016.00194.
[110] L. Steinstraesser, T. Hirsch, M. Schulte, M. Kueckelhaus, F. Jacobsen, E.A. Mersch, I. Stricker, N. Afacan, H. Jenssen, R.E.W. Hancock, J. Kindrachuk, Innate defense regulator peptide 1018 in wound healing and wound infection, PLoS One 7 (2012), e39373, https://doi.org/10.1371/journal.pone.0039373.
[111] A. Hollmann, M. Martinez, P. Maturana, L.C. Semorile, P.C. Maffia, Antimicrobial peptides: interaction with model and biological membranes and synergism with chemical antibiotics, Front. Chem. 6 (2018) 204, https://doi.org/10.3389/fchem.2018.00204.
[112] J. Li, P. Fernández-Millán, E. Boix, Synergism between host defence peptides and antibiotics against bacterial infections, Curr. Top. Med. Chem. 20 (2020) 1238–1263, https://doi.org/10.2174/1568026620666200303122626.
[113] B. Mishra, S. Reiling, D. Zarena, G. Wang, Host defense antimicrobial peptides as antibiotics: design and application strategies, Curr. Opin. Chem. Biol. 38 (2017) 87–96, https://doi.org/10.1016/j.cbpa.2017.03.014.
[114] A. Motos, L.M. Avery, K.J. DeRonde, E.M. Mullane, J.L. Kuti, D.P. Nicolau, Where should antibiotic gradient diffusion strips be crossed to assess synergy? A comparison of the standard method with a novel method using steady-state antimicrobial concentrations, Int. J. Antimicrob. Agents 53 (2019) 698–702, https://doi.org/10.1016/j.ijantimicag.2019.03.006.
[115] P.G. Lima, P.F.N. Souza, C.D.T. Freitas, L.P. Bezerra, N.A.S. Neto, A.F.B. Silva, J.T. A. Oliveira, D.O.B. Sousa, Synthetic peptides against Trichophyton mentagrophytes and T. rubrum: mechanisms of action and efficiency compared to griseofulvin and itraconazole, Life Sci. (2020), https://doi.org/10.1016/j.lfs.2020.118803.
[116] William Porto, Luz Irazazabal, Eliane Alvez, Suzana Ribeiro, et al., In silico optimization of a guava antimicrobial peptide enables combinatorial exploration for peptide design, Nat. Commun. (2019), https://doi.org/10.1038/s41467-018-03746-3.
[117] Marlon Cardoso, Raquel Orozco, Camila Rezende, et al., Computer-Aided Design of Antimicrobial Peptides: Are We Generating Effective Drug Candidates? Front. Micro. (2020) https://doi.org/10.3389/fmicb.2019.03097.
[118] William Porto, Isabel Fensterseifer, Suzana Ribeiro, Octavio Franco, Joker: An algorithm to insert patterns into sequences for designing antimicrobial peptides, Bioc. Biophys. Acta (BBA) Gen. Sub. (2018), https://doi.org/10.1016/j.bbagen.2018.06.011.
[119] Isabel Fensterseifer, Mario Felicio, Eliane Alves, et al., Selective antibacterial activity of the cationic peptide PaDBS1R6 against Gram-negative bacteria, Bioc. Biophys. Acta (BBA) Gen. Sub. (2019), https://doi.org/10.1016/j.bbamem.2019.03.016.
[120] Domenico Schillaci, Maria Cusimano, Vincenzo Cunsolo, et al., Immune mediators of sea-cucumber Holothuria tubulosa (Echinodermata) as source of novel antimicrobial and anti-staphylococcal biofilm agents, AMB Exp. (2013), https://doi.org/10.1186/2191-0855-3-35.
[121] Maria Cusimano, Angelo Spinello, Giampaolo Barone, et al., A Synthetic Derivative of Antimicrobial Peptide Holothuroidin 2 from Mediterranean Sea Cucumber (Holothuria tubulosa) in the Control of Listeria monocytogenes, Mar. Drugs (2019), https://doi.org/10.3390/md17030159.
[122] Erica O Mello, Suzanna F F Ribeiro, et al., Antifungal activity of PvD1 defensin involves plasma membrane permeabilization, inhibition of medium acidification, and induction of ROS in fungi cells, Curr. Micro. (2011), https://doi.org/10.1007/s00284-010-9847-3.
[123] Erica Mello, Gabriel Taveira, Andre Carvalho, Valdirene Gomes, Improved smallest peptides based on positive charge increase of the γ-core motif from *Pv* D $_1$ and their mechanism of action against *Candida* species, Intern. J. Nano. (2019), https://doi.org/10.2147/IJN.S187957.
[124] Viviane Nascimento, Érica Mello, Laís Carvalho, et al., PvD1 defensin, a plant antimicrobial peptide with inhibitory activity against Leishmania amazonensis, Biosci. Rep. (2015), https://doi.org/10.1042/BSR20150060.
[125] Genoveva Samblanx, Inge Goderis, Karin Thevissen, et al., Mutational Analysis of a Plant Defensin from Radish (Raphanus sativus L.) Reveals Two Adjacent Sites Important for Antifungal Activity, J. Bio. Chem. (1997), https://doi.org/10.1074/jbc.272.2.1171.
[126] Karin Thevissen, Isabelle François, Lolke Sijtsma, et al., Antifungal activity of synthetic peptides derived from Impatiens balsamina antimicrobial peptides Ib-AMP1 and Ib-AMP4, Peptides (2005), https://doi.org/10.1016/j.peptides.2005.01.008.
[127] Miquel Vila-Perelló, Andrea Sánchez-Vallet, Francisco García-Olmedo, Antonio Mollina, David Andreu, Synthetic and structural studies on Pyrularia pubera thionin: a single-residue mutation enhances activity against Gram-negative bacteria, FEBS letters (2003), https://doi.org/10.1016/s0014-5793(03)00053-x.

APÊNDICE D - COMBINED ANTIBIOFILM ACTIVITY OF SYNTHETIC PEPTIDES AND ANTIFUNGAL DRUGS AGAINST *CANDIDA* SPP.

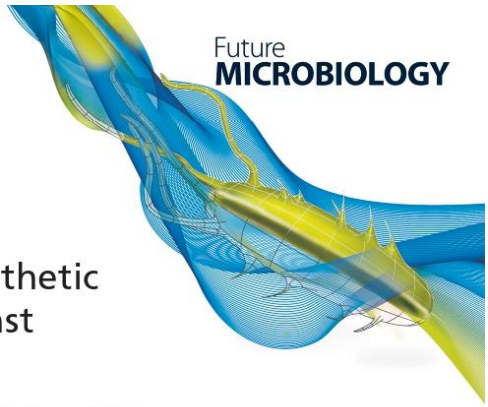

Research Article

For reprint orders, please contact: reprints@futuremedicine.com

Combined antibiofilm activity of synthetic peptides and antifungal drugs against *Candida* spp.

Leandro P Bezerra[‡,1], Ayrles FB Silva[‡,2], Ralph Santos-Oliveira[3], Luciana MR Alencar[4], Jackson L Amaral[1,2], Nilton AS Neto[1], Rafael GG Silva[5], Mônica O Belém[6], Claudia R de Andrade[6], Jose TA Oliveira[1], Cleverson DT Freitas[1] & Pedro FN Souza*[,1,7]

[1]Department of Biochemistry & Molecular Biology, Federal University of Ceará, Fortaleza, Ceará, 60451, Brazil
[2]Department of Physic, Federal University of Ceará, Fortaleza, Ceará, 60451, Brazil
[3]Nanoradiopharmaceuticals & Radiopharmacy, Zona Oeste State University, Brazilian Nuclear Energy Commission, Rio de Janeiro, Rio de Janeiro, 23070200, Brazil
[4]Department of Physics, Laboratory of Biophysics & Nanosystems, Federal University of Maranhao, São Luís, Maranhão, 65080-805, Brazil
[5]Department of Biology, Federal University of Ceará, Fortaleza, Ceará, 60451, Brazil
[6]Laboratory of Translational Research, Christus University Center, Fortaleza, Ceará, 60192, Brazil
[7]Drug Research & Development Center, Department of Physiology & Pharmacology, Federal University of Ceará, Fortaleza, Ceará, 60430-275, Brazil
*Author for correspondence: Tel.: +55 853 366 9823; pedrofilhobio@gmail.com
‡These authors contributed equally to this work

Introduction: *Candida krusei* and *Candida albicans* are biofilm-forming drug-resistant yeasts that cause bloodstream infections that can lead to death. Materials & methods: nystatin and itraconazole were combined with two synthetic peptides, PepGAT and PepKAA, to evaluate the synergistic effect against *Candida* biofilms. Additionally, scanning electron and fluorescence microscopies were employed to understand the mechanism behind the synergistic activity. **Results:** Peptides enhanced the action of drugs to inhibit the biofilm formation of *C. krusei* and *C. albicans* and the degradation of mature biofilms of *C. krusei*. In combination with antifungal drugs, peptides' mechanism of action involved cell wall and membrane damage and overproduction of reactive oxygen species. Additionally, in combination, the peptides reduced the toxicity of drugs to red blood cells. **Conclusion:** These results reveal that the synthetic peptides enhanced the antibiofilm activity of drugs, in addition to reducing their toxicity. Thus, these peptides have strong potential as adjuvants and to decrease the toxicity of drugs.

Plain language summary: *Candida krusei* and *Candida albicans* are biofilm-forming, drug-resistant yeasts that cause bloodstream infections that can lead to death. In this study, biofilms of *C. krusei* and *C. albicans* were treated with a solution composed of synthetic peptides and antifungal drugs, none of which were effective alone. The synthetic peptides reduced the toxicity of drugs to red blood cells. These results may pave the way to the application of synthetic peptides as a beneficial additional to antifungal drugs to treat fungi that cannot be killed by drugs alone.

First draft submitted: 1 March 2022; Accepted for publication: 1 July 2022; Published online: 26 July 2022

Keywords: action mechanisms • antibiofilm activity • antifungal drugs • *Candida* • candidiasis • clinical application • nystatin and itraconazole • synergism • synthetic peptides

The rapid increase of antimicrobial resistance to drugs globally is leading to a 'post-antibiotic era' in which most available drugs will no longer work [1]. In this scenario, infections caused by fungi have gained attention. Estimates suggest 200 million new cases of infection by resistant fungi occur every year, with approximately 1 million deaths [2]. Among the fungi infecting humans, those of the *Candida* genus have the highest prevalence, ten cases per 100 patients [3–5].

Future Medicine

10.2217/fmb-2022-0053 © 2022 Future Medicine Ltd **Future Microbiol.** (Epub ahead of print) ISSN 1746-0913

Candida generally affect debilitated individuals, such as transplanted, cancer and immunocompromised patients, leading to bloodstream infection, prolonged hospital stays and high mortality rates [3–5]. Until 2010, *C. albicans* with resistance to multiple drugs was responsible for at least 60% of clinical infections [5]. This scenario has changed. Today, infections caused by non-*C. albicans* account for 56.5% of *Candida* infections. The pathogens causing the new cases are divided into *C. glabrata* (33.3%), *C. tropicalis* (20.3%), *C. krusei* (1.4%) and *C. kefyr* (1.4%) [6]. Another important non-*C. albicans* pathogenic yeast is *C. auris*, first described in 2009 in Japan. Today, *C. auris* is considered a pan-resistant yeast with high resistance rates to azoles, polyenes and echinocandins [7]. Despite this development, *C. albicans* still causes the highest number of cases (43.5%) [6].

Many pathogenic yeasts like *Candida* spp. have developed a wide spectrum of drug-resistance mechanisms. One of the most important is the ability to form biofilms. The production of biofilms can increase drug resistance up to 1000-fold in relation to conventional drugs in studies using free cells [8]. Besides altering the pH and osmolarity, preventing nutrient scarcity and alleviating mechanical and shear forces, the matrix of biofilms boosts the resistance by protecting yeast cells from drugs and the host's immune response [8–11]. It is not entirely clear what triggers *quorum sense* gene expression, but a known factor is the composition of the matrix, which is rich in carbohydrates, proteins, lipids, nucleic acids and water [9].

The ability to develop biofilms increases the resistance of *Candida* spp. to antifungal drugs, with negative clinical implications worldwide [12]. In this context, antimicrobial peptides active against biofilms could be an alternative to address this problem. Many research groups have analyzed antimicrobial peptides active against fungal biofilms, alone or in combination with conventional drugs [13]. However, biofilm-active peptides have not yet reached clinical trials, much less commercial use. Therefore, design, development and optimization of such molecules are needed to fight fungal biofilms [14].

To overcome the threat imposed by yeasts' resistance to drugs, synthetic antimicrobial peptides are an alternative either as new drugs for administration alone or as adjuvants to enhance the activity of drugs [1,15]. Synthetic antimicrobial peptides are typically designed to have a positive charge (at least +1), amphipathic properties, acceptable hydrophobic rates (40–66%) [16–18] and no host toxicity. Breakthroughs in chemical synthesis technologies have reduced the costs of synthesizing high-purity synthetic antimicrobial peptides [1]. The most advantageous technology developed in terms of costs allows the recovery and recycling of solvents used during synthesis, increasing the clinical application of synthetic peptides. For example, fuzeon and rybelsus are synthetic peptides already used to treat HIV and diabetes, respectively [19,20].

Recently, two synthetic peptides (PepGAT and PepKKA) were reported to strongly inhibit the growth of species of the *Candida* genus at low concentrations [18]. Thus, we reasoned that both peptides could be effective against biofilms of the *Candida* genus and would have synergistic effects with drugs that have lost acceptable activity. The antibiofilm activity and action mechanisms of PepGAT and PepKAA against *C. albicans* and *C. krusei* are described and characterized based on advanced microscopic techniques. Furthermore, the results reveal that the synergistic effects of peptides enhanced antibiofilm activity of the commercial drugs nystatin (NYS) and itraconazole (ITR), which are no longer active against *Candida* biofilms.

This study's novelty lies in the fact that synthetic peptides enhanced the activity of antifungal drugs toward *Candida* biofilms, which are the structure of resistance. Additionally, it was shown that synthetic peptides reduced the toxicity of drugs to erythrocytes. The results presented here report the potential of peptides to act as adjuvants of antifungal drugs that are becoming useless.

Methods

Biological materials

The clinical isolates of *C. albicans* (ATCC 10231), *C. krusei* (ATCC 6258) and *C. parapsilosis* (ATCC 22019) were obtained from the Laboratory of Plant Toxins of the Department of Biochemistry and Molecular Biology of Federal University of Ceará (UFC), Fortaleza, Brazil.

Peptide synthesis

The synthetic peptides PepGAT and PepKAA [18] were chemically synthesized by the company GenOne (São Paulo, Brazil), which analyzed their quality and purity (≥95%) by reverse-phase HPLC and mass spectrometry [18].

Biological activity

Antibiofilm effect of peptides and drugs, alone or combined

The effects of PepGAT and PepKAA on the *Candida* spp. biofilm formation were evaluated in flat-bottom 96-well polystyrene microtiter plates [16]. The concentrations of peptides and drugs used were those defined in previous studies by our group [16,21,22]. The cell suspensions were prepared from yeasts cultured for 18 h at 37 °C in Sabouraud broth (Kasvi, Brazil). The cell concentration was diluted to 10^6 cells ml^{-1} in the growth medium. One hundred microliters of the cell suspensions (10^6 cells ml^{-1}) were incubated at 37 °C for 48 h in the dark with 100 µl of the synthetic peptides at concentration of 50 $\mu g/ml^{-1}$ in a solution composed of 5% DMSO in 0.15 M NaCl. After that, the supernatant was discarded and the wells were washed with sterile NaCl, air-dried for 30 min and the biofilm formed was stained with an aqueous solution of 0.1% (m/v) crystal violet (Sigma-Aldrich, São Paulo, Brazil), for 15 min at room temperature (24 ± 2 °C). Excess crystal violet was removed by washing three times with sterile NaCl [16]. Afterward, 250 µl of 95% (v/v) ethanol was added to solubilize the bound crystal violet, and absorbance was read with a microplate reader (BioTek ELx800TM, BioTek Instruments, Inc., VT, USA) at a wavelength of 570 nm. The inhibition of biofilm formation was calculated by comparing the absorbance readings of cells treated with synthetic peptides and those obtained from cells treated with DMSO-NaCl solution (negative control), ITR (1000 $\mu g/ml^{-1}$) and NYS (1000 $\mu g/ml^{-1}$), both used as positive controls [16].

A second experiment was carried out to evaluate the effect of the peptides on the degradation of the mature biofilms [16]. Two hundred microliters of each cell suspension (10^6 cells ml^{-1}, prepared as described earlier) was incubated at 37 °C for 24 h in the dark to form the biofilm. Then the supernatant was gently aspirated with a micropipette to remove the planktonic cells. In each well, 100 µl of each synthetic peptide (50 $\mu g/ml^{-1}$) or controls plus 100 µl of growth medium (Sabouraud broth, Kasvi, Brazil) were added. The plates were incubated for 24 h at 37 °C in the dark. The culture medium was again discarded, and the aforementioned procedure was used to quantify the biofilm biomass remaining after incubation with the peptide [16]. The controls used were the same as those used for inhibition of biofilm formation.

The synergism assays were performed by combining peptides with either antifungal NYS or ITR: the combinations were constituted of each peptide (50 $\mu g/ml^{-1}$) + NYS or ITR (1000 $\mu g/ml^{-1}$) [23]. The control to evaluate the effectiveness of synergism was the activity presented by peptides or drugs alone. After the formulation of combinations, the antibiofilm assays for synergism analyses of *Candida* spp. were conducted as described earlier.

Mechanisms of action of peptides against biofilms

Biofilm integrity by scanning electron microscopy

Morphological changes in the biofilms of *C. albicans* and *C. krusei* were evaluated by scanning electron microscopy (SEM), as previously described [18]. The assay was performed as described earlier (see the Antibiofilm section), but this time, the biofilm was grown on a coverslip (previously treated with 0.1% gelatin; Sigma-Aldrich) inside six-well plates. Next, the biofilm was fixed with fixation buffer (1% [v/v] glutaraldehyde + 4% [v/v] formaldehyde in 0.15 M sodium phosphate buffer at pH 7.0). The wells were then treated with 0.2% (m/v) osmium tetroxide (Sigma-Aldrich) for 30 min in the dark and successively dehydrated with ethanol concentration (30, 70, 100, 100 and 100% [v/v]) for 10 min each. After each centrifugation, the ethanol was aspirated with an automatic pipette. The final dehydration was carried out with 50/50 HMDS for 10 min and then with 100% HMDS (Sigma-Aldrich). Each coverslip was removed from its well and assembled on stubs and coated with a 20-nm gold layer using a PET coating machine (Emitech-Q150TES, Quorum Technologies, Lewes, UK). Images were acquired with an FEI Inspect 50 scanning electron microscope (OR, USA), equipped with a low energy Everhart-Thornley detector using acceleration beam voltage of 20,000 kV and 20,000× detector magnification. The treatments for this assay were peptides alone, drugs alone and solutions of peptides combined with drugs.

Biofilm integrity determined by propidium iodide uptake

The biofilms were produced as described in the biofilm assays and the SEM microscopy sections. Afterward, biofilms treated with peptides alone, drugs alone, and mixed solutions were incubated with 10^{-3} M of propidium iodide (PI, Sigma-Aldrich, São Paulo, Brazil), in the dark, at 37 °C for 30 min [23]. Then the biofilm-containing coverslips were washed with 0.15 M of NaCl three times to remove the unbound PI and observed under a fluorescent microscope (Olympus System BX 60, Japan) with an excitation wavelength of 490 nm and emission wavelength of 520 nm.

10.2217/fmb-2022-0053

Overproduction of reactive oxygen species by biofilms

The overproduction of reactive oxygen species (ROS) was evaluated as described by Dias *et al.* [16]. The biofilms were produced as described in the biofilm assays and the SEM sections. Afterward, biofilms treated with peptides alone, drugs alone and mixed drug–peptide solutions were incubated with 10 µM of DCFH-DA (Sigma-Aldrich, MO, USA) at 37 °C in the dark for 30 min. Then the biofilm-containing coverslips were washed with 0.15 M of NaCl three times to remove the unbound DCFH-DA and observed under a fluorescent microscope (Olympus System BX 60, Tokyo, Japan) with an excitation wavelength of 488 nm and emission wavelength of 525 nm.

Hemolytic assay

The hemolytic activity of synthetic peptides, NYS, ITR and their combination was tested in human red blood cells (HRBCs; types A, B and O), according to Souza *et al.* [18]. The combined solutions of peptides and either NYS or ITR were the same as used in the synergism assays. The HRBCs of types A, B and O were provided by the Ceará Hematology and Hemotherapy Center (Ceará, Brazil).

The blood was collected in the presence of heparin (5 IU ml^{-1}, Sigma-Aldrich, São Paulo, Brazil), centrifuged at 300× *g* for 5 min at 4 °C and gently dissolved in sterile NaCl. The blood was washed three times with 0.15 M NaCl and diluted to a concentration of 2.5% in 0.15 M NaCl as used in the assay. One hundred microliters of each blood type were incubated individually with solutions of synthetic peptides (50 µg/ml^{-1}), NYS (1000 µg/ml^{-1}), ITR (1000 µg/ml^{-1}), the solution formed by peptides and drugs, DMSO-NaCl and 0.1% (v/v) Triton X-100 (the positive control for hemolysis) for 30 min at 37 °C, followed by centrifugation (300× *g* for 5 min at 4 °C, in an Eppendorf 5810 centrifuge (Hamburg, Germany). The supernatants were collected and transferred to 96-well microtiter plates. Hemolysis (%) was calculated by measuring the supernatant absorbance at 414 nm using an automated absorbance microplate reader. Negative (0%) and positive (100%) hemolysis were determined by treating HRBCs with 5% DMSO in 0.15 M NaCl (vehicle for peptides) and 0.1% (v/v) Triton X-100, respectively. The following equation was used to calculate the hemolysis: ([Abs_{414nm} of HRBC treated with peptides-Abs_{414nm} HRBCs treated with 0.15 M NaCl]/([Abs_{414nm} of HRBCs treated with 0.1% TritonX-100-Abs_{414nm} of HRBCs treated with 0.15 M NaCl]) × 100.

Statistical analysis

All the experiments were performed three times, and the descriptive statistics are expressed as the mean ± standard error. The data were submitted to one-way analysis of variance followed by the Tukey test, using GraphPad Prism 5.01 (GraphPad Software, CA, USA), with the significance of $p < 0.05$.

Results

Antibiofilm activity of peptides and synergistic effect with antifungal drugs

The peptides (50 µg/ml^{-1}) presented different behaviors toward the biofilms of *Candida* spp. (Figure 1). The peptides, antifungal drugs and combinations had no activity against the biofilm of *C. parapsilosis* or *C. tropicalis* (Supplementary Figure 1C & D). The first assay was performed to evaluate the ability of peptides to inhibit the biofilm formation of *C. krusei* and *C. albicans* (Figure 1A & B). Against *C. krusei*, both peptides barely reach 10% inhibition. ITR and NYS reached 20% ± 0.012 and 0% inhibition of biofilm formation by *C. krusei* (Figure 1A). In contrast, the combinations of both PepGAT (50 µg/ml^{-1}) + ITR (1000 µg/ml^{-1}) and PepKAA (50 µg/ml^{-1}) + ITR (1000 µg/ml^{-1}) led to inhibitions, respectively, of 80% ± 0.008 and 76% ± 0.032 of *C. krusei* biofilm (Figure 1A). The combination of peptides with NYS was not effective. Regarding *C. albicans*, NYS, PepGAT and PepKAA inhibited biofilm formation by 40% ± 0.01, 10% ± 0.001 and 20%. An interesting result was the synergism found for the combinations of PepGAT + ITR, PepGAT + NYS and PepKAA + NYS, which inhibited the biofilm formation of *C. albicans* by 40% ± 0.030, 95% ± 0.002 and 98% ± 0.005, respectively (Figure 1B).

Regarding the degradation of mature biofilm, none of the combinations or molecules alone were effective to reduce biofilm biomass of *C. albicans*, *C. parapsilosis* and *C. tropicalis* (Supplementary Figure 1A & B), which were only effective against *C. krusei* (Figure 1C). ITR, PepGAT and PepKAA alone did not reduce biomass of mature biofilm of *C. krusei* (Figure 1C). In contrast, NYS was able to reduce the biomass of mature *C. albicans* biofilm by 20% ± 0.005 (Figure 1C). The PepGAT + NYS combination was the only one that did not significantly decrease biomass, whereas PepGAT + ITR, PepKAA + ITR and PepKAA + NYS reduced the mature biofilms *C. albicans* by 50% ± 0.001, 30% ± 0.005 and 15% ± 0.002, respectively (Figure 1C).

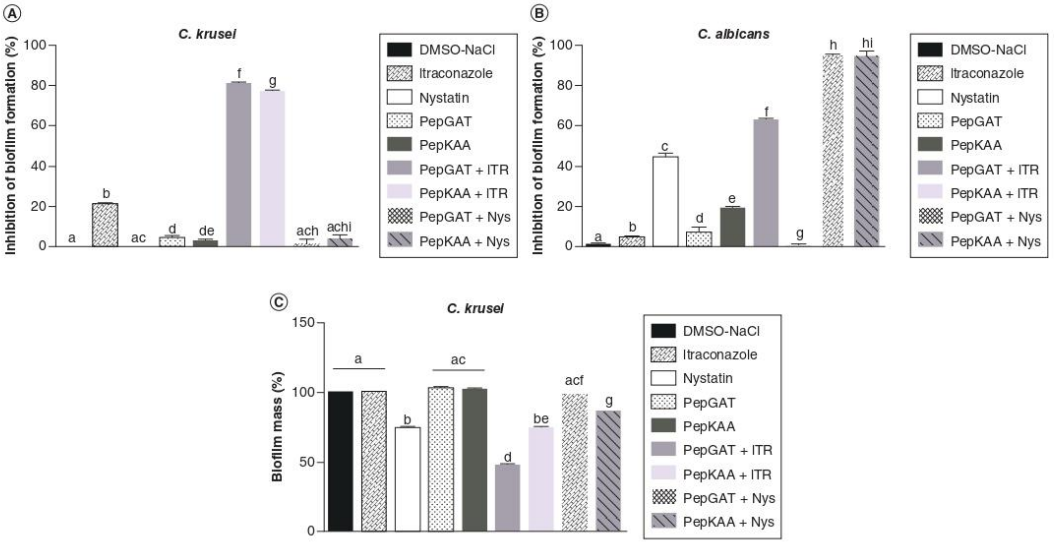

Figure 1. Antibiofilm activity and synergistic effect with NYS and ITR of synthetic peptides PepGAT and PepKAA. (A & B) Inhibition of biofilm formation, respectively, of *Candida krusei* and *Candida albicans*. **(C)** Biofilm degradation of *C. krusei*. All peptides were used at 50 μg/ml^{-1}. NYS and ITR at 1000 μg/ml^{-1}. DMSO-NaCl as a negative control. The letters represent the mean ± standard deviation of three replicates.
Different lowercase letters indicate statically significant difference compared with DMSO by analysis of variance ($p < 0.05$).
ITR: Itraconazole; NYS: Nystatin.

Biofilm integrity and ROS overproduction

The peptides alone and the combination with drugs affected the membrane of the biofilm cells, as revealed by fluorescence microscopy (Figures 2–5). PI is a fluorophore that binds to DNA, releasing red fluorescence. However, PI only crosses damaged cell membranes, whereas healthy membranes block the movement of PI, leading to no fluorescence at all. As expected, in all cases the control (DMSO-NaCl solution, the vehicle of peptides) presented no fluorescence, suggesting the membranes of the control cells had no pores formed (Figures 2–5). An interesting result was the absence of fluorescence in biofilms treated with drugs alone (NYS and ITR) (Figures 2–5).

PepGAT induced fluorescence in all treatments, both regarding inhibition of biofilm formation (Figures 2–4) and degradation of mature biofilms, although at different intensities (Figure 5). The PepKAA presented different behavior. In the case of inhibition of biofilm formation by *C. krusei*, PepKAA alone did not cause damage to the membrane to allow PI to pass and emit fluorescence (Figure 2). In contrast, PepKAA-induced fluorescence by inhibiting biofilm formation by *C. albicans* (Figure 4). In the case of combinations of peptides and antifungal drugs, all presented fluorescence (Figures 2–5). This is an exciting result for three reasons: first, drugs alone did not cause any fluorescence (Figures 2–5); second, in the case of PepKAA, the combination with ITR led to fluorescence (Figures 2 & 3); third, in some cases of PepGAT + ITR (Figures 3 & 5), the fluorescence produced by the combination was higher than that produced by drugs alone, suggesting a larger number of damaged cells.

The experiments to evaluate the ROS overproduction in the biofilms revealed a different pattern than the PI experiments. All positive or negative controls did not produce any fluorescence, indicating no ROS production (Figures 2–5). Regarding inhibiting the biofilm formation of *C. krusei*, both peptides induced ROS production at different intensities, as revealed by fluorescence. In this case, the cells treated with PepGAT were brighter than those treated with PepKAA. Following this pattern, the combinations applied to test inhibition of biofilm formation by *C. krusei* produced only slight fluorescence, indicating low ROS levels (Figure 2). With respect to the inhibition of biofilm formation by *C. albicans*, only a slight production of ROS was indicated, by faint fluorescence in the treatment with PepKAA (Figure 4). In contrast, brighter fluorescence indicated higher production of ROS by

10.2217/fmb-2022-0053

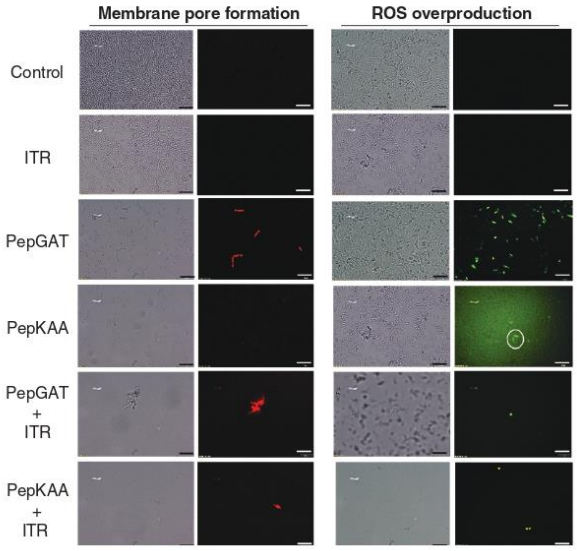

Figure 2. Fluorescence images showing membrane pore formation and ROS overproduction as mechanism of action to inhibit biofilm formation of *Candida krusei*. Control solution of DMSO-NaCl, treated with ITR alone at 1000 μg/ml^{-1}, PepGAT and PepKAA each alone at 50 μg/ml^{-1} and synergistic activity of PepGAT and PepKAA with ITR. Membrane pore formation was measured by propidium iodide uptake assay and ROS overproduction was detected using DCFH-DA.
Bars: 100 μm; ITR: Itraconazole; ROS: Reactive oxygen species.

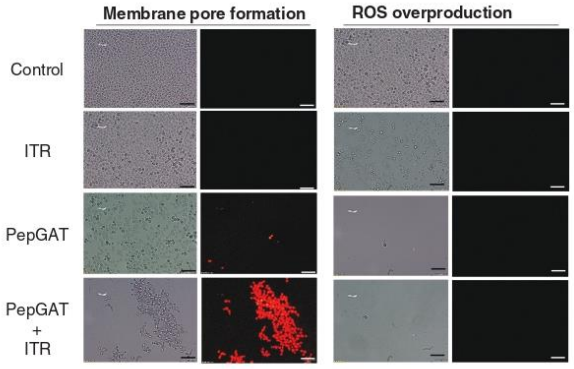

Figure 3. Fluorescence images showing membrane pore formation and ROS overproduction as mechanisms of action to inhibit biofilm formation of *Candida albicans*. Control solution of DMSO-NaCl, treated with ITR alone at 1000 μg/ml^{-1}, PepGAT and PepKAA each alone at 50 μg/ml^{-1} and synergistic activity of PepGAT and PepKAA with ITR. Membrane pore formation was measured by propidium iodide uptake assay and ROS overproduction was detected using DCFH-DA.
Bars: 100 μm; ITR: Itraconazole; ROS: Reactive oxygen species.

treatment both with PepGAT alone and combined with ITR, thus causing degradation of mature biofilms of *C. krusei* (Figure 5), suggesting that ROS overproduction is indeed an important mechanism to degrade biofilms.

SEM analyses of biofilm

SEM images revealed that in all control treatments with DMSO-NaCl solution, the cells in biofilms had healthy spherical shape, with no cracks or other damage to the membrane or cell wall (Figures 6–8). Furthermore, the cells involved in biofilm formation (Figures 6 & 7) and mature biofilm (Figure 8) were not affected by the treatment with either ITR or NYS, both at 1000 μg/ml^{-1}.

Damage revealed by fluorescence microscopy in *Candida* cells (Figures 2–5) confirmed the SEM analysis (Figures 6–8). To inhibit the formation of *C. krusei*, PepGAT induced significant damage to cells, such as cavities (Figure 6, PepGAT and PepKAA panels, white dashed circle), indicating damage to the cell wall. Also, tiny blebs, new buds, scars on new buds and cells and rings of truncated bud scars were present in the cells treated with both peptides (Figure 6, white arrowheads). In both treatments with peptides, cells presented wrinkles and scars all over the structure.

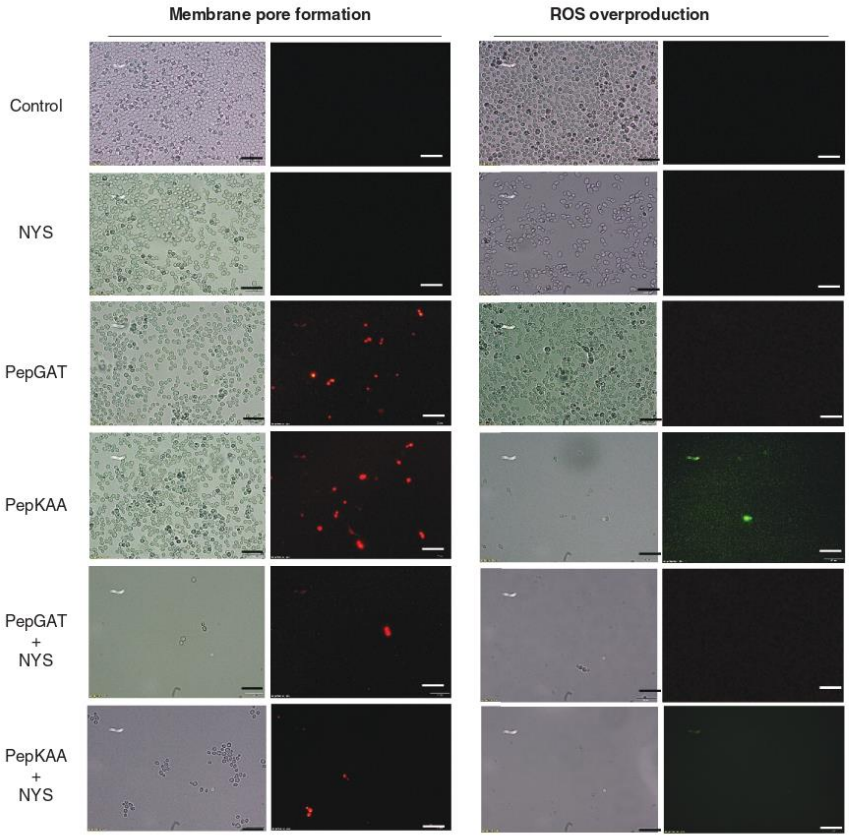

Figure 4. Fluorescence images showing membrane pore formation and reactive oxygen species (ROS) overproduction as mechanisms of action to inhibit biofilm formation of *Candida albicans*. Control solution of DMSO-NaCl, treated with NYS alone at 1000 μg/ml^{-1}, PepGAT and PepKAA each alone at 50 μg/ml^{-1} and synergistic activity of PepGAT and PepKAA with NYS. Membrane pore formation was measured by propidium iodide uptake assay, and ROS overproduction was detected using DCFH-DA.
Bars: 100 μm; NYS: Nystatin; ROS: Reactive oxygen species.

In contrast to what was seen in the treatment with drugs alone, the combination of peptides and drugs led to various types of cell damage, thus inhibiting biofilm formation. In both cases, many cells presented cavities (Figure 6, PepGAT+ITR and PepKAA+ITR panels, white dashed circle), indicating damage to the cell wall. In addition, alterations in cell shape, wrinkles and scars, small blebs, new buds, scars on new buds and cells and rings of truncated bud scars in the treatment with both peptides (Figure 6, white arrowheads) were seen, with no presence of a solid point in the septum junction (Figure 6, white open arrows).

SEM analysis revealed a different pattern of inhibited biofilm formation of *C. albicans* (Figure 7). Treatment with DMSO-NaCl solution, ITR and NYS at 1000 μg/ml^{-1} caused no significant alteration of *C. albicans* cells (Figure 7). Treatment with PepGAT induced small blebs, new buds and scars on new buds and cells (Figure 7, white arrowheads). In contrast, treatment with PepKAA caused damage to all cells. Cells were adhered to each other with poor conformation and pieces of other cells on top of them (Figure 7, panel PepKAA). SEM analysis revealed that the combination of PepGAT + ITR killed almost all cells (Figure 7), and the rest were heavily damaged and unable to form biofilm. The combination of PepKAA + ITR was far less effective than PepGAT + ITR, causing scars and

10.2217/fmb-2022-0053

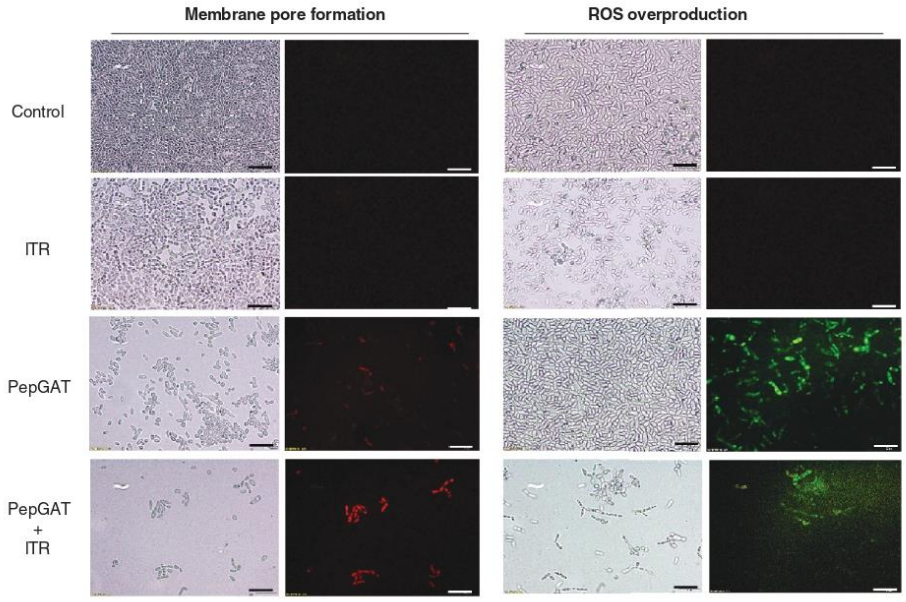

Figure 5. Fluorescence images showing membrane pore formation and ROS overproduction as mechanisms of action to degrade biofilm formation of *Candida krusei*. Control solution of DMSO-NaCl, treated with ITR alone at 1000 μg/ml^{-1}, PepGAT and PepKAA each alone at 50 μg/ml^{-1} and synergistic activity of PepGAT and PepKAA with ITR. Membrane pore formation was measured by propidium iodide uptake assay, and ROS overproduction was detected using DCFH-DA.
Bars: 100 μm; ITR: Itraconazole; ROS: Reactive oxygen species.

wrinkles on cells and abnormal shape. Small blebs, new buds, scars on new buds and cells and rings of truncated bud scars in the treatment with both peptides (Figure 7, white arrowheads) were also observed. The combination of both peptides with NYS was more efficient than the peptides in combination with ITR. In both cases, all cells were dead (Figure 7, PepGAT and PepKAA panels).

Regarding the degradation of mature *C. krusei* biofilm, SEM analysis of ITR-treated biofilm revealed no damage (Figure 8). Treatment with both peptides alone or in combination with ITR resulted in damage to the biofilm cell wall, loss of internal content, tiny blebs, new buds, multiple scars and wrinkles on new buds and cells (Figure 8 white arrowheads), and rings of truncated bud scars (Figure 8, white open arrows).

Hemolytic assay

A previous study (Souza *et al.*, 2020a) showed that the synthetic peptides had no hemolytic activity against any human blood type tested (Table 1), even at 50 μg/ml^{-1}. In contrast, NYS at 1000 μg/ml^{-1} caused 100% ± 0.001 hemolysis in all human blood types, and ITR at 1000 μg/ml^{-1} caused 80% ± 0.040, 75% ± 0.007 and 69% ± 0.003 hemolysis, respectively, to types A, B and O HRBCs (Table 1).

In general, synthetic peptides with antifungal drugs had lower hemolytic effect (Table 1). PepGAT with NYS resulted in reduced hemolytic effects of 54% ± 0.001, 43% ± 0.003 and 12% ± 0.015, respectively, in types A, B and O HRBCs. PepGAT with ITR caused 17% ± 0.013, 45% ± 0.003 and 43% ± 0.009 hemolysis levels, respectively, to types A, B and O HRBCs (Table 1). The combination of PepKAA with NYS hemolyzed 15% ± 0.001, 10% ± 0.011 and 21% ± 0.006, respectively, of types A, B and O HRBCs, whereas the combination of PepKAA with ITR hemolyzed 21% ± 0.011, 34% ± 0.019 and 12% ± 0.002, respectively, of types A, B and O HRBCs (Table 1).

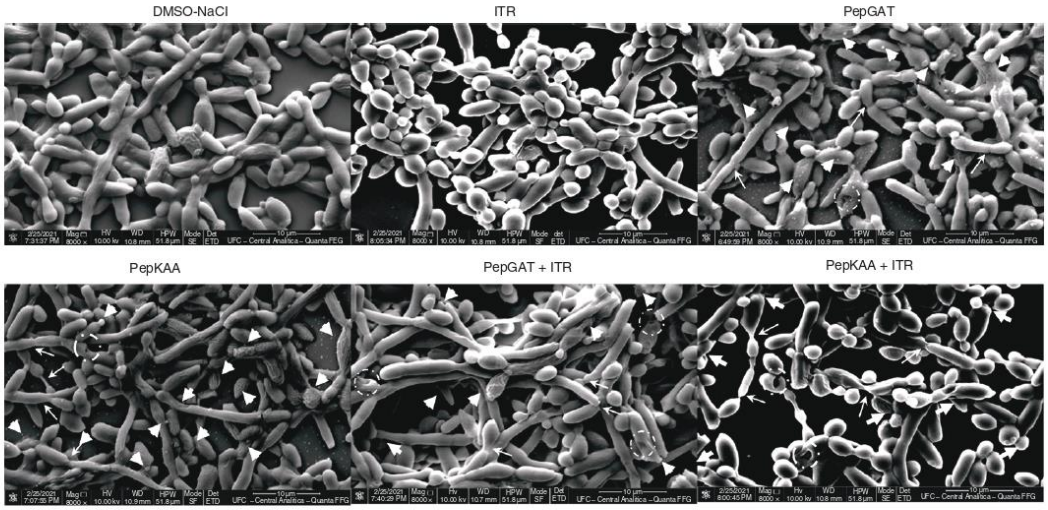

Figure 6. Scanning electron microscopy images showing alterations in the biofilm of *Candida krusei* cells after incubation with synthetic peptides, antifungal drugs and a combination of the two. The surface of biofilm control (DMSO-NaCl panel) cells is covered by well-defined and organized structures. Biofilm cells exposed to ITR, showed alterations in the cell surface. PepGAT and PepKAA-treated cells showed some alterations in cell structure, such as scars, bud scars and distortion in the shape of the cells. Biofilm cells were incubated with PepGAT and PepKAA in contact with ITR, resulting in strong alterations in the cell membrane, scars, bud scars and cell deformation. ITR: Itraconazole.

Table 1. Hemolytic activity of synthetic peptides, antifungal drugs and their combination in human red blood cells, types A, B and O.

Peptides/combinations	Hemolysis (%)		
	Type A	Type B	Type O
0.1% Triton X-100	100 ± 0.001	100 ± 0.001	100 ± 0.001
DMSO-NaCl solution	0	0	0
NYS (1000 $\mu g/ml^{-1}$)	100 ± 0.010	100 ± 0.005	100 ± 0.009
ITR (1000 $\mu g/ml^{-1}$)	80 ± 0.040	75 ± 0.007	69 ± 0.003
PepGAT (50 $\mu g/ml^{-1}$)	0	0	0
PepKAA (50 $\mu g/ml^{-1}$)	0	0	0
PepGAT (50 $\mu g/ml^{-1}$) + NYS (1000 $\mu g/ml^{-1}$)	54 ± 0.001	43 ± 0.003	12 ± 0.015
PepGAT (50 $\mu g/ml^{-1}$) + ITR (1000 $\mu g/ml^{-1}$)	17 ± 0.013	45 ± 0.003	43 ± 0.009
PepKAA (50 $\mu g/ml^{-1}$) + NYS (1000 $\mu g/ml^{-1}$)	15 ± 0.001	10 ± 0.011	21 ± 0.006
PepKAA (50 $\mu g/ml^{-1}$) + ITR (1000 $\mu g/ml^{-1}$)	21 ± 0.011	34 ± 0.019	12 ± 0.002

ITR: Itraconazole; NYS: Nystatin.

Discussion

Fungal infection caused by *Candida* species yeasts poses a critical problem in the healthcare field worldwide, leading to high mortality rates and high medical care costs for hospitalized patients, placing a burden on public health systems [24,25]. Drug-resistant *C. albicans* is the most severe threat to human health and is responsible for infections caused in immunocompromised, HIV-positive and intensive care unit patients [5,10].

C. albicans and *C. krusei* have developed resistance to many antifungal drugs, such as azoles (ITR), echinocandins and polyenes (NYS), among others [26]. Overall, the mechanisms of resistance developed by yeasts involve overexpression or alteration of the target development of efflux pumps to remove excess drugs from the cytoplasm, modification of the drug and biofilm production [1,26–28].

10.2217/fmb-2022-0053

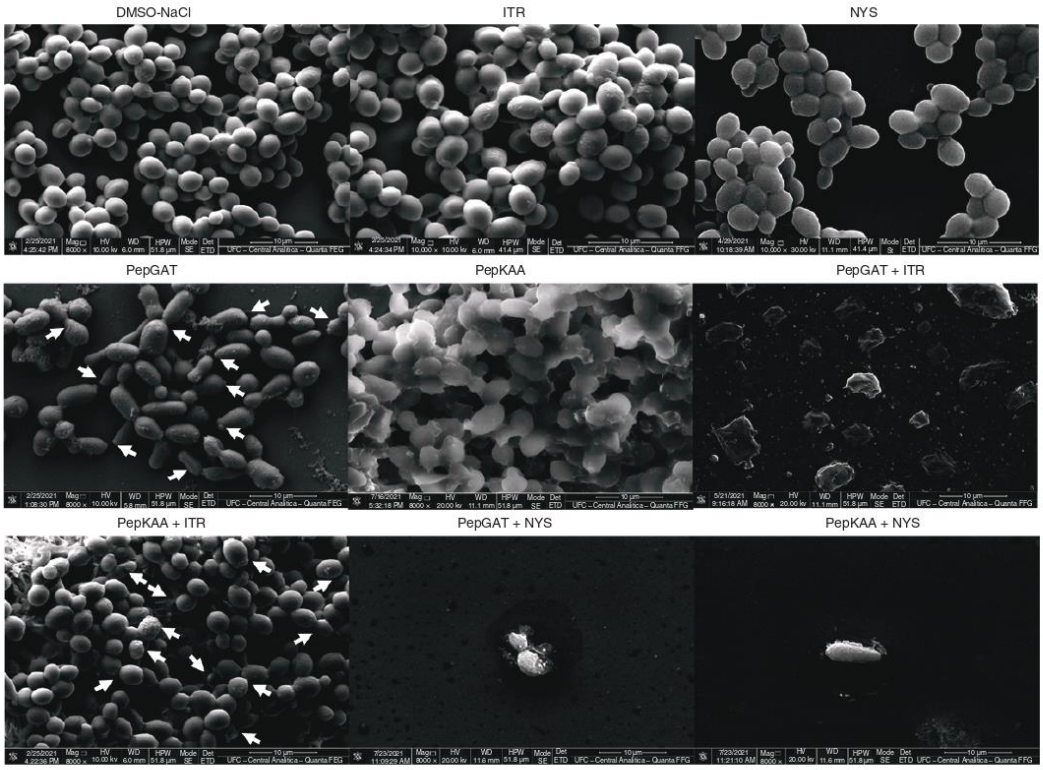

Figure 7. Scanning electron microscopy images showing alterations in the biofilm of *Candida albicans* cells after incubation with synthetic peptides, antifungal drugs and a combination of the two. The surface of biofilm control (DMSO-NaCl panel) cells is covered by well-defined structures. No relevant changes are seen in the biofilm exposed to ITR and NYS. PepGAT- and PepKAA-treated biofilm shows alterations in the cell membrane, scars, bud scars and distorted biofilm structure. Biofilm exposed to combinations of PepGAT and PepKAA in synergistic action with ITR shows strong alterations in cell shape and bud scars. For biofilm incubated with PepGAT and PepKAA with NYS, there is no biofilm observed, and only dead cells remain.
ITR: Itraconazole; NYS: Nystatin.

Biofilm is an excellent resistance structure, and all yeasts of the *Candida* genera can produce it [9]. Biofilm production by *Candida* provides a different environment than planktonic life. For example, cells living in the biofilm community can permanently attach to any surface (e.g., inert material, living tissue, medical devices such as prostheses and cardioverter defibrillators), in addition to increasing the expression of virulence factors and causing higher resistance to antifungal drugs [1,9]. Thus, biofilm formation is a serious threat to overcome.

The effect of synthetic peptides has been tested against *Candida* biofilms. For instance, the synthetic peptides KU4 (96 $\mu g/ml^{-1}$), uperin 3.6 (96 $\mu g/ml^{-1}$), upn-lys4 (96 $\mu g/ml^{-1}$), upn-lys5 (192 $\mu g/ml^{-1}$) and upn-lys6 (96 $\mu g/ml^{-1}$) reduced the viability of the biofilm of *C. albicans* only by 20, 35, 15, 40 and 30%, respectively [29]. In the case of *C. krusei*, the synthetic peptide VLL-28 at 72 $\mu g/ml^{-1}$ reduced the viability of *C. krusei* biofilms by 35% [30]. Paulone *et al.* [31] reported a peptide that presented IC_{50} value against *C. albicans* biofilm of 126 $\mu g/ml^{-1}$.

In addition to those activities of synthetic peptides against *Candida* biofilms, some studies have reported synergism of synthetic peptides with antifungal drugs such as fluconazole and amphotericin B, but only against *Candida* planktonic cells [32–36]. For example, the combination of the synthetic peptide WMR (110 $\mu g/ml^{-1}$) + fluconazole (10 $\mu g/ml^{-1}$) inhibited the growth of *C. albicans* by 50% [35]. Regarding the synergistic effect of peptides and antifungal drugs against *Candida* biofilms, studies are scare – particularly in the case of synthetic peptides. The

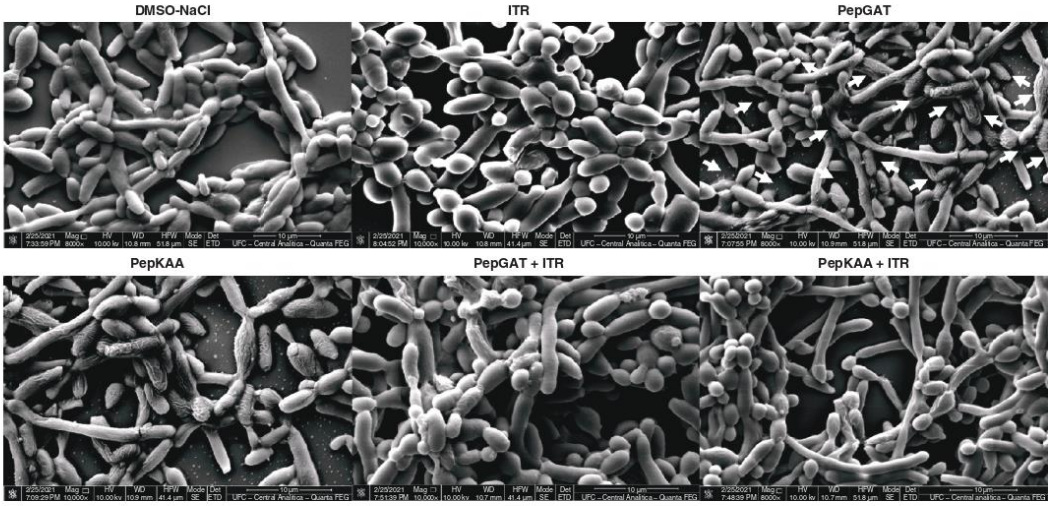

Figure 8. Scanning electron microscopy images showing alterations in the biofilm of *Candida krusei* cells after incubation with synthetic peptides, antifungal drugs and the combination of synthetic peptides and drugs. The surface of biofilm control (DMSO-NaCl solution) is well defined and organized. Biofilm exposed to ITR, showed few alterations in the cell surface. PepGAT and PepKAA-treated biofilm showed alterations in cell structure, such as scars, bud scars and distortion in the shape of the cells. Biofilm incubated with a combination of PepGAT or PepKAA and ITR resulted in strong alterations in the cell membrane, scars, bud scars, deformation of cell structures and leakage of internal content.
ITR: Itraconazole.

combination of the peptide HsLin06_18 (100 $\mu g/ml^{-1}$) with caspofungin (10 $\mu g/ml^{-1}$) inhibited biofilm formation of *C. albicans* by 50% [37]. Analysis of the action mechanism revealed that this combination led to membrane permeability of *C. albicans* cells in biofilms [37].

In another study, the synergistic action of the lipopeptide AC7BS (1000 $\mu g/ml^{-1}$) + fluconazole (1000 $\mu g/ml^{-1}$) reduced mature biofilm of *C. albicans* by 60% [38]. Mora-Navarro *et al.* [39] showed that a β-synthetic peptide (200 $\mu g/ml^{-1}$) + ketoconazole (200 $\mu g/ml^{-1}$) inhibited biofilm formation by 60%. The authors did not report any mechanism of action of the combination. Compared with those results, we found exciting results about the synergistic effect of peptides in combination with antifungal drugs to inhibit the biofilm formation and reduce the mass of mature *Candida* biofilms (Figure 1), whereas PepKAA + NYS inhibited the biofilm formation of *C. albicans* biofilms by 98% and PepGAT + ITR reduced the biomass of mature *C. krusei* biofilms by 55% (Figure 1). It is important to note that none of the studies mentioned here reported results about the reduction of biomass of mature biofilms. This is the most important finding of the present work.

Here, fluorescence (Figures 2–5) and SEM (Figures 5–9) analysis revealed the mechanisms behind the lethal damage of the studied combinations to *Candida* biofilms. Here, additionally, fluorescence analyses revealed an exciting result. In some cases, the combination of peptides with antifungal drugs led to ROS overproduction (Figure 2, panels PepGAT + ITR and PepKAA + ITR; Figure 3, PepGAT + ITR). Interestingly, ROS overproduction only occurred from treatment with the combinations of either PepGAT or PepKAA with ITR, which presented the best inhibition of biofilm formation (Figure 1A) or degradation of mature biofilm (Figure 1C). ROS is essential to biofilm biogenesis, development and formation, as well as to the genetic variability of cells [40]. However, there is a fine line between benefits and lethal effects that is easy to cross. A slight imbalance of ROS levels can lead to ROS accumulation, which is lethal because it inactivates vital molecules such as carbohydrates, nucleic acids, proteins and lipids, triggering programmed cell death [41].

Our results clearly suggest that peptides enhance the antibiofilm activity of NYS and ITR. Two hypotheses explain the improvement of antifungal drugs when combined with peptides. The first is directly related to the action mechanism of ITR and NYS. Although of different classes, ITR and NYS have the same target. ITR

interacts with the enzyme lanosterol 14α-demethylase to inhibit ergosterol biosynthesis, and NYS interacts with the ergosterol in the membrane, causing an imbalance in the membrane [42,43]. By interacting with chitin in the cell walls, both PepGAT and PepKAA cause rupture of the cell wall (Figures 6–8), facilitating the access of lanosterol 14α-demethylase and ergosterol, respectively, by ITR and NYS and thus enhancing their activity. The second explanation is that the peptides attack the membrane directly, as revealed by fluorescence microscopy (Figures 2–5). During the treatment of yeasts with combinations of peptides and antifungal drugs, membranes are doubly attacked. Peptides attack the membrane to form pores, and drugs attack their target in the membranes.

Both ITR and NYS have many undesirable side effects. ITR can cause vomiting, diarrhea, headache and dizziness. In addition, cardiotoxicity and hypertension have been attributed to ITR use [44]. In one study, unpleasant taste was reported for NYS (in 61.5% of subjects in one study), along with adverse gastrointestinal reactions, including vomiting, nausea, diarrhea, anorexia and abdominal pain [44]. The interesting result of the present study is that the combination of peptides with antifungal drugs reduced their toxicity in human erythrocytes (Table 1). In both combination treatments, we found a reduction in toxicity of antifungal drugs of at least twofold, and approaching 8.3-fold (Table 1).

Conclusion

This is a pioneering study showing the activity, mechanism of action and synergistic effects of two synthetic peptides (PepGAT and PepKAA) with NYS and ITR against biofilms of *C. albicans* and *C. krusei*. In the most effective combinations, peptides enhanced the antibiofilm activity of both drugs by at least fivefold and reduced their toxic effect against red blood cells up to 10-fold. Synthetic peptides may be employed as adjuvants to ITR and NYS to decrease the toxicity of these drugs.

Summary points

- Commercial antifungal drugs (itraconazole [ITR] and Nystatin [NYS]) commonly used against fungal infections have not been effective against *Candida albicans* and *Candida krusei* biofilms.
- Synthetic peptides (PepGAT and PepKAA) appear to act synergistically with NYS and ITR, enhancing their activity against *C. albicans* and *C. krusei* biofilms.
- Synergistic actions of peptides and drugs were effective in both experiments to inhibit biofilm formation and to reduce biomass of mature biofilms.
- Scanning electron microscopy and fluorescence microscopy provided important insight into the mechanisms of synergistic action of peptides and drugs against *C. albicans* and *C. krusei* biofilms.
- In addition to improving the antifungal activity of drugs, the synthetic peptides also reduced their toxicity to red blood cells. This suggests that synthetic peptides are potential alternative molecules to act as adjuvants of NYS and ITR to overcome the resistance of biofilms.

Supplementary data

To view the supplementary data that accompany this paper please visit the journal website at: www.futuremedicine.com/doi/suppl/10.2217/fmb-2022-0053

Author contributions

Conceptualization – LP Bezerra, PFN Souza. Data curation – LP Bezerra, AFB Silva, JL Amaral, NAS Neto, CR de Andrade, RGG Silva, R Santos-Oliveira, LM Rebelo Alencar and PFN Souza. Formal analysis – CDT Freitas, JTA Oliveira, and PFN Souza. Funding acquisition – CDT Freitas, R Santos-Oliveira, LM Rebelo Alencar and TA Oliveira. Methodology – LP Bezerra, AFB Silva, JL Amaral, NAS Neto, MO Belém, RGG Silva and PFN Souza. Resources – CDT Freitas, R Santos-Oliveira, LM Rebelo Alencar and TA Oliveira. Supervision – PFN Souza. Writing of original draft – MO Belém, CR de Andrade, R Santos-Oliveira, LM Rebelo Alencar and PFN Souza. Writing, review and editing – R Santos-Oliveira, LM Rebelo Alencar and PFN Souza.

Acknowledgments

The authors are grateful to the staff of the central analytical facilities of UFC, Brazil.

Financial & competing interests disclosure

This work was supported by grants from the following Brazilian agencies: Conselho Nacional de Desenvolvimento Científico e Tecnológico (CNPq); Coordenação de Aperfeiçoamento de Pessoal de Nível Superior (CAPES); and Fundação Cearense de Apoio

ao Desenvolvimento Científico e Tecnológico (FUNCAP). Special thanks go to CAPES (grant no. 88887.318820/2019-00) for postdoctoral research of PFN Souza. The authors have no other relevant affiliations or financial involvement with any organization or entity with a financial interest in or financial conflict with the subject matter or materials discussed in the manuscript apart from those disclosed.

English revision for writing assistance was utilized in the production of this manuscript and paid with funding provided to Pedro F. N. Souza by CAPES grant (no. 88887.318820/2019-00).

References

1. Lima PG, Oliveira JTA, Amaral JL *et al.* Synthetic antimicrobial peptides: characteristics, design, and potential as alternative molecules to overcome microbial resistance. *Life Sci.* 278, 119647 (2021).
2. Sanguinett M, Posteraro B, Lass-Florl C. Antifungal drug resistance among *Candida* species: mechanisms and clinical impact. *Mycoses* 58(Suppl. 2), 2–13 (2015).
3. Morgan J, Meltzer MI, Plikaytis BD *et al.* Excess mortality, hospital stay, and cost due to candidemia: a case-control study using data from Population-Based Candidemia Surveillance. *Infect. Control Hosp. Epidemiol.* 26(6), 540–547 (2005).
4. Brown GD, Denning DW, Grow NAR *et al.* Hidden killers: human fungal infections. *Sci. Transl. Med.* 4(165), 1–18 (2012).
5. Antinori S, Milazzo L, Sollima S *et al.* Candidemia and invasive candidiasis in adults: anarrative review. *Eur. J. Intern. Med.* 34, 21–28 (2016).
6. Fu J, Ding Y, Wei B *et al.* Epidemiology of *Candida albicans* and non-*C. albicans* of neonatal candidemia at a tertiary care hospital in western China. *BMC Infect. Dis.* 17(1), 329 (2017).
7. Ademe M, Girma F. *Candida auris*: from multidrug resistance to pan-resistant strains. *Infect. Drug Resist.* 13, 1287 (2020).
8. De La Fuente-Núñez C, Cardoso MH, De Souza CE *et al.* Synthetic antibiofilm peptides. *Biochim. Biophys. Acta – Biomembr.* 1858(5), 1061–1069 (2016).
9. Cavalheiro M, Teixeira MC. *Candida* biofilms: threats, challenges, and promising strategies. *Front. Med.* 5, 28 (2018).
10. Costa-de-Oliveira S, Rodrigues AG. *Candida albicans* antifungal resistance and tolerance in bloodstream infections: the triad yeast–host–antifungal. *Microorganisms* 8(2), 1–11 (2020).
11. Marak MB, Dhanashree B. Antifungal susceptibility and biofilm production of *Candida* spp. isolated from clinical samples. *Int. J. Microbiol.* 2018, 7495218 (2018).
12. Chowdhary A, Sharma C, Meis JF. Azole-resistant aspergillosis: epidemiology, molecular mechanisms, and treatment. *J. Infect. Dis.* 216(Suppl. 3), S436–S444 (2017).
13. Fjell CD, Hiss JA, Hancock REW *et al.* Designing antimicrobial peptides: form follows function. *Nat. Rev. Drug Discov.* 11(1), 37–51 (2012).
14. Duncan VMS, O'Neil DA. Commercialization of antifungal peptides. *Fungal Biol. Rev.* 26(4), 156–165 (2013).
15. Mohamed MF, Abdelkhalek A, Seleem MN. Evaluation of short synthetic antimicrobial peptides for treatment of drug-resistant and intracellular *Staphylococcus aureus*. *Sci. Reports* 6(1), 1–14 (2016).
16. Dias LP, Souza PFN, Oliveira JTA *et al.* RcAlb-PepII, a synthetic small peptide bioinspired in the 2S albumin from the seed cake of *Ricinus communis*, is a potent antimicrobial agent against *Klebsiella pneumoniae* and *Candida parapsilosis*. *Biochim. Biophys. Acta Biomembr.* 1862(2), 183092 (2020).
17. Oliveira JTA, Souza PFN, Vasconcelos IM *et al.* Mo-CBP3-PepI, Mo-CBP3-PepII, and Mo-CBP3-PepIII are synthetic antimicrobial peptides active against human pathogens by stimulating ROS generation and increasing plasma membrane permeability. *Biochimie* 157, 10–21 (2019).
18. Souza PFN, Marques LSM, Oliveira JTA *et al.* Synthetic antimicrobial peptides: from choice of the best sequences to action mechanisms. *Biochimie* 175, 132–145 (2020).
19. Pennington MW, Zell B, Bai CJ. Commercial manufacturing of current good manufacturing practice peptides spanning the gamut from neoantigen to commercial large-scale products. *Med. Drug Discov.* 9, 100071 (2021).
20. Buckley ST, Bækdal TA, Vegge A *et al.* Transcellular stomach absorption of a derivatized glucagon-like peptide-1 receptor agonist. *Sci. Transl. Med.* 10(468), 7047 (2018).
21. Lima PG, Souza PFN, Freitas CDT *et al.* Anticandidal activity of synthetic peptides: mechanism of action revealed by scanning electron and fluorescence microscopies and synergism effect with nystatin. *J. Pept. Sci.* 26(6), e3249 (2020).
22. PFN S, PG L, CDT F *et al.* Antidermatophytic activity of synthetic peptides: action mechanisms and clinical application as adjuvants to enhance the activity and decrease the toxicity of Griseofulvin. *Mycoses* 63(9), 979–992 (2020).
23. Souza PFN, Lima PG, Freitas CDT *et al.* Antidermatophytic activity of synthetic peptides: action mechanisms and clinical application as adjuvants to enhance the activity and decrease the toxicity of Griseofulvin. *Mycoses* 63(9), 979–992 (2020).

24. Nami S, Mohammadi R, Vakili M *et al.* Fungal vaccines, mechanism of actions and immunology: a comprehensive review. *Biomed. Pharmacother.* 109, 333–344 (2019).
25. Pristov KE, Ghannoum MA. Resistance of *Candida* to azoles and echinocandins worldwide. *Clin. Microbiol. Infect.* 25(7), 792–798 (2019).
26. Jamiu AT, Albertyn J, Sebolai OM, Pohl CH *et al.* Update on *Candida krusei*, a potential multidrug-resistant pathogen. *Med. Mycol.* 59(1), 14–30 (2021).
27. Orozco AS, Higginbotham LM, Hitchcock CA *et al.* Mechanism of fluconazole resistance in *Candida krusei*. *Antimicrob. Agents Chemother.* 42(10), 2645 (1998).
28. Guinea J, Sánchez-Somolinos M, Cuevas O *et al.* Fluconazole resistance mechanisms in *Candida krusei*: the contribution of efflux-pumps. *Med. Mycol.* 44(6), 575–578 (2006).
29. Lum KY, Tay ST, Le CF *et al.* Activity of novel synthetic peptides against *Candida albicans*. *Sci. Rep.* 5, 9657 (2015).
30. Roscetto E, Contursi P, Vollaro A *et al.* Antifungal and anti-biofilm activity of the first cryptic antimicrobial peptide from an archaeal protein against *Candida* spp. clinical isolates. *Sci. Reports* 8(1), 1–11 (2018).
31. Paulone S, Ardizzoni A, Tavanti A *et al.* The synthetic killer peptide KP impairs *Candida albicans* biofilm *in vitro*. *PLOS ONE* 12(7), e0181278 (2017).
32. Park SC, Kim YM, Lee JK *et al.* Targeting and synergistic action of an antifungal peptide in an antibiotic drug-delivery system. *J. Control Release* 256, 46–55 (2017).
33. MacCallum DM, Desbois AP, Coote PJ. Enhanced efficacy of synergistic combinations of antimicrobial peptides with caspofungin versus *Candida albicans* in insect and murine models of systemic infection. *Eur. J. Clin. Microbiol. Infect. Dis.* 32(8), 1055–1062 (2013).
34. do Nascimento Dias J, de Souza Silva C, de Araújo AR *et al.* Mechanisms of action of antimicrobial peptides ToAP2 and NDBP-5.7 against *Candida albicans* planktonic and biofilm cells. *Sci. Rep.* 10(1), 1–14 (2020).
35. Maione A, Bellavita R, Alteriis ED *et al.* WMR peptide as antifungal and antibiofilm against *Candida albicans* and Non-*C. albicans* species: shreds of evidence on the mechanism of action. *Int. J. Mol. Sci.* 23(4), 2151 (2022).
36. Czechowicz P, Neubauer D, Nowicka J *et al.* Antifungal activity of linear and disulfide-cyclized ultrashort cationic lipopeptides alone and in combination with fluconazole against vulvovaginal *Candida* spp. *Pharmaceutics* 13(10), 22–45 (2021).
37. Cools TL, Struyfs C, Drijfhout JW *et al.* A linear 19-mer plant defensin-derived peptide acts synergistically with caspofungin against *Candida albicans* biofilms. *Front. Microbiol.* 8, 1–14 (2017).
38. Ceresa C, Rinaldi M, Tessarolo F *et al.* Inhibitory effects of lipopeptides and glycolipids on *C. albicans*-Staphylococcus spp. dual-species biofilms. *Front. Microbiol.* 11, 3516 (2021).
39. Mora-Navarro C, Méndez-Vega J, Caraballo-León J *et al.* Hydrophobicity of antifungal β-Peptides is associated with their cytotoxic effect on *in vitro* human colon Caco-2 and liver HepG2 cells. *PLOS ONE* 11(3), e0149271 (2016).
40. Čáp M, Váchová L, Palková Z. Reactive oxygen species in the signaling and adaptation of multicellular microbial communities. *Oxid. Med. Cell. Longev.* 2012, 13 (2012).
41. Maurya IK, Pathak S, Sharma M *et al.* Antifungal activity of novel synthetic peptides by accumulation of reactive oxygen species (ROS) and disruption of cell wall against *Candida albicans*. *Peptides* 32(8), 1732–1740 (2011).
42. Borgers M, Van de Ven MA. Mode of action of itraconazole: morphological aspects. *Mycoses* 32, 53–59 (1989).
43. dos Santos AG, Marquês JT, Carreira AC *et al.* The molecular mechanism of Nystatin action is dependent on the membrane biophysical properties and lipid composition. *Phys. Chem. Chem. Phys.* 19(44), 30078–30088 (2017).
44. Queiroz-Telles F, Silva N, Carvalho MM *et al.* Evaluation of efficacy and safety of itraconazole oral solution for the treatment of oropharyngeal candidiasis in aids patients. *Braz. J. Infect. Dis.* 5(2), 60–66 (2001).

APÊNDICE E - SYNERGISTIC ANTIFUNGAL ACTIVITY OF SYNTHETIC PEPTIDES AND ANTIFUNGAL DRUGS AGAINST *CANDIDA ALBICANS* AND *C. PARAPSILOSIS* BIOFILMS

antibiotics

MDPI

Article

Synergistic Antifungal Activity of Synthetic Peptides and Antifungal Drugs against *Candida albicans* and *C. parapsilosis* Biofilms

Leandro P. Bezerra [1], Cleverson D. T. Freitas [1,*], Ayrles F. B. Silva [1], Jackson L. Amaral [1], Nilton A. S. Neto [1], Rafael G. G. Silva [2], Aura L. C. Parra [1], Gustavo H. Goldman [3], Jose T. A. Oliveira [1], Felipe P. Mesquita [4] and Pedro F. N. Souza [1,4,*]

[1] Department of Biochemistry and Molecular Biology, Federal University of Ceará, Fortaleza 60451, CE, Brazil; leandro.bioquimica@gmail.com (L.P.B.); ayrlesbrandao@gmail.com (A.F.B.S.); jacksoncesarc@gmail.com (J.L.A.); niltonararipeneto@hotmail.com (N.A.S.N.); alchaconp@unal.edu.co (A.L.C.P.); jtaolive@ufc.br (J.T.A.O.)
[2] Department of Biology, Federal University of Ceará, Fortaleza 60451, CE, Brazil; rafaelguimaraes@ufc.br
[3] Faculty of Pharmaceutical Sciences of Ribeirão Preto, University of São Paulo, São Paulo P.O. Box 05508-000, SP, Brazil; ggoldman@usp.br
[4] Drug Research and Development Center, Department of Physiology and Pharmacology, Federal University of Ceará, Rua Coronel, Nunes de Melo 100, Caixa, Fortaleza 60430-275, CE, Brazil; felipe_mesquita05@hotmail.com
* Correspondence: cleversondiniz@hotmail.com (C.D.T.F.); pedrofilhobio@gmail.com (P.F.N.S.)

check for updates

Citation: Bezerra, L.P.; Freitas, C.D.T.; Silva, A.F.B.; Amaral, J.L.; Neto, N.A.S.; Silva, R.G.G.; Parra, A.L.C.; Goldman, G.H.; Oliveira, J.T.A.; Mesquita, F.P.; et al. Synergistic Antifungal Activity of Synthetic Peptides and Antifungal Drugs against *Candida albicans* and *C. parapsilosis* Biofilms. *Antibiotics* **2022**, *11*, 553. https://doi.org/10.3390/antibiotics11050553

Academic Editor: Charlotte A. Huber

Received: 29 March 2022
Accepted: 20 April 2022
Published: 21 April 2022

Publisher's Note: MDPI stays neutral with regard to jurisdictional claims in published maps and institutional affiliations.

Copyright: © 2022 by the authors. Licensee MDPI, Basel, Switzerland. This article is an open access article distributed under the terms and conditions of the Creative Commons Attribution (CC BY) license (https://creativecommons.org/licenses/by/4.0/).

Abstract: *C. albicans* and *C. parapsilosis* are biofilm-forming yeasts responsible for bloodstream infections that can cause death. Synthetic antimicrobial peptides (SAMPs) are considered to be new weapons to combat these infections, alone or combined with drugs. Here, two SAMPs, called *Mo*-CBP_3-PepI and *Mo*-CBP_3-PepIII, were tested alone or combined with nystatin (NYS) and itraconazole (ITR) against *C. albicans* and *C. parapsilosis* biofilms. Furthermore, the mechanism of antibiofilm activity was evaluated by fluorescence and scanning electron microscopies. When combined with SAMPs, the results revealed a 2- to 4-fold improvement of NYS and ITR antibiofilm activity. Microscopic analyses showed cell membrane and wall damage and ROS overproduction, which caused leakage of internal content and cell death. Taken together, these results suggest the potential of *Mo*-CBP_3-PepI and *Mo*-CBP_3-PepIII as new drugs and adjuvants to increase the activity of conventional drugs for the treatment of clinical infections caused by *C. albicans* and *C. parapsilosis*.

Keywords: antibiofilm activity; candidiasis; synergism; synthetic peptides; antifungal drugs

1. Introduction

Biofilms are established by microbial cells on an inert or living surface, promoting the development of microcolonies with polymeric matrices and enhancing the resistance to various antimicrobial agents [1,2]. *Candida* species are biofilm-forming yeasts responsible for up to 15% of hospital-acquired cases of sepsis [3]. A mature biofilm produced by *Candida* spp. consists of an extracellular matrix composed of glycoproteins (55%), carbohydrates (25%), lipids (15%), and nucleic acids (5%) [4]. The National Institute of Health (NIH) in the USA considers biofilms to be a public health problem and estimated that they can be responsible for 80% of the difficulties in curing human infections [1,2,4,5]. The most susceptible people are immunocompromised patients, AIDS+ patients, patients under chemotherapy treatment or immunosuppressive therapies, and patients fitted with medical devices (catheters, pacemakers, and heart valves) [6,7].

C. albicans and *C. parapsilosis* are common opportunistic fungal pathogens that asymptomatically colonize the mucosal surfaces and skin of healthy individuals. However, in

some circumstances they can cause an infection called candidiasis [8]. In addition, *C. albicans* and *C. parapsilosis* are responsible for bloodstream infections termed candidemia, which are common in immunocompromised patients, including those in intensive care units [9]. Currently, the treatment of infections caused by *C. albicans* and *C. parapsilosis* involves the use of antifungal agents that interrupt different metabolic pathways of the cell. However, some studies have reported *Candida* resistance to these antifungal molecules [10–12]. A study by Katiyar and collaborators [13] described *Candida* clinical isolates that contain genes responsible for resistance to some commercial antifungal agents [13]. To counter this problem, synthetic antimicrobial peptides (SAMPs) have been described as new alternatives, either alone or combined with commercial antifungal drugs, to control *Candida* infection and overcome the pathogens' resistance [1]. SAMPs have some important antimicrobial characteristics found in natural antimicrobial peptides, such as positive net charge, α-helical structure, low molecular weight (600–1200 Da), high hydrophobic ratio (40–60%) and amphipathicity [1,14].

Recently, our research group designed, characterized, and evaluated the antimicrobial activity of two synthetic peptides, called *Mo*-CBP_3-PepI (CPIAQRCC) and *Mo*-CBP_3-PepIII (AIQRCC). These peptides were designed based on the structure of *Mo*-CBP_3, a chitin-binding protein purified from *Moringa oleifera* seeds [15,16]. The anticandidal activity and mechanism of action of these peptides were evaluated by Oliveira et al. (2019) and Lima et al. (2020). Therefore, the aim of this study was to evaluate the antifungal activity and action mechanism of *Mo*-CBP_3-PepI and *Mo*-CBP_3-PepIII, alone or combined with NYS and ITR, against *C. albicans* and *C. parapsilosis* biofilms.

2. Results

2.1. Antibiofilm Activity of Synthetic Peptides and Two Commercial Drugs

The activities of *Mo*-CBP_3-PepI and *Mo*-CBP_3-PepIII (50 μg mL^{-1}) against *C. albicans* and *C. parapsilosis* biofilms are shown in Figure 1. The biofilm formation of *C. albicans* was inhibited 10% by *Mo*-CBP_3-PepI, whereas *Mo*-CBP_3-PepIII did not show any activity. Interestingly, the commercial drugs ITR and NYS inhibited biofilm formation by only 7% and 40%, respectively (Figure 1A). Regarding the synergistic effect, the combination of both peptides *Mo*-CBP_3-PepI and *Mo*-CBP_3-PepIII with ITR or NYS significantly enhanced the inhibition of *C. albicans* biofilm formation. For instance, the two peptides combined with NYS increased the inhibition of *C. albicans* biofilm formation by 40% to 80% (Figure 1A). ITR and NYS inhibited *C. parapsilosis* biofilm formation by 45% and 43%, respectively. In contrast, *Mo*-CBP_3-PepI and *Mo*-CBP_3-PepIII inhibited this by only 15% and 25%, respectively (Figure 1B). On the other hand, combinations of *Mo*-CBP_3-PepI + ITR, *Mo*-CBP_3-PepIII + ITR, *Mo*-CBP_3-PepI + NYS, and *Mo*-CBP_3-PepIII + NYS inhibited the biofilm formation by about 98%, 96%, 79%, and 82%, respectively (Figure 1B).

Regarding the degradation of mature *C. albicans* biofilm, ITR and NYS decreased the biofilm mass by about 50% and 30%, while *Mo*-CBP_3-PepI and *Mo*-CBP_3-PepIII only degrading it by 60% and 30%, respectively (Figure 1C). Remarkably, the combinations *Mo*-CBP_3-PepI + ITR and *Mo*-CBP_3-PepIII + ITR did not have any effect (Figure 1C). However, the combinations *Mo*-CBP_3-PepI + NYS and *Mo*-CBP_3-PepIII + NYS degraded 85% and 50% of the mature *C. albicans* biofilm (Figure 1C). Concerning the degradation of mature *C. parapsilosis* biofilm, only the combination Mo-CBP3-PepI + NYS showed activity, reducing the biofilm biomass by 50% (Figure 1D).

2.2. Analysis of Candida Biofilm Morphology

Scanning electron microscopy (SEM) was used to evaluate damage to *C. albicans* and *C. parapsilosis* biofilms after all treatments (Figures 2 and 3). The control cells did not show any damage or alterations on the surface; only spherical-shaped cells were observed without cracks or scars. The treatment with peptides or drugs caused only mild damage, such as wrinkles and slight changes to the morphology of cells, which had a very similar appearance to the control (Figures 2 and 3). In contrast, the combination of both peptides

with the two drugs caused a significant reduction in the mature biofilm compared to control, and it was possible to see damage such as small blebs, new buds, scars, and rings of truncated bud scars. *Mo*-CBP$_3$-PepI + NYS and *Mo*-CBP$_3$-PepIII + NYS were by far the most lethal to *C. albicans* and *C. parapsilosis*. In those treatments, the cells were greatly damaged, with high roughness levels, severe alterations in morphology, and a clear indication of cell lysis leading to loss of cytoplasm (Figures 2 and 3).

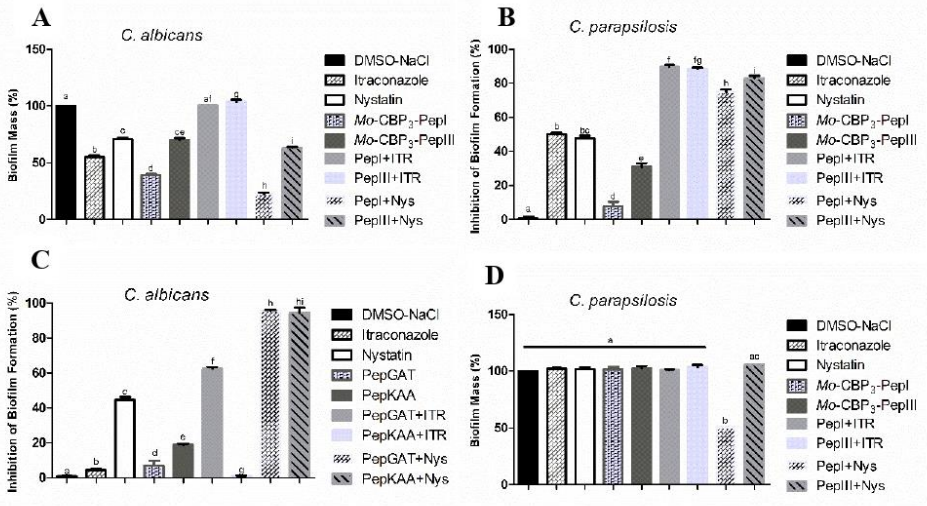

Figure 1. (**A**,**B**) Inhibitory activity of biofilm formation and (**C**,**D**) degradation of mature biofilm of *C. albicans* and *C. parapsilosis*. DMSO-NaCl was used as a negative control and ITR and NYS as positive controls. The letters represent the mean ± standard deviation of three replicates. Different lowercase letters indicate a statistically significant difference compared to DMSO-NaCl by analysis of variance ($p < 0.05$).

Because *Mo*-CBP$_3$-PepI + NYS showed the best inhibitory activity against biofilm formation, this sample was chosen to investigate alteration of mature biofilms of *C. albicans* and *C. parapsilosis* (Figure 4). The control biofilm (treated with DMSO-NaCl) did not present any damage, while the biofilms treated with NYS or *Mo*-CBP$_3$-PepI presented mild damage, such as altered morphology and wrinkles, distortion, and apparent reduction in biomass compared to the controls. However, *Mo*-CBP$_3$-PepI + NYS was highly lethal to mature *C. albicans* and *C. parapsilosis* biofilms (Figure 4). These biofilms had a large reduction in biomass, as well as severe cell damage, such as depression-like cavities and damage to the cell wall, alterations in cell shape, wrinkles and scars, and loss of internal content (Figure 4).

Figure 2. *Cont.*

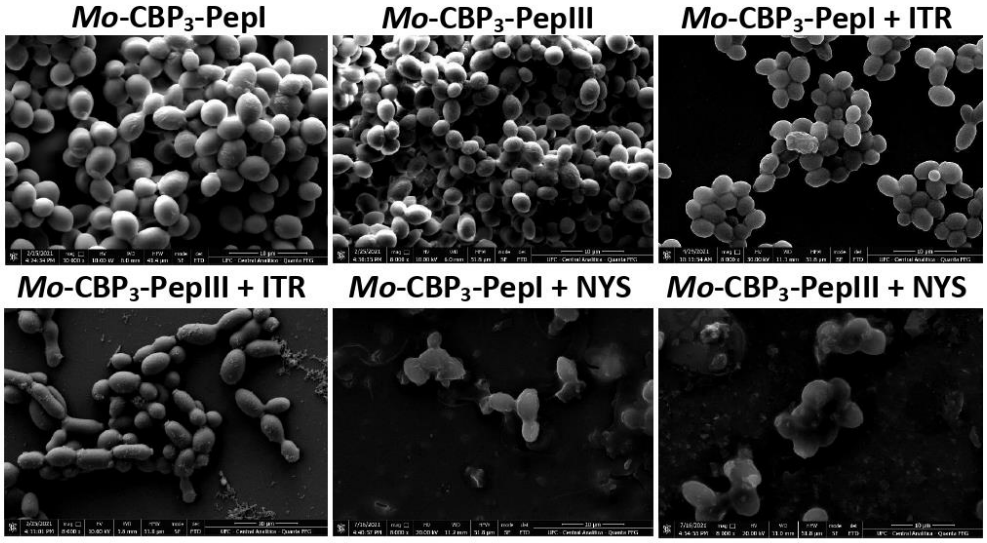

Figure 2. SEM images showing *C. albicans* biofilms after treatment with ITR, NYS, *Mo*-CBP$_3$-PepI, *Mo*-CBP$_3$-PepIII, and their combinations. Control: DMSO-NaCl solution.

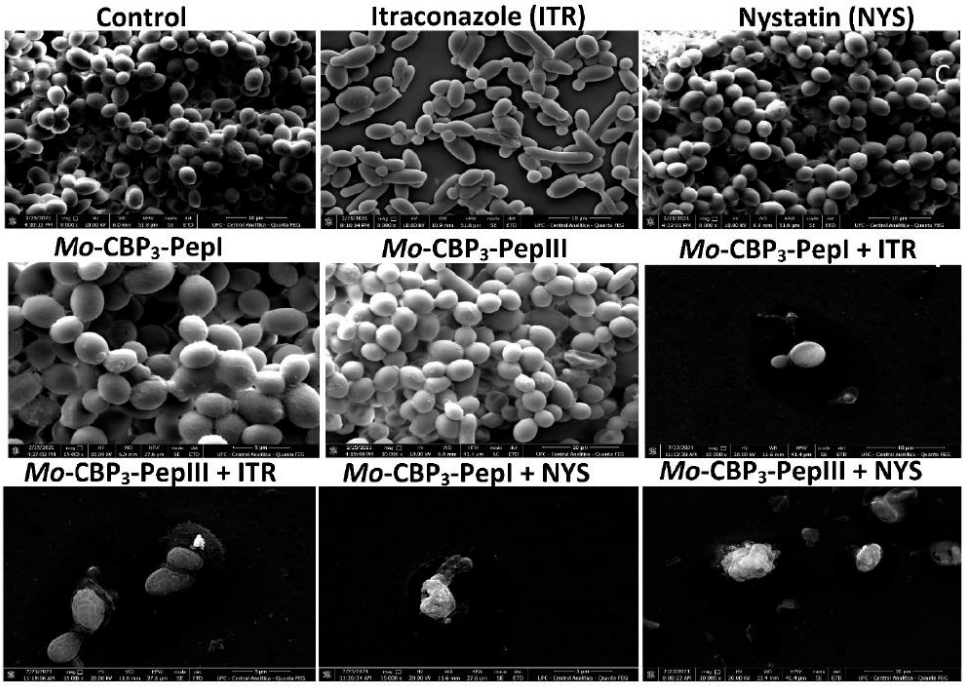

Figure 3. SEM images showing *C. parapsilosis* biofilms after treatment with ITR, NYS, *Mo*-CBP$_3$-PepI, *Mo*-CBP$_3$-PepIII, and their combinations. Control: DMSO-NaCl solution.

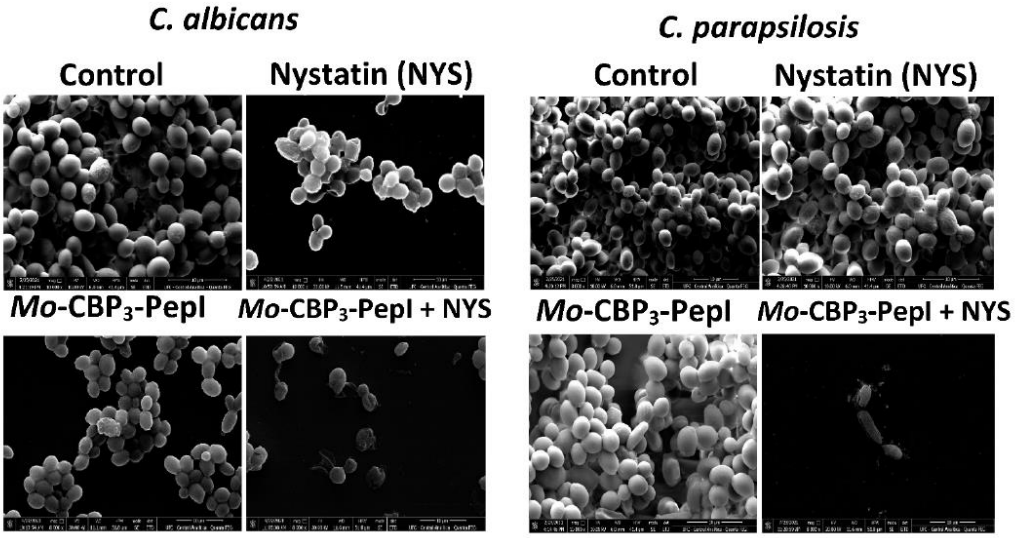

Figure 4. SEM images showing alterations of mature biofilm of *C. albicans* and *C. parapsilosis* after treatment with *Mo*-CBP$_3$-PepI, NYS and *Mo*-CBP$_3$-PepI + NYS. Control: DMSO-NaCl solution.

2.3. Membrane Pore Formation

The propidium iodide (PI) uptake assay was used to evaluate possible damage to the yeast cell membranes. PI interacts with DNA, releasing red fluorescence, but this is only possible when the membrane is damaged, since healthy membranes are impermeable to PI. As expected, the control (DMSO-NaCl solution) did not damage the cell membranes, because no fluorescence was detected. Similarly, cells treated with NYS and ITR did not show any fluorescence. However, *Mo*-CBP$_3$-PepI and *Mo*-CBP$_3$-PepIII, alone or in combination with NYS or ITR, induced red fluorescence in *C. albicans* and *C. parapsilosis* cells, indicating these cells membranes were damaged (Figures 5–9).

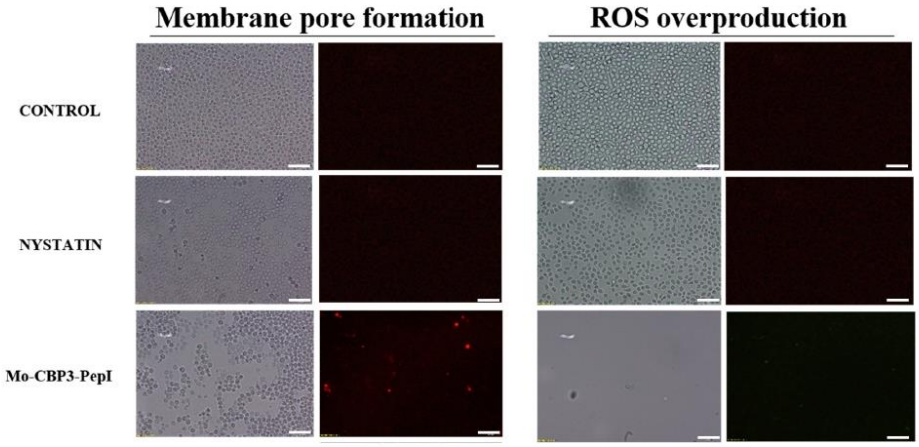

Figure 5. *Cont.*

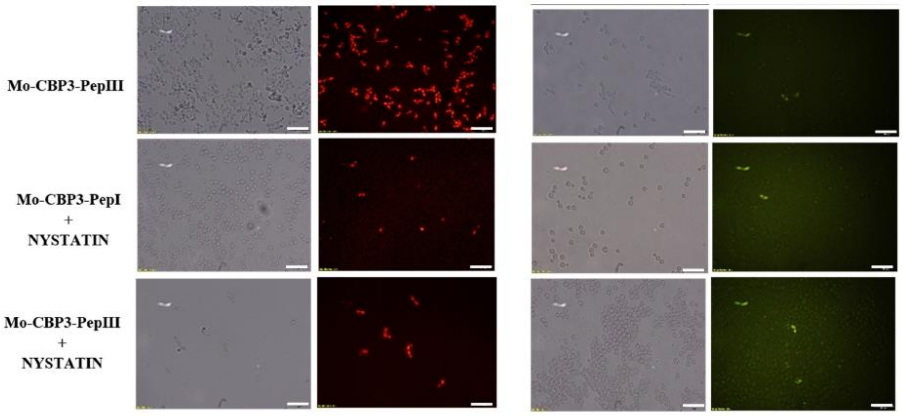

Figure 5. Fluorescence images showing membrane pore formation and ROS overproduction on inhibition of biofilm of *C. albicans* cells. Control solution of DMSO-NaCl, treated with *Mo*-CBP_3-PepI and *Mo*-CBP_3-PepIII at 50 μg mL^{-1} and synergistic activity of both peptides with NYS. Membrane pore formation was measured by the propidium iodide (PI) uptake assay, and ROS overproduction was detected using 2′, 7′ dichlorofluorescein diacetate (DCFH-DA). Bars: 100 μm.

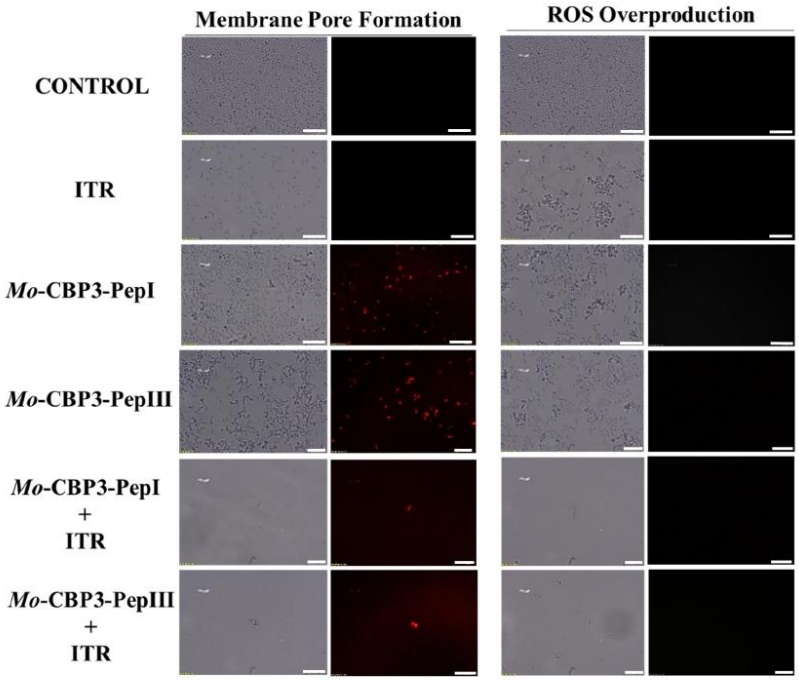

Figure 6. Fluorescence images showing membrane pore formation and ROS overproduction on inhibition of the biofilm of *C. parapsilosis* cells. Control solution of DMSO-NaCl, treated with *Mo*-CBP_3-PepI and *Mo*-CBP_3-PepIII at 50 μg mL^{-1} and synergistic activity of both peptides with ITR. Membrane pore formation was measured by the PI uptake assay, and ROS overproduction was detected using 2′, 7′ dichlorofluorescein diacetate (DCFH-DA). Bars: 100 μm.

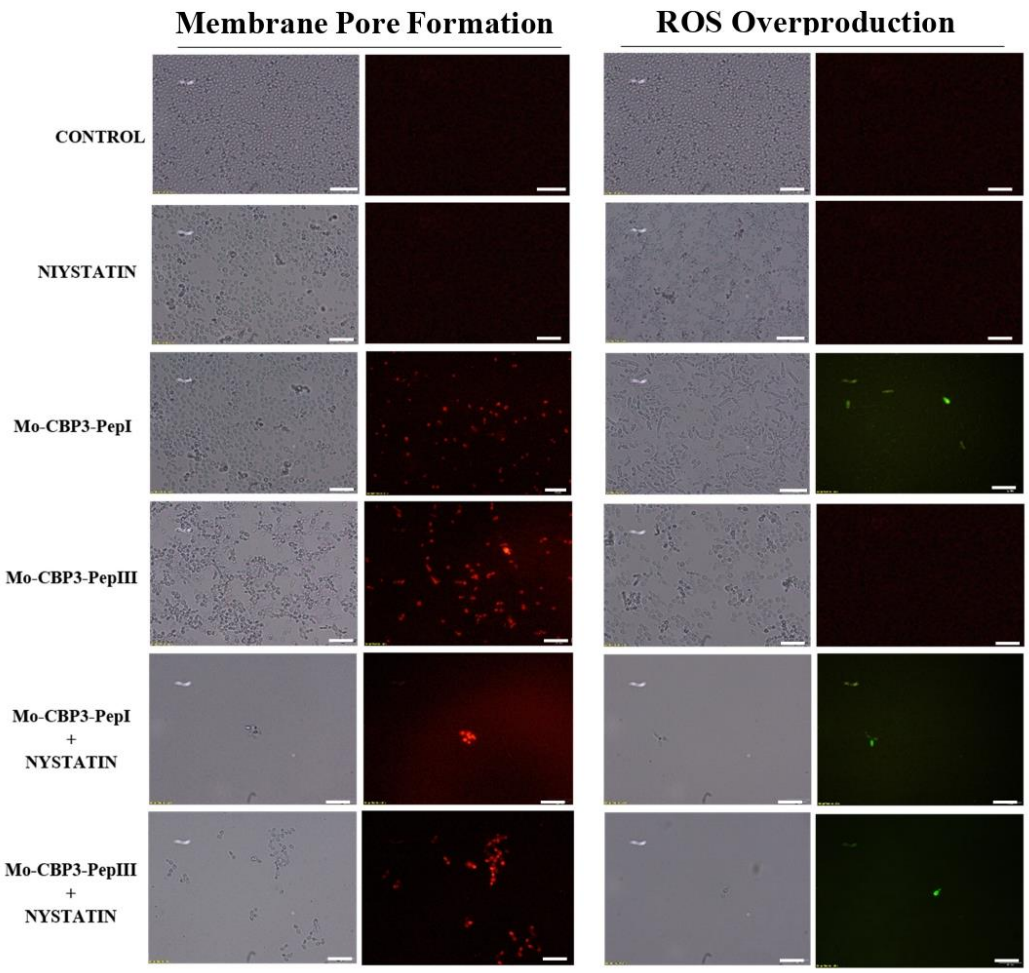

Figure 7. Fluorescence images showing membrane pore formation and ROS overproduction on inhibition of the biofilm of *C. parapsilosis* cells. Control solution of DMSO-NaCl, treated with *Mo*-CBP3-PepI and Mo-CBP3-PepIII at 50 μg mL^{-1} and synergistic activity of both peptides with NYS. Membrane pore formation was measured by the PI uptake assay, and ROS overproduction was detected using 2′, 7′ dichlorofluorescein diacetate (DCFH-DA). Bars: 100 μm.

ROS overproduction is another mechanism employed by peptides to inhibit biofilm formation. The results showed that treatment of *C. albicans* cells with NYS or ITR did not induce ROS overproduction, whereas both peptides and their combination with NYS induced a slight production of ROS. None of the treatments induced ROS overproduction by *C. parapsilosis* biofilms (Figures 5–9).

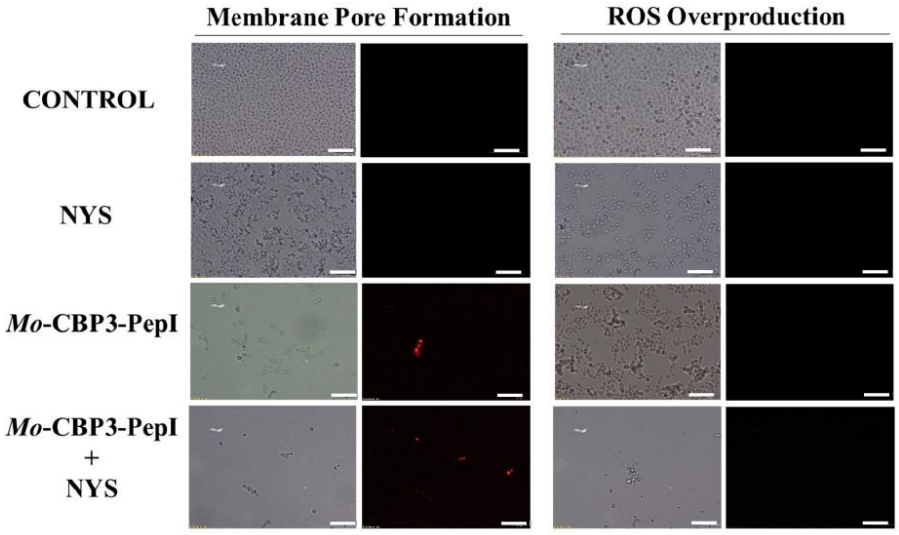

Figure 8. Fluorescence images showing membrane pore formation and ROS overproduction on degradation of the biofilm of *C. albicans* cells. Control solution of DMSO-NaCl, treated with *Mo*-CBP3-PepI at 50 μg mL^{-1} and synergistic activity with NYS. Membrane pore formation was measured by the PI uptake assay, and ROS overproduction was detected using 2′, 7′ dichlorofluorescein diacetate (DCFH-DA). Bars: 100 μm.

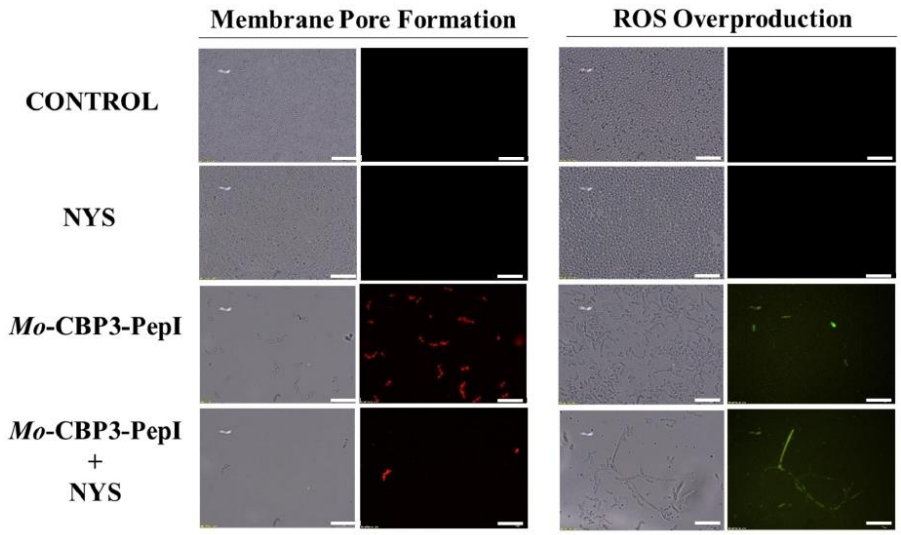

Figure 9. Fluorescence images showing membrane pore formation and ROS overproduction on degradation of the biofilm of *C. parapsilosis* cells. Control solution of DMSO-NaCl, treated with *Mo*-CBP_3-PepI at 50 μg mL^{-1} and synergistic activity with NYS. Membrane pore formation was measured by the PI uptake assay, and ROS overproduction was detected using 2′, 7′ dichlorofluorescein diacetate (DCFH-DA). Bars: 100 μm.

2.4. Molecular Docking

The molecular docking assays were performed to evaluate the possible interactions of the peptides with NYS and ITR. *Mo*-CBP$_3$-PepI interacted with ITR and NYS with binding interaction energy (LBIE) values of −4.5 and −4.2 kcal.mol^{-1}, respectively (Figure 10A,B). The amino acid residues Pro2 and Ile4 of the Mo-CBP3-PepI peptide showed Pi-Alkyl interactions with the phenyl (4.5 Å), piperazine (4.2 Å), and dichlorophenyl (4.5 Å) groups of ITR. Cys8 had a Pi-Anion (3.4 Å, triazole group) and a Pi-Sulfur (5.1 Å, dichlorophenyl group) interaction with ITR, and Arg6 presented only van der Waals interaction (Figure 10C). *Mo*-CBP$_3$-PepI interacted with NYS by van der Waals forces between Cys8, Gln5, and Cys1. An Alkyl (5.0 Å) interaction with Pro2 and an unfavorable donor-donor (1.3 Å) with Arg6 were also observed (Figure 10D).

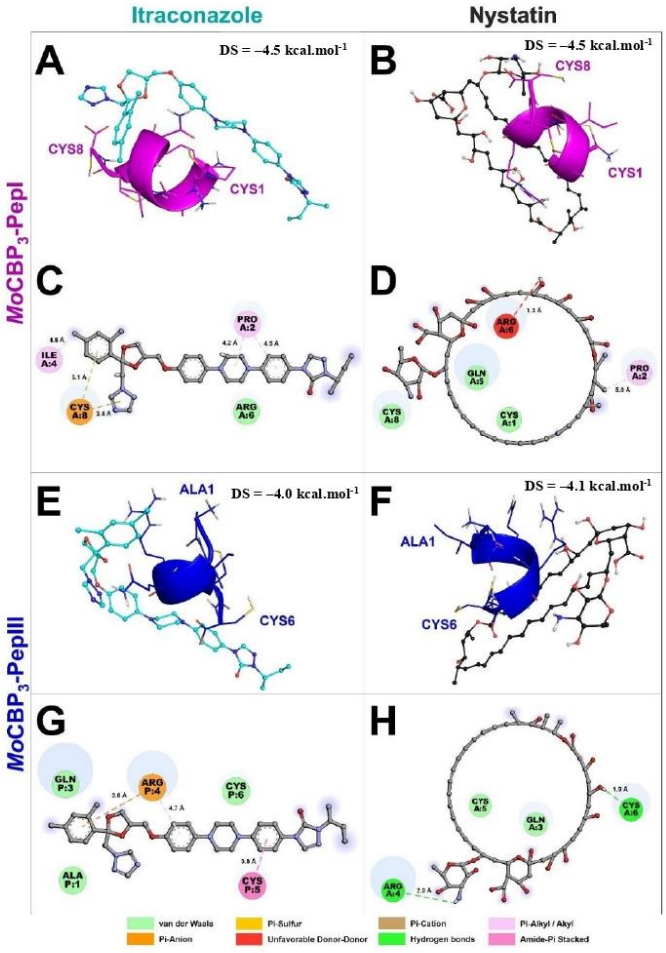

Figure 10. Molecular docking revealed that *Mo*-CBP$_3$-PepI and *Mo*-CBP$_3$-PepIII interact with ITR and NYS. *Mo*-CBP$_3$-PepI is represented in pink (**A**,**B**) and *Mo*-CBP$_3$-PepIII in blue (**E**,**F**). (**C**,**D**,**G**,**H**) show the binding sites of *Mo*-CBP$_3$-PepI and *Mo*-CBP$_3$-PepIII with ITR and NYS.

Mo-CBP$_3$-PepIII presented docking scores of −4.0 and −4.1 kcal.mol^{-1} with ITR and NYS, respectively (Figure 10E,F). *Mo*-CBP$_3$-PepIII interacted through van der Waals forces through residues Ala1, Gln3, and Cys6 with ITR. Cys5 interacted through an Amide-Pi stacked (3.8 Å) with the phenyl group of ITR. The Arg4 of *Mo*-CBP$_3$-PepIII established a Pi-Cation interaction with the dichlorophenyl group (3.8 Å) and a Pi-Alkyl interaction (4.7 Å) with the methoxyphenyl group of itraconazole (Figure 10E,G). The interaction between *Mo*-CBP$_3$-PepIII and NYS was supported by hydrogen bonds between residues Arg4 (2.0 Å) and Cys6 (1.9 Å), as well as through van der Waals interactions through residues Gln3 and Cys5 (Figure 10F,H).

2.5. Hemolytic Assay

As shown in a previous study [16], *Mo*-CBP$_3$-PepI and *Mo*-CBP$_3$-PepIII had no hemolytic activity against any human blood type tested (Table 1), even at 50 μg mL^{-1}. In contrast, NYS (1000 μg mL^{-1}) caused 100% hemolysis in all human blood types, and ITR (1000 μg mL^{-1}) caused 75%, 68%, and 58% hemolysis to Type A, B, and O red blood cells, respectively (Table 1).

Table 1. Hemolytic activity of *Mo*-CBP$_3$-PepI and *Mo*-CBP$_3$-PepIII, antifungal drugs, and combined solutions on human red blood cells.

Peptides/Combinations	% Hemolysis		
	Type A Blood	Type B Blood	Type O Blood
0.1% Triton X-100	100 ± 0.002	100 ± 0.001	100 ± 0.007
DMSO-NaCl Solution	0	0	0
NYS (1000 μg mL^{-1})	100 ± 0.005	100 ± 0.001	100 ± 0.002
ITR (1000 μg mL^{-1})	75 ± 0.007	68 ± 0.004	58 ± 0.003
Mo-CBP$_3$-PepI (50 μg mL^{-1})	0	0	0
Mo-CBP$_3$-PepIII (50 μg mL^{-1})	0	0	0
Mo-CBP$_3$-PepI (50 μg mL^{-1}) + NYS (1000 μg mL^{-1})	14 ± 0.006	23 ± 0.009	2 ± 0.001
Mo-CBP$_3$-PepI (50 μg mL^{-1}) + ITR (1000 μg mL^{-1})	0	4 ± 0.003	8 ± 0.005
Mo-CBP$_3$-PepIII (50 μg mL^{-1}) + NYS (1000 μg mL^{-1})	45 ± 0.001	30 ± 0.001	18 ± 0.007
Mo-CBP$_3$-PepIII (50 μg mL^{-1}) + ITR (1000 μg mL^{-1})	50 ± 0.005	15 ± 0.008	2 ± 0.001

The mean ± standard deviation of three replicates according to ANOVA ($p < 0.05$).

In general, the combination of synthetic peptides decreased the hemolytic effect of both drugs (Table 1). The combination of *Mo*-CBP$_3$-PepI with NYS resulted in hemolytic effects of 14%, 23%, and 2%, and the combination of *Mo*-CBP$_3$-PepI with ITR resulted in 0%, 4%, and 8% hemolysis to Type A, B, and O red blood cells, respectively (Table 1). The combination of *Mo*-CBP$_3$-PepIII with NYS hemolyzed 45%, 30%, and 18%, while the combination of *Mo*-CBP$_3$-PepI with ITR resulted in 50%, 15%, and 2% for Type A, B, and O red blood cells, respectively (Table 1).

3. Discussion

Natural antimicrobial peptides (AMPs) are promising molecules to act as substitutes or adjuvants to treat infections. However, they have some disadvantages, such as toxicity, low resistance to proteolysis, and the high cost of isolation and purification. The development of synthetic antimicrobial peptides (SAMPs) is an alternative solution to overcome these drawbacks, since they have low or no toxicity to mammalian cells, and low chance of developing antimicrobial resistance based on their mechanism of action [1,14].

Bioinspired SAMPs based on natural AMPs can have attributes that are not present in the natural molecule [17,18]. A good example is the synthetic peptide LAH4, designed based on the Magainin 2 sequence, which presented potent activity against *Escherichia coli* and *Staphylococcus aureus* compared with the natural peptide Magainin 2 [17,18]. Recently, our research group designed peptides derived from *Mo*-CBP$_3$ and antifungal chitin-binding protein from *M. oleifera* seeds. *Mo*-CBP$_3$-PepI and *Mo*-CBP$_3$-pepIII inhibited the growth of

C. albicans and *C. parapsilosis* planktonic cells by the stimulation of ROS production, cell wall damage, and membrane pore formation, leading to death [15,16]. It is important to mention that *Mo*-CBP_3 did not present anticandidal activity. Based on that, we decided to evaluate the potential of *Mo*-CBP_3-PepI and *Mo*-CBP_3-pepIII to inhibit biofilm formation and its capacity to promote degradation of mature biofilms of *C. albicans* and *C. parapsilosis*.

Regarding degradation of the mature biofilms of *C. albicans*, *Mo*-CBP_3-PepI and *Mo*-CBP_3-PepIII had activity of 40% and 70%, respectively (Figure 1). These results corroborate those involving gH625, a peptide analog from gH625-M, which reduced by 61% the biomass of mature biofilms of *C. albicans* [19]. SEM analysis of *C. albicans* and *C. parapsilosis* treated with *Mo*-CBP_3-PepI and *Mo*-CBP_3-PepIII showed that the biofilms suffered severe structural damage. Furthermore, SEM images suggested that the two peptides induced rupture of the cell wall and membrane pore formation, leading to internal content loss and death. The images also showed the presence of scars, buds, and cracks. These results corroborate those reported by Belmadani and collaborators [20], who observed that Dermaseptin-S1, an antimicrobial peptide from *Phyllomedusa sauvagii*, decreased *C. albicans* biofilm formation by causing changes in the cell wall structure, membrane pore formation, and leakage of internal content. Similar behavior was observed by Sierra et al., where a *C. albicans* biofilm suffered severe damage by the antimicrobial peptide called Histatin-5 [21]. This severe damage observed in the cell wall of both cells via SEM analysis can be explained since *Mo*-CBP_3-PepI and *Mo*-CBP_3-PepIII are designed based on the sequence of *Mo*-CBP_3, which is a chitin-binding protein from *M. oleifera* seeds [16]. Both peptides can interact with the chitin present in the fungal cell wall and cause destabilization of the cell, leading to rupture, electrolyte imbalance, and thus cell death.

Unlike many commercial drugs that have specific targets, SAMPs target the cell membrane and/or the cell wall [14]. The ability of SAMPs to alter the microbial membrane permeability is considered the most common mechanism of action of these molecules, making the development of resistance mechanisms by microorganisms very difficult [1,14]. Fluorescence microscopy analyses were performed to evaluate if our peptides could induce membrane damage. *Mo*-CBP_3-PepI and *Mo*-CBP_3-PepIII induced PI uptake in *C. albicans* and *C. parapsilosis* biofilms, suggesting pore formation or cell membrane damage, as observed by SEM analysis. Furthermore, the peptides induced ROS overproduction in *C. parapsilosis* and *C. albicans* biofilms. A similar profile was observed using the peptides KP and MCh-AMP1, which are synthetic peptides able to induce ROS overproduction in *C. albicans* biofilm, leading to cell death. ROS are involved in the damage of essential molecules such as proteins, lipids, and DNA [22].

There are some explanations for the synergistic effect of the peptides and antifungal drugs tested here. First, the interactions between both peptides and NYS and ITR (Figure 6) can explain the synergistic activity obtained, where both peptides enhanced the activity of both drugs. Additionally, molecular docking studies were performed to evaluate whether both peptides could interact with NYS and ITR. Similar behavior was detected by Souza et al. [23], where *Mo*-CBP_3-PepI and *Mo*-CBP_3-PepIII interacted with griseofulvin by weak interactions, such as hydrogen bonds and hydrophobic interactions. The interaction of peptides with griseofulvin enhanced its activity against dermatophytes and reduced the toxicity of the drug, as was also shown in this study.

Two hypotheses can could explain the synergistic action between peptides and NYS. First, peptides target membranes and NYS targets the ergosterol. The interaction between peptides and NYS could result in a coordinated attack on the *Candida* membrane, enhancing the deleterious effect on it. Second, besides targeting the ergosterol in the membrane, NYS also has intracellular targets [24]. Once within the cytoplasm, NYS can attack the vacuole, causing its enlargement and impairing its function. Due to membrane-pore formation, the peptides might facilitate the access of NYS to the cytoplasm. It is known that *Mo*-CBP_3-PepI and *Mo*-CBP_3-PepIII form pores of 6 and 20 kDa, respectively, in *C. albicans* and *C. parapsilosis* membranes [15,16]. NYS has a molecular weight of 926.1 Da, so it is feasible to suggest that NYS passes through the membrane and attacks the cellular vacuole.

The synergistic effect of peptides with ITR, which has a molecular weight of 705 Da, could be explained by its the passage through the membrane by the pores formed in it as a result of the peptides' action. The facilitated passage of ITR through the pores formed by peptides in the membrane enhances its activity of inhibiting the cholesterol biosynthesis pathways, and thus the ergosterol synthesis [25]. One relevant fact is that both *Mo*-CBP_3-PepI and *Mo*-CBP_3-PepIII improved the activity of NYS and ITR by up to 50% regarding the inhibition of biofilm formation of *C. albicans* and *C. parapsilosis*. Moreover, the results showed that *Mo*-CBP_3-PepI enhanced NYS activity up to 60% in degrading the mature biofilms and preformed biofilm of both yeasts. The peptides also enhanced the antifungal activity of NYS and ITR against *C. albicans* and *C. parapsilosis* biofilms.

ITR and NYS can cause undesired effects, such as vomiting, nausea, diarrhea, anorexia, abdominal pain, and dizziness. Besides these side effects, cardiotoxicity and hypertension have been attributed to ITR usage. An unexpected and interesting result was that the association of peptides with antifungal drugs reduced their toxicity to human erythrocytes. For example, NYS alone caused hemolysis of 100% in type-A erythrocytes, while *Mo*-CBP_3-PepI + NYS and *Mo*-CBP_3-PepIII + NYS induced hemolysis of 0 and 45%, respectively, for type A blood. All treatments combining peptides with antifungal drugs were able to reduce the drugs' hemolytic effects.

Molecular docking analysis between peptides and drugs revealed a clue about how peptides reduced these hemolytic effects. The membrane of erythrocytes has neutral phospholipids, which means that any interaction with those membranes must be driven by hydrophobic interactions [24]. It is known that NYS and ITR are hydrophobic drugs [25,26]. Thus, hydrophobic interactions with membranes of erythrocytes may drive the hemolytic activity of NYS and ITR. The molecular docking experiments revealed that peptides had hydrophobic interactions with NYS and ITR, suggesting that the hydrophobic interactions between peptides and both drugs prevented the interaction with the erythrocyte membranes, reducing their hemolytic effect.

4. Materials and Methods

4.1. Ethics Statement

Does not apply to this study.

4.2. Biological and Chemical Materials

C. albicans (ATCC 10231) and *C. parapsilosis* (ATCC 22019) were obtained from the Laboratory of Plant Toxins of the Department of Biochemistry and Molecular Biology of Federal University of Ceará, Brazil. All chemicals were purchased from Sigma-Aldrich Co. (St. Louis, MO, USA).

4.3. Peptide Synthesis

The synthetic peptides *Mo*-CBP_3-PepI (CPIAQRCC) and *Mo*-CBP_3-PepIII (AIQRCC) were chemically synthesized by the company GenOne (São Paulo, Brazil), and the quality and purity (≥95%) were analyzed by reverse-phase high-performance liquid chromatography (RP-HPLC, Jasco, Easton, MD, USA) and mass spectrometry (Waltham, MA, USA).

4.4. Biological Activity

Antibiofilm Assay

The assays against *C. albicans* and *C. parapsilosis* biofilms were performed following the method described by [27–29], with some modifications. To evaluate the inhibition of the biofilm formation, 100 µL of *C. albicans* or *C. parapsilosis* suspension (2.5×10^3 CFU/mL in Sabouraud liquid medium) was incubated in 96-well plates with 100 µL of *Mo*-CBP_3-PepI, *Mo*-CBP_3-PepII or *Mo*-CBP_3-PepIII (50 µg mL^{-1}, as defined by [14–16,23]), at 37 °C for 48 h. The supernatant was removed and the wells were washed three times with sterile 0.15 M NaCl. Next, the cells were fixed with 100 µL of 100% methanol for 15 min at 37 °C and the plates were air-dried under the same conditions. Then, 200 µL of an aqueous solution

of 0.1% crystal violet was added and incubated for 30 min at 24 °C. To remove the excess crystal violet, the plates were washed three times with distilled water and finally 100 µL of 33% acetic acid to solubilize the dye bound in the biofilm. After 15 min, the absorbance was measured at 600 nm using an automated microplate reader (Epoch, Biotek, Santa Clara, CA, USA).

To evaluate the degradation of mature biofilm, the cell suspensions of both yeasts (100 µL, 2.5 × 10^3 CFU/mL in Sabouraud liquid medium) were first incubated at 37 °C for 24 h in 96-well plates. Then, the supernatant was removed, and 100 µL of the Sabouraud liquid medium and 100 µL of each peptide (50 µg mL^{-1}) were added and incubated again for 24 h. The culture medium was again discarded, and the same procedure that used 0.1% crystal violet was employed to quantify the biofilm mass. In both experiments, a solution of 5% DMSO in 0.9% NaCl was used as a negative control. NYS (1000 µg mL^{-1}) and ITR (1000 µg mL^{-1}) were used as positive controls. The synergism assays were carried out by combining the peptides (50 µg mL^{-1}) with NYS or ITR (1000 µg mL^{-1}) and the effectiveness was compared with the activity of the peptides and drugs alone.

4.5. Overproduction of Reactive Oxygen Species (ROS)

The ROS overproduction was determined following the method described by Dias et al. [29], with some modifications. *C. albicans* and *C. parapsilosis* were incubated with the three peptides under the same conditions as described above. Then, 50 µL of cell suspension (2.5 × 10^3 CFU/mL) was incubated with 50 µL of each peptide (50 µg mL^{-1}) for 24 h and the formed biofilm was washed with 0.15 M NaCl three times to remove the Sabouraud liquid medium. Next, 20 µL of 2′,7′ dichlorofluorescein diacetate (DCFH-DA, Sigma, St. Louis, MI, USA) was added and incubated in the dark for 30 min at 24 °C. Finally, the biofilms were washed with 0.15 M NaCl and observed under a fluorescence microscope (Olympus System BX 41, Tokyo, Japan) with an excitation wavelength of 488 nm and emission wavelength of 525 nm.

4.6. Cell Membrane Integrity Assay

The cell membrane integrity of *C. albicans* and *C. parapsilosis* was tested as described by Dias et al. [29], with some modifications. The biofilms were treated as described for ROS overproduction analysis. Thus, 20 µL of propidium iodide (PI, Sigma, St. Louis, MI, USA) was added and incubated in the dark for 30 min at 24 °C. Then the samples were washed three times with 0.15 M NaCl to remove the excess of PI and observed with a fluorescence microscope (Olympus System BX 41, Tokyo, Japan) with an excitation wavelength of 535 nm and emission wavelength of 617 nm.

4.7. Scanning Electron Microscopy (SEM) Analysis

The morphological changes in the cells of *C. albicans* and *C. parapsilosis* were evaluated by SEM (Billerica, MA, USA), using the method described by Staniszewska et al. [30]. Biofilms were fixed with 1% (*v*/*v*) glutaraldehyde in 0.15 M sodium phosphate buffer at pH 7.0 for 16 h. Then the biofilms were washed with 0.15 M sodium phosphate buffer (pH 7.0) three times. Next, 0.2% (*v*/*v*) osmium tetroxide was added to the samples and incubated for 30 min at 37 °C and washed again under the same conditions described above. Samples were successively dehydrated with increased ethanol concentrations (30%, 50%, 70% 100% and 100% [*v*/*v*]) for 10 min each at 24 °C. Last, the final dehydration was realized with 50% hexamethyldisilane (HMDS, Sigma, St. Louis, MI, USA) diluted in ethanol for 10 min and then 100% HDMS. The biofilms were placed on stubs and coated with a 20 nm gold layer using a positron-emission tomography (PET) coating machine (Emitech-Q150TES, Quorum Technologies, Lewes, England). The images were obtained with an FEI inspectTM50 scanning electron microscope, equipped with a low energy detector (Everhart-Thornley), and the acceleration used was 20,000 kV and 20,000× detector magnification.

4.8. Obtainment, File Preparation, and Molecular Docking

The three-dimensional (3D) structures of *Mo*-CBP$_3$-PepI and *Mo*-CBP$_3$-PepIII were predicted using the PepFold server 3 (https://bioserv.rpbs.univ-paris-diderot.fr/services/PEP-FOLD/ accessed on 15 February 2022) [31]. The amino acid protonation of the peptides was adjusted to pH 7.4 using Protein Prepare [32]. NYS (accession number CID 16219709) and ITR (accession number CID 55283) 3D structures were obtained from the database of PubChem (https://pubchem.ncbi.nlm.nih.gov/ accessed on 15 February 2022) [33]. The protonation of the ligands was adjusted using the Marvin Sketch software version 15.6.15. The energy minimization of the peptide hydrogens and the ligand was conducted using Discovery Studio v. 20.1 (https://discover.3ds.com/discovery-studio-visualizer-download accessed on 15 March 2022) and Open Babel version 2.4.0 (https://osdn.net/projects/sfnet_openbabel/downloads/openbabel/2.4.0/OpenBabel-2.4.0.exe/ accessed on 5 March 2022).

Molecular docking assays were carried out using Autodock Vina, version 1.1.2 [34]. Additionally, the Autodock graphical interface version 1.5.6 was used to maintain polar hydrogens and provide charges to peptides and drugs using Kollman united charges [35]. The *Mo*-CBP$_3$-PepI and *Mo*-CBP$_3$-PepIII were considered rigid molecules, and NYS and ITR were docked as flexible molecules. The grid box was defined as a 24 Å × 24 Å × 24 Å cube with the peptides in the center. The exhaustiveness was set to 16, and all other parameters were used as default. The software Discovery Studio v. 20.1 and the 3D interaction representations were realized using the Pymol program (https://pymol.org/2/ accessed on 8 March 2022).

4.9. Hemolytic Assay

The hemolytic activities of *Mo*-CBP$_3$-PepI, *Mo*-CBP$_3$-PepIII, NYS, and ITR, alone and in their different combinations, were assessed using A, B, and O types of human erythrocytes as described by Souza et al. [14]. The concentrations of all solutions were the same as used in the synergism assays. The blood types were provided by the Hematology and Hemotherapy Center of Ceará (Fortaleza, Brazil).

The blood was collected in a tube with heparin (5 IU mL^{-1}, Sigma Aldrich, São Paulo, Brazil), centrifuged at 300× *g* for 5 min at 4 °C, washed with sterile 0.15 M NaCl, and diluted to a concentration of 2.5%. Each blood type was incubated (100 µL) with solutions of Mo-CBP3-PepI, Mo-CBP3-PepIII (50 µg mL^{-1}), NYS (1000 µg mL^{-1}), or ITR (1000 µg mL^{-1}) for 30 min at 37 °C, followed by centrifugation (300× *g* for 5 min at 4 °C, centrifuge Eppendorf 5810, Hannover, Germany). Supernatants were collected and transferred to 96-well microtiter plates and the hemolysis (%) was calculated by reading the absorbance at 414 nm using an automated absorbance microplate reader using DMSO-NaCl solution (0%) and 0.1% Triton X-100 (100%) as negative and positive controls for hemolysis, respectively. The hemolysis was calculated by the equation: [(Abs$_{414nm}$ of sample treated with peptides or drugs-Abs$_{414nm}$ of samples treated with DMSO-NaCl)/[(Abs$_{414nm}$ of samples treated with 0.1% TritonX-100-Abs$_{414nm}$ of samples treated with DMSO-NaCl] × 100.

4.10. Statistical Analysis

All the assays were performed individually three times and the values are expressed as the mean ± standard error. The data were submitted to ANOVA followed by the Tukey test. GraphPad Prism version 5.01 (GraphPad Software company, Santa Clara, CA, USA) was used to generate all graphics, with a significance of $p < 0.05$.

5. Conclusions

The antibiofilm activity, absence of toxicity, and synergistic effect enhancing the activity of NYS and ITR, strongly indicated that *Mo*-CBP$_3$-PepI and *Mo*-CBP$_3$-PepIII are promising antibiofilm peptides which could act as new antimicrobial agents. We also highlight their use for clinical application or adjuvants to conventional drugs to overcome resistance developed by *Candida* species.

Author Contributions: All authors made substantial contributions. The conception and design of the study and acquisition of data, analysis, docking analysis, and interpretation were performed by L.P.B., C.D.T.F., A.F.B.S., N.A.S.N., J.L.A., A.L.C.P., J.T.A.O. and P.F.N.S. Microscopic analyses were carried out by R.G.G.S. and A.F.B.S. Writing or revising the article was done by L.P.B., A.L.C.P., G.H.G., F.P.M. and P.F.N.S. P.F.N.S. gave final approval of the version to be submitted. All authors have read and agreed to the published version of the manuscript.

Funding: This work was supported by grants from the following Brazilian agencies: Conselho Nacional de Desenvolvimento Científico e Tecnológico (CNPq) (process numbers 308107/2013-6 and 306202/2017-4); Coordenação de Aperfeiçoamento de Pessoal de Nível Superior (CAPES); Instituto Nacional de Ciências e Tecnologia de Bioinspiração (Process Number: 465507/2014-0) and Fundação Cearense de Apoio ao Desenvolvimento Científico e Tecnológico (FUNCAP). CAPES provided the postdoctoral grant to Pedro F. N. Souza (grant number 88887.318820/2019-00). We are also grateful to the staff of the central analytical facilities of UFC, Brazil.

Institutional Review Board Statement: Not applicable.

Informed Consent Statement: Not applicable.

Data Availability Statement: The data that support the findings of this study are available on request from the corresponding author.

Acknowledgments: Special thanks to CAPES for providing the postdoctoral grant to Pedro F. N. Souza. We are also grateful to the staff of the central analytical facilities of UFC, Brazil.

Conflicts of Interest: The authors report no conflict of interest. The authors alone are responsible for the content and the writing of the paper.

References

1. Lima, P.G.; Oliveira, J.T.A.; Amaral, J.L.; Freitas, C.D.T.; Souza, P.F.N. Synthetic antimicrobial peptides: Characteristics, design, and potential as alternative molecules to overcome microbial resistance. *Life Sci.* **2021**, *278*, 119647–119660. [CrossRef] [PubMed]
2. Kumar, A.; Alam, A.; Rani, M.; Ehtesham, N.Z.; Hasnain, S.E. Biofilms: Survival and defense strategy for pathogens. *Int. J. Med. Microbiol.* **2017**, *307*, 481–489. [CrossRef] [PubMed]
3. Kovács, R.; Majoros, L. Fungal quorum-sensing molecules: A review of their antifungal effect against *Candida* biofilms. *J. Fungi* **2020**, *6*, 99. [CrossRef] [PubMed]
4. Zarnowski, R.; Westler, W.M.; Lacmbouh, G.A.; Marita, J.M.; Bothe, J.R.; Bernhardt, J.; Lounes-Hadj Sahraoui, A.; Fontaine, J.; Sanchez, H.; Hatfield, R.D.; et al. Novel entries in a fungal biofilm matrix encyclopedia. *MBio* **2014**, *5*, e01333-14. [CrossRef]
5. Fox, E.P.; Nobile, C.J. A sticky situation. *Transcription* **2012**, *3*, 315–322. [CrossRef] [PubMed]
6. Kullberg, B.J.; Oude Lashof, A.M.L. Epidemiology of opportunistic invasive mycoses. *Eur. J. Med. Res.* **2002**, *7*, 183–191. [PubMed]
7. Weig, M. Clinical aspects and pathogenesis of *Candida* Infection. *Trends Microbiol.* **1998**, *6*, 468–470. [CrossRef]
8. Baillie, G.S. Matrix polymers of *Candida* biofilms and their possible role in biofilm resistance to antifungal agents. *J. Antimicrob. Chemother.* **2000**, *46*, 397–403. [CrossRef]
9. Sasso, M.; Roger, C.; Sasso, M.; Poujol, H.; Barbar, S.; Lefrant, J.-Y.; Lachaud, L. Changes in the distribution of colonising and infecting *Candida* Spp. isolates, antifungal drug consumption and susceptibility in a french intensive care unit: A 10-year study. *Mycoses* **2017**, *60*, 770–780. [CrossRef]
10. LaFleur, M.D.; Kumamoto, C.A.; Lewis, K. *Candida albicans* biofilms produce antifungal-tolerant persister cells. *Antimicrob. Agents Chemother.* **2006**, *50*, 3839–3846. [CrossRef]
11. Ramage, G. Investigation of multidrug efflux pumps in relation to fluconazole resistance in *Candida albicans* biofilms. *J. Antimicrob. Chemother.* **2002**, *49*, 973–980. [CrossRef] [PubMed]
12. Arendrup, M.C.; Patterson, T.F. Multidrug-resistant *Candida*: Epidemiology, molecular mechanisms, and treatment. *J. Infect. Dis.* **2017**, *216*, S445–S451. [CrossRef] [PubMed]
13. Katiyar, S.; Pfaller, M.; Edlind, T. *Candida albicans* and *Candida glabrata* clinical isolates exhibiting reduced echinocandin susceptibility. *Antimicrob. Agents Chemother.* **2006**, *50*, 2892–2894. [CrossRef] [PubMed]
14. Souza, P.F.N.; Marques, L.S.M.; Oliveira, J.T.A.; Lima, P.G.; Dias, L.P.; Neto, N.A.S.; Lopes, F.E.S.; Sousa, J.S.; Silva, A.F.B.; Caneiro, R.F.; et al. Synthetic antimicrobial peptides: From choice of the best sequences to action mechanisms. *Biochimie* **2020**, *175*, 132–145. [CrossRef]
15. Lima, P.G.; Souza, P.F.N.; Freitas, C.D.T.; Oliveira, J.T.A.; Dias, L.P.; Neto, J.X.S.; Vasconcelos, I.M.; Lopes, J.L.S.; Sousa, D.O.B. Anticandidal activity of synthetic peptides: Mechanism of action revealed by scanning electron and fluorescence microscopies and synergism effect with nystatin. *J. Pept. Sci.* **2020**, *26*, e3249. [CrossRef]
16. Oliveira, J.T.A.; Souza, P.F.N.; Vasconcelos, I.M.; Dias, L.P.; Martins, T.F.; Van Tilburg, M.F.; Guedes, M.I.F.; Sousa, D.O.B. *Mo*-CBP_3-PepI, *Mo*-CBP_3-PepII, and *Mo*-CBP_3-PepIII are synthetic antimicrobial peptides active against human pathogens by stimulating ROS generation and increasing plasma membrane permeability. *Biochimie* **2019**, *157*, 10–21. [CrossRef]

17. Mason, A.J.; Moussaoui, W.; Abdelrahman, T.; Boukhari, A.; Bertani, P.; Marquette, A.; Shooshtarizaheh, P.; Moulay, G.; Boehm, N.; Guerold, B. Structural determinants of antimicrobial and antiplasmodial activity and selectivity in histidine-rich amphipathic cationic peptides. *J. Biol. Chem.* **2009**, *284*, 119–133. [CrossRef]
18. Mason, A.J.; Gasnier, C.; Kichler, A.; Prévost, G.; Aunis, D.; Metz-Boutigue, M.H.; Bechinger, B. Enhanced membrane disruption and antibiotic action against pathogenic bacteria by designed histidine-rich peptides at acidic PH. *Antimicrob. Agents Chemother.* **2006**, *50*, 3305–3311. [CrossRef]
19. Galdiero, E.; de Alteriis, E.; De Natale, A.; D'Alterio, A.; Siciliano, A.; Guida, M.; Lombardi, L.; Falanga, A.; Galdiero, S. Eradication of *Candida albicans* persister cell biofilm by the membranotropic peptide GH625. *Sci. Rep.* **2020**, *10*, 5780–5791. [CrossRef]
20. Belmadani, A.; Semlali, A.; Rouabhia, M. Dermaseptin-S1 decreases *Candida albicans* growth, biofilm formation and the expression of hyphal wall protein 1 and aspartic protease genes. *J. Appl. Microbiol.* **2018**, *125*, 72–83. [CrossRef]
21. Sierra, J.M.; Fusté, E.; Rabanal, F.; Vinuesa, T.; Viñas, M. An overview of antimicrobial peptides and the latest advances in their development. *Expert Opin. Biol. Ther.* **2017**, *17*, 663–676. [CrossRef] [PubMed]
22. Seyedjavadi, S.S.; Khani, S.; Eslamifar, A.; Ajdary, S.; Goudarzi, M.; Halabian, R.; Akbari, R.; Zare-Zardini, H.; Imani Fooladi, A.A.; Amani, J.; et al. The antifungal peptide MCh-AMP1 derived from *Matricaria chamomilla* inhibits *Candida albicans* growth via inducing ROS generation and altering fungal cell membrane permeability. *Front. Microbiol.* **2020**, *10*, 3150. [CrossRef] [PubMed]
23. Souza, P.F.N.; Lima, P.G.; Freitas, C.D.T.; Sousa, D.O.B.; Neto, N.A.S.; Dias, L.P.; Vasconcelos, I.M.; Freitas, L.B.N.; Silva, R.G.G.; Sousa, J.S.; et al. Antidermatophytic activity of synthetic peptides: Action mechanisms and clinical application as adjuvants to enhance the activity and decrease the toxicity of griseofulvin. *Mycoses* **2020**, *63*, 979–992. [CrossRef] [PubMed]
24. Bhuiyan, M.S.A.; Ito, Y.; Nakamura, A.; Tanaka, N.; Fujita, K.; Fukui, H.; Takegawa, K. Nystatin effects on vacuolar function in *Saccharomyce. Biosci. Biotechnol. Biochem.* **1999**, *63*, 1075–1082. [CrossRef] [PubMed]
25. Borgers, M.; Van de Ven, M.-A. Mode of action of itraconazole: Morphological aspects. *Mycoses* **1989**, *32* (Suppl. 1), 53–59. [CrossRef] [PubMed]
26. Huang, Y.; Huang, J.; Chen, Y. Alpha-helical cationic antimicrobial peptides: Relationships of structure and function. *Protein Cell* **2010**, *1*, 143–152. [CrossRef]
27. Benavent, C.; García-Herrero, V.; Torrado, C.; Torrado-Santiago, S. Nystatin antifungal micellar systems on endotracheal tubes: Development, characterization and in vitro evaluation. *Pharmazie* **2019**, *74*, 34–38. [CrossRef]
28. Lang, B.; Liu, S.; McGinity, J.W.; Williams, R.O. Effect of hydrophilic additives on the dissolution and pharmacokinetic properties of itraconazole-enteric polymer hot-melt extruded amorphous solid dispersions. *Drug Dev. Ind. Pharm.* **2016**, *42*, 429–445. [CrossRef]
29. Dias, L.P.; Souza, P.F.N.; Oliveira, J.T.A.; Vasconcelos, I.M.; Araújo, N.M.S.; Tilburg, M.F.V.; Guedes, M.I.F.; Carneiro, R.F.; Lopes, J.L.S.; Sousa, D.O.B. RcAlb-PepII, a synthetic small peptide bioinspired in the 2S albumin from the seed cake of *Ricinus communis*, is a potent antimicrobial agent against *Klebsiella pneumoniae* and *Candida parapsilosis*. *Biochim. Biophys. Acta-Biomembr.* **2020**, *1862*, 183092–183102. [CrossRef]
30. Staniszewska, M.; Bondaryk, M.; Swoboda-Kopec, E.; Siennicka, K.; Sygitowicz, G.; Kurzatkowski, W. *Candida albicans* morphologies revealed by scanning electron microscopy analysis. *Braz. J. Microbiol.* **2013**, *44*, 813–821. [CrossRef]
31. Lamiable, A.; Thévenet, P.; Rey, J.; Vavrusa, M.; Derreumaux, P.; Tufféry, P. PEP-FOLD3: Faster de novo structure prediction for linear peptides in solution and in complex. *Nucleic Acids Res.* **2016**, *44*, W449–W454. [CrossRef] [PubMed]
32. Martínez-Rosell, G.; Giorgino, T.; De Fabritiis, G. PlayMolecule ProteinPrepare: A web application for protein preparation for molecular dynamics simulations. *J. Chem. Inf. Model.* **2017**, *57*, 1511–1516. [CrossRef] [PubMed]
33. Kim, S.; Chen, J.; Cheng, T.; Gindulyte, A.; He, J.; He, S.; Li, Q.; Shoemaker, B.A.; Thiessen, P.A.; Yu, B.; et al. PubChem 2019 update: Improved access to chemical data. *Nucleic Acids Res.* **2019**, *47*, D1102–D1109. [CrossRef]
34. Trott, O.; Olson, A.J. AutoDock Vina: Improving the speed and accuracy of docking with a new scoring function, efficient optimization, and multithreading. *J. Comput. Chem.* **2009**, *31*, 455–461. [CrossRef]
35. Morris, G.M.; Huey, R.; Lindstrom, W.; Sanner, M.F.; Belew, R.K.; Goodsell, D.S.; Olson, A.J. AutoDock4 and autodocktools4: Automated docking with selective receptor flexibility. *J. Comput. Chem.* **2009**, *30*, 2785–2791. [CrossRef] [PubMed]

APÊNDICE F - A MOLECULAR DOCKING STUDY REVEALED THAT SYNTHETIC PEPTIDES INDUCED CONFORMATIONAL CHANGES IN THE STRUCTURE OF SARS-COV-2 SPIKE GLYCOPROTEIN, DISRUPTING THE INTERACTION WITH HUMAN ACE2 RECEPTOR

International Journal of Biological Macromolecules 164 (2020) 66–76

Contents lists available at ScienceDirect

International Journal of Biological Macromolecules

journal homepage: http://www.elsevier.com/locate/ijbiomac

A molecular docking study revealed that synthetic peptides induced conformational changes in the structure of SARS-CoV-2 spike glycoprotein, disrupting the interaction with human ACE2 receptor

Pedro F.N. Souza *, Francisco E.S. Lopes, Jackson L. Amaral, Cleverson D.T. Freitas, Jose T.A. Oliveira

Department of Biochemistry and Molecular Biology, Federal University of Ceará, Fortaleza, Ceará CEP 60.440-554, Brazil

ARTICLE INFO

Article history:
Received 2 June 2020
Received in revised form 14 July 2020
Accepted 14 July 2020
Available online 18 July 2020

Keywords:
SARS-CoV-2
COVID-19
Synthetic peptides
Molecular docking
ACE2 receptor

ABSTRACT

The global outbreak of COVID-19 (Coronavirus Disease 2019) caused by SARS-CoV-2 (Severe Acute Respiratory Syndrome caused by Coronavirus 2) began in December 2019. Its closest relative, SARS-CoV-1, has a slightly mutated Spike (S) protein, which interacts with ACE2 receptor in human cells to start the infection. So far, there are no vaccines or drugs to treat COVID-19. So, research groups worldwide are seeking new molecules targeting the S protein to prevent infection by SARS-CoV-2 and COVID-19 establishment. We performed molecular docking analysis of eight synthetic peptides against SARS-CoV-2 S protein. All interacted with the protein, but *Mo*-CBP_3-PepII and PepKAA had the highest affinity with it. By binding to the S protein, both peptides led to conformational alterations in the protein, resulting in incorrect interaction with ACE2. Therefore, given the importance of the S protein-ACE2 interaction for SARS-CoV-2 infection, synthetic peptides could block SARS-CoV-2 infection. Moreover, unlike other antiviral drugs, peptides have no toxicity to human cells. Thus, these peptides are potential molecules to be tested against SARS-CoV-2 and to develop new drugs to treat COVID-19.

© 2020 Elsevier B.V. All rights reserved.

1. Introduction

Coronaviruses (CoV) are a group of non-segmented positive single-stranded RNA, with size up to 32 kb, belonging to the Coronaviridae family and Nidovirales order [1,2]. Seventeen coronaviruses can infect humans. Typically, this infection presents slight symptoms, like a common cold. However, among them, three cause the same symptoms but with higher intensity and are also responsible for atypically severe pneumonia complications, which increases their mortality compared to other viruses [1–5].

In the last two decades, three CoV outbreaks have spread widely, becoming world pandemics. The first began in the winter of 2002 in China, where viral pneumonia caused by CoVs resulted in severe acute respiratory syndrome coronavirus (SARS-CoV-1), officially infecting 8906 people in 26 countries and leading to 774 deaths [6,7]. The second was 2012 in Saudi Arabia, called Middle East respiratory syndrome coronavirus (MERS-CoV), which led to death of 37% of infected patients. MERS-CoV spread to 27 countries, infecting 2254 people and causing 800 deaths worldwide [6,8].

The third outbreak is ongoing, a pandemic situation that started in December 2019 in China. Patients developed new severe pneumonia (COVID-19) caused by SARS-CoV-2.COVID-19. The disease spread rapidly to 210 countries, at this writing infecting almost 5 million people and causing around 362 thousand deaths [9,10], figures that are rising steeply. The origin of SARS-CoV-2 is obscure. Although there are similarities between SARS-CoV-2 and bat SARS-CoV-like coronaviruses, the progenitor is hard identify [3,11,12].

Genome sequence data has revealed at least 70% similarity between SARS-CoV-1 and SARS-CoV-2 [3,12–14]. Both coronaviruses share the same entry path in human cells, but with particularities. SARS-CoV-1 and SARS-CoV-2 possess a membrane-bound trimeric spike (S) protein, which has a receptor-binding domain (RBD) able to interact with Angiotensin I Converting Enzyme 2 (ACE2) receptor in human cells [7,15]. Despite the similarities, the S protein from SARS-CoV-2 has modifications in the RBD sequence that enhance the affinity with ACE2 of humans. Indeed, the SARS-CoV-2 S protein has a 20-fold higher affinity with human ACE2 than the S protein from SARS-CoV-1, leading to faster spread from human to human [3,7,13–15].

As yet there are no drugs for clinical treatment or vaccines to prevent human infection by SARS-CoV-2. Drug repositioning seems to be a faster method to find an effective medicine to treat clinical symptoms of COVID-19 [16]. However, in this chaotic scenario, computational screening and molecular docking (MD) are promising alternatives to find a new or existing drug to treat symptoms of COVID-19. In all those MD analyses, a common target has been tested, the SARS-CoV-2 S protein, because it is essential to the entry in cells to start the infection process [17–21].

* Corresponding author at: Biochemistry and Molecular Biology Department, Federal University of Ceará, Laboratory of Plant Defense Proteins, Av. Mister Hull, P.O. Box: 60451, Fortaleza, CE, Brazil.
E-mail address: pedrofilhobio@gmail.com (P.F.N. Souza).

https://doi.org/10.1016/j.ijbiomac.2020.07.174
0141-8130/© 2020 Elsevier B.V. All rights reserved.

Here we report a MD study using eight antimicrobial peptides (*Mo*-CBP_3-PepI, *Mo*-CBP_3-PepII, *Mo*-CBP_3-PepIII [22,23], *RcAlb*-PepI, *RcAlb*-PepII, *RcAlb*-PepIII [24], PepGAT and PepKAA [25] (unpublished data)) that target the SARS-CoV-2 S protein. With different affinities, all peptides interact with the RBD from the SARS-CoV-2 S protein. By interacting with SARS-CoV-2 S protein, peptides change its native conformation, inducing incorrect interaction with the ACE2 receptor and thus blocking the entry of SARS-CoV-2 into the cell. The MD results suggest peptides as potential alternative molecules to be used against SARS-CoV-2. To the best of our knowledge, this is the first study to employ synthetic peptides as drugs to target spike protein from SARS-CoV-2.

2. Methodology

2.1. Three-dimensional (3D) structures

The 3D structures of *Mo*-CBP_3-PepI, *Mo*-CBP_3-PepII, and *Mo*-CBP_3-PepIII were the same reported by Oliveira et al. [22]. The 3D structures of *Rc*Alb-PepI, *Rc*Alb-PepII, *Rc*Alb-PepIII were the same as employed by Dias et al. [24]. The 3D structures of PepGAT and PepKAA were the same as employed by Souza et al. [25]. The 3D structure files of SARS-CoV-2 Spike protein (open state, PDB: 6VYB; closed state, PDB: 6VXX) and human ACE2 (ACE2; PDB: 1R42) were downloaded from Protein Data Bank (PDB, https://www.rcsb.org/).

2.2. Bioinformatic analyses of antiviral potential of synthetic peptides

Bioinformatics was employed to evaluate whether the peptides presented any antiviral potential. We used the free server iAMPPred (http://cabgrid.res.in:8080/amppred/).

2.3. Molecular docking (MD) assays

Blind molecular docking assays were carried out in two systems. First, the molecular docking experiments involved synthetic peptides (ligands) against SARS-CoV-2 spike glycoprotein in the open state (6VYB) and closed state (6VXX). Second, SARS-CoV-2 spike-peptide complexes were tested by molecular docking against the ACE2 human receptor. All molecular docking experiments were performed using the ClusPro 2.0 server (https://cluspro.org), which is the best performing server currently available for the CAPRI challenge [26]. It is also used for the study of inhibitor-enzyme, peptide-protein, and inhibitor-protein complexes, additionally allowing the analysis and choice of the most appropriate scoring scheme for the complex in this study [27–29].

The GPU option was selected because it uses more specific computer graphic units of the Massachusetts Green High-Performance Computing Center (MGHPC). The choice of models was standardized and followed the criteria use of the same scoring scheme (Balanced) and balance between the number of members and lowest binding energy. The balanced scoring scheme has the best weight coefficients for the energy used in the structures. The best complexes generated by molecular docking studies were analyzed in terms of interface energy and interaction between surface residues, and for models with a high number of members. The first 12 models of the balanced energy parameter were used for the analysis of waste and interface energy, and models with less than 20 anchored structures were excluded from the analysis. The models were also selected from the analysis of the PIPER energy in the center of the cluster, that is, the structure that has the largest number of neighboring structures in the center of the cluster, as well as from the analysis of the structure that had the lowest energy of the cluster.

2.4. Minimization and equilibration by molecular dynamics simulation

To reach a higher stabilized state, the six systems of interest (S protein closed:: ACE2; S protein open::ACE2; S protein closed::*Mo*-CBP_3-PepII::ACE2; S protein open::*Mo*-CBP_3-PepII::ACE2; S protein closed::PepKAA:: ACE2; and S protein open::PepKAA:: ACE2) were minimized and equilibrated using Gromacs version 2018.4 [30]. Initially, the topology was recorded using the OPLS-AA/L all-atom force field [31,32], after a cubic box was created with 2 nm from the box edge. The box solvation was done with the SPC/E water model. The systems were neutralized and Na^+ and Cl^- ions were added at a concentration of 0.15 M. The minimization was carried out until reaching negative potential energy and maximum force under 1000 kJ mol^{-1} nm^{-1}. Finally, the equilibration of temperature and pressure was performed for 100 ps.

2.5. Analysis of the complexes interface

The database for structural analysis of 3D structures PDBdum (EMBL - EBI; http://www.ebi.ac.uk/pdbsum) was used to analyze the general content of the interface region resulting from the molecular docking tests. The Ligplot software was used to generate the 2D figures with the hydrogen bonds and the hydrophobic interactions, and the Pymol software was used to generate the figures with 3D structures [28]. The Pymol software, in addition to being used to visualize the molecular structure of models, was also used to identify molecular interactions between complexes, identify polar and non-polar interactions, and perform the alignment of structures. PyMol was also used to calculate RMSD and generate the score for the overlapping of structures.

2.6. Refinement and validation of structures

The complex structures generated by the molecular docking tests were refined by the Galaxy Refine Complex, a tool belonging to the molecular interaction server GalaxyWEB. All 3D structures were validated for steric impediment by the MolProbity and PROCHECK servers.

3. Results

3.1. Antiviral potential of synthetic peptides

Before molecular docking analyses, the peptides were analyzed in an antiviral sever to evaluate whether or not they had antiviral potential. We only considered peptides that were at least 70% antiviral to be promising. Among all peptides tested, only four that criterion: *Mo*-CBP_3-PepI, *Mo*-CBP_3-PepII, *RcAlb*-PepIII, and PepKAA, respectively with 70, 85, 84, 74% being antiviral (Supplementary Table 1).

3.2. Interaction of SARS-Cov-2 spike glycoprotein with human ACE2 receptor

The subunits and domains of spike protein are represented in Fig. 1, in which their two conformational states are also observed: the closed state (Fig. 1A) and the open state (Fig. 1B). As expected, in the open state (Fig. 1B) the receptor-binding domain (RBD) responsible for interacting with the human ACE2 receptor was positioned outside the structure, favoring interaction with ACE2 (Fig. 1B). Additionally, it the S1 and S2 domains of spike protein, which are respectively responsible for the S1 domain's interaction with human ACE2 and viral and cell membrane fusion before entrance (Fig. 1A and B) [7]. The results of blind molecular docking assays performed by Cluspro 2.0 revealed that in both closed (Fig. 1C) and open (Fig. 1D) state, the spike protein can interact with ACE2. Fig. 1D insert is a zoom view of the interaction between spike protein and ACE2 receptor.

The interface region of the spike protein in the open state with ACE2 had the lowest energy among all the models generated, with the lowest binding energy (LBE), −1032.0 kJ·mol^{-1}. Thus it was used as a control for the analysis of the interaction between peptides and spike protein. In the closed state, spike protein binds to a different region of ACE2 with an LBE of −899.0 kJ·mol^{-1} and interaction with 33 members. This model correlates with the literature data for the ACE2 region (31–41 interaction with spike protein; Uniprot: Q9BYF1 [33]), demonstrating the

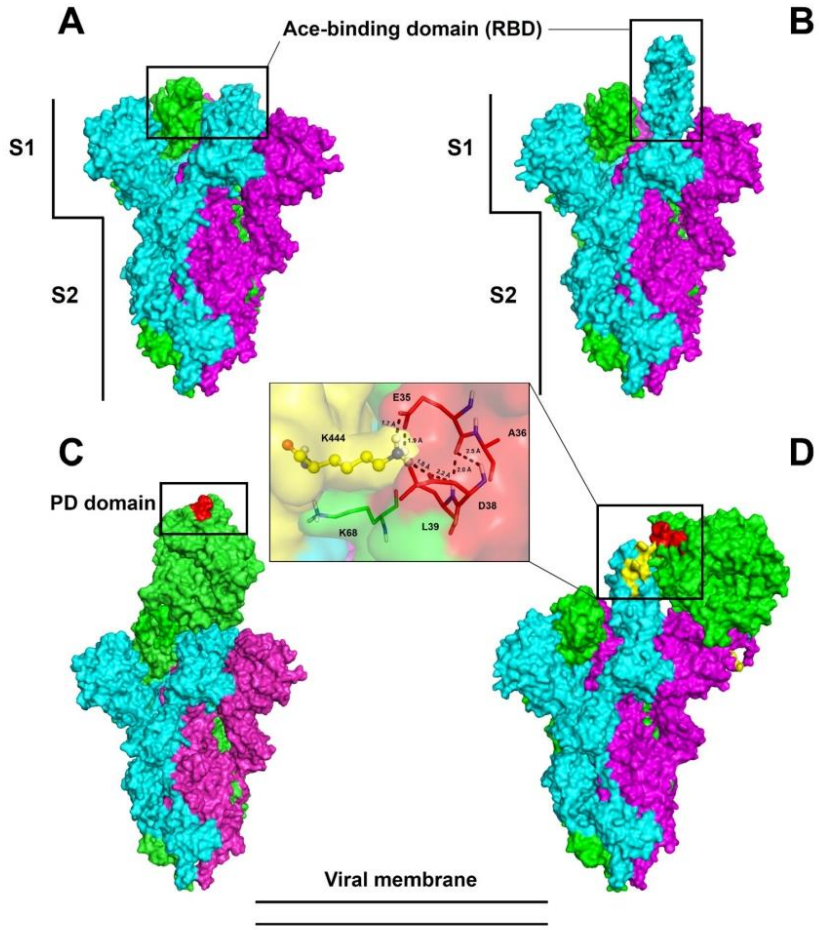

Fig. 1. Trimeric structure of SARS-CoV-2 spike glycoprotein. The conformational states closed (A) and partially open (B) define the effectiveness of the connection to ACE2. The regions indicated by rectangles correspond to the RBD domains of the glycoprotein spike (A, B) and the PD domain (C, D) of ACE2. The vertical bars define the S1 and S2 subunits that are essential for initial SARS-CoV-2 infection. The enlarged area shows some interaction amino acids according to the crystals in the literature. The trimer chains are highlighted by the colors cyan, magenta, and green.

importance of open conformational state for binding with ACE2 and onset of infection (Fig. 1C).

These results confirm the predictions identified by [33], who suggested that spike protein must be in the open conformation to interact with the PD domain of ACE2 on the cell surface. The spike glycoprotein must expose the RBD domain for the interaction to occur, because in the closed conformational state, the ACE2 recognition motifs (RBDs) are buried at the interface between the proteins.

3.3. Molecular docking of SARS-Cov-2 S protein with peptides

The molecular docking experiments were performed using the eight peptides against spike protein in both open (Fig. 2) and closed (Fig. 3) states. MD assays with the open state of spike protein showed that *Mo*-CBP$_3$-PepI, *Mo*-CBP$_3$-PepII, *Mo*-CBP$_3$-PepIII, *RcAlb*-PepI, *RcAlb*-PepII and PepGAT interact with the S1 domain (Fig. 2A–E, G). In contrast, RcAlb-PepIII and PepKAA interacted with the S2 domain (Fig. 2F and H). Similar results were found out during the MD assays with peptides against the closed state of spike protein (Fig. 3). Only one difference was observed: in this model, *RcAlb*-PepIII interacted with the S1 domain of the spike protein instead of S2 as in the open state (Fig. 3G).

The number of hydrogen bonds and hydrophobic interactions of the peptides and spike protein suggests their strong interaction, in both open (Table 1) and closed (Table 2) states. Our results revealed distinct behaviors of peptides when in contact with spike protein. Among the peptides that interacted with the S1 domain, *Mo*-CBP$_3$-PepII presented the lowest binding energy, of −814.4 kJ·mol^{-1} (Table 1), and the highest number of interactions (185), of which 170 were hydrophobic interactions and 15 were hydrogen bonds in the open state, and 173 were hydrophobic interactions and 12 were hydrogen bonds in the closed state (Tables 1 and 2).

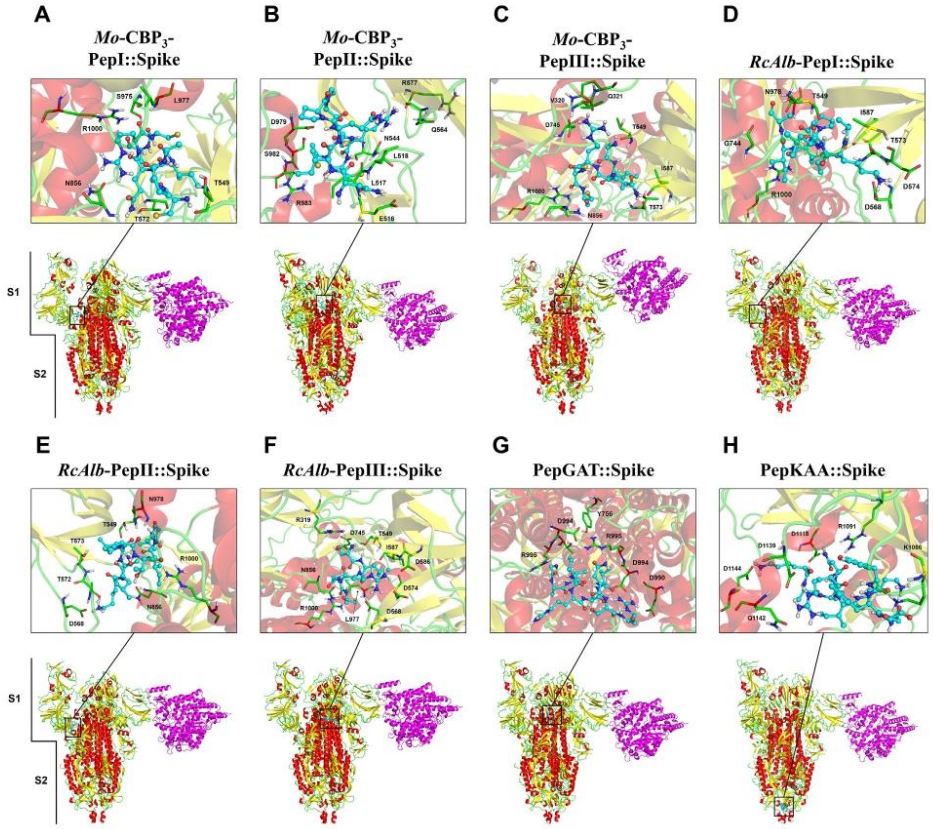

Fig. 2. 3D structures of the spike glycoprotein in the open state complexed with synthetic peptides and ACE2. The representation shows the viral protein in the partially open state. The RBD and PD domains of ACE2 (magenta) are altered due to the interaction between spike glycoprotein and the peptides. The connection to ACE2 does not occur between the RBD and PD domains. In the S protein, colors are defined by SS: alpha-helix in red, beta-sheets in yellow, and loops in green.

3.4. Stable and balanced structures

All structures were minimized with potential energy of about -2.5×10^{-7} after 5500 energy minimization steps and maximum force of less than 1000 kJ mol^{-1} nm^{-1} (Fig. 4A). The minimized structures occurred at the equilibrium of temperature. From 5 to 100 ps, the temperature of all complexes was balanced at 300 K, with small variations (Fig. 4B). Finally, with variable pressure and density it was possible to observe equilibrium after 5 ps and continuing stability until 100 ps. The pressure and density equilibrium were achieved at about 0 bar and 1015 kg m^{-3}, respectively (Fig. 4C and D). The final stable complexes were used in the subsequent analyses.

3.5. Interaction of SARS-Cov-2 S protein with peptides

Mo-CBP_3-PepII interacted with the α-helices spike S1 domain (Fig. 5A). This interaction is mainly supported by hydrogen bonds formed by Asn^1, Gln^3, Pro^4, and Arg^7 from *Mo*-CBP_3-PepII, respectively with Glu^{516}, Asp^{40}, Arg^{567}, Gln^{564}, from the S1 domain of the S protein (Fig. 5B). Moreover, other interactions were also crucial for this interaction, as revealed by Ligplot analyses, such as hydrogen bonds Asn^1, Cys^6, Arg^7, and Cys^8, from *Mo*-CBP_3-PepII with, respectively, Leu^{517}, Leu^{518}, Asp^{979}, Arg^{577}, Asn^{544}, Cys^{391} (Fig. 5C) from the S protein. Several hydrophobic interactions were observed in the residues with spoked red arcs.

Regarding peptides that interacted with the S2 domain close to the transmembrane region of the spike protein (Fig. 6A), PepKAA was the best, with 171 interactions, including 10 hydrogen bonds and 161 hydrophobic interactions and an LBE value of -674.9 kJ·mol^{-1} in the open state (Table 1). The hydrogen bond interactions that support this were Lys^1, Asn^4, Arg^5, and Lys^7 from PepKAA, respectively, with Glu^{1144}, Asp^{1139}, Asp^{1118}, and Lys^{1086} S2 domain of the S protein (Fig. 6B). Moreover, Ligplot analyses revealed several hydrophobic interactions with all PepKAA, represented by residues in spoked red arcs (Fig. 6C).

3.6. Peptide-induced conformational changes in SARS-Cov-2 spike

Unfortunately, *Mo*-CBP_3-PepII did not bind to the RBD domain of the spike protein in the S1 subunit. However, a meticulous analysis revealed an interesting point. The analysis of conformational alignment and overlapping of S protein structures, before and after interaction with *Mo*-CBP_3-PepII, revealed that by interacting with the S1 subunit, *Mo*-CBP_3-PepII induced a change in the conformational state of the S protein

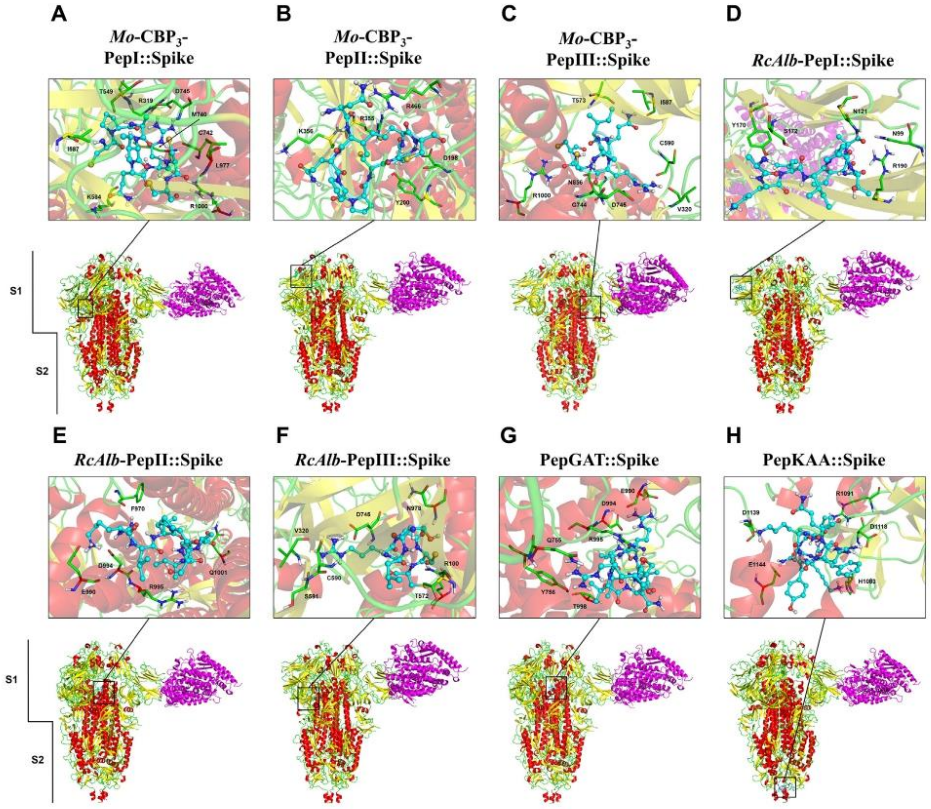

Fig. 3. 3D structures of the spike glycoprotein in the closed state complexed with synthetic peptides and ACE2. The representation shows the viral protein in the partially closed state. The RBD and PD domains of ACE2 (magenta) are altered due to the interaction between spike glycoprotein and the peptides. The connection to ACE2 does not occur between the RBD and PD domains. In the S protein, colors are defined by SS: alpha-helix in red, beta-sheets in yellow, and loops in green.

Table 1
Molecular interaction docking between synthetic peptides and SARS-CoV-2 spike protein in the open state. The molecular docking assay was performed using the *ClusPro server 2.0* and structural analysis was performed by using the *Pymol* program.

Complexes	Lowest binding energy[a]	Hydrogen bonds[b]	Number of hydrophobic interactions[c]
SARS-CoV2 spike protein/*Mo*-CBP_3-PepI	−658.0	THR_{549} (CYS_1); ARG_{567} (CYS_8); THR_{572} (GLN_5); TYR_{741} (ARG_6); ASN_{856} (GLN_5, ARG_6); SER_{975} (CYS_7); LEU_{977} (ARG_6)	111
SARS-CoV2 spike protein/*Mo*-CBP_3-PepII	−814.4	CYS_{391} (CYS_8); GLU_{516} (ASN_1); LEU_{517} (CYS_6, ASN_1); ASN_{544} (ARG_7); GLN_{564} (ARG_7); ARG_{567} (PRO_4, GLN_3); ARG_{577} (ARG_7); ASP_{979} (CYS_6); SER_{982} (CYS_9); ARG_{983} (CYS_9).	170
SARS-CoV2 spike protein/*Mo*-CBP_3-PepIII	−700.8	ASP_{745} (ARG_4); SER_{975} (CYS_6); ARG_{1000} (CYS_5, CYS_6); THR_{549} (ARG_4); THR_{573} (GLN_3); ILE_{587} (GLN_3); CYS_{590} (ARG_4)	134
SARS-CoV2 spike protein/*RcAlb*-PepI	−649.8	ASP_{568} (LYS_2); THR_{573} (ALA_1); ASP_{574} (LYS_2); LEU_{977} (PRO_5); ASN_{978} (ALA_8); ARG_{1000} (THR_6)	116
SARS-CoV2 spike protein/*RcAlb*-PepII	−744.8	THE_{549} (ALA_1); GLY_{744} (ALA_8); ASN_{856} (LEU_3); ASN_{978} (PRO_5); ARG_{1000} (THR_6).	143
SARS-CoV2 spike protein/*RcAlb*-PepIII	−703.0	ASP_{745} (SER_1); ASN_{856} (GLY_4); SER_{975} (CYS_6); ARG_{1000} (CYS_5); THR_{549} (LEU_2, SER_1); ASP_{568} (ARG_3); ASP_{574} (ARG_3); ILE_{587} (ARG_3);	123
SARS-CoV2 spike protein/PepGAT	−593.1	TYR_{756} (GLY_1); TYR_{756} (ALA_2); GLU_{990} (ARG_5); ASP_{994} (ARG_5); ARG_{995} (ARG_5); ARG_{995} (SER_9); THR_{998} (THR_3); GLU_{990} (ARG_{10}); ASP_{994} (ARG_{10}); ARG_{995} (ASN_8)	141
SARS-CoV2 spike protein/PepKAA	−674.9	LYS_{1086} (PHE_9); HIS_{1088} (TYR_8); ARG_{1091} (ASN_4); ASP_{1118} (ASN_4); GLN_{1142} (ARG_5); GLU_{1144} (LYS_1); GLN_{1113} (LYS_7); ASP_{1118} (LYS_1); ASP_{1139} (LYS_1); ASP_{1139} (LYS_1)	161

[a] Calculated by the ClusPro server 2.0.
[b] Analyzed in the Pymol program.
[c] Analyzed in the Ligplot program.

Table 2
Molecular interaction docking between synthetic peptides and SARS-CoV-2 spike protein in the closed state. The molecular docking assay was performed using the *ClusPro server 2.0* and structural analysis was performed by using the *Pymol* program.

Complexes	Lowest binding energy[a]	Hydrogen bonds[b]	Number of hydrophobic interactions[c]
SARS-CoV2 spike protein/*Mo*-CBP_3-PepI	−703.0	THR_{549} (CYS_1); ASP_{568} (GLN_5); ASP_{571} (CYS_8); THR_{572} (GLN_5); MET_{740} (ARG_6); GLY_{744} (CYS_7); ASP_{745} (ARG_6); PHE_{855} (GLN_5); LEU_{977} (CYS_7); ASN_{978} (CYS_7); ARG_{1000} (ARG_6, CYS_8, CYS_7)	194
SARS-CoV2 spike protein/*Mo*-CBP_3-PepII	−787.3	TRP_{353} (CYS_8); ASN_{354} (ASN_1); ARG_{355} (CYS_8); LYS_{356} (GLN_3); ARG_{357} (GLN_3); ARG_{466} (ASN_1), (CYS_8); THR_{167} (CYS_9,); ASP_{198} (ARG_7); TYR_{200} (ARG_7); ILE_{231} (CYS_9); GLY_{232} (CYS_9).	173
SARS-CoV2 spike protein/*Mo*-CBP_3-PepIII	−723.8	GLY_{744} (ALA_1); ASP_{745} (ARG_4); ASN_{856} (GLN_3); ASN_{978} (ILE_2); ARG_{1000} (CYS_5); THR_{573} (GLN_3); ILE_{587} (GLN_3); CYS_{590} (ARG_4).	135
SARS-CoV2 spike protein/*RcAlb*-PepI	−587.8	ASN_{121} (ALA_8); TYR_{170} (LEU_3); SER_{172} (ALA_1, LEU_3); ARG_{190} (THR_6, ILE_7, ALA_8)	81
SARS-CoV2 spike protein/*RcAlb*-PepII	−671.8	ASP_{994} (LYS_2, LEU_3); ARG_{995} (THR_6, PRO_5); GLN_{1002} (LEU_9); PHE_{970} (ALA_1); ARG_{995} (LYS_2)	139
SARS-CoV2 spike protein/*RcAlb*-PepIII	−674.6	ASN_{978} (GLY_4); ARG_{1000} (CYS_5); THR_{573} (SER_1); CYS_{590} (ARG_3).	91
SARS-CoV2 spike protein/PepGAT	−619.0	GLU_{990} (ARG_5); ASP_{994} (ALA_2, ARG_5); ARG_{995} (ARG_5, SER_9); GLN_{755} (ARG_{10}); TYR_{756} (ARG_{10}); ASP_{994} (ARG_{10}); ARG_{995} (ASN_8).	142
SARS-CoV2 spike protein/PepKAA	−715.6	ASP_{1118} (LYS_7); ASP_{1139} (LYS_7); GLU_{1144} (ASN_4, LYS_7); HIS_{1083} (LYS_1); ARG_{1091} (ALA_2); ASP_{1118} (ARG_5); VAL_{1137} (LYS_1)	175

[a] Calculated by the ClusPro server 2.0.
[b] Analyzed in the Pymol program.
[c] Analyzed in the Ligplot program.

structure in the closed and open states (Fig. 7C and D) in comparison with the spike protein alone in the closed and open states (Fig. 7A and B). The RMSD of the spike protein in the closed and open state was 0, indicating typical 3D conformation. However, after interaction with *Mo*-CBP_3-PepII, the RMSD values changed from 0 to 1.258 and 1.331, respectively, for the open and closed states. PepKAA also induced conformational changes in the S protein after interacting with the S2 domain (Fig. 7E and F), which was revealed by RMSD values that changed from 0 in the control to 1.262 and 1.342, respectively, in open and closed state of the S protein. These data suggest *Mo*-CBP_3-PepII and PepGAT induce changes in the conformation of the S protein, which may decrease the binding affinity of the SARS-CoV-2 spike protein with human ACE2.

3.7. Peptides do not lead to alterations in the structure of ACE2 receptor

MD assays were also carried out to investigate possible interaction between peptides and ACE2 receptor. The results revealed that both peptides interact with the extracellular region of the ACE2 (Fig. 8A and D). Even though interacting in the same region, the interaction energy and amino acids involved were different. *Mo*-CBP_3-PepII had a slightly lower affinity with ACE2, as shown by an LBE value of $-665.5\ kJ \cdot mol^{-1}$. The amino acids involved in this interaction are Ile^2 and C^9 from *Mo*-CBP_3-PepII, respectively, with Try^{158} and Asp^{615} from ACE2 (Fig. 8B). For PepKAA, the LBE was $-700.5\ kJ \cdot mol^{-1}$ and the amino acids involved were Arg^5 and Gln^{10} with Tyr^{158}, Asp^{157}, Asp^{615}, and Ala^{956} from the ACE2 receptor (Fig. 8E).

Even though both peptides bound to ACE2, none of them caused any conformational change in its structure (Fig. 8C and F). This result suggests that despite binding to ACE2, the peptides did not alter structure, and hence its function.

3.8. By interacting with spike protein, peptides block its interaction with ACE2

As shown above, the S protein can interact with ACE receptor in both closed and open state (Fig. 9A and B). However, only in the open state of S protein did the interaction happen correctly by the RBD domain of the S protein with the PD domain of ACE2 (Fig. 9B), allowing the entrance of SARS-CoV into cells [33].

We already found that peptides induced conformational changes in the S protein (Fig. 7). To see if these changes could interfere in the interaction of that protein with ACE2 MD analyses were performed with the S protein:peptides complex with ACE2 (Fig. 9C–F). MD assays carried out with S protein:*Mo*-CBP_3-PeII complexed with ACE2 in both open (Fig. 9C) and closed states (Fig. 9D) revealed that protein S still interacted with ACE2, but this interaction occurred in a different portion rather than the RDB domain. The complex formed by the open state of the S protein and *Mo*-CBP_3-PeII (Fig. 9C) interacted with a portion far from the RBD domain. The same results were found when the complex S protein:PepKAA interacted with ACE2 (Fig. 9E and F). When complexed with PepKAA, the S protein could not correctly interact with ACE2.

4. Discussion

COVID-19 disease is entirely new, and there is no treatment of even vaccine to protect people. Besides respiratory complications, COVID-19 can cause cytokine-mediated inflammatory responses in patients, leading to complications of the heart, kidneys and liver, as well as decreased platelet counts. All these complication are led by the overproduction of response proinflammatory cytokines such as tumor necrosis factor (TNF), interleukin (IL) 6 and 1β [34–36]. The high transmissibility and infectivity of SARS-CoV-2 compared to SARS-CoV-1 and MERS are, in part, the result of a mutation in the spike protein [3,15,20].

The spike protein is a trimeric glycoprotein with two domains, S1 and S2, both critical for SARS-CoV-2 infection. In humans, the interaction between spike protein and ACE2 allows the entrance of SARS-CoV-2 in the lungs. The ability of SARS-CoV-2 to infect many different cells is supported by the interaction between the S protein and ACE2 receptor. ACE2 is expressed in many human tissues, such as lungs, liver, heart, kidneys, gut and brain. Thus, once inside the human body, SARS-CoV-2 can virtually infect all these tissues, leading to multiple infections. Because of that, the spike protein has been the target of many studies worldwide seeking ways to neutralize SARS-CoV-2 infection [7,33,37].

Based on its importance, the spike protein has been targeted by many research groups seeking treatment to COVID-19. Supercomputers and molecular docking assays have been employed to find an existing or develop a new drug that targets this protein and thus prevents SARS-CoV form infecting human cells [18,19,38]. We showed by molecular docking that *Mo*-CBP_3-PepII and PepKAA interact, respectively, with the S1 and S2 domains of the S protein (Fig. 2).

The lowest binding energy values were -814.4 and $-674.9\ kJ \cdot mol^{-1}$, respectively, for *Mo*-CBP_3-PepII and PepKAA. That is 2.71 and 2.24 higher

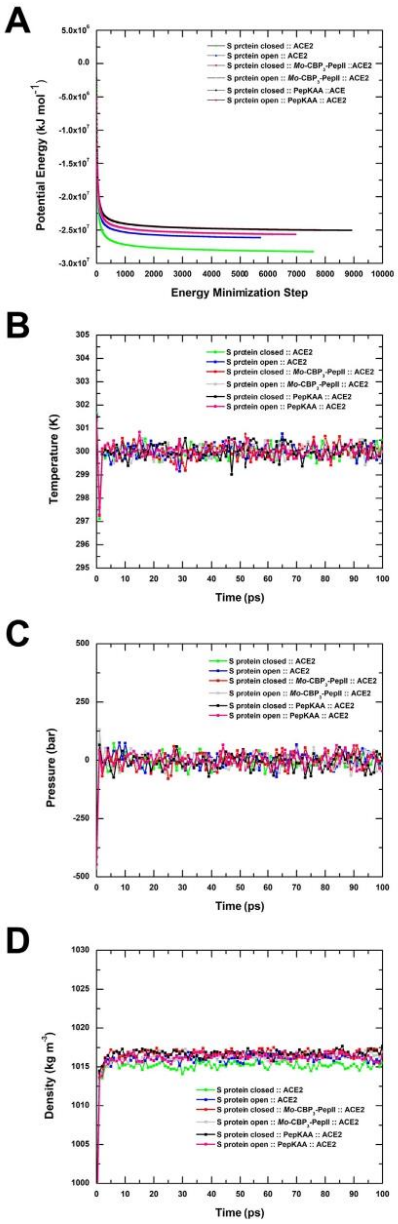

Fig. 4. Minimization and equilibrium of the S protein complexed with *Mo*-CBP$_3$-PepII, PepKAA, and ACE2. The minimizations are observed through potential energy during the energy minimization step (A). The temperature, pressure and density equilibrium along 100 ps (B, C, and D, respectively). The S protein in closed form complexed with ACE2 is represented in green line and square. The open-complexed S protein with ACE2 is represented by the blue line and square. *Mo*-CBP$_3$-PepII with ACE2 and closed S protein is represented by the red line and square. The open S protein is represented in the gray line and square. PepKAA with ACE2 and closed S protein is represented by the black line and square, and when with open S protein is represented by a pink line and square.

than the energy of arbidol to interact with the S protein [38], suggesting that both peptides have more affinity to bind with the S protein than with arbidol. Despite proven toxicity, some researchers are still analyzing chloroquine and hydroxychloroquine to treat COVID-19. Molecular docking analysis revealed that chloroquine and hydroxychloroquine have binding energies of 100 kJ·mol^{-1} and 137 kJ·mol^{-1} to interact with the spike protein. These values are too low compared to the values presented by peptides.

Another study reported molecular docking assays using other drugs against SARS-CoV-2 RNA polymerase (RdRp). The drugs galidesivir, remdesivir, tenofovir, sofosbuvir, and ribavirin bind with SARS-CoV-2 RdRp, with very low binding energies of −7.0, −7.6, −6.9, −7.5, and −7.8 kcal/mol, respectively [39]. Besides the low binding energies, SARS-CoV-2 RpRd might not be a good target because this enzyme can only be assessed during SARS-CoV-2 replication within the cell. By binding to the S protein, peptides prevent cell infection, and thus all the downstream process of SARS-CoV-2 entrance in cells.

Many studies have investigated drug repositioning to an available drug for faster development of treatment for COVID-19 [16,40]. Wu et al. [40] conducted molecular docking screening using many already available drugs such as antihypertensive, antifungal, antibacterial and anticoagulant drugs. Some of them presented low affinity to interact with the S protein, so could not interfere in S protein-ACE2 interaction like the peptides presented here did.

Our experiments revealed that the energy of S protein and ACE2 is 899.0 kJ·mol^{-1}. By showing energies of 814.4 and −674.9 kJ·mol^{-1}, respectively, *Mo*-CBP$_3$-PepII and PepKAA can interfere in the S protein-ACE2 interaction. This interaction raised two questions: (i) What are the consequences of peptide interaction with the S protein?; and (ii) After interact with peptides, could the S protein bind to the ACE2 protein? The first question was solved by employing RMSD analyses. The RMSD values of the S protein after interaction with peptides were 1.331 and 1.342, respectively, for *Mo*-CBP$_3$-PepII and PepKAA (Fig. 7), suggesting that by interaction with the S protein, these peptides induce conformation changes in it, which could lead either to no interaction or wrong interaction with ACE2. Vankadari [38] showed that the RMSD value of arbidol after binding to the S protein was 0.82, indicating a slight alteration in that protein's structure.

Indeed, after binding to peptides, the S protein can still bind to ACE2 but with very low affinity and in the wrong place (Fig. 9). The wrong interaction of the S protein with ACE2 has severe consequences for SARS-Cov-2. In humans, the domain (targeted by *Mo*-CBP$_3$-PepII) is responsible for interacting with ACE2 (angiotensin-converting enzyme 2) receptors in lung cells. After interaction with ACE2, the spike protein is cleaved by a cellular protease, releasing the S2 domain (targeted by PepKAA), responsible for the fusion between viral and cell membranes [7,33,34,41]. These results strongly suggest that both peptides act by targeting the S protein and can block the interaction with ACE2 and thus inhibit the entrance of SARS-CoV-2, first in lung cells and then other cells [2,42]. As happens with other viruses, without a cell to infect, SARS-Cov-2 becomes unstable and thus is naturally degraded.

ACE2 is an essential cellular receptor in many types of cells involved in the conversion of angiotensin (Ang) I and Ang II into Ang 1–9 and Ang 1–7 [37]. Its malfunction can lead to severe multiorgan damages. Based on that, when used in clinical trials, peptides might not show any collateral effects. Molecular docking assays revealed that *Mo*-CBP$_3$-PepII and PepKAA indeed bind to ACE2, but RMSD analyses showed that no conformational changes occur (Fig. 8). This suggests that although peptides bind to ACE2, its function in cells is not affected. In addition, the binding energy values indicate that peptides have more affinity with the spike protein than ACE2, which means that in the same environment, peptides will prefer to bind to the spike protein instead of ACE2.

Antiviral drugs already available, such as arbidol, chloroquine and hydroxychloroquine, have many side effects, such as diarrhea, nausea, vomiting, liver, and heart damage [12,43,44]. Compared to those drugs, the synthetic peptides presented here have no side effects, no

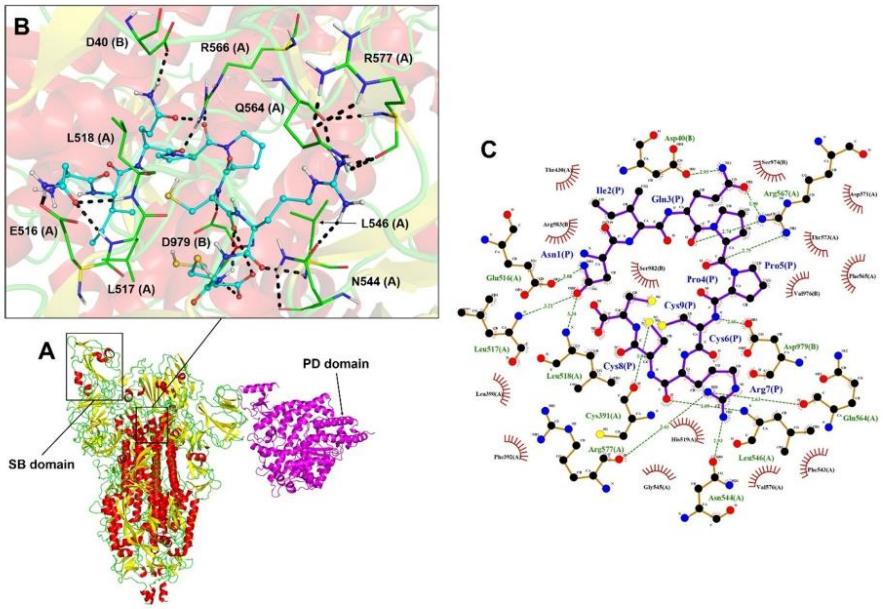

Fig. 5. 3D and flat structure of the S protein complexed with *Mo*-CBP$_3$-PepII and ACE2. Diagram of the interface region showing hydrogen bonds and hydrophobic interactions are visualized in 3D (A, B) and 2D (C). The peptide *Mo*-CBP$_3$-PepII interacts with the α-helix of the S1 subunit. The images were generated automatically by Lig-Plot and analyzed on PyMol. In B, the peptide is shown in cyan and the viral protein in green. LigPlot images show peptide residues in dark blue and viral residues in dark red.

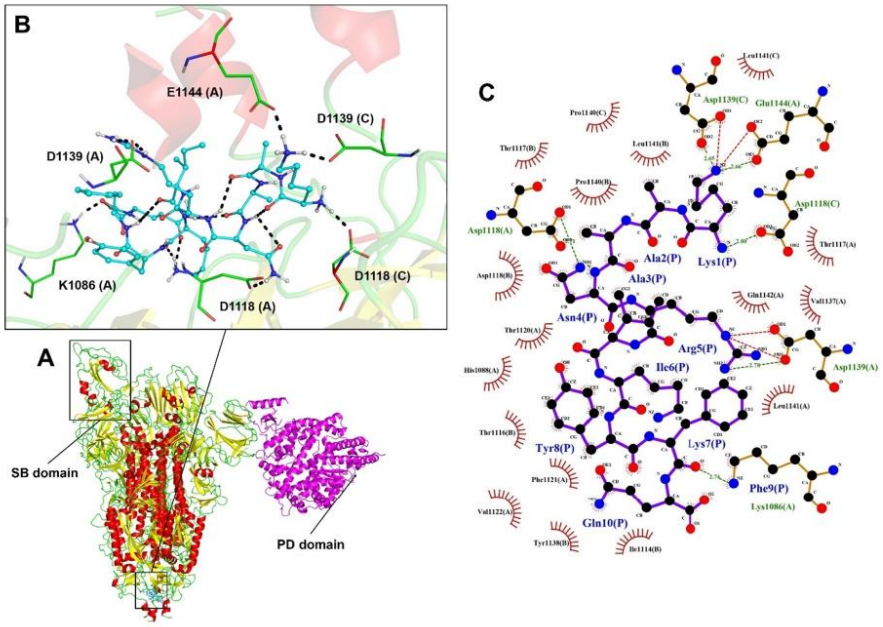

Fig. 6. 3D and flat structure of the S protein complexed with PepKAA and ACE2. Diagram of the interface region showing hydrogen bonds and hydrophobic interactions are visualized in 3D (A, B) and 2D (C). The peptide PepKAA interacts with the α-helix of the S1 subunit. The images were generated automatically by LigPlot and analyzed on the PyMol. In B, the peptide is shown in cyan and the viral protein in green. LigPlot images show peptide residues in dark blue and viral residues in dark red.

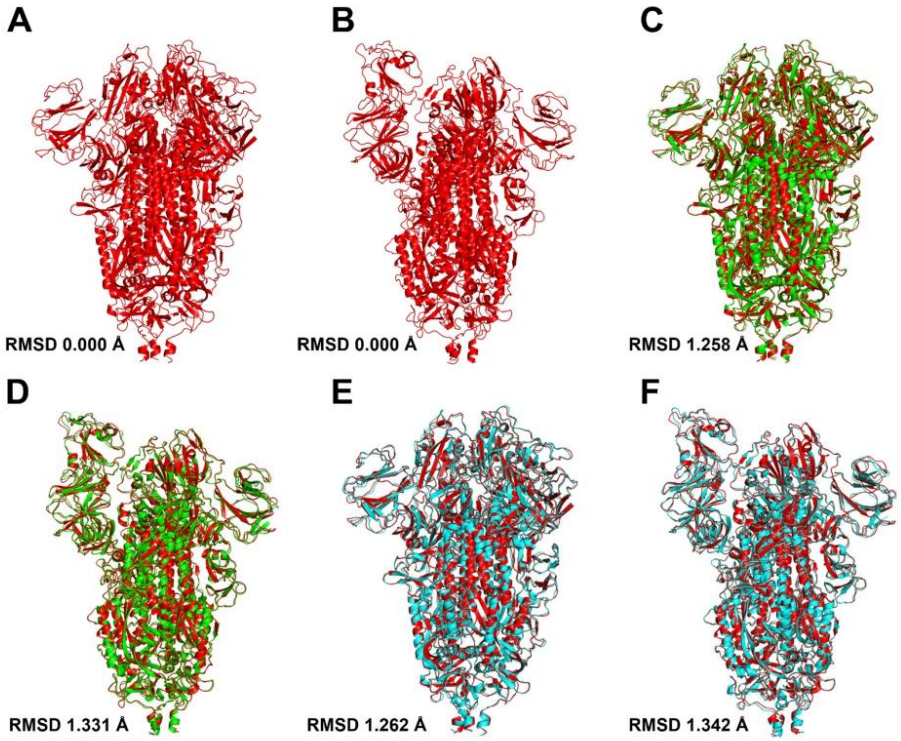

Fig. 7. 3D visualization SARS-CoV-2 S protein:peptides complexes and RMSD calculations. The RMSD calculation of the closed (A) and partially open (B) states of the viral protein before (in red) and after (green and blue) the interaction with the Mo-CBP3-PepII (C, D) peptides and PepKAA (E, F) suggest conformational alteration caused by the peptides. The structure before (red) and after (green) the interaction of *Mo*-CBP_3-PepII and cyan for PepKAA. The structural alignment was carried out by Pymol.

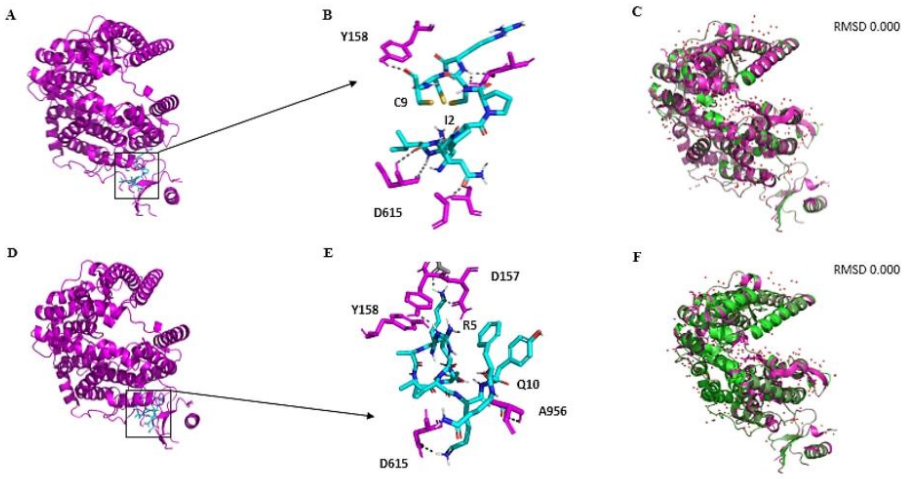

Fig. 8. Representation of the interface of interaction between ACE2 and *Mo*-CBP_3-PepII and PepKAA. *Mo*-CBP_3-PepII (A, B) and PepKAA (D, E) did not bind to the PD domain of ACE2 and did not interfere with the binding to the RBD domain of the spike glycoprotein. RMSD data displayed of *Mo*-CBP_3-PepII (C) and PepKAA (D) suggest that the peptides do not cause a conformational change in the ACE2 protein. Overlapping of crystals before and after interaction with synthetic peptides is shown in magenta and green, respectively.

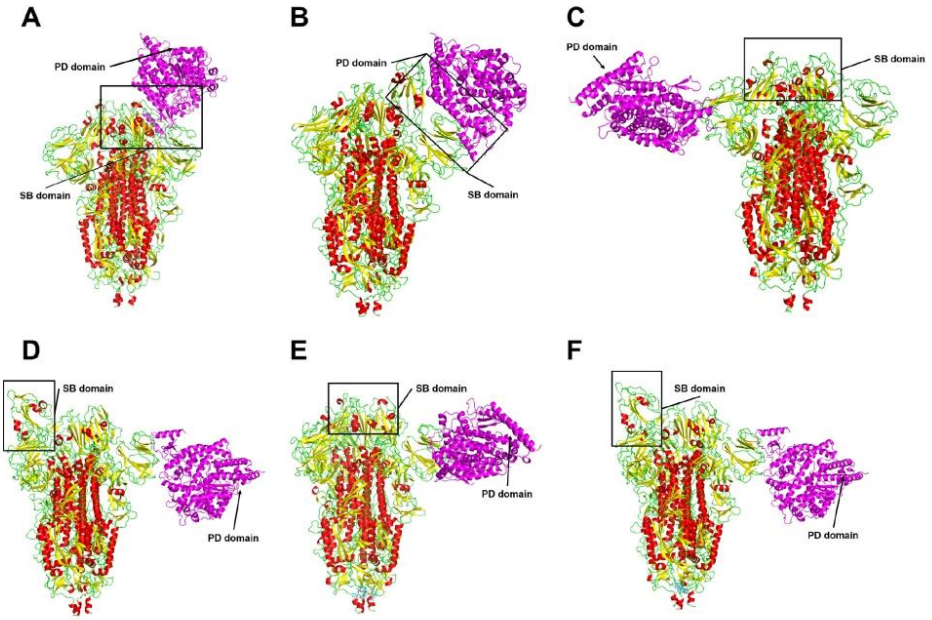

Fig. 9. Effectiveness of the link between SARS-CoV-2 S protein and ACE2 in the presence of peptides. ACE2 binds to the RBD domains in the conformational states closed (A) and open (B) of the spike glycoprotein. Binding to the RBD domains does not occur between the S protein: *Mo*-CBP$_3$-PepII (C, D) and ACE2 complexes, S protein: PepKAA (E, F) and ACE2. Protein S is colored by SS; in magenta ACE2.

hemolytic activity or toxicity to human cells [23]. This indicates that peptides, based on molecular docking, are potential molecules for use to develop new drugs, given their higher affinity with the spike protein without interfering with ACE2 activity, and absence of toxic effects.

The peptides have high potential against SARS-CoV-2. However, some limitations have to solve: (1) The peptides were only tested against the ACE2 receptor. However, there is an alternative receptor in the human lungs cells called CD209L, a C-type lectin (also called L-SIGN), which could be used by coronaviruses to cause infection [45]. (2) SARS-CoV-2 is an RNA virus that suggests a high mutational rate [45,46], which makes it challenging to find a good target. Indeed, the peptides tested here could not prevent the mutations in SARS-CoV-2 RNA. Because of that, at the same time, peptides could be employed to disrupt the interaction between SARS-CoV-2 and ACE2, they also can be tested against the CD209L receptor by molecular dynamics simulations and against the SARS-CoV-2 RNA polymerase, to see if peptides could inhibit its activity. Further analysis will be carried out to increase the broad spectrum of peptides against SARS-CoV-2.

5. Conclusion

This is the first study to report peptides as potential antiviral molecules that can be used to inhibit SARS-CoV-2 entrance in cells. These peptides can interact with SARS-CoV-2 S protein and block its entrance in human cells and thus inhibit infection and COVID-19 development. Further analyses are needed to prove this, but we can suggest that *Mo*-CBP$_3$-PepII and PepKAA have potential for development of new drugs against SARS-CoV-2 and perhaps other viruses.

Supplementary data to this article can be found online at https://doi.org/10.1016/j.ijbiomac.2020.07.174.

Funding and acknowledgments

This work was supported by grants from the following Brazilian agencies: Conselho Nacional de Desenvolvimento Científico e Tecnológico (CNPq) (process numbers 308107/2013-6 and 306202/2017-4); Coordenação de Aperfeiçoamento de Pessoal de Nível Superior (CAPES); and Fundação Cearense de Apoio ao Desenvolvimento Científico e Tecnológico (FUNCAP).

Author contributions

All authors made substantial contributions in the following steps: (1) conception and design of the study by PFNS; (2) acquisition of data, analysis, interpretation of data by FESL and JLA (3) drafting the article or revising it critically with important intellectual content by FESL, CDTF, JTAO, and PFNS; and (3) final approval of the version to be submitted by PFNS.

Ethical approval

None sought.

Declaration of competing interest

All authors declare no conflict of interest.

References

[1] J.S.M. Peiris, Coronaviruses, Med. Microbiol, Eighteenth ed.Elsevier Inc. 2012, pp. 587–593, https://doi.org/10.1016/B978-0-7020-4089-4.00072-X.

[2] C.J. Burrell, C.R. Howard, F.A. Murphy, Fenner and White's medical virology, Chapter 13 - Coronaviruses, Fifth edition 2017, pp. 437–446, https://doi.org/10.1016/B978-0-12-375156-0.00031-X.

[3] K.G. Andersen, A. Rambaut, W.I. Lipkin, E.C. Holmes, R.F. Garry, The proximal origin of SARS-CoV-2, Nat. Med. 26 (2020) 450–452, https://doi.org/10.1038/s41591-020-0820-9.

[4] J. Cui, F. Li, Z.L. Shi, Origin and evolution of pathogenic coronaviruses, Nat. Rev. Microbiol. 17 (2019) 181–192, https://doi.org/10.1038/s41579-018-0118-9.

[5] Q. Li, X. Guan, P. Wu, X. Wang, L. Zhou, Y. Tong, R. Ren, K.S.M. Leung, E.H.Y. Lau, J.Y. Wong, X. Xing, N. Xiang, Y. Wu, C. Li, Q. Chen, D. Li, T. Liu, J. Zhao, M. Liu, W. Tu, C. Chen, L. Jin, R. Yang, Q. Wang, S. Zhou, R. Wang, H. Liu, Y. Luo, Y. Liu, G. Shao, H. Li, Z. Tao, Y. Yang, Z. Deng, B. Liu, Z. Ma, Y. Zhang, G. Shi, T.T.Y. Lam, J.T. Wu, G.F. Gao, B.J. Cowling, B. Yang, G.M. Leung, Z. Feng, Early transmission dynamics in Wuhan, China, of novel coronavirus-infected pneumonia, N. Engl. J. Med. 382 (2020) 1199–1207, https://doi.org/10.1056/NEJMoa2001316.

[6] Z. Song, Y. Xu, L. Bao, L. Zhang, P. Yu, Y. Qu, H. Zhu, W. Zhao, Y. Han, C. Qin, From SARS to MERS, thrusting coronaviruses into the spotlight, Viruses 11 (2019) 59, https://doi.org/10.3390/v11010059.

[7] M. Hoffmann, H. Kleine-Weber, S. Schroeder, N. Krüger, T. Herrler, S. Erichsen, T.S. Schiergens, G. Herrler, N.H. Wu, A. Nitsche, M.A. Müller, C. Drosten, S. Pöhlmann, SARS-CoV-2 cell entry depends on ACE2 and TMPRSS2 and is blocked by a clinically proven protease inhibitor, Cell (2020)https://doi.org/10.1016/j.cell.2020.02.052.

[8] WHO, Middle East Respiratory Syndrome Coronavirus (MERS-CoV), WHO, 2020.

[9] COVIDView weekly summary | CDC, (n.d.). https://www.cdc.gov/coronavirus/2019-ncov/covid-data/covidview/index.html (accessed April 26, 2020).

[10] B.B. Practice, Coronavirus disease 2019, World Heal. Organ. 2020 (2019) 2633, https://doi.org/10.1001/jama.2020.2633.

[11] F. Almazán, I. Sola, S. Zuñiga, S. Marquez-Jurado, L. Morales, M. Becares, L. Enjuanes, Coronavirus reverse genetic systems: infectious clones and replicons, Virus Res. 189 (2014) 262–270, https://doi.org/10.1016/j.virusres.2014.05.026.

[12] H. Li, S.-M. Liu, X.-H. Yu, S.-L. Tang, C.-K. Tang, Coronavirus disease 2019 (COVID-19): current status and future perspective, Int. J. Antimicrob. Agents 105951 (2020)https://doi.org/10.1016/j.ijantimicag.2020.105951.

[13] D.S. Hui, E. I Azhar, T.A. Madani, F. Ntoumi, R. Kock, O. Dar, G. Ippolito, T.D. Mchugh, Z.A. Memish, C. Drosten, A. Zumla, E. Petersen, The continuing 2019-nCoV epidemic threat of novel coronaviruses to global health — the latest 2019 novel coronavirus outbreak in Wuhan, China, Int. J. Infect. Dis. 91 (2020) 264–266, https://doi.org/10.1016/j.ijid.2020.01.009.

[14] A. Wu, Y. Peng, B. Huang, X. Ding, X. Wang, P. Niu, J. Meng, Z. Zhu, Z. Zhang, J. Wang, J. Sheng, L. Quan, Z. Xia, W. Tan, G. Cheng, T. Jiang, Genome composition and divergence of the novel coronavirus (2019-nCoV) originating in China, Cell Host Microbe 27 (2020) 325–328, https://doi.org/10.1016/j.chom.2020.02.001.

[15] Y. Yuan, D. Cao, Y. Zhang, J. Ma, J. Qi, Q. Wang, G. Lu, Y. Wu, J. Yan, Y. Shi, X. Zhang, G.F. Gao, Cryo-EM structures of MERS-CoV and SARS-CoV spike glycoproteins reveal the dynamic receptor binding domains, Nat. Commun. 8 (2017), 15092. https://doi.org/10.1038/ncomms15092.

[16] Drug repositioning is an alternative for the treatment of coronavirus COVID-19, Int. J. Antimicrob. Agents (2020) 105969, https://doi.org/10.1016/J.IJANTIMICAG.2020.105969.

[17] B. Robson, COVID-19 coronavirus spike protein analysis for synthetic vaccines, a peptidomimetic antagonist, and therapeutic drugs, and analysis of a proposed achilles' heel conserved region to minimize probability of escape mutations and drug resistance, Comput. Biol. Med.. (n.d.). doi:https://doi.org/10.1016/J.COMPBIOMED.2020.103749.

[18] D.C. Hall, H.-F. Ji, A search for medications to treat COVID-19 via in silico molecular docking models of the SARS-CoV-2 spike glycoprotein and 3CL protease, Travel Med. Infect. Dis. (2020) 101646, https://doi.org/10.1016/j.tmaid.2020.101646.

[19] C. Wu, Y. Liu, Y. Yang, P. Zhang, W. Zhong, Y. Wang, Q. Wang, Y. Xu, M. Li, X. Li, M. Zheng, L. Chen, H. Li, Analysis of therapeutic targets for SARS-CoV-2 and discovery of potential drugs by computational methods, Acta Pharm. Sin. B (2020)https://doi.org/10.1016/j.apsb.2020.02.008.

[20] T. Fujii, T. Nakamura, A. Iwamoto, Current concepts in SARS treatment, J. Infect. Chemother. 10 (1) (2004)https://doi.org/10.1007/s10156-003-0296-9.

[21] P. Calligari, S. Bobone, G. Ricci, A. Bocedi, Molecular Investigation of SARS – CoV-2 Proteins and, 2020.

[22] J.T.A. Oliveira, P.F.N. Souza, I.M. Vasconcelos, L.P. Dias, T.F. Martins, M.F. Van Tilburg, M.I.F. Guedes, D.O.B. Sousa, Mo-CBP3-PepI, Mo-CBP3-PepII, and Mo-CBP3-PepIII are synthetic antimicrobial peptides active against human pathogens by stimulating ROS generation and increasing plasma membrane permeability, Biochimie 157 (2019) 10–21, https://doi.org/10.1016/j.biochi.2018.10.016.

[23] P.G. Lima, P.F.N. Souza, C.D.T. Freitas, J.T.A. Oliveira, L.P. Dias, J.X.S. Neto, I.M. Vasconcelos, J.L.S. Lopes, D.O.B. Sousa, Anticandidal activity of synthetic peptides: mechanism of action revealed by scanning electron and fluorescence microscopies and synergism effect with nystatin, J. Pept. Sci. (2020) 1–13, https://doi.org/10.1002/psc.3249.

[24] L.P. Dias, P.F.N. Souza, J.T.A. Oliveira, I.M. Vasconcelos, N.M.S. Araújo, M.F.V. Tilburg, M.I.F. Guedes, R.F. Carneiro, J.L.S. Lopes, D.O.B. Sousa, RcAlb-PepII, a synthetic small peptide bioinspired in the 2S albumin from the seed cake of Ricinus communis, is a potent antimicrobial agent against Klebsiella pneumoniae and Candida parapsilosis, Biochim. Biophys. Acta Biomembr. (2019) 183092, https://doi.org/10.1016/j.bbamem.2019.183092.

[25] P.F.N. Souza, L.S.M. Marques, J.T.A. Oliveira, P.G. Lima, L.P. Dias, N.A.S. Neto, F.E.S. Lopes, J.S. Sousa, A.F.B. Silva, R.F. Caneiro, J.L.S. Lopes, M.V. Ramos, C.D.T. Freitas, Synthetic antimicrobial peptides: from choice of the best sequences to action mechanisms, Biochimie 175 (2020) 132–145, https://doi.org/10.1016/j.biochi.2020.05.016.

[26] Y. Inbar, D. Schneidman-Duhovny, I. Halperin, A. Oron, R. Nussinov, H.J. Wolfson, Approaching the CAPRI challenge with an efficient geometry-based docking, Proteins Struct. Funct. Genet., Proteins 2005, pp. 217–223, https://doi.org/10.1002/prot.20561.

[27] D. Kozakov, D.R. Hall, B. Xia, K.A. Porter, D. Padhorny, C. Yueh, D. Beglov, S. Vajda, The ClusPro web server for protein-protein docking, Nat. Protoc. 12 (2017) 255–278, https://doi.org/10.1038/nprot.2016.169.

[28] R.A. Laskowski, J. Jabłońska, L. Pravda, R.S. Vařeková, J.M. Thornton, PDBsum: structural summaries of PDB entries, Protein Sci. 27 (2018) 129–134, https://doi.org/10.1002/pro.3289.

[29] I.H. Moal, P.A. Bates, SwarmDock and the use of normal modes in protein-protein docking, Int. J. Mol. Sci. 11 (2010) 3623–3648, https://doi.org/10.3390/ijms11103623.

[30] D. Van Der Spoel, E. Lindahl, B. Hess, G. Groenhof, A.E. Mark, H.J.C. Berendsen, GROMACS: fast, flexible, and free, J. Comput. Chem. 26 (2005) 1701–1718, https://doi.org/10.1002/jcc.20291.

[31] M.J. Robertson, J. Tirado-Rives, W.L. Jorgensen, Improved peptide and protein torsional energetics with the OPLS-AA force field, J. Chem. Theory Comput. 11 (2015) 3499–3509, https://doi.org/10.1021/acs.jctc.5b00356.

[32] W.L. Jorgensen, D.S. Maxwell, J. Tirado-Rives, Development and testing of the OPLS all-atom force field on conformational energetics and properties of organic liquids, J. Am. Chem. Soc. 118 (1996) 11225–11236, https://doi.org/10.1021/ja9621760.

[33] A.C. Walls, Y.J. Park, M.A. Tortorici, A. Wall, A.T. McGuire, D. Veesler, Structure, function, and antigenicity of the SARS-CoV-2 spike glycoprotein, Cell 181 (e6) (2020) 281–292, https://doi.org/10.1016/j.cell.2020.02.058.

[34] R.J. Jose, A. Manuel, COVID-19 cytokine storm: the interplay between inflammation and coagulation, Lancet Respir. 2019 (2019) 2019–2020, https://doi.org/10.1016/S2213-2600(20)30216-2.

[35] P. Mehta, D.F. McAuley, M. Brown, E. Sanchez, R.S. Tattersall, J.J. Manson, COVID-19: consider cytokine storm syndromes and immunosuppression, Lancet 395 (2020) 1033–1034, https://doi.org/10.1016/S0140-6736(20)30628-0.

[36] M.Z. Tay, C.M. Poh, L. Rénia, P.A. MacAry, L.F.P. Ng, The trinity of COVID-19: immunity, inflammation and intervention, Nat. Rev. Immunol. (2020) 1–12, https://doi.org/10.1038/s41577-020-0311-8.

[37] M. Gheblawi, K. Wang, A. Viveiros, Q. Nguyen, J.-C. Zhong, A.J. Turner, M.K. Raizada, M.B. Grant, G.Y. Oudit, Angiotensin converting enzyme 2: SARS-CoV-2 receptor and regulator of the renin-angiotensin system, Circ. Res. (2020)https://doi.org/10.1161/CIRCRESAHA.120.317015.

[38] N. Vankadari, Arbidol: a potential antiviral drug for the treatment of SARS-CoV-2 by blocking the trimerization of viral spike glycoprotein? Int. J. Antimicrob. Agents (2020) 105998, https://doi.org/10.1016/j.ijantimicag.2020.105998.

[39] A.A. Elfiky, Ribavirin, remdesivir, sofosbuvir, galidesivir, and tenofovir against SARS-CoV-2 RNA dependent RNA polymerase (RdRp): a molecular docking study, Life Sci. 253 (2020)https://doi.org/10.1016/j.lfs.2020.117592.

[40] M. Alifano, P. Alifano, P. Forgez, A. Iannelli, Renin-angiotensin system at the heart of COVID-19 pandemic, Biochimie (2020)https://doi.org/10.1016/j.biochi.2020.04.008.

[41] A.E. Gorbalenya, S.C. Baker, R.S. Baric, R.J. de Groot, C. Drosten, A.A. Gulyaeva, B.L. Haagmans, C. Lauber, A.M. Leontovich, B.W. Neuman, D. Penzar, S. Perlman, L.L. Poon, D. Samborskiy, I.A. Sidorov, I. Sola, J. Ziebuhr, Severe Acute Respiratory Syndrome-related Coronavirus: The Species and Its Viruses-A Statement of the Coronavirus Study Group, (n.d.). doi:https://doi.org/10.1101/2020.02.07.937862.

[42] J.M. Oakes, R.M. Fuchs, J.D. Gardner, E. Lazartigues, X. Yue, Nicotine and the renin-angiotensin system, Am. J. Phys. Regul. Integr. Comp. Phys. 315 (2018) R895–R906, https://doi.org/10.1152/ajpregu.00099.2018.

[43] Q. Liu, H.R. Xiong, L. Lu, Y.Y. Liu, F. Luo, W. Hou, Z.Q. Yang, Antiviral and anti-inflammatory activity of arbidol hydrochloride in influenza A (H1N1) virus infection, Acta Pharmacol. Sin. 34 (2013) 1075–1083, https://doi.org/10.1038/aps.2013.54.

[44] A. Cortegiani, G. Ingoglia, M. Ippolito, A. Giarratano, S. Einav, A systematic review on the efficacy and safety of chloroquine for the treatment of COVID-19, J. Crit. Care 57 (2020) 279–283, https://doi.org/10.1016/j.jcrc.2020.03.005.

[45] S.A. Jeffers, S.M. Tusell, L. Gillim-Ross, E.M. Hemmila, J.E. Achenbach, G.J. Babcock, W.D. Thomas, L.B. Thackray, M.D. Young, R.J. Mason, D.M. Ambrosino, D.E. Wentworth, J.C. DeMartini, K.V. Holmes, CD209L (L-SIGN) is a receptor for severe acute respiratory syndrome coronavirus, Proc. Natl. Acad. Sci. U. S. A. 101 (2004) 15748–15753, https://doi.org/10.1073/pnas.0403812101.

[46] H. Li, L. Liu, D. Zhang, J. Xu, H. Dai, N. Tang, X. Su, B. Cao, SARS-CoV-2 and viral sepsis: observations and hypotheses, Lancet 395 (2020) 1517–1520, https://doi.org/10.1016/S0140-6736(20)30920-X.

APÊNDICE G - THE HUMAN PANDEMIC CORONAVIRUSES ON THE SHOW: THE SPIKE GLYCOPROTEIN AS THE MAIN ACTOR IN THE CORONAVIRUSES PLAY

International Journal of Biological Macromolecules 179 (2021) 1–19

Contents lists available at ScienceDirect

International Journal of Biological Macromolecules

journal homepage: http://www.elsevier.com/locate/ijbiomac

Review

The human pandemic coronaviruses on the show: The spike glycoprotein as the main actor in the coronaviruses play

Pedro F.N. Souza [a,*,1], Felipe P. Mesquita [b,1], Jackson L. Amaral [a], Patrícia G.C. Landim [a], Karollyny R.P. Lima [a], Marília B. Costa [b], Izabelle R. Farias [b], Luina B. Lima [b], Raquel C. Montenegro [b]

[a] Department of Biochemistry and Molecular Biology, Federal University of Ceara, Brazil
[b] Drug research and Development Center, Department of Medicine, Federal University of Ceara, Brazil

ARTICLE INFO

Article history:
Received 23 January 2021
Received in revised form 25 February 2021
Accepted 26 February 2021
Available online 2 March 2021

Keywords:
Coronaviruses
Spike proteins
SARS-CoV-2
SARS-CoV
MERS-CoV
RBD
Mutations

ABSTRACT

Three coronaviruses (CoVs) have threatened the world population by causing outbreaks in the last two decades. In late 2019, the severe acute respiratory syndrome coronavirus-2 (SARS-CoV-2) emerged and caused the coronaviruses to disease 2019 (COVID-19), leading to the ongoing global outbreak. The other pandemic coronaviruses, SARS-CoV and Middle East respiratory syndrome CoV (MERS-CoV), share a considerable level of similarities at genomic and protein levels. However, the differences between them lead to distinct behaviors. These differences result from the accumulation of mutations in the sequence and structure of spike (S) glycoprotein, which plays an essential role in coronavirus infection, pathogenicity, transmission, and evolution. In this review, we brought together many studies narrating a sequence of events and highlighting the differences among S proteins from SARS-CoV, MERS-CoV, and SARS-CoV-2. It was performed here, analysis of S protein sequences and structures from the three pandemic coronaviruses pointing out the mutations among them and what they come through. Additionally, we investigated the receptor-binding domain (RBD) from all S proteins explaining the mutation and biological importance of all of them. Finally, we discuss the mutation in the S protein from several new isolates of SARS-CoV-2, reporting their difference and importance. This review brings into detail how the variations in S protein that make SARS-CoV-2 more aggressive than its relatives coronaviruses and other differences between coronaviruses.

© 2021 Elsevier B.V. All rights reserved.

Contents

* Corresponding author at: Biochemistry and Molecular Biology Department, Federal University of Ceará, CE, Brazil, Laboratory of Plant Defense Proteins, Av. Mister Hull, P.O. Box: 60451, Fortaleza, CE, Brazil.
E-mail address: pedrofilhobio@gmail.com (P.F.N. Souza).
[1] Both authors contributed equally to this article.

https://doi.org/10.1016/j.ijbiomac.2021.02.203
0141-8130/© 2021 Elsevier B.V. All rights reserved.

1. Introduction

Coronaviruses (CoVs) belong to a family of positive-sense, single-stranded, RNA viruses that are lipid-enveloped [1]. The classification by virologists classified coronaviruses into four genera as alpha, beta, gamma, and delta. The most famous are the α- and β-coronaviruses, given their ability to pass through the animal-human barriers, thus becoming clinically relevant to humans [2]. Nowadays, virologists reported seven coronaviruses able to infect humans and named as human coronaviruses (hCoVs). Of these, human coronavirus OC43 (hCoV-OC43), Severe Acute Respiratory Syndrome coronavirus (SARS-CoV), Human coronavirus HKU1 (hCoV-HKU1), MERS-CoV are classified into the beta-genera, and human coronavirus NL-63 (hCoV-NL63) and Human coronavirus 229E (hCoV-229E) into the α-genera [1,3–6].

The hCoVs hCoV-HKU1, hCoV-OC43, hCoV-NL63, and hCoV-229E are not that harmful to humans as their infection results in non-symptomatic infection or, worse case, mild respiratory and less common gastrointestinal infection. Today, 5–30% of common cold cases are attributed to these hCoVs. Therefore, humans did not give the necessary attention to the hCoVs. However, in the last two decades, three outbreaks caused by hCoVs made humans pay more attention to them. The ongoing outbreak showed the human population how devastating hCoVs could be and driven many researchers worldwide to find either a vaccine or a treatment [1–6].

In December 2019, China warned the World Health Organization (WHO) about pneumonia caused by a new virus in Wuhan [7–9]. Later, the new virus was grouped into the coronavirus family and named severe acute respiratory syndrome coronavirus-2 (SARS-CoV-2). SARS-CoV-2 spreads quickly worldwide, and in a few months, more precisely in March 2020, the situation became worse and established a pandemic state [9–11]. The pandemic situation was followed by lockdown strategies adopted by the entire world. Despite that, the health care systems around the world went through high pressure, followed by the shutting down of the economic situation in many countries [7].

Unlike the 2002–2003 SARS-CoV-1 outbreak, SARS-CoV-2 infection reached all continents quickly, proving to be more contagious. Comparing both viruses, the infection caused by SARS-CoV-2 is recognized by a broader clinical spectrum that comes from asymptomatic infection to severe viral pneumonia with respiratory failure and death [8,12,13]. In contrast to SARS-CoV and MERS-CoV, many SARS-CoV-2-infected patients developed low-titer of neutralizing antibody, leading them to suffer with prolonged severe symptoms and illness, suggesting a more effective SARS-CoV-2 immune surveillance evasion than SARS-CoV and MERS-CoV [14–18].

The ongoing outbreak caused by SARS-CoV-2 has taken many lives, threatened thousands more, and destroyed entire families worldwide. Indeed, SARS-CoV-2 (Coronavirus Disease 2019) is by far more transmissible than SARS-CoV-1 and MERS-CoV but is less lethal than they are (Table 1). However, SARS-CoV-2 higher transmissibility has resulted in 113,299,920 million of infected people with 2,512,823 million of death as of 25 February 2021, by far a larger number compared to other outbreaks [19,20].

The coronaviruses outbreak presented different spreads worldwide. Starting in November 2002 in Foshan-China, until March 2003, the SARS-CoV-1 outbreak has spread all over 29 countries (Fig. 1) [21,22]. The WHO status for SARS-CoV-1 today is controlled [21]. The MERS-CoV outbreak started in April 2012 in Zarqa-Jordan, and by September 2012, spread to 27 countries (Fig. 1) [22–25]. The status of MERS-CoV by WHO is sporadic continuous [24]. For SARS-CoV-2, as we know, the status of the outbreak is ongoing and has already spread to 213 countries (Fig. 1) [26].

The higher transmissibility of the SARS-CoV-2 is probable due to the higher number of accumulated positive mutations in the spike glycoprotein (S), which led this protein to be 20 times more effective in recognized human receptors than the spike from SARS-CoV-1 and MERS-CoV [27,28]. Based on that, the review is focused on the discussion and tracking the mutations in the S protein in three recent coronaviruses that posed outbreaks of SARS-CoV-1, MERS-CoV, and SARS-CoV-2. Additionally, we intend to understand the contribution of the S protein to the transmissibility of SARS-CoV-2 compared to SARS-CoV-1 and MERS-CoV.

2. Coronaviruses taxonomy and linking to bats

The coronaviruses are one of the two genera belonging to the *Coronaviridae* family. The other one is the toroviruses [29–31], both included in the *Nidovirales* order. Coronaviruses are highly disseminated among mammals in general, causing mild infections such as cold and gastrointestinal. However, in some cases, they might cause severe respiratory infection. In the past, coronavirus was known the most by an infection caused in animals such as bronchitis virus (IBV) in chickens and pigs and Feline infectious peritonitis (FIP) in cats [7–11,32].

Nowadays, at least 60 coronaviruses have been isolated and described, mainly from bats (BtCoVs). Most of the coronaviruses identified belong to the betacoronavirus group. It has been accepted that the power to flight of bats associated with the ability to migrate to regions far from the original spot has imposed a strong selective pressure for the coexistence with viruses [33–36]. Additionally, bats' immune system is known as permissive, which means that bats can act as a reservoir to coronaviruses without developing the disease [37–40]. Bats, at the same time, could act as a carrier to 10 up to 17 α-coronaviruses and 7 up to 12 β-coronaviruses with the potential to jump to humans passing interspecies barrier causing disease [41]. To corroborate that,

Table 1
Human coronaviruses (hCoV) related-symptoms and their case fatality rates.

hCoV	Case fatality rate	Symptoms	Refs
SARS-CoV	9.6%	Fever Myalgia Headache Malaise Chills Nonproductive cough Dyspnea Respiratory distress Diarrhea	[42,56,113]
MERS -CoV	35.5%	Fever Cough Chills Sore throat Myalgia Arthralgia Dyspnea Pneumonia Diarrhea and vomiting Acute renal impairment	[98,113]
SARS-CoV-2	6.8%	Fever Cough Chills Myalgia Arthralgia Dyspnea Pneumonia Diarrhea and vomiting	[9,111,113]

long-term studies by genome sequencing revealed nucleotide similarity between coronaviruses found in humans and bats using the same cell entry, the Angiotensin-Converting Enzyme 2 receptor (ACE2) [38]. These studies [33–41] helped to track back the hCoVs to bats. For instance, it is hypothesized that the MERS-CoV evolved from a progenitor hosted in bats to infect dromedary and camels with the ability to directly infect humans [6].

3. The pandemic coronaviruses

3.1. SARS-CoV

In 2002, SARS-CoV-1 emerged in Guangdong Province, China, that spread over five continents 29 countries, leading to 8098 cases and 774 deaths in nearly September 2003 [42–44]. The SARS-CoV was the first threat imposed by hCoVs to humankind that outbreaks around the world. During the outbreak, the estimated case fatality rate (CRF) was 9.6%, and the human-to-human transmission of SARS-CoV was confirmed. On 30 January, WHO, warned by China scientific council, declared the SARS-CoV outbreak as an international public health emergency [21]. The first SARS-CoV cases occurred in employees who worked in a restaurant that handled wild mammals served as exotic food. Studies found that Chinese horseshoe bats had sequences of SARS-related CoVs and hosted a virus that shares similarities with SARS-CoV. Based on that, the origin of SARS-CoV is believed to have occurred in Chinese horseshoe bats [44,45].

The first suspected source of SARS-CoV was civets, a small mammal, due to the detection of the virus in those animals. Nonetheless, these animals are only transient hosts and found no evidence in wild civets [46]. Meanwhile, the evidence points to bats as hosts for SARS-CoV since they are permissive to SARS-CoV-like viruses [46].

3.1.1. Origin and evolution of SARS-CoV-1

SARS-CoV belongs to β-coronaviruses (Fig. S1) of *the Coronaviridae* family and is involved in zoonotic transmission and spread among humans through close contact [47]. It was later reported the first patient with SARS-CoV had prior contact with animals before developing the symptoms. The causative agent of SARS was later found in palm civets. However, strains isolated from handled market civets were transmitted from other animals. This suggests civets only as an intermediate host. Based on that, the hypothesis that the bat was the natural host of SARS-CoV came back to the spotlight [48,49].

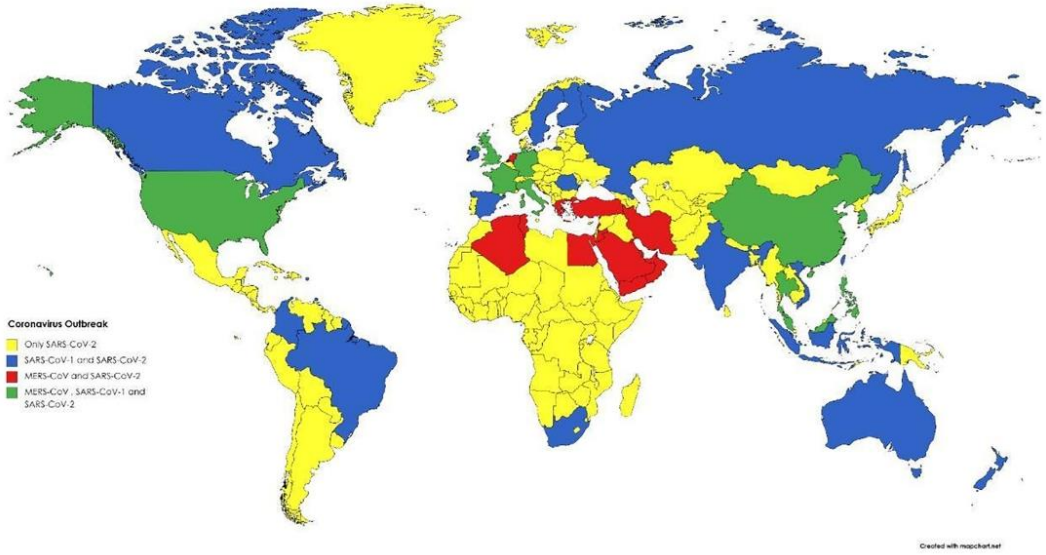

Fig. 1. Worldwide view of Coronaviruses outbreak hotspots: spread locations of SARS-CoV 1, SARS-CoV 2, and MERS-CoV around the globe. Yellow represents dissemination of only SARS-CoV-2, blue represents dissemination of both SARS-CoV-1 and SARS-CoV-2, red represents dissemination of MERS-CoV and SARS-CoV-2, and green represents dissemination of the three coronaviruses. Created with BioRender.com.

Hu et al. [50] provided new information suggesting that the horseshoe bat (*Rhinolophus sinicus*) is the natural host of SARS-CoV. The authors reached that conclusion after the isolation of SARS-like CoVs that was homologous to SARS-CoV. Moreover, evidence shows the possible origin of SARS-CoV was based on the recombination of different SARS-like coronavirus in bats since some potential recombination sites were identified around the S gene [50,51]. Rest and Mindell [52] tried to elucidate the phylogenetic origin of SARS-CoV by comparing RNA dependent RNA polymerase (RdRp) sequences between SARS-CoV and other coronaviruses. The results showed that the SARS-CoV sequence is a recombinant virus. Recently, phylogenetic analyses showed a high similarity (80%) between SARS-CoV and SARS-CoV-2 [53]. Regarding the S gene, the similarity between SARS–CoV-2, and SARS-CoV is about 76% [47,54].

Coronaviruses often undergo mutations and genetic recombination, as they have error-prone RdRP, which results in a bigger diversity, adaptive evolution, and capacity to cause disease. Previous studies have shown that SARS-CoV mutated over the 2002 and 2004 epidemic to better bind to its cellular receptor (ACE2) and replication in human cells, enhancing virulence [55]. The S1 subunit of S protein has a receptor-binding domain (RBD) involved in the direct interaction with the ACE2 receptor [47,53–55].

3.1.2. Pathogenicity

During the SARS-CoV epidemic in 2002, patients usually presented fever, myalgia, headache, malaise, chills, cough, dyspnea, and respiratory distress generally 5 to 7 days later, resulting in death. In some cases, the gastrointestinal tract, liver, kidney, and brain [56]. SARS-CoV infection of the lungs leads to diffuse alveolar damage, epithelial cell proliferation, and an increase in macrophages [57,58].

The high transmission efficiency of the SARS-CoV occurs because it binds to a target (ACE2) on cells that are abundantly expressed, including pneumocytes in the respiratory system. The virus enters and replicates in these cells. Thus, mature virions are then released to infect new target cells [47,52]. SARS-CoV-1 has an incubation period of ~5 days, and 95% of patients develop the disease within 13 days of exposure [46]. SARS-CoV was reported to cause the respiratory system and the gastrointestinal and other organ systems [56]. This is because the SARS-COV human receptor ACE2 is abundantly expressed in the lungs and small intestine [55,57,58].

SARS-CoV has unique pathogenesis because it causes upper and lower respiratory tract infections [55]. Common early symptoms are fever, chills, coughing, malaise, myalgia, headache, and less common symptoms, including diarrhea, vomiting, and nausea. In some cases, not common, SARS-CoV is associated with thrombotic complications and hematologic manifestations [42]. Abnormal chest X-rays are detected in roughly 60% of patients infected with SARS-CoV. It was reported that 20–30% of patients infected with SARS-COV require intensive care and mechanical ventilation [59–61]. In addition, at that time, it was noticed the SARS-CoV had developed high stability in aerosol and other surfaces, which had improved its transmissibility [62,63].

3.2. MERS-CoV

The MERS-CoV was primarily identified in Arabian Peninsula in 2012 as the major agent of a severe respiratory condition with a high case fatality rate (CFR) of ~35% (Table 1) [24]. Saudi Arabia was the first country to report MERS-CoV and the hotspot to its outbreak. MERS-CoV has officially 2279 laboratory-confirmed cases with 806 associated deaths in 27 countries (Fig. 1) [23,24,42,48,64,65]. Nowadays, there are yet reported cases of MERS-CoV infection. For example, WHO [24] has reported nine confirmed infection cases by MERS-CoV with five deaths from April to September 2020. It is proposed that during replicating the genome, the mutation rate of MERS-CoV is 4.81×10^{-4} substitutions per site per year [65,66]. MERS-CoV has the same genome size and produces the same proteins (Fig. 2) of SARS-CoV, which will be in-depth, discussed later [67].

During the infection process, the S glycoprotein plays a central role in cell recognition, attachment, cell entry, and infection [27,28]. Structurally, the S protein is a trimetric protein with two subunits, S1 and

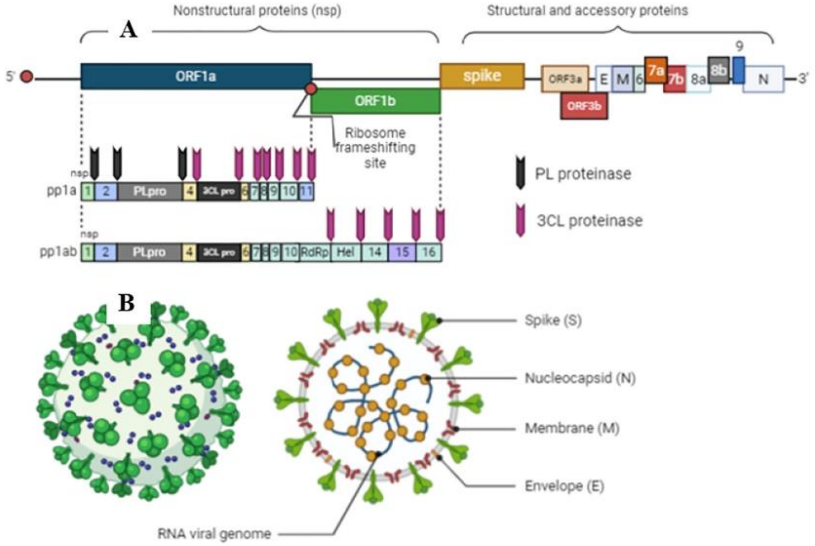

Fig. 2. Schematic diagram of coronaviruses genome and structural proteins of viral particles. A. Genome of coronaviruses produces non-structural proteins (nsp), such as RNA-dependent RNA polymerase involved in genome replication and two proteases involved in polyprotein processing, and structural and accessory proteins involved in composition of viral particles. B. The Genomes of coronaviruses also produce four structural proteins with significant roles in transmission and pathogenesis: spike (S), envelope (E), membrane (M), and nucleocapsid (N). Created with BioRender.com.

S2, in each monomer (Fig. 3A). The S protein from MERS-CoV binds to the cellular receptor dipeptidyl peptidase 4 (DPP4/CD26) driven by S1. At this point, the MERS-CoV infection differs from that presented by SARS-CoV and SARS-CoV-2, which employ interaction with ACE2 receptor (Fig. 3B). SARS-CoV-2 is the only known CoV that could use both ACE2 and DPP4/CD26 receptors. The second step of infection is the same for the three pandemic coronaviruses, which involve the viral membrane and host membrane fusion and virus arrivals into the cytoplasm [64]. The replication process inside the cytoplasm will be later discussed in this review.

3.2.1. Origin and evolution of MERS-CoV

Since the MERS-CoV outbreak, research worldwide has put together pieces of information to decipher the puzzle about MERS-CoV origin, pathogenicity, and transmissibility. The zoonotic event played a non-trivial part in MERS-CoV evolution and transmission [66]. Because a serosurvey study revealed that dromedary camels have antibodies against MERS-CoV, indicating that MERS-CoV has circulated in that area a long time before the outbreak. Harbor viruses that are closely genetically related to humans, the dromedary camels, constitute a source of pathogens that can be harmful to humans [68–72]. However, as to other coronaviruses, bats are believed to be the primary source of MERS-CoV origin and still works as a reservoir host of MERS-CoV. Genome sequence data revealed a similarity of 99.2–99.5% between bat and human MERS-CoV [23,48,68,69,71].

By analyzing 5030 fecal specimens from bats, Annan et al. [73] strongly suggested MERS-CoV likely comes from bats. Studies employing phylogenetic analysis showed two main MERS-CoV clades: A and B hosting camel and human MERS-CoV. MERS-CoV strains from humans from Jordan and Saudi Arabia belong to clade A. In contrast, clade B, divided into five groups (I to V), hosts MERS-CoV collected of humans from other regions and camels. The MERS-CoV from bats and hedgehogs forms a basal paraphyletic group to all camel and human MERS-CoV clades. This result suggests that, in addition to bats, hedgehog could also be the ancestor of camel and human MERS-CoV [36,66].

Additionally, it is known that recombination events can create new viral strains capable of infecting new hosts and evading immune responses from hosts. Overall, those mutations affect the S protein involved in both processes. There is evidence that recombination events on clade B groups, involving camel MERS-CoV and human MERS-CoV of different groups (I to V), produced different recombinant virus types (1 to 7) [66]. It was reported these recombination events might happen frequently and involving group V might happen broadly. Additionally, multiple recombination events indicate double infection, persistent infection, and superinfection during the transmission history [66].

The most recent common MERS-CoV ancestor was estimated as of March 2012, consistent with initial case detection and the beginning of the outbreak [74]. The genetic mechanisms underlying cross-species jumping remain poorly understood. However, it was reported that mutations on MERS-CoV S protein changed its surface charge,

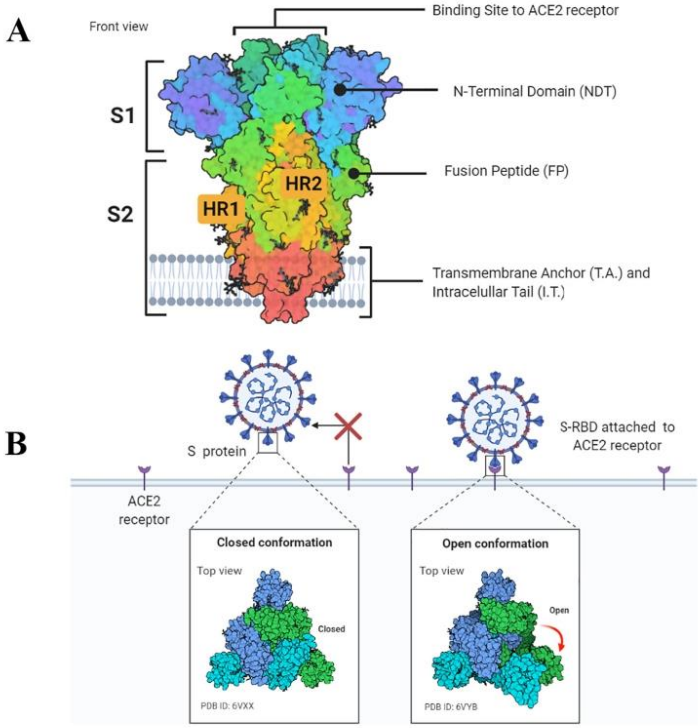

Fig. 3. Schematic representation of the SARS-CoV-2 spike protein. A. Spike protein consists of the S1 and S2 units. In the S1 subunit, there is an extracellular N-terminal domain and a receptor-binding domain which play a role in the viral entrance into the cell through ACE2 receptor. In the S2 subunit, there is the fusion protein (FP), heptapeptide repeat sequence 1 and 2 (HR1 and HR2), as well as the transmembrane domain and a short C-terminal domain. B. Open or closed three dimensional conformation of S protein implicate in the binding of cell receptor ACE2. Created with BioRender.com.

enhancing cross-species jumping and viral entry on cells through suboptimal DPP4 receptor [75–78].

The higher number of positive selections in the S protein is completely comprehensive given the central role played by S protein in MERS-CoV infection [66]. Most of the positive selection sites were in the RBD of S protein. RBD has two portions, one binding region, and one core region. Both are crucial to the virus recognizing and entering host cells and it. It was observed at two sites of mutations in the binding region of RDB, suggesting these amino acid substitutions might improve MERS-CoV binding capability to bind to different host cells and thus facilitate its cross-species transmission [66]. Chen et al. [79] state that most of the recombination and sequence diversity is in the S gene. Those changes may affect the structural conformation of RBD and the interactions with cognate human receptors.

As discussed before, the receptor used by MERS-CoV in the cells is different from that employed by SARS-CoV and SARS-CoV-2. SARS-CoV and SARS-CoV-2 employ the ACE2 receptor, MERS-CoV picked DPP4 [80,81]. As SARS-CoVs, the S1 C-terminal (CTD) of MERS-CoV acts as RBD, with two domains: the core and receptor-binding motif (RBM) [79,82–84]. S1-CTD from MERS-CoV is structurally similar to that from SARS-CoVs, composed of a major β–sheet scaffold. However, while in SARS-CoVs, the RBM has many unordered structures forming loops, the MERS-CoV RDM mainly contains stranded β–sheets. It is postulated these structural differences were responsible for receptor-specificity between viruses [85].

3.2.2. Pathogenicity

The high similarities among the DPP4 from humans, camels, horses, and bats allow MERS-CoV to infect them. However, mutations in the DPP4 receptor from mice, hamsters, and ferrets prevent MERS-CoV infection [86–88]. MERS-CoV isolates sampled from humans and camels are highly similar to each other and use the human DPP4 receptor efficiently [89]. Studies revealed that these mutations change critical residues in mouse DPP4 compared to humans DPP4 affecting host specificity of MERS-CoV. Some of these residues mapped in mouse and hamsters are different from humans; two residues 288 and 330 in mouse DPP4, and five in 291, 295, 336, 341, and 346 in hamsters DPP4 lead to the incompatibility of DPP4 from mouse and hamster with MERS-CoV S proteins thus preventing the infection [89].

Interaction between the residues 330 of DPP4 with MERS-CoV RBD Y499 has been suggested as a key interaction [82,83]. Besides that, Peck et al. [87] observed that the residue 330 mutation knocks out an NXT glycosylation motif in mouse DPP4. These results show that glycosylation acts as a determinant of DPP4-mediated host range and inhibits infection by MERS-CoV. Other nonpermissive hosts (ferret, hamster, guinea pig) also have a nonconserved glycosylation site in the region of DPP4 that interacts with the MERS-RBD. Peck et al. [86] demonstrate that glycosylation is an essential barrier to MERS-CoV infection, yet other species-specific determinants are also responsible. Elegant experiments involving mutations of these residues from mice and hamsters to those correspondents in human DPP4 allow the MERS-CoV to infect mice and hamsters [82–84,86,88,89]. As expected, S protein is a crucial determinant factor of host range MERS-CoV and alteration either on its structure or in its receptor dramatically affects virus success.

Overall, people infected and confirmed by a laboratory test for MERS-CoV were around 49 years old; 65% are males. The hospitalization time for patients to come back healthy was about 41 days [90,91]. MERS-CoV has a median incubation period of 5.2 days, reaching 12 days in normal people conditions, and a more extended period in patients immunocompromised and comorbidities [92,93]. The onset of symptoms to death 11.5 days. Even nowadays, the morbidity is still 36% (WHO, 2020), with more than 50% of patients showing viral accumulation on lungs revealed by radiography of the chest. Generally, the high viral loads on the lungs lead to acute respiratory distress syndrome [92,94,95].

The clinical manifestations of MERS-CoV could be in three forms. First, asymptomatic. Second, flu-like symptoms, cold, fever, cough, dyspnea, pneumonia, myalgia, diarrhea, vomiting, abdominal pain, chills or rigors, and malaise (Table 1). Third, acute progressive infection leading to acute respiratory distress syndrome, septic shock followed by multiorgan failure, and death [96–101]. Nearly 50% of patients developing either form 2 or 3 of MERS-CoV infection require intensive medical care in the intensive care unit (ICU). From those, up to 70% typically go to mechanical ventilation [100,101].

It is reported 50% of patients infected by MERS-CoV develop an atypical symptom called Acute Kidney Injury (AKI), which is a sudden kidney failure or damage. From those, up to 70% will pass by renal replacement therapy given the damage caused by MERS-CoV to kidneys [102–105]. MERS-CoV has been detected in upper and lower respiratory secretions at relatively high virus load and fecal samples [106,107].

3.3. SARS-CoV-2

The outbreak of SARS-CoV-2 leading to the world fully spreading the COVID-19 caused more than 2,041,232 million deaths by now [108,109]. After that, many other countries reported increasing COVID-19 cases [110] (Fig. 1). Since WHO declared a pandemic status in March 2020, the global spread rate has accelerated, and confirmed cases are approaching 95,553,377 million infected people [109]. The SARS-CoV-2 belongs to the beta-coronavirus (2B lineage) of the Coronaviridae family, with a positive-stranded RNA genome composed of 29,800 nucleotides in length allowing the production of the same set of proteins seen in other coronaviruses (Fig. 2) [111].

The genome of SARS-CoV-2 is closely related to SARS-CoV-1 (79%) and to a lesser extent of MERS-CoV (50%) (Supplementary Fig. 1B), deadly human coronavirus described in recent years -*Coronaviridae Study Group of the International Committee on Taxonomy of Viruses* [112]. Although the infection mechanism between these three coronaviruses is similar, the genome sequence reveals some differences [113]. All these epidemics scenarios imposed by coronaviruses have threatened human health, social, and economic context, leading to catastrophic consequences.

3.3.1. Origin and evolution of SARS-CoV-2

SARS-CoV-2 belongs to the Beta-coronavirus B lineage, the same evolutionary branch of SARS-CoV-1 and MERS-CoV, conferring several structural, genetic, and pathogenic characteristics (Supplementary Fig. 1A) [114–116]. Although there is a lack of conclusive evidence, some studies have proposed a plausible explanation for the origin of SARS-CoV-2. The full-length genomic sequence analysis, distinctive phylogenetic distances on the major clade of SARS-CoV-2 provide a clue to the evolutionary relationships among them [116]. However, SARS-CoV-2 shares 79% sequence identity to SARS-CoV-1 and only 50% to MERS-CoV in the genomic sequence. In our genetic distance analysis of the S gene (Supplementary Fig. 1B), SARS-CoV-2 (NC_045512.2) were compared against SARS-CoV-1 (NC_004718.3) and MERS-CoV (NC_038294.1). The evolutionary distance analysis showed considerable differences between SARS-CoV-2 and MERS-CoV, mainly in the N-terminal domain and RBD nucleotide sequence, which are involved in recognizing the cellular receptor (Supplementary Fig. 1B) [117].

Zhou et al. [115] demonstrated SARS-CoV-2 likely evolved from naturally SARS-like coronavirus colonizing bats. Results indicated the closest relationship of SARS-CoV-2 with batCov RatG13 (from *Rhinolophus affinis*), supporting the hypothesis that Bats are a reservoir for SARS-CoV-2 progenitor. However, although these two coronaviruses are identical (96% of genome identity), RaTG13 S protein diverges in the RBD, suggesting it may not bind to human ACE2 [118]. Pangolins (*Manis javanica*) was considered the probable reservoir since the pangolin's coronaviruses exhibit high similarity with RBD of S protein from SARS-CoV-2 [119].

Still, neither bat nor pangolin coronaviruses have polybasic cleavage sites, sequence responsible for determining viral infectivity and host range, which raises the question about the possibility of these SARS-

CoV-2 progenitors [120]. Mutations, insertions, and deletions can occur near the S1–S2 junction of S protein from SARS-CoV-2, increasing the probability of polybasic cleavage site acquisition, enhancing transmission crossing the mammalian-human line, and improving human-to-human [121] (Fig. 3). Once acquired, adaptation was fixed as a new feature in the SARS-CoV-2 genome and enabled the rapid spread of SARS-CoV-2 to pandemic status.

3.3.2. Pathogenicity

Respiratory air droplets, aerosol, direct contact with contaminated surfaces, and fecal-oral transmission drive human coronaviruses. SARS-CoV-2 reaches the host via the respiratory tract, alveolar epithelial cells, vascular endothelial cells, and alveolar macrophages are the primary targets of the viral entry (Supplementary Fig. 2) [122].

Cell entry of SARS-CoV-1 and SARS-CoV-2 depends on the S protein binding with specific cellular receptors, ACE2 and TMPRSS2, playing a crucial role in the entry of both viruses into the host cells [28]. Briefly, the S protein of SARS-CoV-2 consists of two subunits, the S1 domain, and the S2 domain. SARS-CoV-2 utilizes RBD of the S1 domain to bind to the cellular receptor ACE2, which stimulates the TMPRSS2 to cleavages protein S at the S1 and S2 sites, allowing the cell membrane fusion and viral entry [27] (Fig. 3). Later, the role of S protein from three pandemic viruses in cell entry will be more in-depth discussed.

The clinical symptoms of SARS-CoV-2 infection are similar to SARS-CoV-1 and MERS-CoV infections described, being pneumonia the most described in the studies with abnormal chest CT examinations. However, patients infected with SARS-CoV-2 rarely have significant upper respiratory signs indicating the targeted cell may exist in the lower respiratory tract. Indeed, it has been reported SARS-CoV-2 infection mostly triggers deep airway inflammatory reactions and alveolar damage [123]. For SARS-CoV-2, the most common symptoms are cough, dyspnea, chest pain, myalgia/arthralgia, diarrhea, nausea, vomiting, and common systemic symptoms observed: fever, chills, fatigue [124]. Also, SARS-CoV-2 infects several human tissues, such as the lung, intestinal tract, pharynx, heart, kidney, liver, brain, and blood [125,126]. Nevertheless, further studies are necessary to evaluate the effects of SARS-CoV-2 in extra-pulmonary infection sites.

The immune system may play a critical role in the severity of COVID-19. SARS-CoV-2 infection of pneumocytes induces a "cytokine storm", which is an activation cascade of auto-amplifying cytokine production [116]. Local inflammatory responses promote the release of cytokines, including transforming growth factor-β1 (TGF-β1), tumor necrosis factor-α (TNF-α), interleukin-1β (IL-1β), IL-6, IL-2, IL-7, IL-10, granulocyte colony-stimulating factor (G-CSF), monocyte chemotactic protein (MCP), TNF-α and other chemokines to recruit leukocytes for the inflammation region leading to a multiple organ functional failure [116].

A recent study showed a plausible answer for this event: the direct SARS-CoV-2 infection of vascular endothelial cells with concomitant accumulation of inflammatory mononuclear cells in multiple organs in patients with severe COVID-19 [127]. Another plausible point is the involvement of SARS-CoV-2 infection with multiorgan failure due to the ACE2 and TMPRSS2 expression distribution in several human organs [125].

Another aspect is the higher proportion of macrophage and neutrophils observed in the patients with severe symptoms than those with mild symptoms and the chemokine related to these cells [128]. Interestingly, Zuo et al. [129] described the formation of neutrophil extracellular traps (NET) inside the microvessels of severe disease patients that could be a potential factor for severity.

4. Molecular biology of coronaviruses

4.1. Coronaviruses genome organization

Viruses classified as coronaviruses possess a single-stranded, non-segmented, large, and positive-sense RNA. The positive-sense RNA is an advantage acquired over the evolution process that mimics the cellular mRNA making its translation easier. Like cellular mRNAs, coronaviruses RNA possesses both 5′ cap and a tail at 3′ end [130,131] (Fig. 2A). The viral RNA is way larger than cellular mRNA and even compared to other viruses such as picornavirus (four times) and flavivirus (three times). The larger size of the coronaviruses genome varies from 27.3 to 31.3 kb, classified as the bigger RNA molecules are known until now [132].

Coronaviruses genome holds many ORFs (Fig. 2A), another difference compared to cellular mRNA. Precisely, the coronaviruses genome has 10 ORFs. The two largest ORF1a and ORF1b are responsible for producing up to 16 non-structural proteins (nsp) (Fig. 2A). Among those are PL proteinase, 3CL protease, RNA-dependent RNA polymerase (RdRp), and Helicase. The PL proteinase and 3CL protease are involved in polyprotein post-translational processes (Fig. 2A) [67]. The other ORFs are responsible for producing structural and accessory spike glycoprotein (S), an envelope protein (E), membrane attached protein (M), and nucleocapsid protein (N) (Fig. 2B). The genome of coronaviruses produces five canonical proteins. The RdRp at the 5′ end and S, E, M, and N at the 3′ end. This is a common sequence that RNA is translated following the sequence 5′- RdRp-S-*E*-M-N-3′ (Fig. 2A) [130–132].

Holding a positive-sense RNA is an excellent advantage to any viruses. For coronaviruses, it is not different. If only the RNA entry in a permissive cell the infective process starts. These processes have been shown in many studies over the years [131,133–135]. The most recent example of that is the vaccine produced by companies Pfizer and BioNTech (BNT162b2). BNT162b2 is a lipid nanoparticle–formulated, nucleoside-modified positive sense-RNA encoding membrane-anchored SARS-CoV-2 full-length S protein. Given the positive sense, when RNA is absolved by the cell is promptly translated to viral S protein, which is exposed or externalized by the cells and recognized by the immune system producing antibodies against it [136].

During coronaviruses infection, the genome acts as cellular mRNA producing the larger replicase protein. The RNA from coronaviruses also possesses an important site dedicated to a ribosomal frameshifting event. After that, there is a ribosomal frameshifting site [137] (Fig. 2A). Ribosomal frameshifting in the displacement of ribosomal frames, also known as translation recording, is a biological phenomenon that results in multiple protein production from a single mRNA molecule (Fig. 2A). Although it is common in viruses, it goes beyond them. Organisms from all three kingdoms employ frameshifting to regulate gene expression [137–142]. Next, as usual, the genome is a model for protein synthesis, RNA replication, and assembly, producing new virus particles [143].

4.2. Virion particles

Coronavirus particles are spherical, pleomorphic (Fig. 2B) with diameters varying from 80 to 120 nm [144,145]. Attached to it membranes are found two types of the spike. One larger with projection 17–20 nm long produced S protein (Fig. 2B), and a smaller one 5–10 nm long today known as the hemagglutinin-esterase (HE) found in a subset of coronaviruses [144,145]. Recently, the development of advanced microscopy techniques has clarified coronavirus morphology.

Ng and collaborators [146] catch three-dimensional (3D) images from SARS-CoV moving out from the Vero infected cell. By employing scanning electron (SEM) and atomic force (AFM) microscopies, it was possible to notice the small cauliflowers-like structures assumed by viral particles. To see the outside of the virus is not that hard. The problem is to evaluate the inside of a viral particle. To go that far, virion particles have been treated to nonionic detergents, allowing them to look inside the coronavirus particles. It was revealed that coronaviruses possess helical symmetric nucleocapsids, which is not common to positive-sense RNA viruses but for negative-sense RNA viruses. This is a great point of discordance among virologists. However, a few published studies are reporting that, but only we know is that more studies are required to obtain a clear picture of coronavirus virion particles.

5. The coronaviruses proteins

5.1. Membrane protein (M)

The M protein (Fig. 2B) is one of the three main structural proteins in coronaviruses. It is responsible for the viral particle conformation after assembling [147–150]. The M protein holds a small N-terminal domain extended to the outside of the viral particle, which is important to interact with the endoplasmic reticulum during infection [151]. Right after the N-terminal domain, there are three large, highly hydrophobic transmembrane domains followed by an even larger C-terminus domain, which stands inside the viral particle.

The M protein has regular conservation into the coronavirus family. The same is not applied to the coronaviruses groups. A consensus in all groups is that M protein has multiple-glycosylated stages. The preglycolysated stage of M proteins ranges in size from 25 to 30 kDa. However, multiple glycosylations could lead to a high molecular Mass of M protein [152]. Neuman et al., [147] reported the ability of M protein to oligomerizes to form larger structures. In the same study, the authors revealed two stages: the larger and compact. In the larger stage, M protein forms a structure 8 nm long. In contrast, the compact form has structures 6 nm long. The oligomerization stages of M protein are involved in many virion particle assemblies and even genome protection [147,153–155]. The interaction between transmembrane domains drives the interaction between M proteins; this interaction is important to exclude any leftover host membrane during the release of viral particles [147,156].

5.2. Envelope protein (E)

The E (Fig. 2B) is the smallest, membrane-integral, and less known structural protein from coronaviruses. One quite intriguing point is that E protein accumulates the most in the infected cells during viral replication. Still, only a very small portion is inserted in the new viral particle. The function of the excess of E protein in replication is obscure [157,158]. Most of E protein is localized outside the viral particle. This is because it is involved in the viral attachment to the ER and Golgi apparatus controlling virus intracellular traffic [158–160]. Although not known how the E protein is involved in the viral titers, viral particle production, and maturation [159,161–168].

5.3. Nucleocapsid protein (N)

The N (Fig. 2B) protein holds a molecular weight varying from 43 to 50 kDa, larger than M and E proteins but far smaller than S protein. It has a quite essential function to coronaviruses. Interacting with the RNA genome forms a helical structure like a necklace with beads providing stability to the RNA genome [169]. N protein sequence is divided into three domains. The highest part of the molecule has great amounts of Lys and Arg residues leading to a positive charge, which is involved in the interaction with the negative charge of viral RNA. This portion comprehends domains 1 and 2. For example, it was identified that the RNA bind ability of MHV N is attributed to domain 2 [169–171].

An unusual feature of N proteins in the phosphorylation. N protein from some but not all coronaviruses are phosphorylated. Some phosphorylation happens in a Ser and others in the N residues [172,173]. The biological function of phosphorylation in the N until today is obscure. However, the hypothesis is that the phosphorylation helps N protein to recognize only viral RNA. Chen et al. [172], employing Mass spectroscopic analysis and surface plasmon resonance, brought some information about the biological importance of N phosphorylation. The nonphosphorylated and phosphorylated N protein has the same ability to bind to viral RNA. However, the phosphorylated N protein binds only to the viral RNA. In contrast, the nonphosphorylated binds to both viral and non-viral RNA. These experiments by Chen et al. [172] revealed one biological effect of phosphorylation of N protein, which is the recognition exclusively of viral RNA.

5.4. Spike protein (S)

Now, after a brief explanation about coronaviruses and their proteins. It will be deeply discussed about the protein that is the focus of the review and plays essential roles during coronaviruses infection, Spike glycoprotein (S). The S protein is the third protein component and most abundant in the viral envelope (Fig. 2) [174]. The S protein is the larger protein from coronaviruses with about 180–200 kDa [174]. It has a larger N-terminal region (90% of protein) exposed outside the viral envelope and a shorter C-terminal region inside the viral envelope. Between N- and C-terminal regions, there is a transmembrane section liking both N- and C- regions (Fig. 3A) [174].

The S protein possesses high-level glycosylation on its structure. Before post-translational processing, the monomeric structure of S protein that inserts carbohydrates on its structure is about 128–160 kDa. After the glycosylation process, the size of S protein ranges between 180 and 200, which indicates a high amount of carbohydrates are inserted in its structure, most of them N-linked [175]. It is proposed that the biological function of glycosylation in the S proteins is to evade the host immune system during infection [176,177]. For example, a study from Delmas and Laude [177] with the S protein from porcine transmissible gastroenteritis virus revealed the glycosylation process coincides with the translation. The authors also showed that the glycosylation precedes the S protein trimerization. The glycosylation of TGEV S is essential to correct the folding of monomers [177].

S protein is still a huge protein even in the monomeric stage with 1273 amino acid residues. The first 13 amino acids form the signal peptide in the N-terminal site targeting the protein from the endoplasmic reticulum to the viral envelope. The S1 subunit goes from 14 to 685 amino acid residues. The S2 subunit starts at the amino acid 686 until the 1273 residue. Both regions are involved in cell recognition and entry (Fig. 3A and Supplementary 3) [178,179]. Like other proteins, the S protein is synthesized as an inactive precursor present in the viral envelope. During cell infection, the S protein is cleaved by a cellular protease releasing the S1 and S2 subunits activating it and allowing the membrane fusion and virus entry (Fig. 3A) [28,180,181]. This will be discussed later in this review.

5.4.1. The S1 subunit from S protein

The S1 subunit is smaller than the S2 subunit but has a quite relevant coronaviruses function (Fig. 3A and Supplementary 3). The S1 subunit is responsible for recognizing the cell receptor to allow virus entry into the cell cytoplasm. The S1 subunit hosts the RBD responsible for binding to ACE2 in the portion where the aminopeptidase cleavage point is present [181–183]. The S1 region also contains the N-terminal (NTD) and C-terminal (CTD) domains, both involved in the RBD recognition (Fig. 3A and Supplementary 3). For comparison purposes, the SARS-CoV-2 S1 CTD has more amino acid residues (21 aa) directly involved with the ACE2 interaction that SARS-CoV S1 CDT does (17 aa). Additionally, the mutational analysis revealed amino acid substitution from I472 in SARS-CoV S1 CTD for F486 SARS-CoV-2 S1 CTD strength interaction with the ACE2 Y83, the establishment of aromatic-aromatic interaction (15, 16). Yet, the substitution of E484 in SARS-CoV-2 S1 CDT instead of a P470 residue in SARS-CoV S1 CTD increases the ionic interaction with ACE2 leading to higher affinity to the receptor (Fig. S3) [182,183].

The RBD hosted by the S1 domain is critical for recognizing the ACE2 receptor by S protein. There are nine residues fully conserved in all coronaviruses involved in the ACE2-RBD interaction. Given the importance of RBD for the coronavirus, it becomes a great target for the action of neutralizing antibodies [27,28,180,182,183]. Our research group has recently performed a molecular docking with synthetic peptides against S protein from SARS-CoV-2 [184]. Out of eight, two peptides showed up as promising the most to bind toward S protein. Indeed, the peptides do not interact with the RBD domain. However, the interaction with S protein led to conformational changes in the S protein structures. The docking simulation led to a wrong interaction with the ACE2 receptor,

hence inhibiting virus entry in the cell [184]. In another study, Souza et al. [185] designed four peptides from the amino acid sequence of the ACE2 receptor. Those peptides specifically targeted the RBD domain from S protein. After interaction with peptides, RBD presented changes in the conformational structure impairing the correct interaction with ACE2 protein, suggesting that peptides could prevent cell infection by SARS-CoV-2.

5.4.2. The S2 subunit from S protein

The S2 subunit from the S protein hosts many important domains for S protein function. The first domain is the fusion peptide (FP) from 788 to 806 amino acid residues (Fig. 3A and Supplementary 3). FP is a short fragment highly conserved in the coronavirus family. Its composition is essentially made by apolar residues such as Gly and Ala, all-important during the membrane fusion activity of the S2 subunit during viral infection (Fig. 3A and Supplementary 3) [186] [13,23].

Right after the FP domain, two sequences called heptapeptide repeated sequence 1 (HR1) (912–984 residues) and heptapeptide repeated sequence 2 (HR2) (1163–1213) with, respectively, 72 and 50 (Fig. 3A and Supplementary 3) [187]. Both HR1 and HR2 are located at the N-terminus portion of the transmembrane domain (TM) and follow the same structure HPPHCPC where H designates a hydrophobic residue, P regards a polar or hydrophilic, and C is any other charged residue. The HR1 and HR2 are essential to the viral fusion and entry function of the subunit in the cell [187].

The HR1 domains assemble to form a homotrimeric structure with highly conserved hydrophobic surfaces. These hydrophobic surfaces are exposed to the outside of the 3D structure of the S2 subunit to interact with the HR2 domain. In turn, HR2 forms a rigid helix followed by a highly flexible loop in the face that interacts with the HR1 domain. The interaction between HR1 and HR2 domains is strong and supported by hydrophobic and aromatic interactions forming a bigger domain fusion core region [188].

The HR1 and HR2 are essential to infection establishment by hCoVs and are thus highly conserved [188]. Given that, these domains are targeted continuously by potential antiviral molecules. That happens because another critical target, the RBD from the S1 domain of S protein, is highly variable, so it is hard to develop a drug toward RBD. But the high conservation of HR domains makes them a great target [186–189]. For instance, Xia et al. [189] have developed an HR2-derived peptide that targets the HR1 region and inhibits cell infection by human coronaviruses.

6. Biological roles of the S protein

The S protein is the most important factor involved in viral infection. Because of that, it stands exposed on the viral envelope surface. It is a trimetric protein essential to receptor recognition, cell attachment, membrane fusion and virus entry [28,38,54,80,83,85,126,179,182,184,191]. Given S protein roles, it is present in all kinds of hCoVs and other viruses such HIV and Ebola [191] but with other names.

The S protein possesses two conformational states (Fig. 3B). The conformational dynamics of S protein is due to the flexibility of NTD and RBD. The first is the closed state where the RBD domain cannot recognize the ACE2 receptor (Fig. 3B). The closed state is also called perfusion state because it precedes membrane fusion [192]. The closed state (prefusion) of beta coronaviruses was determined by cryo-electron microscopy [193]. In general, the closed state of S protein from coronaviruses is similar to the, considering higher complexity, hemagglutinin from influenza virus. In the closed state conformation, the RBD domain is trapped into a pocket formed by the NTD region and RBD itself, inhibiting the interaction with the ACE2 receptor [85,193].

Additionally, in the closed state, the S1 heads stand on top of S2 subunits to avoid the S2 conformational transitions. In the S2 domain, the HRs domain assumes the helices form to stabilize the S2 subunit. In the coronavirus fusion HR-1 domain, the hydrophobic residues support the formation of a small loop and helix, which are buried inside the prefusion structure. The proteolysis is essential for the conformational transition of S2, one at the S1/S2 border and the other at the N-terminal region [194,195]. The S protein moves to the second stage called an open state (Fig. 3B). In the open state, the RBD is now exposed outside the S protein structure and can recognize and bind to the cellular receptor (Fig. 3B) [27,28,67]. In this stage, the RBD dynamics is modulated by proteolysis allowing the interaction with the ACE2 receptor. After interaction by RBD-ACE2, the virus will start the process to enter within the cell, and the S protein starts to change to another stage called post-fusion, leading to the viral and cellular membrane fusion [27,28,67,189,193–195]. Recently, Wang et al. [196] reported the S protein could have an alternative route to enter cells. Rather than interact with RBD, S protein from hCoVs could interact with a CD147, which is a transmembrane glycoprotein from the immunoglobulin superfamily. It is known for the CD147 involvement in tumor development, bacterial, virus, and *Plasmodium* invasion and infection [196–198].

Wang et al. [196] revealed Vero E6 and BEAS-2B cell lines either lacking or blocked to CD147 or blocking presented no signal of SARS-CoV-2 amplification. Additionally, the expression of CD147 in SARS-CoV-2 non-permissive human cells allowed virus entry and infection. The authors also found high viral loads in the mice lungs expressing human CD147, but not in wild type mice. Indeed, the results presented by Wang and co-authors [196] are quite interesting.

In the same way, since November 2020, a new cellular receptor came up as hosts in facilitating SARS-CoV-2 entry. Those receptors either enhance the ACE2-mediated entry of SARS-CoV-2 or act as alternative receptors for SARS-CoV-2 entry. SARS-CoV-2 could employ these alternative receptors to enter the cell with a low expression of ACE2. For instance, the tyrosine-protein kinase UFO (AXL) acts as a receptor by interacting with the NDT domain of S protein, demonstrated by in vitro cell culture model and COVID-19 patients samples [201]. Another in vitro model study showed the high-density lipoprotein (HDL) scavenger receptor B type 1 (SR-B1) as a facilitator of ACE2-dependent entry of SARS-CoV-2 through the interaction of the S1 subunit. Blocking the S protein interaction with a specific monoclonal antibody against cholesterol/HDL inhibits the HDL-enhanced SARS-CoV-2 infection [202].

Cantuti-Castelvetri et al. [203] and Daly et al. [204] revealed that neuropilin-1 (NRP1), which is known to bind furin-cleaved substrates, potentiates SARS-CoV-2 infectivity. The NRP1 protein is highly expressed in the respiratory and olfactory epithelium, with the highest expression in endothelial and epithelial cells. Those cells present a low expression of ACE2 receptors, which is why SARS-CoV-2 employs this protein to enter the cell [203,204]. Amraei et al. [205] reported that CD209L and CD209 are members of the C-type lectin superfamily and could act as mediators of SARS-CoV-2 entry cell and increase viral pathogenesis. The CD209L is highly expressed in human type II alveolar cells, lungs, and liver, whereas CD209 protein is expressed in alveolar macrophages. Both CD209L and CD209 interact with the RBD of S protein from SARS-CoV-2 to enter cells. The mechanism of these proteins is quite similar to ACE2-mediated cell entry by SARS-CoV-2.

Recently, in an elegant experiment, Tang et al. [206] revealed a new candidate molecule used by SARS-CoV-2 to enter cells. ACE2-knockout mice are not protected from SARS-CoV-2 infection. The authors showed that the transferrin receptor (TfR) is the target by S protein to allow SARS-CoV-2 entry on cells. Even though new finding supports alternative molecule employment to invade cells by SARS-CoV-2, little is known about the role of these receptors for SARS-CoV-2 entry on cells. Based on that, the discussion below will be mainly focused on the ACE2-S protein interaction, which there more information allowing a deeper discussion has been supported by the literature.

Most of the CoVs enter cells by interacting with the RBD domain from S protein with the ACE2 receptor [199]. The ACE2 receptor is a widely expressed protein in the cell membrane of many tissues such as lungs, heart, kidney, renal, cardiovascular, and intestine [200].

Discovered in 2000, ACE2 holds 61% of similarity with ACE. Structural analysis of ACE2 protein revealed an N- and C-terminal followed by a unique transmembrane α-helix domain followed by an intracellular portion [113]. The difference between ACE and ACE2 is the most related to their activity. At the time, ACE catalyzed the conversion of angiotensin I in angiotensin II. ACE2 acts in angiotensin II conversion in two forms: angiotensin 1–1 and angiotensin 1–9 [201]. Until the pandemic situation imposed by the coronaviruses, ACE2 moves from the shadow to light as an important protein to viral infection. Now, it is quite clear that SARS-CoV-2 and other coronaviruses employ the ACE2 to come into a cell and start an infection.

The infectious process starts when a coronavirus-infected person sneezes, releasing air droplets containing virus particles into the environment (Fig. 4). Without a social distancing, a healthy person intake, by natural breathing, the contaminated air allowing the air droplets infected with the virus to reach the lungs (Fig. S2). At that point, the S protein becomes the principal actor in the coronavirus infection by driving viral recognition and entry on cells. The S1 subunit from the S protein starts the process by promoting RBD interaction with ACE2 (Fig. 4 - 1). After the attachment of the virus supported by S protein and low pH conditions act as targets to the viral fusion of membranes [178,179,182].

After the attachment, the S protein, driven by the S2 subunit, promotes the viral fusion, which is the fusion of the viral membrane with the host cell membrane. The trigger to initiate the membrane fusion is the proteolytic action suffered by S protein after the attachment to the receptor. As a result of the cleavage, the S protein is separated into two parts, S1 and S2, by cellular proteases. Even after the cleavage, the subunit S1 and S2 remain non covalently bonded to ensure the membrane fusion follows through [202,203].

Hasan et al. [203] and Millet et al. [202] revealed that in the SARS-like coronaviruses such as SARS-CoV and SARS-CoV-2, the S protein has an uncleaved state. In contrast, other coronaviruses possess S protein mainly in the cleaved state. Additionally, the mutational analysis revealed that SARS-CoV-2 had accumulated mutations increasing the number of cleavage sites on S protein, leading to higher cleavage rates and cell entry and infectivity [202,203]. Many studies over the years [28,180] revealed host proteases involved the most in S protein cleavage are TMPRSS2 and trypsin, even for SARS-CoV and SARS-CoV-2. The S protein from SARS-CoV and SARS-CoV-2 are essentially the same. However, the high number of cleavage sites in the SARS-CoV-2 S protein might be involved in higher contagious levels of SARS-CoV-2 compared to SARS-CoV.

Back to viral fusion, the domains FP and both HR on S2 is critical to viral fusion. The cleavage of S protein exposes the FP domain, which is, in turn, inserted in the host membrane triggering the viral fusion [114,178,191]. Once anchored in the host membrane by the FP domain, the distances between viral and host membrane are dramatically reduced, and HR1 stands close to the cell membrane, and HR2 is yet anchored in the viral membrane. Now starts the last and crucial process in membrane fusion. The HR2 domain turns up toward the HR1. Both domains form a helix structure to produce a fusion core, and the viral membrane is pushed over toward the cell membrane tightly, and both membranes fuse. The virus reaches the cytoplasm. Now it is just a matter of making the cell work in virus replication. Once inside the cytoplasm, the virus hijacks cellular proteins and supplies to replicate the genome and produce thousands of new viral particles [204,205].

Inside the cell, the positive-sense RNA from coronaviruses, which works as mRNA, is released, and translated by the cellular ribosomes (Fig. 4 - 2). The first protein produced is the huge replicase polyprotein complex (Fig. 4 - 3). The positive-sense RNA is then used as a model by the replicase to produce the negative-sense RNA, the subgenomic RNAs, and thus new positive-sense RNA molecules (Fig. 4 - 4). The subgenomic RNAs were used to produce S, E, M, N proteins (Fig. 4 - 5 and 6). The proteins S, E, and M move to the ER and attach to its membrane. At the same time, the N protein interacts with the RNA molecules to form the nucleocapsid particles (Fig. 4 - 7). Now, induced by structural membrane-bounded protein, the membrane of ER suffers conformation changes to assume a spherical format with the nucleocapsid particle inside, which is the new virion particle. The new viral particle moves now out to infect new cells (Fig. 4 8–9). This is the common way of CoVs replication. S protein is not called here as a principal actor without a motive. In some cases, during CoVs, the infection can lead to the formation of syncytia [206–208].

Syncytia are giant infected cells induced by some viruses, like coronaviruses. All pandemic coronaviruses, SARS-CoV-1, MERS-CoV and SARS-CoV-2 [206–208] have the ability to induce syncytia formation. Somehow, in coronavirus infection, the host cell showed the S protein on the membrane, which is a quite important function of S protein. The S protein interacts with the ACE2 with neighboring healthy cells and thus induces membrane fusion of many cells forming giant known syncytia. By inducing the syncytia formation, the coronaviruses can continuously infect cells without moving out cells. This is an incredible and essential ability acquired by S protein over evolution. The syncytia formation induced by S protein allows the virus to keep spreading without extracellular virus particles working as an evasion mechanism of the immune system.

7. S protein in the pandemic coronaviruses

As discussed above, in the last two decades, the human king faced three outbreaks caused by hCoVs. These coronaviruses have threatened and taken many lives worldwide with different spreading rates, fatality cases, and regions affected (Fig. 1 and Table 1). The pandemic hCoVs had present different spread and human-to-human transmissible rates. That factor could be attributed to the mutation in the S protein from all of them. Over the years, hCoVs have accumulated many mutations, some negative, some positive, which culminate in the current pandemic scenario. This section will discuss the characteristics and differences of S protein from the pandemic hCoVs. Most of the comparisons are made between SARS-CoV and SARS-CoV-2 when pertinent MERS-CoV will be included.

The mutations that lead to the change in amino acid in the S protein could be important information to track the natural sources of CoVs, allowing intra-species or inter-species jumping of the virus. For example, genomic sequence experiments revealed that SARS-CoV-2 is closer to bat CoVs than other hCoVs, which indicates its origin [37,51,62,69,115,117,121,190,209]. The RatG13, CoV from bats, has a similarity of 93.1% in the gene and 98% in the protein sequence of S protein with SARS-CoV-2. In contrast, SARS-CoV-2 has only 80% similarity in the S protein with other hCoVs [37,51,62,69,115,117,121,190,209].

In contrast to other CoVs, SARS-CoV-2 has accumulated many mutations in S protein conserved regions (Fig. S3). Because of that, even with some similarities, SARS-CoV-2 is much sufficiently different from SARS-CoV and SARS-like coronaviruses [40,47,51,111]. In comparison to pandemic hCoVs, SARS-CoV-2 is, indeed, closer to SARS-CoV than MERS-CoV (Fig. S1A) [45,93,98,178]. Even though evolutionary studies put SARS-CoV-2 and SARS-CoV in the same group, they still hold remarkable variations between them [111]. Wu et al. [111] revealed high similarities between SARS-CoV-2 and SARS-CoV at the polyprotein level, but many significant alterations exist. For instance, the most remarkable is the absence of protein 8a in SARS-CoV-2 and its presence in the SARS-CoV, which indicates a mutation that deletes or produces a truncated inactive 8a protein in SARS-CoV-2. For sure, the absence of 8a did not affect SARS-CoV-2 fitness [111].

To have a better picture of the S protein changes of the pandemic hCoVs, we performed an alignment comparing the entire sequence of S protein from MERS-CoV (accession number K9N5Q8), SARS-CoV-1 (accession number P59595), and SARS-CoV-2 (accession number P0DTC2) deposited in the UniProt database (Supplementary Fig. 3). By analyzing the results, the first point noticed was the length of S protein in all viruses. The MERS-CoV S protein has a higher number of amino acid residues, 1345. In contrast, S protein from SARS-CoV and SARS-

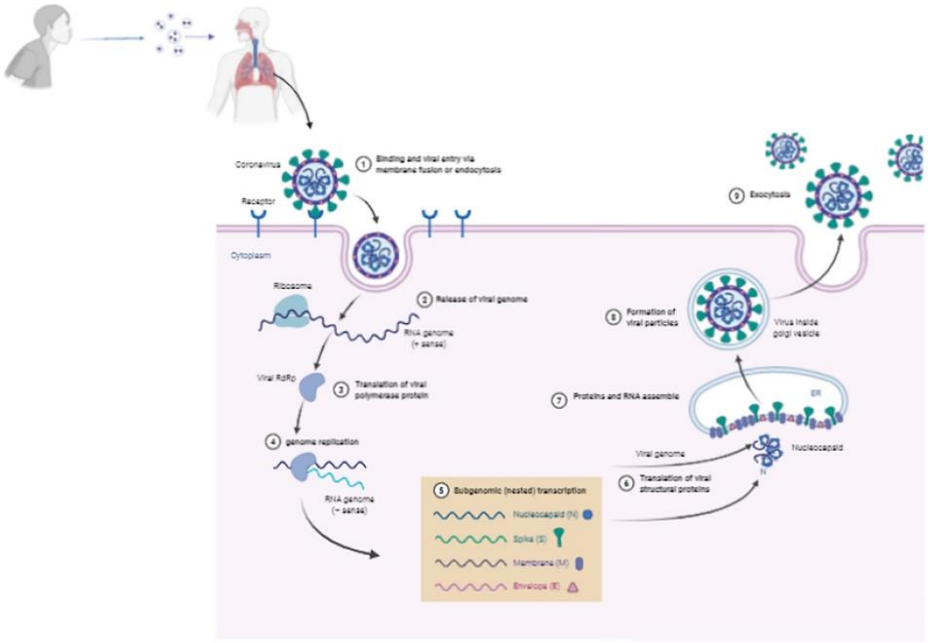

Fig. 4. Schematic model of coronavirus entry in cell. Coronaviruses bind to the host cell surface and release their RNA genomes into the cell through endocytosis. The positive-sense RNA genome is translated to produce the RNA-dependent RNA polymerase (RdRp) complex. Then the RdRp complex produces negative-sense RNA from the RNA genome, which provides the template for synthesis of positive-sense mRNAs. Then these subgenomic mRNAs are translated into structural and accessory proteins for viral particle assembly in endoplasmic reticulum. Finally, The enveloped virion is then exported from the cell by exocytosis. Created with BioRender.com.

CoV-2 has, respectively, 1243 and 1261 amino acid residues (Supplementary Fig. 3). That might be a result of many deletions in S protein from both SARS-CoV and SARS-CoV-2.

The S protein alignment from the pandemic hCoVs revealed that compared to the MERS-CoV S protein, the S protein from SARS-CoV-1 and SARS-CoV-2 has 14 points of deletions. Probably, because of those deletions, the S protein from SARS-CoV-1 and SARS-CoV-2 are smaller than the MERS-CoV S protein (Supplementary Fig. 3). Of these, 12 points of deletions are present in the S1 subunit and 2 on the S2 subunit. Most of the point mutations are situated in regions that have no important domains for the infection process. But somehow alter the 3D of S protein, making it more compact in both SARS-CoV and SARS-CoV-2 than MERS-CoV.

Another great difference between S protein from SARS-CoV and SARS-CoV-2 is the pattern of glycosylation [210–212]. The presence of an additional glycosylation spot in Asn^{370} in SARS-CoV-2 compared to S protein from SARS-CoV provides an additional glycosylation state in S protein from SARS-CoV-2. This spot belongs to a domain involved in the membrane attachment and thereby enhances the interaction with the receptor and membrane fusion [211]. Point mutations in SARS-CoV-2 S protein are said to increase virulence through the instability of the viral machinery and altered viral-to-cell-membrane fusion (Supplementary Fig. 3).

It is already known that the amino acid composition change does not reflect protein structure changes and thereby function. To check that, we provide a root mean square deviation (RMSD) calculation of the atomic position on S protein from the pandemic hCoVs (Fig. 5). The RMSD provides a value: If the value is 0, the atoms from both structures are in the same position, with no alteration in the 3D structure. However, if the value is anyone higher than zero, it indicates the atoms are in different positions, and this value is high, the structures are very different.

To perform the structural alignments was used the 3D structures from S proteins MERS-CoV (PDB ID: 5X5C), SARS-CoV-1 (PDB ID: 5X58), and SARS-CoV-2 (PDB ID: 6Z97) deposited in the UniProt database deposited in the Protein Data Bank (PDB, https://www.rcsb.org/). By performing a structural alignment, it is possible to see structural changes. Fig. 5 shows the structural alignment between the S proteins from MERS-CoV and SARS-CoV. It is possible to analyze in many positions the differences in both proteins. The RMSD value for this alignment was 12.93 A, indicating both atomic positions are quite different. The comparison between S protein from MERS-CoV and SARS-CoV-2 is more interesting (Fig. 5). In some regions such as NDT, the arm of S1 and HR is possible to evaluate that the S protein structure from MERS-CoV is more prominent than S protein than SARS-CoV-2. It seems the S protein from SARS-CoV-2 is more compact with a lower atomic distance than MERS-CoV (Fig. 5). The RMSD value for the structural alignment of S protein from MERS-CoV and SARS-CoV-2 is 15.90 A, which indicates both structures are quite different. Despite the differences in S protein it is important to remember both viruses employed different receptor to come inside the cell. Together these differences are responsible for complete behaviors regarding the spread, infectivity, and severity of the disease.

The RMSD analysis of S protein from SARS-CoV and SARS-CoV-2 (Fig. 5) revealed a lower value, 9.21 A, than that obtained in the comparisons of SARS-CoV x MERS-CoV and SARS-CoV-2 x MERS-CoV. It is important to notice that even the S protein from SARS-CoV and SARS-CoV-2 are similar, they share many differences. By looking at amino acid sequence alignment (Supplementary Fig. 3) it is possible to notice many changes in the amino acid residues at the same position.

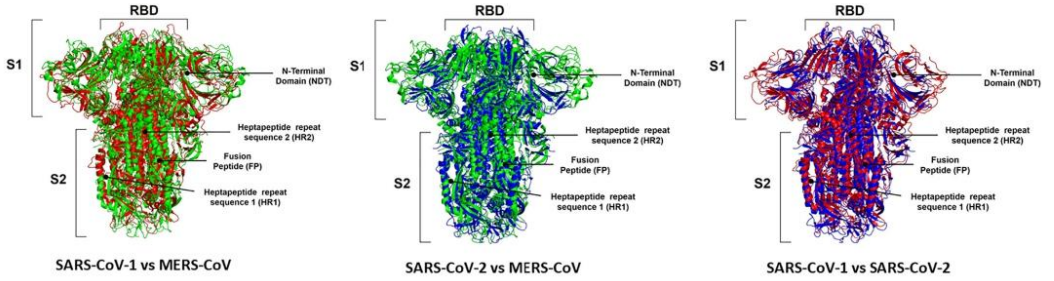

Fig. 5. Three-dimensional structure comparison of Spike protein among SARS-COV-1, MERS-CoV and SARS-COV2 through protein alignment. The spike protein of SARS-CoV-1 is represented in red, MERS-CoV in green and SARS-CoV-2 is blue. The 3D structures from S proteins MERS-CoV (PDB ID: 5X5C), SARS-CoV-1 (PDB ID: 5X58), and SARS-CoV-2 (PDB ID: 6Z97) deposited in the UniProt database deposited in the Protein Data Bank (PDB, https://www.rcsb.org/). RBD: Receptor-binding domain; NDT: N-terminal domain; HR1 and HR2: heptapeptide repeat sequence 1 and 2; FP: fusion peptide of subunit 1 and 2 are identified in the images. The structural alignments were performed in the Pymol program with the educational license.

These changes could be responsible for the altered structures revealed by RMSD analysis.

It is important to notice that some point mutations occur on the RBD site (Supplementary Figs. 3 and 4). To have a better overview it was performed an alignment comparing the sequence of RBD extracted from the sequence of S protein from MERS-CoV (accession number K9N5Q8), SARS-CoV-1 (accession number P59595), and SARS-CoV-2 (accession number P0DTC2) deposited in the UniProt database (Supplementary Fig. 4). For example, the sequences ^{536}EDCDYYRKQLS^{546}, ^{575}VQYC^{578}, and ^{587}KLEFAN^{592} are present in the S protein from MERS-CoV absent in that one from SARS-CoV and SARS-CoV-2 (Supplementary Fig. 4). Deletion points were not an exclusivity from SARS-CoV and SARS-CoV-2. The S protein from MERS-CoV presents 4 points of deletion than SARS-CoV and SARS-CoV-2 (Supplementary Fig. 3).

The RBD portion has nine cysteine residues able to form four disulfide bonds. Comparing the location of these disulfide bonds in the SARS-CoV, MERS-CoV, and SARS-CoV-2, it was possible to see if the positions of disulfide bonds are similar SARS-CoV-2 and SARS-CoV, but in a different position in comparison both with MERS-CoV (Fig. 5 and Supplementary Fig. 3) [183]. This result suggests a closed mode of action between RBD from SARS-CoV and SARS-CoV-2 but not too close to the action of RBD from MERS-CoV.

Regarding S protein, most of the amino acid changes were in RBD, affecting the conformational flexibility of the protein or binding interactions with ACE2 [213]. The mutations accumulated by SARS-CoV-2 lead to five amino acid residues that are different than those in SARS-CoV. In SARS-CoV, the residues are Tyr^{455}, Leu^{486}, Asn^{494}, Asp^{495}, Tre^{501}, and Tyr^{506}. In contrast, in SARS-CoV-2, the residues are Leu^{455}, Phe^{486}, Glu^{494}, Ser^{495}, Asn^{501}, and Tyr^{506} [214] (Supplementary Fig. 4). These differences in the SARS-CoV-2 RBD domain allow it to bind to ACE2 with an affinity 20 times higher than SARS-CoV [214].

A key mutation in the RBD from SARS-CoV-2 compared to SARS-CoV is the presence of a Lys^{417}. The core region of RBD from SARS-CoV-2 has a unique residue of Lys^{417}, forming a salt-bridge interaction with a residue of Asp^{30}. This interaction strengthens the energy bind of SARS-CoV-2 RBD with ACE2. In contrast, this position of RBD from SARS-CoV holds a Val residue that did not allow such type of interaction (Supplementary Fig. 4) [183]. Indeed, the presence of Val residue interrupts the interaction, thus weakens the interaction with ACE2. Besides, the presence of Lys^{417} provides a positively charged patch providing an electrostatic surface, which is not present in the RDB from SARS-CoV [183]. Besides strengthening the SARS-CoV-RBD::ACE2 interaction, the Lys^{417} is also important to S protein immunogenicity (Supplementary Fig. 4). The substitution of a Val to Lys in the RBD from SARS-CoV-2 hinders the interaction of anti-SARS-CoV antibodies and thus the neutralization of SARS-CoV-2 by anti-SARS-CoV antibodies (Supplementary Fig. 4) [183].

The RMSD analysis revealed some important information about the structure of all S proteins from pandemic hCoVs. However, the S protein is a huge protein with a complex structure (Fig. 5). To obtain a better view of the alteration in RBD, it was performed an RMSD analysis of only the RBD portion, comparing in all pandemic hCoVs. The RMSD allowed a more in-depth evaluation of differences (Fig. 6). To perform the structural alignments was used the 3D structures of RBD from MERS-CoV (PDB ID: 6L8Q), SARS-CoV-1 (PDB ID: 2AJF), and SARS-CoV-2 (PDB ID: 6VW1) deposited in the UniProt database deposited in the Protein Data Bank (PDB, https://www.rcsb.org/). The comparison between RBD from MERS-CoV and SARS-CoV revealed at least three positions with a high variation in the structure (Fig. 6 arrows). The RMSD value was 10.34 A. Corroborating the results from S protein RMSD analysis of MERS-CoV and SARS-CoV-2 (Fig. 6), the RBD analysis domain presented a high RMSD value of 11.6 A, indicating the structures were quite different. The arrows highlighted the most prominent differences (Fig. 6).

Regarding the RMSD analysis of RBD follows the same pattern of S protein for SARS-CoV and SARS-CoV-2 (Fig. 6). Although there are many differences in the amino acid sequence of RBD showed by the alignment (Fig. S4). The conformational structure of RBD from SARS-CoV and SARS-CoV-2 is quite similar as represented by the RMSD analysis with a value of 2.09, which is very low compared to other RMSD analysis (Fig. 6). The similarity between RBD sequences from SARS-CoV and SARS-CoV-2 is around 74% allowing both viruses to use ACE2 receptors to a different extent in the cell [118]. Indeed, RBD from SARS-CoV-2 can form a higher number of interactions with ACE2 than RBD from SARS-CoV, supporting the high affinity of SARS-CoV-2 RBD to ACE2 than SARS-CoV. This is possible because RBD from SARS-CoV-2 performs more atomic interaction with the ACE2 compared to SARS-CoV. Experiments have shown the RBD from SARS-CoV-2 binds to ACE2 in an nM scale concentration, with dissociation at 4.7 nM. In contrast, the RBD from SARS-CoV has a constant of dissociation about 31 nM [28,178,183].

All these differences in the atomic arrangement led to suitable differences in S protein are directly involved in the interactions with the ACE2 receptor and thus binding affinities. Based on that, it is feasible to suggest that those alterations are responsible for the higher affinity of SARS-CoV-2 RBD than SARS-CoV RBD by the receptor, and thereby higher transmissibility [28,178,183]. Experimental analysis using animals is an important source of information if the mutations on RBD affect COVID-19 symptomatology and may provide information about the origin of the pandemic situation [215]. Based on RBD sequences' similarities, there have been discussions of convergent evolution between SARS-CoV and SARS-CoV-2 RBD structures enhancing the affinity of SARS-CoV-2 by ACE2 [183,215].

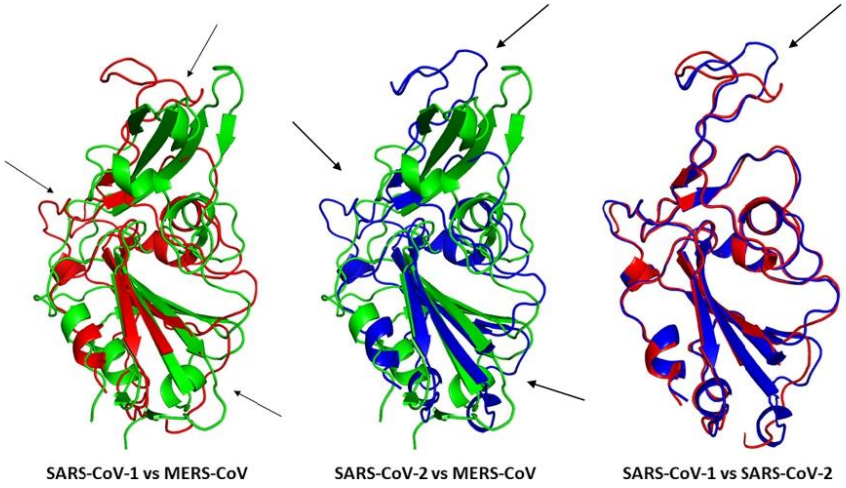

Fig. 6. Three-dimensional structure comparison of Receptor-Binding Domain (RBD) of Spike protein among SARS-COV-1, MERS-CoV and SARS-COV2 through protein alignment. The RBD of SARS-CoV-1 is represented in red, MERS-CoV in green and SARS-CoV-2 is blue. Structural differences are indicated by arrows. To perform the structural alignments was used the 3D structures of RBD from MERS-CoV (PDB ID: 6L8Q), SARS-CoV-1 (PDB ID: 2AJF), and SARS-CoV-2 (PDB ID: 6VW1) deposited in the UniProt database deposited in the Protein Data Bank (PDB, https://www.rcsb.org/). The structural alignments were performed in the Pymol program with the educational license.

Albeit everybody looks for a mutation in the RBD given its interaction with ACE2 receptor, other regions. For example, it was reported that many mutations changed amino acid sequences in the HR1 domain of SARS-CoV-2 compared to SARS-CoV, which might be associated with improved and more robust interaction with the HR2. Thereby enhancing the membrane fusion ability of S protein, which increased SARS-CoV-2 infectivity (Fig. S3) [181,189,193,195]. Comparing SARS-CoV and SARS-CoV-2, the S2 domain is well preserved in both N- and C-terminal domains. All regions involved in viral particle fusion such as FP, HR1, HR2, TM, cytoplasmic portion have similarities, respectively, of 93%, 88%, 100%, 93%, and 97% (Fig. S4) [216].

It was already described how mutations favoring SARS-CoV-2 S protein cleavage improve viral loads and the higher efficiency of spread compared to other hCoVs [27,181,216]. These mutations increase the number of proteases that could cleavage the extracellular portion of S protein from SARS-CoV-2, increasing its infectivity and virulence [118,181,213]. Mutational studies showed that compared to other coronaviruses S protein, one from SARS-CoV-2 has a higher number of hotspots for glycosylation. It is quite possible that SARS-CoV-2 is using these new sites of glycosylation to evade immune system surveillance, making it S protein less antigenic than those from other coronaviruses do and thereby contributing to its pandemic spreading [118,181,207,213,217,218].

8. Mutations in S protein from SARS-CoV-2

Based on all discussion made above, it is quite clear the high mutational rates in hCoVs. Most of the discussion focused on the mutations in the pandemic hCoVs SARS-CoV, MERS-CoV, and SARS-CoV-2. In this topic, the focus will be the mutations that happened in the S protein from SARS-CoV-2 since the beginning of the outbreak.

Mutations are a process intrinsic to all RNA viruses. There are some results from mutation: (1) mutations are a natural process resulting from the errors made by the RNA polymerase during RNA replication; (2) Mutations could be induced by RNA-editing system as a natural defense system from the host; (3) genetic variation from recombination of two viral lineages 8,9,11,12,13. To viruses, mutations could be neutral, which is the majority, harmful or to a less extent represent some advantages to virus [219]. In SARS-CoV-2, the mutations have a lower rate, an estimated 1–2 mutations per month [220], because the RNA polymerase has an unusual proof-reading mechanism [221]. Even so, many mutations have been related to SARS-CoV-2 since the outbreak has started [222,223]. The mutations in SARS-CoV-2 are the most listed in S protein and associated with higher transmissibility and virulence [222,223].

At the beginning of the outbreak, in January of 2020, WHO recognized the circulation of a SARS-CoV-2 variant with a D614G substitution in the S protein (Fig. 7). [7,26,109]. According to WHO [7,26,109], the D614G variant was first identified in China and became the dominant variant worldwide by June 2020. The D614G variant, compared to other SARS-CoV-2, has enhancements in infectivity and transmission [222] but does not lead to higher illness.

The D614G mutation changes a Gly residue by Asp residue at 614 positions located at the C-terminal region of S1 subunits from S protein, a region directly associated with S2 subunit [222,223]. The advantage of D614G mutation is the high transmission, infectivity, and viral loads in patients with COVID-19 [222,223]. Experiments performed by Plante et al. [224] showed that sera from hamsters infected with the wildtype slightly neutralized the D614G variant. This is a concerning result because it has implications in the vaccine efficacy and thus in antibody therapy.

As happens to other mutations discussed in SARS-CoV-2, the D614G is not in the RBD domain and does not improve the affinity of S protein by ACE2. Indeed, the D614G results in a more stable S protein than wild type S protein and increases the assembly of more functional S protein outside viral particles. Both these advantages increase SARS-CoV-2 infectivity [222–224].

Last December 2020, WHO recognized a new SARS-CoV-2 mutant discovered in the United Kingdom from samples collected 20-Sept-2020 in the county of Kent and another on 21-Sept-2020 from London [225]. This mutant was named SARS-CoV-2 lineage B.1.1.7 (SARS-B117). The mutant SARS-B117 has 17 mutations. Of these, eight mutations were found in the gene responsible for S protein production [225]. The mutations in the S protein were: two deletions: HV 69–70 and Y144 (Fig. 7). The deletions in the 69 and 70 position of the S protein are related to the evasion of S protein from the immune response.

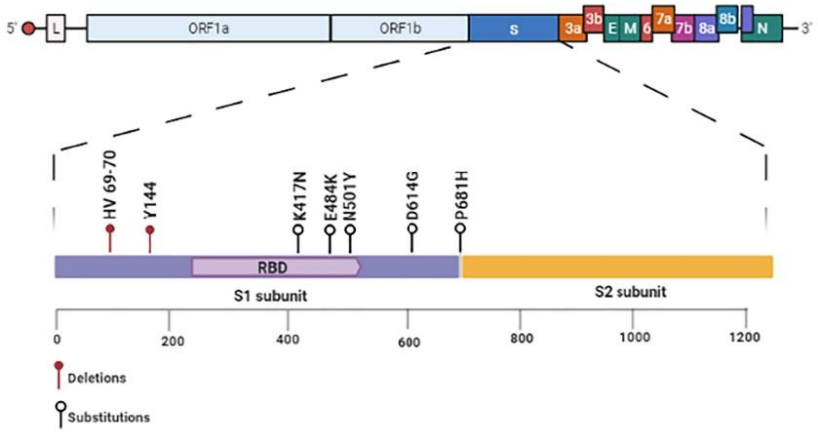

Fig. 7. Schematic diagram of mutations in the Spike protein from SARS-CoV-2. All relevant mutations in the Spike protein that lead to the new variants of SARS-CoV-2 are in the RBD. Among those, the most relevant are deletion: HV 69–70 and Y144. Substitutions: K417N, E484K, N501Y (RBD), D614G, and P681H. Created with BioRender.com.

Probable, the deletions change the shape of the S protein to make it harder for antibodies to attach. Besides, very recent experiments showed these deletions enable the SARS-B117 to infect cells more efficiently than its wildtype counterpart [225].

The other two mutations in SARS-B117 have biological significance. The Mutation N501Y in RBD (Fig. 7) is said to increase its affinity by ACE2 receptor, increase the transmissibility and infectivity, and make SARS-B117 more contagious. The N501Y mutation changes an amino acid residue of Asn by one of Tyr on the top of each S monomer protein. The region that makes keeps in touch with ACE2 on human cells. In a typical CoV, the top of the S protein is like a fitting puzzle piece. Even though it can catch onto human cells, but the fit is so loose that the virus sometimes falls away and fails to infect the cell. The N501Y mutation came to fix that by making the shape sharp of the puzzle piece, allowing a tighter touch, and enhancing the chance of a successful infection [225]. A new variant of SARS-CoV-2 N501Y·V2 (B.1.351) has emerged in South Africa and is rapidly replacing pre-existing variants.

The other mutation, P681H (Fig. 7), creates a new cleavage site in the intersection of S1 and S2 in the S protein. This cleavage site S1/S2 is unique to SARS-CoV-2, being not present in other related coronaviruses and increase the infection of epithelial cells by SARS-B117 [225]. Therefore, the new virus SARS-B177 has some advantages compared to already circulating SARS-CoV-2 is less immunogenic and has a higher affinity to ACE2 ability to enter within cells. These results revealed the potential and brought concerns about the control of SARS-CoV-2. As of 30 December 2020, the SARS-B117 has spread to 31 other countries proving the high transmissibility of this new variant.

Recently, now in January 2021, the researchers from Oswaldo Cruz Foundation (FIOCRUZ) reported a new variant of SARS-CoV-2, name SARS-CoV-2 B.1.1.28 (SARS-B1128) [226]. The SARS-B1128 was first identified in Amazonas, but there are reports of the same variant, Manaus making a new clade of viruses that emerged in Brazil. The analysis of 69 genomes collected at the hospital from Amazonas states revealed this variant SARS-B1128 still maintains the N501Y mutation and acquired two new mutations K417N and E484K S protein (Fig. 7). Specifically, those mutations are in the RBD portion of the S protein.

By now, there is no scientific or experimental support, but these mutations may have enhanced the ability of SARS-B1128 to bind to ACE2, increasing the transmissibility rates. Based on that, it is feasible to suggest that this high transmissibility is behind the dramatic increase of COVID-19 cases in the state of Amazonas that led to the collapse of the public health system and taken many lives.

Since the beginning of the outbreak, the COVID-19 pandemic has reached every continent in the world. The faster COVID-19 spreads started the run to develop vaccines. Today, some vaccines are already licensed in humans after passing by phase 3 clinical trials. These are the recombinant spike glycoprotein: either mRNA based (the Moderna and Pfizer–BioNTech vaccines), via an adenovirus vector (the Oxford–AstraZeneca, CanSino, and Johnson & Johnson vaccines), or via injection of the protein itself (the Novavax vaccine). The rapid development of vaccines is a breakthrough in the history of vaccines. However, one question arises: Are these vaccines effective against the SARS-CoV-2 new variants?

All the vaccines available today are based on the original SARS-CoV-2 that came up in Wuhan. So, in theory, it is feasible to suggest that variants of SARS-CoV-2 could evolve with resistance to immunity induced by recombinant spike protein vaccines once the mutations lead to a new different type of Spike protein. For instance, a 2020 preprint (non-peer-reviewed manuscript) revealed that a convalescent plasma for hCoV 229E does not neutralize the mutant hCoV 229E leading to individuals less able to neutralize new strains.

From this point, this data suggests that mutations in SARS-CoV-2 could lead to new variants not affected by the vaccine. The length of the spike protein used by licensed vaccines is relatively short (~1270 amino acids), leading to vaccines concentrated only in two sections NTD and RBD domains. Based on that, the antibody response is so focused on some parts of the spike protein. Spike protein mutations might be driven by antigenic drift or even by the selection, either during natural infection or due to the vaccine itself. It is already known that a virus grown under the selective pressure imposed by a single monoclonal antibody targeting a single epitope of a viral protein, mutations in that protein sequence will lead to the loss of neutralization. Additionally, notable showed that SARS-CoV-2 could mutate to escape neutralization by polyclonal antibodies.

Undoubtedly, the spike glycoprotein mutations can affect the efficiency of SARS-CoV-2 neutralization by antibodies, either mono- or polyclonal. Besides the effect in the humoral response, mutations in the spike protein could affect cellular response making the cytotoxic effect of T cells useless. However, only clinical trials with vaccine patients could bring to light this concern.

9. Conclusion

As discussed, all over in this review, the S protein play as a principal actor to SARS-CoV-2 became known and spread worldwide in the last

year, causing the third outbreak of coronaviruses. All the new features available to SARS-CoV-2 that led to a higher pathogenesis spectrum, transmissibility, and high affinity to human receptors were enhanced by mutations accumulated by the S protein from SARS-CoV-2 it more efficient than that one from SARS-CoV and MERS-CoV. Even though SARS-CoV and SARS-CoV-2 share similarities, there are differences, which may explain both viruses' completely different behaviors. Most mutations accumulated by S protein from SARS-CoV-2 are hosted in the RBD domain, which is noticeably different from SARS-CoV and MERS-CoV RBD. Here we discuss some mutations that change the amino acid content and atomic location of molecules leading to differences in the S protein from SARS-CoV, MERS-CoV, and SARS-CoV-2. These differences made S protein from SARS-CoV-2 more efficient to bind host receptors than SARS-CoV and MERS-CoV. Mutations also provided an additional cleavage in S1/S2 exclusively from SARS-CoV-2 improving membrane fusion. The unique glycosylation pattern is another advantage accumulated by SARS-CoV-2 S protein playing essential roles in viral tropism, pathogenesis, transmissibility, and evasion of the immune system. Therefore, S protein from pandemic coronaviruses is an essential factor in the show presented by them. Based on that, in-depth studies are required to investigate and understand more about S protein to develop potent drugs and vaccines to eliminate these threats.

CRediT authorship contribution statement

Conceptualization: Pedro F. N. Souza.

Data curation: Pedro F.N. Souza Felipe P. Mesquita, Jackson L. Amaral, Patrícia G. C. Landim, Karollyny R.P. Lima, Marília B. Costa, Izabelle R. Farias, Luina B. Lima.

Formal analysis: Pedro F.N. Souza, Jackson L. Amaral and Felipe P. Mesquita.

Funding acquisition: Pedro F.N. Souza, Felipe P. Mesquita and Raquel C. Montenegro.

Resources: Pedro F.N. Souza, Felipe P. Mesquita and Raquel C. Montenegro.

Supervision: Pedro F.N. Souza.

Writing–original draft: Pedro F.N. Souza, Felipe P. Mesquita, Jackson L. Amaral, Patrícia G. C. Landim, Karollyny R.P. Lima, Marília B. Costa, Izabelle R. Farias, Luina B. Lima.

Writing, review and editing: Pedro F.N. Souza, Felipe P. Mesquita and Raquel C. Montenegro.

Final approve of manuscript and submission: Pedro F.N. Souza.

Ethical approval

Not applicable.

Funding and acknowledgments

Grants from the following Brazilian agencies supported this work: The National Council for Scientific and Technological Development (CNPq), with a doctoral and master grant to JLA and FPM a research grant; the Office to Coordinate Improvement of University Personnel (CAPES) sponsored PFNS with a postdoctoral fellowship.

Declaration of competing interest

All authors declare no conflicts of interest.

Appendix A. Supplementary data

Supplementary data to this article can be found online at https://doi.org/10.1016/j.ijbiomac.2021.02.203.

References

[1] S.R. Weiss, Forty years with coronaviruses, J. Exp. Med. (2020) 217.
[2] C.M. Coleman, M.B. Frieman, Coronaviruses: important emerging human pathogens, J. Virol. 88 (2014) 5209–5212, https://doi.org/10.1128/jvi.03488-13.
[3] A.E. Gorbalenya, S.C. Baker, R.S. Baric, R.J. de Groot, C. Drosten, A.A. Gulyaeva, B.L. Haagmans, C. Lauber, A.M. Leontovich, B.W. Neuman, et al., The species severe acute respiratory syndrome-related coronavirus: classifying 2019-nCoV and naming it SARS-CoV-2, Nat. Microbiol. 5 (2020) 536–544.
[4] ICTV, , Available online: https://talk.ictvonline.org/taxonomy/ (accessed on Jan 21, 2021).
[5] C. Drosten, S. Günther, W. Preiser, S. van der Werf, H.-R. Brodt, S. Becker, H. Rabenau, M. Panning, L. Kolesnikova, R.A.M. Fouchier, et al., Identification of a novel coronavirus in patients with severe acute respiratory syndrome, N. Engl. J. Med. 348 (2003) 1967–1976, https://doi.org/10.1056/nejmoa030747.
[6] A.M. Zaki, S. van Boheemen, T.M. Bestebroer, A.D.M.E. Osterhaus, R.A.M. Fouchier, Isolation of a novel coronavirus from a man with pneumonia in Saudi Arabia, N. Engl. J. Med. 367 (2012) 1814–1820, https://doi.org/10.1056/nejmoa1211721.
[7] Coronavirus disease (COVID-19), , Available online: https://www.who.int/emergencies/diseases/novel-coronavirus-2019 (accessed on Jan 21, 2021).
[8] Q. Ding, P. Lu, Y. Fan, Y. Xia, M. Liu, The clinical characteristics of pneumonia patients coinfected with 2019 novel coronavirus and influenza virus in Wuhan, China, J. Med. Virol. 92 (2020) 1549–1555, https://doi.org/10.1002/jmv.25781.
[9] X. Wu, Y. Cai, X. Huang, X. Yu, L. Zhao, F. Wang, Q. Li, S. Gu, T. Xu, Y. Li, et al., Co-infection with SARS-CoV-2 and influenza a virus in patient with pneumonia, China, Emerg. Infect. Dis. 26 (2020) 1324–1326, https://doi.org/10.3201/EID2606.200299.
[10] Z. Khodamoradi, M. Moghadami, M. Lotfi, Co-infection of coronavirus disease 2019 and influenza a: A report from Iran, Arch. Iran. Med. 23 (2020) 239–243, https://doi.org/10.34172/aim.2020.04.
[11] E. Mahase, Covid-19: outbreak could last until spring 2021 and see 7.9 million hospitalised in the UK, BMJ 368 (2020), m1071, https://doi.org/10.1136/bmj.m1071.
[12] L.M. Vos, R. Bruyndonckx, N.P.A. Zuithoff, P. Little, J.J. Oosterheert, B.D.L. Broekhuizen, C. Lammens, K. Loens, M. Viveen, C.C. Butler, et al., Lower respiratory tract infection in the community: associations between viral aetiology and illness course, Clin. Microbiol. Infect. 27 (2021) 96–104, https://doi.org/10.1016/j.cmi.2020.03.023.
[13] S.A. Meo, A.M. Alhowikan, T.A.L. Khlaiwi, I.M. Meo, D.M. Halepoto, M. Iqbal, A.M. Usmani, W. Hajjar, N. Ahmed, Novel coronavirus 2019-nCoV: prevalence, biological and clinical characteristics comparison with SARS-CoV and MERS-CoV, Eur. Rev. Med. Pharmacol. Sci. 24 (2020) 2012–2019.
[14] Y. Zhang, J. Zhang, Y. Chen, B. Luo, Y. Yuan, F. Huang, T. Yang, F. Yu, J. Liu, B. Liu, et al., The ORF8 Protein of SARS-CoV-2 Mediates Immune Evasion through Potently Downregulating MHC-I. *bioRxiv*, 2020https://doi.org/10.1101/2020.05.24.111823 2020.05.24.111823.
[15] V.K. Shah, P. Firmal, A. Alam, D. Ganguly, S. Chattopadhyay, Overview of immune response during SARS-CoV-2 infection: lessons from the past, Front. Immunol. 11 (2020) 1949.
[16] Y. Tan, F. Tang, SARS-CoV-2-mediated immune system activation and potential application in immunotherapy, Med. Res. Rev. 1 (2020) 1167–1194.
[17] Y. Zhang, J. Zhang, Y. Chen, B. Luo, Y. Yuan, F. Huang, T. Yang, F. Yu, J. Liu, B. Liu, et al., The ORF8 Protein of SARS-CoV-2 Mediates Immune Evasion through Potently Downregulating MHC-I, 2020https://doi.org/10.1101/2020.05.24.111823.
[18] M.D. Park, Immune evasion via SARS-CoV-2 ORF8 protein? Nat. Rev. Immunol. 20 (2020) 408, https://doi.org/10.1038/s41577-020-0360-z.
[19] Coronavirus Update (Live), 97,633,202 cases and 2,091,064 deaths from COVID-19 virus pandemic - Worldometer, Available online: https://www.worldometers.info/coronavirus/.
[20] W. Wang, J. Tang, F. Wei, Updated understanding of the outbreak of 2019 novel coronavirus (2019-nCoV) in Wuhan, China, J. Med. Virol. 92 (2020) 441–447, https://doi.org/10.1002/jmv.25689.
[21] Severe Acute Respiratory Syndrome (SARS), , Available online: https://www.who.int/health-topics/severe-acute-respiratory-syndrome#tab=tab_1 (accessed on Jan 21, 2021).
[22] N.S. Zhong, B.J. Zheng, Y.M. Li, L.L.M. Poon, Z.H. Xie, K.H. Chan, P.H. Li, S.Y. Tan, Q. Chang, J.P. Xie, et al., Epidemiology and cause of severe acute respiratory syndrome (SARS) in Guangdong, People's Republic of China, in February, 2003, Lancet 362 (2003) 1353–1358, https://doi.org/10.1016/S0140-6736(03)14630-2.
[23] Z.A. Memish, S. Perlman, M.D. Van Kerkhove, A. Zumla, Middle East respiratory syndrome, Lancet 395 (2020) 1063–1077.
[24] Middle East respiratory syndrome coronavirus (MERS-CoV), Available online: https://www.who.int/health-topics/middle-east-respiratory-syndrome-coronavirus-mers#tab=tab_1 (accessed on Jan 21, 2021).
[25] Evidence of person-to-person transmission within a family cluster of novel coronavirus infections, United Kingdom, February 2013, Eurosurveillance 18 (2013) https://doi.org/10.2807/ese.18.11.20427-en.
[26] Coronavirus disease (COVID-19) situation reports, Available online: https://www.who.int/emergencies/diseases/novel-coronavirus-2019/situation-reports.
[27] A.C. Walls, Y.J. Park, M.A. Tortorici, A. Wall, A.T. McGuire, D. Veesler, Structure, function, and antigenicity of the SARS-CoV-2 spike glycoprotein, Cell 181 (2020) 281–292.e6, https://doi.org/10.1016/j.cell.2020.02.058.
[28] M. Hoffmann, H. Kleine-Weber, S. Schroeder, N. Krüger, T. Herrler, S. Erichsen, T.S. Schiergens, G. Herrler, N.H. Wu, A. Nitsche, et al., SARS-CoV-2 cell entry depends on ACE2 and TMPRSS2 and is blocked by a clinically proven protease inhibitor, Cell (2020)https://doi.org/10.1016/j.cell.2020.02.052.

[29] E.J. Snijder, M.C. Horzinek, Toroviruses: replication, evolution and comparison with other members of the coronavirus-like superfamily, J. Gen. Virol. 74 (1993) 2305–2316.
[30] L. Enjuanes, I. Sola, S. Alonso, D. Escors, S. Zúñiga, Coronavirus reverse genetics and development of vectors for gene expression, Curr. Top. Microbiol. Immunol. 287 (2005) 161–197.
[31] M.H.V. van Regenmortel, C.M. Fauquet, D.H.L. Bishop, E.B. Carstens, M.K. Estes, S.M. Lemon, J. Maniloff, M.A. Mayo, D.J. McGeoch, C.R. Pringle, et al., Virus taxonomy: classification and nomenclature of viruses. Seventh report of the international committee on taxonomy of viruses, Virus Taxon. Classif. Nomencl. viruses. Seventh Rep. Int. Comm. Taxon. Viruses 1 (2000) 1123–1128.
[32] X. Pan, D.M. Ojcius, T. Gao, Z. Li, C. Pan, C. Pan, Lessons learned from the 2019-nCoV epidemic on prevention of future infectious diseases, Microbes Infect. 22 (2020) 86–91, https://doi.org/10.1016/j.micinf.2020.02.004.
[33] E.C. Teeling, M.S. Springer, O. Madsen, P. Bates, S.J. O'Brien, W.J. Murphy, A molecular phylogeny for bats illuminates biogeography and the fossil record, Science (80-.) 307 (2005) 580–584, https://doi.org/10.1126/science.1105113.
[34] S.K.P. Lau, P.C.Y. Woo, K.S.M. Li, Y. Huang, H.W. Tsoi, B.H.L. Wong, S.S.Y. Wong, S.Y. Leung, K.H. Chan, K.Y. Yuen, Severe acute respiratory syndrome coronavirus-like virus in Chinese horseshoe bats, Proc. Natl. Acad. Sci. U. S. A. 102 (2005) 14040–14045, https://doi.org/10.1073/pnas.0506735102.
[35] Y. Guan, B.J. Zheng, Y.Q. He, X.L. Liu, Z.X. Zhuang, C.L. Cheung, S.W. Luo, P.H. Li, L.J. Zhang, Y.J. Guan, et al., Isolation and characterization of viruses related to the SARS coronavirus from animals in southern China, Science (80-.) 302 (2003) 276–278, https://doi.org/10.1126/science.1087139.
[36] W. Wang, X.D. Lin, W.P. Guo, R.H. Zhou, M.R. Wang, C.Q. Wang, S. Ge, S.H. Mei, M.H. Li, M. Shi, et al., Discovery, diversity and evolution of novel coronaviruses sampled from rodents in China, Virology 474 (2015) 19–27, https://doi.org/10.1016/j.virol.2014.10.017.
[37] Y. Tao, M. Shi, C. Chommanard, K. Queen, J. Zhang, W. Markotter, I.V. Kuzmin, E.C. Holmes, S. Tong, Surveillance of bat coronaviruses in Kenya identifies relatives of human coronaviruses NL63 and 229E and their recombination history, J. Virol. 91 (2017)https://doi.org/10.1128/jvi.01953-16.
[38] X.Y. Ge, J.L. Li, X. Lou Yang, A.A. Chmura, G. Zhu, J.H. Epstein, J.K. Mazet, B. Hu, W. Zhang, C. Peng, et al., Isolation and characterization of a bat SARS-like coronavirus that uses the ACE2 receptor, Nature 503 (2013) 535–538, https://doi.org/10.1038/nature12711.
[39] A. Lacroix, V. Duong, V. Hul, S. San, H. Davun, K. Omaliss, S. Chea, A. Hassanin, W. Theppangna, S. Silithammavong, et al., Genetic diversity of coronaviruses in bats in Lao PDR and Cambodia, Infect. Genet. Evol. 48 (2017) 10–18, https://doi.org/10.1016/j.meegid.2016.11.029.
[40] W. Li, Z. Shi, M. Yu, W. Ren, C. Smith, J.H. Epstein, H. Wang, G. Crameri, Z. Hu, H. Zhang, et al., Bats are natural reservoirs of SARS-like coronaviruses, Science (80-.) 310 (2005) 676–679, https://doi.org/10.1126/science.1118391.
[41] S. Leopardi, E.C. Holmes, M. Gastaldelli, L. Tassoni, P. Priori, D. Scaravelli, G. Zamperin, P. De Benedictis, Interplay between co-divergence and cross-species transmission in the evolutionary history of bat coronaviruses, Infect. Genet. Evol. 58 (2018) 279–289, https://doi.org/10.1016/j.meegid.2018.01.012.
[42] D. Giannis, I.A. Ziogas, P. Gianni, Coagulation disorders in coronavirus infected patients: COVID-19, SARS-CoV-1, MERS-CoV and lessons from the past, J. Clin. Virol. 127 (2020), 104362, https://doi.org/10.1016/j.jcv.2020.104362.
[43] C. Cao, W. Chen, S. Zheng, J. Zhao, J. Wang, W. Cao, Analysis of spatiotemporal characteristics of pandemic SARS spread in mainland China, Biomed. Res. Int. 2016 (2016)https://doi.org/10.1155/2016/7247983.
[44] L.E. Gralinski, V.D. Menachery, Return of the coronavirus: 2019-nCoV, Viruses 12 (2020).
[45] Z. Wu, J.M. McGoogan, Characteristics of and important lessons from the coronavirus disease 2019 (COVID-19) outbreak in China: summary of a report of 72314 cases from the Chinese Center for Disease Control and Prevention, JAMA - J. Am. Med. Assoc. 323 (2020) 1239–1242.
[46] E. De Wit, N. Van Doremalen, D. Falzarano, V.J. Munster, SARS and MERS: recent insights into emerging coronaviruses, Nat. Rev. Microbiol. 14 (2016) 523–534.
[47] A.A.T. Naqvi, K. Fatima, T. Mohammad, U. Fatima, I.K. Singh, A. Singh, S.M. Atif, G. Hariprasad, G.M. Hasan, M.I. Hassan, Insights into SARS-CoV-2 genome, structure, evolution, pathogenesis and therapies: structural genomics approach, Biochim. Biophys. Acta Mol. basis Dis. 1866 (2020).
[48] J. Cui, F. Li, Z.L. Shi, Origin and evolution of pathogenic coronaviruses, Nat. Rev. Microbiol. 17 (2019) 181–192.
[49] M.R. Alam, M.R. Kabir, S. Reza, Comorbidities might be a risk factor for the incidence of COVID-19: evidence from a web-based survey, Prev. Med. Rep. 21 (2021), 101319, https://doi.org/10.1016/j.pmedr.2021.101319.
[50] B. Hu, L.P. Zeng, X. Lou Yang, X.Y. Ge, W. Zhang, B. Li, J.Z. Xie, X.R. Shen, Y.Z. Zhang, N. Wang, et al., Discovery of a rich gene pool of bat SARS-related coronaviruses provides new insights into the origin of SARS coronavirus, PLoS Pathog. 13 (2017)https://doi.org/10.1371/journal.ppat.1006698.
[51] B. Hu, X. Ge, L.F. Wang, Z. Shi, Bat origin of human coronaviruses coronaviruses: emerging and re-emerging pathogens in humans and animals Susanna Lau positive-strand RNA viruses, Virol. J. (2015) 12.
[52] J.S. Rest, D.P. Mindell, SARS associated coronavirus has a recombinant polymerase and coronaviruses have a history of host-shifting, Infect. Genet. Evol. 3 (2003) 219–225, https://doi.org/10.1016/j.meegid.2003.08.001.
[53] S.P. Anand, Y. Chen, J. Prévost, R. Gasser, G. Beaudoin-Bussières, C.F. Abrams, M. Pazgier, A. Finzi, Interaction of human ACE2 to membrane-bound SARS-CoV-1 and SARS-CoV-2 S glycoproteins, Viruses 12 (2020)https://doi.org/10.3390/v12101104.
[54] A.L. Arndt, B.J. Larson, B.G. Hogue, A conserved domain in the coronavirus membrane protein tail is important for virus assembly, J. Virol. 84 (2010) 11418–11428, https://doi.org/10.1128/jvi.01131-10.
[55] J. Chen, Pathogenicity and transmissibility of 2019-nCoV—A quick overview and comparison with other emerging viruses, Microbes Infect. 22 (2020) 69–71, https://doi.org/10.1016/j.micinf.2020.01.004.
[56] Antibody-Dependent Enhancement of SARS Coronavirus Infection and its Role in the Pathogenesis of SARS | HKMJ Available online: https://www.hkmj.org/abstracts/v22n3Suppl 4/25.htm (accessed on Jan 21, 2021).
[57] T. Yoshikawa, T. Hill, K. Li, C.J. Peters, C.-T.K. Tseng, Severe acute respiratory syndrome (SARS) coronavirus-induced lung epithelial cytokines exacerbate SARS pathogenesis by modulating intrinsic functions of monocyte-derived macrophages and dendritic cells, J. Virol. 83 (2009) 3039–3048, https://doi.org/10.1128/jvi.01792-08.
[58] A.C. Sims, R.S. Baric, B. Yount, S.E. Burkett, P.L. Collins, R.J. Pickles, Severe acute respiratory syndrome coronavirus infection of human ciliated airway epithelia: role of ciliated cells in viral spread in the conducting Airways of the Lungs, J. Virol. 79 (2005) 15511–15524, https://doi.org/10.1128/jvi.79.24.15511-15524.2005.
[59] S.M. Abate, S. Ahmed Ali, B. Mantfardo, B. Basu, Rate of intensive care unit admission and outcomes among patients with coronavirus: a systematic review and meta-analysis, PLoS One 15 (2020), e0235653, https://doi.org/10.1371/journal.pone.0235653.
[60] G.M. Joynt, H.Y. Yap, SARS in the intensive care unit, Curr. Infect. Dis. Rep. 6 (2004) 228–233.
[61] F. Guimarães, Atuação do fisioterapeuta em unidades de terapia intensiva no contexto da pandemia de COVID-19, Fisioter. em Mov. 33 (2020)https://doi.org/10.1590/1980-5918.033.ed01.
[62] F. Wu, S. Zhao, B. Yu, Y.M. Chen, W. Wang, Z.G. Song, Y. Hu, Z.W. Tao, J.H. Tian, Y.Y. Pei, et al., A new coronavirus associated with human respiratory disease in China, Nature 579 (2020) 265–269, https://doi.org/10.1038/s41586-020-2008-3.
[63] Aerosol and surface stability of SARS-CoV-2 as compared with SARS-CoV-1. 2020, doi:https://doi.org/10.1056/NEJMc2001737.
[64] H. Kleine-Weber, M.T. Elzayat, M. Hoffmann, S. Pöhlmann, Functional analysis of potential cleavage sites in the MERS-coronavirus spike protein, Sci. Rep. 8 (2018) 1–11, https://doi.org/10.1038/s41598-018-34859-w.
[65] S.K.P. Lau, A.C.P. Wong, T.C.K. Lau, P.C.Y. Woo, Molecular evolution of MERS coronavirus: dromedaries as a recent intermediate host or long-time animal reservoir? Int. J. Mol. Sci. 18 (2017)https://doi.org/10.3390/ijms18102138.
[66] Z. Zhang, L. Shen, X. Gu, Evolutionary dynamics of MERS-CoV: potential recombination, positive selection and transmission, Sci. Rep. 6 (2016), 25049, https://doi.org/10.1038/srep25049.
[67] J.S.M. Peiris, Coronaviruses, Medical Microbiology, Eighteenth editionElsevier Inc. 2012, pp. 587–593 , (ISBN 9780702040894).
[68] S.K.P. Lau, K.S.M. Li, H.K.H. Luk, Z. He, J.L.L. Teng, K.-Y. Yuen, U. Wernery, P.C.Y. Woo, Middle East respiratory syndrome coronavirus antibodies in Bactrian and hybrid camels from Dubai, mSphere 5 (2020)https://doi.org/10.1128/msphere.00898-19.
[69] M.A. Ali, R. El-Shesheny, A. Kandeil, M. Shehata, B. Elsokary, M. Gomaa, N. Hassan, A. El Sayed, A. El-Taweel, H. Sobhy, et al., Cross-sectional surveillance of middle east respiratory syndrome coronavirus (MERS-CoV) in dromedary camels and other mammals in Egypt, august 2015 to January 2016, Eurosurveillance 22 (2017)https://doi.org/10.2807/1560-7917.ES.2017.22.11.30487.
[70] B. Meyer, M.A. Müller, V.M. Corman, C.B.E.M. Reusken, D. Ritz, G.J. Godeke, E. Lattwein, S. Kallies, A. Siemens, J. van Beek, et al., Antibodies against MERS coronavirus in dromedaries, United Arab Emirates, 2003 and 2013, Emerg. Infect. Dis. 20 (2014) 552–559, https://doi.org/10.3201/eid2004.131746.
[71] M.A. Müller, V.M. Corman, J. Jores, B. Meyer, M. Younan, A. Liljander, B.J. Bosch, E. Lattwein, M. Hilali, B.E. Musa, et al., Mers coronavirus neutralizing antibodies in camels, eastern Africa, 1983–1997, Emerg. Infect. Dis. 20 (2014) 2093–2095, https://doi.org/10.3201/eid2012.141026.
[72] V.M. Corman, J. Jores, B. Meyer, M. Younan, A. Liljander, M.Y. Said, I. Gluecks, E. Lattwein, B.J. Bosch, J.F. Drexler, et al., Antibodies against MERS coronavirus in dromedary camels, Kenya, 1992-2013, Emerg. Infect. Dis. 20 (2014) 1319–1322, https://doi.org/10.3201/eid2008.140596.
[73] A. Annan, H.J. Baldwin, V.M. Corman, S.M. Klose, M. Owusu, E.E. Nkrumah, E.K. Badu, P. Anti, O. Agbenyega, B. Meyer, et al., Human betacoronavirus 2c EMC/2012-related viruses in bats, Ghana and Europe, Emerg. Infect. Dis. 19 (2013) 456–459, https://doi.org/10.3201/eid1903.121503.
[74] M. Cotten, S.J. Watson, A.I. Zumla, H.Q. Makhdoom, A.L. Palser, S.H. Ong, A.A. Al Rabeeah, R.F. Alhakeem, A. Assiri, J.A. Al-Tawfiq, et al., Spread, circulation, and evolution of the Middle East respiratory syndrome coronavirus, MBio 5 (2014)https://doi.org/10.1128/mBio.01062-13.
[75] M. Letko, K. Miazgowicz, R. McMinn, S.N. Seifert, I. Sola, L. Enjuanes, A. Carmody, N. van Doremalen, V. Munster, Adaptive evolution of MERS-CoV to species variation in DPP4, Cell Rep. 24 (2018) 1730–1737, https://doi.org/10.1016/j.celrep.2018.07.045.
[76] C.M. Coleman, K.L. Matthews, L. Goicochea, M.B. Matthew, Wild-type and innate immune-deficient mice are not susceptible to the Middle East respiratory syndrome coronavirus, J. Gen. Virol. 95 (2014) 408–412, https://doi.org/10.1128/jvi.00534-17.
[77] W. Tai, Y. Wang, C.A. Fett, G. Zhao, F. Li, S. Perlman, S. Jiang, Y. Zhou, L. Du, Recombinant receptor-binding domains of multiple Middle East respiratory syndrome coronaviruses (MERS-CoVs) induce cross-neutralizing antibodies against divergent human and camel MERS-CoVs and antibody escape mutants, J. Virol. 91 (2017) https://doi.org/10.1128/jvi.01651-16.
[78] M.G. Douglas, J.F. Kocher, T. Scobey, R.S. Baric, A.S. Cockrell, Adaptive evolution influences the infectious dose of MERS-CoV necessary to achieve severe respiratory disease, Virology 517 (2018) 98–107, https://doi.org/10.1016/j.virol.2017.12.006.

[79] Y. Chen, K.R. Rajashankar, Y. Yang, S.S. Agnihothram, C. Liu, Y.-L. Lin, R.S. Baric, F. Li, Crystal structure of the receptor-binding domain from newly emerged Middle East respiratory syndrome coronavirus, J. Virol. 87 (2013) 10777–10783, https://doi.org/10.1128/jvi.01756-13.
[80] L. Du, G. Zhao, Z. Kou, C. Ma, S. Sun, V.K.M. Poon, L. Lu, L. Wang, A.K. Debnath, B.-J. Zheng, et al., Identification of a receptor-binding domain in the S protein of the novel human coronavirus Middle East respiratory syndrome coronavirus as an essential target for vaccine development, J. Virol. 87 (2013) 9939–9942, https://doi.org/10.1128/jvi.01048-13.
[81] V.S. Raj, H. Mou, S.L. Smits, D.H.W. Dekkers, M.A. Müller, R. Dijkman, D. Muth, J.A.A. Demmers, A. Zaki, R.A.M. Fouchier, et al., Dipeptidyl peptidase 4 is a functional receptor for the emerging human coronavirus-EMC, Nature 495 (2013) 251–254, https://doi.org/10.1038/nature12005.
[82] G. Lu, Y. Hu, Q. Wang, J. Qi, F. Gao, Y. Li, Y. Zhang, W. Zhang, Y. Yuan, J. Bao, et al., Molecular basis of binding between novel human coronavirus MERS-CoV and its receptor CD26, Nature 500 (2013) 227–231, https://doi.org/10.1038/nature12328.
[83] N. Wang, X. Shi, L. Jiang, S. Zhang, D. Wang, P. Tong, D. Guo, L. Fu, Y. Cui, X. Liu, et al., Structure of MERS-CoV spike receptor-binding domain complexed with human receptor DPP4, Cell Res. 23 (2013) 986–993, https://doi.org/10.1038/cr.2013.92.
[84] H. Mou, V.S. Raj, F.J.M. van Kuppeveld, P.J.M. Rottier, B.L. Haagmans, B.J. Bosch, The receptor binding domain of the new Middle East respiratory syndrome coronavirus maps to a 231-residue region in the spike protein that efficiently elicits neutralizing antibodies, J. Virol. 87 (2013) 9379–9383, https://doi.org/10.1128/jvi.01277-13.
[85] F. Li, Receptor recognition mechanisms of coronaviruses: a decade of structural studies, J. Virol. 89 (2015) 1954–1964, https://doi.org/10.1128/jvi.02615-14.
[86] K.M. Peck, T. Scobey, J. Swanstrom, K.L. Jensen, C.L. Burch, R.S. Baric, M.T. Heise, Permissivity of dipeptidyl peptidase 4 orthologs to Middle East respiratory syndrome coronavirus is governed by glycosylation and other complex determinants, J. Virol. 91 (2017)https://doi.org/10.1128/jvi.00534-17.
[87] K.M. Peck, A.S. Cockrell, B.L. Yount, T. Scobey, R.S. Baric, M.T. Heise, Glycosylation of mouse DPP4 plays a role in inhibiting Middle East respiratory syndrome coronavirus infection, J. Virol. 89 (2015) 4696–4699, https://doi.org/10.1128/jvi.03445-14.
[88] A.S. Cockrell, K.M. Peck, B.L. Yount, S.S. Agnihothram, T. Scobey, N.R. Curnes, R.S. Baric, M.T. Heise, Mouse Dipeptidyl peptidase 4 is not a functional receptor for Middle East respiratory syndrome coronavirus infection, J. Virol. 88 (2014) 5195–5199, https://doi.org/10.1128/jvi.03764-13.
[89] A. Barlan, J. Zhao, M.K. Sarkar, K. Li, P.B. McCray, S. Perlman, T. Gallagher, Receptor variation and susceptibility to Middle East respiratory syndrome coronavirus infection, J. Virol. 88 (2014) 4953–4961, https://doi.org/10.1128/jvi.00161-14.
[90] Y.M. Arabi, A. Al-Omari, Y. Mandourah, F. Al-Hameed, A.A. Sindi, B. Alraddadi, S. Shalhoub, A. Almotairi, K. Al Khatib, A. Abdulmomen, et al., Critically ill patients with the middle east respiratory syndrome: a multicenter retrospective cohort study, Crit. Care Med. 45 (2017) 1683–1695, https://doi.org/10.1097/CCM.0000000000002621.
[91] Y.M. Arabi, A.A. Arifi, H.H. Balkhy, H. Najm, A.S. Aldawood, A. Ghabashi, H. Hawa, A. Alothman, A. Khaldi, B. Al Raiy, Clinical course and outcomes of critically ill patients with middle east respiratory syndrome coronavirus infection, Ann. Intern. Med. 160 (2014), 389–397, https://doi.org/10.7326/m13-2486.
[92] A.M. Al-Osail, M.J. Al-Wazzah, The history and epidemiology of Middle East respiratory syndrome corona virus, Multidiscip. Respir. Med. 12 (2017).
[93] N. Zhu, D. Zhang, W. Wang, X. Li, B. Yang, J. Song, X. Zhao, B. Huang, W. Shi, R. Lu, et al., A novel coronavirus from patients with pneumonia in China, 2019, N. Engl. J. Med. 382 (2020) 727–733, https://doi.org/10.1056/nejmoa2001017.
[94] E.I. Azhar, S. Lanini, G. Ippolito, A. Zumla, The middle east respiratory syndrome coronavirus – a continuing risk to global health security, Advances in Experimental Medicine and Biology, vol. 972, Springer, New York LLC 2017, pp. 49–60.
[95] A. Zumla, J.F.W. Chan, E.I. Azhar, D.S.C. Hui, K.Y. Yuen, Coronaviruses-drug discovery and therapeutic options, Nat. Rev. Drug Discov. 15 (2016) 327–347.
[96] H.M. Al-Dorzi, S. Alsolamy, Y.M. Arabi, Critically ill patients with Middle East respiratory syndrome coronavirus infection, Crit. Care 20 (2016).
[97] K. Kupferschmidt, Camel vaccine offers hope to stop MERS: vaccinated animals shed less virus, but is that good enough to prevent human outbreaks? Science (80-.). 350 (2015) 1453.
[98] A. Zumla, D.S. Hui, S. Perlman, Middle East respiratory syndrome, Lancet 386 (2015) 995–1007.
[99] C. Drosten, B. Meyer, M.A. Müller, V.M. Corman, M. Al-Masri, R. Hossain, H. Madani, A. Sieberg, B.J. Bosch, E. Lattwein, et al., Transmission of MERS-coronavirus in household contacts, N. Engl. J. Med. 371 (2014) 828–835, https://doi.org/10.1056/nejmoa1405858.
[100] I.K. Oboho, S.M. Tomczyk, A.M. Al-Asmari, A.A. Banjar, H. Al-Mugti, M.S. Aloraini, K.Z. Alkhaldi, E.L. Almohammadi, B.M. Alraddadi, S.I. Gerber, et al., 2014 MERS-CoV outbreak in Jeddah — a link to health care facilities, N. Engl. J. Med. 372 (2015) 846–854, https://doi.org/10.1056/nejmoa1408636.
[101] M. Senga, Y.M. Arabi, R.A. Fowler, Clinical spectrum of the Middle East respiratory syndrome coronavirus (MERS-CoV), J. Infect. Public Health 10 (2017) 191–194, https://doi.org/10.1016/j.jiph.2016.04.008.
[102] M. Alghamdi, F. Mushtaq, N. Awn, S. Shalhoub, MERS CoV infection in two renal transplant recipients: case report, Am. J. Transplant. 15 (2015) 1101–1104, https://doi.org/10.1111/ajt.13085.
[103] K.O. Alsaad, A.H. Hajeer, M. Al Balwi, M. Al Moaiqel, N. Al Oudah, A. Al Ajlan, S. AlJohani, S. Alsolamy, G.E. Gmati, H. Balkhy, et al., Histopathology of Middle East respiratory syndrome coronovirus (MERS-CoV) infection – clinicopathological and ultrastructural study, Histopathology 72 (2018) 516–524, https://doi.org/10.1111/his.13379.
[104] R.H. Cha, J.S. Joh, I. Jeong, J.Y. Lee, H.S. Shin, G. Kim, Y. Kim, Renal complications and their prognosis in Korean patients with Middle East respiratory syndrome-coronavirus from the central MERS-CoV designated hospital, J. Korean Med. Sci. 30 (2015) 1807–1814, https://doi.org/10.3346/jkms.2015.30.12.1807.
[105] D.L. Ng, F. Al Hosani, M.K. Keating, S.I. Gerber, T.L. Jones, M.G. Metcalfe, S. Tong, Y. Tao, N.N. Alami, L.M. Haynes, et al., Clinicopathologic, immunohistochemical, and ultrastructural findings of a fatal case of middle east respiratory syndrome coronavirus infection in the United Arab Emirates, April 2014, Am. J. Pathol. 186 (2016) 652–658, https://doi.org/10.1016/j.ajpath.2015.10.024.
[106] A. Assiri, J.A. Al-Tawfiq, A.A. Al-Rabeeah, F.A. Al-Rabiah, S. Al-Hajjar, A. Al-Barrak, H. Flemban, W.N. Al-Nassir, H.H. Balkhy, R.F. Al-Hakeem, et al., Epidemiological, demographic, and clinical characteristics of 47 cases of Middle East respiratory syndrome coronavirus disease from Saudi Arabia: a descriptive study, Lancet Infect. Dis. 13 (2013) 752–761, https://doi.org/10.1016/S1473-3099(13)70204-4.
[107] A. Assiri, A. McGeer, T.M. Perl, C.S. Price, A.A. Al Rabeeah, D.A.T. Cummings, Z.N. Alabdullatif, M. Assad, A. Almulhim, H. Makhdoom, et al., Hospital outbreak of Middle East respiratory syndrome coronavirus, N. Engl. J. Med. 369 (2013) 407–416, https://doi.org/10.1056/nejmoa1306742.
[108] C. Wang, P.W. Horby, F.G. Hayden, G.F. Gao, A novel coronavirus outbreak of global health concern, Lancet 395 (2020) 470–473.
[109] WHO Coronavirus Disease (COVID-19), Dashboard | WHO coronavirus disease (COVID-19) dashboard, Available online: https://covid19.who.int/.
[110] M. Bassetti, A. Vena, D.R. Giacobbe, The novel Chinese coronavirus (2019-nCoV) infections: challenges for fighting the storm, Eur. J. Clin. Investig. (2020) 50.
[111] A. Wu, Y. Peng, B. Huang, X. Ding, X. Wang, P. Niu, J. Meng, Z. Zhu, Z. Zhang, J. Wang, et al., Genome composition and divergence of the novel coronavirus (2019-nCoV) originating in China, Cell Host Microbe 27 (2020) 325–328, https://doi.org/10.1016/j.chom.2020.02.001.
[112] A.G. Harrison, T. Lin, P. Wang, et al., Mechanisms of SARS-CoV-2 transmission and pathogenesis, Trends. Immunol. 41 (2020) 1100–1115.
[113] R. Lu, X. Zhao, J. Li, P. Niu, B. Yang, H. Wu, W. Wang, H. Song, B. Huang, N. Zhu, et al., Genomic characterisation and epidemiology of 2019 novel coronavirus: implications for virus origins and receptor binding, Lancet 395 (2020) 565–574, https://doi.org/10.1016/S0140-6736(20)30251-8.
[114] X. Tang, C. Wu, X. Li, Y. Song, X. Yao, X. Wu, Y. Duan, H. Zhang, Y. Wang, Z. Qian, et al., On the origin and continuing evolution of SARS-CoV-2, Natl. Sci. Rev. 7 (2020) 1012–1023, https://doi.org/10.1093/nsr/nwaa036.
[115] P. Zhou, X. Lou Yang, X.G. Wang, B. Hu, L. Zhang, W. Zhang, H.R. Si, Y. Zhu, B. Li, C.L. Huang, et al., A pneumonia outbreak associated with a new coronavirus of probable bat origin, Nature 579 (2020) 270–273, https://doi.org/10.1038/s41586-020-2012-7.
[116] Y. Tang, J. Liu, D. Zhang, Z. Xu, J. Ji, C. Wen, Cytokine storm in COVID-19: the current evidence and treatment strategies, Front. Immunol. 11 (2020) 1708.
[117] M.G. Hemida, M.M. Ba Abduallah, The SARS-CoV-2 outbreak from a one health perspective, One Heal 10 (2020)https://doi.org/10.1016/j.onehlt.2020.100127.
[118] Y. Wan, J. Shang, R. Graham, R.S. Baric, F. Li, Receptor recognition by the novel coronavirus from Wuhan: an analysis based on decade-long structural studies of SARS coronavirus, J. Virol. 94 (2020) 127–147, https://doi.org/10.1128/jvi.00127-20.
[119] T. Zhang, Q. Wu, Z. Zhang, Pangolin Homology Associated with 2019-nCoV. *bioRxiv*, 2020https://doi.org/10.1101/2020.02.19.950253 2020.02.19.950253.
[120] N. Nao, J. Yamagishi, H. Miyamoto, M. Igarashi, R. Manzoor, A. Ohnuma, Y. Tsuda, W. Furuyama, A. Shigeno, M. Kajihara, et al., Genetic predisposition to acquire a polybasic cleavage site for highly pathogenic avian influenza virus hemagglutinin, MBio (2017) 8, https://doi.org/10.1128/mBio.02298-16.
[121] Y.R. Rastogi, A. Sharma, R. Nagraik, A. Aygün, F. Şen, The novel coronavirus 2019-nCoV: its evolution and transmission into humans causing global COVID-19 pandemic, Nat. Rev. Microbiol. 26 (2020) 1–8.
[122] L. Sabioni, A. De Lorenzo, C. Lamas, F. Muccillo, H.C. Castro-Faria-Neto, V. Estato, E. Tibiricа, Systemic microvascular endothelial dysfunction and disease severity in COVID-19 patients: evaluation by laser Doppler perfusion monitoring and cytokine/chemokine analysis, Microvasc. Res. 134 (2021), 104119, https://doi.org/10.1016/j.mvr.2020.104119.
[123] Z. Xu, L. Shi, Y. Wang, J. Zhang, L. Huang, C. Zhang, S. Liu, P. Zhao, H. Liu, L. Zhu, et al., Pathological findings of COVID-19 associated with acute respiratory distress syndrome, Lancet Respir. Med. 8 (2020) 420–422, https://doi.org/10.1016/S2213-2600(20)30076-X.
[124] D. Wang, B. Hu, C. Hu, F. Zhu, X. Liu, J. Zhang, B. Wang, H. Xiang, Z. Cheng, Y. Xiong, et al., Clinical characteristics of 138 hospitalized patients with 2019 novel coronavirus-infected pneumonia in Wuhan, China, JAMA - J. Am. Med. Assoc. 323 (2020) 1061–1069, https://doi.org/10.1001/jama.2020.1585.
[125] M. Dong, J. Zhang, X. Ma, J. Tan, L. Chen, S. Liu, Y. Xin, L. Zhuang, ACE2, TMPRSS2 distribution and extrapulmonary organ injury in patients with COVID-19, Biomed. Pharmacother. 131 (2020), 110678.
[126] V.G. Puelles, M. Lütgehetmann, M.T. Lindenmeyer, J.P. Sperhake, M.N. Wong, L. Allweiss, S. Chilla, A. Heinemann, N. Wanner, S. Liu, et al., Multiorgan and renal tropism of SARS-CoV-2, N. Engl. J. Med. 383 (2020) 590–592, https://doi.org/10.1056/nejmc2011400.
[127] Z. Varga, A.J. Flammer, P. Steiger, M. Haberecker, R. Andermatt, A.S. Zinkernagel, M.R. Mehra, R.A. Schuepbach, F. Ruschitzka, H. Moch, Endothelial cell infection and endotheliitis in COVID-19, Lancet 395 (2020) 1417–1418.
[128] M. Liao, Y. Liu, J. Yuan, Y. Wen, G. Xu, J. Zhao, L. Cheng, J. Li, X. Wang, F. Wang, et al., Single-cell landscape of bronchoalveolar immune cells in patients with COVID-19, Nat. Med. 26 (2020) 842–844, https://doi.org/10.1038/s41591-020-0901-9.
[129] Y. Zuo, S. Yalavarthi, H. Shi, K. Gockman, M. Zuo, J.A. Madison, C. Blair, A. Weber, B.J. Barnes, M. Egeblad, et al., Neutrophil extracellular traps in COVID-19, JCI Insight 5 (2020)https://doi.org/10.1172/jci.insight.138999.
[130] B. Lomniczi, Biological properties of avian coronavirus RNA, J. Gen. Virol. 36 (1977) 531–533, https://doi.org/10.1099/0022-1317-36-3-531.

[131] M.M. Lai, C.L. Liao, Y.J. Lin, X. Zhang, Coronavirus: how a large RNA viral genome is replicated and transcribed, Infect. Agents Dis. 3 (1994) 98–105.
[132] C.A.M. de Haan, P.S. Masters, X. Shen, S. Weiss, P.J.M. Rottier, The group-specific murine coronavirus genes are not essential, but their deletion, by reverse genetics, is attenuating in the natural host, Virology 296 (2002) 177–189, https://doi.org/10.1006/viro.2002.1412.
[133] J.O. Norman, A.W. McClurkin, H.L. Bachrach, Infectious nucleic acid from a transmissible agent causing gastroenteritis in pigs, J. Comp. Pathol. 78 (1968) 227–235, https://doi.org/10.1016/0021-9975(68)90099-6.
[134] G. Schochetman, R.H. Stevens, R.W. Simpson, Presence of infectious polyadenylated RNA in coronavirus avian bronchitis virus, Virology 77 (1977) 772–782, https://doi.org/10.1016/0042-6822(77)90498-6.
[135] H. Wege, A. Mueller, V. Ter Meulen, Genomic RNA of the murine coronavirus JHM, J. Gen. Virol. 41 (1978) 217–227, https://doi.org/10.1099/0022-1317-41-2-217.
[136] F.P. Polack, S.J. Thomas, N. Kitchin, J. Absalon, A. Gurtman, S. Lockhart, J.L. Perez, G. Pérez Marc, E.D. Moreira, C. Zerbini, et al., Safety and efficacy of the BNT162b2 mRNA Covid-19 vaccine, N. Engl. J. Med. 383 (2020) 2603–2615, https://doi.org/10.1056/nejmoa2034577.
[137] J.D. Dinman, Programmed ribosomal frameshifting goes beyond viruses, Microbe 1 (2006) 521–527.
[138] J.L. Jacobs, A.T. Belew, R. Rakauskaite, J.D. Dinman, Identification of functional, endogenous programmed - 1 ribosomal frameshift signals in the genome of Saccharomyces cerevisiae, Nucleic Acids Res. 35 (2007) 165–174, https://doi.org/10.1093/nar/gkl1033.
[139] L.A. Klobutcher, P.J. Farabaugh, Shifty ciliates: frequent programmed translational frameshifting in euplotids, Cell 111 (2002) 763–766, https://doi.org/10.1016/s0092-8674(02)01138-8.
[140] A.B. Hammell, R.C. Taylor, S.W. Peltz, J.D. Dinman, Identification of putative programmed −1 ribosomal frameshift signals in large DNA databases, Genome Res. 9 (1999) 417–427, https://doi.org/10.1101/gr.9.5.417.
[141] P.V. Baranov, R.F. Gesteland, J.F. Atkins, Recoding: translational bifurcations in gene expression, Gene 286 (2002) 187–201, https://doi.org/10.1016/s0378-1119(02)00423-7.
[142] B. Cobucci-Ponzano, M. Rossi, M. Moracci, Translational recoding in archaea, Extremophiles 16 (2012) 793–803, https://doi.org/10.1007/s00792-012-0482-8.
[143] R.S. Baric, B. Yount, Subgenomic negative-strand RNA function during mouse hepatitis virus infection, J. Virol. 74 (2000) 4039–4046, https://doi.org/10.1128/jvi.74.9.4039-4046.2000.
[144] A. Dalton, F. Haguenau, Ultrastructure of Animal Viruses and Bacteriophages : An Atlas, 1973.
[145] H.A. Davies, M.R. Macnaughton, Comparison of the morphology of three coronaviruses, Arch. Virol. 59 (1979) 25–33, https://doi.org/10.1007/BF01317891.
[146] M.L. Ng, J.W.M. Lee, M.L.N. Leong, A.E. Ling, H.C. Tan, E.E. Ooi, Topographic changes in SARS coronavirus-infected cells during late stages of infection, Emerg. Infect. Dis. 10 (2004) 1907–1914, https://doi.org/10.3201/eid1011.040195.
[147] B.W. Neuman, G. Kiss, A.H. Kunding, D. Bhella, M.F. Baksh, S. Connelly, B. Droese, J.P. Klaus, S. Makino, S.G. Sawicki, et al., A structural analysis of M protein in coronavirus assembly and morphology, J. Struct. Biol. 174 (2011) 11–22, https://doi.org/10.1016/j.jsb.2010.11.021.
[148] B.W. Neuman, J.S. Joseph, K.S. Saikatendu, P. Serrano, A. Chatterjee, M.A. Johnson, L. Liao, J.P. Klaus, J.R. Yates 3rd, K. Wüthrich, et al., Proteomics analysis unravels the functional repertoire of coronavirus nonstructural protein 3, J. Virol. 82 (2008) 5279–5294, https://doi.org/10.1128/JVI.02631-07.
[149] M. Bárcena, G.T. Oostergetel, W. Bartelink, F.G.A. Faas, A. Verkleij, P.J.M. Rottier, A.J. Koster, B.J. Bosch, Cryo-electron tomography of mouse hepatitis virus: insights into the structure of the coronavirion, Proc. Natl. Acad. Sci. U. S. A. 106 (2009) 582–587, https://doi.org/10.1073/pnas.0805270106.
[150] K. Narayanan, A. Maeda, J. Maeda, S. Makino, Characterization of the coronavirus M protein and nucleocapsid interaction in infected cells, J. Virol. 74 (2000) 8127–8134, https://doi.org/10.1128/jvi.74.17.8127-8134.2000.
[151] C.A.M. de Haan, L. Kuo, P.S. Masters, H. Vennema, P.J.M. Rottier, Coronavirus particle assembly: primary structure requirements of the membrane protein, J. Virol. 72 (1998) 6838–6850, https://doi.org/10.1128/jvi.72.8.6838-6850.1998.
[152] J.K. Locker, G. Griffiths, M.C. Horzinek, P.J. Rottier, O-glycosylation of the coronavirus M protein. Differential localization of sialyltransferases in N- and O-linked glycosylation, J. Biol. Chem. 267 (1992) 14094–14101.
[153] D. Escors, E. Camafeita, J. Ortego, H. Laude, L. Enjuanes, Organization of two Transmissible Gastroenteritis Coronavirus Membrane Protein Topologies within the Virion and Core, J. Virol. 75 (2001) 12228–12240, https://doi.org/10.1128/jvi.75.24.12228-12240.2001.
[154] D. Escors, J. Ortego, H. Laude, L. Enjuanes, The membrane M protein carboxy terminus binds to transmissible gastroenteritis coronavirus core and contributes to core stability, J. Virol. 75 (2001) 1312–1324, https://doi.org/10.1128/JVI.75.3.1312-1324.2001.
[155] L. Kuo, P.S. Masters, Genetic evidence for a structural interaction between the carboxy termini of the membrane and nucleocapsid proteins of mouse hepatitis virus, J. Virol. 76 (2002) 4987–4999, https://doi.org/10.1128/jvi.76.10.4987-4999.2002.
[156] C.A.M. de Haan, H. Vennema, P.J.M. Rottier, Assembly of the coronavirus envelope: Homotypic interactions between the M proteins, J. Virol. 74 (2000) 4967–4978, https://doi.org/10.1128/jvi.74.11.4967-4978.2000.
[157] P. Venkatagopalan, S.M. Daskalova, L.A. Lopez, K.A. Dolezal, B.G. Hogue, Coronavirus envelope (E) protein remains at the site of assembly, Virology 478 (2015) 75–85, https://doi.org/10.1016/j.virol.2015.02.005.
[158] J.L. Nieto-Torres, M.L. DeDiego, C. Verdiá-Báguena, J.M. Jimenez-Guardeño, J.A. Regla-Nava, R. Fernandez-Delgado, C. Castaño-Rodriguez, A. Alcaraz, J. Torres, V.M. Aguilella, et al., Severe acute respiratory syndrome coronavirus envelope protein ion channel activity promotes virus fitness and pathogenesis, PLoS Pathog. 10 (2014), e1004077, https://doi.org/10.1371/journal.ppat.1004077.
[159] J. Ortego, D. Escors, H. Laude, L. Enjuanes, Generation of a replication-competent, propagation-deficient virus vector based on the transmissible gastroenteritis coronavirus genome, J. Virol. 76 (2002) 11518–11529, https://doi.org/10.1128/jvi.76.22.11518-11529.2002.
[160] K.M. Curtis, B. Yount, R.S. Baric, Heterologous gene expression from transmissible gastroenteritis virus replicon particles, J. Virol. 76 (2002) 1422–1434, https://doi.org/10.1128/jvi.76.3.1422-1434.2002.
[161] E. Corse, C.E. Machamer, Infectious bronchitis virus E protein is targeted to the Golgi complex and directs release of virus-like particles, J. Virol. 74 (2000) 4319–4326, https://doi.org/10.1128/jvi.74.9.4319-4326.2000.
[162] M.L. DeDiego, E. Alvarez, F. Almazán, M.T. Rejas, E. Lamirande, A. Roberts, W.-J. Shieh, S.R. Zaki, K. Subbarao, L. Enjuanes, A severe acute respiratory syndrome coronavirus that lacks the E gene is attenuated in vitro and in vivo, J. Virol. 81 (2007) 1701–1713, https://doi.org/10.1128/JVI.01467-06.
[163] L. Kuo, K.R. Hurst, P.S. Masters, Exceptional flexibility in the sequence requirements for coronavirus small envelope protein function, J. Virol. 81 (2007) 2249–2262, https://doi.org/10.1128/JVI.01577-06.
[164] J.L. Nieto-Torres, M.L. DeDiego, E. Álvarez, J.M. Jiménez-Guardeño, J.A. Regla-Nava, M. Llorente, L. Kremer, S. Shuo, L. Enjuanes, Subcellular location and topology of severe acute respiratory syndrome coronavirus envelope protein, Virology 415 (2011) 69–82, https://doi.org/10.1016/j.virol.2011.03.029.
[165] Y. Li, W. Surya, S. Claudine, J. Torres, Structure of a conserved Golgi complex-targeting signal in coronavirus envelope proteins, J. Biol. Chem. 289 (2014) 12535–12549, https://doi.org/10.1074/jbc.M114.560094.
[166] C. Verdiá-Báguena, J.L. Nieto-Torres, A. Alcaraz, M.L. DeDiego, J. Torres, V.M. Aguilella, L. Enjuanes, Coronavirus E protein forms ion channels with functionally and structurally-involved membrane lipids, Virology 432 (2012) 485–494, https://doi.org/10.1016/j.virol.2012.07.005.
[167] C. Verdiá-Báguena, J.L. Nieto-Torres, A. Alcaraz, M.L. Dediego, L. Enjuanes, V.M. Aguilella, Analysis of SARS-CoV E protein ion channel activity by tuning the protein and lipid charge, Biochim. Biophys. Acta 1828 (2013) 2026–2031, https://doi.org/10.1016/j.bbamem.2013.05.008.
[168] J. Torres, U. Maheswari, K. Parthasarathy, L. Ng, D.X. Liu, X. Gong, Conductance and amantadine binding of a pore formed by a lysine-flanked transmembrane domain of SARS coronavirus envelope protein, Protein Sci. 16 (2007) 2065–2071, https://doi.org/10.1110/ps.062730007.
[169] H. Laude, D. Rasschaert, J.C. Huet, Sequence and N-terminal processing of the transmembrane protein E1 of the coronavirus transmissible gastroenterits virus, J. Gen. Virol. 68 (1987) 1687–1693, https://doi.org/10.1099/0022-1317-68-6-1687.
[170] K.R. Hurst, L. Kuo, C.A. Koetzner, R. Ye, B. Hsue, P.S. Masters, A major determinant for membrane protein interaction localizes to the carboxy-terminal domain of the mouse coronavirus Nucleocapsid protein, J. Virol. 79 (2005) 13285–13297, https://doi.org/10.1128/jvi.79.21.13285-13297.2005.
[171] K. Narayanan, C.-J. Chen, J. Maeda, S. Makino, Nucleocapsid-independent specific viral RNA packaging via viral envelope protein and viral RNA signal, J. Virol. 77 (2003) 2922–2927, https://doi.org/10.1128/jvi.77.5.2922-2927.2003.
[172] H. Chen, A. Gill, B.K. Dove, S.R. Emmett, C.F. Kemp, M.A. Ritchie, M. Dee, J.A. Hiscox, Mass spectroscopic characterization of the coronavirus infectious bronchitis virus nucleoprotein and elucidation of the role of phosphorylation in RNA binding by using surface plasmon resonance, J. Virol. 79 (2005) 1164–1179, https://doi.org/10.1128/JVI.79.2.1164-1179.2005.
[173] A.N. Zakhartchouk, S. Viswanathan, J.B. Mahony, J. Gauldie, L.A. Babiuk, Severe acute respiratory syndrome coronavirus nucleocapsid protein expressed by an adenovirus vector is phosphorylated and immunogenic in mice, J. Gen. Virol. 86 (2005) 211–215, https://doi.org/10.1099/vir.0.80530-0.
[174] H.C. Song, M.-Y. Seo, K. Stadler, B.J. Yoo, Q.-L. Choo, S.R. Coates, Y. Uematsu, T. Harada, C.E. Greer, J.M. Polo, et al., Synthesis and characterization of a native, oligomeric form of recombinant severe acute respiratory syndrome coronavirus spike glycoprotein, J. Virol. 78 (2004) 10328–10335, https://doi.org/10.1128/JVI.78.19.10328-10335.2004.
[175] O. Krokhin, Y. Li, A. Andonov, H. Feldmann, R. Flick, S. Jones, U. Stroeher, N. Bastien, K.V.N. Dasuri, K. Cheng, et al., Mass spectrometric characterization of proteins from the SARS virus: a preliminary report, Mol. Cell. Proteomics 2 (2003) 346–356, https://doi.org/10.1074/mcp.M300048-MCP200.
[176] Y. Watanabe, J.D. Allen, D. Wrapp, J.S. McLellan, M. Crispin, Site-specific glycan analysis of the SARS-CoV-2 spike, Science 369 (2020) 330–333, https://doi.org/10.1126/science.abb9983.
[177] B. Delmas, H. Laude, Assembly of coronavirus spike protein into trimers and its role in epitope expression, J. Virol. 64 (1990) 5367–5375, https://doi.org/10.1128/jvi.64.11.5367-5375.1990.
[178] D. Wrapp, N. Wang, K.S. Corbett, J.A. Goldsmith, C.-L. Hsieh, O. Abiona, B.S. Graham, J.S. McLellan, Cryo-EM structure of the 2019-nCoV spike in the prefusion conformation, Science 367 (2020) 1260–1263, https://doi.org/10.1126/science.abb2507.
[179] J. Shang, W. Yushun, L. Chuming, Y. Gang, G. Qibin, A. Ashley, L. Fang, et al., Cell entry mechanisms of SARS-CoV-2, PNAS 117 (2020) 11727–11734, https://doi.org/10.1016/j.cell.2020.02.052 e8.
[180] S. Bertram, R. Dijkman, M. Habjan, A. Heurich, S. Gierer, I. Glowacka, K. Welsch, M. Winkler, H. Schneider, H. Hofmann-Winkler, et al., TMPRSS2 activates the human coronavirus 229E for cathepsin-independent host cell entry and is expressed in viral target cells in the respiratory epithelium, J. Virol. 87 (2013) 6150–6160, https://doi.org/10.1128/JVI.03372-12.
[181] L. Du, R.Y. Kao, Y. Zhou, Y. He, G. Zhao, C. Wong, S. Jiang, K.-Y. Yuen, D.-Y. Jin, B.-J. Zheng, Cleavage of spike protein of SARS coronavirus by protease factor Xa is

associated with viral infectivity, Biochem. Biophys. Res. Commun. 359 (2007) 174–179, https://doi.org/10.1016/j.bbrc.2007.05.092.
[182] Q. Wang, Y. Zhang, L. Wu, S. Niu, C. Song, Z. Zhang, G. Lu, C. Qiao, Y. Hu, K.-Y. Yuen, et al., Structural and functional basis of SARS-CoV-2 entry by using human ACE2, Cell 181 (2020) 894–904 , e9 https://doi.org/10.1016/j.cell.2020.03.045.
[183] J. Lan, J. Ge, J. Yu, S. Shan, H. Zhou, S. Fan, Q. Zhang, X. Shi, Q. Wang, L. Zhang, et al., Structure of the SARS-CoV-2 spike receptor-binding domain bound to the ACE2 receptor, Nature 581 (2020) 215–220, https://doi.org/10.1038/s41586-020-2180-5.
[184] P.F.N. Souza, F.E.S. Lopes, J.L. Amaral, C.D.T. Freitas, J.T.A. Oliveira, International journal of biological macromolecules a molecular docking study revealed that synthetic peptides induced conformational changes in the structure of SARS-CoV-2 spike glycoprotein , disrupting the interaction with human ACE2 receptor, Int. J. Biol. Macromol. 164 (2020) 66–76, https://doi.org/10.1016/j.ijbiomac.2020.07.174.
[185] P.F.N. Souza, J.L. Amaral, L.P. Bezerra, F.E.S. Lopes, V.N. Freire, J.T.A. Oliveira, C.D.T. Freitas, ACE2-derived peptides interact with the RBD domain of SARS-CoV-2 spike glycoprotein, disrupting the interaction with the human ACE2 receptor, J. Biomol. Struct. Dyn. (2021) 1–14, https://doi.org/10.1080/07391102.2020.1871415.
[186] J.K. Millet, G.R. Whittaker, Physiological and molecular triggers for SARS-CoV membrane fusion and entry into host cells, Virology 517 (2018) 3–8, https://doi.org/10.1016/j.virol.2017.12.015.
[187] Chambers, P.; Pringle, C.R.; Easton, A.J. Heptad repeat sequences are located adjacent to hydrophobic regions in several types of virus fusion glycoproteins. J. Gen. Virol. 1990, 71 (Pt 12, 3075–3080, doi:https://doi.org/10.1099/0022-1317-71-12-3075.
[188] S. Liu, G. Xiao, Y. Chen, Y. He, J. Niu, C.R. Escalante, H. Xiong, J. Farmar, A.K. Debnath, P. Tien, et al., Interaction between heptad repeat 1 and 2 regions in spike protein of SARS-associated coronavirus: implications for virus fusogenic mechanism and identification of fusion inhibitors, Lancet (London, England) 363 (2004) 938–947, https://doi.org/10.1016/S0140-6736(04)15788-7.
[189] S. Xia, L. Yan, W. Xu, A.S. Agrawal, A. Algaissi, C.-T.K. Tseng, Q. Wang, L. Du, W. Tan, I.A. Wilson, et al., A pan-coronavirus fusion inhibitor targeting the HR1 domain of human coronavirus spike, Sci. Adv. 5 (2019), eaav4580, https://doi.org/10.1126/sciadv.aav4580.
[190] W. Widagdo, N.M.A. Okba, W. Li, A. de Jong, R.L. de Swart, L. Begeman, J.M.A. van den Brand, B.-J. Bosch, B.L. Haagmans, Species-specific Colocalization of Middle East respiratory syndrome coronavirus attachment and entry receptors, J. Virol. 93 (2019)https://doi.org/10.1128/jvi.00107-19.
[191] W. Weissenhorn, A. Dessen, L.J. Calder, S.C. Harrison, J.J. Skehel, D.C. Wiley, Structural basis for membrane fusion by enveloped viruses, Mol. Membr. Biol. 16 (1999) 3–9, https://doi.org/10.1080/096876899294706.
[192] F. Li, Structure, function, and evolution of coronavirus spike proteins, Annu. Rev. Virol. 3 (2016) 237–261, https://doi.org/10.1146/annurev-virology-110615-042301.
[193] R.N. Kirchdoerfer, C.A. Cottrell, N. Wang, J. Pallesen, H.M. Yassine, H.L. Turner, K.S. Corbett, B.S. Graham, J.S. McLellan, A.B. Ward, Pre-fusion structure of a human coronavirus spike protein, Nature 531 (2016) 118–121, https://doi.org/10.1038/nature17200.
[194] T. Heald-Sargent, T. Gallagher, Ready, set, fuse! The coronavirus spike protein and acquisition of fusion competence, Viruses 4 (2012) 557–580, https://doi.org/10.3390/v4040557.
[195] S. Belouzard, J.K. Millet, B.N. Licitra, G.R. Whittaker, Mechanisms of coronavirus cell entry mediated by the viral spike protein, Viruses 4 (2012) 1011–1033, https://doi.org/10.3390/v4061011.
[196] K. Wang, W. Chen, Z. Zhang, Y. Deng, J.Q. Lian, P. Du, D. Wei, Y. Zhang, X.X. Sun, L. Gong, et al., CD147-spike protein is a novel route for SARS-CoV-2 infection to host cells, Signal Transduct. Target. Ther. 5 (2020) 1–10, https://doi.org/10.1038/s41392-020-00426-x.
[197] Y. Li, J. Xu, L. Chen, W. De Zhong, Z. Zhang, L. Mi, Y. Zhang, C.G. Liao, H.J. Bian, J.L. Jiang, et al., HAb18G (CD147), a cancer-associated biomarker and its role in cancer detection, Histopathology 54 (2009) 677–687, https://doi.org/10.1111/j.1365-2559.2009.03280.x.
[198] T. Pushkarsky, G. Zybarth, L. Dubrovsky, V. Yurchenko, H. Tang, H. Guo, B. Toole, B. Sherry, M. Bukrinsky, CD147 facilitates HIV-1 infection by interacting with virus-associated cyclophilin a, Proc. Natl. Acad. Sci. U. S. A. 98 (2001) 6360–6365, https://doi.org/10.1073/pnas.111583198.
[199] R. Yan, Y. Zhang, Y. Li, L. Xia, Y. Guo, Q. Zhou, Structural basis for the recognition of SARS-CoV-2 by full-length human ACE2, Science 367 (2020) 1444–1448, https://doi.org/10.1126/science.abb2762.
[200] S. Wang, Z. Qiu, Y. Hou, X. Deng, W. Xu, T. Zheng, P. Wu, S. Xie, W. Bian, C. Zhang, Z. Sun, K. Liu, C. Shan, A. Lin, S. Jiang, Y. Xie, Q. Zhou, L. Lu, J. Huang, X. Li, AXL is a candidate receptor for SARS-CoV-2 that promotes infection of pulmonary and bronchial epithelial cells, Cell Res. 31 (2021) 126–140https://doi.org/10.1038/s41422-020-00460-y.
[201] L. Chen, W. Liu, Q. Zhang, K. Xu, G. Ye, W. Wu, Z. Sun, F. Liu, K. Wu, B. Zhong, et al., RNA based mNGS approach identifies a novel human coronavirus from two individual pneumonia cases in 2019 Wuhan outbreak, Emerg. Microbes Infect. 9 (2020) 313–319, https://doi.org/10.1080/22221751.2020.1725399.
[202] C. Wei, L. Wan, Q. Yan, X. Wang, J. Zhang, X. Yang, Y. Zhang, C. Fan, D. Li, Y. Deng, J. Sun, J. Gong, X. Yang, Y. Wang, X. Wang, J. Li, H. Yang, H. Li, Z. Zhang, R. Wang, P. Du, Y. Zong, F. Yin, W. Zhang, N. Wang, Y. Peng, H. Lin, J. Feng, C. Qin, W. Chen, Q. Gao, R. Zhang, Y. Cao, H. Zhong, HDL-scavenger receptor B type 1 facilitates SARS-CoV-2 entry, Nat. Metab. 2 (2020) 1391–1400https://doi.org/10.1038/s42255-020-00324-0.
[203] L. Cantuti-Castelvetri, R. Ojha, L.D. Pedro, M. Djannatian, J. Franz, S. Kuivanen, F. van der Meer, K. Kallio, T. Kaya, M. Anastasina, T. Smura, L. Levanov, L. Szirovicza, A. Tobi, H. Kallio-Kokko, P. Österlund, M. Joensuu, F.A. Meunier, S.J. Butcher, M.S. Winkler, B. Mollenhauer, A. Helenius, O. Gokce, T. Teesalu, J. Hepojoki, O. Vapalahti, C. Stadelmann, G. Balistreri, M. Simons, Neuropilin-1 facilitates SARS-CoV-2 cell entry and infectivity, Science (80-.) 370 (2020) 856–860https://doi.org/10.1126/science.abd2985.
[204] J.L. Daly, B. Simonetti, C. Antón-Plágaro, M.K. Williamson, D.K. Shoemark, L. Simón-Gracia, K. Klein, M. Bauer, R. Hollandi, U.F. Greber, P. Horvath, R.B. Sessions, A. Helenius, J.A. Hiscox, T. Teesalu, D.A. Matthews, A.D. Davidson, P.J. Cullen, Y. Yamauchi, Neuropilin-1 is a host factor for SARS-CoV-2 infection, BioRxiv 865 (2020) 861–865https://doi.org/10.1101/2020.06.05.134114.
[205] X. Tang, M. Yang, Z. Duan, Z. Liao, L. Liu, R. Cheng, M. Fang, G. Wang, H. Liu, J. Xu, P.M. Kamau, Z. Zhang, L. Yang, X. Zhao, X. Peng, R. Lai, Transferrin receptor is another receptor for SARS-CoV-2 entry, BioRxiv 20 (2020) , 2020.10.23.350348 http://biorxiv.org/content/early/2020/10/23/2020.10.23.350348.abstract.
[206] R. Amraei, W. Yin, M.A. Napoleon, E.L. Suder, J. Berrigan, Q. Zhao, J. Olejnik, K.B. Chandler, C. Xia, J. Feldman, B.M. Hauser, T.M. Caradonna, A.G. Schmidt, S. Gummuluru, E. Mühlberger, V. Chitalia, ,6,7 , (2020).
[207] S. Matsuyama, N. Nagata, K. Shirato, M. Kawase, M. Takeda, F. Taguchi, Efficient activation of the severe acute respiratory syndrome coronavirus spike protein by the transmembrane protease TMPRSS2, J. Virol. 84 (2010) 12658–12664, https://doi.org/10.1128/JVI.01542-10.
[208] P.F.N. Souza, F.E.L. Carvalho, Killing two birds with one stone: how do Plant viruses break down plant defenses and manipulate cellular processes to replicate themselves? J. Plant Biol. 62 (2019) 170–180, https://doi.org/10.1007/s12374-019-0056-8.
[209] Y. Fan, K. Zhao, Z.L. Shi, P. Zhou, Bat coronaviruses in China, Viruses 11 (2019).
[210] M. Yuan, N.C. Wu, X. Zhu, C.-C.D. Lee, R.T.Y. So, H. Lv, C.K.P. Mok, I.A. Wilson, A highly conserved cryptic epitope in the receptor binding domains of SARS-CoV-2 and SARS-CoV, Science 368 (2020) 630–633, https://doi.org/10.1126/science.abb7269.
[211] P.F.N. Souza, Masters of manipulation: how do positive-sense RNA viruses employ plant proteins to replicate, move from cell to cell, and overcome antiviral immunity? J. Plant Dis. Prot. (2020)https://doi.org/10.1007/s41348-020-00342-w.
[212] A. Brufsky, Distinct viral clades of SARS-CoV-2: implications for modeling of viral spread, J. Med. Virol. 92 (2020) 1386–1390, https://doi.org/10.1002/jmv.25902.
[213] A. Spinello, A. Saltalamacchia, A. Magistrato, Is the rigidity of SARS-CoV-2 spike receptor-binding motif the Hallmark for its enhanced infectivity? Insights from all-atom simulations, J. Phys. Chem. Lett. 11 (2020) 4785–4790, https://doi.org/10.1021/acs.jpclett.0c01148.
[214] K.G. Andersen, A. Rambaut, W.I. Lipkin, E.C. Holmes, R.F. Garry, The proximal origin of SARS-CoV-2, Nat. Med. 26 (2020) 450–452, https://doi.org/10.1038/s41591-020-0820-9.
[215] T.-J. Chang, D.-M. Yang, M.-L. Wang, K.-H. Liang, P.-H. Tsai, S.-H. Chiou, T.-H. Lin, C.-T. Wang, Genomic analysis and comparative multiple sequences of SARS-CoV2, J. Chin. Med. Assoc. 83 (2020) 537–543, https://doi.org/10.1097/JCMA.0000000000000335.
[216] B. Coutard, C. Valle, X. de Lamballerie, B. Canard, N.G. Seidah, E. Decroly, The spike glycoprotein of the new coronavirus 2019-nCoV contains a furin-like cleavage site absent in CoV of the same clade, Antivir. Res. 176 (2020), 104742, https://doi.org/10.1016/j.antiviral.2020.104742.
[217] J. Buchrieser, J. Dufloo, M. Hubert, B. Monel, D. Planas, M.M. Rajah, C. Planchais, F. Porrot, F. Guivel-Benhassine, S. Van der Werf, et al., Syncytia formation by SARS-CoV-2-infected cells, EMBO J. 39 (2020)https://doi.org/10.15252/embj.2020106267.
[218] A. Heurich, H. Hofmann-Winkler, S. Gierer, T. Liepold, O. Jahn, S. Pohlmann, TMPRSS2 and ADAM17 cleave ACE2 differentially and only proteolysis by TMPRSS2 augments entry driven by the severe acute respiratory syndrome coronavirus spike protein, J. Virol. 88 (2014) 1293–1307, https://doi.org/10.1128/jvi.02202-13.
[219] M. Kimura, T. Ota, On the rate of molecular evolution, J. Mol. Evol. 1 (1971) 1–17, https://doi.org/10.1007/BF01659390.
[220] S. Duchene, L. Featherstone, M. Haritopoulou-Sinanidou, A. Rambaut, P. Lemey, G. Baele, Temporal signal and the phylodynamic threshold of SARS-CoV-2, Virus Evol. 6 (2020), veaa061, https://doi.org/10.1093/ve/veaa061.
[221] E. Minskaia, T. Hertzig, A.E. Gorbalenya, V. Campanacci, C. Cambillau, B. Canard, J. Ziebuhr, Discovery of an RNA virus 3′->5′ exoribonuclease that is critically involved in coronavirus RNA synthesis, Proc. Natl. Acad. Sci. U. S. A. 103 (2006) 5108–5113, https://doi.org/10.1073/pnas.0508200103.
[222] L. Zhang, C. Jackson, H. Mou, A. Ojha, E. Rangarajan, T. Izard, M. Farzan, H. Choe, The D614G mutation in the SARS-CoV-2 spike protein reduces S1 shedding and increases infectivity, bioRxiv Prepr. Serv. Biol. (2020)https://doi.org/10.1101/2020.06.12.148726.
[223] B. Korber, W.M. Fischer, S. Gnanakaran, H. Yoon, J. Theiler, W. Abfalterer, N. Hengartner, E.E. Giorgi, T. Bhattacharya, B. Foley, et al., Tracking changes in SARS-CoV-2 spike: evidence that D614G increases infectivity of the COVID-19 virus, Cell (2020)https://doi.org/10.1016/j.cell.2020.06.043.
[224] J.A. Plante, Y. Liu, J. Liu, H. Xia, B.A. Johnson, K.G. Lokugamage, X. Zhang, A.E. Muruato, J. Zou, C.R. Fontes-Garfias, et al., Spike mutation D614G alters SARS-CoV-2 fitness, Nature (2020) 1–6, https://doi.org/10.1038/s41586-020-2895-3.
[225] Preliminary genomic characterisation of an emergent SARS-CoV-2 lineage in the UK defined by a novel set of spike mutations - SARS-CoV-2 coronavirus / nCoV-2019 genomic epidemiology - Virological, Available online: https://virological.org/t/preliminary-genomic-characterisation-of-an-emergent-sars-cov-2-lineage-in-the-uk-defined-by-a-novel-set-of-spike-mutations/563.
[226] Fiocruz publica Nota Técnica sobre nova variante do Sars-CoV-2 no Amazonas, Available online: https://portal.fiocruz.br/noticia/fiocruz-publica-nota-tecnica-sobre-nova-variante-do-sars-cov-2-no-amazonas (accessed on Jan 22, 2021).

APÊNDICE H - NEUTRALIZING EFFECT OF SYNTHETIC PEPTIDES TOWARD SARS-COV-2

ACS OMEGA

http://pubs.acs.org/journal/acsodf

Article

Neutralizing Effect of Synthetic Peptides toward SARS-CoV-2

Pedro F.N. Souza,* Maurício F. vanTilburg, Felipe P. Mesquita, Jackson L. Amaral, Luina B. Lima, Raquel C. Montenegro, Francisco E.S. Lopes, Rafael X. Martins, Leonardo Vieira, Davi F. Farias, Ana C. O. Monteiro-Moreira, Cleverson D.T. Freitas, Arnaldo S. Bezerra, Maria I. F. Guedes, Débora S.C.M. Castelo-Branco, and Jose T.A. Oliveira

Cite This: *ACS Omega* 2022, 7, 16222−16234 Read Online

ACCESS | Metrics & More | Article Recommendations | Supporting Information

ABSTRACT: The outbreak caused by SARS-CoV-2 has taken many lives worldwide. Although vaccination has started, the development of drugs to either alleviate or abolish symptoms of COVID-19 is still necessary. Here, four synthetic peptides were assayed regarding their ability to protect Vero E6 cells from SARS-CoV-2 infection and their toxicity to human cells and zebrafish embryos. All peptides had some ability to protect cells from infection by SARS-CoV-2 with the D614G mutation. Molecular docking predicted the ability of all peptides to interact with and induce conformational alterations in the spike protein containing the D614G mutation. PepKAA was the most effective peptide, by having the highest docking score regarding the spike protein and reducing the SARS-CoV-2 plaque number by 50% (EC_{50}) at a concentration of 0.15 mg mL^{-1}. Additionally, all peptides had no toxicity to three lines of human cells as well as to zebrafish larvae and embryos. Thus, these peptides have potential activity against SARS-CoV-2, making them promising to develop new drugs to inhibit cell infection by SARS-CoV-2.

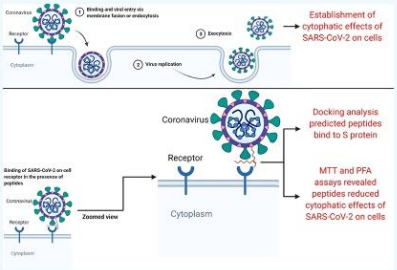

Downloaded via UNIV FED DO CEARA on November 2, 2022 at 15:32:11 (UTC).
See https://pubs.acs.org/sharingguidelines for options on how to legitimately share published articles.

INTRODUCTION

The outbreak of the coronavirus disease in late 2019 (COVID-19) is still ongoing and has already claimed more than 4 million lives worldwide.[1,2] The causative agent of COVID-19 was later identified as SARS-CoV-2 (Severe Acute Respiratory Syndrome Coronavirus 2), which is 96 and 79% similar, respectively, to BatCoV RatG13 (a coronavirus from bats) and another pandemic coronavirus, SARS-CoV.[3] Coronaviruses are a group of viruses belonging to the family *Coronaviridae*, a group of enveloped positive-stranded RNA viruses with both medical and veterinary importance. The RNA genome produces a larger polyprotein composed of non-structural (NSPs) and structural proteins (SPs). The NSPs are classified from 1 to 16 and the SPs are identified as spike (S), envelope (E), membrane (M), and nucleocapsid (N) proteins.[4]

Due to the huge effort of scientists worldwide, an unprecedented breakthrough was achieved. In less than a year, vaccination campaigns began in virtually all countries.[5] However, two problems have arisen: (1) the rate of vaccination is not fast enough to reach herd immunity worldwide, and (2) countries with low vaccination rates are a repository of SARS-CoV-2 mutants that threaten the efficacy of the vaccines, causing vaccinated people to be jeopardized by COVID-19.[4,6] Most of the mutations in the SARS-CoV-2 genome are concentrated in the RBD domain of S protein. S protein is the main focus of most vaccines developed, so mutations on it could reduce their efficacy.[6] Other points are that poor countries that cannot afford to buy vaccines are still struggling with COVID-19, and the development of specific drugs for clinical treatment of the symptoms is still necessary. Therefore, the development of drugs for COVID-19, despite the availability of vaccines, is still urgent.[7] Drug repositioning has been employed to accelerate the process of drug development. This entails testing drugs already approved for the treatment of other diseases against SARS-CoV-2. Despite reaching good results in computational simulations, in vitro tests have so far revealed the inefficiency of the targeted drugs.[7]

In this context, in two previous studies, our research group employed computational simulations to drive antimicrobial peptides toward the S protein[8] and Mpro[9] of SARS-CoV-2. In the first study, Souza et al.[8] reported that out of 8 peptides, two peptides, *Mo*-CBP_3-PepII and PepKAA, strongly bonded to the S protein, leading to changes in structural conformation and interaction with the ACE2 receptor. In the second study, Amaral et al.[9] employed the same peptides against Mpro. Of these, three

Received: April 8, 2022
Accepted: April 20, 2022
Published: April 28, 2022

ACS Publications

© 2022 The Authors. Published by American Chemical Society

https://doi.org/10.1021/acsomega.2c02203
ACS Omega 2022, 7, 16222−16234

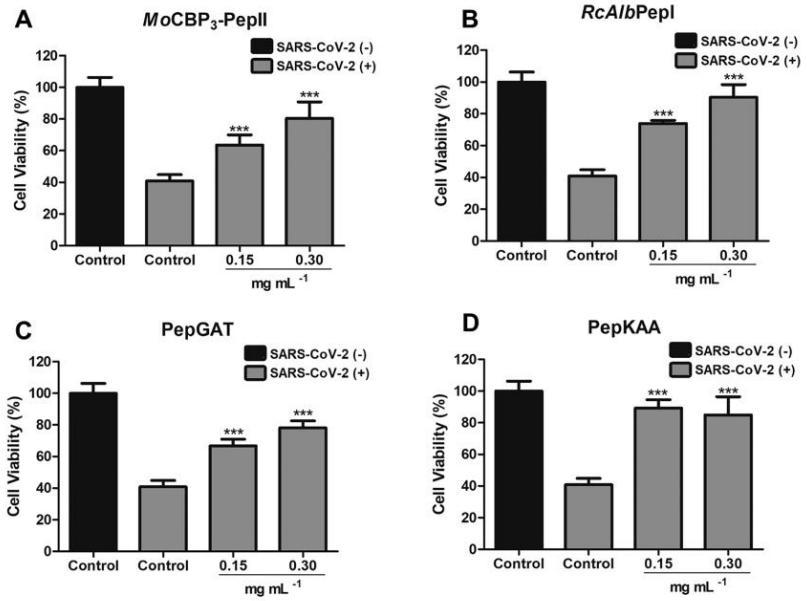

Figure 1. Inhibitory activity of synthetic peptides against SARS-CoV-2 infection. (A) *Mo*-CBP3-PepII, (B) *Rc*Alb-PepI, (C) PepGAT, and (D) PepKAA inhibiting Vero E6 cell infection by SARS-CoV-2 as revealed by MTT assay for cell viability. Peptides at different concentrations were incubated with SARS-CoV-2 for 30 min; then, SARS-CoV-2 was mixed with Vero E6 cells for 4 h. After that, cells were incubated for 96 h, and cell viability was evaluated by MTT assay. Vero E6 cells with and without SARS-CoV-2 infection were used as controls for cell viability. Data are shown as mean ± standard deviation of three independent experiments. ***$P < 0.001$. The neutralizing effect of peptides against SARS-CoV-2.

peptides, *Rc*Alb-PepI, PepGAT, and PepKAA, interacted the best with Mpro, leading to conformational changes and reduction in the catalytic site. The results of both studies suggested that those peptides could have anti-SARS-CoV-2 action in vitro, making them potential candidates for the development of a specific drug to treat COVID-19 symptoms.

The four peptides tested here were designed from plant proteins.[10−12] *Mo*-CBP$_3$-PepII and *Rc*Alb-PepI were designed, respectively, from a chitin-binding protein of *Moringa oleifera* and a 2S albumin of *Ricinus communis*.[10,11] PepGAT and PepKAA were designed from a chitinase from *Arabidopsis thaliana*.[12] All peptides are positively charged, have hydrophobic ratio from 40 to 65%, were predicted to have antiviral action, and are resistant to intestinal enzymes, indicating the potential for oral administration.[10−12] Here, we report the in vitro activity of those peptides against SARS-CoV-2 in addition to their level of toxicity.

RESULTS

Anti-SARS-CoV-2 Potential of Synthetic Peptides. To test whether the peptides can suppress virus-induced cytopathic effects, a simple and fast MTT [3-(4,5-dimethylthiazol-2-yl)-2,5-diphenyltetrazolium] bioassay for screening drugs against SARS-CoV-2 was used. The MTT assay is a simple colorimetric test to assess cell metabolic activity in a microplate reader. It is based on the activity of the NAD(P)H-dependent cellular oxidoreductase, which transforms the tetrazolium bromide from MTT into formazan, which has a purple color, allowing the determination of presence of the number of viable cells.[13] Based on that, we expected that the cells infected by SARS-CoV-2 would not convert the MTT into formazan because they had been killed by SARS-CoV-2, and the control cells (without SARS-CoV-2 exposure) would convert all MTT into formazan because they would be metabolically active (Figure 1).

All peptides were able to inhibit virus-induced cytopathic effects, with EC_{50} values in the microgram/milliliter range (Table 1). Thus, we performed a test with a fixed concentration

Table 1. EC50 Values for Peptides Treatment in Vero E6 Cell Culture Infected with SARS-CoV-2[a]

peptides	EC50 (mg mL^{-1})	CI95%
*Mo*CBP3-PepII	0.09	0.04−0.19
*RcAlb*PepI	0.05	0.03−0.07
PepGAT	0.08	0.07−0.09
PepKAA	0.04	0.02−0.07

[a]EC50: concentration of a drug that gives a half-maximal response. CI95%: 95% confidence interval.

to investigate the inhibition of virus-induced cytopathic effects at 0.15 and 0.30 mg mL^{-1}. The positive control cells [exposed to dimethyl sulfoxide (DMSO)] presented 100% viability, while the cells infected with SARS-CoV-2 presented about 40% viability (Figure 1). At 0.15 mg mL^{-1}, the peptides *Mo*-CBP3-PepII, *RcAlb*-PepI, PepGAT, and PepKAA reduced the SARS-CoV-2 cytopathic effects by 60, 75, 65, and 90%, respectively (Figure 1). At 0.30 mg mL^{-1}, the reductions of SARS-CoV-2 cytopathic effects were 75, 90, 85, and 80%, respectively, for *Mo*-

https://doi.org/10.1021/acsomega.2c02203
ACS Omega 2022, 7, 16222−16234

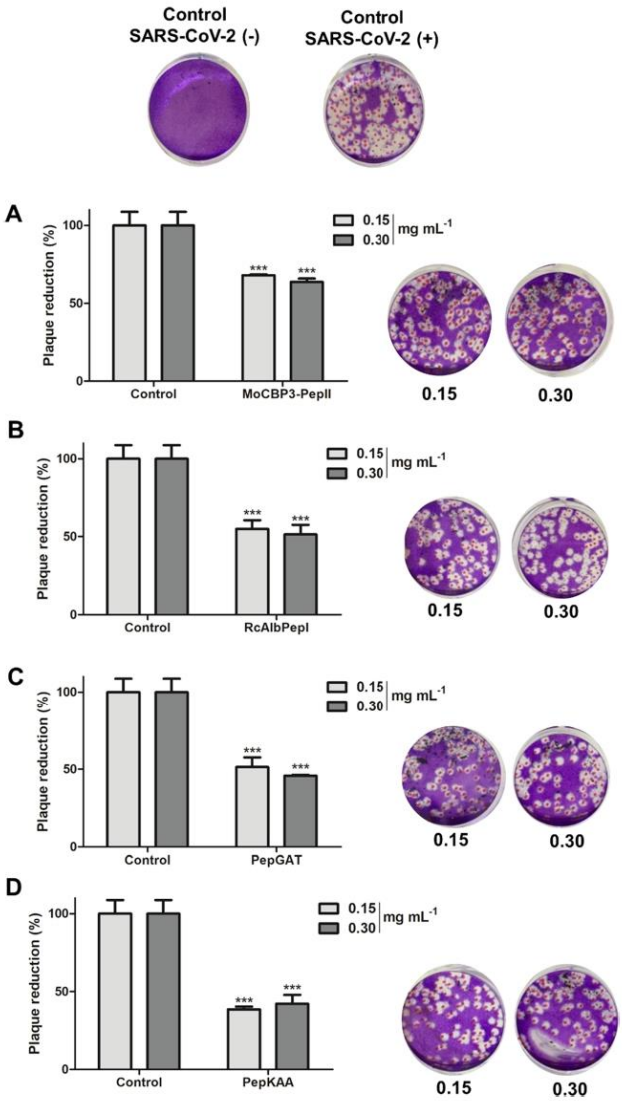

Figure 2. Plaque reduction neutralization effect of synthetic peptides against SARS-CoV-2. (A) *Mo*-CBP3-PepII, (B) *Rc*Alb-PepI, (C) PepGAT, and (D) PepKAA inhibiting SARS-CoV-2 plaque formation on Vero E6 cells. One hundred PFU of SARS-CoV-2 were incubated with the peptides at different at 37 °C for 1 h. Then, they were added to pre-seeded Vero E6 cells at 90−100% confluence. After fixation for 1 h, the overlay was removed, and cells were stained with 0.5% crystal violet. Vero E6 cells with and without SARS-CoV-2 were used as negative controls for SARS-CoV-2 neutralization. Data are shown as mean ± standard deviation of three independent experiments. ***$P < 0.001$.

CBP3-PepII, *RcAlb*-PepI, PepGAT, and PepKAA (Figure 1). The best peptides and concentrations were PepKAA at 0.15 mg mL^{-1} and *RcAlb*-PepI at 0.30 mg mL^{-1}, in both cases reaching 90% cell viability.

To confirm the neutralizing effect of peptides against SARS-CoV-2, the peptides were first incubated with SARS-CoV-2 and then added to a Vero E6 cell monolayer. All tested peptides (0.15 and 0.30 mg mL^{-1}) significantly reduced the plaque formation in Vero E6 cell co-cultures with SARS-CoV-2 (Figure 2). The least effective peptide was *Mo*-CBP_3-PepII, which inhibited plaque formation only by about 35 at both concentrations (Figure 2A). In turn, the most effective peptide was PepKAA, which achieved inhibition of around 60% at both concentrations (Figure 2D).

https://doi.org/10.1021/acsomega.2c02203
ACS Omega 2022, 7, 16222−16234

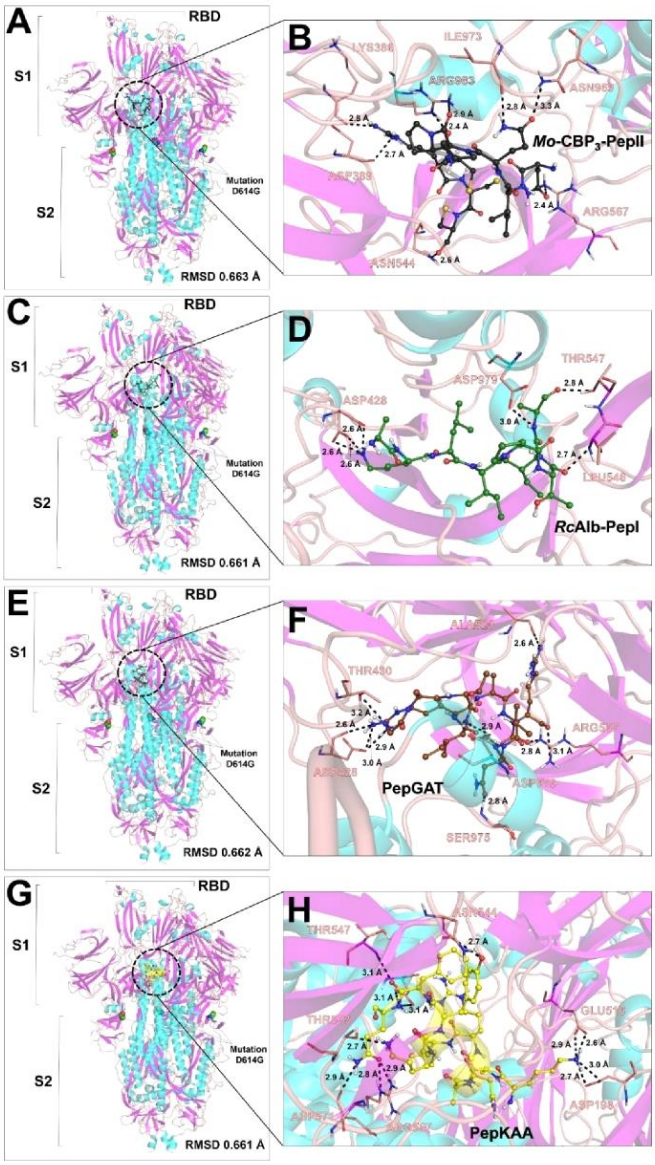

Figure 3. Peptides *Mo*-CBP$_3$-PepII, *Rc*Alb-PepI, PepGAT, and PepKAA interacting with the mutated S protein (S^{D614G}) of SARS-CoV-2. (A,C,E,G) General view of the interaction between S^{D614G} with *Mo*-CBP$_3$-PepII, *Rc*Alb-PepI, PepGAT, and PepKAA, respectively. (B,D,F,H) Zoomed overview of the interaction and the hydrogen bonds between S^{D614G} and peptides *Mo*-CBP$_3$-PepII, *Rc*Alb-PepI, PepGAT, and PepKAA, respectively. Toxicity of peptides to human cells.

Molecular Docking of Peptides toward the D614G Mutant of S Protein. The results of a recent study[8] revealed that all peptides tested interacted with the S protein from the Wuhan isolate of SARS-CoV-2. Of these, *Mo*-CBP$_3$-PepII and PepKAA presented the strongest interaction energies.[8] In our study, sequencing revealed that the SARS-CoV-2 isolate contained D614G on the S protein (Figure S1). Thus, we

https://doi.org/10.1021/acsomega.2c02203
ACS Omega 2022, 7, 16222−16234

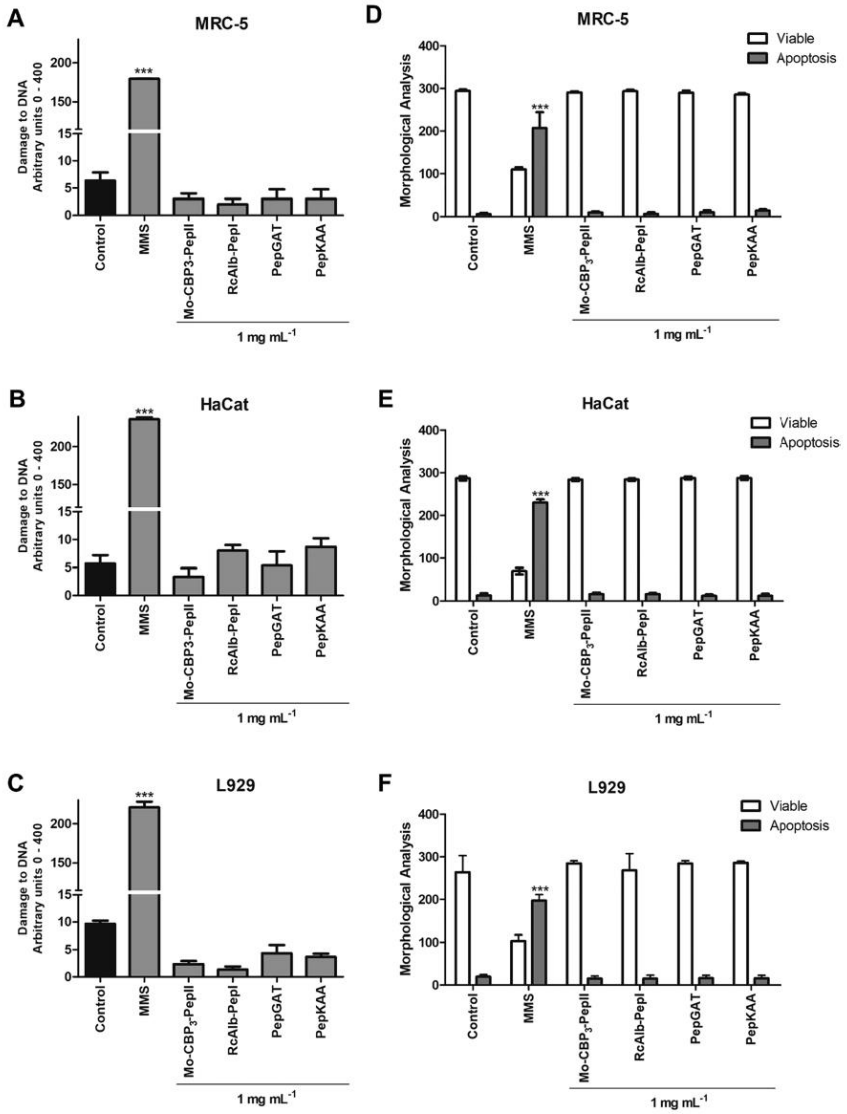

Figure 4. Assessment of toxicity of *Mo*-CBP_3-PepII, *Rc*Alb-PepI, PepGAT, and PepKAA to human cell lines. (A) L929, (B) HaCat, and (C) MRC-5 lines were incubated with synthetic peptides at a concentration of 1 mg mL to evaluate the damage to DNA by comet assay. (D−F) Cell lines were incubated with peptides as described and evaluated for viable cells and cells in apoptosis. MMS (4×10^{-5} M) was employed as a positive control for cell toxicity and healthy cells as a negative control for toxicity. Data are shown as mean ± standard deviation of three independent experiments. ***$P < 0.001$.

performed a new docking analysis to see if the peptides would still interact with this mutant protein.

The molecular docking analysis predicted that *Mo*-CBP_3-PepII, *Rc*Alb-PepI, PepGAT, and PepKAA would interact in the S1 region of the mutant protein S (D614G) of SARS-CoV-2 (Figure 3A,C,E,G). We observed alterations in the atomic positions of the S protein after interaction with peptides, revealed by variations in RMSD values of 0.663, 0.661, 0.662, and 0.661 Å, respectively, to *Mo*-CBP_3-PepII, *Rc*Alb-PepI, PepGAT, and PepKAA.

Mo-CBP_3-PepII presented the lowest binding energy of interaction (LBEI), −676.1 kJ·mol^{-1} with S^{D614G}. The

https://doi.org/10.1021/acsomega.2c02203
ACS Omega 2022, 7, 16222−16234

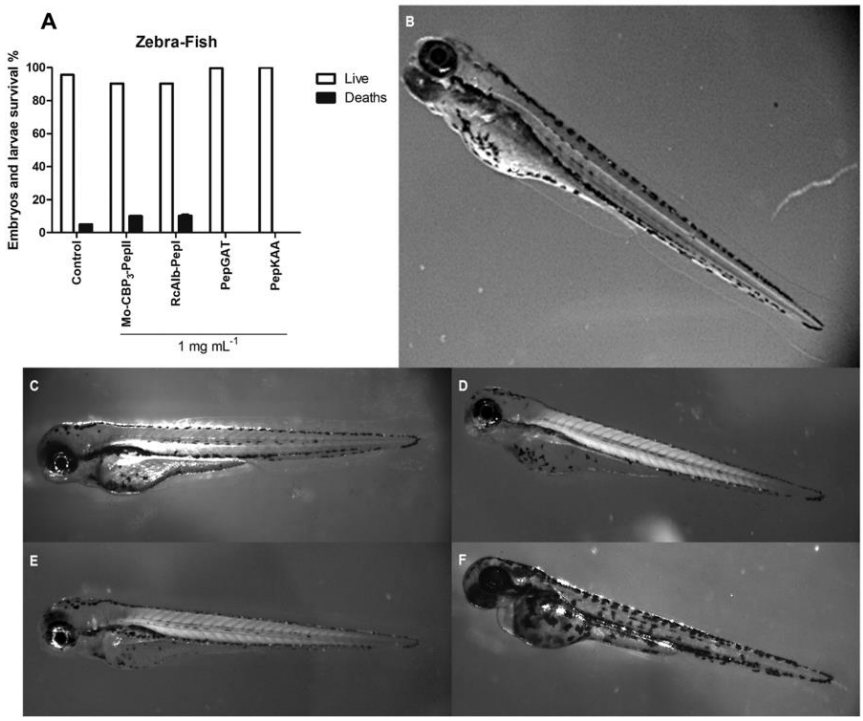

Figure 5. Assessment of toxicity of *Mo*-CBP$_3$-PepII, *Rc*Alb-PepI, PepGAT, and PepKAA to zebrafish embryos. (A) Survival rate (%) of zebrafish embryos and larvae exposed to 1 mg mL of each synthetic peptide and control (E3 medium) samples after 96 h. (B−F) Zebrafish larvae exposed to, respectively, control (E3 medium), *Mo*-CBP$_3$-PepII, *Rc*Alb-PepI, PepGAT, and PepKAA 1 mg mL^{-1} for 96 h. All organisms presented normal development even exposed to peptides. Data are shown as mean ± standard deviation of three independent experiments.

interaction was supported by hydrogen bonds among amino acid residues of S^{D614G} Lys^{386}, Asp^{389}, Asn^{544}, Arg^{567}, Asn^{969}, Ile^{973} and Arg^{983}, with respective distances of 2.8, 2.7, 2.6, 2.4, 3.3, 2.8, and 2.4 Å (Figure 3B). *Mo*-CBP$_3$-PepII also exhibited hydrophobic interactions with the residues Leu^{518}, Ser^{974}, Leu^{517}, Thr^{430}, Phe^{565}, His^{519}, Cys^{391}, Ala^{522}, Gly^{545}, Leu^{546}, Ser^{982}, and Leu^{390} of S^{D614G} (Figure S2A).

*Rc*Alb-PepI had a LBEI value with S^{D614G} of −646.9 kJ·mol^{-1}, supported by six hydrogen bonds and 14 hydrophobic interactions with S^{D614G}. The hydrogen bonds were with the residues Asp^{428}, Leu^{546}, Thr^{547}, and Asp^{979}, with distances of 2.6, 2.6, 2.6, 2.7, 2.8, and 3.0 Å (Figure 3D). The hydrophobic interactions were formed by Ile^{973}, Thr^{430}, Ser^{974}, Leu^{518}, Ser^{982}, His^{519}, Arg^{983}, Leu^{517}, Gln^{564}, Phe^{565}, Gly^{545}, Leu^{390}, Cys^{391}, and Asn^{544} of S^{D614G} (Figure S2B).

The LBEI between PepGAT and S^{D614G} was −605.5 kJ·mol^{-1}. Ten hydrogen bonds between the PepGAT and the amino acid residues Thr^{430}, Asp^{979}, Asp^{428}, Arg^{567}, Ser^{975}, and Ala^{520} of S^{D614G} and 10 hydrophobic interactions between Arg^{983}, Ile^{973}, Cys^{391}, Leu^{390}, Leu^{518}, Leu^{517}, Ser^{974}, Asp40, Phe^{565}, Val^{42}, and His^{519} supported the PepGAT-S^{D614G} complex (Figures 3F and S2C).

PepKAA (LBEI, −779.4 kJ·mol^{-1}) interacted with S^{D614G} by hydrogen bonds with the amino acid residues Asp^{198}, Glu^{516}, Arg^{567}, Asp^{571}, Thr^{547}, Thr^{573}, and Asn^{544}, with distances of 2.7, 2.6, 2.8, 2.9, 3.1, 2.7, and 2.7 Å, respectively (Figure 3H). PepKAA also exhibited hydrophobic interactions with Tyr^{200}, Leu^{517}, Leu^{518}, Ser^{974}, Asn^{969}, His^{519}, Arg^{983}, Ser^{975}, Val^{976}, Phe^{565}, Ala^{522}, Leu^{390}, Gly^{545}, Leu^{546}, and Cys^{391} of S^{D614G} with PepKAA (Figure S2D).

To find possible clinical applications of peptides, their toxicity to human cells was assessed (Figure 4). The MTT assay revealed that the peptides were not toxic to the human cells tested. All cells treated with peptides presented 100% viability (Figure S3). Additionally, we performed two other experiments to evaluate the peptides' safety on human cells. In the first experiment, we tested whether the peptides would induce DNA damage (Figure 4A−C) to three cell lines: L929 fibroblast cells from mice and two human lines—human fetal lung fibroblast (MRC-5 line) and human keratinocytes (HaCaT line). At a concentration of 1 mg mL^{-1}, the comet assay revealed that all peptides caused no damage to DNA (Figure 4A−C). In contrast, in the positive control for DNA damage, the methyl methanesulfonate (MMS) (4×10^{-5} M) agent caused severe damages to the cells' DNA.

The second experiment analyzed whether peptides can induce apoptosis in the same cell line at a concentration of 1 mg mL^{-1} (Figure 4D−F). At that concentration of peptides, the treated cells presented no characteristics of apoptosis (Figure 4D,E). In contrast, cells treated with 4×10^{-5} M presented all aspects of apoptosis, such as small cell volume, fragmented nucleus,

https://doi.org/10.1021/acsomega.2c02203
ACS Omega 2022, 7, 16222−16234

peripheral condensation of chromatin, and apoptotic bodies (Figure 4D,E).

Toxicity of Peptides to Zebrafish Embryos. To assess in depth the safety of peptides, the toxicology to zebrafish embryos was evaluated (Figure 5). The survival rates of zebrafish larvae and embryos after exposure to 1 mg mL^{-1} of the peptides for 96 h were ≥90% (Figure 5A). After 96 h of treatment, morphological analysis revealed no alterations (nonlethal effects) in the embryos exposed to the control (Figure 5B) and peptides (Figure 5C−F). The embryo coagulation rates were ≤20% in the control and peptide-tested embryos (Figure 5B−F). This is an expected and spontaneous natural process that happens in zebrafish embryos, leading to a mortality rate of 5−25%.

DISCUSSION

At the beginning of the current outbreak, it was thought that vaccines would be the only way to fight back SARS-CoV-2. Thus, an unprecedented collaboration worldwide led to the development of vaccines in record times.[14,15] However, together with the beginning of vaccination came SARS-CoV-2 variants not affected or weakly affected by the immune response produced by vaccines.[16] The first vaccines applied brought widespread hope that vaccination would end the pandemic. However, what nobody expected was the emergence of many SARS-CoV-2 variants due to mutations, reducing the vaccines' efficiency. For example, a mutation in the RBD of the S protein at position E484 reduced the SARS-CoV-2 neutralization by monoclonal antibodies and convalescent sera.[16] Thus far, there are more than 3.5 billion people vaccinated worldwide.[17,18] Even though this number has been reached in short a time, the WHO and American Centers for Disease Control (CDC) have reported that some fully vaccinated people have still been infected by SARS-CoV-2. Thus, they are advising even fully vaccinated people to continue using masks to prevent infection by variants.[19−21]

The emergence of these SARS-CoV-2 variants and the existence of people at greater risk such as immunosuppressed patients and those who cannot be vaccinated, such as young children, makes it important to develop drug/treatments specific for SARS-CoV-2 that can abolish or alleviate the symptoms of infected patients. To find such drugs quickly, many groups have examined drug repositioning, so far without success. Many antiviral drugs such as arbidol, an anti-influenza drug targeting the S protein, and galidesivir, remdesivir, tenofovir, sofosbuvir, and ribavirin, which target the RdRp, have been submitted to in silico assays for use against SARS-CoV-2.[22,23] Of these drugs, the studies with arbidol have gone the furthest. Wang et al.[24] reported that at a concentration of 1.9 mg mL^{-1}, arbidol achieved EC_{50} to SARS-CoV-2. They also suggested a dosage of 200 mg 3 times/day or even higher to alleviate COVID-19 symptoms. In another study, Yang et al.[25] revealed that in a group of 82 health professionals treated prophylactically with arbidol, 48 people (58.5%) were infected by SARS-CoV-2 and hospitalized and 34 (41.5%) developed mild symptoms of COVID-19. Altogether, these results suggest that arbidol is not very effective, so new drugs need to be developed. Nevertheless, it was approved for the treatment of patients with COVID-19 by the National Medical Products Administration of China.

In our previous study,[8] it was shown that *Mo*-CBP_3-PepII and PepKAA strongly bind to the S protein, leading to changes in three-dimensional (3D) conformational structures and misplaced interactions with the ACE2 receptor.[8] Here, we have shown that all four peptides interact with S^{D614G}, altering its conformational structure (Figures 3 and S2). Thus, it is feasible to suggest that these peptides block the entrance of SARS-CoV-2 in cells by interacting with the S protein. In silico studies predicted that PepKAA, by strongly interacting with both S^{8} and S^{D614G} (Figures 3 and S2) and changing their 3D, could be the best peptide to block SARS-CoV-2 entrance in cells. Those results were confirmed by in vitro experiments (Figures 1 and 2). Based on all our results, PepKAA is the best peptide to inhibit SARS-CoV-2 S^{D614G} in cells, by reducing the virus plaque number by 60% at the lowest concentration (0.15 mg mL^{-1}). This study is very important because the active concentration of PepKAA is 47.5-fold lower than that of arbidol, the most widely studied drug against SARS-CoV-2.[24,25]

Studying the repositioning of other antiviral drugs, Sacramento et al.[26] employed a combination of daclatasvir and sofosbuvir, two anti-HCV drugs (Hepatitis C virus), against SARS-CoV-2 at concentrations higher than that employed to treat HCV. Wang et al.[27] reported that other antiviral drugs such as penciclovir, ribavirin, faviparin, and remdesivir had EC_{50} values in vitro against SARS-CoV-2, respectively, of 0.1, 0.98, 0.062, and 0.062 mg mL^{-1}. These results show that PepKAA is a good candidate to be used as a source to develop a new drug against SARS-CoV-2. Of these drugs, only arbidol and remdesivir have been investigated beyond in vitro tests. However, as reported above, arbidol was not very efficient.[25] Although approved by the FDA (U.S. Food and Drug Administration), the results of remdesivir in clinical trials presented no significant differences between the placebo and the drug-treated group of patients.[28] Therefore, the search for new drugs to block SARS-CoV-2 is still necessary.

Based on our data, of all peptides tested here, PepKAA is likely the best one to neutralize SARS-CoV-2 S^{D614G}, by preventing cell infection (Figures 1 and 2). However, other peptides are also promising to inhibit SARS-CoV-2, such as *RcAlb*-PepI and PepGAT (Figures 1 and 2). Here, data from in vitro (Figures 1 and 2) and in silico tests (Figures 3 and S2) of PepKAA are in harmony and may explain its high efficiency against SARS-CoV-2. Souza et al.[8] reported that PepKAA interacted with the S protein with an LBEI of −715.6 kJ·mol^{-1}, by inducing a conformational change in the S protein. The authors showed that PepKAA led to the incorrect interaction of S protein and ACE2 receptor, suggesting that the formation of the PepKAA-S protein complex inhibits the entrance of SARS-CoV-2 in cells.[8]

In another study, Amaral et al.[9] predicted that PepKAA has a strong interaction with M^{pro} of SARS-CoV-2, leading to conformational changes and reduction of the active site. These findings suggest that PepKAA reduced the M^{pro} activity. M^{pro} is vital for SARS-CoV-2 replication because SARS-CoV-2 is an RNA virus producing a polyprotein that is cleaved by Mpro, releasing SARS-CoV-2 proteins.[4,9] Here, the molecular docking study predicted that PepKKA has the highest LBEI for S^{D614G} compared to other peptides (Figure 3). The LBEI of PepKAA to S^{D614G} was −779.4 kJ·mol^{-1}, which is very similar to that presented for the wild-type S protein, −715.6 kJ·mol^{-1}.[8] PepKAA did not interact close to the G614 mutation, but the interaction was still important to induce conformational changes in the S^{D614G} protein, which could induce the wrong interaction with the ACE2 receptor.

Here, in all assays, PepKAA was first incubated with SARS-CoV-2 for 30 min to interact with the S^{D614G} protein before infecting cells. Interestingly, even when the virus, peptides, and cells were incubated at the same time, PepKAA could not

https://doi.org/10.1021/acsomega.2c02203
ACS Omega 2022, 7, 16222−16234

prevent cell infection by SARS-CoV-2 (data not shown). These results strongly suggest that the mechanism behind PepKAA's anti-SARS-CoV-2 activity is by interacting with S^{D614G}, inducing conformational changes (as revealed by docking), wrongly interacting with the ACE2 receptor,[8] and thus inhibiting SARS-CoV-2 from invading the cell. Also, it is feasible to suggest that by a so-far-unclear mechanism, PepKAA inhibits M^{pro} activity, which also prevents SARS-CoV-2 replication and infection. We hypothesize this because PepKAA is a membrane-penetrating peptide[12] and SARS-CoV-2 has a lipid envelope.[4] Thus, PepKAA could also target the SARS-CoV-2 membrane, inactivating it. In that case, PepKAA could inhibit SARS-CoV-2 by different mechanisms.

Recently, other synthetic peptides have been tested against SARS-CoV-2.[29−31] Curreli et al.[29] have analyzed the interaction of RBD from SARS-CoV-2 with human ACE2. From this analysis, the authors designed and synthesized four peptides. Among those, the synthetic peptide NYBSP-4 presented an IC_{50} of 1.97 μM against SARS-CoV-2. This result is better than that showed for PepKAA, which reached the same inhibition at a concentration of 12.1 μM. However, compared to results reported by Larue et al.,[30] PepKAA seems to be more effective. Larue et al.[30] reported that synthetic peptides SAP1, SAP2, and SAP6 derived from human ACE2 receptor displayed an IC_{50} toward SARS-CoV-2 at concentrations of, 2.39, 3.72, and 1.90 mM, respectively, which are much higher than the concentration of 12.1 μM presented by PepKAA. In another study, Han et al.[31] reported that the peptide GK-7, also derived from human ACE2, presented an IC_{50} toward SARS-CoV-2 at a concentration of 3.8 μM, which is lower than the concentration presented by PepKAA (12.1 μM). It is important to notice that all studies performed the antiviral assay using a pseudovirus expressing the S protein.[29−31] In our case, we employed the entire natural virus isolated from a patient with full fitness to infect cells in the assay, which is closer than what occurs during infection. This could be an explanation for the elevated concentration required for PepKAA to reach the same concentration presented by other peptides. This result still highlights the efficiency and the potential of PepKAA toward SARS-CoV-2.

One important feature of a candidate drug is safety. New drugs must cause no or very low side effects. In the case of arbidol and remdesivir, this is not true. Both have considerable side effects.[32−34] Yet despite this, they were approved for treatment given the emergency faced by the population from the SARS-CoV-2 outbreak. Arbidol was hastily approved to treat COVID-19 in China, even without satisfactory results. The use of arbidol was associated in rats with loss of body weight, loss of organ weight (mainly liver), and piloerection in females.[34] In the case of remdesivir, the side effects reported were from patients with COVID-19 using the drug to treat symptoms. The side effects reported were increased nausea, diarrhea, vomiting, gastroparesis, atrial fibrillation, cardiac arrest, and acute kidney injury.[35] It is important to state that we are not criticizing or judging the use of these drugs. Because they were approved, they should be used. However, it is also urgently necessary to seek a new type of drug that has lower or no toxic effects.

In this context, PepKAA is a strong candidate. PepKAA was meticulously designed to prevent any kind of toxic effect.[12] Indeed, the bioinformatics analysis revealed no allergic or toxic potential. The hemolytic analysis revealed only 5% chance to cause hemolysis on erythrocytes. However, the in vitro tests against erythrocytes revealed no hemolysis. PepKAA did not present any toxicity to Vero cells.[12] Here, looking toward clinical trials with PepKAA and/or other peptides, we performed additional toxicity tests. Not only PepKAA but also all synthetic peptides presented no genotoxicity or pro-apoptotic effects on human cells L929, MRC-5, and HaCaT (Figure 4) at a concentration of 1 mg mL^{-1}, which is threefold higher than the highest concentration tested (Figure 1). To shed more light on the toxicity of peptides, we employed an important tool for drug development: testing by the zebrafish model.[36] At a concentration of 1 mg mL, none of the peptides presented toxicity to zebrafish larvae and embryos (Figure 5). That concentration (1 mg mL^{-1}) is 25-fold higher than the EC50 value of PepKAA against SARS-CoV-2. In this assay, we used 20 zebrafish embryos, and the embryos incubated with the peptides had a survival of ≥95%. In the case of PepKAA, the survival was 100% (Figure 5A), and no damage was found in the zebrafish (Figure 5C−H). Altogether, the results of efficacy against SARS-CoV-2 and safety indicated PepKAA as a potential substance for testing the development of new drugs against SARS-CoV-2.

PepKAA is a synthetic peptide. One question always arises when working with synthetic peptides: are they cost-effective for commercial use? During the 1990s, the employment of synthetic peptides was impossible given the high cost of chemicals used in the synthesis combined with a very low yield. However, new technologies allowing the recovery and recycling of solvents used during synthesis have made it feasible to produce with a kilogram scale, leading to a dramatic reduction in the cost of peptide synthesis.[37] The synthetic peptide Fuzeon is an example. It is a peptide used in the treatment of HIV requiring kilogram-scale production (≥100 kg), which is possible due to these new technologies.[38] In 2018, the FDA approved a glucagon-like synthetic peptide, Rybelsus, used in the treatment of type II diabetes.[39] Therefore, if the pharmaceutical industry demonstrates interest, the application of synthetic peptides is surely practicable. Based on the potential of our peptides, we filed a patent application in Brazil with the National Industrial Property Institute, under number BR 10 2020 023728 4.

■ CONCLUSIONS

Here, all synthetic peptides were active against SARS-CoV-2 to some extent. The ability to interact with S^{D614G} provided a clue about how peptides act to inhibit SARS-CoV-2. PepKAA was the most prominent peptide to inhibit SARS-CoV-2 while showing no toxicity to human cells and zebrafish embryos. PepKAA thus has a higher potential to develop new anti-SARS-CoV-2 drugs that are effective without adverse effects.

■ METHODOLOGY

Ethical Statement. This experiment conducted with a human patient in this study was approved by the Research Ethics Committee involving human beings on the use of humans in experiments of the Federal Univerisity of Ceará, with authorization documented by protocol no. 4.029.490. All experiments with SARS-CoV-2 were done in accordance with relevant guidelines and regulations. Additionally, the informed consent was obtained from all participants and/or their legal guardian(s).

The experiments conducted with zebrafish in this study were approved by the Ethics Committee in the Use of Animals of the Federal University of Paraíba, with authorization documented by protocol no. 4460140920. In addition to this, animal use methods were carried out in compliance with the ARRIVE

https://doi.org/10.1021/acsomega.2c02203
ACS Omega 2022, 7, 16222−16234

guidelines and in accordance with relevant guidelines and regulations.

Sample Collection. The clinical sample was collected from a patient with positive real-time (RT)-qPCR result and presenting symptoms of SARS-CoV-2 infection. A nasopharyngeal swab was used to collect the sample, and the sample was placed into a 3 mL tube containing a viral transportation solution, as described by Holshue et al.[40] All experiments were carried out in the biosafety level 3 facility (NB-3) of the Laboratory of Emerging and Reemerging Pathogens of the Federal University of Ceará (Fortaleza, Brazil).

Viral Isolation and Titration. The SARS-CoV-2 isolation was performed following the protocol described by Harcourt et al.[41] with modifications. Vero E6 cells (ATCC number CCL-81) were cultured in a Leibovitz medium (L-15) supplemented with 2% heat-inactivated fetal bovine serum (FBS) and 1% penicillin/streptomycin solution (GIBCO). The frozen sample was thawed and passed through a 22 μm syringe filter. The viral isolation was carried out in a 96-well plate containing a Vero cell monolayer with 90−100% confluence. Then, 50 μL of the L-15 medium without FBS was added to 100 μL of the clinical material. Then, the plate was incubated for 2 h at 37 °C, with shaking every 15 min to facilitate the infection of cells by the virus. After the incubation, the medium was removed and added to all wells containing 100 μL of L-15 with 2% FCS and 1% penicillin/streptomycin, incubated at 37 °C and observed daily for the presence of cytopathic effects. The material in the wells in which cytopathic effects were observed was submitted to confirmatory testing using RT reverse transcription PCR. The supernatant from the infected Vero cells was collected, placed into cryotubes, and stored at −80 °C. The virus titration was done following the method described by Mendoza et al.[42]

RT PCR and Sequencing. SARS-CoV-2 RNA was extracted using the QIAamp Viral RNA kit (Qiagen) following the manufacturer's instructions for SARS-CoV-2 detection using a one-step procedure. For RT PCR (qPCR), the CDC 2019-nCoV qPCR diagnostic panel was followed, using specific primers to confirm the presence of SARS-CoV-2 in all cell cultures. In this kit, the primer−probe mixes target two regions of the nucleocapsid gene (N1 and N2) as well as the human endogenous control (RNase P gene), a control for sample integrity.

Thereafter, a specific RBD region of the spike gene was amplified from the cDNA sample using the paired primers (F-AATCTATCAGGCCGGTAGCAC and R-CACCAATGGG-TATGTCACACT) and Platinum Taq DNA Polymerase High-Fidelity kit (Invitrogen). The PCR product was analyzed by electrophoresis through 1.5% agarose gel and purified using the PureLink PCR Purification Kit (Thermo Fisher). The purified product was sequenced using the BigDye Terminator v1.1 Cycle Sequencing Kit (Thermo Fisher) according to the manufacturer's instructions. The basic local alignment search tool software was used for the computer analysis of sequence data with the reference sequence from Wuhan, China (NC_045512.2).

By amplifying the N gene as a target, we confirmed the presence of SARS-CoV-2. After the confirmation, we performed partial sequencing of the RBD region of the S protein, revealing the presence of mutation A23231G, which corresponds to the D614G mutation in the spike protein (S^{D614G}).

Anti-SARS-CoV-2 Activity of Peptides by the MTT Assay. The peptides were diluted to a concentration ranging from 0 to 2.5 mg mL^{-1} in the L-15 medium (Cultilab, Brazil) without fetal serum and filtered through 22 μm filters. The peptides were mixed with an equal volume of viral solution and incubated for 30 min at 37 °C. After incubation, the mixture from each peptide dilution and a multiplicity of infection (MOI) of 1.85 were added in triplicate to a 96-well plate containing 2.5 × 10^5 cells per well. After 2 h of incubation at 37 °C, the virus-containing mixtures were removed from the wells and replaced by fresh L-15 medium containing 2% FBS and 1% antibiotic. The plate was incubated for 4 days at 37 °C. The negative control wells received only the culture medium, and the positive control wells received the virus. After this period, the medium was removed, and 50 μL of 5 mg mL^{-1} MTT (3-4,5-dimethylthiazol-2-yl)-25 diphenyl tetrazolium bromide (Life Technologies, USA) was added. The plate remained for 4 h at 37 °C, after which the solution was removed, and the formazan crystals were diluted with 50 μL DMSO. The plate was read at 540 nm, and the percentage of protection (PP) was calculated by the following formula: PP = [(AB)/(CB) × 100], where A, B, and C indicate the absorbance of the peptide, virus, and control cells, respectively.[43]

Plaque Reduction Neutralization Tests. The neutralization assay was performed as described by Muruato et al.[44] Vero E6 cells (6 × 10^5 per well) were seeded in 12-well plates and left at rest overnight. Then, SARS-CoV-2 samples at an MOI of 1.85 were incubated with the peptides at concentrations of 0.15 and 0.30 mg mL^{-1} at 37 °C for 1 h. The virus−peptide mixture was added in triplicate to pre-seeded Vero E6 cells at 90−100% confluence. After 2 h of incubation at 37 °C, 1 mL of the overlay containing 1.5% carboxymethylcellulose in L-15 containing 2% FBS and 1% penicillin/streptomycin antibiotics (GIBCO) was added to the infected cells. After 3 days of incubation, 1 mL of 3.65% formaldehyde in phosphate-buffered saline (PBS) was added to the overlay-covered cells. After fixation for 1 h, the overlay was removed, and the contents of the cells were stained with 0.5% crystal violet. The plates were washed with water to remove excess dye, photographed, and submitted for counting using the ImageJ program. Percentage plaque reduction was calculated using the following formula: [(sample × 100)/positive control] −100.

Molecular Docking Analysis. The crystallographic data of the mutant (D614G) SARS-CoV-2 protein S was obtained from the Protein Data Bank, with accession number PDB ID: 7DX1. The 3D structures of peptides *Mo*-CBP_3-PepII, *Rc*Alb-PepI, PepGAT, and PepKAA were predicted using the PEP-FOLD 3.5 software.[45] The protein and peptide structures were determined and the protonation states were adjusted using the ProteinPrepare software.[46]

To carry out molecular docking between the peptides and the mutated protein S of SARS-CoV-2, we used the ClusPro 2.0 server,[47] which showed the best results in the CAPRI challenge.[48] The results were analyzed using the number of members in each cluster and the lowest energies calculated through the Balanced software method, which considers the energies obtained from electrostatic and hydrophobic interactions.

To analyze the interactions between the peptides and the mutated S protein, the software LigPlot$^+$ v. 2.2.4 was used.[49] The preparation of figures and measurement of the variation in rmsd were performed with the Pymol software.

Assessment of Cytotoxicity. The cytotoxicity was quantified by the ability of live cells to reduce the yellow dye 3-(4,5-dimethyl-2-thiozolyl)-2,5-diphenyl-2H-tetrazolium bromide (MTT) to formazan.[50] Cytotoxicity was checked against

https://doi.org/10.1021/acsomega.2c02203
ACS Omega 2022, 7, 16222−16234

L929 (murine fibroblasts, ATCC number CCL-1), MRC-5 (human lung fibroblasts, ATCC number CCL-171), and HaCat (human keratinocytes), provided by the Rio de Janeiro Cell Bank (BCRJ, Brazil). All cell lines were washed and resuspended in the DMEM medium supplemented with 10% FBS, 2 mM of glutamine, 100 U/mL of penicillin, and 100 μg/mL of streptomycin, at 37 °C under 5% CO_2. For the experiments, cells were plated in 96-well plates (0.1×10^6 cells/mL for HaCat cells and 0.1×10^4 cells/mL for L929 and MRC-5 cell lines). After 24 h, the tested peptides (1 mg mL^{-1} in the culture medium) were added to each well, and the cells were incubated for 72 h. MMS (4×10^{-5} M) was used as the positive control. Thereafter, the plates were centrifuged, and the medium was replaced with a fresh medium (150 μL) containing 0.5 mg mL of MTT. Three hours later, the MTT formazan product was dissolved in 150 μL DMSO, and the absorbance was measured using a multiplate reader (Spectra Count, Packard, Ontario, Canada). Drug effect was quantified as the percentage of control absorbance of the reduced dye at 595 nm.

Comet Assay. For this assay, the concentration of peptides was 1 mg mL^{-1}. DMSO−NaCl was the negative control for damage, and MMS (4×10^{-5} M) was used as the positive control for DNA damage. The standard alkaline comet assay (single-cell gel electrophoresis) was performed as previously described.[51] After treatment (24 h), cells were washed with ice-cold PBS, trypsinized, and resuspended in the complete medium. Then, 20 μL of cell suspension (0.7×10^5 cells/mL) was dissolved in 0.75% low-melting-point agarose and immediately spread onto a glass microscope slide pre-coated with a layer of 1% agarose with a normal melting point. The agarose was allowed to set at 4 °C for 5 min. Slides were incubated in an ice-cold lysis solution (2.5 M NaCl, 0.01 M Tris, 0.1 M EDTA, 1% Triton X-100, and 10% DMSO, pH 10.0) at 4 °C for at least 1 h to remove cell membranes, leaving DNA as "nucleoids".

After that, the slides were placed in a horizontal electrophoresis unit and incubated with a fresh buffer solution (0.3 M NaOH, 0.001 M EDTA, pH 13.0) at 4 °C for 20 min to allow DNA unwinding and the expression of alkali-labile sites. Electrophoresis was conducted for 20 min at 25 V (94 V/cm). All the above steps were performed in the dark to prevent additional DNA damage. Slides were neutralized (0.4 M Tris, pH 7.5) and stained using 20 μg mL ethidium bromide (EB). One hundred and fifty cells (50 cells from each of the three replicate slides for each treatment) were selected, coded, and blindly analyzed for DNA migration. These cells were visually scored according to the tail length into five classes: (1) class 0: undamaged, without a tail; (2) class 1: with a tail shorter than the diameter of the head nucleus; (3) class 2: with a tail length 1−2× the diameter of the head; (4) class 3: with a tail longer than 2× the diameter of the head; and (5) class 4: comets with no heads. The damage index (DI) value was assigned to each sample. DI is an arbitrary score based on the number of cells in the different damage classes, which are visually scored by measuring the DNA migration length and the amount of DNA in the tail. DI ranges from 0 (no tail: 100 cells × 0) to 400 (with maximum migration: 100 cells × 4).[52]

Morphological Characterization of Apoptotic PBLs. For this assay, the concentration of peptides was 1 mg mL^{-1}. DMSO−NaCl was the negative control for damage, and MMS (4×10^{-5} M) was used as the positive control for DNA damage. The peptide and control solutions were incubated as described above. Then, cells with morphological characteristics of apoptosis (i.e., small cell volume, peripheral condensation of chromatin, fragmented nucleus, and apoptotic bodies) were determined after each treatment (24 h) by the acridine orange (AO)/EB staining assay: 25 μL of the cell suspension was mixed with 1 μL of the staining solution (100 μg/mL AO + 100 μg/mL EB in PBS) and spread on a slide, where 300 cells were counted per data point. The percentage of apoptotic cells was then calculated.[53]

Zebrafish Toxicity. *Zebrafish Embryos.* Zebrafish embryos (AB wild-type strain) with approximately 1 HPF (hour post-fertilization) were provided by the Production Unit for Alternative Model Organisms (UniPOM), Federal University of Paraiba, João Pessoa, Brazil. The parents were maintained in a recirculation system with regular monitoring of water quality parameters (pH, ammonia, and nitrite levels) in a room with controlled temperature (26 ± 1 °C) and photoperiod (14:10 light/dark cycle). Fish were fed daily with commercial feed (Color Bits Tetra, Melle, Germany) and freeze-dried spirulina (Fazenda Tamanduá, Patos, Brazil) and were monitored for abnormal behavior or disease development.

Before the experiment, adult zebrafish (male-to-female ratio of 2:1) were transferred to a 7 L spawning tank with a bottom mesh and a quick-opening valve for embryo collection. Embryos were collected on the day of the experiment and cultured in an adapted embryonic medium E3 (5.0 mM NaCl, 0.17 mM KCl, 0.33 mM CaCl, and 0.33 mM MgSO4) containing 0.005% methylene blue. Only spawning samples with a fertilization rate ≥90% were used. Viable embryos (normal cleavage pattern and without morphological changes) were selected under an inverted light microscope (Televal 31, Zeiss, Germany), at 50× magnification.

Acute Toxicity Test. The fish embryo acute toxicity test was independently conducted with four peptides according to the OECD Guideline number 236[54] adapted for 96-well plates by Muniz et al.[55] Zebrafish embryos with up to 3 hpf were exposed to 1 mg mL^{-1} of each sample. For each test and control sample, 20 wells were filled with 0.3 mL of solution and 1 embryo.

Additionally, 20 embryos were exposed only to the E3 medium (the solvent control). Lethal and non-lethal effects were observed daily for 96 h. Embryos showing lethality endpoints (coagulation, no formation of somites, no detachment of tail, or absence of heartbeat) were considered dead. This number was used to determine the survival percentage (number of live organisms/total number of organisms × 100) per tested sample. The exposures were under static conditions (without the renovation of the exposure solution). Observations were performed with a stereomicroscope (Olympus SZX7, Japan) at 56× magnification and photographed (Moticam 5+, China). After 96 h, surviving larvae were euthanized with eugenol and properly discarded.

Statistical Analysis. The assays were performed in three independent experiments. The statistics were expressed as the mean ± standard deviation. The data were submitted to ANOVA followed by the Tukey test, using GraphPad Prisma 5.01, with a significance of $p < 0.05$.

■ ASSOCIATED CONTENT

Supporting Information

The Supporting Information is available free of charge at https://pubs.acs.org/doi/10.1021/acsomega.2c02203.

Clustal alignment of the SARS-CoV-2 nucleotide sequence of the receptor-binding domain from S protein; two-dimensional demonstration of the interaction

https://doi.org/10.1021/acsomega.2c02203
ACS Omega 2022, 7, 16222−16234

between peptides and mutated protein SD^{614G}; and assessment of the toxicity of Mo-CBP3-PepII, RcAlb-PepI, PepGAT, and PepKAA to human cell lines by cell viability assay (PDF)

AUTHOR INFORMATION

Corresponding Author

Pedro F.N. Souza − *Department of Biochemistry and Molecular Biology, Federal University of Ceará, Fortaleza, Ceará 60020-181, Brazil; Drug Research and Development Center, Department of Physiology and Pharmacology, Federal University of Ceará, Fortaleza, Ceará 60020-181, Brazil;* orcid.org/0000-0003-2524-4434; Email: pedrofilhobio@gmail.com

Authors

Maurício F. vanTilburg − *Biotechnology and Molecular Biology Laboratory, Renorbio, State University of Ceará, Fortaleza, Ceará 60020-181, Brazil*

Felipe P. Mesquita − *Drug Research and Development Center, Department of Physiology and Pharmacology, Federal University of Ceará, Fortaleza, Ceará 60020-181, Brazil*

Jackson L. Amaral − *Department of Biochemistry and Molecular Biology, Federal University of Ceará, Fortaleza, Ceará 60020-181, Brazil*

Luina B. Lima − *Drug Research and Development Center, Department of Physiology and Pharmacology, Federal University of Ceará, Fortaleza, Ceará 60020-181, Brazil*

Raquel C. Montenegro − *Drug Research and Development Center, Department of Physiology and Pharmacology, Federal University of Ceará, Fortaleza, Ceará 60020-181, Brazil*

Francisco E.S. Lopes − *Department of Biochemistry and Molecular Biology, Federal University of Ceará, Fortaleza, Ceará 60020-181, Brazil*

Rafael X. Martins − *Laboratory for Risk Assessment of Novel Technologies (LabRisk), Department of Molecular Biology, Federal University of Paraiba, João Pessoa, Paraíba 58051-900, Brazil*

Leonardo Vieira − *Laboratory for Risk Assessment of Novel Technologies (LabRisk), Department of Molecular Biology, Federal University of Paraiba, João Pessoa, Paraíba 58051-900, Brazil*

Davi F. Farias − *Laboratory for Risk Assessment of Novel Technologies (LabRisk), Department of Molecular Biology, Federal University of Paraiba, João Pessoa, Paraíba 58051-900, Brazil*

Ana C. O. Monteiro-Moreira − *School of Pharmacy, University of Fortaleza, Fortaleza, Ceará 60811-690, Brazil*

Cleverson D.T. Freitas − *Department of Biochemistry and Molecular Biology, Federal University of Ceará, Fortaleza, Ceará 60020-181, Brazil*

Arnaldo S. Bezerra − *Biotechnology and Molecular Biology Laboratory, Renorbio, State University of Ceará, Fortaleza, Ceará 60020-181, Brazil*

Maria I. F. Guedes − *Biotechnology and Molecular Biology Laboratory, Renorbio, State University of Ceará, Fortaleza, Ceará 60020-181, Brazil*

Débora S.C.M. Castelo-Branco − *Department of Pathology and Legal Medicine, Federal University of Ceará, Fortaleza, Ceará 60020-181, Brazil*

Jose T.A. Oliveira − *Department of Biochemistry and Molecular Biology, Federal University of Ceará, Fortaleza, Ceará 60020-181, Brazil;* orcid.org/0000-0003-1207-1140

Complete contact information is available at: https://pubs.acs.org/10.1021/acsomega.2c02203

Author Contributions

Conceptualization: P.F.N.S., M.F.T., F.P.M. Data curation: P.F.N.S., M.F.T., F.P.M., J.L.A., L.B.L., R.X.M., L.V., D.F.F., A.S.B. Formal analysis: P.F.N.S., D.F.F., M.F.T., F.P.M., J.L.A., Funding acquisition: R.C.M., D.F.F., A.C.O.M.M., C.D.T.F., M.I.F.G., D.S.C.M.C.-B. J.T.A.O. Methodology: P.F.N.S., M.F.T., F.P.M., J.L.A., A.S.B. Resources: P.F.N.S., R.C.M., D.F.F., A.C.O.M.M., C.D.T.F., M.I.F.G., D.S.C.M.C.-B. J.T.A.O. Supervision: P.F.N.S., and F.P.M. Writing original draft: P.F.N.S., and F.P.M. Writing, review, and editing: F.P.M., M.F.T., F.P.M., D.S.C.M.C.-B., P.F.N.S.

Notes

The authors declare no competing financial interest.

ACKNOWLEDGMENTS

Special thanks go to the Office to Coordinate Improvement of Higher Education Personnel (CAPES) for providing the postdoctoral grant to P.F.N.S. This work was also supported by grants from the following Brazilian agencies: National Council for Scientific and Technological Development, for a research productivity grant to R.C.M.; CAPES for the grant to R.C.M. (number 88881.505364/2020-01—Announcement 9/2020); National Institute of Science and Technology of Bioinspiration and Cearense Foundation to Support Scientific and Technological Development for the grant to R.C.M. (Number 03195011/2020). R.C.M. and D.éS.C.M.C.-B. give special thanks to the School of Medicine of Federal University of Ceará for supporting this research through a COVID-19 research grant.

REFERENCES

(1) WHO Coronavirus (COVID-19) Dashboard | WHO Coronavirus (COVID-19) Dashboard With Vaccination Data https://covid19.who.int/(accessed Jul 9, 2021).

(2) Wang, C.; Horby, P. W.; Hayden, F. G.; Gao, G. F. A Novel Coronavirus Outbreak of Global Health Concern. *Lancet* **2020**, *395*, 470−473.

(3) Zhang, T.; Wu, Q.; Zhang, Z. Probable Pangolin Origin of SARS-CoV-2 Associated with the COVID-19 Outbreak. *Curr. Biol.* **2020**, *30*, 1346−1351.

(4) Souza, P. F. N.; Mesquita, F. P.; Amaral, J. L.; Landim, P. G. C.; Lima, K. R. P.; Costa, M. B.; Farias, I. R.; Lima, L. B.; Montenegro, R. C. The Human Pandemic Coronaviruses on the Show: The Spike Glycoprotein as the Main Actor in the Coronaviruses Play. *Int. J. Biol. Macromol.* **2021**, *179*, 1−19.

(5) Lazarus, J. V.; Ratzan, S. C.; Gostin, L. O.; Larson, H. J.; Rabin, K.; Kimball, S. A Global Survey of Potential Acceptance of a COVID-19 Vaccine. *Nat. Med.* **2021**, *27*, 225−228.

(6) Alam, I.; Radovanovic, A.; Incitti, R.; Kamau, A. A.; Alarawi, M.; Azhar, E. I.; Gojobori, T. CovMT: An Interactive SARS-CoV-2 Mutation Tracker, with a Focus on Critical Variants. *Lancet Infect. Dis.* **2021**, *21*, 602.

(7) Serafin, M. B.; Bottega, A.; Foletto, V. S. Drug Repositioning Is an Alternative for the Treatment of Coronavirus COVID-19. *Int. J. Antimicrob. Agents* **2020**, *55*, 105969.

(8) Souza, P. F. N.; Lopes, F. E. S.; Amaral, J. L.; Freitas, C. D. T.; Oliveira, J. T. A. A Molecular Docking Study Revealed That Synthetic Peptides Induced Conformational Changes in the Structure of SARS-CoV-2 Spike Glycoprotein, Disrupting the Interaction with Human ACE2 Receptor. *Int. J. Biol. Macromol.* **2020**, *164*, 66−76.

(9) Amaral, J. L.; Oliveira, J. T. A.; Lopes, F. E. S.; Freitas, C. D. T.; Freire, V. N.; Abreu, L. V.; Souza, P. F. N. Quantum Biochemistry,

Molecular Docking, and Dynamics Simulation Revealed Synthetic Peptides Induced Conformational Changes Affecting the Topology of the Catalytic Site of SARS-CoV-2 Main Protease. *J. Biomol. Struct. Dyn.* **2021**, 1.

(10) Dias, L. P.; Souza, P. F. N.; Oliveira, J. T. A.; Vasconcelos, I. M.; Araújo, N. M. S.; Tilburg, M. F. V.; Guedes, M. I. F.; Carneiro, R. F.; Lopes, J. L. S.; Sousa, D. O. B. RcAlb-PepII, a Synthetic Small Peptide Bioinspired in the 2S Albumin from the Seed Cake of Ricinus Communis, Is a Potent Antimicrobial Agent against Klebsiella Pneumoniae and Candida Parapsilosis. *Biochim. Biophys. Acta Biomembr.* **2020**, *1862*, 183092.

(11) Oliveira, J. T. A.; Souza, P. F. N.; Vasconcelos, I. M.; Dias, L. P.; Martins, T. F.; Van Tilburg, M. F.; Guedes, M. I. F.; Sousa, D. O. B. Mo-CBP3-PepI, Mo-CBP3-PepII, and Mo-CBP3-PepIII Are Synthetic Antimicrobial Peptides Active against Human Pathogens by Stimulating ROS Generation and Increasing Plasma Membrane Permeability. *Biochimie* **2019**, *157*, 10−21.

(12) Souza, P. F. N.; Marques, L. S. M.; Oliveira, J. T. A.; Lima, P. G.; Dias, L. P.; Neto, N. A. S.; Lopes, F. E. S.; Sousa, J. S.; Silva, A. F. B.; Caneiro.; et al. Synthetic Antimicrobial Peptides: From Choice of the Best Sequences to Action Mechanisms. *Biochimie* **2020**, *175*, 132−145.

(13) Stockert, J. C.; Horobin, R. W.; Colombo, L. L.; Blázquez-Castro, A. Tetrazolium Salts and Formazan Products in Cell Biology: Viability Assessment, Fluorescence Imaging, and Labeling Perspectives. *Acta Histochem.* **2018**, *120*, 159−167.

(14) Abu-Raddad, L. J.; Chemaitelly, H.; Butt, A. A. Effectiveness of the BNT162b2 Covid-19 Vaccine against the B.1.1.7 and B.1.351 Variants. *N. Engl. J. Med.* **2021**, *385*, 187.

(15) Heath, P. T.; Galiza, E. P.; Baxter, D. N.; Boffito, M.; Browne, D.; Burns, F.; Chadwick, D. R.; Clark, R.; Cosgrove, C.; Galloway, J.; et al. Safety and Efficacy of NVX-CoV2373 Covid-19 Vaccine. *N. Engl. J. Med.* **2021**, *385*, 1172.

(16) Gupta, R. K. Will SARS-CoV-2 Variants of Concern Affect the Promise of Vaccines? *Nat. Rev. Immunol.* **2021**, *21*, 340−341.

(17) Coronavirus (COVID-19) Vaccinations - Statistics and Research - Our World in Data https://ourworldindata.org/covid-vaccinations (accessed Jul 15, 2021).

(18) Mathieu, E.; Ritchie, H.; Ortiz-Ospina, E.; Roser, M.; Hasell, J.; Appel, C.; Giattino, C.; Rodés-Guirao, L. A Global Database of COVID-19 Vaccinations. *Nat. Hum. Behav.* **2021**, *5*, 947−953, DOI: 10.1038/S41562-021-01122-8.

(19) COVID-19 Breakthrough Case Investigations and Reporting | CDC https://www.cdc.gov/vaccines/covid-19/health-departments/breakthrough-cases.html (accessed Jul 15, 2021).

(20) What You Should Know About the Possibility of COVID-19 Illness After Vaccination|CDC https://www.cdc.gov/coronavirus/2019-ncov/vaccines/effectiveness/why-measure-effectiveness/breakthrough-cases.html (accessed Jul 15, 2021).

(21) COVID-19 Vaccines Advice https://www.who.int/emergencies/diseases/novel-coronavirus-2019/covid-19-vaccines/advice (accessed Jul 15, 2021).

(22) Elfiky, A. A. Ribavirin, Remdesivir, Sofosbuvir, Galidesivir, and Tenofovir against SARS-CoV-2 RNA Dependent RNA Polymerase (RdRp): A Molecular Docking Study. *Life Sci* **2020**, *253*, 117592.

(23) Vankadari, N. Arbidol: A Potential Antiviral Drug for the Treatment of SARS-CoV-2 by Blocking Trimerization of the Spike Glycoprotein. *Int. J. Antimicrob. Agents* **2020**, *56*, 105998.

(24) Wang, X.; Cao, R.; Zhang, H.; Liu, J.; Xu, M.; Hu, H.; Li, Y.; Zhao, L.; Li, W.; Sun, X.; Yang, X.; et al. The Anti-Influenza Virus Drug, Arbidol Is an Efficient Inhibitor of SARS-CoV-2 in Vitro. *Cell Discov.* **2020**, *6*, 1−5.

(25) Yang, C.; Ke, C.; Yue, D.; Li, W.; Hu, Z.; Liu, W.; Hu, S.; Wang, S.; Liu, J. Effectiveness of Arbidol for COVID-19 Prevention in Health Professionals. *Front. Public Health* **2020**, *0*, 249.

(26) Sacramento, C. Q.; Fintelman-Rodrigues, N.; Temerozo, J. R.; et al. In Vitro Antiviral Activity of the Anti-HCV Drugs Daclatasvir and Sofosbuvir against SARS-CoV-2, the Aetiological Agent of COVID-19. *J. Antimicrob. Chemother.* **2021**, *76*, 1874−1885.

(27) Wang, M.; Cao, R.; Zhang, L.; Yang, X.; Liu, J.; Xu, M.; Shi, Z.; Hu, Z.; Zhong, W.; Xiao, G. Remdesivir and Chloroquine Effectively Inhibit the Recently Emerged Novel Coronavirus (2019-NCoV) in Vitro. *Cell Res.* **2020**, *30*, 269−271.

(28) Beigel, J. H.; Tomashek, K. M.; Dodd, L. E.; Mehta, A. K.; Zingman, B. S.; Kalil, A. C.; Hohmann, E.; Chu, H. Y.; Luetkemeyer, A.; Kline, S.; et al. Remdesivir for the Treatment of Covid-19 — Final Report. *N. Engl. J. Med.* **2020**, *383*, 1813−1826.

(29) Curreli, A. F.; Victor, S. M. B.; Ahmed, S.; Drelich, B.; Tong, X.; Chien-Te, K.; Tseng, C. D. H.; Debnatha, A. K. Stapled Peptides Based on Human Angiotensin-Converting. *mBio* **2020**, *11*, 1−13.

(30) Larue, R. C.; Xing, E.; Kenney, A. D.; Zhang, Y.; Tuazon, J. A.; Li, J.; Yount, J. S.; Li, P. K.; Sharma, A. Rationally Designed ACE2-Derived Peptides Inhibit SARS-CoV-2. *Bioconjugate Chem.* **2021**, *32*, 215−223.

(31) Han, S.; Zhao, G.; Wei, Z.; Chen, Y.; Zhao, J.; He, Y.; He, Y. J.; Gao, J.; Chen, S.; Du, C.; et al. An Angiotensin-Converting Enzyme-2-Derived Heptapeptide GK-7 for SARS-CoV-2 Spike Blockade. *Peptides* **2021**, *145*, 170638.

(32) FDA. *Fact Sheet For Healthcare Providers G Medical Vsms Ecg Patch*, 2020.

(33) Adamsick, M. L.; Gandhi, R. G.; Bidell, M. R.; Elshaboury, R. H.; Bhattacharyya, R. P.; Kim, A. Y.; Nigwekar, S.; Rhee, E. P.; Sise, M. E. Remdesivir in Patients with Acute or Chronic Kidney Disease and COVID-19. *J. Am. Soc. Nephrol.* **2020**, *31*, 1384−1386.

(34) Wang, M.; Shu, B.; Bai, W.-X.; Liu, J.; Yao, J. A 4-Week Oral Toxicity Study of an Antiviral Drug Combination Consisting of Arbidol and Acetaminophen in Rats. *Drug Chem. Toxicol.* **2010**, *33*, 244−253.

(35) Fan, Q.; Zhang, B.; Ma, J.; Zhang, S. Safety Profile of the Antiviral Drug Remdesivir: An Update. *Biomed. Pharmacother.* **2020**, *130*, 110532.

(36) MacRae, C. A.; Peterson, R. T. Zebrafish as Tools for Drug Discovery. *Nat. Rev. Drug Discovery* **2015**, *14*, 721−731.

(37) Zhang, T.; Chen, Z.; Tian, Y.; Han, B.; Zhang, N.; Song, W.; Liu, Z.; Zhao, J.; Liu, J. Kilogram-Scale Synthesis of Osteogenic Growth Peptide (10-14) Using a Fragment Coupling Approach. *Org. Process Res. Dev.* **2015**, *19*, 1257−1262.

(38) Pennington, M. W.; Zell, B.; Bai, C. J. Commercial Manufacturing of Current Good Manufacturing Practice Peptides Spanning the Gamut from Neoantigen to Commercial Large-Scale Products. *Med. Drug Discovery* **2021**, *9*, 100071.

(39) Buckley, S. T.; Bækdal, T. A.; Vegge, A.; Maarbjerg, S. J.; Pyke, C.; Ahnfelt-Rønne, J.; Madsen, K. G.; Schéele, S. G.; Alanentalo, T.; Kirk, R. K.; et al. Transcellular Stomach Absorption of a Derivatized Glucagon-like Peptide-1 Receptor Agonist. *Sci. Transl. Med.* **2018**, *10*, 7047.

(40) Holshue, M. L.; DeBolt, C.; Lindquist, S.; Lofy, K. H.; Wiesman, J.; Bruce, H.; Spitters, C.; Ericson, K.; Wilkerson, S.; Tural, A.; et al. First Case of 2019 Novel Coronavirus in the United States. *N. Engl. J. Med.* **2020**, *382*, 929−936.

(41) Harcourt, J.; Tamin, A.; Lu, X.; Kamili, S.; Sakthivel, S. K.; Murray, J.; Queen, K.; Tao, Y.; Paden, C. R.; Zhang, J.; Li, Y.; et al. Severe Acute Respiratory Syndrome Coronavirus 2 from Patient with Coronavirus Disease, United States - Volume 26, Number 6—June 2020 - Emerging Infectious Diseases Journal - CDC. *Emerg. Infect. Dis.* **2020**, *26*, 1266−1273.

(42) Mendoza, E. J.; Manguiat, K.; Wood, H. Two Detailed Plaque Assay Protocols for the Quantification of Infectious SARS-CoV-2. *Curr. Protoc. Microbiol.* **2020**, *57*, cpmc105.

(43) López-Martínez, R.; Ramírez-Salinas, G. L.; Correa-Basurto, J.; Barrón, B. L. Inhibition of Influenza A Virus Infection In Vitro by Peptides Designed In Silico. *PLoS One* **2013**, *8*, No. e76876.

(44) Muruato, A. E.; Fontes-Garfias, C. R.; Ren, P.; Garcia-Blanco, M. A.; Menachery, V. D.; Xie, X.; Shi, P.-Y. A High-Throughput Neutralizing Antibody Assay for COVID-19 Diagnosis and Vaccine Evaluation. *Nat. Commun.* **2020**, *11*, 1−6.

(45) Lamiable, A.; Thévenet, T.; Rey, R.; Vavrusa, M. PEP-FOLD3: Faster de Novo Structure Prediction for Linear Peptides in Solution and in Complex. *Nucleic Acids Res.* **2016**, *44*, W449−W454.

https://doi.org/10.1021/acsomega.2c02203
ACS Omega 2022, 7, 16222−16234

(46) Martínez-Rosell, G.; Giorgino, T.; De Fabritiis, G. PlayMolecule ProteinPrepare: A Web Application for Protein Preparation for Molecular Dynamics Simulations. *J. Chem. Inf. Model.* **2017**, *57*, 1511−1516.
(47) Kozakov, D.; Hall, D. R.; Xia, B.; Porter, K. A.; Padhorny, D.; Yueh, C.; Beglov, D.; Vajda, S. The ClusPro Web Server for Protein−Protein Docking. *Nat. Protoc.* **2017**, *12*, 255−278.
(48) Lensink, M. F.; Nadzirin, N.; Velankar, S.; Wodak, S. J. Modeling Protein-protein, Protein-peptide, and Protein-oligosaccharide Complexes: CAPRI 7th Edition. *Proteins: Struct., Funct., Bioinf.* **2020**, *88*, 916−938.
(49) Laskowski, R. A.; Swindells, M. B. LigPlot+: Multiple Ligand−Protein Interaction Diagrams for Drug Discovery. *J. Chem. Inf. Model.* **2011**, *51*, 2778−2786.
(50) T, M. Rapid Colorimetric Assay for Cellular Growth and Survival: Application to Proliferation and Cytotoxicity Assays. *J. Immunol. Methods* **1983**, *65*, 55−63.
(51) Collins, A. R. The Comet Assay for DNA Damage and Repair: Principles, Applications, and Limitations. *Mol. Biotechnol.* **2004**, *26*, 249−261.
(52) Burlinson, B.; Tice, R. R.; Speit, G.; Agurell, E.; Brendler-Schwaab, S. Y.; Collins, A. R.; Escobar, P.; Honma, M.; Kumaravel, T. S.; et al. Fourth International Workgroup on Genotoxicity Testing: Results of the in Vivo Comet Assay Workgroup. *Mutat. Res. Genet. Toxicol. Environ. Mutagen* **2007**, *627*, 31−35.
(53) McGahon, A. J.; Martin, S. J.; Bissonnette, R. P.; Mahboubi, A.; Shi, Y.; Mogil, R. J.; Nishioka, W. K.; Green, D. R. Chapter 9 The End of the (Cell) Line: Methods for the Study of Apoptosis in Vitro. *Methods Cell Biol.* **1995**, *46*, 153−185.
(54) Test No. 236: Fish Embryo Acute Toxicity (FET) Test | READ online https://read.oecd-ilibrary.org/environment/test-no-236-fish-embryo-acute-toxicity-fet-test_9789264203709-en#page1 (accessed Jul 12, 2021).
(55) Muniz, M. S.; Halbach, K.; Alves Araruna, I. C.; Martins, R. X.; Seiwert, B.; Lechtenfeld, O.; Reemtsma, T.; Farias, D. Moxidectin Toxicity to Zebrafish Embryos: Bioaccumulation and Biomarker Responses. *Environ. Pollut.* **2021**, *283*, 117096.

Recommended by ACS

Inactivation of SARS-CoV-2 Spike Protein Pseudotyped Virus Infection Using ACE2-Tethered Gold Nanorods under Near-Infrared Laser Irradiation
Ian Peng, Ching-An Peng, *et al.*
OCTOBER 07, 2022
ACS APPLIED NANO MATERIALS
READ

Peptide–Antibody Fusions Engineered by Phage Display Exhibit an Ultrapotent and Broad Neutralization of SARS-CoV-2 Variants
Jonathan M. Labriola, Sachdev S. Sidhu, *et al.*
JUNE 22, 2022
ACS CHEMICAL BIOLOGY
READ

Peptide from SARS-CoV-2 spike protein forms amyloids
Celia Henry Arnaud.
JUNE 06, 2022
C&EN GLOBAL ENTERPRISE
READ

Stapled Peptides Targeting SARS-CoV-2 Spike Protein HR1 Inhibit the Fusion of Virus to Its Cell Receptor
Mengjun Zheng, Xiang Li, *et al.*
NOVEMBER 24, 2021
JOURNAL OF MEDICINAL CHEMISTRY
READ

Get More Suggestions >

https://doi.org/10.1021/acsomega.2c02203
ACS Omega 2022, 7, 16222−16234

APÊNDICE I - THE SPIKE GLYCOPROTEIN OF SARS-COV-2: A REVIEW OF HOW MUTATIONS OF SPIKE GLYCOPROTEINS HAVE DRIVEN THE EMERGENCE OF VARIANTS WITH HIGH TRANSMISSIBILITY AND IMMUNE ESCAPE

International Journal of Biological Macromolecules 208 (2022) 105–125

Contents lists available at ScienceDirect

International Journal of Biological Macromolecules

journal homepage: www.elsevier.com/locate/ijbiomac

Review

The spike glycoprotein of SARS-CoV-2: A review of how mutations of spike glycoproteins have driven the emergence of variants with high transmissibility and immune escape

Pedro F.N. Souza [a,b,*], Felipe P. Mesquita [b], Jackson L. Amaral [a], Patrícia G.C. Landim [a], Karollyny R.P. Lima [a], Marília B. Costa [b], Izabelle R. Farias [b], Mônica O. Belém [c], Yago O. Pinto [d], Heline H.T. Moreira [d], Ilana C.L. Magalhaes [e], Débora S.C.M. Castelo-Branco [f], Raquel C. Montenegro [b], Claudia R. de Andrade [c]

[a] Department of Biochemistry and Molecular Biology, Federal University of Ceará, Brazil
[b] Drug research and Development Center, Department of Medicine, Federal University of Ceará, Brazil
[c] Laboratory of Translational Research, Christus University Center, Fortaleza, Ceará 60192, Brazil
[d] Medical Education Institution-Idomed, Canindé, Ceará, Brazil
[e] State University of Ceara, Fortaleza, Ceara, Brazil
[f] Department of Pathology and Legal Medicine, Postgraduate Program in Medical Microbiology, Group of Applied Medical Microbiology, Federal University of Ceará, Fortaleza, Ceará, Brazil

ARTICLE INFO

Keywords:
Coronaviruses
Spike proteins
SARS-CoV-2
RBD
Mutations

ABSTRACT

Late in 2019, SARS-CoV-2 (severe acute respiratory syndrome coronavirus-2) emerged, causing an unknown type of pneumonia today called coronaviruses disease 2019 (COVID-19). COVID-19 is still an ongoing global outbreak that has claimed and threatened many lives worldwide. Along with the fastest vaccine developed in history to fight SARS-CoV-2 came a critical problem, SARS-CoV-2. These new variants are a result of the accumulation of mutations in the sequence and structure of spike (S) glycoprotein, which is by far the most critical protein for SARS-CoV-2 to recognize cells and escape the immune system, in addition to playing a role in SARS-CoV-2 infection, pathogenicity, transmission, and evolution. In this review, we discuss mutation of S protein and how these mutations have led to new variants that are usually more transmissible and can thus mitigate the immunity produced by vaccination. Here, analysis of S protein sequences and structures from variants point out the mutations among them, how they emerge, and the behavior of S protein from each variant. This review brings details in an understandable way about how the variants of SARS-CoV-2 are a result of mutations in S protein, making them more transmissible and even more aggressive than their relatives.

1. Introduction

SARS-CoV-2 belongs to the Coronavirus family, consisting of positive-sense, single-stranded RNA viruses that are lipid-enveloped [1]. In December 2019, SARS-CoV-2 infected its first patient, starting what would be a new pandemic established by the World Health Organization (WHO) [2,3]. The ongoing outbreak showed how devastating a virus can be even though SARS-CoV-2 is not that dangerous compared to other deadly viruses [4–8].

Unlike SARS-CoV-1 and MERS-CoV outbreaks, which were more endemic than a pandemic, SARS-CoV-2 quickly became global, based on high transmissibility [2,3,9,10]. At the beginning of the pandemic, COVID-19 was compared to other viral diseases caused by coronaviruses, even the flu (Table 1). Earlier in the outbreak, even some scientists did not give the necessary attention to COVID-19. However, as a completely new disease, COVID-19 showed that it cannot be neglected [11–15].

For example, in comparison with flu, COVID-19 has higher values of R_0, CRF, incubation time, and hospitalization rates (Table 1). Those results indicate that COVID-19 is not only just a strain of flu and deserves

* Corresponding author at: Drug research and Development Center, Department of Physiology and Pharmacology, Federal University of Ceará, Brazil, Rua Coronel Nunes de Melo 100, Caixa 60430-275 Fortaleza, CE, Brazil.
E-mail address: pedrofilhobio@gmail.com (P.F.N. Souza).

https://doi.org/10.1016/j.ijbiomac.2022.03.058
Received 8 December 2021; Received in revised form 8 March 2022; Accepted 10 March 2022
Available online 15 March 2022
0141-8130/© 2022 Elsevier B.V. All rights reserved.

Table 1
Data comparison of COVID-19 with other viral diseases.

	Influenza	SARS-CoV-2	SARS-CoV	MERS-CoV
Basic reproductive rate (R_0)	1.3	5.9–6.8	3	0.3–0.8
Case fatality rate (CRF)	0.05–0.1%	6.8%	9.6–11%	34.4%
Incubation time (days)	1–4	4–14	2–7	6
Hospitalization rate	2%	20%	70–85%	90%
Community attack rate	10%	30–40%	10–60%	4–13%

attention [16–19]. Compared to diseases caused by SARS-CoV and MERS-CoV, COVID-19 presents low CRF value, so that SARS-CoV and MERS-CoV have higher mortality than SARS-CoV-2 (Table 1). The infection caused by SARS-CoV-2 has a broader clinical spectrum, ranging from asymptomatic infection to severe viral pneumonia with respiratory failure and death [18,20,21].

The high R_0 of SARS-CoV-2 (Table 1) is probably due to the S protein's higher affinity (20 times more) than S protein from SARS-CoV-1 and MERS-CoV. The accumulation of favorable mutations in the S protein from SARS-CoV-2 made it more effective in recognizing human receptors than the spike from [14,22–26]. The mutations' accumulation in S proteins changed the S protein among different coronaviruses. It also led to genetically different lineages of SARS-CoV-2, called variants, that emerged and spread worldwide since the beginning of SARS-CoV-2 (Fig. 1) [27–31]. Today, there are two definitions of the variants of SARS-CoV-2: 1) variants of interest – VoI; and variants of concern – VoC (Table 2). VoIs possess mutations that improve SARS-CoV-2 fitness. VoCs arise from genetic changes that increase SARS-CoV-2 transmissibility and virulence, and can decrease the effectiveness of vaccines and treatments (Fig. 1) [27]. In the case of VoCs of SARS-CoV-2, these variants accumulated mutations on the S protein that either enhanced the transmissibility or the escape from the immune system. Sometimes these mutations are shared between the variants, while in other cases they are not (Fig. 1).

To the best of our knowledge, so far, no study has been published containing all the relevant information about SARS-CoV-2 VoCs, discussing how the mutations accumulate and affect the fitness of the S protein, and hence SARS-CoV-2. Based on that, this review is focused on the discussion and tracking of the mutations in the S protein that have led to the emergence of VoCs (Table 1). Additionally, we aim to understand the contribution of mutations to the S protein's three-dimensional structure and how these alterations affect the transmissibility and virulence of SARS-CoV-2 VoCs compared to the wild-type version that first came from Wuhan.

2. General aspects of SARS-CoV-2

2.1. Molecular biology of SARS-CoV-2

SARS-CoV-2 is a single-stranded, non-segmented, positive-sense RNA with both 5cap and a tail at 3end [32,33]. The SARS-CoV-2 RNA is similar to cellular mRNA, which is an essential evolutionary advantage, by mimicking the cellular mRNA, directly driving viral RNA for translation [34]. The positive-sense RNA of SARS-CoV-2 allows the infection in any permissive cell [33,35–37]. This characteristic of SARS-CoV-2 and other coronaviruses led Pfizer and BioNTech to produce the first mRNA vaccine (BNT162b2). BNT162b2 is a nucleoside-modified positive sense-RNA encoding the full-length membrane-anchored SARS-CoV-2 S protein enclosed in a lipid nanoparticle. After the shot, the skin promptly dissolves the positive-sense RNA and is translated by cell machinery of protein synthesis to viral S protein. Furthermore, S protein is exposed and externalized to be recognized by the immune system leading to the production of anti-SARS-CoV-2 antibodies [38].

During the SARS-CoV-2 replication cycle, the first protein produced is a large replication complex. Then RNA, which has a ribosomal frameshifting site [39], undergoes this frameshifting event. This event leads to the displacement of ribosomal frames, also known as translation

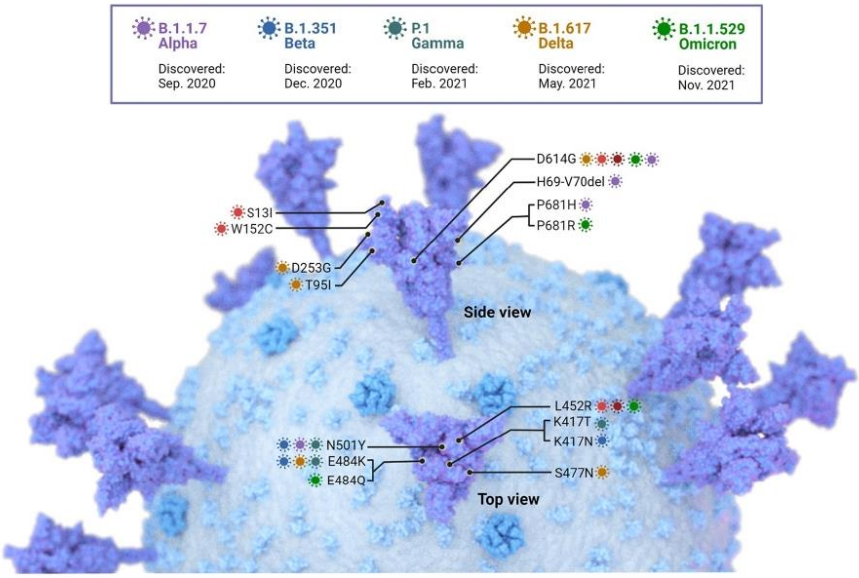

Fig. 1. Scheme model showing all the mutation on Spike protein from variants. In this model is possible to all the shared mutations among the variants and all the unique mutation of each variant. Created with www.BioRender.com.

Table 2
Variants of SARS-CoV-2.

Type	Name	Pango classification	Origin	Type	Name	Pango classification	Origin
Variants of interest	Lambda	C.37	Peru	Variants of concern	Alpha	B.1.1.7	United Kingdom
	Mu	B.1.621	Colombia				
	Epsilon	B.1.427 B.1.429	United States		Beta	B.1.351	South Africa
	Kappa	B.1.617.1	India		Gamma	P1	Brazil
	Eta	B.1.525	United Kingdom		Delta	B.1.617.2	India
					Omicron	B.1.1.529	Discovered on South Africa
	Iota	B.1.526	United States				
	Zeta	P2	Brazil				

recording, resulting in multiple protein production from a single mRNA molecule [39–44]. Moreover, the RNA serves for protein synthesis, RNA replication, and assembly, producing new virus particles [45]. The SARS-CoV-2 genome produces 16 non-structural proteins (nsp), including PL proteinase, 3CL protease, RNA-dependent RNA polymerase (RdRp), and helicase. The genome of SARS-CoV-2 also produces five structural envelope proteins (E), a membrane attached protein (M), nucleocapsid protein (N), and S protein (Fig. 2A).

2.2. Origin and evolution of SARS-CoV-2

SARS-CoV-2 is grouped in the B lineage of Beta-coronaviruses, the same as SARS-CoV [46–48]. Both SARS-CoV and SARS-CoV-2 share 79% of genomic identity, allowing similar structural, genetic, and pathogenic characteristics [48]. Despite many gas in knowledge of SARS-CoV-2 origins, the WHO has started an investigation of SARS-CoV-2 [49–51]. This investigation is essential to avoid unbiased speculation that SARS-CoV-2 was developed at laboratory. Today, there are two front lines of investigations. First, the SARS-CoV-2 resulted from a laboratory incident at the Wuhan Institute of Virology (WIV). Second, whether SARS-CoV-2 came out from Wuhan markets, mainly the Huanan market, which is involved in trading of thousands of wild animals, including species with high risk, such as civets and raccoons [46]. The positive results for SARS-CoV-2 in environmental samples from the Huanan market support this theory [49–51].

Rather than speculation, here only findings based on scientific data will be discussed. Although there are many gaps in knowledge about the ribosomal frameshifting site's influence on SARS-CoV-2's origin, some studies have proposed a plausible explanation. Zhou et al. [52] suggested that SARS-CoV-2 very likely came from an ancestor of naturally SARS-like coronavirus from bats. The analysis of the genomic sequence of SARS-CoV-2 provided a clue to the evolutionary aspect of SARS-CoV-2

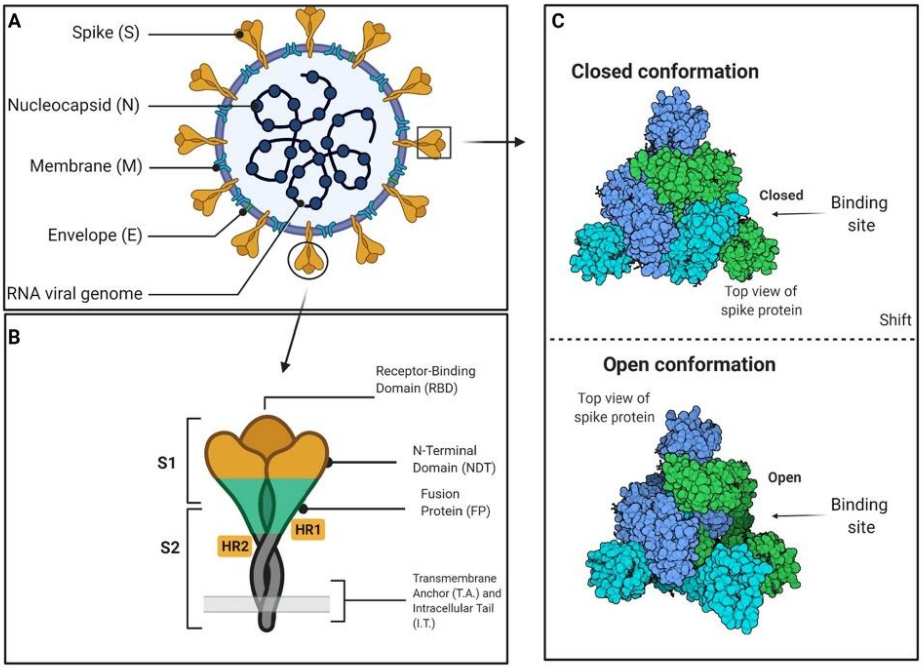

Fig. 2. Schematic representation of the SARS-CoV-2 particle and spike protein. (A) SARS-CoV-2 particle closuring the viral genome. (B) Spike protein consists of the S1 (holding the NDT and RBD regions) and S2 (holding the FP, HR1 and HR2 regions) units. (C) The two conformations assumed by Spike protein. The closed conformation with RBD inside the structure and the open conformation with RBD exposed to recognize ACE2 receptor. Created with www.BioRender.com.

[52]. Genetic analysis revealed an identity of 96% between SARS-CoV-2 and RatG13 (from *Rhinolophus affinis*). These data support the idea that bats are reservoirs of SARS-CoV-2 progenitor's and SARS-CoV-2 ancestors' spillover from bats to humans. It is intriguing that even with higher genetic similarities, the RaTG13 S protein diverges in the RBD region from the S protein from SARS-CoV-2, suggesting it may not bind to human ACE2 [53]. Moreover, based on RBD sequencing and host-receptor interactions, Pangolins (*Manis Javanica*) were considered a possible reservoir based on high similarity with RBD of S protein from SARS-CoV-2 [14].

Unexpectedly, the analysis revealed that S protein coronaviruses from neither pangolins nor bats possess the polybasic cleavage site, essential for SARS-CoV-2 infectivity and host range [54]. Mutational analysis revealed the presence of insertions and deletions close to the S1-S2 junction of S protein from SARS-CoV-2. This change indicates acquisition of polybasic cleavage sites by SARS-CoV-2, established as a new feature in the SARS-CoV-2 genome, had improved transmission, species spillover, and human-human transmission [55–58]. This gain of function by S protein from SARS-CoV-2 may lead to higher affinity, which is 20 times that compared to S protein from SARS-CoV [59]. This improved S protein led to a higher spread of SARS-CoV-2, reaching pandemic dimensions four months after the first case [5,11,60,61]. To date, COVID-19 caused by SARS-CoV-2 has infected more than 245 million people and claimed more than 5 million lives.

2.3. Pathogenicity of SARS-CoV-2

The improvement of S protein in SARS-CoV-2 changes aspects of its infection. SARS-CoV-2 contacts are hosted by contaminated respiratory air droplets and human airway epithelium cells [62,63]. Zhu et al. [63] showed that although sharing the same receptor (ACE2) to reach cells, S protein from SARS-CoV-2 is more efficient in infecting human airway epithelium cells than human coronavirus NL63 (HCoV-NL63) and SARS-CoV. SARS-CoV-2 entries in cells interact, causing S protein binding with specific cell receptors, ACE2 and TMPRSS2 [64]. In summary, the RBD present in the S1 subunit from S protein binds to ACE2 in the host cell. Then, the TMPRSS2 catalyzes the cleavage of S protein on the S1-S2 domain to start the membrane fusion process and viral entry [65]. Later, this mechanism will be detailed in the section about S protein.

SARS-CoV-2 infection can result in three situations: 1) asymptomatic, 2) mild symptoms, and 3) severe acute pneumonia and death [66–69]. In situations 2 and 3, the symptoms vary from mild, such as fever, chills, fatigue, cough, dyspnea, chest pain, myalgia/arthralgia, diarrhea, nausea and vomiting to severe such as infections in the lungs, intestinal tract, pharynx, heart, kidney, liver, brain, blood, inflammatory reactions and alveolar damage [66–69]. Most of the problems during COVID-19 are caused by an overreaction of the immune system. A process called "cytokine storm" produces a high level of pro-inflammatory cytokines such as growth factor-β1 (TGF-β1), tumor necrosis factor-α (TNF-α), interleukin-1β (IL-1β), IL-6, IL-2, IL-7, IL-10, and granulocyte colony-stimulating factor (G-CSF), leading to local inflammation and multiple organ functional failure [68,70–73].

3. The S protein

Before moving forward with the discussion about S protein in VoCs I, it is essential to understand how this protein works. Like other viral attachment proteins, S protein is synthesized and deposited in viral particles in inactive form. Thus, during the viral infection, it is activated by a host protease, which releases the S1 and S2 subunits, activating them and allowing the membrane fusion and virus entry as an inactive precursor present in the viral envelope. The S protein is cleaved during cell infection by a cellular protease, releasing [64,74,75]. An exciting characteristic of S protein is the high level of glycosylation. Before post-translational processing, S protein is present in amounts ranging from 128 to 160 kDa. After carbohydrate insertion, mostly by N-links, the size of S protein increases to 180–200 [76–78]. It has been hypothesized that the biological function of glycosylation in the S proteins is to evade the host immune system during infection [76–78]. S protein has an N-terminal region that is about 90% of protein length exposed to the outside of the viral particle, a transmembrane section, and an inside C-terminal region [79]. Even at the monomeric stage with 1273 amino acid residues, S protein reveals its size [80], being divided into S1 (1-685) and S2 (686-1273).

The S1 subunit is involved in host cell recognition and attachment to it. The receptor-binding domain (RBD) responsible for binding to the ACE2 is hosted by the S1 subunit [58,75,81]. By holding the RBD domain, the S1 subunit is the most likely target for the action of neutralizing antibodies and developing drugs [58,64,65,74,81]. Additionally, S1 contains the N-terminal (NTD) and C-terminal (CTD) domains, both involved in the RBD recognition. For comparison, the SARS-CoV-2 S1 CTD has an insertion of 21 amino acid residues (21 aa) directly involved with the ACE2 interaction compared to SARS-CoV S1 CDT. The amino acid residues F486 and E484 from SARS-CoV-2 S1 CTD determine the strength of the interaction with ACE2 receptor compared to I472 and P470 from SARS-CoV S1 CTD [58,81].

The S2 subunit is involved in membrane fusion and virus entry in cells. To develop this function, the S2 subunit hosts three critical domains: fusion peptide (FP, 788–806), heptapeptide repeated sequence 1 (HR1) (912–984 residues), and heptapeptide repeated sequence 2 (HR2) (1163–1213). FP is a small apolar fragment composed of Gly and Ala, allowing the interaction with the membrane, densely conserved in the coronavirus family [21,82,83]. Two FP domains are found in two repeated sequences, HR1 and HR2. These amphipathic sequences with hydrophobic and hydrophilic amino acid residues allow all types of interactions with phospholipids in the membrane. HR1 and HR2 interact to form a domain fusion core region [84] that drives the S2 subunit to the cell membrane and initiates the fusion process [82,84–86].

Many other viruses present S-like proteins critical to receptor recognition, cell attachment, membrane fusion, and virus entry. HIV and Ebola possess S-like proteins with other names [64,69,81,87–95]. In SARS-CoV-2, the S protein in its trimeric form is found exposed outside the viral particle with an extension of 15 nm playing an essential role in viral infection. Exposed in the viral particle and before interacting with the ACE2 receptor, so the S protein is found in inactive form. The S protein possesses two conformational moments (Fig. 2C), the open and closed states.

This conformational flexibility is based on the presence of NTD and RBD. The RBD is enclosed inside the S protein structure in the closed state and cannot interact with the ACE2 receptor (Fig. 2C). The closed conformation is also known as the perfusion state [93,96,97]. At this stage, the RBD is found in a pocket inside the S protein structure, covered by the NTD region. At this moment, the S1 stays on the top of the S2 subunit to prevent early conformational change to the post-fusion structure [98,99].

Some elegant studies have shown that a proteolytic cleavage of S protein changes from perfusion to post-fusion state. This cleavage of S protein is made by a cellular protease attached to the cell membrane. The protease is TMPRSS2 and happens at a polybasic cleavage site on S protein. Interestingly, S protein from SARS-CoV-2 has a higher cleavage than S protein from SARS-CoV. Higher levels of S protein cleavage might be involved in the faster entrance in cells and thus faster replication of the virus [64,74].

The RBD is pulled out of the S protein structure during the open state and can recognize and interact with the ACE2 receptor (Fig. 2C) [64,65,100]. After the RBD and ACE2 receptor interaction, the complex RBD-ACE2 initializes the conformational changes of the S protein structure to the fusion state (post-fusion). The S2 subunit and membrane control this reaction. Membrane fusion leads to SARS-CoV-2 entry in cells [64,65,86,97–100]. Right after SARS-CoV-2 reaches the cytoplasm, the infection process starts [80,81,101,102].

4. How mutants of S protein led to VoCs

4.1. Mutation on coronavirus genome

As described above, viruses classified in the coronavirus family have the giant single-stranded RNA genomes. The complexity of the genome requires a complex mechanism to repair possible mistakes in the replication process. So, coronaviruses possess a massive polymerase complex, and a multifunctional protein (nsp14) proofreading the Exo N domain. In contrast, this proofreading function is not found in other RNA viruses with smaller genome sizes [93]. The domain with residues compatible with Exo N activity has been described in other proteins. Genetic diversity in SARS-CoV-2 is very likely low [103–105].

However, natural selection can cause rare but favorable mutations. For example, mutations in the influenza virus during each year's flu season leads to a complex balance between immunological resistance developed across populations and mutations, providing antibody resistance [61], which requires the development of new influenza vaccines every season [106]. In a recent study, Sehra et al. [107] suggested the establishment of SARS-CoV-2 as a seasonal infection like flu. However, the long duration of the outbreak can lead to the accumulation of immunologically relevant mutations of the SARS-CoV-2 genome even in the vaccinated population.

4.2. Could VoCs overshadow the breakthrough of vaccines?

To have an overview of the impact of mutations that generate VoCs on vaccine efficacy as revealed by experiments with SARS-CoV-2 itself or pseudoviruses expressing combined or individual mutations on S protein that led to VoCs, sera of 20 post-vaccinated volunteers immunized with BNT162b2 (Pfizer–BioNTech) or mRNA-1273 (Moderna), both mRNA vaccines, presented levels of anti-spike IgM and IgG and RBD-specific antibodies similar to people that were naturally infected by SARS-CoV-2 [108–111]. The results revealed a reduction in the neutralization of SARS-CoV-2 or pseudoviruses carrying mutations compared to the Wuhan isolate.

In another experiment, the effect was evaluated of a single N501Y mutation on neutralization. Results showed that sera from 20 participants in a trial of BNT162b2 presented a modest reduction in the neutralization of virus, with N501Y mutation [109,110,112,113]. Regarding the virus holding the E484K mutation, results revealed a 6.7-fold reduction of the neutralization of post-vaccination sera from people vaccinated with the BNT162b2 [114]. Experiments with Alpha and Beta variants showed a higher neutralization action against live-viral antibodies from sera of people vaccinated with ChAdOx1 nCoV-19 (Oxford–AstraZeneca) [115]. Gamma variant was able to escape from antibodies produced by BNT162b2 (5.8-fold) and mRNA-1273 (4.5-fold and 2.9-fold, respectively), reducing the neutralization of vaccines, respectively, by 6 and 4.5-fold post-vaccination [116]. Both Beta and Gamma VoCs share the E484K; suggesting this mutation could be a determinant for low neutralization of post-vaccinated sera.

The NVX-CoV2373 (Novavax) S protein-based vaccine showed 95.6% efficacy against the wild type. However, this efficacy dropped to 85.6% and 60.0%, respectively, for the Alpha and Beta variants [117]. Likewise, the vaccine JNJ-78436735 (Johnson & Johnson/Janssen) showed efficacy of 72% for wild types, but this number dropped to 57% for the Beta variant [118]. These data indicate the Beta variant has accumulated mutations that reduced the efficacy of NVX-CoV2373 and JNJ-78436735, but these vaccines are still clinically efficacious.

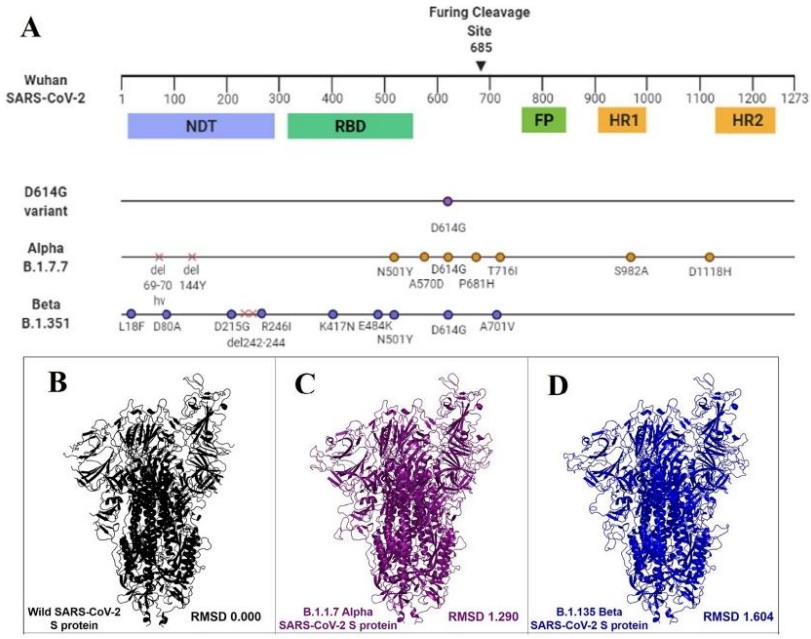

Fig. 3. Scheme presenting the mutations on variants and structural alignments of the variants compared to wildtype version Spike protein from SARS-CoV-2. (A) Comparison of Spike protein sequences from wildtype version of SARS-CoV-2 and mutations on Spike protein presenting in the variants D614, Alpha and Beta. (B) structural analysis of Spike protein from wildtype version of SARS-CoV-2, (C) Spike protein from Alpha variant and (D) Spike protein from Beta variant. RMSD analysis indicates changes in the structure.

5. S protein holding D614G mutation

The isolate of SARS-CoV-2 hosting the SD614G (Fig. 3A) emerged and spread globally in January to March 2020 [119,120]. Besides showing up early in 2020, the D614G is a well-conserved substitution presented by all new SARS-CoV-2 VoCs that came after suggesting it as a well-established successful mutation [119]. SD614G brought many benefits to SARS-CoV-2 fitness, which will be discussed, such as enhanced replication and infectivity. It facilitates S protein incorporation into the virion, increases virion stability, leads to higher viral loads in COVID-19 patients, modulates glycosylation at the nearby N616 site, but has higher infectivity and transmissibility of SARS-CoV-2 [119–123].

At the molecular level, the D614G mutation increases the stability and density of the S protein. It decreases the S1 subunit shedding, keeping both S1 and S2 subunits more closely supported by stronger intermolecular association, leading to a highly stabilized S1–S2 interface in SD614G. It was known that S1 shedding limits the infectivity of the original SARS-CoV-2 (without SD614G) by releasing S1 from S2 during viral fusion. The D614G mutation fixed this problem by strengthening the intramolecular interaction between S1 and S2, blocking S1 dissociation and thus virus infectivity and transmission [119–123].

6. Alpha variant of SARS-CoV-2

In December 2020, a variant that spread quickly and increased the risk of death was detected in the United Kingdom (UK). The variant derived from the SARS-CoV-2 20B clade was confirmed as B.1.1.7, now known as the Alpha variant. In the early investigation stage, increased transmissibility of up to 71% over the previously circulating strains of SARS-CoV-2 [124,125] was estimated. The high transmissibility of the Alpha variant has been described in several studies in different countries, with a transmissibility range between 50 and 80% [126–128]. *In vitro* and *in vivo* experiments supported the observed behavior of the Alpha variant. It was demonstrated that the Alpha variant can multiply and shed more effectively in the nasal cavity of hamsters than other variants, even at low viral loads and short time of exposure [129]. Based on that, the Alpha variant was defined as VoC in December 2020. It was later defined as a variant, being monitored (VBM) because it had no longer been detected or was circulating at very low levels [130].

In January 2021, 45 countries reported the Alpha variant's presence. A group of British scientists proposed that the Alpha variant is responsible for the third wave of the pandemic in Scotland, associated with severe cases of COVID-19. The study results showed that the Alpha variant of SARS-CoV-2 has 5 times higher permeability than other co-circulating variants, hence its rapid spread in Scotland [131].

In a UK case-control study of 54,906 participants who tested positive for SARS-CoV-2, in comparison with the Alpha variant and previously circulating variants reported a mortality hazard ratio associated with infection with VOC-202012/1 compared with infection with previously circulating variants (hazard ratio of 1.64 [95% CI 1.32–2.04]) [132]. The Biwako Ohashi Hospital in Japan described a specific sign called red face after Alpha variant infection, which may be predictive of a sudden deterioration of patients [133].

Interestingly, in September 2021, a French group had already identified the SARS-CoV-2 Alpha variant in cats and dogs in France [134]. Recently, scientists in the UK identified cases of severe myocarditis in cats and dogs associated with the Alpha variant that crossed the interspecies line in the that country, raising questions regarding its potential pathogenicity in these animals [135]. The Alpha variant results from the accumulation of 17 mutations compared to the original SARS-CoV-2 virus discovered in Wuhan, China. Here, as reported before, we focus on the mutations accumulated in the S protein (Fig. 3A). These mutations are expected to lead to expanded spread and increased severity of the associated disease, requiring more effective vaccines, therapeutic drugs, diagnostic tools, and other public health measures.

The Alpha variant has eight spike mutations, including two deletions in the S protein (Fig. 3A). These mutations led to two deletions, both in the NDT region: 1) 69–70del (*i.e.*, a deletion of 6 bases coding for histidine and valine at positions 69 and 70, respectively, in the viral S gene); and 2) 144del (deletion of Tyr residue). Usually, deletions of SARS-CoV-2 result in escape from the immune system. However, the 69–70del has a different purpose. The 69–70del is very likely a genetic compensation. As we will discuss further, mutations of RBD to escape from the host's immune system led to reduced affinity for ACE2 receptors. So, 69–70del can increase the affinity of S protein for ACE2 receptors [136]. Kemp et al. [136] revealed *in vitro* that 69–70del is not involved in the escape of antibodies from convalescent sera but does increase infectivity, incorporation of cleaved S protein on viral membrane, and spike infectivity. The authors discussed the idea that this deletion came about to compensate for small infectivity defects induced by RBD mutations N501Y, N439K, and Y453F in the S protein sequence [136]. The 144del is a deletion of Tyr residue. It is supposed that deletion changes the NDT loop based on the high volume of Tyr residue. This alteration in the NDT loop might indicate that neutralization by 144del is more efficient in reducing neutralization by NTD-specific neutralizing antibodies (9 of 10; 90%) than RBD-specific neutralizing antibodies (5 of 31, 16%) [110,137–140].

The next mutation in the S protein from Alpha is N501Y (*i.e.*, an asparagine to tyrosine amino acid substitution at position 501 in the viral S gene) (Fig. 3A). It is the first time this mutation was detected in SARS-CoV-2. The 501 position is at the RBD–ACE2 interface. N501 forms part of the binding loop in the contact region of hACE2, forming a hydrogen bond with Y41 in hACE2. It also stabilizes K353, one of the virus-binding hotspot residues in hACE2. The N501Y substitution is an advantage to variants holding it, maybe because it is present in Alpha, Beta, and Gama variants (Figs. 3 and 4). The substitution of an asparagine (polar) with a tyrosine (hydrophobic) increases the affinity of RBD for ACE2a [141,142]. Molecular investigations showed that the N501Y mutation of the SARS-CoV-2 variant identified in the UK and South Africa evolved separately [143]. N501Y mutation slowed the dissociation of the RBD from the ACE2 receptor. Additionally, it seems that N501Y reduces neutralization by antibodies [110,124].

The effect of a mutation that replaces an alanine with an aspartate residue at position 570 in the S protein remains unclear. It has only been detected in the Alpha variant (Fig. 3A). The same happens with the T716I, S982A, and D1118H mutations; they have only been found in the Alpha variant, and their functions are still unclear (Fig. 3A). However, the mutation replacing proline with arginine (P681H) increases the positive net effect of S protein right before the 685 position, which is the furin cleavage site (Fig. 3A). It has been proposed that P681H enhances the cleavage by a furin protease, which is involved in the activation of membrane fusion during viral infection [64,144,145].

All those mutations change the S protein, and root mean square deviation (RMSD) calculation revealed the atomic position on the S protein of variants compared with the wild-type S protein from the Wuhan isolate (Figs. 3 and 4). The RMSD calculation provides a clue about the alterations in protein structure through a score: a score of 0 indicates the atoms from both structures are in the same position, which means no alteration in the 3D structure. Any score different from 0 indicates the atoms are in different positions, and the higher this value is, the greater the differences are between structures. The S protein from the Alpha variant has accumulated mutations on the HR1 and HR2 portions of the S2 subunit, leading to conformational changes in those regions, which are essential to membrane fusion.

Research has shown that vaccines still provide reliable protection against the variant, although they may be less effective. Different studies have described the impact of the Alpha variant on vaccine efficiency. The BNT162b2 vaccine (Pfizer) showed 0.81- to 1.46-fold reductions in geometric mean titers (GMTs) against mutations in B.1.1.7 and B.1.351 variants relative to the parental virus from Wuhan [112,113]. The mRNA-1273 vaccine (Moderna) demonstrated no reduction against the

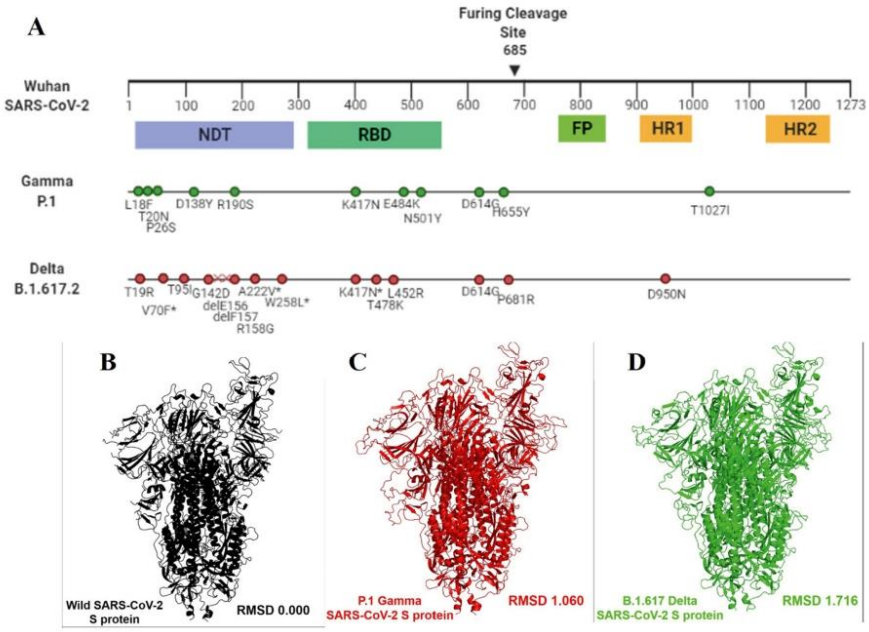

Fig. 4. Scheme presenting the mutations on variants and structural alignments of the variants compared to wildtype version Spike protein from SARS-CoV-2. (A) Comparison of Spike protein sequences from wildtype version of SARS-CoV-2 and mutations on Spike protein presenting in the variants Gamma and Delta. (B) structural analysis of Spike protein from wildtype version of SARS-CoV-2, (C) Spike protein from Gamma variant and (D) Spike protein from Delta variant. RMSD analysis indicates changes in the structure.

B.1.1.7 variant [111]. ChAdOx1-nCoV-19-elicited sera with 9-fold lower *in vitro* neutralization activity against the B.1.1.7 variant [114]. Based on these findings, scientists suggest that in countries with low vaccination coverage, where the Alpha variant is not yet dominant, there is an urgent need to improve health facilities to meet medical requirements of possible Alpha outbreaks.

7. Beta variants of SARS-CoV-2

The Beta variant (B 1.351) emerged in Nelson Mandela Bay, Eastern Cape, in October and November 2020 and soon became predominant in South Africa, overcoming the previously dominant variants B.1.1.54, B.1.1.56, and C.1 lineages [146]. By December of 2020 and January of 2021, the Beta variant had arrived in Botswana, France, Scotland, South Korea, Sweden, Switzerland, the United Kingdom, Austria, Belgium, Denmark, Finland, Germany, Ireland, Netherlands, Norway, Australia, Brazil, Canada, China, Japan, Taiwan, United States, and Zambia [147]. This fast spread led to over 95% of infections during and after the second epidemic wave, between November 2020 and February 2021 [142,146,148].

The Beta variant was initially classified as a new monophyletic cluster (501Y·V2), replacing the three main South African lineages (B.1.1.54, B.1.1.56, and C.1) that were circulating during the first epidemic wave [148]. The high transmissibility and increased infection duration explain why the Beta variant became predominant [149,150]. According to the mutational profile observed at the first sampling point, this lineage had accumulated, in addition to D614G, five other non-synonymous mutations in the spike protein (D80A, D215G, E484K, N501Y, and A701V). Three further spike mutations emerged by the end of November (L18F, R246I, and K417N). Additionally, the Beta variant has two deletions in the NDT region (Fig. 3A) [148].

The substitutions are: L18F, involving the exchange of a leucine (apolar amino acid) by a phenylalanine (a hydrophobic amino acid); D80A, the replacement of aspartic acid (negative) with alanine (apolar); D215G, replacement of an aspartic acid (negative) with a glycine (apolar); and R246I, involving replacement of an arginine (positive) with an isoleucine (apolar). Also, deletions in the NDT region (Fig. 3A) are involved in the escape from neutralization by antibodies such as NTD-binding mAbs30 and 4A8 [140].

Three of the spike mutations are in critical residues in the receptor-binding domain (RBD) (K417K, E484K, and N501Y) (Fig. 3A). The K417 position of the S protein has been designated an epitope of RBD of class 1 and 2 antibodies [109]. Moreover, very likely the alteration of this spot affects the ability of class 1 and 2 antibodies to bind and neutralize the RBD, preventing the interaction with the ACE2 receptor [141,142]. In the Beta variant, a substitution of lysine (positive) by asparagine (polar uncharged) is involved in the ability of the S protein from the Beta variant to escape from immune antibodies. Besides that, this substitution has a negative effect. It was noticed that K417N slightly reduces the affinity of RBD for ACE2, but it seems this collateral effect did not change the Beta variant's fitness [142].

The substations E484K and on RBD possibly enhanced the binding affinity of the Beta variant for the ACE2 receptor. The E484K mutation is uncommon and interacts with the K31 hotspot residue of hACE2 [142,151]. The position E484 of the S protein indicates it is an immunodominant residue, which means the immune response is focused against it. So, mutation in this position could completely disarm the immune response toward a variant holding it. The Beta variant was the first VoC to show substitution at position 484, in which a proline (apolar) was replaced by lysine (positive). The E484K is involved in

escape from antibodies in convalescent plasma (C121 and C144 monoclonal antibodies) [151–155]. Baum et al. [155] showed that a pseudovirus with the mutation E484K could escape neutralization by combining two monoclonal antibodies, REGN10989 and REGN10934, used to treat severe cases of COVID-19.

The mutation N501Y (see the Alpha variant section) is present in Alpha and Beta. It is involved in the binding phase of the S protein with ACE2, allowing an increase in affinity for ACE2 and modifying the structural mechanics of the RBD-ACE2 complex. The N501Y enables escape from the immune system but reduces the affinity of the S protein for the ACE2 receptor (see the Alpha variant section). However, in the Beta variant, the presence of K417N and E484K mutations slightly reduce the affinity for RBD, as they abolish the interfacial salt bridges that help bind RBD-ACE2 and stabilize the complex. Therefore, these two additional mutations in the Beta variant could overshadow in part the increase in the RBD-ACE2 caused by N501Y. However, those mutations facilitate the escape of the Beta variant from the neutralizing effect of antibodies. Based on that, it is feasible to suggest that the positive effect of K417N and E484K mutations is greater than the negative effect, enhancing the Beta variant's fitness and thus being kept by the virus and even developed by other variants [50,156].

As discussed above, the Beta variant presents many non-synonymous amino acid substitutions. These amino acid changes alter the three-dimensional structure of the S protein. For example, N501Y replaces an asparagine with a tyrosine. The side-chain volume of asparagine is 114.1 $Å^3$, compared to the side-chain volume of 193.6 $Å^3$ of tyrosine. This difference in the size of lateral chains affects the S protein's structure. To verify that, a root mean square deviation (RMSD) calculation of the atomic position on the S protein from the variants was performed in comparison with the wild-type S protein from the Wuhan isolate (Figs. 3). To perform the structural alignments, the 3D structures of S proteins of the Wuhan isolate (PDB ID: 6Z97) were deposited in the Protein Data Bank (PDB, https://www.rcsb.org/) and the database of the Beta variant (modeled in this study). The RMSD analysis revealed significant structural changes between Wuhan S protein and Beta variant S protein (Fig. 3D). It is possible to analyze in many positions the differences of the two proteins. The RMSD value for this alignment was 1.604 A, indicating that both atomic positions are quite different. The greatest alteration was in regions such as NDT, the arm of S1, and RBD (Fig. 3D). These alterations are responsible for the differential interaction of the S protein with the ACE2 receptor, and thus the spread, infectivity, and severity of the disease.

Given the ability to escape from the immune system, the Beta variant overtook the Alpha variant in regions with naturally acquired immunity, by about 20% to 40%. To date, modest clinical trials have shown that two doses of the Pfizer-BioNTech vaccine had 75% effectiveness against Beta variant infection. In contrast, Novavax's vaccine showed 89% efficacy in the UK compared to South Africa, with 60%. Similarly, the Johnson & Johnson vaccine trials reported lower levels of protection against moderate to severe COVID-19 in South Africa than in the United States. Meanwhile, South Africa ceased plans to roll out the AstraZeneca vaccine because clinical trials did not show protection against mild or moderate illness caused by the Beta variant [145,156,157]. Experiments using viruses expressing RBD with K417N + E484K + N501Y revealed a reduction of 2 to 3-fold in neutralization by antibodies in plasma from vaccinated individuals [111].

8. Gama variant of SARS-CoV-2

Since SARS-CoV-2 became pandemic, it has evolved genetically, leading to different variants (Fig. 1), with different genetic profiles, and thus different degrees of severity. The genomic sequencing of viral samples has been fundamental to detect the new variants of SARS-CoV-2 [25,65]. The new VoC, the P.1 lineage, known today as the Gama variant, was detected in about 42% of the analyzed genomic sequences in samples from Manaus in December 2020 and presented important mutations with biological significance.

The Gamma variant was also identified in January 2021 in Brazilian travelers at Japanese airports [158]. After that, this variant was identified in different Brazilian regions [159–161]. Manaus, the capital of Amazonas State, was the most affected and became an epicenter of the outbreak of the Gamma variant, which quickly spread through the Solimões River course, causing the collapse of public and private health systems [162]. Notably, the cases of Gamma variant in January represented 85.4% (41/48) of COVID-19 cases in Manaus [163]. In February 2021, it had spread in South America and was responsible for nearly 40% of COVID-19 cases [164–166]. These results revealed the high infectivity rate of this variant, which is estimated to be 2.6 times more infectious.

In February 2021, two cases of a new SARS-CoV-2 variant were described in Alagoas State [167]. One person came from Amazonas, and the other was characterized as community transmission in Alagoas, confirming the presence of the Gamma variant [161]. According to data gathered by the FIOCRUZ-COVID-19 Genomics Surveillance Network of the Brazilian Ministry of Health, the Gamma variant was mainly responsible for Covid-19 cases in Brazil from February to July 2021. For comparison, in December 2020, 26% of deposited genomes were the Gamma variant (P.1); six months later, in June, 64.6% were the Gamma variant, and in August, 99% of the sequenced samples were the Gamma variant [168].

After the first detection on 23 December 2020 in Manaus [163], the Gamma variant was found in 71 countries. It was detected in South America, Central America, North America, Europe, Angola, Turkey, Japan, the Philippines and Australia. The Gamma variant was not detected following a logical geographical sequence concerning the first case, since it was detected in Uruguay, Canada, India and Australia in the same period. Brazil and the United States had the greatest number of Gamma infections globally [169]. The Gamma variant was classified as VoC based on its greater transmissibility, pathogenicity, and immune escape. The Gamma variant carries multiple mutations in the NDT and RBD domains [170,171].

The analysis of sequences revealed that the SARS-CoV-2 Gamma variant has 37 mutations, including 22 missense, 10 synonymous, three intergenic, one frameshift, and one in-frameshift mutation. In the spike protein, 12 missense mutations (L18F, T20N, P26S, D138Y, R190S, K417T, E484K, N501Y, D614G, H655Y, T1027I, and V1176F) were observed [163,171,172]. Three mutations (K417T, E484K, and N501Y) were also identified in the RBD region of the spike protein [158,170].

Although the emergence was in different in most countries, the Gamma and Beta variants share some important mutations in RBD, such as L18F, K417T, and E484K, in addition to D614G (Figs. 3 and 4 panel A). The N501Y is shared by the Alpha, Beta, and Gamma variants. The appearance of those mutations in different variants that emerged in different countries has two possible explanations: first, the selective pressure on SARS-CoV-2, probably induced by either natural or artificial immunity, drove the emergence of the mutation in different individuals; or second, it is a clear case of convergent evolution. The implication of these mutations (L18F, K417T, E484K and N501Y) has already been discussed in the Alpha and Beta sections.

In addition to shared mutations, some mutations are exclusive to the Gamma variant (Fig. 4A). Those mutations are T20N, P26S, D138Y, R190S in the NDT region; H655Y, close to the furin site, and T1027I in the junction between the HR1 and HR2 regions. The mutations T20N (replacing a threonine with an asparagine) and P26S (replacing a proline with a serine) are located in the NDT supersite region. The NDT supersite is highly targeted by antibodies [137,140,163]. Studies by McCallum et al. [137] and Suryadevara et al. [173] revealed that antibodies with higher neutralizing power preferably attack the NDT supersite region. Thus, a mutation in this region helps the Gamma variant to escape from the immune system. Additionally, the mutation T20N provides an N site for glycosylation, which could create a shield, protecting the region from antibody recognition [174]. Although D138Y, R190S, H655Y, and

T1027I are non-synonymous mutations, it seems that their mutations have not affected or conferred any additional fitness to the S protein, or at best, their effects are still unclear. What is known is that those mutations are lineage-defining.

RMSD analysis comparing the S protein from the Gamma variant with the S protein from the Wuhan isolate produced a score of 1.060 Å, indicating the differences between S proteins (Fig. 4B and C). Compared to other variants, the S protein from the Gamma variant is the one closest to the S protein from the Wuhan isolate. The most exciting alterations in the 3D structure are in the NDT region (Fig. 4C), and the mutation T20N, which potentially increases the glycosylation, covering the entire region, preventing the antibodies' attachment. The RMSD analysis suggests that the S protein from the Gamma variant has adapted its structure mainly to escape from the immune system. The Gamma variant is responsible for the first case of reinfection in Manaus, Brazil [174]. This observation indicates the Gamma variant has excellent ability to mitigate or escape from the immune system, which might be related to a higher mortality rate of the Gamma variant, estimated to be 1.7 to 2.4-fold higher than the rate of the Wuhan isolate [174].

The Gamma variant has a high attack rate even in people that have completed the vaccination regimen. By July 2021, the Gamma variant was predominant in French Guiana, threatening the hospital capacity by causing the third wave [175]. The reduced vaccine efficiency toward the Gamma variant was a surprise, because *in vitro* trials showed strong neutralization of antibodies in people vaccinated with the BNT162b2 vaccine [38,110–113,116]. The unexpectedly high attack rate of the Gamma variant could result from problems with the vaccine storage, but this is just speculation. A Gamma outbreak among persons fully vaccinated with the BNT162b2 vaccine shows the ability of the Gamma variant to escape from the immune system. This uncommon infection of the Gamma variant in vaccinated people demands surveillance and studies of BNT162b2's effectiveness in regard to the Gamma variant.

9. Delta variant

First reported in India, in late December 2020, the double-mutated Delta VoC, a coronavirus variant formerly known as Indian VoC or B.1.617.2, is 40% more transmissible than the Alpha variant and two times more transmissible than the original Wuhan strain of SARS-CoV-2, leading to new lockdowns [176,177]. The Delta variant required only a few months to spread to 98 countries, becoming the dominant variant in all of them. Delta is the causative agent of more than 83% of COVID-19 cases in the U.S. and 91% of infections in the UK. The UK and many countries in Europe have faced increased new infections and deaths by the Delta variant, which rapidly became the dominant variant worldwide [178].

The advantage of this Delta variant is the combination of high transmissibility and immune system evasion, besides being less sensitive to neutralizing antibodies. Mutations of the S protein may have enhanced its ability to bind to the ACE2 receptor [179]. As discussed above, the S protein must be cut twice by host proteins to enter human cells. However, the Delta variant has earlier processing of the S protein, and newly formed viral particles emerge rapidly from infected cells, infecting other cells more efficiently [180].

The Delta variant has accumulated multiple mutations in the S1 subunit, specifically in the NDT and RBD regions. Mutations in NDT are related to escape from the immune system, and mutation in RBD seems to improve its stability and ability to bind to ACE2 and evade the immune system [181]. However, despite this knowledge, many unknowns surround the Delta variant. For instance, it is not yet understood for sure how Delta's mutations lead to a supercharged variant [181].

According to the Center for Disease Control (CDC), Delta has exclusive signature mutations including T19R, V70F*, T95I, G142D, delE156-, delF157-, R158G, A222V*, W258L*, L452R, T478K, P681R, and D950N (Fig. 4A) [181]. The Delta variant also has the mutations D614G, shared with all variants, and K417N, shared with the Beta and Gamma variants. The implication of D614G and K417N has already been discussed in this study. Delta variants presenting the K417N mutation shared with Gamma and Beta variants belong to lineages AY.1, AY.2, and AY.3, being called Delta plus variants (Figs. 3A and 4A) [177–180,182–185].

The mutations T19R, V70F*, T95I, G142D, delE156-, delF157-, R158G, A222V* and W258L* are all located in the NDT (Fig. 4) region, covering the NDT supersite, which is the target of anti-NTD neutralizing antibodies [109,116,137,140]. The NDT region has a stabilizing effect on the S protein [186] because it is targeted by potent neutralizing antibodies [137,173,186–188]. The NDT supersite is divided into five loops, named N1 to N5, covering different residue gaps in N1 (residues 14–26), N2 (residues 67–79), N3 (residues 141–156), N4 (residues 177–186), and N5 (residues 246–260) [186,187,189].

The Delta variant has accumulated many non-synonymous mutations in the NDT supersite, changing its structure to reduce the neutralizing effect of anti-NDT antibodies. A meticulous analysis of the Delta variant's mutations in the NDT region shows that T19R is in the N1 region, V70F is in the N2 region, G142D and delE156- are in N3, and A222V and W258L are in the N5 region. The Delta variant showed three mutations in the RBD region (K417N, L452R, T478K). One of them, K417N, shared with the Beta and Gamma variants, has already been discussed. Here we focus on the two exclusive regions of the Delta variants L452R and T478K (Fig. 4A).

It was shown that the Alpha, Beta, and Gamma variants share the mutation N501Y, which is involved in escaping from the immune system. However, this mutation slightly reduces the affinity of RBD for the ACE receptor. It seems that the Delta variant has accumulated mutations to overcome that obstacle. The Delta variant lacks the mutation N501Y. In contrast, it has the mutations L452R and T478K, which are involved in the escape from anti-RBD antibodies and do not reduce the affinity of RBD for ACE2 [28,46,93,136,137,186,187,190,191]. The mutation L452R (changing a leucine for an arginine) is closely related to the escape of monoclonal antibodies [142]. For example, the monoclonal antibody Bamlanivimab lost its antiviral effect against the Delta variant, contrasting with its continuing activity against other variants [142]. The unique change of T478K in the RBD region of the Delta S protein was found precisely in the epitope region recognized by monoclonal antibodies known as Class 1 [192].

The mutation P681R, adjacent to the furin cleavage site (685), seems to be one of the greatest advantages of the Delta variant. The Alpha variant has a mutation at the same P681H site. This mutation increases the Alpha transmissibility by 40% in comparison with the original SARS-CoV-2 from Wuhan. The mutation replaces the proline residue with an arginine residue in the Delta variant at position 681. Both mutations in the Alpha and Delta variants lead to a less acidic environment, favoring the basic cleavage at the furin site. The fact is that arginine is the most basic ever, with a pK of the side chain of 12.5. Based on that, arginine provides a perfect environment for furin cleavage and activation of the S protein.

Furin cuts indicate the existence of more S proteins primed to invade human cells. For example, in SARS-CoV virions, only 10% of S protein is primed and can infect cells. In the Alpha variant, with P681H, the primed S protein is about 50%. In contrast, in the Delta variant, holding the mutation P681R, 75% of S proteins are primed and can infect human cells. The P681R is not just one more mutation; it is behind the fast spread of the Delta variant and probably is the essential advantage gained by Delta [180].

Liu and researchers reported that the S protein is cut more efficiently in the Delta variant than others [193]. The P681R at a furin cleavage site separates the S1 and S2 subunits [180]. The authors stated that it seems the viral particles of the Delta variant are produced with the primed S protein and then infect cells more efficiently. Virologists at the University of Tokyo showed that the P681R mutation speeds up the infection of uninfected cells through plasma membrane fusion, three times more than the other variants [185].

The D950N (Fig. 4A) region is located at the interface of the S protein trimer. It is suggested that this mutation regulates S protein dynamics between monomeric and trimeric phases [194]. The RMSD analysis (Fig. 4D) revealed that the S protein from Delta is the most different from the original S protein from the Wuhan isolate (Fig. 4B). The S protein from the Delta variant presented the highest value of RMSD, 1.716 (Fig. 4D). The most altered region is the NDT region due to accumulating a higher number of mutations.

The Delta variant is more aggressive [184]. Delta-infected people present a viral load 1260 times higher than people infected with the original coronavirus strain [195,196]. Li et al. [195] reported that high viral loads in people infected with the Delta variant are reached in up to four days after contact with an infected person. In contrast, in people infected with the original SARS-CoV-2, this only happened six days after contact. This result indicates a higher replication rate of the Delta variant, which has a perfect combination to spread. The high viral loads plus short incubation time make sense to explain the greater transmissibility of the Delta variant compared to the original SARS-CoV-2 or even the other variants.

The Delta variant's ability to strongly bind to the receptors of lung cells and escape from immune response might overcome immunization gained from vaccination [184]. Recent data indicate that fully vaccinated people can still be vectors to spread the Delta variant more efficiently than other variants [197–199]. The fully vaccinated people are protected against severe COVID-19 and death by Delta variants. However, those people still present a high level of transmission. This fact is intriguing to scientists worldwide, and the recommendation is for vaccinated people to continue taking precautions such as social distancing and wearing face masks.

10. Omicron variant

On 24 November 2021, a new variant was identified in South Africa, variant B.1.1.529, later designated as Omicron by the WHO. Two days later, Omicron was classified as a VoC, a classification that occurred faster than the other variants [200]. The Omicron variant is highly mutated, with more than 50 mutations (30 mutations in the S protein alone). There have been more than 200 cases detected in 23 countries on all 6 continents [200]. Most surprisingly, cases were detected in Scotland, where 6 cases of these variants were identified. None of them were related to travelers from South Africa, which may indicate community transmission of the variant [201].

Initial results show that this variant has many mutations in relation to the Alpha and Delta variants, linked to the sudden increase in transmission, infectivity, and escape from the immune system. Initial modeling studies using artificial intelligence showed that Omicron's protein S could escape from T lymphocyte cells, but more *in vitro* studies need to be conducted to confirm this finding [201]. Like three patients in Brazil, some people infected by Omicron were fully vaccinated, indicating that Omicron can defeat the immunity caused by vaccines.

Preliminary studies have shown that the S protein of this new variant has an insertion at position 214 of the NTD region. This insertion was likely acquired from a host infected by SARS-CoV-2. Therefore, sequencing in the search for new variants is of paramount importance for understanding how mutations affect the behavior of protein S in human infection and the discovery of new animal hosts. That is why it is essential to continue monitoring people infected with SARS-CoV-2.

Of the 30 mutations of the S protein of the Omicron variant, some are shared with previous variants, and others are unique. Among the mutations, Omicron has one insertion of three amino acids in the NDT region together with three small deletions compared to wild-type SARS-CoV-2 from Wuhan. Insertions and deletions in the S protein from Omicron lead to a loss of three amino acid residues in the Omicron S protein compared to the wild-type version of the virus.

Indeed, mutations lead to a different S protein in the Omicron variant compared to S protein from Wuhan SARS-CoV-2 (Fig. 5). The Delta variants have the most different S protein among the variants compared to Wuhan SARS-CoV-2 (Figs. 3 and 4). However, RMSD analysis of the S protein from Omicron revealed a new winner. The S protein from the Omicron variant had an RMSD score of 2.156 (Fig. 5C), compared to the S protein structure of Wuhan isolate (Fig. 5A), with score of 1.716 (Fig. 5B). This analysis showed many alterations in atoms' positions, leading to a structural difference in S protein spatial arrangement. The most different parts of S protein from the Omicron variant have been found in the NDT region, which has suffered from many mutations, including insertions and deletions.

First of all, the D614G substitution in all variants is also conserved in Omicron S protein. Omicron shares mutations that were previously exclusive to Alpha, such as del69–70 and P681H. Omicron has no mutation shared only with the Beta variant, and the H655Y substitution is the only mutation that Omicron shares only with the Gamma variant. With the Delta variant, Omicron shares T95I, G142D and T478K. Omicron shares the N501Y region with Alpha, Beta, and Gamma variants. Additionally, Omicron shares the K417N substitution with Beta, Gamma, and Delta variants.

The Omicron variant has 24 signature mutations (A67V, Δ211/L212I, ins214EPE, G339D, S371L, S373P, S375F, N440K, G446S, S477N, E484A, Q493K, G496S, Q498R, Y505H, T547K, N679K, N764K, D796Y, N856K, Q954H, N969K, and L981F [201]. These mutations are found in the NDT region, in the RBD, around the furin cleavage region, in the fusion peptide and HR1 regions. The shared mutation between Omicron and other variants has already been discussed throughout this review. When important, it is possible to further develop some discussion. However, the focus here is on the signature mutations presented by

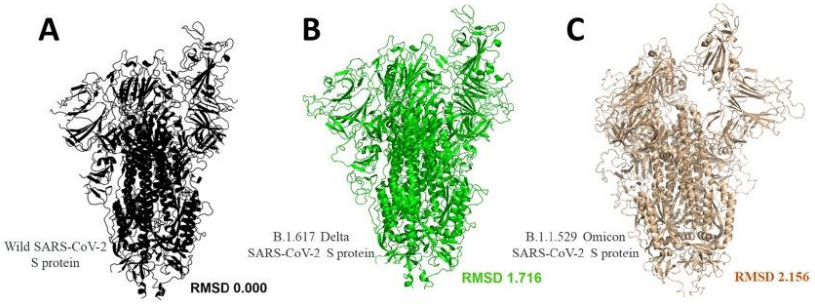

Fig. 5. Structural alignment among Spike protein from Wildtype and variants of SARS-CoV-2. (A) structural analysis of Spike protein from wildtype version of SARS-CoV-2, (B) Spike protein from Delta variant and (C) Spike protein from Omicron variant. RMSD analysis indicates changes in the structure.

Omicron.

An interesting point regarding Omicron is the substitution of E484A rather than the E484K present in the Beta and Gamma variants (Figs. 3A and 4A). As discussed above, the E484K is related to escape from neutralizing antibodies. In the Omicron variant, the E484A is more involved in escaping from 2B04 and 1B07monoclonal antibodies [201].

As happens in other variants, the mutation in the NTD region was mostly involved in two points: stabilizing the S1 to allow strong interaction between RBD and ACE2, and escape from neutralizing antibodies. With the deletion shared with the Alpha variant, Omicron also has another del211, a substitution of L212I, and an ins214EPE of three amino acids in the NDT region. As discussed above, NDT is a supersite of recognition by antibodies. By changing this region, Omicron can be more efficient in escaping from the immune system [43,202]. These alterations could be involved in the ability of Omicron to infect fully vaccinated people.

This is not the first substitution where N440K is present. One SARS-CoV-2 sample isolated from a re-infected patient presented this mutation [151] and is related to escape from human monoclonal antibodies. This mutation is predicted to result from selective pressure imposed by antibodies [203]. Other mutations in RBD such as G446S, S477N, T478K (also in the Delta variant), E484A, and Q498R, are all involved in the escape of RBD from anti-RBD neutralizing antibodies [142,193,204].

Q493 is an important site for interaction between RBD and ACE2. However, mutations at this site are generally either Q493R/K, and the Omicron variant has the Q4 substitution It seems that this mutation is tolerated and does not affect the interaction between ACE2 and RBD [205]. Indeed, this mutation is involved in the escape from LY-CoV555, LY-CoV016, and REGN10989/10934 monoclonal antibodies [155,205].

S477N, N501Y, P681H, and N679K are very likely to support the Omicron variant's higher transmissibility. Before Delta, Alpha was the most transmissible variant in the world. This was possible because compared to wild-type SARS-CoV-2, the Alpha variant has a histidine rather than a proline at position 681 in the polybasic cleavage site in the spike protein at the S1/S2 junction (residues 681–685) to the furin site of cleavage. The furin cleavage requires a basic environment to occur, so the replacement of proline (apolar) by histidine (positively charged) in the Alpha variant improved the furin cleavage, producing more activity of S proteins able to infect the cell. Additionally, the Alpha variant loses glycosylation at this position by removing the proline residue. This is important because carbohydrates hinder the cleavage site, inhibiting access by the protease. Elimination of proline removed a glycosylation site found in the ancestral Wuhan strain.

In the case of Delta, there has been improvement. The Delta variant has substitution at position 681, but the Delta variant has an arginine replacing the proline residue instead of lysine. By being the essential amino acid residue, the Delta variant improved the cleavage of S protein, enhancing its cell recognition and infection, leading to higher transmissibility than that presented by the Alpha variant. The Omicron preserves the same substitution presented by the Alpha variant, P681H. The replacement of proline by an arginine instead of histidine is a significant evolutionary advantage. In contrast to histidine, which is only positive at mildly basic pH, arginine is positive under all cell conditions. This is thought to be responsible for the higher transmissibility of the Delta variant [206].

At first glance it was reasonable to assume that Omicron could be less transmissible than the Delta variant. However, Omicron also showed a new mutation near the cleavage site, N679K. This substitution also added a positively charged lysine residue, making the neighborhood satisfactory for furin cleavage. So, these two mutations, P681H and N679K seem to be associated with mutations that provide a more efficient S1-S2 cleavage, leading to a more infective S protein. Although this makes total sense, it needs more investigation for confirmation. However, the rapid replacement of the Delta variant by Omicron in South Africa reinforces the hypothesis of high transmissibility rates of the Omicron variant. Another explanation for higher transmissibility of Omicron is that these mutations also promote escape from the immune system.

There is no doubt about the higher transmissibility rates of Omicron. However, it needs to be quantified. The reproductive number (R_0) is a measure of transmissibility (Fig. 6). For example, the R_0 of wild-type SARS-CoV-2 is 1, which means one infected person transmits the virus to one person. The R_0 for the Alpha variant is 1.76, indicating more transmissibility (Fig. 6). For the Delta variant, the R_0 value is 5.01 (Fig. 6), indicating that one person infected with the Delta variant can spread the virus to up to five other people. This is a high increase of transmissibility compared to wild-type SARS-CoV-2. However, there are no reliable data on R_0 for Omicron (Fig. 6). Based on preliminary infection in South Africa, it is postulated to be higher than the Delta variant.

Regarding the severity of COVID-19 caused by Omicron, the knowledge is insufficient to reach any conclusions. However, there is some information available. For example, the COVID-19 caused by Omicron has new symptoms not described before regarding other variants, such as fatigue, body aches and headache. Additionally to these symptoms, one patient also presented a fever and a very high pulse rate [207,208]. Some patients have been found to be positive for Omicron infection but without symptoms [207].

Some vaccinated people have become infected with the Omicron variant, indicating this variant can to some extent, break immunity acquired with vaccination. The escape from the immune system of vaccinated people might be related to the higher number of mutations in the RBD region, allowing the escape from anti-RBD neutralizing antibodies. It has been indicated but not confirmed that Omicron can escape from memory immunity conferred by T cells and durable immunity.

Among vaccinated people infected with Omicron, some are asymptomatic and some have only mild symptoms. There have been no severe cases, hospitalization, or death caused by Omicron. This indicates that vaccination does not prevent Omicron infection, but it protects from severe cases, hospitalization, and death [200,201,207,208]. This information suggests how important it is to expand vaccination worldwide to prevent severe COVID-19 caused by the Omicron variant.

11. Interaction of S protein from variants with ACE2

Although it is known that the S protein from variants has a higher affinity for ACE2 than the wild-type version, nobody has quantified this interaction. What is known and accepted is that variants are more transmissible than wild-type versions. Here, we have used the wild-type S protein from the Protein Data Bank (https://www.rcsb.org/, PDB ID: 6Z97) to build the three-dimensional (3D) models of protein from the Alpha, Beta, Gamma, Delta and Omicron variants using the Swiss Model Server (https://swissmodel.expasy.org/) [209]. All the structure showed in the manuscript were validated. The models were created using the SWISS-model that already make the check in the structure using the Molprobity. Additionally, we have checked the structures on Molprobity server (http://molprobity.biochem.duke.edu/) [210] by Ramachandran plot analysis. Also, the global quality factor and the reliability of the models' folding were evaluated by ERRAT2 (http://servicesn.mbi.ucla.edu/ERRAT/) and Verify3D (http://servicesn.mbi.ucla.edu/Verify3D/), respectively. The 3D model built was docked against the ACE2 (PDB ID: 7KMD) using the FRODOCK Interactive protein-protein docking server (http://frodock.chaconlab.org/) [211].

The FRODOCK server provides a docking score (DS) that indicates the interaction between the protein and ligand. In this case, higher DS values are associated with higher affinity of the interaction. Based on the corresponding DS value, this only enables suggesting which protein has more affinity than any other protein. As a control, the interaction between the wild-type S protein from Wuhan isolate with ACE2 (Fig. 7A) has been used. This interaction has a DS value of 3025.00 (Fig. 7A). All S proteins from variants have higher DS values, indicating they have a higher affinity for ACE2 than wild-type S protein (Fig. 7). This was

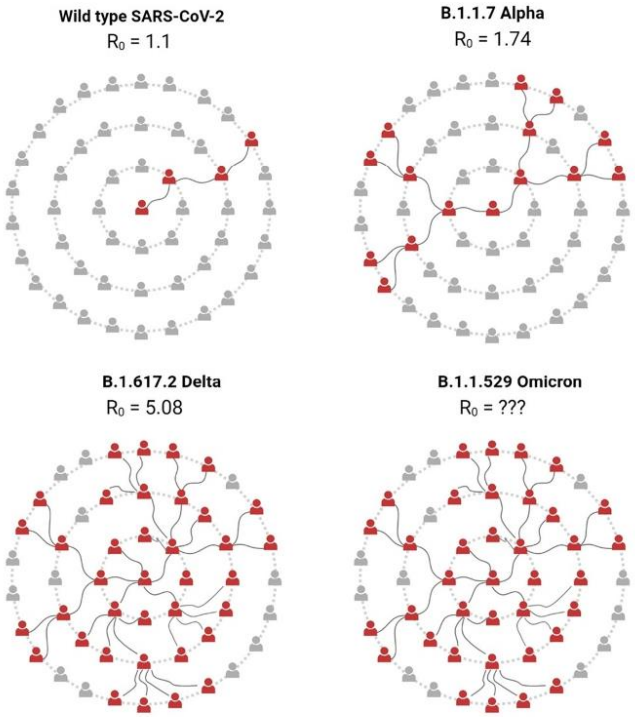

Fig. 6. The reproductive number (R_0) wildtype and variants of SARS-CoV-2. The R_0 of the variants is higher than the wildtype version of SARS-CoV-2 suggesting the variants are more transmissible.

expected, because, to some extent, all variants are more transmissible than wild-type SARS-CoV-2 from Wuhan. The S proteins from Beta and Gamma variants presented DS values, respectively, of 3102.00 and 3200.00, which mean increases of 2.5% and 5.85% in the DS interaction with ACE2 (Fig. 7C and D). This result suggests the S protein from those variants has a slight increase in the ability to interact with ACE2 compared to the wild-type versions of S protein.

The DS values for Alpha, Delta, and Omicron were, respectively,3341.00, 3415.00, and 4150.00 representing increases of 10.44%, 12.89%, and 37.23% in the ability to bind to ACE2 (Fig. 7B, E, and F). These three variants were classified as transmissible and presented the highest DS values compared to other wild-type variants of S protein. Not surprisingly, the S protein from the Omicron variant, which has many mutations, presented the highest value of DS, suggesting the S protein from the Omicron variant is the most optimized protein for interaction with the ACE2 receptor. These results are in accordance with the higher transmissibility of the Omicron variant.

12. Conclusion

It is clear that the S protein from variants has been changing with two goals: 1) to improve the interaction with ACE2; and 2) to escape from the immune system. Spike amino acid substitutions, deletions, and insertions (Omicron) have a direct impact on how neutralizing antibodies interact with S protein from variants, leading to reinfection and even infection of fully vaccinated people. However, it looks like the mutations in the spike of variants are more driven to improve the interaction with the ACE. The fast interaction with ACE2 reduces time when SARS-CoV-2 is exposed to neutralizing antibodies. The results presented lead to the conclusion that the Omicron S protein is optimized to bind to the ACE2 receptor and escape from the immune system. It is clear that SARS-CoV-2 is under selective pressure caused by vaccines and is changing in response to that pressure. So, an understanding of spike mutations in antigenic positions will help monitor and improve vaccine effectiveness. Additionally, it is essential to continue collecting virus information by sequencing and studies with vaccines to elucidate the SARS-CoV-2 behavior.

Funding and acknowledgments.

Special thanks go to CAPES for providing the postdoctoral grant (grant number 88887.318820/2019-00) to Pedro F. N. Souza. This work was supported by grants from the following Brazilian agencies: National Council for Scientific and Technological Development (CNPq), research productivity grant to Raquel C. Montenegro; Office to Coordinate Improvement of Higher Education Personnel (CAPES) for the grant to Raquel C. Montenegro (number 88881.505364/2020-01 - Call No. 9/2020; National Institute for Science and Technology of Bioinspiration and Cearense Foundation to Support Scientific and Technological Development (FUNCAP), for the grant to Raquel C. Montenegro (Number: 03195011/2020). Raquel C. Montenegro and Débora S.C.M. Castelo-Branco acknowledge the School of Medicine (FAMED) of Federal University of Ceará for supporting this research by the COVID-19 research program.

CRediT authorship contribution statement

Conceptualization: Pedro F. N. Souza.

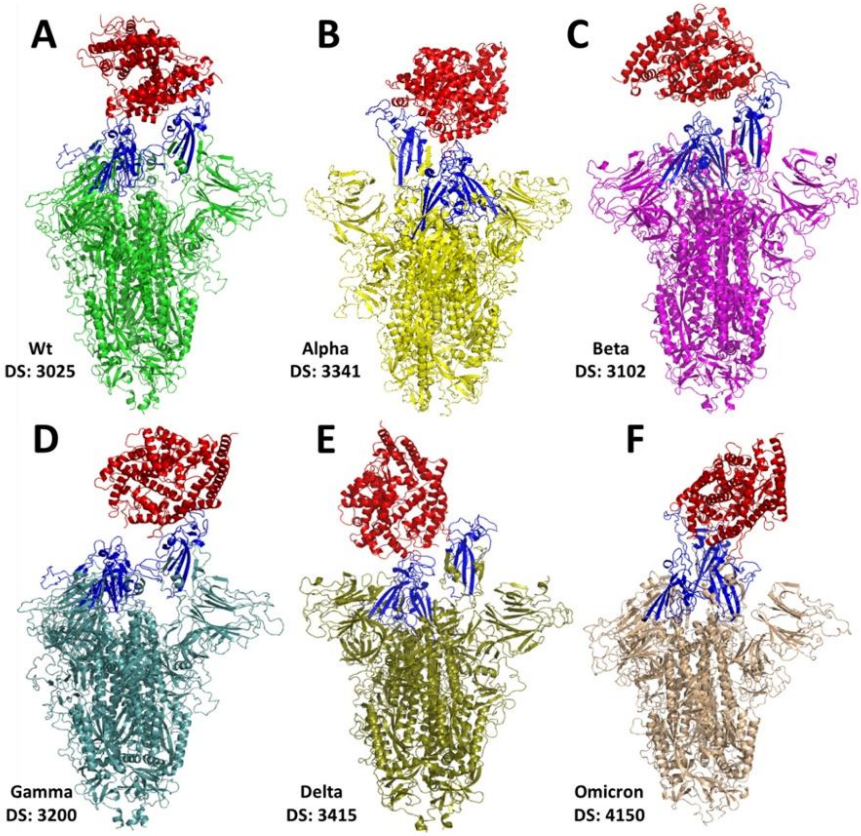

Fig. 7. Docking analysis of Spike protein with ACE2 receptor. (A) Docking analysis of Spike protein of Spike protein from (A) wildtype version, (B) Alpha variant, (C) Beta variant, (D) Gamma variant, (E) Delta variant and (F) Omicron variant with the ACE2 receptor. DS is a docking score produced by FRODDOCK server and indicates strength of interaction between proteins.

Data curation: Pedro F.N. Souza, Felipe P. Mesquita, Jackson L. Amaral, Patrícia G. C. Landim, Karollyny R.P. Lima, Marília B. Costa, Izabelle R. Farias, Mônica O. Belém, Yago O. Pinto, Heline H. T. Moreira, Ilana C.L. Magalhaes, Claudia R. de Andrade.

Formal analysis: Pedro F.N. Souza, Felipe P. Mesquita, Jackson L. Amaral, Patrícia G. C. Landim, Karollyny R.P. Lima, Marília B. Costa, Izabelle R. Farias, Mônica O. Belém, Yago O. Pinto, Heline H. T. Moreira, Ilana C.L. Magalhaes, Claudia R. de Andrade.

Funding acquisition: Pedro F.N. Souza.

Resources: Pedro F.N. Souza.

Supervision: Pedro F.N. Souza.

Writing–original draft: Pedro F.N. Souza, Patrícia G. C. Landim, and Claudia R. de Andrade.

Writing, review, and editing: Pedro F.N. Souza.

Final approval of the manuscript and submission: Pedro F.N. Souza.

Ethical approval

Not applicable.

Declaration of competing interest

All authors declare no conflicts of interest.

References

[1] S.R. Weiss, Forty years with coronaviruses, J. Exp. Med. 217 (2020), https://doi.org/10.1084/jem.20200537.

[2] Coronavirus Disease (COVID-19) situation reports, (n.d.). https://www.who.int/emergencies/diseases/novel-coronavirus-2019/situation-reports (accessed January 21, 2021).

[3] Coronavirus disease (COVID-19), (n.d.). https://www.who.int/emergencies/diseases/novel-coronavirus-2019 (accessed January 21, 2021).

[4] Coronavirus update (live): 97,633,202 cases and 2,091,064 deaths from COVID-19 virus pandemic - Worldometer, (n.d.). https://www.worldometers.info/coronavirus/ (accessed January 21, 2021).

[5] WHO Coronavirus Disease (COVID-19) dashboard | WHO Coronavirus Disease (COVID-19) dashboard, (n.d.). https://covid19.who.int/ (accessed January 22, 2021).

[6] C. Drosten, B. Meyer, M.A. Müller, V.M. Corman, M. Al-Masri, R. Hossain, H. Madani, A. Sieberg, B.J. Bosch, E. Lattwein, R.F. Alhakeem, A.M. Assiri, W. Hajomar, A.M. Albarrak, J.A. Al-Tawfiq, A.I. Zumla, Z.A. Memish, Transmission of MERS-coronavirus in household contacts, N. Engl. J. Med. 371 (2014) 828–835, https://doi.org/10.1056/nejmoa1405858.

[7] A.M. Zaki, S. van Boheemen, T.M. Bestebroer, A.D.M.E. Osterhaus, R.A. M. Fouchier, Isolation of a novel coronavirus from a man with pneumonia in

Saudi Arabia, N. Engl. J. Med. 367 (2012) 1814–1820, https://doi.org/10.1056/nejmoa1211721.
[8] Preliminary genomic characterisation of an emergent SARS-CoV-2 lineage in the UK defined by a novel set of spike mutations - SARS-CoV-2 coronavirus / nCoV-2019 Genomic Epidemiology - Virological, (n.d.). https://virological.org/t/preliminary-genomic-characterisation-of-an-emergent-sars-cov-2-lineage-in-the-uk-defined-by-a-novel-set-of-spike-mutations/563 (accessed January 22, 2021).
[9] Severe Acute Respiratory Syndrome (SARS), (n.d.). https://www.who.int/health-topics/severe-acute-respiratory-syndrome#tab=tab_1 (accessed January 21, 2021).
[10] Middle East respiratory syndrome coronavirus (MERS-CoV), (n.d.). https://www.who.int/health-topics/middle-east-respiratory-syndrome-coronavirus-mers#tab=tab_1 (accessed January 21, 2021).
[11] M. Bassetti, A. Vena, D.R. Giacobbe, The novel chinese coronavirus (2019-nCoV) infections: challenges for fighting the storm, Eur. J. Clin. Investig. 50 (2020), https://doi.org/10.1111/eci.13209.
[12] M.G. Hemida, M.M. Ba Abduallah, The SARS-CoV-2 outbreak from a one health perspective, One Heal. 10 (2020), https://doi.org/10.1016/j.onehlt.2020.100127.
[13] A. Brufsky, Distinct viral clades of SARS-CoV-2: implications for modeling of viral spread, J. Med. Virol. 92 (2020) 1386–1390, https://doi.org/10.1002/jmv.25902.
[14] T. Zhang, Q. Wu, Z. Zhang, Pangolin Homology Associated With 2019-nCoV, BioRxiv, 2020, https://doi.org/10.1101/2020.02.19.950253, 2020.02.19.950253.
[15] A.E. Gorbalenya, S.C. Baker, R.S. Baric, R.J. de Groot, C. Drosten, A.A. Gulyaeva, B.L. Haagmans, C. Lauber, A.M. Leontovich, B.W. Neuman, D. Penzar, S. Perlman, L.L.M. Poon, D.V. Samborskiy, I.A. Sidorov, I. Sola, J. Ziebuhr, The species severe acute respiratory syndrome-related coronavirus: classifying 2019-nCoV and naming it SARS-CoV-2, Nat. Microbiol. 5 (2020) 536–544, https://doi.org/10.1038/s41564-020-0695-z.
[16] X. Wu, Y. Cai, X. Huang, X. Yu, L. Zhao, F. Wang, Q. Li, S. Gu, T. Xu, Y. Li, B. Lu, Q. Zhan, Co-infection with SARS-CoV-2 and influenza a virus in patient with pneumonia, China, Emerg. Infect. Dis. 26 (2020) 1324–1326, https://doi.org/10.3201/EID2606.200299.
[17] V.K. Shah, P. Firmal, A. Alam, D. Ganguly, S. Chattopadhyay, Overview of immune response during SARS-CoV-2 infection: lessons from the past, Front. Immunol. 11 (2020) 1949, https://doi.org/10.3389/fimmu.2020.01949.
[18] Q. Ding, P. Lu, Y. Fan, Y. Xia, M. Liu, The clinical characteristics of pneumonia patients coinfected with 2019 novel coronavirus and influenza virus in Wuhan, China, J. Med. Virol. 92 (2020) 1549–1555, https://doi.org/10.1002/jmv.25781.
[19] Z. Khodamoradi, M. Moghadami, M. Lotfi, Co-infection of coronavirus disease 2019 and influenza a: a report from Iran, Arch. Iran. Med. 23 (2020) 239–243, https://doi.org/10.34172/aim.2020.04.
[20] L.M. Vos, R. Bruyndonckx, N.P.A. Zuithoff, P. Little, J.J. Oosterheert, B.D. L. Broekhuizen, C. Lammens, K. Loens, M. Viveen, C.C. Butler, D. Crook, K. Zlateva, H. Goossens, E.C.J. Claas, M. Ieven, A.M. Van Loon, T.J.M. Verheij, F. E.J. Coenjaerts, Lower respiratory tract infection in the community: associations between viral aetiology and illness course, Clin. Microbiol. Infect. 27 (2021) 96–104, https://doi.org/10.1016/j.cmi.2020.03.023.
[21] S.A. Meo, A.M. Alhowikan, T.A.L. Khlaiwi, I.M. Meo, D.M. Halepoto, M. Iqbal, A. M. Usmani, W. Hajjar, N. Ahmed, Novel coronavirus 2019-nCoV: prevalence, biological and clinical characteristics comparison with SARS-CoV and MERS-CoV, Eur. Rev. Med. Pharmacol. Sci. 24 (2020) 2012–2019, https://doi.org/10.26355/eurrev_202002_20379.
[22] M.G. Douglas, J.F. Kocher, T. Scobey, R.S. Baric, A.S. Cockrell, Adaptive evolution influences the infectious dose of MERS-CoV necessary to achieve severe respiratory disease, Virology 517 (2018) 98–107, https://doi.org/10.1016/j.virol.2017.12.006.
[23] J.L. Nieto-Torres, M.L. DeDiego, C. Verdiá-Báguena, J.M. Jimenez-Guardeño, J. A. Regla-Nava, R. Fernandez-Delgado, C. Castaño-Rodriguez, A. Alcaraz, J. Torres, V.M. Aguilella, L. Enjuanes, Severe acute respiratory syndrome coronavirus envelope protein ion channel activity promotes virus fitness and pathogenesis, PLoS Pathog. 10 (2014), e1004077, https://doi.org/10.1371/journal.ppat.1004077.
[24] A.A.T. Naqvi, K. Fatima, T. Mohammad, U. Fatima, I.K. Singh, A. Singh, S.M. Atif, G. Hariprasad, G.M. Hasan, M.I. Hassan, Insights into SARS-CoV-2 genome, structure, evolution, pathogenesis and therapies: structural genomics approach, Biochim. Biophys. Acta - Mol. Basis Dis. 1866 (2020), https://doi.org/10.1016/j.bbadis.2020.165878.
[25] B. Korber, W.M. Fischer, S. Gnanakaran, H. Yoon, J. Theiler, W. Abfalterer, N. Hengartner, E.E. Giorgi, T. Bhattacharya, B. Foley, K.M. Hastie, D.G. Parker, Tracking changes in SARS-CoV-2 spike: evidence that D614G increases infectivity of the COVID-19 virus, Cell (2020), https://doi.org/10.1016/j.cell.2020.06.043.
[26] K.R. Hurst, L. Kuo, C.A. Koetzner, R. Ye, B. Hsue, P.S. Masters, A major determinant for membrane protein interaction localizes to the carboxy-terminal domain of the mouse coronavirus nucleocapsid protein, J. Virol. 79 (2005) 13285–13297, https://doi.org/10.1128/jvi.79.21.13285-13297.2005.
[27] Tracking SARS-CoV-2 variants, (n.d.). https://www.who.int/en/activities/tracking-SARS-CoV-2-variants/ (accessed December 7, 2021).
[28] P. Wang, L. Liu, S. Iketani, Y. Luo, Y. Guo, M. Wang, J. Yu, B. Zhang, P.D. Kwong, B.S. Graham, J.R. Mascola, J.Y. Chang, M.T. Yin, M. Sobieszczyk, C.A. Kyratsous, L. Shapiro, Z. Sheng, M.S. Nair, Y. Huang, D.D. Ho, Increased resistance of SARS-CoV-2 variants B.1.351 and B.1.1.7 to antibody neutralization, BioRxiv Prepr. Serv. Biol. (2021), https://doi.org/10.1101/2021.01.25.428137.
[29] W.T. Harvey, A.M. Carabelli, B. Jackson, R.K. Gupta, E.C. Thomson, E. M. Harrison, C. Ludden, R. Reeve, A. Rambaut, S.J. Peacock, D.L. Robertson, SARS-CoV-2 variants, spike mutations and immune escape, Nat. Rev. Microbiol. 197 (19) (2021) 409–424, https://doi.org/10.1038/s41579-021-00573-0, 2021.
[30] S.M. Kissler, J.R. Fauver, C. Mack, C.G. Tai, M.I. Breban, A.E. Watkins, R. M. Samant, D.J. Anderson, J. Metti, G. Khullar, R. Baits, M. MacKay, D. Salgado, T. Baker, J.T. Dudley, C.E. Mason, D.D. Ho, N.D. Grubaugh, Y.H. Grad, Viral Dynamics of SARS-CoV-2 Variants in Vaccinated and Unvaccinated Persons, 2021, https://doi.org/10.1056/NEJMc2102507 doi:10.1056/NEJMC2102507.
[31] W. Wang, X.D. Lin, W.P. Guo, R.H. Zhou, M.R. Wang, C.Q. Wang, S. Ge, S.H. Mei, M.H. Li, M. Shi, E.C. Holmes, Y.Z. Zhang, Discovery, diversity and evolution of novel coronaviruses sampled from rodents in China, Virology 474 (2015) 19–27, https://doi.org/10.1016/j.virol.2014.10.017.
[32] B. Lomniczi, Biological properties of avian coronavirus RNA, J. Gen. Virol. 36 (1977) 531–533, https://doi.org/10.1099/0022-1317-36-3-531.
[33] M.M. Lai, C.L. Liao, Y.J. Lin, X. Zhang, Coronavirus: how a large RNA viral genome is replicated and transcribed, Infect. Agents Dis. 3 (1994) 98–105.
[34] C.A.M. de Haan, H. Vennema, P.J.M. Rottier, Assembly of the coronavirus envelope: homotypic interactions between the M proteins, J. Virol. 74 (2000) 4967–4978, https://doi.org/10.1128/jvi.74.11.4967-4978.2000.
[35] J.O. Norman, A.W. McClurkin, H.L. Bachrach, Infectious nucleic acid from a transmissible agent causing gastroenteritis in pigs, J. Comp. Pathol. 78 (1968) 227–235, https://doi.org/10.1016/0021-9975(68)90099-6.
[36] G. Schochetman, R.H. Stevens, R.W. Simpson, Presence of infectious polyadenylated RNA in coronavirus avian bronchitis virus, Virology 77 (1977) 772–782, https://doi.org/10.1016/0042-6822(77)90498-6.
[37] H. Wege, A. Mueller, V. Ter Meulen, Genomic RNA of the murine coronavirus JHM, J. Gen. Virol. 41 (1978) 217–227, https://doi.org/10.1099/0022-1317-41-2-217.
[38] F.P. Polack, S.J. Thomas, N. Kitchin, J. Absalon, A. Gurtman, S. Lockhart, J. L. Perez, G. Pérez Marc, E.D. Moreira, C. Zerbini, R. Bailey, K.A. Swanson, S. Roychoudhury, K. Koury, P. Li, W.V. Kalina, D. Cooper, R.W. Frenck, L. L. Hammitt, Ö. Türeci, H. Nell, A. Schaefer, S. Ünal, D.B. Tresnan, S. Mather, P. R. Dormitzer, U. Şahin, K.U. Jansen, W.C. Gruber, Safety and efficacy of the BNT162b2 mRNA Covid-19 vaccine, N. Engl. J. Med. 383 (2020) 2603–2615, https://doi.org/10.1056/nejmoa2034577.
[39] J.D. Dinman, Programmed ribosomal frameshifting goes beyond viruses, Microbe 1 (2006) 521–527, https://doi.org/10.1128/microbe.1.521.1.
[40] J.L. Jacobs, A.T. Belew, R. Rakauskaite, J.D. Dinman, Identification of functional, endogenous programmed - 1 ribosomal frameshift signals in the genome of Saccharomyces cerevisiae, Nucleic Acids Res. 35 (2007) 165–174, https://doi.org/10.1093/nar/gkl1033.
[41] L.A. Klobutcher, P.J. Farabaugh, Shifty ciliates: frequent programmed translational frameshifting in euplotids, Cell 111 (2002) 763–766, https://doi.org/10.1016/s0092-8674(02)01138-8.
[42] A.B. Hammell, R.C. Taylor, S.W. Peltz, J.D. Dinman, Identification of putative programmed -1 ribosomal frameshift signals in large DNA databases, Genome Res. 9 (1999) 417–427, https://doi.org/10.1101/gr.9.5.417.
[43] P.V. Baranov, R.F. Gesteland, J.F. Atkins, Recoding: translational bifurcations in gene expression, Gene 286 (2002) 187–201, https://doi.org/10.1016/s0378-1119(02)00423-7.
[44] B. Cobucci-Ponzano, M. Rossi, M. Moracci, Translational recoding in archaea, Extremophiles 16 (2012) 793–803, https://doi.org/10.1007/s00792-012-0482-8.
[45] R.S. Baric, B. Yount, Subgenomic negative-strand RNA function during mouse hepatitis virus infection, J. Virol. 74 (2000) 4039–4046, https://doi.org/10.1128/jvi.74.9.4039-4046.2000.
[46] X. Tang, C. Wu, X. Li, Y. Song, X. Yao, X. Wu, Y. Duan, H. Zhang, Y. Wang, Z. Qian, J. Cui, J. Lu, On the origin and continuing evolution of SARS-CoV-2, Natl. Sci. Rev. 7 (2020) 1012–1023, https://doi.org/10.1093/nsr/nwaa036.
[47] B. Zhou, T.T.N. Thao, D. Hoffmann, A. Taddeo, N. Ebert, F. Labroussaa, A. Pohlmann, J. King, S. Steiner, J.N. Kelly, J. Portmann, N.J. Halwe, L. Ulrich, B. S. Trüeb, X. Fan, B. Hoffmann, L. Wang, L. Thomann, X. Lin, H. Stalder, B. Pozzi, S. de Brot, N. Jiang, D. Cui, J. Hossain, M.M. Wilson, M.W. Keller, T.J. Stark, J. R. Barnes, R. Dijkman, J. Jores, C. Benarafa, D.E. Wentworth, V. Thiel, M. Beer, SARS-CoV-2 spike D614G change enhances replication and transmission, Nature 592 (2021) 122–127, https://doi.org/10.1038/S41586-021-03361-1.
[48] X. Tang, M. Yang, Z. Duan, Z. Liao, L. Liu, R. Cheng, M. Fang, G. Wang, H. Liu, J. Xu, P.M. Kamau, Z. Zhang, L. Yang, X. Zhao, X. Peng, R. Lai, Transferrin receptor is another receptor for SARS-CoV-2 entry, BioRxiv, 2020. http://biorxiv.org/content/early/2020/10/23/2020.10.23.350348.abstract.
[49] A. Maxmen, WHO report into COVID pandemic origins zeroes in on animal markets, not labs, Nature 592 (2021) 173–174, https://doi.org/10.1038/D41586-021-00865-8.
[50] J. Pekar, M. Worobey, N. Moshiri, K. Scheffler, J.O. Wertheim, Timing the SARS-CoV-2 index case in Hubei province, Science (80-.) 372 (2021) 412–417, https://doi.org/10.1126/SCIENCE.ABF8003.
[51] A. Maxmen, WHO report into COVID pandemic origins zeroes in on animal markets, not labs, Nature 2021 (2021), 5927853 (accessed December 7, 2021), https://www.nature.com/articles/d41586-021-00865-8.
[52] P. Zhou, X. Lou Yang, X.G. Wang, B. Hu, L. Zhang, W. Zhang, H.R. Si, Y. Zhu, B. Li, C.L. Huang, H.D. Chen, J. Chen, Y. Luo, H. Guo, R. Di Jiang, M.Q. Liu, Y. Chen, X.R. Shen, X. Wang, X.S. Zheng, K. Zhao, Q.J. Chen, F. Deng, L.L. Liu, B. Yan, F.X. Zhan, Y.Y. Wang, G.F. Xiao, Z.L. Shi, A pneumonia outbreak associated with a new coronavirus of probable bat origin, Nature 579 (2020) 270–273, https://doi.org/10.1038/s41586-020-2012-7.

[53] Y. Wan, J. Shang, R. Graham, R.S. Baric, F. Li, Receptor recognition by the novel coronavirus from Wuhan: an analysis based on decade-long structural studies of SARS coronavirus, J. Virol. 94 (2020) 127–147, https://doi.org/10.1128/jvi.00127-20.

[54] N. Nao, J. Yamagishi, H. Miyamoto, M. Igarashi, R. Manzoor, A. Ohnuma, Y. Tsuda, W. Furuyama, A. Shigeno, M. Kajihara, N. Kishida, R. Yoshida, A. Takadaa, Genetic predisposition to acquire a polybasic cleavage site for highly pathogenic avian influenza virus hemagglutinin, MBio 8 (2017), https://doi.org/10.1128/mBio.02298-16.

[55] R. Lu, X. Zhao, J. Li, P. Niu, B. Yang, H. Wu, W. Wang, H. Song, B. Huang, N. Zhu, Y. Bi, X. Ma, F. Zhan, L. Wang, T. Hu, H. Zhou, Z. Hu, W. Zhou, L. Zhao, J. Chen, Y. Meng, J. Wang, Y. Lin, J. Yuan, Z. Xie, J. Ma, W.J. Liu, D. Wang, W. Xu, E. C. Holmes, G.F. Gao, G. Wu, W. Chen, W. Shi, W. Tan, Genomic characterisation and epidemiology of 2019 novel coronavirus: implications for virus origins and receptor binding, Lancet 395 (2020) 565–574, https://doi.org/10.1016/S0140-6736(20)30251-8.

[56] Y. Tao, M. Shi, C. Chommanard, K. Queen, J. Zhang, W. Markotter, I.V. Kuzmin, E.C. Holmes, S. Tong, Surveillance of bat coronaviruses in Kenya identifies relatives of human coronaviruses NL63 and 229E and their recombination history, J. Virol. 91 (2017), https://doi.org/10.1128/jvi.01953-16.

[57] B. Hu, L.P. Zeng, X. Lou Yang, X.Y. Ge, W. Zhang, B. Li, J.Z. Xie, X.R. Shen, Y. Z. Zhang, N. Wang, D.S. Luo, X.S. Zheng, M.N. Wang, P. Daszak, L.F. Wang, J. Cui, Z.L. Shi, Discovery of a rich gene pool of bat SARS-related coronaviruses provides new insights into the origin of SARS coronavirus, PLoS Pathog. 13 (2017), https://doi.org/10.1371/journal.ppat.1006698.

[58] J. Lan, J. Ge, J. Yu, S. Shan, H. Zhou, S. Fan, Q. Zhang, X. Shi, Q. Wang, L. Zhang, X. Wang, Structure of the SARS-CoV-2 spike receptor-binding domain bound to the ACE2 receptor, Nature 581 (2020) 215–220, https://doi.org/10.1038/s41586-020-2180-5.

[59] K.G. Andersen, A. Rambaut, W.I. Lipkin, E.C. Holmes, R.F. Garry, The proximal origin of SARS-CoV-2, Nat. Med. 26 (2020) 450–452, https://doi.org/10.1038/s41591-020-0820-9.

[60] C. Wang, P.W. Horby, F.G. Hayden, G.F. Gao, A novel coronavirus outbreak of global health concern, Lancet 395 (2020) 470–473, https://doi.org/10.1016/S0140-6736(20)30185-9.

[61] A. Wu, Y. Peng, B. Huang, X. Ding, X. Wang, P. Niu, J. Meng, Z. Zhu, Z. Zhang, J. Wang, J. Sheng, L. Quan, Z. Xia, W. Tan, G. Cheng, T. Jiang, Genome composition and divergence of the novel coronavirus (2019-nCoV) originating in China, Cell Host Microbe 27 (2020) 325–328, https://doi.org/10.1016/j.chom.2020.02.001.

[62] M.R. Alam, M.R. Kabir, S. Reza, Comorbidities might be a risk factor for the incidence of COVID-19: evidence from a web-based survey, Prev. Med. Reports. 21 (2021), 101319, https://doi.org/10.1016/j.pmedr.2021.101319.

[63] N. Zhu, W. Wang, Z. Liu, C. Liang, W. Wang, F. Ye, B. Huang, L. Zhao, H. Wang, W. Zhou, Y. Deng, L. Mao, C. Su, G. Qiang, T. Jiang, J. Zhao, G. Wu, J. Song, W. Tan, Morphogenesis and cytopathic effect of SARS-CoV-2 infection in human airway epithelial cells, Nat. Commun. 111 (11) (2020) 1–8, https://doi.org/10.1038/s41467-020-17796-z, 2020.

[64] M. Hoffmann, H. Kleine-Weber, S. Schroeder, N. Krüger, T. Herrler, S. Erichsen, T. S. Schiergens, G. Herrler, N.H. Wu, A. Nitsche, M.A. Müller, C. Drosten, S. Pöhlmann, SARS-CoV-2 cell entry depends on ACE2 and TMPRSS2 and is blocked by a clinically proven protease inhibitor, Cell (2020), https://doi.org/10.1016/j.cell.2020.02.052.

[65] A.C. Walls, Y.J. Park, M.A. Tortorici, A. Wall, A.T. McGuire, D. Veesler, Structure, function, and antigenicity of the SARS-CoV-2 spike glycoprotein, Cell 181 (2020) 281–292, https://doi.org/10.1016/j.cell.2020.02.058, e6.

[66] Z. Xu, L. Shi, Y. Wang, J. Zhang, L. Huang, C. Zhang, S. Liu, P. Zhao, H. Liu, L. Zhu, Y. Tai, C. Bai, T. Gao, J. Song, P. Xia, J. Dong, J. Zhao, F.S. Wang, Pathological findings of COVID-19 associated with acute respiratory distress syndrome, Lancet Respir. Med. 8 (2020) 420–422, https://doi.org/10.1016/S2213-2600(20)30076-X.

[67] D. Wang, B. Hu, C. Hu, F. Zhu, X. Liu, J. Zhang, B. Wang, H. Xiang, Z. Cheng, Y. Xiong, Y. Zhao, Y. Li, X. Wang, Z. Peng, Clinical characteristics of 138 hospitalized patients with 2019 novel coronavirus-infected pneumonia in Wuhan, China, JAMA, J. Am. Med. Assoc. 323 (2020) 1061–1069, https://doi.org/10.1001/jama.2020.1585.

[68] M. Dong, J. Zhang, X. Ma, J. Tan, L. Chen, S. Liu, Y. Xin, L. Zhuang, ACE2, TMPRSS2 distribution and extrapulmonary organ injury in patients with COVID-19, Biomed. Pharmacother. 131 (2020), 110678, https://doi.org/10.1016/j.biopha.2020.110678.

[69] V.G. Puelles, M. Lütgehetmann, M.T. Lindenmeyer, J.P. Sperhake, M.N. Wong, L. Allweiss, S. Chilla, A. Heinemann, N. Wanner, S. Liu, F. Braun, S. Lu, S. Pfefferle, A.S. Schröder, C. Edler, O. Gross, M. Glatzel, D. Wichmann, T. Wiech, S. Kluge, K. Pueschel, M. Aepfelbacher, T.B. Huber, Multiorgan and renal tropism of SARS-CoV-2, N. Engl. J. Med. 383 (2020) 590–592, https://doi.org/10.1056/nejmc2011400.

[70] Y. Tang, J. Liu, D. Zhang, Z. Xu, J. Ji, C. Wen, Cytokine storm in COVID-19: the current evidence and treatment strategies, Front. Immunol. 11 (2020) 1708, https://doi.org/10.3389/fimmu.2020.01708.

[71] Z. Varga, A.J. Flammer, P. Steiger, M. Haberecker, R. Andermatt, A. S. Zinkernagel, M.R. Mehra, R.A. Schuepbach, F. Ruschitzka, H. Moch, Endothelial cell infection and endotheliitis in COVID-19, Lancet 395 (2020) 1417–1418, https://doi.org/10.1016/S0140-6736(20)30937-5.

[72] M. Liao, Y. Liu, J. Yuan, Y. Wen, G. Xu, J. Zhao, L. Cheng, J. Li, X. Wang, F. Wang, L. Liu, I. Amit, S. Zhang, Z. Zhang, Single-cell landscape of bronchoalveolar immune cells in patients with COVID-19, Nat. Med. 26 (2020) 842–844, https://doi.org/10.1038/s41591-020-0901-9.

[73] Y. Zuo, S. Yalavarthi, H. Shi, K. Gockman, M. Zuo, J.A. Madison, C. Blair, A. Weber, B.J. Barnes, M. Egeblad, R.J. Woods, Y. Kanthi, J.S. Knight, Neutrophil extracellular traps in COVID-19, JCI Insighs 5 (2020), https://doi.org/10.1172/jci.insight.138999.

[74] S. Bertram, R. Dijkman, M. Habjan, A. Heurich, S. Gierer, I. Glowacka, K. Welsch, M. Winkler, H. Schneider, H. Hofmann-Winkler, V. Thiel, S. Pöhlmann, TMPRSS2 activates the human coronavirus 229E for cathepsin-independent host cell entry and is expressed in viral target cells in the respiratory epithelium, J. Virol. 87 (2013) 6150–6160, https://doi.org/10.1128/JVI.03372-12.

[75] L. Du, R.Y. Kao, Y. Zhou, Y. He, G. Zhao, C. Wong, S. Jiang, K.-Y. Yuen, D.-Y. Jin, B.-J. Zheng, Cleavage of spike protein of SARS coronavirus by protease factor xa is associated with viral infectivity, Biochem. Biophys. Res. Commun. 359 (2007) 174–179, https://doi.org/10.1016/j.bbrc.2007.05.092.

[76] O. Krokhin, Y. Li, A. Andonov, H. Feldmann, R. Flick, S. Jones, U. Stroeher, N. Bastien, K.V.N. Dasuri, K. Cheng, J.N. Simonsen, H. Perreault, J. Wilkins, W. Ens, F. Plummer, K.G. Standing, Mass spectrometric characterization of proteins from the SARS virus: a preliminary report, Mol. Cell. Proteomics 2 (2003) 346–356, https://doi.org/10.1074/mcp.M300048-MCP200.

[77] B. Delmas, H. Laude, Assembly of coronavirus spike protein into trimers and its role in epitope expression, J. Virol. 64 (1990) 5367–5375, https://doi.org/10.1128/jvi.64.11.5367-5375.1990.

[78] Y. Watanabe, J.D. Allen, D. Wrapp, J.S. McLellan, M. Crispin, Site-specific glycan analysis of the SARS-CoV-2 spike, Science 369 (2020) 330–333, https://doi.org/10.1126/science.abb9983.

[79] H.C. Song, M.-Y. Seo, K. Stadler, B.J. Yoo, Q.-L. Choo, S.R. Coates, Y. Uematsu, T. Harada, C.E. Greer, J.M. Polo, P. Pileri, M. Eickmann, R. Rappuoli, S. Abrignani, M. Houghton, J.H. Han, Synthesis and characterization of a native, oligomeric form of recombinant severe acute respiratory syndrome coronavirus spike glycoprotein, J. Virol. 78 (2004) 10328–10335, https://doi.org/10.1128/JVI.78.19.10328-10335.2004.

[80] D. Wrapp, N. Wang, K.S. Corbett, J.A. Goldsmith, C.-L. Hsieh, O. Abiona, B. S. Graham, J.S. McLellan, Cryo-EM structure of the 2019-nCoV spike in the prefusion conformation, Science 367 (2020) 1260–1263, https://doi.org/10.1126/science.abb2507.

[81] Q. Wang, Y. Zhang, L. Wu, S. Niu, C. Song, Z. Zhang, G. Lu, C. Qiao, Y. Hu, K.-Y. Yuen, Q. Wang, H. Zhou, J. Yan, J. Qi, Structural and functional basis of SARS-CoV-2 entry by using human ACE2, Cell 181 (2020) 894–904, https://doi.org/10.1016/j.cell.2020.03.045, e9.

[82] J.K. Millet, G.R. Whittaker, Physiological and molecular triggers for SARS-CoV membrane fusion and entry into host cells, Virology 517 (2018) 3–8, https://doi.org/10.1016/j.virol.2017.12.015.

[83] Z.A. Memish, S. Perlman, M.D. Van Kerkhove, A. Zumla, Middle East respiratory syndrome, Lancet 395 (2020) 1063–1077, https://doi.org/10.1016/S0140-6736(19)33221-0.

[84] S. Liu, G. Xiao, Y. Chen, Y. He, J. Niu, C.R. Escalante, H. Xiong, J. Farmar, A. K. Debnath, P. Tien, S. Jiang, Interaction between heptad repeat 1 and 2 regions in spike protein of SARS-associated coronavirus: implications for virus fusogenic mechanism and identification of fusion inhibitors, Lancet (London, England) 363 (2004) 938–947, https://doi.org/10.1016/S0140-6736(04)15788-7.

[85] P. Chambers, C.R. Pringle, A.J. Easton, Heptad repeat sequences are located adjacent to hydrophobic regions in several types of virus fusion glycoproteins, J. Gen. Virol. 71 (Pt 12) (1990) 3075–3080, https://doi.org/10.1099/0022-1317-71-12-3075.

[86] S. Xia, L. Yan, W. Xu, A.S. Agrawal, A. Algaissi, C.-T.K. Tseng, Q. Wang, L. Du, W. Tan, I.A. Wilson, S. Jiang, B. Yang, L. Lu, A pan-coronavirus fusion inhibitor targeting the HR1 domain of human coronavirus spike, Sci. Adv. 5 (2019), eaav4580, https://doi.org/10.1126/sciadv.aav4580.

[87] A.L. Arndt, B.J. Larson, B.G. Hogue, A conserved domain in the coronavirus membrane protein tail is important for virus assembly, J. Virol. 84 (2010) 11418–11428, https://doi.org/10.1128/jvi.01131-10.

[88] X.Y. Ge, J.L. Li, X. Lou Yang, A.A. Chmura, G. Zhu, J.H. Epstein, J.K. Mazet, B. Hu, W. Zhang, C. Peng, Y.J. Zhang, C.M. Luo, B. Tan, N. Wang, Y. Zhu, G. Crameri, S.Y. Zhang, L.F. Wang, P. Daszak, Z.L. Shi, Isolation and characterization of a bat SARS-like coronavirus that uses the ACE2 receptor, Nature 503 (2013) 535–538, https://doi.org/10.1038/nature12711.

[89] W. Weissenhorn, A. Dessen, L.J. Calder, S.C. Harrison, J.J. Skehel, D.C. Wiley, Structural basis for membrane fusion by enveloped viruses, Mol. Membr. Biol. 16 (1999) 3–9, https://doi.org/10.1080/096876899294706.

[90] P.F.N. Souza, F.E.S. Lopes, J.L. Amaral, C.D.T. Freitas, J.T.A. Oliveira, International journal of biological macromolecules a molecular docking study revealed that synthetic peptides induced conformational changes in the structure of SARS-CoV-2 spike glycoprotein, disrupting the interaction with human ACE2 receptor, Int. J. Biol. Macromol. 164 (2020) 66–76, https://doi.org/10.1016/j.ijbiomac.2020.07.174.

[91] P.F.N. Souza, J.L. Amaral, L.P. Bezerra, F.E.S. Lopes, V.N. Freire, J.T.A. Oliveira, C.D.T. Freitas, ACE2-derived peptides interact with the RBD domain of SARS-CoV-2 spike glycoprotein, disrupting the interaction with the human ACE2 receptor, J. Biomol. Struct. Dyn. (2021) 1–14, https://doi.org/10.1080/07391102.2020.1871415.

[92] K. Wang, W. Chen, Z. Zhang, Y. Deng, J.Q. Lian, P. Du, D. Wei, Y. Zhang, X. X. Sun, L. Gong, X. Yang, L. He, L. Zhang, Z. Yang, J.J. Geng, R. Chen, H. Zhang, B. Wang, Y.M. Zhu, G. Nan, J.L. Jiang, L. Li, J. Wu, P. Lin, W. Huang, L. Xie, Z. H. Zheng, K. Zhang, J.L. Miao, H.Y. Cui, M. Huang, J. Zhang, L. Fu, X.M. Yang, Z. Zhao, S. Sun, H. Gu, Z. Wang, C.F. Wang, Y. Lu, Y.Y. Liu, Q.Y. Wang, H. Bian,

P. Zhu, Z.N. Chen, CD147-spike protein is a novel route for SARS-CoV-2 infection to host cells, Signal Transduct. Target. Ther. 5 (2020) 1–10, https://doi.org/10.1038/s41392-020-00426-x.

[93] F. Li, Receptor recognition mechanisms of coronaviruses: a decade of structural studies, J. Virol. 89 (2015) 1954–1964, https://doi.org/10.1128/jvi.02615-14.

[94] N. Wang, X. Shi, L. Jiang, S. Zhang, D. Wang, P. Tong, D. Guo, L. Fu, Y. Cui, X. Liu, K.C. Arledge, Y.H. Chen, L. Zhang, X. Wang, Structure of MERS-CoV spike receptor-binding domain complexed with human receptor DPP4, Cell Res. 23 (2013) 986–993, https://doi.org/10.1038/cr.2013.92.

[95] L. Du, G. Zhao, Z. Kou, C. Ma, S. Sun, V.K.M. Poon, L. Lu, L. Wang, A.K. Debnath, B.-J. Zheng, Y. Zhou, S. Jiang, Identification of a receptor-binding domain in the S protein of the novel human coronavirus Middle East respiratory syndrome coronavirus as an essential target for vaccine development, J. Virol. 87 (2013) 9939–9942, https://doi.org/10.1128/jvi.01048-13.

[96] F. Li, Structure, function, and evolution of coronavirus spike proteins, Annu. Rev. Virol. 3 (2016) 237–261, https://doi.org/10.1146/annurev-virology-110615-042301.

[97] R.N. Kirchdoerfer, C.A. Cottrell, N. Wang, J. Pallesen, H.M. Yassine, H.L. Turner, K.S. Corbett, B.S. Graham, J.S. McLellan, A.B. Ward, Pre-fusion structure of a human coronavirus spike protein, Nature 531 (2016) 118–121, https://doi.org/10.1038/nature17200.

[98] T. Heald-Sargent, T. Gallagher, Ready, set, fuse! The coronavirus spike protein and acquisition of fusion competence, Viruses 4 (2012) 557–580, https://doi.org/10.3390/v4040557.

[99] S. Belouzard, J.K. Millet, B.N. Licitra, G.R. Whittaker, Mechanisms of coronavirus cell entry mediated by the viral spike protein, Viruses 4 (2012) 1011–1033, https://doi.org/10.3390/v4061011.

[100] J.S.M. Peiris, Coronaviruses, in: Med. Microbiol, Eighteenth Ed, Elsevier Inc, 2012, pp. 587–593, https://doi.org/10.1016/B978-0-7020-4089-4.00072-X.

[101] C. Wei, L. Wan, Q. Yan, X. Wang, J. Zhang, X. Yang, Y. Zhang, C. Fan, D. Li, Y. Deng, J. Sun, J. Gong, X. Yang, Y. Wang, X. Wang, J. Li, H. Yang, H. Li, Z. Zhang, R. Wang, P. Du, Y. Zong, F. Yin, W. Zhang, N. Wang, Y. Peng, H. Lin, J. Feng, C. Qin, W. Chen, Q. Gao, R. Zhang, Y. Cao, H. Zhong, HDL-scavenger receptor B type 1 facilitates SARS-CoV-2 entry, Nat. Metab. 2 (2020) 1391–1400, https://doi.org/10.1038/s42255-020-00324-0.

[102] L. Cantuti-Castelvetri, R. Ojha, L.D. Pedro, M. Djannatian, J. Franz, S. Kuivanen, F. van der Meer, K. Kallio, T. Kaya, M. Anastasina, T. Smura, L. Levanov, L. Szirovicza, A. Tobi, H. Kallio-Kokko, P. Österlund, M. Joensuu, F.A. Meunier, S. J. Butcher, M.S. Winkler, B. Mollenhauer, A. Helenius, O. Gokce, T. Teesalu, J. Hepojoki, O. Vapalahti, C. Stadelmann, G. Balistreri, M. Simons, Neuropilin-1 facilitates SARS-CoV-2 cell entry and infectivity, Science (80-.) 70 (2020) 856–860, https://doi.org/10.1126/science.abd2985.

[103] J.R. Fauver, M.E. Petrone, E.B. Hodcroft, K. Shioda, H.Y. Ehrlich, A.G. Watts, C.B. F. Vogels, A.F. Brito, T. Alpert, A. Muyombwe, J. Razeq, R. Downing, N. R. Cheemarla, A.L. Wyllie, C.C. Kalinich, I.M. Ott, J. Quick, N.J. Loman, K. M. Neugebauer, A.L. Greninger, K.R. Jerome, P. Roychoudhury, H. Xie, L. Shrestha, M.L. Huang, V.E. Pitzer, A. Iwasaki, S.B. Omer, K. Khan, I.I. Bogoch, R.A. Martinello, E.F. Foxman, M.L. Landry, R.A. Neher, A.I. Ko, N.D. Grubaugh, coast-to-coast spread of SARS-CoV-2 during the early epidemic in the United States, Cell 181 (2020) 990–996, https://doi.org/10.1016/J.CELL.2020.04.021/ATTACHMENT/5CB77A1F-2086-46B8-8ED7-62CEFF34DAE8/MMC3.XLSX, e5.

[104] M. Sevajol, L. Subissi, E. Decroly, B. Canard, I. Imbert, Insights into RNA synthesis, capping, and proofreading mechanisms of SARS-coronavirus, Virus Res. 194 (2014) 90–99, https://doi.org/10.1016/J.VIRUSRES.2014.10.008.

[105] E.C. Smith, H. Blanc, M. Vignuzzi, M.R. Denison, Coronaviruses lacking exoribonuclease activity are susceptible to lethal mutagenesis: evidence for proofreading and potential therapeutics, PLoS Pathog. 9 (2013), https://doi.org/10.1371/JOURNAL.PPAT.1003565.

[106] M.F. Boni, J.R. Gog, V. Andreasen, M.W. Feldman, Epidemic dynamics and antigenic evolution in a single season of influenza a, Proc. R. Soc. B Biol. Sci. 273 (2006) 1307, https://doi.org/10.1098/RSPB.2006.3466.

[107] S.T. Sehra, J.D. Salciccioli, D.J. Wiebe, S. Fundin, J.F. Baker, Maximum daily temperature, precipitation, ultraviolet light, and rates of transmission of severe acute respiratory syndrome coronavirus 2 in the United States, Clin. Infect. Dis. 71 (2020) 2482–2487, https://doi.org/10.1093/CID/CIAA681.

[108] N. Faulkner, K.W. Ng, M. Wu, R. Harvey, M. Margaritis, S. Paraskevopoulou, C. F. Houlihan, S. Hussain, M. Greco, W. Bolland, S. Warchal, J. Heaney, H. Rickman, M.J. Spyer, D. Frampton, M. Byott, T. de Oliveira, A. Sigal, S. Kjaer, C. Swanton, S. Gandhi, R. Beale, S.J. Gamblin, J. McCauley, R. Daniels, M. Howell, D.L.V. Bauer, E. Nastouli, S. Investigators, G. Kassiotis, C.C.-19 Consortium, Reduced Antibody Cross-reactivity Following Infection With B.1.1.7 Than With Parental SARS-CoV-2 Strains, BioRxiv, 2021, https://doi.org/10.1101/2021.03.01.433314, 2021.03.01.433314.

[109] A.P. West, J.O. Wertheim, J.C. Wang, T.I. Vasylyeva, J.L. Havens, M. A. Chowdhury, E. Gonzalez, C.E. Fang, S.S.Di Lonardo, S. Hughes, J.L. Rakeman, H.H. Lee, C.O. Barnes, P.N.P. Gnanapragasam, Z. Yang, C. Gaebler, M. Caskey, M. C. Nussenzweig, J.R. Keeffe, P.J. Bjorkman, Detection and Characterization of the SARS-CoV-2 Lineage B.1.526 in New York, BioRxiv, 2021, https://doi.org/10.1101/2021.02.14.431043, 2021.02.14.431043.

[110] D.A. Collier, A.De Marco, I.A.T.M. Ferreira, B. Meng, R.P. Datir, A.C. Walls, S. A. Kemp, J. Bassi, D. Pinto, C. Silacci-Fregni, S. Bianchi, M.A. Tortorici, J. Bowen, K. Culap, S. Jaconi, E. Cameroni, G. Snell, M.S. Pizzuto, A.F. Pellanda, C. Garzoni, A. Riva, S. Baker, G. Dougan, C. Hess, N. Kingston, P.J. Lehner, P.A. Lyons, N. J. Matheson, W.H. Owehand, C. Saunders, C. Summers, J.E.D. Thaventhiran, M. Toshner, M.P. Weekes, A. Bucke, J. Calder, L. Canna, J. Domingo, A. Elmer, S. Fuller, J. Harris, S. Hewitt, J. Kennet, S. Jose, J. Kourampa, A. Meadows, C. O'Brien, J. Price, C. Publico, R. Rastall, C. Ribeiro, J. Rowlands, V. Ruffolo, H. Tordesillas, B. Bullman, B.J. Dunmore, S. Fawke, S. Gräf, J. Hodgson, C. Huang, K. Hunter, E. Jones, E. Legchenko, C. Matara, J. Martin, F. Mescia, C. O'Donnell, L. Pointon, N. Pond, J. Shih, R. Sutcliffe, T. Tilly, C. Treacy, Z. Tong, J. Wood, M. Wylot, L. Bergamaschi, A. Betancourt, G. Bower, C. Cossetti, A.De Sa, M. Epping, R. Grenfell, A. Hinch, O. Huhn, S. Jackson, I. Jarvis, D. Lewis, J. Marsden, F. Nice, G. Okecha, O. Omarjee, M. Perera, N. Richoz, V. Romashova, N.S. Yarkoni, R. Sharma, L. Stefanucci, J. Stephens, M. Strezlecki, L. Turner, E.M. D.D.De Bie, K. Bunclark, M. Josipovic, M. Mackay, S. Rossi, M. Selvan, S. Spencer, C. Yong, A. Ansaripour, A. Michael, L. Mwaura, C. Patterson, G. Polwarth, P. Polgarova, G. di Stefano, C. Fahey, R. Michel, S.H. Bong, J.D. Coudert, E. Holmes, J. Allison, H. Butcher, D. Caputo, D. Clapham-Riley, E. Dewhurst, A. Furlong, B. Graves, J. Gray, T. Ivers, M. Kasanicki, E.Le Gresley, R. Linger, S. Meloy, F. Muldoon, N. Ovington, S. Papadia, I. Phelan, H. Stark, K.E. Stirrups, P. Townsend, N. Walker, J. Webster, A. Elmer, N. Kingston, B. Graves, L. E. McCoy, K.G.C. Smith, J.R. Bradley, N. Temperton, L. Ceron-Gutierrez, G. Barcenas-Morales, S.C. Robson, N.J. Loman, T.R. Connor, T. Golubchik, R.T. Martinez Nunez, C. Ludden, S. Corden, I. Johnston, D. Bonsall, C.P. Smith, A. R. Awan, G. Bucca, M.E. Torok, K. Saeed, J.A. Prieto, D.K. Jackson, W. L. Hamilton, L.B. Snell, C. Moore, E.M. Harrison, S. Goncalves, D.J. Fairley, M. W. Loose, J. Watkins, R. Livett, S. Moses, R. Amato, S. Nicholls, M. Bull, D. L. Smith, J. Barrett, D.M. Aanensen, M.D. Curran, S. Parmar, D. Aggarwal, J. G. Shepherd, M.D. Parker, S. Glaysher, M. Bashton, A.P. Underwood, N. Pacchiarini, K.F. Loveson, A.M. Carabelli, K.E. Templeton, C.F. Langford, J. Sillitoe, T.I. de Silva, D. Wang, D. Kwiatkowski, A. Rambaut, J. O'Grady, S. Cottrell, M.T.G. Holden, E.C. Thomson, H. Osman, M. Andersson, A. J. Chauhan, M.O. Hassan-Ibrahim, M. Lawniczak, A. Alderton, M. Chand, C. Constantinidou, M. Unnikrishnan, A.C. Darby, J.A. Hiscox, S. Paterson, I. Martincorena, D.L. Robertson, E.M. Volz, A.J. Page, O.G. Pybus, A.R. Bassett, C. V. Ariani, M.H.Spencer Chapman, K.K. Li, R.N. Shah, N.G. Jesudason, Y. Taha, M. P. McHugh, R. Dewar, A.S. Jahun, C. McMurray, S. Pandey, J.P. McKenna, A. Nelson, G.R. Young, C.M. McCann, S. Elliott, H. Lowe, B. Temperton, S. Roy, A. Price, S. Rey, M. Wyles, S. Rooke, S. Shaaban, M. de Cesare, L. Letchford, S. Silveira, E. Pelosi, E. Wilson-Davies, M. Hosmillo, Á. O'Toole, A.R. Hesketh, R. Stark, L. du Plessis, C. Ruis, H. Adams, Y. Bourgeois, S.L. Michell, D. Gramatopoulos, J. Edgeworth, J. Breuer, J.A. Todd, C. Fraser, D. Buck, M. John, G.L. Kay, S. Palmer, S.J. Peacock, D. Heyburn, D. Weldon, E. Robinson, A. McNally, P. Muir, I.B. Vipond, J. Boyes, V. Sivaprakasam, T. Salluja, S. Dervisevic, E.J. Meader, N.R. Park, K. Oliver, A.R. Jeffries, S. Ott, A. da Silva Filipe, D.A. Simpson, C. Williams, J.A.H. Masoli, B.A. Knight, C.R. Jones, C. Koshy, A. Ash, A. Casey, A. Bosworth, L. Ratcliffe, L. Xu-McCrae, H.M. Pymont, S. Hutchings, L. Berry, K. Jones, F. Halstead, T. Davis, C. Holmes, M. Iturriza-Gomara, A.O. Lucaci, P.A. Randell, A. Cox, P. Madona, K.A. Harris, J.R. Brown, T. W. Mahungu, D. Irish-Tavares, T. Haque, J. Hart, E. Witele, M.L. Fenton, S. Liggett, C. Graham, E. Swindells, J. Collins, G. Eltringham, S. Campbell, P. C. McClure, G. Clark, T.J. Sloan, C. Jones, J. Lynch, B. Warne, S. Leonard, J. Durham, T. Williams, S.T. Haldenby, N. Storey, N.F. Alikhan, N. Holmes, C. Moore, M. Carlile, M. Perry, N. Craine, R.A. Lyons, A.H. Beckett, S. Goudarzi, C. Fearn, K. Cook, H. Dent, H. Paul, R. Davies, B. Blane, S.T. Girgis, M.A. Beale, K. L. Bellis, M.J. Dorman, E. Drury, L. Kane, S. Kay, S. McGuigan, R. Nelson, L. Prestwood, S. Rajatileka, R. Batra, R.J. Williams, M. Kristiansen, A. Green, A. Justice, A.I.K. Mahanama, B. Samaraweera, N.F. Hadjirin, J. Quick, R. Poplawski, L.M. Kermack, N. Reynolds, G. Hall, Y. Chaudhry, M.L. Pinckert, I. Georgana, R.J. Moll, A. Thornton, R. Myers, J. Stockton, C.A. Williams, W. C. Yew, A.J. Trotter, A. Trebes, G. MacIntyre-Cockett, A. Birchley, A. Adams, A. Plimmer, B. Gatica-Wilcox, C. McKerr, E. Hilvers, H. Jones, H. Asad, J. Coombes, J.M. Evans, L. Fina, L. Gilbert, L. Graham, M. Cronin, S. Kumziene-Summerhayes, S. Taylor, S. Jones, D.C. Groves, P. Zhang, M. Gallis, S.F. Louka, I. Starinskij, C. Jackson, M. Gourtovaia, G. Tonkin-Hill, K. Lewis, J.M. Tovar-Corona, K. James, L. Baxter, M.T. Alam, R.J. Orton, J. Hughes, S. Vattipally, M. Ragonnet-Cronin, F.F. Nascimento, D. Jorgensen, O. Boyd, L. Geidelberg, A. E. Zarebski, J. Raghwani, M.U.G. Kraemer, J. Southgate, B.B. Lindsey, T. M. Freeman, J.P. Keatley, J.B. Singer, L. de Oliveira Martins, C.A. Yeats, K. Abudahab, B.E.W. Taylor, M. Menegazzo, J. Danesh, W. Hogsden, S. Eldirdiri, A. Kenyon, J. Mason, T.I. Robinson, A. Holmes, J. Price, J.A. Hartley, T. Curran, A.E. Mather, G. Shankar, R. Jones, R. Howe, S. Morgan, E. Wastenge, M. R. Chapman, S. Mookerjee, R. Stanley, W. Smith, T. Peto, D. Eyre, D. Crook, G. Vernet, C. Kitchen, H. Gulliver, I. Merrick, M. Guest, R. Munn, D.T. Bradley, T. Wyatt, C. Beaver, L. Foulser, S. Palmer, C.M. Churcher, E. Brooks, K.S. Smith, K. Galai, G.M. McManus, F. Bolt, F. Coll, L. Meadows, S.W. Attwood, A. Davies, E. De Lacy, F. Downing, S. Edwards, G.P. Scarlett, S. Jeremiah, N. Smith, D. Leek, S. Sridhar, S. Forrest, C. Cormie, H.K. Gill, J. Dias, E.E. Higginson, M. Maes, J. Young, M. Wantoch, D. Jamrozy, S. Lo, M. Patel, V. Hill, C.M. Bewshea, S. Ellard, C. Auckland, I. Harrison, C. Bishop, V. Chalker, A. Richter, A. Beggs, A. Best, B. Percival, J. Mirza, O. Megram, M. Mayhew, L. Crawford, F. Ashcroft, E. Moles-Garcia, N. Cumley, R. Hopes, P. Asamaphan, M.O. Niebel, R.N. Gunson, A. Bradley, A. Maclean, G. Mollett, R. Blacow, P. Bird, T. Helmer, K. Fallon, J. Tang, A.D. Hale, L.R. Macfarlane-Smith, K.L. Harper, H. Carden, N.W. Machin, K.A. Jackson, S.S.Y. Ahmad, R.P. George, L. Turtle, E. O'Toole, J. Watts, C. Breen, A. Cowell, A. Alcolea-Medina, T. Charalampous, A. Patel, L.J. Levett, J. Heaney, A. Rowan, G.P. Taylor, D. Shah, L. Atkinson, J.C.D. Lee, A.P. Westhorpe, R. Jannoo, H.L. Lowe, A. Karamani, L. Ensell, W. Chatterton, M. Pusok, A. Dadrah, A. Symmonds, G. Sluga, Z. Molnar, P. Baker, S. Bonner, S. Essex, E. Barton, D. Padgett, G. Scott, J. Greenaway, B.A.I. Payne, S. Burton-Fanning, S. Waugh, V. Raviprakash, N. Sheriff, V. Blakey, L.A. Williams, J. Moore, S. Stonehouse, L. Smith, R.K. Davidson, L. Bedford, L. Coupland, V. Wright, J.G. Chappell,

T. Tsoleridis, J. Ball, M. Khakh, V.M. Fleming, M.M. Lister, H.C. Howson-Wells, L. Berry, T. Boswell, A. Joseph, I. Willingham, N. Duckworth, S. Walsh, E. Wise, N. Moore, M. Mori, N. Cortes, S. Kidd, R. Williams, L. Gifford, K. Bicknell, S. Wyllie, A. Lloyd, R. Impey, C.S. Malone, B.J. Cogger, N. Levene, L. Monaghan, A.J. Keeley, D.G. Partridge, M. Raza, C. Evans, K. Johnson, E. Betteridge, B. W. Farr, S. Goodwin, M.A. Quail, C. Scott, L. Shirley, S.A.J. Thurston, D. Rajan, I. F. Bronner, L. Aigrain, N.M. Redshaw, S.V. Lensing, S. McCarthy, A. Makunin, C. E. Balcazar, M.D. Gallagher, K.A. Williamson, T.D. Stanton, M.L. Michelsen, J. Warwick-Dugdale, R. Manley, A. Farbos, J.W. Harrison, C.M. Sambles, D. J. Studholme, A. Lackenby, T. Mbisa, S. Platt, S. Miah, D. Bibby, C. Manso, J. Hubb, G. Dabrera, M. Ramsay, D. Bradshaw, U. Schaefer, N. Groves, E. Gallagher, D. Lee, D. Williams, N. Ellaby, H. Hartman, N. Manesis, V. Patel, J. Ledesma, K.A. Twohig, E. Allara, C. Pearson, J.K.J. Cheng, H.E. Bridgewater, L. R. Frost, G. Taylor-Joyce, P.E. Brown, L. Tong, A. Broos, D. Mair, J. Nichols, S. N. Carmichael, K.L. Smollett, K. Nomikou, E. Aranday-Cortes, N. Johnson, S. Nickbakhsh, E.E. Vamos, M. Hughes, L. Rainbow, R. Eccles, C. Nelson, M. Whitehead, R. Gregory, M. Gemmell, C. Wierzbicki, H.J. Webster, C.L. Fisher, A.W. Signell, G. Betancor, H.D. Wilson, G. Nebbia, F. Flaviani, A.C. Cerda, T. V. Merrill, R.E. Wilson, M. Cotic, N. Bayzid, T. Thompson, E. Acheson, S. Rushton, S. O'Brien, D.J. Baker, S. Rudder, A. Aydin, F. Sang, J. Debebe, S. Francois, T. I. Vasylyeva, M.E. Zamudio, B. Gutierrez, A. Marchbank, J. Maksimovic, K. Spellman, K. McCluggage, M. Morgan, R. Beer, S. Afifi, T. Workman, W. Fuller, C. Bresner, A. Angyal, L.R. Green, P.J. Parsons, R.M. Tucker, R. Brown, M. Whiteley, J. Bonfield, C. Puethe, A. Whitwham, J. Liddle, W. Rowe, I. Siveroni, T. Le-Viet, A. Gaskin, R. Johnson, I. Abnizova, L. Aigrain, A. Alderton, M. Ali, L. Allen, R. Amato, R. Anderson, C. Ariani, S. Austin-Guest, S. Bala, J. Barrett, A. Bassett, K. Battleday, J. Beal, M. Beale, C. Beaver, S. Bellany, T. Bellerby, K. Bellis, D. Berger, M. Berriman, E. Betteridge, P. Bevan, S. Binley, J. Bishop, K. Blackburn, J. Bonfield, N. Boughton, S. Bowker, T. Brendler-Spaeth, I. Bronner, T. Brooklyn, S.K. Buddenborg, R. Bush, C. Caetano, A. Cagan, N. Carter, J. Cartwright, T.C. Monteiro, L. Chapman, T.J. Chillingworth, P. Clapham, R. Clark, A. Clarke, C. Clarke, D. Cole, E. Cook, M. Coppola, L. Cornell, C. Cornwell, C. Corton, A. Crackett, A. Cranage, H. Craven, S. Craw, M. Crawford, T. Cutts, M. Dabrowska, M. Davies, R. Davies, J. Dawson, C. Day, A. Densem, T. Dibling, C. Dockree, D. Dodd, S. Dogga, M. Dorman, G. Dougan, M. Dougherty, A. Dove, L. Drummond, E. Drury, M. Dudek, J. Durham, L. Durrant, E. Easthope, S. Eckert, P. Ellis, B. Farr, M. Fenton, M. Ferrero, N. Flack, H. Fordham, G. Forsythe, L. Foulser, M. Francis, A. Fraser, A. Freeman, A. Galvin, M. Garcia-Casado, A. Gedny, S. Girgis, J. Glover, S. Goncalves, S. Goodwin, O. Gould, M. Gourtovaia, A. Gray, E. Gray, C. Griffiths, Y. Gu, F. Guerin, W. Hamilton, H. Hanks, E. Harrison, A. Harrott, E. Harry, J. Harvison, P. Heath, A. Hernandez-Koutoucheva, R. Hobbs, D. Holland, S. Holmes, G. Hornett, N. Hough, L. Huckle, L. Hughes-Hallet, A. Hunter, S. Inglis, S. Iqbal, A. Jackson, D. Jackson, K. James, D. Jamrozy, C.J. Verdejo, I. Johnston, M. Jones, K. Kallepally, L. Kane, K. Kay, S. Kay, J. Keatley, A. Keith, A. King, L. Kitchin, M. Kleanthous, M. Klimekova, P. Korlevic, K. Krasheninnkova, D. Kwiatkowski, G. Lane, C. Langford, A. Laverack, K. Law, M. Lawniczak, S. Lensing, S. Leonard, L. Letchford, K. Lewis, A. Lewis-Wade, J. Liddle, Q. Lin, S. Lindsay, S. Linsdell, R. Livett, S. Lo, R. Long, J. Lovell, J. Lovell, C. Ludden, J. Mack, M. Maddison, A. Makunin, I. Mamun, J. Mansfield, N. Marriott, M. Martin, I. Martincorena, M. Mayho, S. McCarthy, J. McClintock, S. McGuigan, S. McHugh, L. McMinn, C. Meadows, E. Mobley, R. Moll, M. Morra, L. Morrow, K. Murie, S. Nash, C. Nathwani, P. Naydenova, A. Neaverson, R. Nelson, E. Nerou, J. Nicholson, T. Nimz, G.G. Noell, S. O'Meara, V. Ohan, K. Oliver, C. Olney, D. Ormond, A. Oszlanczi, S. Palmer, Y.F. Pang, B. Pardubska, N. Park, A. Parmar, G. Patel, M. Patel, M. Payne, S. Peacock, A. Petersen, D. Plowman, T. Preston, L. Prestwood, C. Puethe, M. Quail, D. Rajan, S. Rajatileka, R. Rance, S. Rawlings, N. Redshaw, J. Reynolds, M. Reynolds, S. Rice, M. Richardson, C. Roberts, K. Robinson, M. Robinson, D. Robinson, H. Rogers, E.M. Rojo, D. Roopra, M. Rose, L. Rudd, R. Sadri, N. Salmon, D. Saul, F. Schwach, C. Scott, P. Seekings, L. Shirley, J. Sillitoe, A. Simms, M. Sinnott, S. Sivadasan, B. Siwek, D. Sizer, K. Skeldon, J. Skelton, J. Slater-Tunstill, L. Sloper, N. Smerdon, C. Smith, C. Smith, J. Smith, K. Smith, M. Smith, S. Smith, T. Smith, L. Sneade, C.D. Soria, C. Sousa, E. Souster, A. Sparkes, M. Spencer-Chapman, J. Squares, R. Stanley, C. Steed, T. Stickland, I. Still, M. Stratton, M. Strickland, A. Swann, A. Swiatkowska, N. Sycamore, E. Swift, E. Symons, S. Szluha, E. Taluy, N. Tao, K. Taylor, S. Taylor, S. Thompson, M. Thompson, M. Thomson, N. Thomson, S. Thurston, G. Tonkin-Hill, D. Toombs, B. Topping, J. Tovar-Corona, D. Ungureanu, J. Uphill, J. Urbanova, P.J. Van, V. Vancollie, P. Voak, D. Walker, M. Walker, M. Waller, G. Ward, C. Weatherhogg, N. Webb, D. Weldon, A. Wells, E. Wells, L. Westwood, T. Whipp, T. Whiteley, G. Whitton, A. Whitwham, S. Widaa, M. Williams, M. Wilson, S. Wright, W. Harvey, H. W. Virgin, A. Lanzavecchia, L. Piccoli, R. Doffinger, M. Wills, D. Veesler, D. Corti, R.K. Gupta, Sensitivity of SARS-CoV-2 B.1.1.7 to mRNA vaccine-elicited antibodies, Nature 5937857 (593) (2021) 136–141, https://doi.org/10.1038/s41586-021-03412-7 (2021.

[111] Z. Wang, F. Schmidt, Y. Weisblum, F. Muecksch, C.O. Barnes, S. Finkin, D. Schaefer-Babajew, M. Cipolla, C. Gaebler, J.A. Lieberman, T.Y. Oliveira, Z. Yang, M.E. Abernathy, K.E. Huey-Tubman, A. Hurley, M. Turroja, K.A. West, K. Gordon, K.G. Millard, V. Ramos, J.Da Silva, J. Xu, R.A. Colbert, R. Patel, J. Dizon, C. Unson-O'Brien, I. Shimeliovich, A. Gazumyan, M. Caskey, P. J. Bjorkman, R. Casellas, T. Hatziioannou, P.D. Bieniasz, M.C. Nussenzweig, mRNA vaccine-elicited antibodies to SARS-CoV-2 and circulating variants, Nature 592 (2021) 616–622, https://doi.org/10.1038/S41586-021-03324-6.

[112] X. Xie, J. Zou, C.R. Fontes-Garfias, H. Xia, K.A. Swanson, M. Cutler, D. Cooper, V. D. Menachery, S. Weaver, P.R. Dormitzer, P.-Y. Shi, Neutralization of N501Y Mutant SARS-CoV-2 by BNT162b2 Vaccine-elicited Sera, BioRxiv, 2021, https://doi.org/10.1101/2021.01.07.425740.

[113] X. Xie, Y. Liu, J. Liu, X. Zhang, J. Zou, C.R. Fontes-Garfias, H. Xia, K.A. Swanson, M. Cutler, D. Cooper, V.D. Menachery, S.C. Weaver, P.R. Dormitzer, P.Y. Shi, Neutralization of SARS-CoV-2 spike 69/70 deletion, E484K and N501Y variants by BNT162b2 vaccine-elicited sera, Nat. Med. 274 (27) (2021) 620–621, https://doi.org/10.1038/s41591-021-01270-4, 2021.

[114] K.R.W. Emary, T. Golubchik, P.K. Aley, C.V. Ariani, B. Angus, S. Bibi, B. Blane, D. Bonsall, P. Cicconi, S. Charlton, E.A. Clutterbuck, A.M. Collins, T. Cox, T. C. Darton, C. Dold, A.D. Douglas, C.J.A. Duncan, K.J. Ewer, A.L. Flaxman, S. N. Faust, D.M. Ferreira, S. Feng, A. Finn, P.M. Folegatti, M. Fuskova, E. Galiza, A. L. Goodman, C.M. Green, C.A. Green, M. Greenland, B. Hallis, P.T. Heath, J. Hay, H.C. Hill, D. Jenkin, S. Kerridge, R. Lazarus, V. Libri, P.J. Lillie, C. Ludden, N. G. Marchevsky, A.M. Minassian, A.C. McGregor, Y.F. Mujadidi, D.J. Phillips, E. Plested, K.M. Pollock, H. Robinson, A. Smith, R. Song, M.D. Snape, R. K. Sutherland, E.C. Thomson, M. Toshner, D.P.J. Turner, J. Vekemans, T. L. Villafana, C.J. Williams, A.V.S. Hill, T. Lambe, S.C. Gilbert, M. Voysey, M. N. Ramasamy, A.J. Pollard, Efficacy of ChAdOx1 nCoV-19 (AZD1222) vaccine against SARS-CoV-2 variant of concern 202012/01 (B.1.1.7): an exploratory analysis of a randomised controlled trial, Lancet 397 (2021) 1351–1362, https://doi.org/10.1016/S0140-6736(21)00628-0/ATTACHMENT/5AC30D10-B090-4650-A3B7-014B635234DA/MMC1.PDF.

[115] S.A. Madhi, V. Baillie, C.L. Cutland, M. Voysey, A.L. Koen, L. Fairlie, S. D. Padayachee, K. Dheda, S.L. Barnabas, Q.E. Bhorat, C. Briner, G. Kwatra, K. Ahmed, P. Aley, S. Bhikha, J.N. Bhiman, A.E. Bhorat, J. du Plessis, A. Esmail, M. Groenewald, E. Horne, S.-H. Hwa, A. Jose, T. Lambe, M. Laubscher, M. Malahleha, M. Masenya, M. Masilela, S. McKenzie, K. Molapo, A. Moultrie, S. Oelofse, F. Patel, S. Pillay, S. Rhead, H. Rodel, L. Rossouw, C. Taoushanis, H. Tegally, A. Thombrayil, S. van Eck, C.K. Wibmer, N.M. Durham, E.J. Kelly, T. L. Villafana, S. Gilbert, A.J. Pollard, T. de Oliveira, P.L. Moore, A. Sigal, A. Izu, Efficacy of the ChAdOx1 nCoV-19 Covid-19 vaccine against the B.1.351 variant, N. Engl. J. Med. 384 (2021) 1885–1898, https://doi.org/10.1056/NEJMOA2102214/SUPPL_FILE/NEJMOA2102214_DATA-SHARING.PDF.

[116] W.F. Garcia-Beltran, E.C. Lam, K. St, A.D. Denis, Z.H. Nitido, B.M. Garcia, J. Hauser, M.N. Feldman, D.J. Pavlovic, M.C. Gregory, A. Poznansky, A.G. Sigal, A.J. Schmidt, V. Iafrate, A.B.Balazs Naranbhai, Multiple SARS-CoV-2 variants escape neutralization by vaccine-induced humoral immunity, Cell 184 (2021) 2372–2383, https://doi.org/10.1016/J.CELL.2021.03.013, e9.

[117] E. Mahase, Covid-19: novavax vaccine efficacy is 86% against UK variant and 60% against south african variant, BMJ 372 (2021), https://doi.org/10.1136/BMJ.N296.

[118] E. Mahase, Covid-19: where are we on vaccines and variants? BMJ 372 (2021), n597 https://doi.org/10.1136/BMJ.N597.

[119] R.K. Gupta, Will SARS-CoV-2 variants of concern affect the promise of vaccines? Nat. Rev. Immunol. 216 (21) (2021) 340–341, https://doi.org/10.1038/s41577-021-00556-5, 2021.

[120] K. B, F. WM, G. EE, H. KM, P. MD, P. DG, E. CM, F. TM, P. LG, W. SP, L. CC, S. EO, M. DC, Tracking changes in SARS-CoV-2 spike: evidence that D614G increases infectivity of the COVID-19 virus, Cell 182 (2020) 812–827, https://doi.org/10.1016/J.CELL.2020.06.043, e19.

[121] C.B. Jackson, L. Zhang, M. Farzan, H. Choe, Functional importance of the D614G mutation in the SARS-CoV-2 spike protein, Biochem. Biophys. Res. Commun. 538 (2021) 108, https://doi.org/10.1016/J.BBRC.2020.11.026.

[122] B. Korber, W.M. Fischer, S. Gnanakaran, H. Yoon, J. Theiler, W. Abfalterer, N. Hengartner, E.E. Giorgi, T. Bhattacharya, B. Foley, K.M. Hastie, M.D. Parker, D. G. Partridge, C.M. Evans, T.M. Freeman, T.I. de Silva, A. Angyal, R.L. Brown, L. Carrilero, L.R. Green, D.C. Groves, K.J. Johnson, A.J. Keeley, B.B. Lindsey, P. J. Parsons, M. Raza, S. Rowland-Jones, N. Smith, R.M. Tucker, D. Wang, M. D. Wyles, C. McDanal, L.G. Perez, H. Tang, A. Moon-Walker, S.P. Whelan, C. C. LaBranche, E.O. Saphire, D.C. Montefiori, Tracking changes in SARS-CoV-2 spike: evidence that D614G increases infectivity of the COVID-19 virus, Cell 182 (2020) 812–827, https://doi.org/10.1016/J.CELL.2020.06.043, e19.

[123] J.A. Plante, Y. Liu, J. Liu, H. Xia, B.A. Johnson, K.G. Lokugamage, X. Zhang, A. E. Muruato, J. Zou, C.R. Fontes-Garfias, D. Mirchandani, D. Scharton, J.P. Bilello, Z. Ku, Z. An, B. Kalveram, A.N. Freiberg, V.D. Menachery, X. Xie, K.S. Plante, S. C. Weaver, P.-Y. Shi, Spike mutation D614G alters SARS-CoV-2 fitness, Nat. 5927852 (592) (2020) 116–121, https://doi.org/10.1038/s41586-020-2895-3, 2020.

[124] T. Kirby, New variant of SARS-CoV-2 in UK causes surge of COVID-19, Lancet Respir. Med. 9 (2021) e20–e21, https://doi.org/10.1016/S2213-2600(21)00005-9.

[125] J.W. Tang, P.A. Tambyah, D.S. Hui, Emergence of a new SARS-CoV-2 variant in the UK, J. Infect. 82 (2021) e27–e28, https://doi.org/10.1016/J.JINF.2020.12.024.

[126] N.G. Davies, S. Abbott, R.C. Barnard, C.I. Jarvis, A.J. Kucharski, J.D. Munday, C. A.B. Pearson, T.W. Russell, D.C. Tully, A.D. Washburne, T. Wenseleers, A. Gimma, W. Waites, K.L.M. Wong, K. van Zandvoort, J.D. Silverman, K. Diaz-Ordaz, R. Keogh, R.M. Eggo, S. Funk, M. Jit, K.E. Atkins, W.J. Edmunds, Estimated transmissibility and impact of SARS-CoV-2 lineage B.1.1.7 in England, Science 372 (2021), https://doi.org/10.1126/SCIENCE.ABG3055.

[127] K. Leung, M.H.H. Shum, G.M. Leung, T.T.Y. Lam, J.T. Wu, Early transmissibility assessment of the N501Y mutant strains of SARS-CoV-2 in the United Kingdom, october to november 2020, Euro Surveill. 26 (2021), https://doi.org/10.2807/1560-7917.ES.2020.26.1.2002106.

[128] H. Fort, A Very Simple Model to Account for the Rapid Rise of the British Variant of SARS-CoV-2 in Several Countries and the World, MedRxiv, 2021, https://doi.org/10.1101/2021.04.13.21254841, 2021.04.13.21254841.
[129] B.W.Y. Mok, H. Liu, S. Deng, J. Liu, A.J. Zhang, S.Y. Lau, S. Liu, R.C.Y. Tam, C. J. Cremin, T.T.L. Ng, J.S.L. Leung, L.K. Lee, P. Wang, K.K.W. To, J.F.W. Chan, K. H. Chan, K.Y. Yuen, G.K.H. Siu, H. Chen, Low dose inocula of SARS-CoV-2 alpha variant transmits more efficiently than earlier variants in hamsters, Commun. Biol. 41 (4) (2021) 1–8, https://doi.org/10.1038/s42003-021-02640-x, 2021.
[130] SARS-CoV-2 variant classifications and definitions, (n.d.). https://www.cdc.gov/coronavirus/2019-ncov/variants/variant-classifications.html?CDC_AA_refVal=https%3A%2F%2Fwww.cdc.gov%2Fcoronavirus%2F2019-ncov%2Fvariants%2Fvariant-info.html (accessed December 7, 2021).
[131] D.J. Pascall, G. Mollett, R. Blacow, N. Bulteel, R. Campbell, A. Campbell, S. Clifford, C. Davis, A.da S. Filipe, L. Fjodorova, R. Forrest, E. Goldstein, R. Gunson, J. Haughney, M.T.G. Holden, P. Honour, J. Hughes, E. James, T. Lewis, S. Lycett, M. McHugh, Y. Onishi, B. Parcell, D.L. Robertson, N.El Sakka, S. Shabaan, J.G. Shepherd, K. Smollett, K. Templeton, E. Vink, E. Wastnedge, T. Williams, T.C.-19 G.U. (COG-U. consortium, E.C. Thomson, The SARS-CoV-2 Alpha Variant Causes Increased Clinical Severity of Disease, MedRxiv, 2021, https://doi.org/10.1101/2021.08.17.21260128, 2021.08.17.21260128.
[132] R. Challen, E. Brooks-Pollock, J.M. Read, L. Dyson, K. Tsaneva-Atanasova, L. Danon, Risk of mortality in patients infected with SARS-CoV-2 variant of concern 202012/1: matched cohort study, BMJ 372 (2021), https://doi.org/10.1136/BMJ.N579.
[133] A. Nakaya, E. Ogura, Y. Katayama, M. Yoshii, E. Yoshino, K. Hozumi, S. Tago, Y. Teranishi, Y. Minamibashi, M. Harada, M. Yoshioka, Y. Kawano, Y. Arai, K. Yoshida, S. Shimizu, K. Ogura, K. Iwashita, Red face may be a specific sign of SARS-CoV-2 alpha variantAlpha v\, IDCases 25 (2021), https://doi.org/10.1016/J.IDCR.2021.E01214.
[134] E. Krafft, S. Denolly, B. Boson, S. Angelloz-Pessey, S. Levaltier, N. Nesi, S. Corbet, B. Leterrier, M. Fritz, E.M. Leroy, M.A. Gouilh, F.L. Cosset, A. Kodjo, V. Legros, Report of one-year prospective surveillance of SARS-CoV-2 in dogs and cats in france with various exposure risks: confirmation of a low prevalence of shedding, detection and complete sequencing of an alpha variant in a cat, Viruses 13 (2021) 1759, https://doi.org/10.3390/V13091759, 13 (2021) 1759.
[135] L. Ferasin, M. Fritz, H. Ferasin, P. Becquart, S. Corbet, M.A. Gouilh, V. Legros, E. M. Leroy, Infection with SARS-CoV-2 variant B.1.1.7 detected in a group of dogs and cats with suspected myocarditis, Vet. Rec. 189 (2021), https://doi.org/10.1002/VETR.944 no-no.
[136] S.A. Kemp, B. Meng, I.A. Ferriera, R. Datir, W.T. Harvey, G. Papa, S. Lytras, D. A. Collier, A. Mohamed, G. Gallo, N. Thakur, T.C.-19 G.U. (COG-U. Consortium, A.M. Carabelli, J.C. Kenyon, A.M. Lever, A.De Marco, C. Saliba, K. Culap, E. Cameroni, L. Piccoli, D. Corti, L.C. James, D. Bailey, D.L. Robertson, R. K. Gupta, Recurrent Emergence and Transmission of a SARS-CoV-2 Spike Deletion H69/V70, BioRxiv, 2021, https://doi.org/10.1101/2020.12.14.422555, 2020.12.14.422555.
[137] M. McCallum, A. De Marco, F.A. Lempp, M.A. Tortorici, D. Pinto, A.C. Walls, M. Beltramello, A. Chen, Z. Liu, F. Zatta, S. Zepeda, J. di Iulio, J.E. Bowen, M. Montiel-Ruiz, J. Zhou, L.E. Rosen, S. Bianchi, B. Guarino, C.S. Fregni, R. Abdelnabi, S.Y.C. Foo, P.W. Rothlauf, L.M. Bloyet, F. Benigni, E. Cameroni, J. Neyts, A. Riva, G. Snell, A. Telenti, S.P.J. Whelan, H.W. Virgin, D. Corti, M. S. Pizzuto, D. Veesler, N-terminal domain antigenic mapping reveals a site of vulnerability for SARS-CoV-2, Cell 184 (2021) 2332–2347, https://doi.org/10.1016/J.CELL.2021.03.028/ATTACHMENT/F72F3A1A-8DD6-4517-A111-A1E4C49E33DD/MMC1.PDF, e16.
[138] J. Hu, P. Peng, K. Wang, L. Fang, F. Yang Luo, A. Shun Jin, B. Zhong Liu, N. Tang, A. Long Huang, Emerging SARS-CoV-2 variants reduce neutralization sensitivity to convalescent sera and monoclonal antibodies, Cell. Mol. Immunol. 18 (2021) 1061–1063, https://doi.org/10.1038/S41423-021-00648-1.
[139] C. Rees-Spear, L. Muir, S. Griffith, J. Heaney, Y. Aldon, J. Snitselaar, P. Thomas, C. Graham, J. Seow, N. Lee, A. Rosa, C. Roustan, C. Houlihan, R. Sanders, R. Gupta, P. Cherepanov, H. Stauss, E. Nastouli, , on behalf of the S. Investigators, K. Doores, M. van Gils, L. McCoy, The Impact of Spike Mutations on SARS-CoV-2 Neutralization, BioRxiv, 2021, https://doi.org/10.1101/2021.01.15.426849, 2021.01.15.426849.
[140] B. Meng, S.A. Kemp, G. Papa, R. Datir, I.A.T.M. Ferreira, S. Marelli, W.T. Harvey, S. Lytras, A. Mohamed, G. Gallo, N. Thakur, D.A. Collier, P. Mlcochova, S. C. Robson, N.J. Loman, T.R. Connor, T. Golubchik, R.T.Martinez Nunez, C. Ludden, S. Corden, I. Johnston, D. Bonsall, C.P. Smith, A.R. Awan, G. Bucca, M. E. Torok, K. Saeed, J.A. Prieto, D.K. Jackson, W.L. Hamilton, L.B. Snell, C. Moore, E.M. Harrison, S. Goncalves, D.J. Fairley, M.W. Loose, J. Watkins, R. Livett, S. Moses, R. Amato, S. Nicholls, M. Bull, D.L. Smith, J. Barrett, D.M. Aanensen, M. D. Curran, S. Parmar, D. Aggarwal, J.G. Shepherd, M.D. Parker, S. Glaysher, M. Bashton, A.P. Underwood, N. Pacchiarini, K.F. Loveson, K.E. Templeton, C. F. Langford, J. Sillitoe, T.I. de Silva, D. Wang, D. Kwiatkowski, A. Rambaut, J. O'Grady, S. Cottrell, M.T.G. Holden, E.C. Thomson, H. Osman, M. Andersson, A.J. Chauhan, M.O. Hassan-Ibrahim, M. Lawniczak, A. Alderton, M. Chand, C. Constantinidou, M. Unnikrishnan, A.C. Darby, J.A. Hiscox, S. Paterson, I. Martincorena, E.M. Volz, A.J. Page, O.G. Pybus, A.R. Bassett, C.V. Ariani, M.H. S. Chapman, K.K. Li, R.N. Shah, N.G. Jesudason, Y. Taha, M.P. McHugh, R. Dewar, A.S. Jahun, C. McMurray, S. Pandey, J.P. McKenna, A. Nelson, G. R. Young, C.M. McCann, S. Elliott, H. Lowe, B. Temperton, S. Roy, A. Price, S. Rey, M. Wyles, S. Rooke, S. Shaaban, M. de Cesare, L. Letchford, S. Silveira, E. Pelosi, E. Wilson-Davies, M. Hosmillo, Á. O'Toole, A.R. Hesketh, R. Stark, L. du Plessis, C. Ruis, H. Adams, Y. Bourgeois, S.L. Michell, D. Gramatopoulos, J. Edgeworth, J. Breuer, J.A. Todd, C. Fraser, D. Buck, M. John, G.L. Kay, S. Palmer, S.J. Peacock, D. Heyburn, D. Weldon, E. Robinson, A. McNally, P. Muir, I.B. Vipond, J. Boyes, V. Sivaprakasam, T. Salluja, S. Dervisevic, E.J. Meader, N. R. Park, K. Oliver, A.R. Jeffries, S. Ott, A. da Silva Filipe, D.A. Simpson, C. Williams, J.A.H. Masoli, B.A. Knight, C.R. Jones, C. Koshy, A. Ash, A. Casey, A. Bosworth, L. Ratcliffe, L. Xu-McCrae, H.M. Pymont, S. Hutchings, L. Berry, K. Jones, F. Halstead, T. Davis, C. Holmes, M. Iturriza-Gomara, A.O. Lucaci, P. A. Randell, A. Cox, P. Madona, K.A. Harris, J.R. Brown, T.W. Mahungu, D. Irish-Tavares, T. Haque, J. Hart, E. Witele, M.L. Fenton, S. Liggett, C. Graham, E. Swindells, J. Collins, G. Eltringham, S. Campbell, P.C. McClure, G. Clark, T. J. Sloan, C. Jones, J. Lynch, B. Warne, S. Leonard, J. Durham, T. Williams, S. T. Haldenby, N. Storey, N.F. Alikhan, N. Holmes, C. Moore, M. Carlile, M. Perry, N. Craine, R.A. Lyons, A.H. Beckett, S. Goudarzi, C. Fearn, K. Cook, H. Dent, H. Paul, R. Davies, B. Blane, S.T. Girgis, M.A. Beale, K.L. Bellis, M.J. Dorman, E. Drury, L. Kane, S. Kay, S. McGuigan, R. Nelson, L. Prestwood, S. Rajatileka, R. Batra, R.J. Williams, M. Kristiansen, A. Green, A. Justice, A.I.K. Mahanama, B. Samaraweera, N.F. Hadjirin, J. Quick, R. Poplawski, L.M. Kermack, N. Reynolds, G. Hall, Y. Chaudhry, M.L. Pinckert, I. Georgana, R.J. Moll, A. Thornton, R. Myers, J. Stockton, C.A. Williams, W.C. Yew, A.J. Trotter, A. Trebes, G. MacIntyre-Cockett, A. Birchley, A. Adams, A. Plimmer, B. Gatica-Wilcox, C. McKerr, E. Hilvers, H. Jones, H. Asad, J. Coombes, J.M. Evans, L. Fina, L. Gilbert, L. Graham, M. Cronin, S. Kumziene-Summerhayes, S. Taylor, S. Jones, D.C. Groves, P. Zhang, M. Gallis, S.F. Louka, I. Starinskij, C. Jackson, M. Gourtovaia, G. Tonkin-Hill, K. Lewis, J.M. Tovar-Corona, K. James, L. Baxter, M.T. Alam, R.J. Orton, J. Hughes, S. Vattipally, M. Ragonnet-Cronin, F. F. Nascimento, D. Jorgensen, O. Boyd, L. Geidelberg, A.E. Zarebski, J. Raghwani, M.U.G. Kraemer, J. Southgate, B.B. Lindsey, T.M. Freeman, J.P. Keatley, J. B. Singer, L. de Oliveira Martins, C.A. Yeats, K. Abudahab, B.E.W. Taylor, M. Menegazzo, J. Danesh, W. Hogsden, S. Eldirdiri, A. Kenyon, J. Mason, T. I. Robinson, A. Holmes, J. Price, J.A. Hartley, T. Curran, A.E. Mather, G. Shankar, R. Jones, R. Howe, S. Morgan, E. Wastenge, M.R. Chapman, S. Mookerjee, R. Stanley, W. Smith, T. Peto, D. Eyre, D. Crook, G. Vernet, C. Kitchen, H. Gulliver, I. Merrick, M. Guest, R. Munn, D.T. Bradley, T. Wyatt, C. Beaver, L. Foulser, S. Palmer, C.M. Churcher, E. Brooks, K.S. Smith, K. Galai, G. M. McManus, F. Bolt, F. Coll, L. Meadows, S.W. Attwood, A. Davies, E.De Lacy, F. Downing, S. Edwards, G.P. Scarlett, S. Jeremiah, N. Smith, D. Leek, S. Sridhar, S. Forrest, C. Cormie, H.K. Gill, J. Dias, E.E. Higginson, M. Maes, J. Young, M. Wantoch, D. Jamrozy, S. Lo, M. Patel, V. Hill, C.M. Bewshea, S. Ellard, C. Auckland, I. Harrison, C. Bishop, V. Chalker, A. Richter, A. Beggs, A. Best, B. Percival, J. Mirza, O. Megram, M. Mayhew, L. Crawford, F. Ashcroft, E. Moles-Garcia, N. Cumley, R. Hopes, P. Asamaphan, M.O. Niebel, R.N. Gunson, A. Bradley, A. Maclean, G. Mollett, R. Blacow, P. Bird, T. Helmer, K. Fallon, J. Tang, A.D. Hale, L.R. Macfarlane-Smith, K.L. Harper, H. Carden, N.W. Machin, K.A. Jackson, S.S.Y. Ahmad, R.P. George, L. Turtle, E. O'Toole, J. Watts, C. Breen, A. Cowell, A. Alcolea-Medina, T. Charalampous, A. Patel, L.J. Levett, J. Heaney, A. Rowan, G.P. Taylor, D. Shah, L. Atkinson, J.C.D. Lee, A.P. Westhorpe, R. Jannoo, H.L. Lowe, A. Karamani, L. Ensell, W. Chatterton, M. Pusok, A. Dadrah, A. Symmonds, G. Sluga, Z. Molnar, P. Baker, S. Bonner, S. Essex, E. Barton, D. Padgett, G. Scott, J. Greenaway, B.A.I. Payne, S. Burton-Fanning, S. Waugh, V. Raviprakash, N. Sheriff, V. Blakey, L.A. Williams, J. Moore, S. Stonehouse, L. Smith, R.K. Davidson, L. Bedford, L. Coupland, V. Wright, J.G. Chappell, T. Tsoleridis, J. Ball, M. Khakh, V.M. Fleming, M.M. Lister, H.C. Howson-Wells, L. Berry, T. Boswell, A. Joseph, I. Willingham, N. Duckworth, S. Walsh, E. Wise, N. Moore, M. Mori, N. Cortes, S. Kidd, R. Williams, L. Gifford, K. Bicknell, S. Wyllie, A. Lloyd, R. Impey, C.S. Malone, B.J. Cogger, N. Levene, L. Monaghan, A.J. Keeley, D.G. Partridge, M. Raza, C. Evans, K. Johnson, E. Betteridge, B. W. Farr, S. Goodwin, M.A. Quail, C. Scott, L. Shirley, S.A.J. Thurston, D. Rajan, I. F. Bronner, L. Aigrain, N.M. Redshaw, S.V. Lensing, S. McCarthy, A. Makunin, C. E. Balcazar, M.D. Gallagher, K.A. Williamson, T.D. Stanton, M.L. Michelsen, J. Warwick-Dugdale, R. Manley, A. Farbos, J.W. Harrison, C.M. Sambles, D. J. Studholme, A. Lackenby, T. Mbisa, S. Platt, S. Miah, D. Bibby, C. Manso, J. Hubb, G. Dabrera, M. Ramsay, D. Bradshaw, U. Schaefer, N. Groves, E. Gallagher, D. Lee, D. Williams, N. Ellaby, H. Hartman, N. Manesis, V. Patel, J. Ledesma, K.A. Twohig, E. Allara, C. Pearson, J.K.J. Cheng, H.E. Bridgewater, L. R. Frost, G. Taylor-Joyce, P.E. Brown, L. Tong, A. Broos, D. Mair, J. Nichols, S. N. Carmichael, K.L. Smollett, K. Nomikou, E. Aranday-Cortes, N. Johnson, S. Nickbakhsh, E.E. Vamos, M. Hughes, L. Rainbow, R. Eccles, C. Nelson, M. Whitehead, R. Gregory, M. Gemmell, C. Wierzbicki, H.J. Webster, C.L. Fisher, A.W. Signell, G. Betancor, H.D. Wilson, G. Nebbia, F. Flaviani, A.C. Cerda, T. V. Merrill, R.E. Wilson, M. Cotic, N. Bayzid, T. Thompson, E. Acheson, S. Rushton, S. O'Brien, D.J. Baker, S. Rudder, A. Aydin, F. Sang, J. Debebe, S. Francois, T. I. Vasylyeva, M.E. Zamudio, B. Gutierrez, A. Marchbank, J. Maksimovic, K. Spellman, K. McCluggage, M. Morgan, R. Beer, S. Afifi, T. Workman, W. Fuller, C. Bresner, A. Angyal, L.R. Green, P.J. Parsons, R.M. Tucker, R. Brown, M. Whiteley, J. Bonfield, C. Puethe, A. Whitwham, J. Liddle, W. Rowe, I. Siveroni, T. Le-Viet, A. Gaskin, R. Johnson, I. Abnizova, M. Ali, L. Allen, R. Anderson, C. Ariani, S. Austin-Guest, S. Bala, J. Barrett, A. Bassett, K. Battleday, J. Beal, M. Beale, S. Bellany, T. Bellerby, K. Bellis, D. Berger, M. Berriman, P. Bevan, S. Binley, J. Bishop, K. Blackburn, N. Boughton, S. Bowker, T. Brendler-Spaeth, I. Bronner, T. Brooklyn, S.K. Buddenborg, R. Bush, C. Caetano, A. Cagan, N. Carter, J. Cartwright, T.C. Monteiro, L. Chapman, T.J. Chillingworth, P. Clapham, R. Clark, A. Clarke, C. Clarke, D. Cole, E. Cook, M. Coppola, L. Cornell, C. Cornwell, C. Corton, A. Crackett, A. Cranage, H. Craven, S. Craw, M. Crawford, T. Cutts, M. Dabrowska, M. Davies, J. Dawson, C. Day, A. Densem, T. Dibling, C. Dockree, D. Dodd, S. Dogga, M. Dorman, G. Dougan, M. Dougherty, A. Dove, L. Drummond, M. Dudek, L. Durrant, E. Easthope, S. Eckert, P. Ellis, B. Farr, M. Fenton, M. Ferrero, N. Flack, H. Fordham, G. Forsythe, M. Francis,

A. Fraser, A. Freeman, A. Galvin, M. Garcia-Casado, A. Gedny, S. Girgis, J. Glover, O. Gould, A. Gray, E. Gray, C. Griffiths, Y. Gu, F. Guerin, W. Hamilton, H. Hanks, E. Harrison, A. Harrott, E. Harry, J. Harvison, P. Heath, A. Hernandez-Koutoucheva, R. Hobbs, D. Holland, S. Holmes, G. Hornett, N. Hough, L. Huckle, L. Hughes-Hallet, A. Hunter, S. Inglis, S. Iqbal, A. Jackson, D. Jackson, C. J. Verdejo, M. Jones, K. Kallepally, K. Kay, J. Keatley, A. Keith, A. King, L. Kitchin, M. Kleanthous, M. Klimekova, P. Korlevic, K. Krasheninnkova, G. Lane, C. Langford, A. Laverack, K. Law, S. Lensing, A. Lewis-Wade, J. Liddle, Q. Lin, S. Lindsay, S. Linsdell, R. Long, J. Lovell, J. Lovell, J. Mack, M. Maddison, A. Makunin, I. Mamun, J. Mansfield, N. Marriott, M. Martin, M. Mayho, J. McClintock, S. McHugh, L. MapcMinn, C. Meadows, E. Mobley, R. Moll, M. Morra, L. Morrow, K. Murie, S. Nash, C. Nathwani, P. Naydenova, A. Neaverson, E. Nerou, J. Nicholson, T. Nimz, G.G. Noell, S. O'Meara, V. Ohan, C. Olney, D. Ormond, A. Oszlanczi, Y.F. Pang, B. Pardubska, N. Park, A. Parmar, G. Patel, M. Payne, S. Peacock, A. Petersen, D. Plowman, T. Preston, M. Quail, R. Rance, S. Rawlings, N. Redshaw, J. Reynolds, M. Reynolds, S. Rice, M. Richardson, C. Roberts, K. Robinson, M. Robinson, D. Robinson, H. Rogers, E. M. Rojo, D. Roopra, M. Rose, L. Rudd, R. Sadri, N. Salmon, D. Saul, F. Schwach, P. Seekings, A. Simms, M. Sinnott, S. Sivadasan, B. Siwek, D. Sizer, K. Skeldon, J. Skelton, J. Slater-Tunstill, L. Sloper, N. Smerdon, C. Smith, C. Smith, J. Smith, K. Smith, M. Smith, S. Smith, T. Smith, L. Sneade, C.D. Soria, C. Sousa, E. Souster, A. Sparkes, M. Spencer-Chapman, J. Squares, R. Stanley, C. Steed, T. Stickland, I. Still, M. Stratton, M. Strickland, A. Swann, A. Swiatkowska, N. Sycamore, E. Swift, E. Symons, S. Szluha, E. Taluy, N. Tao, K. Taylor, S. Taylor, S. Thompson, M. Thompson, M. Thomson, N. Thomson, S. Thurston, D. Toombs, B. Topping, J. Tovar-Corona, D. Ungureanu, J. Uphill, J. Urbanova, P.J. Van, V. Vancollie, P. Voak, D. Walker, M. Walker, M. Waller, G. Ward, C. Weatherhogg, N. Webb, A. Wells, E. Wells, L. Westwood, T. Whipp, T. Whiteley, G. Whitton, S. Widaa, M. Williams, M. Wilson, S. Wright, L.M. Duncan, A.M. Carabelli, J.C. Kenyon, A. M. Lever, A.De Marco, C. Saliba, K. Culap, E. Cameroni, N.J. Matheson, L. Piccoli, D. Corti, L.C. James, D.L. Robertson, D. Bailey, R.K. Gupta, Recurrent emergence of SARS-CoV-2 spike deletion H69/V70 and its role in the Alpha variant B.1.1.7, Cell Rep. 35 (2021), https://doi.org/10.1016/J.CELREP.2021.109292, 2021.07.07.21260122.

[141] J. Zahradník, S. Marciano, M. Shemesh, E. Zoler, J. Chiaravalli, B. Meyer, Y. Rudich, O. Dym, N. Elad, G. Schreiber, SARS-CoV-2 RBD in Vitro Evolution Follows Contagious Mutation Spread, Yet Generates an Able Infection Inhibitor, BioRxiv, 2021, https://doi.org/10.1101/2021.01.06.425392, 2021.01.06.425392.

[142] T.N. Starr, A.J. Greaney, S.K. Hilton, D. Ellis, K.H.D. Crawford, A.S. Dingens, M. J. Navarro, J.E. Bowen, M.A. Tortorici, A.C. Walls, N.P. King, D. Veesler, J. D. Bloom, Deep mutational scanning of SARS-CoV-2 receptor binding domain reveals constraints on folding and ACE2 binding, Cell 182 (2020) 1295–1310, https://doi.org/10.1016/J.CELL.2020.08.012, e20.

[143] S. Kannan, P.S.S. Ali, A. Sheeza, Evolving biothreat of variant SARS-CoV-2 - molecular properties, virulence and epidemiology, Eur. Rev. Med. Pharmacol. Sci. 25 (2021) 4405–4412, https://doi.org/10.26355/EURREV_202106_26151.

[144] Preliminary genomic characterisation of an emergent SARS-CoV-2 lineage in the UK defined by a novel set of spike mutations - SARS-CoV-2 coronavirus / nCoV-2019 Genomic Epidemiology - Virological, (n.d.). https://virological.org/t/preliminary-genomic-characterisation-of-an-emergent-sars-cov-2-lineage-in-the-uk-defined-by-a-novel-set-of-spike-mutations/563 (accessed December 8, 2021).

[145] D.L. Bugembe, M.V.T. Phan, I. Ssewanyana, P. Semanda, H. Nansumba, B. Dhaala, S. Nabadda, Á.N. O'Toole, A. Rambaut, P. Kaleebu, M. Cotten, Emergence and spread of a SARS-CoV-2 lineage a variant (A.23.1) with altered spike protein in Uganda, Nat. Microbiol. 68 (6) (2021) 1094–1101, https://doi.org/10.1038/s41564-021-00933-9, 2021.

[146] H. Tegally, E. Wilkinson, M. Giovanetti, A. Iranzadeh, V. Fonseca, J. Giandhari, D. Doolabh, S. Pillay, E.J. San, N. Msomi, K. Mlisana, A. von Gottberg, S. Walaza, M. Allam, A. Ismail, T. Mohale, A.J. Glass, S. Engelbrecht, G.Van Zyl, W. Preiser, F. Petruccione, A. Sigal, D. Hardie, G. Marais, M. Hsiao, S. Korsman, M.-A. Davies, L. Tyers, I. Mudau, D. York, C. Maslo, D. Goedhals, S. Abrahams, O. Laguda-Akingba, A. Alisoltani-Dehkordi, A. Godzik, C.K. Wibmer, B.T. Sewell, J. Lourenço, L.C.J. Alcantara, S.L.K. Pond, S. Weaver, D. Martin, R.J. Lessells, J. N. Bhiman, C. Williamson, T. de Oliveira, Emergence and Rapid Spread of a New Severe Acute Respiratory Syndrome-related Coronavirus 2 (SARS-CoV-2) Lineage With Multiple Spike Mutations in South Africa, MedRxiv, 2020, https://doi.org/10.1101/2020.12.21.20248640, 2020.12.21.20248640.

[147] J.W. Tang, O.T.R. Toovey, K.N. Harvey, D.D.S. Hui, Introduction of the south african SARS-CoV-2 variant 501Y.V2 into the UK, J. Infect. 82 (2021) e8–e10, https://doi.org/10.1016/J.JINF.2021.01.007/ATTACHMENT/7ECE48C8-0894-4954-B74F-4D9DDA7DFB40/MMC1.PDF.

[148] H. Tegally, E. Wilkinson, C.L. Althaus, M. Giovanetti, J.E. San, J. Giandhari, S. Pillay, Y. Naidoo, U. Ramphal, N. Msomi, K. Mlisana, D.G. Amoako, J. Everatt, T. Mohale, A. Nguni, B. Mahlangu, N. Ntuli, Z.T. Khumalo, Z. Makatini, N. Wolter, C. Scheepers, A. Ismail, D. Doolabh, R. Joseph, A. Strydom, A. Mendes, M. Davis, S.H. Mayaphi, Y. Ramphal, A. Maharaj, W.A. Karim, D. Tshiabuila, U.J. Anyaneji, L. Singh, S. Engelbrecht, V. Fonseca, K. Marais, S. Korsman, D. Hardie, N. Hsiao, T. Maponga, G. van Zyl, G. Marais, A. Iranzadeh, D. Martin, L.C.J. Alcantara, P. A. Bester, M.M. Nyaga, K. Subramoney, F.K. Treurnicht, M. Venter, D. Goedhals, W. Preiser, J.N. Bhiman, A. von Gottberg, C. Williamson, R.J. Lessells, T. de Oliveira, Rapid Replacement of the Beta Variant by the Delta Variant in South Africa, MedRxiv, 2021, https://doi.org/10.1101/2021.09.23.21264018, 2021.09.23.21264018.

[149] A tale of two variants: spread of SARS-CoV-2 variants Alpha in Geneva, Switzerland, and Beta in South Africa. https://medrxiv.org/cgi/content/short/2021.06.10.21258468, 2021 (accessed December 8, 2021).

[150] Estimates of severity and transmissibility of novel SARS-CoV-2 variant 501Y.V2 in South Africa | CMMID Repository, (n.d.). https://cmmid.github.io/topics/covid19/sa-novel-variant.html (accessed December 8, 2021).

[151] Y. Weisblum, F. Schmidt, F. Zhang, J. DaSilva, D. Poston, J.C.C. Lorenzi, F. Muecksch, M. Rutkowska, H.H. Hoffmann, E. Michailidis, C. Gaebler, M. Agudelo, A. Cho, Z. Wang, A. Gazumyan, M. Cipolla, L. Luchsinger, C. D. Hillyer, M. Caskey, D.F. Robbiani, C.M. Rice, M.C. Nussenzweig, T. Hatziioannou, P.D. Bieniasz, Escape from neutralizing antibodies by SARS-CoV-2 spike protein variants, elife 9 (2020) 1, https://doi.org/10.7554/ELIFE.61312.

[152] Z. Liu, L.A. VanBlargan, L.M. Bloyet, P.W. Rothlauf, R.E. Chen, S. Stumpf, H. Zhao, J.M. Errico, E.S. Theel, M.J. Liebeskind, B. Alford, W.J. Buchser, A. H. Ellebedy, D.H. Fremont, M.S. Diamond, S.P.J. Whelan, Identification of SARS-CoV-2 spike mutations that attenuate monoclonal and serum antibody neutralization, Cell Host Microbe 29 (2021) 477–488, https://doi.org/10.1016/J.CHOM.2021.01.014, e4.

[153] E. Andreano, G. Piccini, D. Licastro, L. Casalino, N.V. Johnson, I. Paciello, S. Dal Monego, E. Pantano, N. Manganaro, A. Manenti, R. Manna, E. Casa, I. Hyseni, L. Benincasa, E. Montomoli, R.E. Amaro, J.S. McLellan, R. Rappuoli, SARS-CoV-2 escape in vitro from a highly neutralizing COVID-19 convalescent plasma, BioRxiv Prepr. Serv. Biol. (2020), https://doi.org/10.1101/2020.12.28.424451.

[154] T. Moyo-Gwete, M. Madzivhandila, Z. Makhado, F. Ayres, D. Mhlanga, B. Oosthuysen, B.E. Lambson, P. Kgagudi, H. Tegally, A. Iranzadeh, D. Doolabh, L. Tyers, L.R. Chinhoyi, M. Mennen, S. Skelem, G. Marais, C.K. Wibmer, J. N. Bhiman, V. Ueckermann, T. Rossouw, M. Boswell, T. de Oliveira, C. Williamson, W.A. Burgers, N. Ntusi, L. Morris, P.L. Moore, Cross-reactive neutralizing antibody responses elicited by SARS-CoV-2 501Y.V2 (B.1.351), N. Engl. J. Med. 384 (2021) 2161–2163, https://doi.org/10.1056/NEJMC2104192/SUPPL_FILE/NEJMC2104192_DISCLOSURES.PDF.

[155] A. Baum, B.O. Fulton, E. Wloga, R. Copin, K.E. Pascal, V. Russo, S. Giordano, K. Lanza, N. Negron, M. Ni, Y. Wei, G.S. Atwal, A.J. Murphy, N. Stahl, G. D. Yancopoulos, C.A. Kyratsous, Antibody cocktail to SARS-CoV-2 spike protein prevents rapid mutational escape seen with individual antibodies, Science 369 (2020) 1014–1018, https://doi.org/10.1126/SCIENCE.ABD0831.

[156] S. Duchene, L. Featherstone, M. Haritopoulou-Sinanidou, A. Rambaut, P. Lemey, G. Baele, Temporal signal and the phylodynamic threshold of SARS-CoV-2, Virus Evol. 6 (2020), veaa061, https://doi.org/10.1093/ve/veaa061.

[157] E. Volz, V. Hill, J.T. McCrone, A. Price, D. Jorgensen, Á. O'Toole, J. Southgate, R. Johnson, B. Jackson, F.F. Nascimento, S.M. Rey, S.M. Nicholls, R. M. Colquhoun, A. da Silva Filipe, J. Shepherd, D.J. Pascall, R. Shah, N. Jesudason, K. Li, R. Jarrett, N. Pacchiarini, M. Bull, L. Geidelberg, I. Siveroni, C. Koshy, E. Wise, N. Cortes, J. Lynch, S. Kidd, M. Mori, D.J. Fairley, T. Curran, J. P. McKenna, H. Adams, C. Fraser, T. Golubchik, D. Bonsall, C. Moore, S.L. Caddy, F.A. Khokhar, M. Wantoch, N. Reynolds, B. Warne, J. Maksimovic, K. Spellman, K. McCluggage, M. John, R. Beer, S. Afifi, S. Morgan, A. Marchbank, C. Kitchen, H. Gulliver, I. Merrick, M. Guest, R. Munn, T. Workman, T.R. Connor, W. Fuller, C. Bresner, L.B. Snell, T. Charalampous, G. Nebbia, R. Batra, J. Edgeworth, S. C. Robson, A. Beckett, K.F. Loveson, D.M. Aanensen, A.P. Underwood, C.A. Yeats, K. Abudahab, B.E.W. Taylor, M. Menegazzo, G. Clark, W. Smith, M. Khakh, V. M. Fleming, M.M. Lister, H.C. Howson-Wells, L. Berry, T. Boswell, A. Joseph, I. Willingham, P. Bird, T. Helmer, K. Fallon, C. Holmes, J. Tang, V. Raviprakash, S. Campbell, N. Sheriff, M.W. Loose, N. Holmes, C. Moore, M. Carlile, V. Wright, F. Sang, J. Debebe, F. Coll, A.W. Signell, G. Betancor, H.D. Wilson, T. Feltwell, C. J. Houldcroft, S. Eldirdiri, A. Kenyon, T. Davis, O. Pybus, L. du Plessis, A. Zarebski, J. Raghwani, M. Kraemer, S. Francois, S. Attwood, T. Vasylyeva, M. E. Torok, W.L. Hamilton, I.G. Goodfellow, G. Hall, A.S. Jahun, Y. Chaudhry, M. Hosmillo, M.L. Pinckert, I. Georgana, A. Yakovleva, L.W. Meredith, S. Moses, H. Lowe, F. Ryan, C.L. Fisher, A.R. Awan, J. Boyes, J. Breuer, K.A. Harris, J. R. Brown, D. Shah, L. Atkinson, J.C.D. Lee, A. Alcolea-Medina, N. Moore, N. Cortes, R. Williams, M.R. Chapman, L.J. Levett, J. Heaney, D.L. Smith, M. Bashton, G.R. Young, J. Allan, J. Loh, P.A. Randell, A. Cox, P. Madona, A. Holmes, F. Bolt, J. Price, S. Mookerjee, A. Rowan, G.P. Taylor, M. Ragonnet-Cronin, R. Johnson, O. Boyd, E.M. Volz, K. Brunker, K.L. Smollett, N.J. Loman, J. Quick, C. McMurray, J. Stockton, S. Nicholls, W. Rowe, R. Poplawski, R. T. Martinez-Nunez, J. Mason, T.I. Robinson, E. O'Toole, J. Watts, C. Breen, A. Cowell, C. Ludden, G. Sluga, N.W. Machin, S.S.Y. Ahmad, R.P. George, F. Halstead, V. Sivaprakasam, E.C. Thomson, J.G. Shepherd, P. Asamaphan, M. O. Niebel, K.K. Li, R.N. Shah, N.G. Jesudason, Y.A. Parr, L. Tong, A. Broos, D. Mair, J. Nichols, S.N. Carmichael, K. Nomikou, E. Aranday-Cortes, N. Johnson, I. Starinskij, D.L. Robertson, R.J. Orton, J. Hughes, S. Vattipally, J.B. Singer, A. D. Hale, L.R. Macfarlane-Smith, K.L. Harper, Y. Taha, B.A.I. Payne, S. Burton-Fanning, S. Waugh, J. Collins, G. Eltringham, K.E. Templeton, M.P. McHugh, R. Dewar, E. Wastenge, S. Dervisevic, R. Stanley, R. Prakash, C. Stuart, N. Elumogo, D.K. Sethi, E.J. Meader, L.J. Coupland, W. Potter, C. Graham, E. Barton, D. Padgett, G. Scott, E. Swindells, J. Greenaway, A. Nelson, W.C. Yew, P.C. Resende Silva, M. Andersson, R. Shaw, T. Peto, A. Justice, D. Eyre, D. Crooke, S. Hoosdally, T.J. Sloan, N. Duckworth, S. Walsh, A.J. Chauhan, S. Glaysher, K. Bicknell, S. Wyllie, E. Butcher, S. Elliott, A. Lloyd, R. Impey, N. Levene, L. Monaghan, D.T. Bradley, E. Allara, C. Pearson, P. Muir, I.B. Vipond, R. Hopes, H.M. Pymont, S. Hutchings, M.D. Curran, S. Parmar, A. Lackenby, T. Mbisa, S. Platt, S. Miah, D. Bibby, C. Manso, J. Hubb, M. Chand, G. Dabrera, M. Ramsay, D. Bradshaw, A. Thornton, R. Myers, U. Schaefer, N. Groves, E. Gallagher, D. Lee, D. Williams, N. Ellaby, I. Harrison, H. Hartman, N. Manesis, V. Patel, C. Bishop,

V. Chalker, H. Osman, A. Bosworth, E. Robinson, M.T.G. Holden, S. Shaaban, A. Birchley, A. Adams, A. Davies, A. Gaskin, A. Plimmer, B. Gatica-Wilcox, C. McKerr, C. Moore, C. Williams, D. Heyburn, E. De Lacy, E. Hilvers, F. Downing, G. Shankar, H. Jones, H. Asad, J. Coombes, J. Watkins, J.M. Evans, L. Fina, L. Gifford, L. Gilbert, L. Graham, M. Perry, M. Morgan, M. Cronin, N. Craine, R. Jones, R. Howe, S. Corden, S. Rey, S. Kumziene-Summerhayes, S. Taylor, S. Cottrell, S. Jones, S. Edwards, J. O'Grady, A.J. Page, J. Wain, M.A. Webber, A. E. Mather, D.J. Baker, S. Rudder, M. Yasir, N.M. Thomson, A. Aydin, A.P. Tedim, G.L. Kay, A.J. Trotter, R.A.J. Gilroy, N.F. Alikhan, L. de Oliveira Martins, T. Le-Viet, L. Meadows, A. Kolyva, M. Diaz, A. Bell, A.V. Gutierrez, I.G. Charles, E. M. Adriaenssens, R.A. Kingsley, A. Casey, D.A. Simpson, Z. Molnar, T. Thompson, E. Acheson, J.A.H. Masoli, B.A. Knight, A. Hattersley, S. Ellard, C. Auckland, T. W. Mahungu, D. Irish-Tavares, T. Haque, Y. Bourgeois, G.P. Scarlett, D. G. Partridge, M. Raza, C. Evans, K. Johnson, S. Liggett, P. Baker, S. Essex, R. A. Lyons, L.G. Caller, S. Castellano, R.J. Williams, M. Kristiansen, S. Roy, C. A. Williams, P.L. Dyal, H.J. Tutill, Y.N. Panchbhaya, L.M. Forrest, P. Niola, J. Findlay, T.T. Brooks, A. Gavriil, L. Mestek-Boukhibar, S. Weeks, S. Pandey, L. Berry, K. Jones, A. Richter, A. Beggs, C.P. Smith, G. Bucca, A.R. Hesketh, E. M. Harrison, S.J. Peacock, S. Palmer, C.M. Churcher, K.L. Bellis, S.T. Girgis, P. Naydenova, B. Blane, S. Sridhar, C. Ruis, S. Forrest, C. Cormie, H.K. Gill, J. Dias, E.E. Higginson, M. Maes, J. Young, L.M. Kermack, N.F. Hadjirin, D. Aggarwal, L. Griffith, T. Swingler, R.K. Davidson, A. Rambaut, T. Williams, C. E. Balcazar, M.D. Gallagher, Á. O'Toole, S. Rooke, R. Colquhoun, J. Ashworth, J. T. McCrone, E. Scher, X. Yu, K.A. Williamson, T.D. Stanton, S.L. Michell, C. M. Bewshea, B. Temperton, M.L. Michelsen, J. Warwick-Dugdale, R. Manley, A. Farbos, J.W. Harrison, C.M. Sambles, D.J. Studholme, A.R. Jeffries, A.C. Darby, J.A. Hiscox, S. Paterson, M. Iturriza-Gomara, K.A. Jackson, A.O. Lucaci, E. E. Vamos, M. Hughes, L. Rainbow, R. Eccles, C. Nelson, M. Whitehead, L. Turtle, S.T. Haldenby, R. Gregory, M. Gemmell, D. Kwiatkowski, T.I. de Silva, N. Smith, A. Angyal, B.B. Lindsey, D.C. Groves, L.R. Green, D. Wang, T.M. Freeman, M. D. Parker, A.J. Keeley, P.J. Parsons, R.M. Tucker, R. Brown, M. Wyles, C. Constantinidou, M. Unnikrishnan, S. Ott, J.K.J. Cheng, H.E. Bridgewater, L. R. Frost, G. Taylor-Joyce, R. Stark, L. Baxter, M.T. Alam, P.E. Brown, P. C. McClure, J.G. Chappell, T. Tsoleridis, J. Ball, D. Gramatopoulos, D. Buck, J. A. Todd, A. Green, A. Trebes, G. MacIntyre-Cockett, M. de Cesare, C. Langford, A. Alderton, R. Amato, S. Goncalves, D.K. Jackson, I. Johnston, J. Sillitoe, S. Palmer, M. Lawniczak, M. Berriman, J. Danesh, R. Livett, L. Shirley, B. Farr, M. Quail, S. Thurston, N. Park, E. Betteridge, D. Weldon, S. Goodwin, R. Nelson, C. Beaver, L. Letchford, D.A. Jackson, L. Foulser, L. McMinn, L. Prestwood, S. Kay, L. Kane, M.J. Dorman, I. Martincorena, C. Puethe, J.P. Keatley, G. Tonkin-Hill, C. Smith, D. Jamrozy, M.A. Beale, M. Patel, C. Ariani, M. Spencer-Chapman, E. Drury, S. Lo, S. Rajatileka, C. Scott, K. James, S.K. Buddenborg, D.J. Berger, G. Patel, M.V. Garcia-Casado, T. Dibling, S. McGuigan, H.A. Rogers, A.D. Hunter, E. Souster, A.S. Neaverson, I. Goodfellow, O.G. Pybus, Evaluating the effects of SARS-CoV-2 spike mutation D614G on transmissibility and pathogenicity, Cell 184 (2021) 64–75, https://doi.org/10.1016/J.CELL.2020.11.020, e11.

[158] Y. Hirotsu, M. Omata, Discovery of a SARS-CoV-2 variant from the P. 1 lineage harboring K417T/E484K/N501Y mutations in Kofu, Japan, J. Infect. 82 (2021) 276–316.

[159] A.P. Lamarca, L.G.P. de Almeida, R. da Silva Francisco, L.F.A. Lima, K. C. Scortecci, V.P. Perez, O.J. Brustolini, E.S.S. Sousa, D.A. Secco, A.M.G. Santos, Genomic Surveillance of SARS-CoV-2 Tracks Early Interstate Transmission of P. 1 Lineage and Diversification Within P. 2 Clade in Brazil, MedRxiv, 2021.

[160] A.R.R. Freitas, O.A. Beckedorff, A.M. Siqueira, D.B. Castro, C.F. da Costa, D.R. Q. Lemos, E.N.C. Barros, L.P.de G. Cavalcanti, The Emergence of Novel SARS-CoV-2 Variant P. 1 in Amazonas (Brazil) was Temporally Associated with a Change in the Age and Gender Profile of COVID-19 Mortality, 2021. Available SSRN 3804788.

[161] J.C. da Silva, V.B. Félix, S.A.B.F. Leão, E.M. Trindade Filho, F.A. Scorza, New brazilian variant of the SARS-CoV-2 (P1) of COVID-19 in Alagoas state, brazilian, J. Infect. Dis. 25 (2021) 101588–101590, https://doi.org/10.1016/j.bjid.2021.101588.

[162] F.G. Naveca, V. Nascimento, V.C. de Souza, A. de Lima Corado, F. Nascimento, G. Silva, Á. Costa, D. Duarte, K. Pessoa, M. Mejía, COVID-19 in Amazonas, Brazil, was driven by the persistence of endemic lineages and P. 1 emergence, Nat. Med. (2021) 1–9.

[163] N.R. Faria, T.A. Mellan, C. Whittaker, I.M. Claro, S. Mishra, M.A.E. Crispim, F.C. S. Sales, I. Hawryluk, J.T. McCrone, D.da S. Candido, Genomics and epidemiology of the P. 1 SARS-CoV-2 lineage in Manaus, Brazil, Science (80-.) 372 (2021) 815–821.

[164] E. Boehm, I. Kronig, R.A. Neher, I. Eckerle, P. Vetter, L. Kaiser, Novel SARS-CoV-2 variants: the pandemics within the pandemic, Clin. Microbiol. Infect. 27 (2021) 1109–1117.

[165] M.S. Tagliamonte, C. Mavian, K. Zainabadi, M.N. Cash, J.A. Lednicky, B. R. Magalis, A. Riva, M.M. Deschamps, B. Liautaud, V. Rouzier, Rapid emergence and spread of severe acute respiratory syndrome coronavirus 2 gamma (P. 1) variant in Haiti, Clin. Infect. Dis. 1 (2021) 1–4.

[166] R.M. Coutinho, F.M.D. Marquitti, L.S. Ferreira, M.E. Borges, R.L.P. da Silva, O. Canton, T.P. Portella, S.P. Lyra, C. Franco, M.M. Plucinski, Model-based Estimation of Transmissibility and Reinfection of SARS-CoV-2 P. 1 Variant, MedRxiv, 2021.

[167] M.S. da Silva, M. Demoliner, A.W. Hansen, J.S. Gularte, F. Silveira, F.H. Heldt, M. Filippi, F.P. da Silva, L. Mallmann, P. Fink, Early Detection of SARS-CoV-2 P. 1 Variant in Southern Brazil and Reinfection of the Same Patient by P. 2, 2021.

[168] J. Sallas, G.A. Elidio, D.B. Rohlfs, A.C. de Medeiros, D.B. Guilhem, A vigilância genômica do SARS-CoV-2 no brasil na resposta à pandemia da COVID-19, Rev. Panam. Salud Publica 45 (2021), e75.

[169] D.M. Altmann, R.J. Boyton, R. Beale, Immunity to SARS-CoV-2 variants of concern, Science (80-.) 371 (2021) 1103–1104.

[170] T. Fujino, H. Nomoto, S. Kutsuna, M. Ujiie, T. Suzuki, R. Sato, T. Fujimoto, M. Kuroda, T. Wakita, N. Ohmagari, Novel SARS-CoV-2 variant in travelers from Brazil to Japan, Emerg. Infect. Dis. 27 (2021) 1243.

[171] C.K.V. Nonaka, M.M. Franco, T. Gräf, C.A. de Lorenzo Barcia, R.N. de Ávila Mendonça, K.A.F. De Sousa, L.M.C. Neiva, V. Fosenca, A.V.A. Mendes, R.S. De Aguiar, Genomic evidence of SARS-CoV-2 reinfection involving E484K spike mutation, Brazil, Emerg. Infect. Dis. 27 (2021) 1522.

[172] M.J. Firestone, A.J. Lorentz, S. Meyer, X. Wang, K. Como-Sabetti, S. Vetter, K. Smith, S. Holzbauer, A. Beaudoin, J. Garfin, First identified cases of SARS-CoV-2 variant P. 1 in the United States—Minnesota, January 2021, Morb. Mortal. Wkly Rep. 70 (2021) 346.

[173] N. Suryadevara, S. Shrihari, P. Gilchuk, L.A. VanBlargan, E. Binshtein, S.J. Zost, R.S. Nargi, R.E. Sutton, E.S. Winkler, E.C. Chen, M.E. Fouch, E. Davidson, B. J. Doranz, R.E. Chen, P.Y. Shi, R.H. Carnahan, L.B. Thackray, M.S. Diamond, J. E. Crowe, Neutralizing and protective human monoclonal antibodies recognizing the N-terminal domain of the SARS-CoV-2 spike protein, Cell 184 (2021) 2316–2331, https://doi.org/10.1016/J.CELL.2021.03.029, e15.

[174] SARS-CoV-2 reinfection by the new Variant of Concern (VOC) P.1 in Amazonas, Brazil - SARS-CoV-2 coronavirus / nCoV-2019 Genomic Epidemiology - Virological, (n.d.). https://virological.org/t/sars-cov-2-reinfection-by-the-new-variant-of-concern-voc-p-1-in-amazonas-brazil/596 (accessed December 8, 2021).

[175] M. Letko, A. Marzi, V. Munster, Functional assessment of cell entry and receptor usage for SARS-CoV-2 and other lineage B betacoronaviruses, Nat. Microbiol. 54 (5) (2020) 562–569, https://doi.org/10.1038/s41564-020-0688-y, 2020.

[176] A.A. Moona, S. Daria, M. Asaduzzaman, M.R. Islam, Bangladesh reported delta variant of coronavirus among its citizen: actionable items to tackle the potential massive third wave, Infect. Prev. Pract. 3 (2021), 100159, https://doi.org/10.1016/j.infpip.2021.100159.

[177] A. O'Dowd, Covid-19: cases of delta variant rise by 79%, but rate of growth slows, BMJ (2021), https://doi.org/10.1136/bmj.n1596 n1596-n1596.

[178] A. Vaughan, Delta to dominate world, New Sci. 250 (2021) 9, https://doi.org/10.1016/S0262-4079(21)01121-0.

[179] A. Sheikh, J. McMenamin, B. Taylor, C. Robertson, SARS-CoV-2 Delta VOC in Scotland: demographics, risk of hospital admission, and vaccine effectiveness, Lancet 397 (2021) 2461–2462, https://doi.org/10.1016/S0140-6736(21)01358-1.

[180] E. Callaway, The mutation that helps Delta spread like wildfire, Nature 596 (2021) 472–473, https://doi.org/10.1038/d41586-021-02275-2.

[181] J. Khateeb, Y. Li, H. Zhang, Emerging SARS-CoV-2 variants of concern and potential intervention approaches, Crit. Care 25 (2021) 1–8.

[182] S.R. Kannan, A.N. Spratt, A.R. Cohen, S.H. Naqvi, H.S. Chand, T.P. Quinn, C. L. Lorson, S.N. Byrareddy, K. Singh, Evolutionary analysis of the Delta and Delta plus variants of the SARS-CoV-2 viruses, J. Autoimmun. 124 (2021), 102715, https://doi.org/10.1016/j.jaut.2021.102715.

[183] F.K.Majid Monajjemi Fatemeh Mollaamin, Delta variant of Covid-19 study, and why it is a concern: an overview, Biointerface Res. Appl. Chem. 12 (2021) 14, https://doi.org/10.33263/BRIAC125.57975810.

[184] R.B. Malabadi, K.P. Kolkar, N.T. Meti, R.K. Chalannavar, Outbreak of coronavirus (SARS-CoV-2) Delta variant (B.1.617.2) and Delta plus (AY. 1) with fungal infections, mucormycosis: herbal medicine treatment, Int. J. Res. Sci. Innov. 08 (2021) 59–70, https://doi.org/10.51244/IJRSI.2021.8603.

[185] A. Saito, T. Irie, R. Suzuki, T. Maemura, H. Nasser, K. Uriu, Y. Kosugi, K. Shirakawa, K. Sadamasu, I. Kimura, J. Ito, J. Wu, K. Iwatsuki-Horimoto, M. Ito, S. Yamayoshi, S. Ozono, E.P. Butlertanaka, Y.L. Tanaka, R. Shimizu, K. Shimizu, K. Yoshimatsu, R. Kawabata, T. Sakaguchi, K. Tokunaga, I. Yoshida, H. Asakura, M. Nagashima, Y. Kazuma, R. Nomura, Y. Horisawa, K. Yoshimura, A. Takaori-Kondo, M. Imai, T.G. to Phenotype Japan (G2P-Japan) Consortium, S. Nakagawa, T. Ikeda, T. Fukuhara, Y. Kawaoka, K. Sato, SARS-CoV-2 Spike P681R Mutation, a Hallmark of the Delta Variant, Enhances Viral Fusogenicity and Pathogenicity, BioRxiv, 2021, https://doi.org/10.1101/2021.06.17.448820.

[186] X. Chi, R. Yan, J. Zhang, G. Zhang, Y. Zhang, M. Hao, Z. Zhang, P. Fan, Y. Dong, Y. Yang, Z. Chen, Y. Guo, J. Zhang, Y. Li, X. Song, Y. Chen, L. Xia, L. Fu, L. Hou, J. Xu, C. Yu, J. Li, Q. Zhou, W. Chen, A neutralizing human antibody binds to the N-terminal domain of the spike protein of SARS-CoV-2, Science 369 (2020) 650, https://doi.org/10.1126/SCIENCE.ABC6952.

[187] G. Cerutti, Y. Guo, T. Zhou, J. Gorman, M. Lee, M. Rapp, E.R. Reddem, J. Yu, F. Bahna, J. Bimela, Y. Huang, P.S. Katsamba, L. Liu, M.S. Nair, R. Rawi, A.S. Olia, P. Wang, B. Zhang, G.Y. Chuang, D.D. Ho, Z. Sheng, P.D. Kwong, L. Shapiro, Potent SARS-CoV-2 neutralizing antibodies directed against spike N-terminal domain target a single supersite, Cell Host Microbe 29 (2021) 819, https://doi.org/10.1016/J.CHOM.2021.03.005.

[188] S. Liu, Q. Zheng, Z. Wang, Potential covalent drugs targeting the main protease of the SARS-CoV-2 coronavirus, Bioinformatics 36 (2020) 3295–3298, https://doi.org/10.1093/bioinformatics/btaa224.

[189] S.M. Lok, An NTD supersite of attack, Cell Host Microbe 29 (2021) 744, https://doi.org/10.1016/J.CHOM.2021.04.010.

[190] M. Yuan, N.C. Wu, X. Zhu, C.-C.D. Lee, R.T.Y. So, H. Lv, C.K.P. Mok, I.A. Wilson, A highly conserved cryptic epitope in the receptor binding domains of SARS-CoV-2 and SARS-CoV, Science 368 (2020) 630–633, https://doi.org/10.1126/science.abb7269.

[191] G. Lu, Y. Hu, Q. Wang, J. Qi, F. Gao, Y. Li, Y. Zhang, W. Zhang, Y. Yuan, J. Bao, B. Zhang, Y. Shi, J. Yan, G.F. Gao, Molecular basis of binding between novel human coronavirus MERS-CoV and its receptor CD26, Nature 500 (2013) 227–231, https://doi.org/10.1038/nature12328.

[192] C.O. Barnes, C.A. Jette, M.E. Abernathy, K.M.A. Dam, S.R. Esswein, H.B. Gristick, A.G. Malyutin, N.G. Sharaf, K.E. Huey-Tubman, Y.E. Lee, D.F. Robbiani, M. C. Nussenzweig, A.P. West, P.J. Bjorkman, SARS-CoV-2 neutralizing antibody structures inform therapeutic strategies, Nat. 5887839 (588) (2020) 682–687, https://doi.org/10.1038/s41586-020-2852-1, 2020.

[193] Y. Liu, J. Liu, B.A. Johnson, H. Xia, Z. Ku, C. Schindewolf, S.G. Widen, Z. An, S. C. Weaver, V.D. Menachery, X. Xie, P.-Y. Shi, Delta Spike P681R Mutation Enhances SARS-CoV-2 Fitness Over Alpha Variant, BioRxiv, 2021, https://doi.org/10.1101/2021.08.12.456173.

[194] J.A. Plante, B.M. Mitchell, K.S. Plante, K. Debbink, S.C. Weaver, V.D. Menachery, The variant gambit: COVID-19's next move, Cell Host Microbe 29 (2021) 508–515, https://doi.org/10.1016/J.CHOM.2021.02.020.

[195] B. Li, A. Deng, K. Li, Y. Hu, Z. Li, Q. Xiong, Z. Liu, Q. Guo, L. Zou, H. Zhang, M. Zhang, F. Ouyang, J. Su, W. Su, J. Xu, H. Lin, J. Sun, J. Peng, H. Jiang, P. Zhou, T. Hu, M. Luo, Y. Zhang, H. Zheng, J. Xiao, T. Liu, R. Che, H. Zeng, Z. Zheng, Y. Huang, J. Yu, L. Yi, J. Wu, J. Chen, H. Zhong, X. Deng, M. Kang, O.G. Pybus, M. Hall, K.A. Lythgoe, Y. Li, J. Yuan, J. He, J. Lu, Viral Infection and Transmission in a Large, Well-traced Outbreak Caused by the SARS-CoV-2 Delta Variant, MedRxiv, 2021, https://doi.org/10.1101/2021.07.07.21260122, 2021.07.07.21260122.

[196] S. Reardon, How the Delta variant achieves its ultrafast spread, Nature (2021), https://doi.org/10.1038/D41586-021-01986-W.

[197] J.M. Musser, P.A. Christensen, R.J. Olsen, S.W. Long, S. Subedi, J.J. Davis, P. Hodjat, D.R. Walley, J.C. Kinskey, J. Gollihar, Delta Variants of SARS-CoV-2 Cause Significantly Increased Vaccine Breakthrough COVID-19 Cases in Houston, Texas, MedRxiv, 2021, https://doi.org/10.1101/2021.07.19.21260808, 2021.07.19.21260808.

[198] K.K. Riemersma, B.E. Grogan, A. Kita-Yarbro, G.E. Jeppson, D.H. O'Connor, T. C. Friedrich, K.M. Grande, Vaccinated and Unvaccinated Individuals Have Similar Viral Loads in Communities With a High Prevalence of the SARS-CoV-2 Delta Variant, MedRxiv, 2021, https://doi.org/10.1101/2021.07.31.21261387, 2021.07.31.21261387.

[199] N. Subbaraman, How do vaccinated people spread Delta? What the science says, Nature 596 (2021) 327–328, https://doi.org/10.1038/D41586-021-02187-1.

[200] Classification of Omicron (B.1.1.529): SARS-CoV-2 variant of concern, (n.d.). https://www.who.int/news/item/26-11-2021-classification-of-omicron-(b.1.1.529)-sars-cov-2-variant-of-concern (accessed December 8, 2021).

[201] E. Callaway, Heavily mutated coronavirus variant puts scientists on alert, Nature (2021), https://doi.org/10.1038/D41586-021-03552-W.

[202] K.R. McCarthy, L.J. Rennick, S. Nambulli, L.R. Robinson-McCarthy, W.G. Bain, G. Haidar, W.Paul Duprex, Recurrent deletions in the SARS-CoV-2 spike glycoprotein drive antibody escape, Science 371 (2021) 1139–1142, https://doi.org/10.1126/SCIENCE.ABF6950.

[203] P.R. Rani, M. Imran, J.V. Lakshmi, B. Jolly, A. Jain, A. Surekha, V. Senthivel, P. Chandrasekhar, M.K. Divakar, D. Srinivasulu, R.C. Bhoyar, P.R. Vanaja, V. Scaria, S. Sivasubbu, Symptomatic reinfection of SARS-CoV-2 with spike protein variant N440K associated with immune escape, J. Med. Virol. 93 (2021) 4163–4165, https://doi.org/10.1002/JMV.26997.

[204] P. Arora, C. Rocha, A. Kempf, I. Nehlmeier, L. Graichen, M.S. Winkler, M. Lier, S. Schulz, H.-M. Jäck, A. Cossmann, M.V. Stankov, G.M.N. Behrens, S. Pöhlmann, M. Hoffmann, The spike protein of SARS-CoV-2 variant a.30 is heavily mutated and evades vaccine-induced antibodies with high efficiency, Cell. Mol. Immunol. 18 (2021) 2673–2675, https://doi.org/10.1038/S41423-021-00779-5.

[205] T.N. Starr, A.J. Greaney, A.S. Dingens, J.D. Bloom, Complete map of SARS-CoV-2 RBD mutations that escape the monoclonal antibody LY-CoV555 and its cocktail with LY-CoV016, Cell Rep. Med. 2 (2021), https://doi.org/10.1016/J.XCRM.2021.100255/ATTACHMENT/E8FBD729-E3F2-4C6C-8D37-4ED237399D59/MMC2.CSV.

[206] L. Zhang, M. Mann, Z.A. Syed, H.M. Reynolds, E. Tian, N.L. Samara, D.C. Zeldin, L.A. Tabak, K.G. Ten Hagen, Furin cleavage of the SARS-CoV-2 spike is modulated by O-glycosylation, Proc. Natl. Acad. Sci. 118 (2021), e2109905118, https://doi.org/10.1073/PNAS.2109905118.

[207] How bad is Omicron? What scientists know so far, (n.d.). https://www.nature.com/articles/d41586-021-03614-z (accessed December 8, 2021).

[208] Omicron-variant border bans ignore the evidence, say scientists, (n.d.). https://www.nature.com/articles/d41586-021-03608-x (accessed December 8, 2021).

[209] A. Waterhouse, M. Bertoni, S. Bienert, G. Studer, G. Tauriello, R. Gumienny, F. T. Heer, T.A.P. De Beer, C. Rempfer, L. Bordoli, R. Lepore, T. Schwede, SWISS-MODEL: homology modelling of protein structures and complexes, Nucleic Acids Res. 46 (2018) W296–W303, https://doi.org/10.1093/NAR/GKY427.

[210] C.J. Williams, J.J. Headd, N.W. Moriarty, M.G. Prisant, L.L. Videau, L.N. Deis, V. Verma, D.A. Keedy, B.J. Hintze, V.B. Chen, S. Jain, S.M. Lewis, W.B. Arendall, J. Snoeyink, P.D. Adams, S.C. Lovell, J.S. Richardson, D.C. Richardson, MolProbity: more and better reference data for improved all-atom structure validation, Protein Sci. 27 (2018) 293–315, https://doi.org/10.1002/PRO.3330.

[211] E. Ramírez-Aportela, J.R. López-Blanco, P. Chacón, FRODOCK 2.0: fast protein–protein docking server, Bioinformatics 32 (2016) 2386–2388, https://doi.org/10.1093/BIOINFORMATICS/BTW141 (accessed December 8, 2021).

APÊNDICE J - MOLECULAR INSIGHT ON THE BINDING OF STEVIA GLYCOSIDES TO BOVINE SERUM ALBUMIN

Chemico-Biological Interactions 344 (2021) 109526

Contents lists available at ScienceDirect

Chemico-Biological Interactions

journal homepage: www.elsevier.com/locate/chembioint

Molecular insight on the binding of stevia glycosides to bovine serum albumin

Luciana M. Sergio [a,1], Yandara A. Martins [a,1], Jackson L. Amaral [b], Victor L.B. França [b], Camila F. de Freitas [c], Antônio Medina Neto [d], Noboru Hioka [c], Maria I. Ravanelli [a], Cecília Mareze-Costa [a], Sílvio Claudio da Costa [e], Valder N. Freire [b], Kellen Brunaldi [a,*]

[a] Departamento de Ciências Fisiológicas, Universidade Estadual de Maringá, Maringá, 87020-900, Brazil
[b] Departamento de Física, Universidade Federal Do Ceará, Fortaleza, 60440-900, Brazil
[c] Departamento de Química, Universidade Estadual de Maringá, Maringá, 87020-900, Brazil
[d] Departamento de Física, Universidade Estadual de Maringá, Maringá, 87020-900, Brazil
[e] Departamento de Bioquímica, Universidade Estadual de Maringá, Maringá, 87020-900, Brazil

ARTICLE INFO

Keywords:
Steviol
Rebaudioside A
Steviolbioside
Albumin
Molecular docking analysis
Fluorescence spectroscopy

ABSTRACT

The interaction of the steviol and its glycosides (SG), steviolbioside, and rebaudioside A, with bovine serum albumin (BSA) was studied by absorption and fluorescence spectroscopy techniques alongside molecular docking. The stevia derivatives quenched the fluorescence of BSA by a dynamic quenching mechanism, indicating the interaction between the stevia derivatives and BSA. The binding constant (K_b) of steviol was 100-1000-fold higher than those of SG. The stevia derivative/BSA binding reaction was spontaneous and involved the formation of hydrogen bonds and van der Waals interactions between steviol and steviolbioside with BSA, and water reorganization around the rebaudioside A/BSA complex. Molecular docking pointed out the FA1 and FA9 binding sites of BSA as the probable binding sites of steviol and SG, respectively. In conclusion, steviol enhanced hydrophobicity and small size compared to SG may favor its binding to BSA. As steviol and its glycosides share binding sites on BSA with free fatty acids and drugs, they may be competitively displaced from plasma albumin under various physiological states or disease conditions. These findings are clinically relevant and provide an insight into the pharmacokinetics and pharmacodynamics of the stevia glycosides.

1. Introduction

Steviol glycosides (SG), extracted from the leaves of *Stevia rebaudiana* (Bertoni) Bertoni, have been emerging as safe substitutes to artificial sweeteners and as promising food additives to reduce calories in food and beverages [1]. SG have also shown health-promoting properties with therapeutic potential against chronic diseases, such as hypertension and diabetes [2,3].

SG are *ent*-kaurane-type of diterpenes derived from the steviol aglycone, a diterpenoid carboxylic alcohol built up by a perhydrophenanthrene unit fused with a cyclopentane unit. SG are formed by the linking of sugar chains (glucose, rhamnose or xylose) at the hydroxyl and carboxyl groups in the C-13 and C-19 positions, respectively (Fig. 1) [4].

Typically, stevioside and rebaudioside A are the most abundant SG in the stevia leaves, but more than 30 SG have been described up to date. Rebaudioside A is more employed by the food industry than stevioside due to its sweeter and less bitter taste. Steviolbioside, found in less quantity in the leaves of *S. rebaudiana,* is the main metabolite of rebaudioside A and stevioside [6,7]. It can also be produced by alkaline or enzymatic hydrolysis of stevioside [8,9]. Moreover, steviolbioside is a promising scaffold in the synthesis of novel drugs [10].

When orally administered, SG are poorly absorbed by the upper small intestine. Alternatively, SG are cleaved by colon bacteria, resulting in free steviol which is easily absorbed. In the liver, steviol is converted in steviol glucuronide and excreted in the urine [11,12]. Once in the bloodstream, steviol and likely steviol glucuronide may interact with serum albumins, known by their remarkable capacity to bind an

* Corresponding author. Av. Colombo 5790, Sala 117, Bloco H79, Departamento de Ciências Fisiológicas, Universidade Estadual de Maringá, Maringá, PR, 870020-900, Brazil.
E-mail address: kbrunaldi@uem.br (K. Brunaldi).
[1] Co-authors share the first authorship.

https://doi.org/10.1016/j.cbi.2021.109526
Received 10 February 2021; Received in revised form 9 April 2021; Accepted 16 May 2021
Available online 21 May 2021
0009-2797/© 2021 Elsevier B.V. All rights reserved.

extensive diversity of endogenous ligands and drugs [13].

Binding to plasma proteins represents a key pharmacological parameter since it frequently affects the pharmacokinetics and pharmacodynamics of drugs [13,14]. Even though much is reported about the *in vivo* metabolism of SG and their therapeutic value [11,12,15,16], the interaction of SG with serum albumins is still poorly understood. Zhang et al. (2018) reported the binding of rebaudioside A to bovine serum albumin (BSA), with the compromise of the secondary structure and esterase activity of the protein [17]. Mudgal et al. (2016) proposed the use of BSA to limit the access of rebaudioside A to taste receptors to hinder its bitter aftertaste [18].

Thus, in this present study, spectrofluorometric quenching and absorption spectral experiments along with molecular docking were carried out to evaluate the biophysical interaction of steviol and SG, rebaudioside A and steviolbioside, with BSA. Ultimately, this study will provide further understanding regarding the pharmacokinetics and pharmacodynamics of steviol and its glycosides.

BSA was used as a model of albumin molecule due to its high homology with human serum albumin (HSA) [13]. BSA is arranged in three homologous helical domains I-III, comprising two sub-domains A and B each. The major drug-binding sites of BSA are located in the hydrophobic pockets of sub-domains II-A (Sudlow's site I) and III-A (Sudlow's site II) [5,19]. The intrinsic fluorescence of BSA is mainly due to the tryptophan (Trp) residues 134 and 213 presented in domains I and II, respectively [5,20,21].

2. Materials and methods

2.1. Materials

Steviol, steviolbioside and rebaudioside A with approximately 99.9% purity were obtained from the leaves of a variety of *Stevia rebaudiana* with high content in rebaudioside A (UEM 320 cultivar) [22]. BSA, free of fatty acids (Sigma-Aldrich), was dissolved in an aqueous solution containing 25 mM Hepes at pH 7.4 (Sigma-Aldrich). The concentration of protein was determined spectrophotometrically using a molar absorptivity of 44720 M^{-1} cm^{-1} at 280 nm [23].

2.2. Fluorescence spectroscopy

Fluorescence measurements were obtained with a Varian Cary Eclipse spectrofluorometer (Santa Clara, CA, EUA) equipped with a 1 cm quartz cell and a thermostatic bath. For the steady-state fluorescence quenching studies, BSA was excited (λ_{exc}) at 280 and 295 nm and, emission recorded between 300 and 500 nm. The excitation and emission slit widths were set to 2.5 and 10.0 nm, respectively. Spectra were recorded at 15, 20, 25, 30, 35, 40 and 45 °C. Measurements were performed in triplicate. Fluorescence spectra were obtained at a fixed concentration of BSA (10.0 μM in 2.0 mL of Hepes buffer solution, pH 7.4) titrated with the stevia derivatives (5.0 μl of a stock solution in DMSO). The volume increment given by the addition of stock solutions was negligible and did not affect the measurements. The final molar ratios of the stevia derivatives/BSA complexes were 1:10; 1:2; 1:1; 1.5:1;

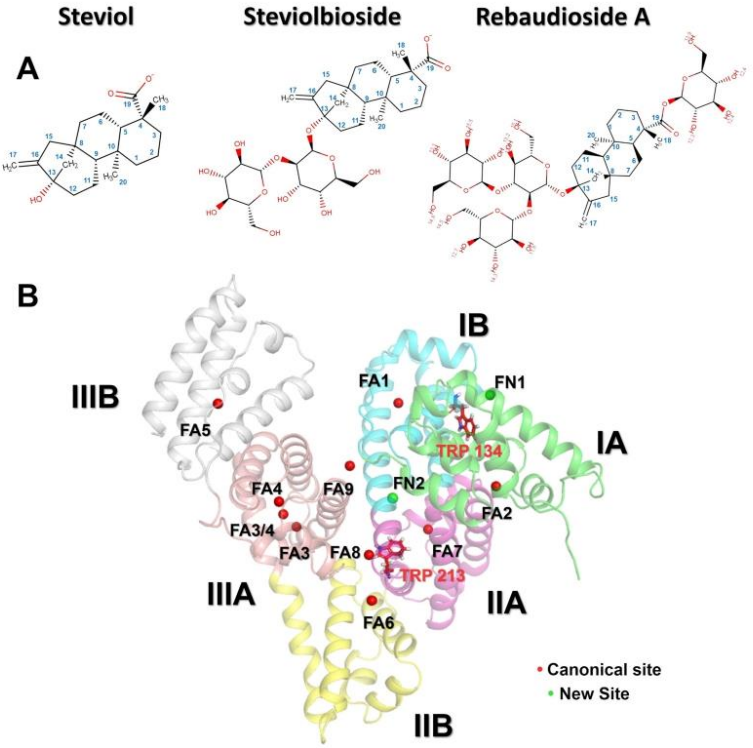

Fig. 1. (A) Molecular structure of steviol, steviolbioside, rebaudioside A. (B) The overall structure of BSA (PDB ID: 4F5S) [5] showing its subdomains, the canonical fatty acid binding sites (FA1-FA9) and the new binding sites (FN1 and FN2; prediction from the blind docking) and the tryptophan (TRP) residues.

2:1; 3:1; 4:1; 5:1 and 6:1 (final concentration of the stevia derivatives of 1, 5, 10, 15, 20, 30, 40, 50 and 60 μM).

2.3. Molecular absorption spectroscopy

Absorption spectra were recorded with a Varian-Cary 60 UV–vis spectrophotometer (Santa Clara, CA, EUA) equipped with a 1.0 cm quartz cell and a thermostatic bath. The range of wavelengths was from 250 to 350 nm. Spectra were obtained at the same experimental conditions used in the fluorescence experiments.

2.4. Molecular docking

The structure information of BSA was obtained from the PDB ID: 4F5S containing X-ray diffraction data with a resolution of 2.47 Å [5]. The molecular structures of steviol, steviolbioside and rebaudioside A were obtained from the National Center for Biotechnology Information, PubChem Database (https://pubchem.ncbi.nlm.nih.gov).

The preparation and the protonation state of the stevia derivatives at physiological pH 7.4 were obtained by using the Marvin Sketch code version 5.5.0.1 (Marvin Beans Suite, ChemAxon) and adjusted with the Discovery Studio package. The protonation state of the protein was adjusted according to data from the PROPKA 3.1 web server tool (http://propka.ki.ku.dk/) and the Protonation tool in the Discovery Studio package.

Molecular docking was performed with Autodock Vina, version 1.1.2 [24]. The Autodock graphical interface (AutoDockTools, version 1.5.6) was used to retain polar hydrogens and to add partial charges to the protein and ligands (Kollman united charges). The receptor BSA and the ligands (the stevia derivatives) were treated as rigid and flexible molecules, respectively. The grid box was defined as a 60 Å × 60 Å x 60 Å cube with the receptors in the center. Exhaustiveness was set up to 15. The twenty conformations of each ligand, top-ranked based on the predicted binding affinity (kcal mol^{-1}), were analyzed using the Discovery Studio package.

2.5. Data analysis

Data were expressed as mean ± standard error (S.E) of three independent measurements. Data fitting was done with OriginLab software (USA).

3. Results and discussion

3.1. Fluorescence quenching of BSA

As illustrated in Fig. 2a,b,c, fluorescence quenching experiments demonstrate the binding of the stevia derivatives to BSA. The fluorescence intensity of BSA (λ_{exc} 280 nm, tryptophan (Trp) and tyrosine (Tyr) are both excited) was gradually reduced with the increasing concentration of the stevia derivatives. No further reduction in fluorescence occurred at molar ratios higher than 1 BSA: 6 stevia derivatives. As expected, the hydrophobic steviol aglycone was more efficient in suppressing BSA fluorescence (40–50%) compared to the hydrophilic SG (10%). The emission spectra of BSA in the presence of steviol were slightly blue shifted (from 3 nm to 8 nm), indicating a likely increase in the hydrophobicity of the immediate microenvironment surrounding Trp residues [25–27].

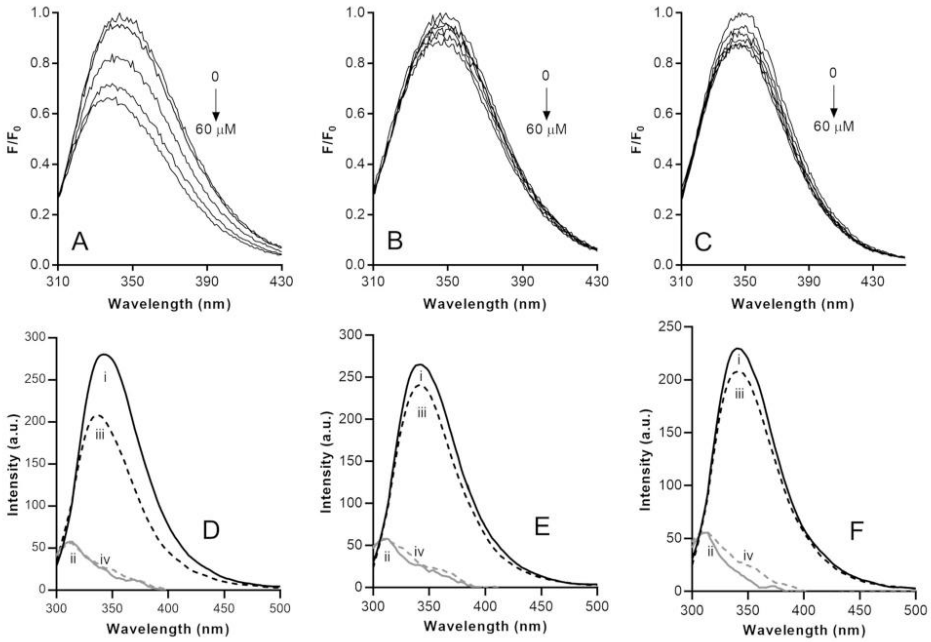

Fig. 2. Fluorescence emission spectra of BSA titrated with steviol (A), steviolbioside (B) and rebaudioside A (C) upon excitation at 280 nm. The contribution of Trp and Tyr to the emission spectra of BSA before and after the addition of steviol (D), steviolbioside (E) and rebaudioside A (D). i: normalized emission spectra of Trp with excitation at 295 nm; ii: emission spectra of Tyr determined by subtracting (i) from that with excitation at 280 nm (not shown); iii and iv: Trp and Tyr spectra in the presence of stevia derivatives, respectively. BSA: 10 μM. Stevia derivatives: 1, 10, 20, 40, and 60 μM (A, B, C); 60 μM (D, E, F). 35 °C. Excitation and emission slits of 2.5 and 10 nm (A, B, C) or 2.5 and 5 nm (C, D, E), respectively.

To differentiate whether the fluorescence quenching (λ_{exc} 280 nm) was related to Trp or Tyr residues, the emission spectra of BSA were deconvoluted using a simple alternative approach described by Bobone, Weert and Stella (2014) (Fig. S1) [28]. As depicted in Fig. 2d,e,f, the binding of the stevia derivatives to BSA produced a reduction only in the Trp emission. Although BSA contains 20 Tyr residues and only two Trp residues (Fig. 1), the intrinsic fluorescence of Trp dominates [20,21].

As observed previously, steviol caused a blue-shift (from 346 nm to 340 nm) only in the Trp emission spectrum (Fig. 2d), probably by increasing the hydrophobicity of the immediate microenvironment around the Trp residues. Fluorescence of Trp is very sensitive to solvent polarity, with fluorescence maximum shifts from about 350 nm in the water down to almost 305 nm in the interior of a hydrophobic protein [25–27]. On the other hand, Tyr emission is much less sensitive to the environment polarity, and its emission maximum is always around 303–305 nm [29].

Fluorescence quenching occurs typically by static or dynamic collisional quenching. These mechanisms are differentiated according to the variation of the quenching constant K_{sv} with temperature. In the static quenching, higher temperatures typically induce the formation of nonfluorescent ground-state species, resulting in a reduction of K_{sv} with a temperature rise. Conversely, in dynamic quenching, the collision between quencher and fluorophore elicits the K_{sv} increase with temperature rise [25].

Therefore, to elucidate the mechanism of fluorescence quenching, the steady-state fluorescence data were analyzed using the modified Stern–Volmer equation $F_0/(F_0–F) = 1/f_a + 1/K_a f_a[Q]$, where F_0 is the initial fluorescence intensity, F is the fluorescence intensity in the presence of the quencher, f_a is the fraction of the initial fluorescence accessible to the quencher, K_a is the Stern-Volmer quenching constant for the accessible fraction of fluorophores, and [Q] is the concentration of quencher.

As displayed in Fig. 3a, modified Stern-Volmer plots within the investigated concentration exhibited a good linear relationship. The intercept and the slope of the plots yield $1/f_a$ and $1/(f_a K_a)$, respectively. The K_a and f_a values of the BSA/stevia derivative systems as a function of temperature are presented in Table 1. K_a values for all BSA/stevia derivative systems were positively correlated with the increasing temperature, which implied that the probable quenching mechanism of stevia derivative/BSA binding reaction is by dynamic collision rather than by a static quenching process.

F_a values (<1) pointed out the partial accessibility of Trp residues for the stevia derivatives. Trp-134 is located in the sub-domain IB (FA1 binding site) and is more exposed to the external hydrophilic environment, whereas Trp-213 is buried in the hydrophobic pocket of domain II [20,21,25,30]. As expected, f_a values calculated for steviol were higher than those of the SG. Steviol enhanced hydrophobicity and small size compared to SG may favor its access into the BSA structure. Additionally, f_a values of steviol and steviolbioside were negatively correlated with temperature, indicating a reduction in the binding affinity to BSA.

3.2. Determination of the binding constants and binding sites

When small molecules bind independently to a set of equivalent sites on a protein, the equilibrium between free and bound molecules is given by the equation $\log(F_0– F)/F = \log K_b + n\log[Q]$, where K_b is the apparent binding constant, n is the number of binding sites per BSA molecule, [Q] is the total quencher concentration and, F_0 and F are steady-state fluorescence intensities before and after the addition of the quencher, respectively [31].

As shown in Fig. 3b, the plot of $\log(F_0–F/F)$ *versus* $\log[Q]$ yields a straight line. The interception with the Y-axis and the slope corresponds to $\log K_b$ and n, respectively. Table 2 gives the calculated K_b and n at different temperatures for the stevia derivative/BSA systems. As expected, K_b of the steviol/BSA complex was 10 to 100-fold higher than those for SG. Steviolbioside (2 glucosyl residues) presented a slightly higher affinity for BSA than rebaudioside A (4 glucosyl residues) at 25 °C. However, this relationship was inverted at 40 °C since the binding of rebaudioside A to BSA was favored by temperature.

K_b of the steviol and steviolbioside/BSA complexes increased from 25 to 30–35 °C and then reduced with further rising in temperature. These results can be interpreted as a reflection of the BSA complex stability (the higher K_b, the more stable are the complexes with BSA). Conversely, binding of rebaudioside A to BSA was clearly favored by temperature as indicated by the increase in K_b with temperature.

The number of binding sites between BSA and steviol (n) was approximately 1, pointing out the presence of just a single binding site in the BSA molecule for steviol. However, it cannot be ruled out the interaction of steviol with multiple binding sites of BSA when considering that the maximum fluorescence quenching was achieved with the molar ratio of 1 BSA: 6 steviol (Fig. 2). For the SG, the number of binding sites was lower than 1, indicating the presence of free uncomplexed BSA molecules.

Altogether, these data suggest a higher binding affinity of steviol towards BSA compared to the SG. However, binding interactions of the SG and even steviol can be considered weaker when compared to some

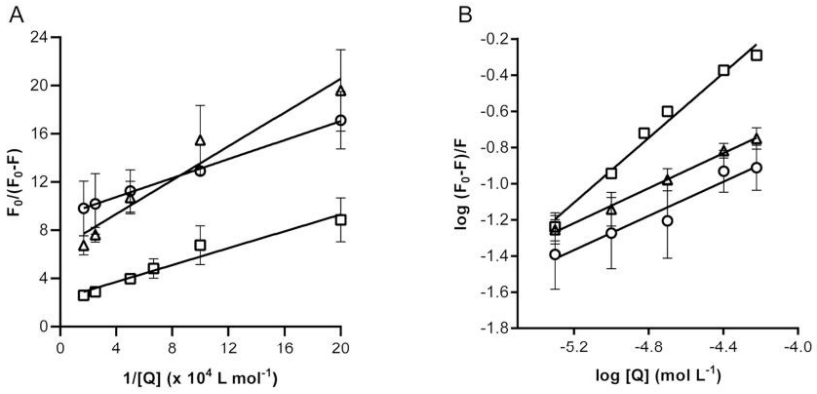

Fig. 3. Modified Stern-Volmer plots for the quenching of BSA by steviol (□), steviolbioside (O), and rebaudioside A (△). (A). Plot of $\log(F_0–F/F)$ as a function of log [quencher] (B). BSA: 10 μM. 40 °C. Data are presented as mean ± SE.

Table 1
Stern-Volmer quenching constant for the accessible fraction (K_a) and the fraction of the initial fluorescence that is accessible to the stevia derivatives (f_a).

	Steviol			Steviolbioside			Rebaudioside A		
T °C	$K_a \times 10^3$ (L mol^{-1})	f_a	R^2	$K_a \times 10^3$ (L mol^{-1})	f_a	R^2	$K_a \times 10^3$ (L mol^{-1})	f_a	R^2
25	10.85 ±0.64	0.96	0.99	7.70 ±1.30	0.30	0.97	51.20 ±6.32	0.07	0.97
30	13.93 ±0.19	0.71	0.99	24.26 ±4.04	0.14	0.92	–	–	–
35	14.53 ±0.29	0.76	0.99	50.73 ±15.25	0.12	0.92			
40	66.29 ±7.16	0.43	0.95	233.99 ±5.52	0.11	0.99	49.38 ±1.98	0.19	0.99
45	43.56 ±0.52	0.43	0.99	–	–	–	93.27 ±12.95	0.15	0.95

Data are presented as mean ± SE of three independent experiments. R^2 is the correlation coefficient.

Table 2
Binding constant (K_b) and number of binding sites (n) of the stevia derivatives/BSA complexes at different temperatures.

	Steviol			Steviolbioside			Rebaudioside A		
T °C	$K_b \times 10^3$ (L mol^{-1})	n	R^2	K_b (L mol^{-1})	n	R^2	K_b (L mol^{-1})	n	R^2
25	4.51 ±0.33	0.93	0.99	144.54 ±16.37	0.77	0.99	8.75 ±1.53	0.50	0.99
30	9.53 ±0.76	1.01	0.98	356.45 ±75.42	0.84	0.96	–	–	–
35	9.44 ±0.92	1.00	0.98	26.79 ±8.87	0.56	0.94	–	–	–
40	3.56 ±0.29	0.90	0.98	12.25 ±3.38	0.47	0.95	19.68 ± 1.29	0.48	0.99
45	0.33 ±0.02	0.70	0.98	–	–	–	37.50 ± 4.74	0.52	0.97

Data are presented as mean ± SE of three independent experiments. R^2 is the correlation coefficient.

common serum albumin ligands [13,32,33]. Additionally, the SG probably presents poor bioavailability as a consequence of their conversion into steviol by colon bacteria and weak binding to BSA [11,12].

3.3. Determination of the thermodynamic parameters

The interaction forces between drugs and biomolecules may include electrostatic interaction, hydrogen bond, van der Waals interaction and hydrophobic interaction. The thermodynamic parameters of a binding reaction are considered evidence of the binding mode interaction [34]. If the enthalpy change (ΔH) does not vary significantly in the temperature range studied, both the ΔH and entropy change (ΔS) are obtained from the van't Hoff equation $\ln K_b = -1(\Delta H/RT) + (\Delta S/R)$, where K_b is analogous to the associative binding constants at the corresponding temperature and R is the gas constant [34,35].

The van't Hoff plots of stevia derivatives/BSA complexes are depicted in Fig. S2 and ΔH, ΔS and ΔG values are presented in Table S1. ΔH and ΔS are obtained as the slope and the ordinate at the origin of the linear relationship between $\ln K_b$ and the reciprocal absolute temperature, respectively. The free energy change (ΔG) is then estimated as $\Delta G = \Delta H - T\Delta S$.

For typical hydrophobic interactions, both ΔH and ΔS values are positive, whereas negative ΔH and ΔS values arise from hydrogen bonding and van der Waals interactions. Conversely, very low positive or negative ΔH and positive ΔS values are characterized by electrostatic interactions between ionic species in an aqueous solution [34]. Accordingly, hydrogen bonding and van der Waals interactions might play a role in the interaction of steviol and steviolbioside with BSA. For both molecules, the negative values of ΔG indicate the spontaneity of complex formation with BSA, an exothermic reaction (ΔH<0) accompanied by a negative ΔS. Under these conditions, the interaction between steviol or steviolbioside with BSA is mainly enthalpy driven. Moreover, the system becomes more organized as steviol and steviolbioside are incorporated in BSA as reflected by the negative ΔS.

The binding reaction between rebaudioside A to BSA was spontaneous (ΔG<0), endothermic (ΔH>0) and entropy-driven (ΔS>0). Therefore, hydrophobic interactions (an interaction that causes hydrophobic moieties to aggregate [36] between rebaudioside A and BSA might be involved, as previously reported [18]. Additionally, positive ΔS may also indicate ionic interactions. However, it seems unlikely since rebaudioside A is neutral at the physiological pH (Fig. S3). However, others have argued a positive value of both ΔH and ΔS usually features the loss of preferential polar interactions, commonly incorrectly attributed to hydrophobic interactions [36–39]. In this manner, the reorganization of water molecules around the rebaudioside A (no longer interaction of glycosyl residues with water) and BSA may explain the positive ΔS. It would compensate for the unfavorable endothermic enthalpy and enable the formation of the rebaudioside A/BSA complex.

3.4. Molecular absorption spectral studies

The absorption spectra of BSA presented a strong and characteristic absorption peak with maximum wavelength at 278 nm due to the aromatic amino acids (mainly Tyr and Trp, with a minor contribution of phenylalanine) (Fig. S4) [25]. The peak intensity slightly increased with the gradual addition of steviol and steviolbioside, whereas rebaudioside A did not affect the absorption spectra of BSA. These data corroborate the fluorescence quenching results, indicating the interaction between steviol and steviolbioside with BSA.

3.5. Molecular docking analysis

Molecular docking was used to further elucidate the stevia derivatives/BSA binding interaction (BSA crystal structure from PDB ID:

4F5S) [5]. The pK_a and protonation pattern of stevia derivatives were also taken into account in the docking analysis. Steviol, steviolbioside and rebaudioside A presented 3, 85 and 14 protonation states, respectively. In the experimental pH 7.4 prevailed the ionized form of steviol and steviolbioside (99,84% of the molecules with the carboxyl group ionized) and the neutral form of rebaudioside A (all of the hydroxyl groups protonated) (Fig. S3).

Fig. 4 shows the binding pockets of BSA that present a high affinity for long-chain and medium-chain fatty acids (FA) and the binding sites (FN1 and FN2) predicted by the blind docking [40,41]. Although the FA binding sites were primarily described in HSA, the high similarity between BSA and HSA suggests that the positions and affinities of the FA binding sites are comparable in these two serum albumins [5].

The application of 2D NMR to characterize FA binding to HSA led to

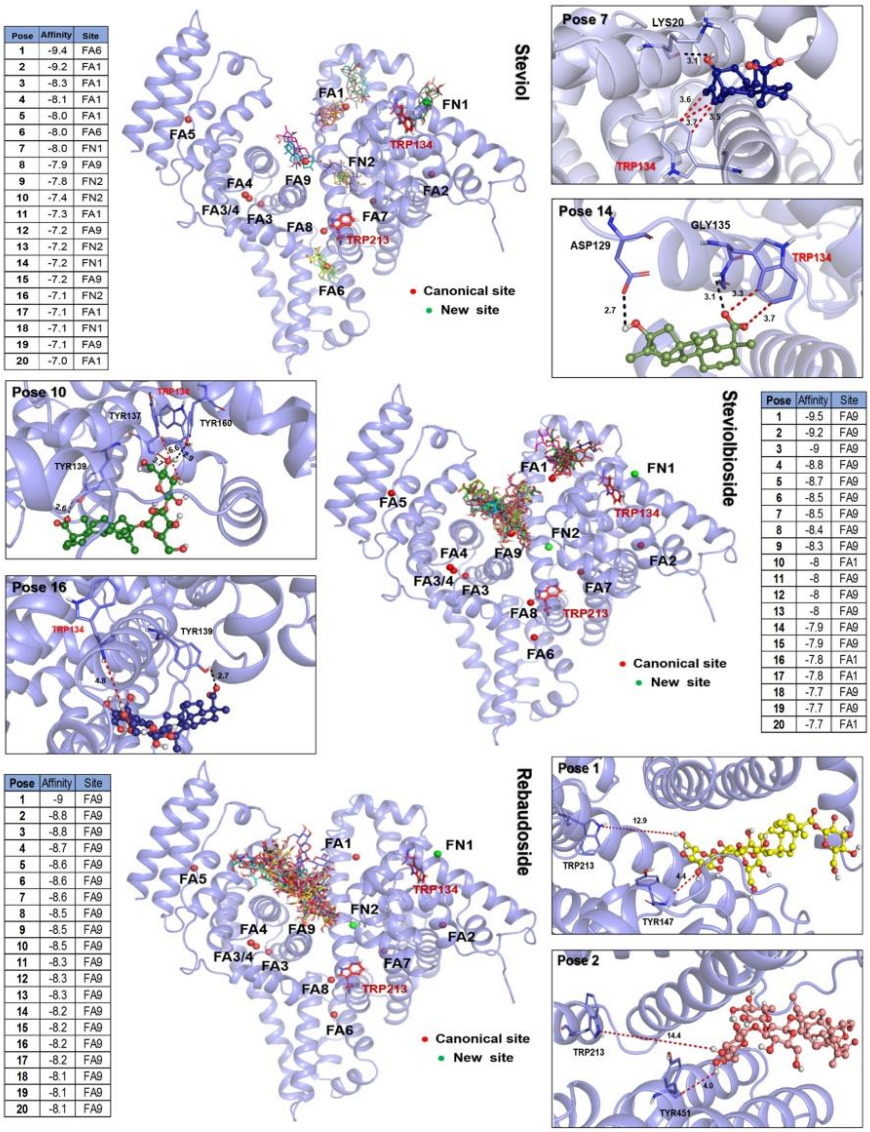

Pose	Affinity	Site
1	-9.4	FA6
2	-9.2	FA1
3	-8.3	FA1
4	-8.1	FA1
5	-8.0	FA1
6	-8.0	FA6
7	-8.0	FN1
8	-7.9	FA9
9	-7.8	FN2
10	-7.4	FN2
11	-7.3	FA1
12	-7.2	FA9
13	-7.2	FN2
14	-7.2	FN1
15	-7.2	FA9
16	-7.1	FN2
17	-7.1	FA1
18	-7.1	FN1
19	-7.1	FA9
20	-7.0	FA1

Pose	Affinity	Site
1	-9.5	FA9
2	-9.2	FA9
3	-9	FA9
4	-8.8	FA9
5	-8.7	FA9
6	-8.5	FA9
7	-8.5	FA9
8	-8.4	FA9
9	-8.3	FA9
10	-8	FA1
11	-8	FA9
12	-8	FA9
13	-8	FA9
14	-7.9	FA9
15	-7.9	FA9
16	-7.8	FA1
17	-7.8	FA1
18	-7.7	FA9
19	-7.7	FA9
20	-7.7	FA1

Pose	Affinity	Site
1	-9	FA9
2	-8.8	FA9
3	-8.8	FA9
4	-8.7	FA9
5	-8.6	FA9
6	-8.6	FA9
7	-8.6	FA9
8	-8.5	FA9
9	-8.5	FA9
10	-8.5	FA9
11	-8.3	FA9
12	-8.3	FA9
13	-8.3	FA9
14	-8.2	FA9
15	-8.2	FA9
16	-8.2	FA9
17	-8.2	FA9
18	-8.1	FA9
19	-8.1	FA9
20	-8.1	FA9

Fig. 4. Molecular docking of the stevia derivatives with BSA. The charts present the binding energy and the site of interaction associated with each predicted conformational pose. The BSA is presented with all of 20 conformational poses bound to its structure. The 3D approximation of the stevia derivative/BSA binding interaction is represented in the rectangles, where the red and black dotted lines represent the distance between the stevia derivatives and the residues Tyr and Trp, and hydrogen-bond interactions, respectively.

the identification of nine structurally distinct sites within the 3 domains of HSA in the solution state [41]; seven of these nine binding sites have since been identified in the crystal structure of HSA [42–44]. The FA binding sites are heterogeneously distributed in the protein structure and present different affinities for FA. Sites FA2, FA4 and FA5 bind FA with high affinity and are generally not impacted by competition binding. FA2 lies at the interface between subdomains IA and IIA while sites FA4 and FA5 are located within domain III. FA1 is a medium affinity binding site and FA3, FA6, FA7, FA8, and FA9 exhibit low affinity for FA [40,41].

As depicted in Fig. 4, molecular docking indicated the binding of steviol to different binding sites of BSA. Site FA1 presented 7 pose conformations for binding interaction followed by FN2 and FA9 (4 poses each), and the FN1 (3 poses). Therefore, the most probable binding site of steviol in BSA is FA1 in the sub-domain IB [5,19]. Site FA1 is relatively open and easily accessible to the solvent. It has been characterized in HSA as a narrow and quite deep hollow formed mainly by hydrophobic residues. Additionally, the ability of site FA1 to extend assists the accommodation of ligands with different sizes [42,45,46]. However, there is a considerable variation in the surface structure and charge distribution between BSA and HSA, particularly in the sub-domain IB [5, 19].

As the molecular docking analysis was carried out with defatted BSA, competitive binding between steviol and FA for the binding sites of BSA cannot be ruled out. Even though site FA1 presents a medium affinity for FA [41], BSA binding to FA would prevail on steviol's (binding constant of FA and steviol in the order of 10^7 [13] and 10^3 M^{-1}, respectively). This observation is even more relevant in states of FA excess such as diabetes or cardiovascular disease [13,47]. Therefore, under physiological conditions, FA may compete with and displace steviol from site FA1. In this scenario, the low-affinity binding sites FA6 and FA9 could have a more important role in the binding interaction between steviol and BSA.

Drug-drug interaction can produce marked changes in the plasma concentration of the active/free drug, thus affecting its pharmacokinetic profile, efficacy and toxicity. Of the three main drug binding sites in HSA (drug site I/FA7, drug site II/FA3 and FA6) [41], molecular docking predicted binding of steviol only to site FA6. This site is located at the interface between subdomains IIA and IIB at the base of the protein between drug site I/FA7 (domain IIA) and drug site II/FA3 (domain IIIA) [42,48]. Site FA6 is the main binding site for NSAID ibuprofen and diffusional, which competitively displace FA from site FA6 in drug-FA competition studies [41].

However, molecular docking results have not excluded a direct or even allosteric interaction of steviol with drug site I/FA7 and drug site II/FA3, as recently reported for testosterone/HSA binding [49]. Testosterone binds to at least 3 known FA binding sites in HSA with conformational changes induced at site FA6 by direct binding to site FA3. Futhermore, the molecular docking analyses were based on the crystalline structures of BSA. Additional and undetected binding sites are unveiled when the protein is in solution and consequently more flexible and accessible to the ligands, as observed in studies of HSA/FA binding using 2D NMR [40,41,49].

As shown in poses 7, 14 and 18 (Fig. 4 and S5), sort-range interactions of steviol with Trp-134 in FN1 binding site (3.3–4.1 Å) accounted for the most of the quenching effect of steviol on the BSA intrinsic fluorescence, or at least for the fraction of the initial fluorescence accessible to steviol. In turn, steviol in site FN2 (pose 9) was 5.0–5.6 Å distant from Trp-213 (Fig. S5). At both binding sites, van der Waals interactions occurred between steviol and the indole double ring of Trp, which presents a great hydrophobic surface area [50]. A more detailed analysis of the pose conformations in sites FN1 and FN2 also revealed that the hydroxyl and carboxyl groups of steviol formed hydrogen bonds and electrostatic interactions with other amino acid residues of BSA. Moreover, in all poses, van der Waals interactions dominated the steviol/BSA binding reaction (Fig. 4, S5 and S6).

As shown in Fig. 4, pose predictions indicated binding of steviolbioside (16 out of 20 conformations) and rebaudioside A (all of 20 conformations) to site FA9, a cleft open to the environment formed between domains IB and IIIA [46]. The bulky polar structure of the SG may prevent them from accessing the binding sites located deeper in the BSA structure. Furthermore, the SG in site FA9 can be in contact with water and BSA (i.e. both ends of the FA9 binding pocket have polar side-chains [46]), which may contribute to the stabilization of the SG/BSA complex.

Molecular docking predicted numerous hydrogen bonds between the glycosyl residues of rebaudioside A and BSA (Figs. S5 and S6). As suggested by thermodynamics data (Table S1), the binding of rebaudioside A to BSA may release water molecules from the interaction with rebaudioside A, contributing to the formation of the rebaudioside A/BSA complex. Additionally, the docking data confirmed the suggestion by Mudgal et al. (2016) that the bitterness-causing hydrophobic aglycone part of rebaudioside A would bind to the hydrophobic cores of BSA [18].

Despite the binding of steviolbioside to site FA1, steviolbioside did not interact with Trp-134 (4.8–8.3 Å distant from each other). Similarly, rebaudioside A in site FA9 was considerable distant from the Trp residues to establish any kind of interaction (Fig. 4 and S5). On the other hand, an extensive network of hydrogen bonds between the glycosyl residues of the SG and BSA was observed. Additionally, the carboxyl group of steviolbioside was involved in hydrogen bonds, and van der Waals interactions were reported between the steviolbioside and rebaudioside A with the amino acid residues of BSA (Fig. 4, S5 and S6).

Though, steviolbioside and rebaudioside A formed hydrogen bonds and van der Waals interactions with the Tyr residues (Fig. 4, S5 and S6) the role of SG/Tyr interaction on fluorescence quenching was ruled out by experimental data (Fig. 2). Therefore, interactions of steviolbioside and rebaudioside A with residues surrounding the Trp residues might have indirectly caused the quenching of BSA fluorescence. In the low-polar protein interior, Trp is much more stable if the polar NH-group of the indole ring interacts with some other polar group (mostly, peptide group) [50]. Accordingly, binding of the SG to BSA might somehow have deprived Trp of polar interactions and consequently perturbed its fluorescent properties.

SG are virtually not absorbed by the gut. Instead, they are cleaved by colon bacteria, resulting in free steviol which is easily absorbed [11,12]. Additionally, SG exhibit a low affinity for BSA (Table 2, binding constant in the order of 10-10^2 M^{-1}) [18]. Therefore, under physiological conditions, the binding of steviol to albumin is more significant than that of SG. However, understanding and characterizing the interaction of SG with BSA have a practical application in the food and beverage industry as BSA hinders the bitter aftertaste of SG and enhances their solubility in water [18] (SG are 100-fold less soluble in water than glucose [51–53].

Altogether, the molecular docking and fluorescence data complemented each other: molecular docking predicted interaction of steviol with Trp-134 and lack of interaction of the SG with any of the Trp residues of BSA, which explained the more pronounced quenching of BSA fluorescence by steviol compared to those of SG.

4. Conclusions

In this study, we have shown that the hydrophobic aglycone steviol and in less extension the more hydrophilic steviol glycosides (SG), steviolbioside and rebaudioside A, are able to bind spontaneously to sites FA1 and FA9 of BSA, respectively. Steviol enhanced hydrophobicity and small size compared to SG may favor its binding to BSA. However, based on the calculated binding constants, the binding of the stevia derivatives to BSA is weaker than common binding interactions of ligands with albumins [13,32,33]. Additionally, as steviol and its glycosides share binding sites on BSA with free fatty acids and drugs, they may be competitively displaced from plasma albumin under various physiological states or disease conditions. Taking together, these findings provide valuable information of clinical relevance on the interaction of

the steviol and SG with plasma albumins, which can contribute to understand the pharmacokinetics and pharmacodynamics of the stevia glycosides.

Credit author contribution statement

Luciana M. Sergio and **Yandara A. Martins** share the first authorship. **Luciana M. Sergio**: Validation, Investigation and Writing – Review & Editing. **Yandara A. Martins**: Validation, Formal Analysis, Investigation and Writing – Review & Editing. **Jackson Amaral**: Methodology, Software, Formal Analysis and Writing – Review & Editing. **Victor L. B. França**: Software, Formal Analysis and Writing – Review & Editing. **Camila F. de Freitas**: Conceptualization, Methodology, Investigation and Formal Analysis. **Antônio Medina Neto**: Conceptualization and Methodology. **Hioka Noboru**: Conceptualization, Methodology and Resources. **Maria I. Ravanelli**: Conceptualization, Resources and Writing – Review & Editing. **Cecília E. M. da Costa**: Conceptualization, Resources and Funding Acquisition. **Sílvio Claudio da Costa**: Conceptualization, Resources and Funding Acquisition. **Valder N. Freire**: Conceptualization, Methodology, Resources, Writing – Review & Editing, Project Administration and Funding Acquisition. **Kellen Brunaldi**: Conceptualization, Methodology, Resources, Writing - Original Draft, Writing – Review & Editing, Supervision, Project Administration and Funding Acquisition.

Declaration of competing interest

The authors declare that they have no known competing financial interests or personal relationships that could have appeared to influence the work reported in this paper.

Acknowledgments

This study was financed in part by the Coordenação de Aperfeiçoamento de Pessoal de Nível Superior - Brasil (CAPES) - Finance Code 001 and by the following Brazilian research agencies Secretaria de Estado da Ciência, Tecnologia e Ensino Superior (SETI, Fundo Paraná - Processo n° 6418/2017) and Conselho Nacional de Desenvolvimento Científico e Tecnológico (CNPq).

Appendix A. Supplementary data

Supplementary data to this article can be found online at https://doi.org/10.1016/j.cbi.2021.109526.

References

[1] A. Romo-Romo, C.A. Aguilar-Salinas, R.A. Gómez-Díaz, G.X. Brito-Córdova, D. V. Gómez-Velasco, M.J. López-Rocha, P. Almeda-Valdés, Non-nutritive sweeteners: evidence on their association with metabolic diseases and potential effects on glucose metabolism and appetite, Rev. Investig. Clin. 69 (2017) 129–138.

[2] V. Gupta, S. Bhasin, W. Guo, R. Singh, R. Miki, P. Chauhan, K. Choong, T. Tchkonia, N.K. Lebrasseur, J.N. Flanagan, J.A. Hamilton, J.C. Viereck, N. S. Narula, J.L. Kirkland, R. Jasuja, Effects of dihydrotestosterone on differentiation and proliferation of human mesenchymal stem cells and preadipocytes, Mol. Cell. Endocrinol. 296 (2008) 32–40, https://doi.org/10.1016/j.mce.2008.08.019.

[3] F. Ahsan, S. Bashir, F. ul H. Shah, Nutritional and medicinal properties of stevia rebaudiana, Curr. Res. Diabetes Obes. J. 13 (2020), https://doi.org/10.19080/CRDOJ.2020.13.555867.

[4] N. Kumari, S. Kumar, Chemistry and analytical techniques for ent-kaurene-glycosides of Stevia rebaudiana Bertoni-A review, J. Appl. Nat. Sci. 9 (2017) 2114–2126.

[5] A. Bujacz, Structures of bovine, equine and leporine serum albumin, Acta Crystallogr. Sect. D Biol. Crystallogr. 68 (2012) 1278–1289, https://doi.org/10.1107/S0907444912027047.

[6] S. Ceunen, J.M.C. Geuns, Steviol glycosides: chemical diversity, metabolism, and function, J. Nat. Prod. 76 (2013) 1201–1228, https://doi.org/10.1021/np400203b.

[7] R. Singla, V. Jaitak, Synthesis of rebaudioside A from stevioside and their interaction model with hTAS2R4 bitter taste receptor, Phytochemistry 125 (2016) 106–111.

[8] V.S.P. Chaturvedula, I. Prakash, Acid and alkaline hydrolysis studies of stevioside and rebaudioside A, J. Appl. Pharmaceut. Sci. 1 (2011) 14.

[9] J. Chen, L. Ding, X.-C. Sui, Y. Xia, T. Lu, H. Wan, T. Lu, Production of a bioactive sweetener steviolbioside via specific hydrolyzing ester linkage of stevioside with a β-galactosidase, Food Chem. 196 (2016) 155–160, https://doi.org/10.1016/j.foodchem.2015.09.035.

[10] M.G. Korochkina, R.R. Sharipova, I.Y. Strobykina, A.D. Lantsova, A.D. Voloshina, N.V. Kulik, V.V. Zobov, V.E. Katnev, V.F. Mironov, Synthesis and antimicrobial and antifungal activity of derivatives of the diterpenoid isosteviol and the glycoside steviolbioside containing onium nitrogen atoms, Pharm. Chem. J. 44 (2011) 597.

[11] E. Koyama, N. Sakai, Y. Ohori, K. Kitazawa, O. Izawa, K. Kakegawa, A. Fujino, M. Ui, Absorption and metabolism of glycosidic sweeteners of stevia mixture and their aglycone, steviol, in rats and humans, Food Chem. Toxicol. 41 (2003) 875–883, https://doi.org/10.1016/S0278-6915(03)00039-5.

[12] E. Koyama, K. Kitazawa, Y. Ohori, O. Izawa, K. Kakegawa, A. Fujino, M. Ui, In vitro metabolism of the glycosidic sweeteners, stevia mixture and enzymatically modified stevia in human intestinal microflora, Food Chem. Toxicol. 41 (2003) 359–374, https://doi.org/10.1016/S0278-6915(02)00235-1.

T. Peters Jr., All about albumin: biochemistry, genetics, and medical applications, third ed., Academic press, San Diego, 1995.

[14] U. Kragh-Hansen, V.T.G. Chuang, M. Otagiri, Practical aspects of the ligand-binding and enzymatic properties of human serum albumin, Biol. Pharm. Bull. 25 (2002) 695–704.

[15] J.M.C. Geuns, P. Augustijns, R. Mols, J.G. Buyse, B. Driessen, Metabolism of stevioside in pigs and intestinal absorption characteristics of stevioside, rebaudioside A and steviol, Food Chem. Toxicol. 41 (2003) 1599–1607, https://doi.org/10.1016/S0278-6915(03)00191-1.

[16] C. Gardana, P. Simonetti, E. Canzi, R. Zanchi, P. Pietta, Metabolism of stevioside and rebaudioside A from Stevia rebaudiana extracts by human microflora, J. Agric. Food Chem. 51 (2003) 6618–6622, https://doi.org/10.1021/jf0303619.

[17] H. Zhang, S. Sun, Y. Wang, Z. Fei, J. Cao, Binding mechanism of five typical sweeteners with bovine serum albumin, Spectrochim. Acta Part A Mol. Biomol. Spectrosc. 205 (2018) 40–47.

[18] S. Mudgal, I. Keresztes, G.W. Feigenson, S.S.H.S.H. Rizvi, Controlling the taste receptor accessible structure of rebaudioside A via binding to bovine serum albumin, Food Chem. 197 (2016) 84–91, https://doi.org/10.1016/j.foodchem.2015.10.064.

[19] K.A. Majorek, P.J. Porebski, A. Dayal, M.D. Zimmerman, K. Jablonska, A. J. Stewart, M. Chruszcz, W. Minor, Structural and immunologic characterization of bovine, horse, and rabbit serum albumins, Mol. Immunol. 52 (2012) 174–182, https://doi.org/10.1016/j.molimm.2012.05.011.

[20] Y. Moriyama, D. Ohta, K. Hachiya, Y. Mitsui, K. Takeda, Fluorescence behavior of tryptophan residues of bovine and human serum albumins in ionic surfactant solutions: a comparative study of the two and one tryptophan (s) of bovine and human albumins, J. Protein Chem. 15 (1996) 265–272, https://doi.org/10.1007/BF01887115.

[21] N. Tayeh, T. Rungassamy, J.R. Albani, Fluorescence spectral resolution of tryptophan residues in bovine and human serum albumins, J. Pharmaceut. Biomed. Anal. 50 (2009) 107–116.

[22] A.S. Dacome, C.C. Da Silva, C.E. Da Costa, J.D. Fontana, J. Adelmann, S.C. Da Costa, Sweet diterpenic glycosides balance of a new cultivar of Stevia rebaudiana (Bert.) Bertoni: isolation and quantitative distribution by chromatographic, spectroscopic, and electrophoretic methods, Process Biochem. 40 (2005) 3587–3594, https://doi.org/10.1016/j.procbio.2005.03.035.

[23] D.C. Carter, J.X. Ho, Structure of serum albumin, in: Adv. Protein Chem, Elsevier, 1994, pp. 153–203.

[24] O. Trott, A.J. Olson, AutoDock Vina, Improving the speed and accuracy of docking with a new scoring function, efficient optimization, and multithreading, J. Comput. Chem. 31 (2010) 455–461.

[25] J.R. Lakowicz, Principles of Fluorescence Spectroscopy Principles of Fluorescence Spectroscopy, 2006, https://doi.org/10.1007/978-0-387-46312-4.

[26] C. Shen, R. Menon, D. Das, N. Bansal, N. Nahar, N. Guduru, S. Jaegle, J. Peckham, Y.K. Reshetnyak, The protein fluorescence and structural toolkit: Database and programs for the analysis of protein fluorescence and structural data, Proteins Struct. Funct. Bioinf. 71 (2008) 1744–1754.

[27] G. Gilardi, G. Mei, N. Rosato, G.W. Canters, A. Finazzi-Agro, Unique environment of Trp48 in Pseudomonas aeruginosa azurin as probed by site-directed mutagenesis and dynamic fluorescence spectroscopy, Biochemistry 33 (1994) 1425–1432.

[28] S. Bobone, M. van de Weert, L. Stella, A reassessment of synchronous fluorescence in the separation of Trp and Tyr contributions in protein emission and in the determination of conformational changes, J. Mol. Struct. 1077 (2014) 68–76.

[29] S.T. Ferreira, L. Stella, E. Gratton, Conformational dynamics of bovine Cu, Zn superoxide dismutase revealed by time-resolved fluorescence spectroscopy of the single tyrosine residue, Biophys. J. 66 (1994) 1185–1196.

[30] M. Punyiczki, A. Rosenberg, The effect of viscosity on the accessibility of the single tryptophan in human serum albumin, Biophys. Chem. 42 (1992) 93–100.

[31] V.D. Suryawanshi, L.S. Walekar, A.H. Gore, P.V. Anbhule, G.B. Kolekar, Spectroscopic analysis on the binding interaction of biologically active pyrimidine derivative with bovine serum albumin, J. Pharm. Anal. 6 (2016) 56–63, https://doi.org/10.1016/j.jpha.2015.07.001.

[32] U. Kragh-Hansen, Structure and ligand binding properties of human serum albumin, Dan. Med. Bull. 37 (1990) 57–84. http://europepmc.org/abstract/MED/2155760.

[33] N.A. Kratochwil, W. Huber, F. Müller, M. Kansy, P.R. Gerber, Predicting plasma protein binding of drugs: a new approach, Biochem. Pharmacol. 64 (2002) 1355–1374, https://doi.org/10.1016/S0006-2952(02)01074-2.

[34] P.D. Ross, S. Subramanian, Thermodynamics of protein association reactions: forces contributing to stability, Biochemistry 20 (1981) 3096–3102, https://doi.org/10.1021/bi00514a017.
[35] M.T.W. Hearn, G. Zhao, Investigations into the thermodynamics of polypeptide interaction with nonpolar ligands, Anal. Chem. 71 (1999) 4874–4885.
[36] E.E. Meyer, K.J. Rosenberg, J. Israelachvili, Recent progress in understanding hydrophobic interactions, Proc. Natl. Acad. Sci. Unit. States Am. 103 (2006) 15739–15746.
[37] P.L. Privalov, S.J. Gill, The hydrophobic effect: a reappraisal, Pure Appl. Chem. 61 (1989) 1097–1104.
[38] K.A.T. Silverstein, A.D.J. Haymet, K.A. Dill, A simple model of water and the hydrophobic effect, J. Am. Chem. Soc. 120 (1998) 3166–3175, https://doi.org/10.1021/ja973029k.
[39] S. Lombardo, S. Eyley, C. Schütz, H. Van Gorp, S. Rosenfeldt, G. Van Den Mooter, W. Thielemans, Thermodynamic study of the interaction of bovine serum albumin and amino acids with cellulose nanocrystals, Langmuir 33 (2017) 5473–5481, https://doi.org/10.1021/acs.langmuir.7b00710.
[40] J.R. Simard, P.A. Zunszain, J.A. Hamilton, S. Curry, Location of high and low affinity fatty acid binding sites on human serum albumin revealed by NMR drug-competition analysis, J. Mol. Biol. 361 (2006) 336–351, https://doi.org/10.1016/j.jmb.2006.06.028.
[41] E.S. Krenzel, Z. Chen, J.A. Hamilton, Correspondence of fatty acid and drug binding sites on human serum albumin: a two-dimensional nuclear magnetic resonance study.(Report), Biochemistry 52 (2013) 1559–1567, https://doi.org/10.1021/bi301458b.
[42] A.A. Bhattacharya, T. Grüne, S. Curry, Crystallographic analysis reveals common modes of binding of medium and long-chain fatty acids to human serum albumin, J. Mol. Biol. 303 (2000) 721–732, https://doi.org/10.1006/jmbi.2000.4158.
[43] J. Ghuman, P.A. Zunszain, I. Petitpas, A.A. Bhattacharya, M. Otagiri, S. Curry, Structural basis of the drug-binding specificity of human serum albumin, J. Mol. Biol. 353 (2005) 38–52, https://doi.org/10.1016/j.jmb.2005.07.075.
[44] S. Curry, H. Mandelkow, P. Brick, N. Franks, Crystal structure of human serum albumin complexed with fatty acid reveals an asymmetric distribution of binding sites, Nat. Struct. Biol. 5 (1998) 827–835, https://doi.org/10.1038/1869.
[45] P. Ascenzi, M. Fasano, Serum heme-albumin: an allosteric protein, IUBMB Life 61 (2009) 1118–1122, https://doi.org/10.1002/iub.263.
[46] P.A. Zunszain, J. Ghuman, A.F. Mcdonagh, S. Curry, Crystallographic analysis of human serum albumin complexed with 4Z,15E-bilirubin-IXα, J. Mol. Biol. 381 (2008) 394–406, https://doi.org/10.1016/j.jmb.2008.06.016.
[47] D.P. Cistola, D.M. Small, Fatty acid distribution in systems modeling the normal and diabetic human circulation. A 13C nuclear magnetic resonance study, J. Clin. Invest. 87 (1991) 1431–1441, https://doi.org/10.1172/JCI115149.
[48] I. Petitpas, T. Grüne, A.A. Bhattacharya, S. Curry, Crystal structures of human serum albumin complexed with monounsaturated and polyunsaturated fatty acids, J. Mol. Biol. 314 (2001) 955–960, https://doi.org/10.1006/jmbi.2000.5208.
[49] A. Jayaraj, H.A. Schwanz, D.J. Spencer, S. Bhasin, J.A. Hamilton, B. Jayaram, A. L. Goldman, M. Krishna, M. Krishnan, A. Shah, Z. Jin, E. Krenzel, S.N. Nair, S. Ramesh, W. Guo, G. Wagner, H. Arthanari, L. Peng, B. Lawney, R. Jasuja, Allosterically coupled multisite binding of testosterone to human serum albumin, Endocrinology 162 (2021), https://doi.org/10.1210/endocr/bqaa199.
[50] E.A. Burstein, N.S. Vedenkina, M.N. Ivkova, Fluorescence and the location of tryptophan residues in protein molecules, Photochem. Photobiol. 18 (1973) 263–279, https://doi.org/10.1111/j.1751-1097.1973.tb06422.x.
[51] C.R. Martins, W.A. Lopes, J.B. de Andrade, Solubilidade das substâncias orgânicas, Quim. Nova 36 (2013) 1248–1255.
[52] A. Kinghorn, in: Stevia: the Genus Stevia, 2002.
[53] M. Carakostas, I. Prakash, A.D. Kinghorn, C.D. Wu, D.D. Soejarto, L. O'Brien Nabors, Alternative Sweeteners, 2012.